Dynamic hypoxic pre-conditioning of cells seeded in tissue-engineered scaffold to improve neovascularisation

Submitted in fulfilment of the degree of
Doctor of Philosophy in Tissue Engineering and Regenerative Medicine

Faculty of Brain Sciences, UCL Ear Institute

Jasmine Onn Yee Ho

MBBS BSc (Hons) MSc (Dist) MRCS (Eng)
MRC Clinical Research Training Fellow and Rosetrees Trust Funded PhD Student

Declaration

I, Jasmine Ho, confirm that the work presented in this thesis is my own. Where information has been derived from other sources, I confirm that this has been indicated in the thesis

Signature:

……..

Table of Contents

Acknowledgements

First and foremost, a huge thank you to my family for supporting me through this process. Without their unwavering encouragement, I would not have been able to carry out the laboratory visits at unsociable hours, the extended trip to Yale for the much-needed collaborative experience and the babysitting time whilst I write this thesis. To my husband, Dom, Mum and Dad, thank you so much, I would certainly not be able to accomplish this without your help with life outside of research. You truly deserve to share every bit of the achievements here. To my boys, Michael and Daniel, thank you so much for being so patient with me, cheering me on and checking in on how many pages I have written in this 'book'. It is all finally done now! I hope you both will feel proud of this accomplishment together as a family.

I would also like to express my gratitude to my research team who has seen me through thick and thin - Martin Birchall, Mark Lowdell, Nazia Mehrban and Raffaelo Sbordoni. I feel we are truly like comrades on this rollercoaster ride of this PhD, especially to you Naz. Thank you for always being there and making things work out for Raff and I. To the past and present lab mates at Mark's PD lab – Carla Carvalho, Toby Proctor, Owen Bain, Maria Rodriguez-Giraldez, Aga Zubiak, Xenia Charalambous, Angela Tait, Ben Weil and anyone who has the fortune of being part of the Royal Free Hospital CCGTT team – your family-like atmosphere, warm friendships and eternal fountain of much-need research wisdom along with the source of much-needed cells, I am so grateful for your time and energy showing me the inside workings of a translational focused lab. I will also never forget the times when some of you (Maria!) had to babysit my kids so I could complete my time-sensitive experiments!

I am also forever grateful to my mentor, research 'muse' and a dear friend, Umber Cheema and her past and present team at Charles Bell House – Rawiya, Judith, Deniz, Auxtine, Anuja, Phil and Alessandro. Thank you all so much for being my surrogate lab team and supporting me through this PhD. Your patience and hospitality during difficult circumstances will never be forgotten. Judith – the molecular PCR queen, mental health advocator and secret 'Elfster' santa, thank you

for being that stable lab figure and helping troubleshoot difficult research problems. Thank you Deniz for your constant encouragement even when you were finding it tough. The little ‘sisterhood’ atmosphere you all had was so refreshing, especially during the doom and gloom of the global pandemic. And to Umber, thanking you just doesn’t seem enough, in fact, no amount of words would do. But for your kindness, encouragement and all the extras without the bells and whistles, and for just being the incredible person that you are – thank you. I hope there will be a way to return this gratitude in the future.

To Alan Dardik and his team at Yale University, thank you so much for having me and making me feel part of the team. In so many ways, you have gone above and beyond to help me achieve my goals. I am so grateful for the last-minute accommodation, the hospitality from you and Susan, and the lifts to the lab just so I could avoid prematurely terminating my experiments. I truly rediscovered my passion for research with your team, which is a big credit to you and your department for creating such a progressive and inclusive atmosphere. I do hope to visit again soon.

To all the other people who have helped me in more ways than one: Krishna Kolluri, for helping me understand how to genetically modify cells and helping me through the transduction process. Prasad Sawadkar, for being incredibly helpful with advising and assisting with the CAM assays and Microfil protocol. Colin Butler, for helping me through the research planning, and for your mentorship and advice when I was struggling with my initial methodology.

I am also very grateful to my funders, the Medical Research Council and Rosetrees Trust, for allowing the following research to take flight through their generous financial support.

Finally, most important of all, to the creator God, the giver of all things good and perfect. Nothing can be achieved or gained without you. This thesis is dedicated to You.

Abbreviations

2D - Two-dimensional
3D - Three-dimensional
A/A - Antimicrobial – Antimycotic
ADM - Acellular Dermal Matrix
aMEM - alpha MEM
ANG - Angiogenin
Ang-1 - Angiopoietin-1
ANOVA - One-way analysis of variance
ASPA - Animals (Scientific Procedures) Act 1986
bFGF – Beta fibroblast growth factor
BLI - Bioluminescent imaging
BME - basement membrane matrix
BSA - Bovine Serum Albumin
CAM – Chorioallantoin membrane
cDNA - Complementary DNA
CCD - charge-coupled device
CO_2 – carbon dioxide
CFU - Colony Forming Unit
CFP - colony-forming potential
CXCL16 - Chemokine (C-X-C motif) ligand 16
CM - Conditioned Media
ddH2O – double-distilled water
DH - Dynamic hypoxia (21-1%)
DFO - deferoxamine
DMEM - Dulbecco's Modified Eagle Medium
DMOG - dimethyloxalylglycine
DMSO - Dimethyl Sulfoxide
DNA - Deoxyribonucleic acid
dsDNA – double stranded DNA
DPPIV - Dipeptidyl peptidase IV
EBM-2 - Endothelial Basal Medium-2
EC – Endothelial cells
ECM - Extra-cellular matrix
EGM-2 - Endothelial Growth Medium-2
EHS - Engelbreth-Holm-Swarm
ELISA - Enzyme-linked immunosorbent assay
EPC - Endothelial progenitor cells
EV – Extracellular vesicles
FACS - Fluorescence-activated cell sorting
FBS - Fetal bovine serum
FGF-7 - Fibroblast growth factor 7
FIH, Factor Inhibiting HIF

FP - filter paper
GM-CSF - granulocyte-macrophage colony-stimulating factor
GMP - Good Manufacturing Practice
H&E - Haematoxylin & Eosin
HBSS - Hank's Balanced Salt Solution
HGF - Hepatocyte growth factor
HIF1a - Hypoxia inducible factor 1 alpha
H3K9me3 - Histone 3 lysine 9 trimethylation
HCl - Hydrochloric acid
HRE - Hypoxia-response element
HUVEC – Human umbilical vein endothelial cell
IACUC - Institutional Animal Care and Use Committee
IGFBP-3 - Insulin-like growth factor binding protein-3
IHC - Immunohistochemistry
IL-8 - Interleukin-8
IPC - Ischemic preconditioning
iPSC - induced pluripotent stem cells
IVIS - In Vivo Imaging System
LCA - *Lens culinaris* agglutinin
LV - Lentiviral
MCP-1 - Monocyte chemoattractant protein-1
MEM - Minimum Essential Medium
mg - milligram
µg - microgram
MHC - Major Histocompatibility Complex
mL - millilitre
mM - millimolar
µM - micromolar
M - Molar
MOI - multiplicity of infection
mRNA – messenger RNA
miRNA – microRNA
MSC - Mesenchymal stem cells
    adMSC - adipose-derived MSC
    bmMSC - bone marrow-derived MSC
    ucMSC - umbilical cord-derived MSC
MSC-EV - Mesenchymal stem cells - extracellular vesicles§
N_2 - Nitrogen
NaCl – Sodium chloride
NaOH - sodium hydroxide
NHS - National Health Service
ng – nanogram
nM – nanomolar
Nrf2 - nuclear factor erythroid 2-related factor 2
NF-κB - Nuclear factor-κB

O_2 - Oxygen
OCR - oxygen consumption rate
OSA - obstructive sleep apnoea
PAI - Photoacoustic imaging
PBS - Phosphate buffer solution
PCR – Polymerase chain reaction
qPCR - Quantitative polymerase chain reaction
PD - Population doubling
PDT - population doubling time
PFA - Paraformaldehyde
PEI - polyethyenimine
PHD - prolyl hydroxylases
POD - post-operative day
PTX3 - Pentraxin 3
RIPC - remote IPC
RBC - Red blood cells
RLU – Relative light units
ROI - Region of interest
ROS - Reactive oxygen species
rpm – Revolutions per minute
RNA - Ribonucleic acid
SD – Standard Deviation; Seeding Density
SDR - Scaffolds for dermal regeneration
SEM – Scanning electron microscopy
SH - Static Hypoxia (1%)
SN - Static Normoxia (21%)
STZ - Streptozotocin
TE – Tissue Engineered
TIMP1 - Tissue inhibitor matrix metalloproteinase 1
TIMP-4 - Tissue Inhibitor of Metalloproteinase 4
TSP-1 - thrombospondin-1
uPA - urokinase-type plasminogen activator
VEGF - Vascular endothelial growth factor
VHL, von Hippel-Lindau
WJ - Wharton's Jelly

List of Figures

List of Tables

Abstract

Introduction: Tissue engineering is the potential solution to the global shortage of tissue and organs. However, the lack of adequate angiogenesis to tissue engineered (TE) scaffolds during the initial stages of implantation has hindered its success *in vivo*. Mesenchymal stem cells (MSC) have the most established track record for translational regenerative therapy and have been widely used in combination with TE scaffolds. Hypoxia is one of the main potentiators for upregulating angiogenic factors in MSC. (1) However, fine-tuning their cellular function and behaviour is still not fully understood. This study aims to help increase the understanding of this process by determining the effects of *in vitro* hypoxic conditioning on enhancement of angiogenesis of MSC for the purpose of pre-clinical translational for TE application.

Methods: The angiogenic potential of 3 different tissue sources (bone marrow, umbilical cord and adipose) MSC were initially determined for downstream pre-clinical application. We established the appropriate regime for *in vitro* dynamic hypoxia conditions in 2D and 3D hydrogel to enhance MSC angiogenic pathway using real-time continuous oxygen sensors and angiogenic cytokine profiling. Cell metabolism and proliferation effects were also evaluated using intravital Realtime-glo, D-luciferin (on transduced MSC) and microscopic Live-Dead stain techniques. We optimised seeding of cells on the TE dermal scaffold (INTEGRA®) for *in vivo* translational purpose and used targeted *in vitro* and *ex vivo* angiogenesis assays, which helped to determine aspects of the MSC conditioned media on endothelial migration, proliferation, morphogenesis and matrix degradation. Finally, the functional reproducibility of the *in vitro* angiogenic response was assessed using *in vivo* angiogenesis CAM assay and murine diabetic wound healing models.

Results: Adipose derived MSC (adMSC) were found to have the most angiogenic potential in response to hypoxic conditioning. Dynamic hypoxia (DH) regime of changing oxygen levels from 21% to 1% when transitioning from T-flask subculture to multiwell plate seeding was most effective at eliciting pro-angiogenic response from adMSC for both *in vitro* 2D and 3D models compared to controls using static normoxia (21% oxygen) and static hypoxia (1%). Low seeding density of adMSC was

found to be the most appropriate to ensure optimised cell adherence and survival post-seeding on TE dermal scaffold (INTEGRA®). It also minimised on localised hypoxic gradient induced oxidative stress by the seeded cells when compared to high seeding density techniques found on non-invasive oxygen monitoring. Conditioned media from DH seeded adMSC was shown to have enhanced angiogenic proteomic profile compared to the controls. *In vitro* angiogenesis assays showed better human endothelial cell migration and morphogenesis in scratch assay and tubular formation assay compared to controls. Preliminary *ex vivo* organ assay results using novel human umbilical arterial rings showed better endothelial out-sprouting and migration through embedded matrix compared to controls. Results from *in vivo* transplantation of adMSC seeded INTEGRA® scaffold showed a mixed response in the CAM assay, highlighting an unaccounted INTEGRA® scaffold effect from the host. Histological sections showed increased vascular and host tissue infiltration into the scaffold. When evaluating the functional angiogenesis in murine wound healing models, although DH adMSC seeded scaffolds showed non-statistically significant increased rate of wound closure, there was significantly greater vessel density within the scaffold on histological evaluation in this group compared to controls.

Conclusion: The results provide a better comprehension of how cells behave in 2D and 3D environments when cultured in dynamically changing oxygen environments. The study addresses important issues, such as the effects of chronic hypoxia on MSC, and how dynamic hypoxia can enhance angiogenic signalling. It also offers a crucial understanding of the *in vitro* oxygen culture environments for future research applications. Further insight into cell-scaffold interaction during *in vivo* transplantation was also established. The importance of having an appropriate *in vivo* model to determine if such *in vitro* angiogenic enhancement would translate to functionally improving neoangiogenesis and subsequent tissue regeneration *in vivo* was also highlighted in this study. Improving and advancing research into optimising and evaluating the *in vitro* environment for clinical application will undoubtedly have a huge impact on the future of cell therapy for regenerative medicine purposes.

Hypothesis & Aims of Thesis

I hypothesis that:

1. Pre-conditioning cells in a dynamic oxygen environment will enhance its pro-angiogenic properties
2. The pre-conditioning of seeded mesenchymal stromal stem cells will promote neovascularisation of a tissue engineered scaffold when implanted in vivo.
3. Enhanced neovascularisation will result in functionally improved neo-tissue regeneration when implanted into a tissue defect *in vivo*.

My aim is to:

i. Determine the exact *in vitro* oxygenation conditions through dynamic pre-conditioning in 2D and 3D settings, which can help further potentiate the angiogenic pathway for therapeutic *in vivo* applications.
ii. Optimise seeding of cells on tissue engineered scaffold for *in vivo* tracking of viability and metabolic activity
iii. Determine if angiogenic response would be reproducible in an *in vivo* model for angiogenesis and functional wound healing

Impact Statement

Tissue engineering and regenerative medicine offer considerable potential for solving many unaddressed or poorly served clinical problems. However, despite decades of use of mesenchymal stem cells (MSC) in pre-clinical research, and in licensed and unlicensed therapies, there remains uncertainty surrounding the mechanisms of their therapeutic effects. This study aimed to optimise *in vitro* MSC culture conditions to explore whether hypoxic preconditioning of seeded cells promotes pro-angiogenic factors accelerating neoangiogenesis *in vivo*. Data and observations from the evaluation of MSC for this purpose helped delineate the hypoxic seeding conditions on my chosen scaffold for optimal cellular viability and enhanced pro-angiogenic factor production. The validation of the dynamic hypoxia protocol was facilitated by the innovative non-invasive application of *in vitro* VisiSen oxygen imaging technology and vigorous cellular and cytokine-based proteomics interrogation. Through studying seeding densities and oxygen levels within the seeding vessel, I ascertained the validity of some of the current translational techniques for therapeutic angiogenic manipulation of MSC. These research outputs are novel as there is little published data on how seeding densities and dynamic changes in oxygen saturations *in vitro* can significantly affect MSC therapeutic potential. Thus, considerable translational knowledge gain has resulted.

Two review articles were published to help raise awareness of cell therapy use for clinical applications in ‘Advances in Wound Care’ journal: ‘Current Advancements and Strategies in Tissue Engineering for Wound Healing: A Comprehensive and Systematic Review’, published in 2017, and ‘Innovations in Stem Cell Therapy for Diabetic Wound Healing’ published in 2022. The unique cross-disciplinary nature of this research also brought together experts from a variety of different scientific backgrounds and take advantage of the latest advances via collaborative projects. A collaboration with the UCL Medical Physics department on their photoacoustic imaging technology for tissue engineering purposes delivered a presentation at the Society of Academic and Research Surgery (SARS) international conference in 2017 and an original research paper titled ‘Monitoring neovascularization and integration of

decellularized human scaffolds using photoacoustic imaging in ‘Photoacoustics’ in 2019.

There was also a conscious effect to keep the research translationally focused. Hence all cellular and tissue-engineered products were chosen based on their potential clinical translational impact. Experimental timelines and protocols were also selected based on the practicalities of potential clinical applications. The trial use of novel non-invasive imaging technology, such as bioluminescence, photoacoustic and hyperspectral imaging for microvasculature and oxygen saturation measurements will help introduce new technologies for better quality *in vivo* data collection. This would aid future validations of these techniques for use in pre-clinical and clinical research.

A potential amalgamation of this research with other ongoing related pre-clinical studies on the use of cell therapy and tissue-engineered scaffold will help facilitate the development of GMP-grade products for clinical use. Thus, this work fills a significant knowledge gap in the translational tissue engineering pipeline, and may accelerate novel therapeutic development with considerable potential health and wealth gain in decades to come.

Presentations and Publications

Presentations:

‘Pre-clinical experience with Integra and wound healing’ Oral Presentation; J Ho (First author and presenter); Integra® SkinDays® West Midlands; Dec 2022

‘Dynamic Oxygen Pre-conditioning of Mesenchymal Stromal Cells to Enhance Therapeutic Angiogenesis for Regenerative Medicine Purposes’ J Ho (First author and presenter), TERMIS 6th World Congress 2021, Maastricht, Netherlands (Virtual Conference); Nov 2021

‘A Cellular Approach to Therapeutic Neovascularisation - Application to Tissue Engineering and Regenerative Medicine’ Keynote Lecture, J Ho (Keynote speaker), 55th Congress of European Society of Surgical Research & 44th Congress of Austrian Society of Surgical Research, Austria; Dec 2020

‘Can We Fine-tune Mesenchymal Stem Cells for Therapeutic Angiogenesis? – Preliminary Study on the use of Hypoxic Pre-conditioned Cells’ J Ho(First author and presenter), U Cheema, M Lowdell, P De Coppi , M Birchall, TCES Conference 2019, Nottingham, UK; June 2019

‘Is hypoxic pre-conditioning of mesenchymal stem cells key to angiogenesis of tissue engineering and regenerative medicine research?’ J Ho(First author and presenter), K Stamati, M Birchall, M Lowdell, P De Coppi, U Cheema, TERMIS World Congress 2018, Kyoto, Japan; Sept 2018

‘In Vivo Monitoring of Vascularisation of Decellularised Scaffolds in Tissue Engineering using Photoacoustic Imaging’ J Ho(First author and presenter), O Ogunlade, T Kalber, R Hynds, E Zhang, S Janes, M Birchall, C Butler, Paul Beard, TERMIS World Congress 2018, Kyoto, Japan; Sept 2018

‘In vivo monitoring of vascularisation in tissue engineering scaffolds using photoacoustic tomography’ J Ho (First author and presenter), O Ogunlande, C Butler, S Janes, M Birchall, P Beard, SARS Annual Meeting 2017, Republic of Ireland; Jan 2017

‘Are hypoxic cells the key to angiogenesis of tissue engineered constructs in regenerative medicine research?’ J Ho (First author and presenter), K Stamati, U Cheema, M Birchall. BAPRAS/RBSPS Summer Scientific Meeting, Bruges, Belgium; Jun 2015

Publications:

‘Innovations in Stem Cell Therapy for Diabetic Wound Healing.’ Ho J, Yue D, Cheema U, Hsia HC, Dardik A. Adv Wound Care. 2022 Feb 17. doi: 10.1089/wound.2021.0104.

‘Monitoring neovascularization and integration of decellularized human scaffolds using photoacoustic imaging.’ Ogunlade O, **Ho JOY** (Joint First Author), Kalber TL, Hynds RE, Zhang E, Janes SM, Birchall MA, Butler CR, Beard P. Photoacoustics. 2019 Jan 8;13:76-84. doi: 10.1016/j.pacs.2019.01.001.

‘**In vivo monitoring of vascularisation of decellularised scaffolds in tissue engineering using photoacoustic tomography**’ J. Ho, O. Ogunlande, C. Butler, S. M. Janes, M. A. Birchall, P. Beard, (2017), SARS abstracts. Br J Surg, 104: 7–57. doi:10.1002/bjs.10531

1 Literature Review

1.1 Introduction

We are currently facing an ageing population with greater burden of chronic diseases. With an increased risk of organ failure or loss as the general population lives longer, this increases the need for organ transplants. With a global crisis around organ shortage. Finding other means to meet the population's growing demands is more critical than ever, as the need for a new inexhaustible source of organs and tissues is becoming more apparent (2).

Regenerative medicine, in particular, tissue engineering (TE) aims to regenerate and replace a tissue or organ that has lost its function. This field of research takes advantage of cells, scaffolds and various bioactive stimuli to the growing organ *in vitro* (3). This rapidly expanding field incorporates a highly multidisciplinary approach and applies the principles of engineering, life sciences and medicine toward the development of biological equivalent substitutes with an aim to restore, maintain, or improve tissue function or a whole organ (4).

With advancements in technology, it is now possible to use tissue regenerative techniques to engineer new organs via the use of biological or synthetically created scaffolds to host the cells which make up the target organ. However, one of the major obstacles for growing new artificial organs is the provision of adequate blood supply to these vital cells during the period of initial implantation into the body (5). Lack of blood supply prevents the implanted organ from fully integrating into the body, leading ultimately to failure of the tissue-engineered structure as a whole. Hence, understanding and improving angiogenesis underpins any future success of tissue engineering of organs for transplant. In addition, diseases related to vascular deficiencies, such as peripheral vascular disease, chronic wounds and myocardial infarction, increases with age. Understanding how to use the latest regenerative techniques, such as cell therapy, to improve angiogenesis in the relevant disease models would also benefit and advance research in those fields.

1.2 Understanding the physiology of angiogenesis

Blood vessel formation occurs through two basic physiological mechanisms: 1) vasculogenesis, a *de novo* formation of blood vessels and 2) angiogenesis, the formation of blood vessels from pre-existing blood vessels.

Vasculogenesis is defined as the process of endothelial cell morphogenesis to form new blood vessels. This *de novo* assembly of vessels are usually confined to embryogenesis (6). However, it can also be replicated in an *in vitro* environment and is used in angiogenesis assays such as the endothelial tubular formation assay described in Chapter 5. Angiogenesis, on the other hand, predominantly involves the *in vivo* development of new capillaries from out-sprouting from pre-existing vessels (7). These can include the complex *in vivo* processes such as sprouting morphogenesis, intussusceptive growth, splitting, remodelling, stabilisation and differentiation into arterioles, venules and capillaries (8). The formation of these new vessels can involved some degree of the vasculogenesis process and build on top of it via the expansion and fine-tuning of the initial, more primitive, embryonic vascular network into a hierarchical network of arterioles, venules and highly branched capillaries to provide efficient blood supply and organ specific vascular functions (8).

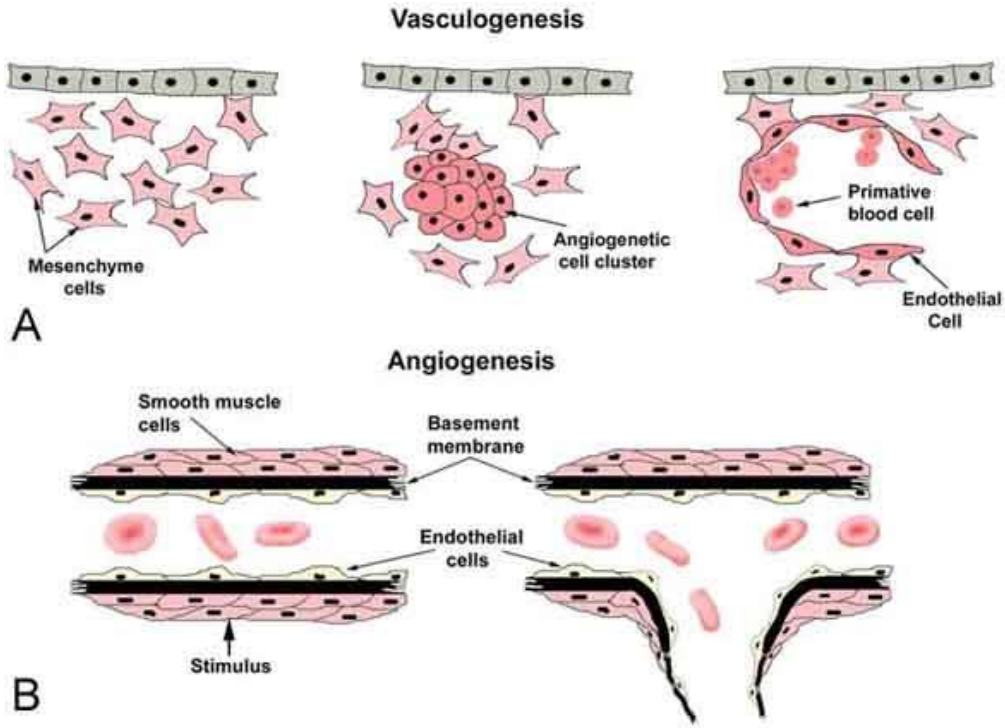

Figure 1-1 Diagram demonstrating the simplified processes involved in (A) vasculogenesis and (B) angiogenesis, from Chinoy 2013 (reproduced with permission from the Creative Commons Attribution 4.0 International License) (9).

Angiogenesis is a process tightly mediated by balance and interplay between pro- and anti-angiogenic factors (7). It also involves a complex cascade of coordinated events (10). This is formed from the recruitment of endothelial cells and endothelial progenitor cells (EPC), alongside supportive mural cells (pericytes and vascular smooth muscle cells) and can occur in both normal and pathological situations. The formed vascular walls are covered by pericytes with a layer of extracellular matrix basement membrane between them (11). This provides stability and support for the newly formed blood vessels. It is not just confined to embryogenesis and can develop postnatally.

The highly dynamic feat is not easily achievable by the use of one single external source for cytokine release. Transplantable cells which secrete the necessary pro-angiogenic growth factors may be the answer to this predicament. They can function as a nature's innate trophic factory, responding spatio-temporally to environmental cues to provide the exact requirements for neoangiogenesis *in vivo*. This is crucial as

development of mature systematic blood vessels requires temporal release of different growth factors at a set chronological sequence as shown in Table 1.1.

As angiogenesis is mainly an *in vivo* process, the process requires observation in a living host. Understanding these definitions are important, as any research involving monitoring of angiogenesis would invariably require an *in vivo* component. The main functional importance of new vascular formation is the provision of oxygen and nutrients to cells and the removal of waste products (12).

1.2.1 Role of bioactive molecules in modulating angiogenesis

Angiogenesis is a highly dynamic process that requires the activation and interaction of several signalling pathways via bioactive molecules in the form of cytokines, chemokines, trophic molecules and growth factors (GF) delivered in a highly coordinated manner. (See Table 1.1) Vascular endothelial growth factor (VEGF) is one of the most crucial cytokines for the initiation of neoangiogenesis. High levels are required to promote EC proliferation and differentiation to form immature vasculature (13). It stimulates ECM degradation required for new vessel sprouting (14). Both VEGF and basic fibroblast growth factor (bFGF) are thought to induce angioblast differentiation in embryogenesis and endothelial progenitor cells differentiation in adults (7,11). It has also been shown that VEGF and bFGF mutually reinforces the angiogenic potential of the other (15).

Whilst VEGF and bFGF are important for the growth phase of vascular development, transforming growth factor beta (TGFβ) 1, platelet-derived growth factor (PDGF)-BB and angiopoietin-1 (Ang-1), with their respective receptors, are essential for the stabilization of the new vessels, as confirmed by both functional knockout of their genes *in vivo* and a number of *in vitro* observations (16). PDGF is responsible for the recruitment of mural cells, such as smooth muscle cells and pericytes (17–19). TGFβ1 has been shown to be important for the production of extracellular matrix, mural cell proliferation, differentiation and recruitment as well as the interaction between ECs and mural cells (7,20). Ang-1 is involved in further remodelling and

maturation of the initial immature vasculature and also plays a role in the maintenance of the quiescence and stability of the mature vessel (13). VEGF and TGFβ1 have been shown to promote EC activation and morphogenesis and EC differentiation and stabilising respectively (see Figure 1-2) (21). Angiostatin and endostatin play a role in preventing hypervascularisation, which produces a large amount of highly irregular, fragile and leaky vessels, such as those seen in tumours (22,23). Table 1.1 provides a summary of the stages of angiogenesis and their corresponding responsible cytokine for reference, and Figure 1-2 offers an overview of the cellular response to angiogenesis and the biomolecules and ECM proteins involved in the process.

Stage of vascularisation	Process	Growth factor	Ref.
Vessel growth	Initial differentiation, proliferation and recruitment of EC to form endothelial tubes	High concentration of VEGF bFGF	(7,11,13,14)
Vessel maturation	Slowing of proliferation and recruitment of pericytes and smooth muscle	TGFß1	(7,16,20)
	Stability and maturation	Ang-1 PDGF-BB	(13,16) (16,17)
Prevention of hypervascularisation	Suppression of EC growth	Angiostatin Endostatin	(22,23)

Table 1.1 Chronicity of normal vascular development with a simplified summary of associated growth factor involved. Adapted from author's own MSc thesis (2015).

Due to the importance of determining the influence of cytokines in these crucial stages of the angiogenesis process, their protein expression levels will be taken into account in this study. The intricate interplay between paracrine and cellular response will be discussed further in the following Section 1.3.

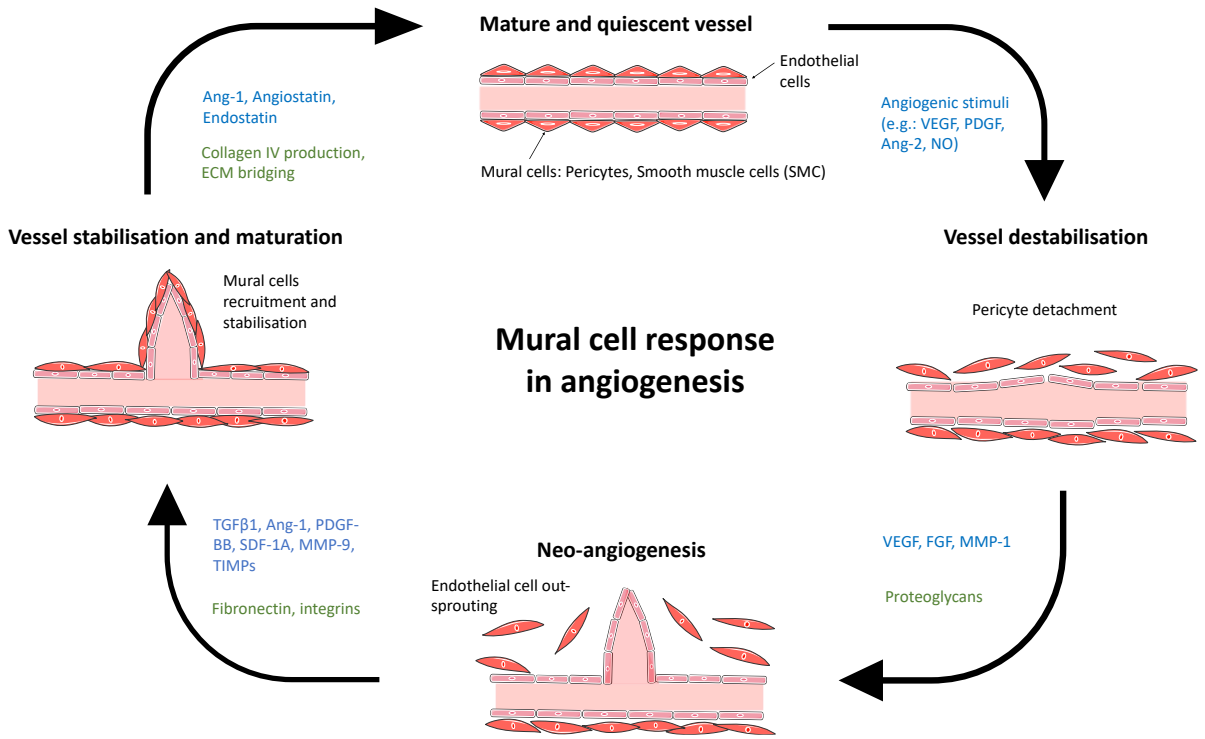

Figure 1-2 Schematic diagram of the role of mural cells in angiogenesis and associated secretome stimuli (text labelled blue) and upregulation of ECM proteins and molecules (text labelled green). Abbreviations: VEGF, vascular endothelial growth factors; PDGF, platelet-derived growth factor; FGF, fibroblast growth factor; Ang, Angiopoietin; NO, nitric oxide; MMP, matrix metalloproteinase; TIMP, tissue inhibitor of metalloproteinase; SDF-1A, stromal cell-derived factor 1A. Adapted from Raza et al (31).

1.2.2 Issues with exogenous cytokines

There are practical issues with the use of exogenous pro-angiogenic growth factors to achieve therapeutic clinical effects. Firstly, there is a high cost when trying to maintain a high level of GF concentration over a length of time to achieve angiogenesis. Secondly, growth factors are known to have a relatively short half-life; VEGF has a half-life of approximately 50 minutes *in vivo* (24). Thirdly, complex pharmacokinetics means that stabilisation of newly formed blood vessels requires long-term release of angiogenic factors in a chronological fashion to ensure blood vessels formed are not dysfunctional and leaky. (see Table 1.1) Researchers have tried to overcome such issues by using newer innovative means by encapsulating therapeutic cytokines into biodegradable scaffolds, which is thought to release factors in a timed, sequential fashion as the scaffold degrades. An early study by Richardson et al. demonstrated this by utilising a new polymer system that allows for the delivery of 2 or more growth factors with distinct kinetics (25). They could

demonstrate that dual delivery of VEGF and PDGF, each with distinct kinetics, results in the rapid formation of a mature vascular network inside polymer scaffolds that had been implanted into the subcutaneous tissue of rats. Despite many other studies which have reported success in this spatial-temporal approach to packaging cytokines and growth factors within scaffolds, biospheres, nanoparticles or bio-printed (26,27), this highly intricate setup is still subjected to high cost and great difficulty in translating to the clinical setting (27,28). Often, the delivery of angiogenic GF by protein or gene therapy can still result in a vasculature that is highly disorganized and leaky (29). A more intuitive means of releasing endogenous GF that is able to sense and respond to the environmental cues of the cells would be more desirable. This thesis will be driven by this notion of harnessing the innate ability of seeded cells to act as a trophic factory for the microenvironment, with the added capability of being able to sense and respond accordingly to the local needs of the cells. This will be discussed in detail in the following sections.

1.3 Role of Cells

Cells play a crucial role in vessel growth, maturation, and stabilisation. It is important to understand and appreciate the physiology of the different cell types and what governs their behaviour in the angiogenic process. This also helps with identifying cell-based strategies and conditions which can further improve and support their role in angiogenesis. Bloods vessels consist of mural cells and EC. Mural cells consist of pericytes, which establish direct cell to cell contact with EC in small diameter blood vessels, such as capillaries and immature vessels, and vascular smooth muscle cells which cover arteries and veins and are separated by a matrix layer from EC (30). Hence, pericytes can be thought to play a more significant role amongst the mural cells in new vessel growth, maturation and stabilisation in neo-angiogenesis processes (31).

The precise angiogenic stimuli which govern the activity of mural cells have been of great interest in tumour angiogenesis and metastasis. The same is true when considering angiogenesis for tissue regeneration and engineering. The conditions that can enhance and promote host EC and mural cells would be beneficial to greater

understanding from further research. In particular, how other cells types and specific paracrine factors could manipulate their behaviour *in vivo* and how to take advantage of these mechanisms to allow for enhanced therapeutic angiogenesis. A summary of the angiogenic process is shown in Figure 1-2 which offers a quick overview on cells, biomolecules and ECM response to new vessel out sprouting. In brief, after an angiogenic stimuli from cytokines such as VEGF, Ang-2 and nitric oxide, a mature and quiescent vessel is destabilised via EC mobilisation and pericyte detachment (32). Further microenvironmental changes include degradation of the basement membrane, vasodilation and an increase in vessel permeability, all of which assist in the recruitment and migration of local and peripheral EC precursors via trophic molecules and local matrix protein, proteoglycans (31). After the initiation of blood flow and the establishment of a basement membrane, the recruitment of mural cells, namely via TGFβ1, PDGF-BB and Ang-1, helps stabilise the new vessels and quiescence is re-established (30). Aside from the cytokine-driven process described above, both EC and their associate mural cells also reside in an extracellular matrix consisting of collagens, laminins, fibronectin, and hydrophilic proteoglycans, amongst other important molecular signals responsible for angiogenesis modulation (33). Hence, modifying the matrix components, as well as fine-tuning the local paracrine signalling to help promote cellular angiogenic response.

Cell-based therapies are emerging as the most promising therapeutic solution for regenerative medical techniques which can be used to treat a plethora of diseases and injuries. Stem cells have gained significant popularity in recent times due to the ability to isolate and grow them successfully from a variety of tissues in the adult body as well as the increasing clinical trial applications. As a result, stem cell therapy has been vigorously studied in organ damage repair and regeneration for numerous diseases.

The recent discovery of induced pluripotent stem cells (iPSC) derived from adult cells has also added to the favourable outlook of stem cell-based research as this would allow for a potentially unlimited bank of autologous stem cells for therapeutic purposes in the future. With the growing number of cell-based products available and the multitude of advanced phase clinical trials and industry pipelines that are in

progress, it is no surprise then that the growing global revenues of cell therapy industry are currently in excess of $1 billion per annum (34,35).

Blood vessels are generally made up of two main cell types: endothelial and mural cells (36). As endothelial cells are known to be highly immunogenic, mural support cells such as mesenchymal stem cells/multipotent stromal cells (MSC) may be a better cellular candidate for therapeutic translational purposes.

Multipotent MSC is of great scientific interest due to their role in the organisation and maintenance of tissue integrity, and involvement in tissue repair and regeneration (37). They have been isolated from many different human tissue sources such as bone marrow, adipose tissue, umbilical cord and other post-natal organs (38). They are capable of self-renewal (37) and have the ability to transdifferentiate into different cell types such as bone, cartilage, adipose, muscle, dermis as well as other connective tissues (39). They are immune evasive in nature as they lack MHC class II molecule (40), hence are attractive from a translational viewpoint. MSC play an important role in supporting haematopoietic stem cells and ensuring normal haematopoiesis function in the body.

MSC have shown vascular regeneration properties *in vitro* and *in vivo*, either by direct differentiation into smooth muscle cells (SMC) and EC, or indirectly via the secretion of paracrine factors which help to recruit endothelial progenitor cells (41,42). MSC are also considered perivascular in nature (43,44), and hence can offer a supportive role to help stabilise newly formed vasculature. From an angiogenic perspective, the ability of MSC to secrete a wide array of pro-angiogenic growth factors renders them an invaluable cell source for therapeutic purposes (see Table 1.2) (45). They have also been indicated as a promising therapy for lymphangiogenesis (46). It comes as no surprise that for therapeutic purposes, MSC are the most extensively translated cell type in translational research, with a total of 1,405 mesenchymal stem cell-based, clinical trials which are currently registered in the US National Institutes of Health (https://clinicaltrials.gov/) as of November 11, 2022 which includes ongoing, withdrawal, complete and unknown status studies (47,48). Figure 1-1 illustrates the extensive array of diseases which have used MSC therapy in clinical trials.

Type of secretome	Active biomolecule	Ref.
Haemopoietic growth factors	SCF, FLT3LG, Thrombopoietin, IL-3, IL-6, GM-CSF, M-CSF	(49–51)
Angiogenic growth factors	HGF, VEGF, Angiopoietin, PDGF, IGF-1, FGF-2, FGF-4, FGF-7	(49,50,52,53)
Trophic molecules	Adiponectin, Adrenomedullin, Osteoprotegerin, MMP10, MMP13, TIMP-1, TIMP-2, TIMP-3, TIMP-4, Leptin, IGFBP-1, IGFBP-2, IGFBP-3, IGFBP-4, BDNF, GDNF, NGF, PIGF	(41,49,50)
Immunomodulatory cytokines	IL-1α, IL-1β, IL-2, TSG-6, OSM, IL-7, IL-10, IL-11, IL-12, IL-13, IL-16γ, IFN-α, LIF, TGF-β, MIF	(49,51,54)
Chemokines	CCL1, CCL2, CCL5, CCL8, CCL11, CCL16, CCL18, CCL22, CCL23, CCL24, CCL26, CXCL1, CXCL2, CXCL3, CXCL5, CXCL6, CXCL8, CXCL11, CXCL12, CXCL13, CX3CL1, XCL1	(49,50,55,56)

Abbreviations: SCF, stem cell factor; FLT3LG, Fms-related tyrosine kinase 3 ligand; IL, interleukin; GM-CSF, granulocyte macrophage colony-stimulating factor; M-CSF, macrophage colony-stimulating factor; HGF, hepatocyte growth factor; VEGF, vascular endothelial growth factors; PDGF, platelet-derived growth factor; IGF, insulin-like growth factor; FGF, fibroblast growth factor; MMP, matrix metalloproteinase; TIMP, tissue inhibitor of metalloproteinase; IGFBP, insulin-like growth factor-binding protein; BDNF, brain-derived neurotrophic factor; GDNF, glial cell-derived neurotrophic factor; NGF, nerve growth factor; PIGF, placenta growth factor; TSG, tumor necrosis factor stimulated gene; OSM, oncostatin; IFN, interferon; TNF, tumor necrosis factor; LIF, leukemia inhibitory factor; TGF, transforming growth factor; MIF, macrophage migration inhibitory factor; CCL, C-C motif chemokine ligand; CXCL, C-X-C motif chemokine ligand; CX3CL, C-X3-C motif chemokine ligand; XCL, X-C motif chemokine ligand

Table 1.2 Secretome produced by mesenchymal stromal stem cells. Reproduced from Nie et al. under the Creative Commons Attribution 4.0 International License (57).

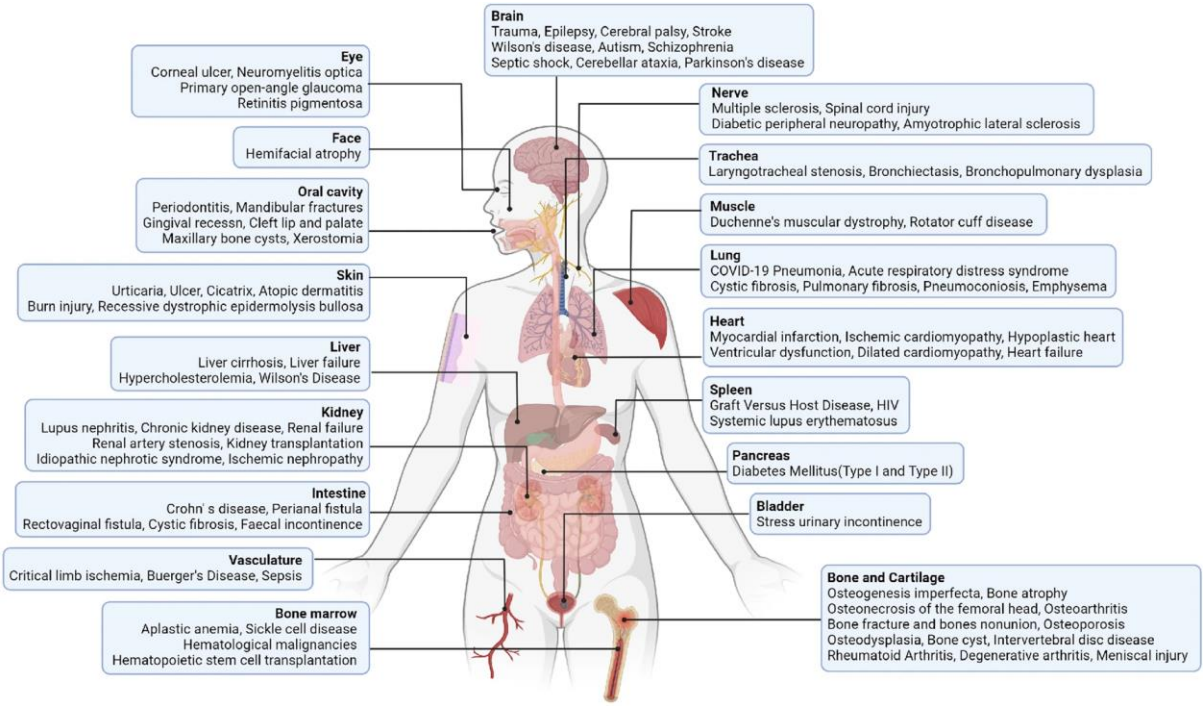

Figure 1-3 This diagram, taken from a recent review article, shows the extensive array of diseases that have completed MSC-based clinical trials (excluding reproductive diseases and ageing). The most widely applied therapy was towards pathologies involving the bone and nervous systems. Reproduced with permission under the Creative Commons Attribution 4.0 International License from a review article by Han et al. (47).

Although the exact mechanism in which mesenchymal stems cells operate as a regenerative source is still not completely understood, it is generally accepted that MSC do not contribute directly to tissue regeneration via differentiation, but instead act as potential trophic mediators, releasing chemotactic, immune-modulatory, and pro-angiogenic factors, which can exploited for therapeutic purposes (41,43,47,58). It is well-researched that under the right conditions, these promoting factors for angiogenesis and cell growth can be harnessed for therapeutic uses (58). Some researchers have showed the possibility of manipulating or ‘pre-activating’ MSC’s paracrine actions via *in vitro* culture methods (59,60).

Unlike delivering a single agent at a specific dose, MSC are sensitive to their microenvironment and can secrete bioactive factors and signals at variable quantities in response to the local microenvironmental cues (58,61). This makes MSC highly advantageous for therapeutic purposes. Hence, under specific pre-activation conditions, their engrafted MSC within TE material can act as a biosensing cellular factory for effective release and regulation of therapeutic growth factors.

1.4 Role of Hypoxia on Cells

Oxygen is a potent biochemical signalling molecule and is one of the major gene-regulator during cellular development (62). It regulates an extensive range of cellular activities critical to the growth of organisms and plays a central role in both normal and pathological physiological states (63). Oxygen exerts significant effects on the cellular processes such as adhesion (64), proliferation (62,65), metabolic activity (66), apoptosis (67), growth factor expression (68), extra-cellular matrix secretion (69,70), and differentiation patterns (66,71,72). Therefore, oxygen availability to cells, particular in the form of hypoxia, can have a major influence on cell behaviour and their biomolecular processes.

Hypoxia is defined as when oxygen tension drop below its normal level in the tissue environment (20–100 mmHg) and has been a long-recognised stimulus for angiogenesis (73). Cellular exposure to hypoxia can be defined as physiological or pathology in nature.

Despite this understanding of the importance of oxygen on cell behaviour and development, cells are still routinely cultured *in vitro* under 'normoxia' conditions of 21% atmospheric O_2 levels. Physiologically, cells are usually not exposed to such high levels of oxygen; cells in our tissues are normally reside between 1 - 14% O_2 as shown in Figure 1-4 (74). The microenvironmental niche of different MSC have been shown to reside in tissues that are physiologically low in oxygen tension. Bone marrow oxygen environments have been shown to vary between 1 - 7% and between 10 - 15% for adipose tissues (75–77). Oxygen tension in umbilical cords has been found to be lower than in the bone marrow, but data is confounded with oxygen measurements at birth, which is not representative of oxygen concentration during gestation (78). Culturing cells in oxygen tension that more closely resembles the native *in vivo* microenvironment can have several positive effects. As early as 1958, studies have described some cells proliferating more rapidly in oxygen tensions that are lower than atmospheric levels (65,79). More recent studies have also shown that culturing cells under lower oxygen tensions increases self-renewal, multipotency,

proliferation rate and potential as well as cell survival (63,80,81). In other words, physiological hypoxia has been shown to have an overall positive effect on cells (82).

However, cells are usually cultured under atmospheric oxygen conditions in the laboratories, subjecting cells to abnormally high oxidative stress compared to their physiological niche. The reasons for this are multiple, largely attributed to traditional cell culture methods and the practical challenges around incubating cells in low oxygen conditions, as well as the lack of awareness of the physiological oxygen environment of the cultured cell, hindering its widespread use. High oxygen culture conditions have been shown to cause early senescence and genetic instability of cells (83).

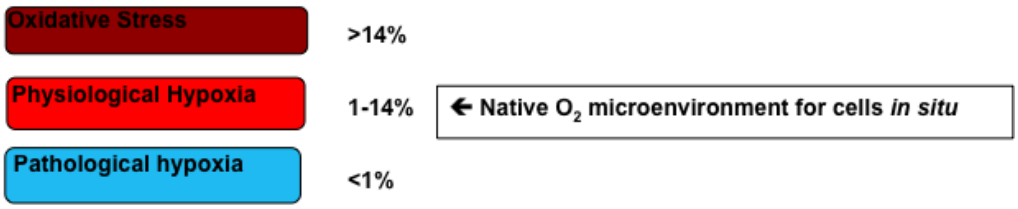

Figure 1-4 Diagram demonstrates values of native oxygen microenvironment of various cells within the mammalian body. Adapted from Stamanti et al. with permission under the journal's 'Gratis Reuse' policy for open access publications, and reproduced from author's own MSc thesis (74).

In a seminal paper by Keeley and Mann in 2018, they set out to define the exact physiological oxygen environments from the cellular to organ level. The paper was a paradigm in the field as it sought to offer valuable insight from macro to microscope variations in oxygen concentration which cell biologists should be aware of. Figure 1-5 (A, B & C) demonstrate crucial changes in the varying oxygen levels within the respiratory and vascular systems (84). This can be very helpful when considering the physiological oxygen tension of the cells of interest during *in vitro* culture and the level of oxygen manipulation which is appropriate for the cell type.

Excess in microvascular shear stress leads to the intraluminal splitting of a vessel into two. However, tissue hypoxia appears to trigger more sprouting angiogenesis of new capillary sprout from a pre-existing vessel (85). However it is unclear the exact paramters of oxygen level which will allow for increased angiogenic factor expression and maintain optimal cell proliferation in order to promote vascular ingrowth via angiogenic cascad (86). If this is understood, then the pre-conditioning of potential

therapeutic cells in hypoxia could be easily translated to pre-transplanting protocol steps for the applications in clinical scenarios such as wound healing (87). Being able to replicate and simulate the physiological oxygen environments within ischaemic tissues, such at sites of wound healing, can help researchers understand in greater depth potential biological response therapeutic MSC would elicit when exposed to harsh conditions at the site of transplant.

With a better appreciation for the cell's physiological niche and advancing technology into cheaper, lower-maintenance hypoxic culture equipment, there will undoubtedly be a greater adoption of hypoxic cell culture from the scientific community. Increasing the knowledge of research around this relatively new and unexploited area of cell engineering can help better engineer culture conditions for desired regenerative and translational clinical applications. More of this will be discussed in the following chapters.

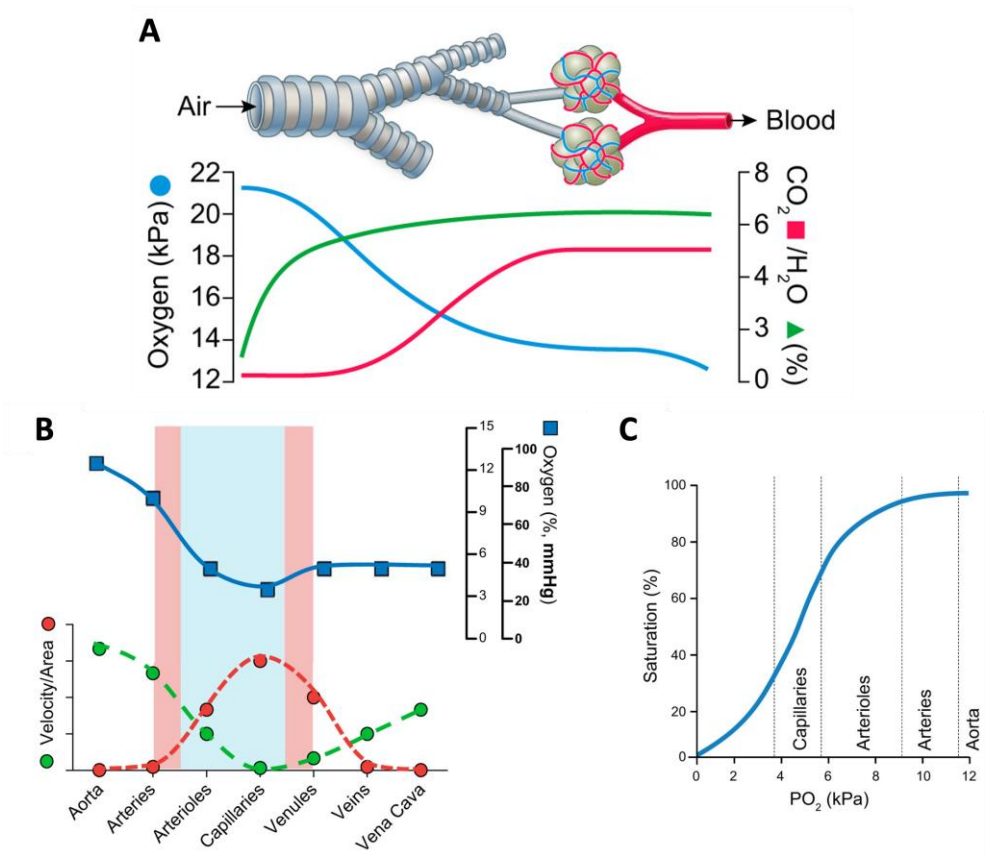

Figure 1-5 Physiological oxygen gradients in the human body. (A) The diagram shows oxygen gradients in the respiratory system. Concentrations, in kPa, of O_2 (●, *left axis*), CO_2 (■, *right axis*), and H_2O (▲, *right axis*) from dry atmosphere to the pulmonary venous circulation are shown. Increases in PH_2O and Pco_2 in the respiratory tract reduce Po_2 proportionally, and venous admixture within the pulmonary vein reduces Po_2 further. (B & C) Diagrams show oxygen gradients in the vascular system. (B) The relationship

between Po_2 (*right axis*), area and velocity throughout the vasculature. Highlighted areas correspond to the vessels in which gaseous (red) and nutrient (blue) exchange would be expected to take place. Velocity and area are arbitrarily by the authors of this figure, and average Po_2 is adapted from Tsai et al. (88). (C) A standard oxyhemoglobin saturation curve, with the average Po_2 values within relevant blood vessels, is annotated as shown. The figures above are reproduced from Keeley and Mann 2019 (84), with permission under the terms and conditions provided by the publisher The American Physiological Society and the Copyright Clearance Center (CCC).

1.4.1 Significance of the HIF1a pathway

Changes in oxygen concentration can act as a physiological stimulus for cells. This can trigger specific intracellular mechanisms to allow cells to adapt to their new microenvironment. Hypoxia can also be deleterious to cells because of hypoxia-mediated, p53-dependent cell death (89). Some cells, such as cancer cells, can thrive under specific oxygen-deprived conditions because of mutations in or a suppressed expression of p53 gene (90). However, hypoxia-inducible factor-1 (HIF-1) expression has been shown to play a greater role in the central cellular adaptive response to hypoxic conditions via the stabilisation of HIF-1α (91).

HIF-1α is considered a master regulator of oxygen homeostasis. HIF-1 an αβ-heterodimer that was first recognized as a DNA-binding factor that mediates hypoxia-inducible activity of the erythropoietin 3′ enhancer (92,93). It soon became clear that it is a key pathway in the mediation of the biological effects of hypoxia. Being a potent oxygen-sensing key transcription factor in the cell, its relative availability is regulated by the presence of oxygen in the local microenvironment. Under normoxia, HIF-1α subunits are hydroxylated by the Fe^{2+}-dependent prolyl hydroxylases (PHD) followed by ubiquitination via binding to von Hippel–Lindau (VHL) tumour suppressor protein, the recognition component of E3 ubiquitin-protein ligases (94). The ubiquitinated HIF-1α is then rapidly degradation by the proteasome (95–97). Under conditions of low oxygen tension (hypoxia or ischemia), PHD activity substantially decreases, enabling HIF-α to accumulate and then translocate into the nucleus to bind to HIF-β (91,98,99). This active HIF-1αβ heterodimer binds to the hypoxic response elements (HRE) and initiates the transcription of target genes (100,101). HIF is thought to control the expression of more than 100 genes downstream and plays a significant role in developmental physiology, health and disease pathogenesis, such as diabetes, cancer, heart disease, inflammation, and immune

function (102–104). These genes are usually involved in the adaptation of the organism to hypoxic conditions, such as metabolic reprogramming (glycolysis, glucose consumption, anaerobic respiration), angiogenesis, cell differentiation, proliferation, survival, and apoptosis (1,91,105–109). One of its most recognised functions is the impact as a key regulator of VEGF gene expression, which plays a pivotal role in angiogenesis (110). Hence, hypoxia can upregulate the expression of different genes which influence the various stages of angiogenesis, such as VEGF, angiopoietin-2, and fibroblast growth factor (1). Lymphangiogenesis can also be initiated by factors released from MSC in hypoxia (132). Table 1.3 summarises the downstream angiogenic transcription targets which are regulated by HIF1.

HIF-1α has been shown to be the main regulator controlling the metabolic fate and multipotency of cells such as MSC (111). In tumour biology, hypoxia has been shown to enhance cancer aggression and progression (89,112–114). In MSC, hypoxia has been shown to enhance neovascularisation capability with positive therapeutic angiogenic effects in a murine hindlimb ischemia model (115). Park et al. demonstrated in MSC that the stabilisation of HIF-1α exerts a selective influence on colony-forming mesenchymal progenitors promoting their self-renewal and proliferation (116). HIF-1α stabilisation in MSC has also been shown to lead to the induction of pluripotent genes (Oct-4 and KLF4) and the inhibition of terminal differentiation into osteogenic and adipogenic lineages (116–118). MSC and other cell types cultured in hypoxic conditions have been shown to increase the expression of anti-apoptotic factors, blocking apoptosis and increasing the survivability of cells in harsh low oxygen tension environments (119,120,106,121,122).

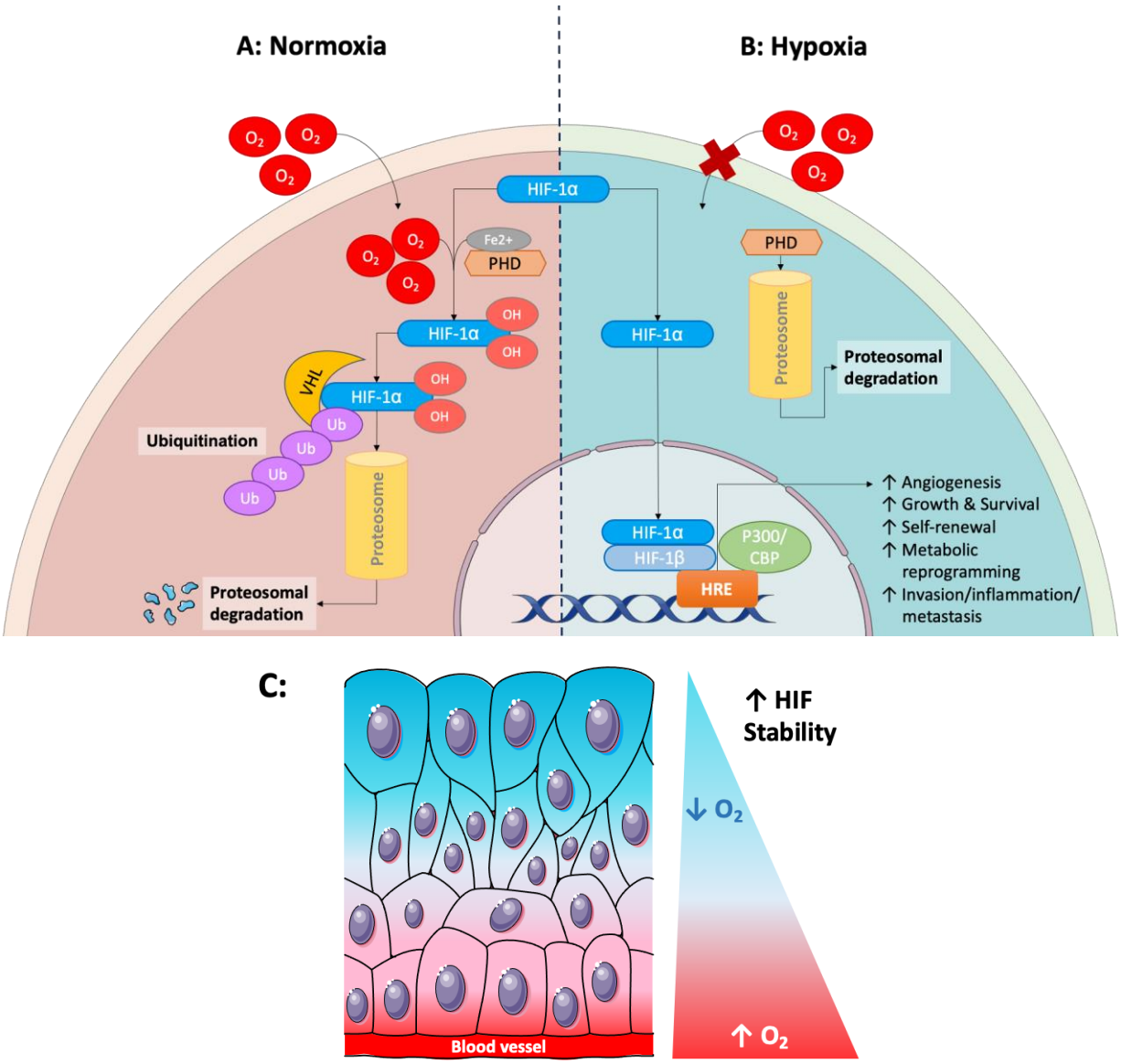

Figure 1-6 HIF-1 α pathways in normoxia and hypoxia. (A) In normoxia, HIF-1α is hydroxylated by prolyl hydroxylases (PHL) in the cytoplasm in an oxygen-dependent manner. It then forms a complex with von Hippel–Lindau (VHL) and other proteins, which is ubiquitinated and subsequently degraded by proteosomes. (B) In hypoxia, the lack of oxygen-dependent hydroxylation and proteasomal degradation of HIF-1α causes it to stabilise and accumulate. It then translocates into the nucleus and forms complexes with HIF-1β as a transcription factor complex that binds to hypoxia response elements (HRE) within the promoter regions of target genes involved in angiogenesis, cell proliferation, growth, and survival, metabolic reprogramming and invasion. Figure adapted from Vito et al. (123). (C) Diagram demonstrating varying oxygen gradient of the local microenvironment around the cells in relation to distance from the nearest blood vessel. HIF stability is increased as oxygen tension decreases with increasing distance from the blood supply.

Direct Transcription downstream effect of HIF1 on HIF	Stimulator (+) or inhibitor (-) of angiogenesis	Ref
VEGF	+	(110,124,125)
Ang-2	+	(126)
NOS	+	(127)
FLT-1 (VEGF-R1)	+	(128,129)
Kdr (VEGF-R2)	+	(130)
Collagen prolyl-4-hydroxylase	+	(131)
MMP	+	(132)
SCF	+	(133)
SDF-1	+	(134)
uPA receptor	+	(135)
PAI-1	+/-	(136,137)
TIMP	+/-	(138–140)
Indirect Transcription Targets of HIF	**Stimulator (+) or inhibitor (-) of angiogenesis**	**Ref**
Ang-1	+	(101)
FGF	+	(141)
PDGF	+	(141,142)
PLGF	+	(101,143,144)
MCP-1	+	(145)
Tie-2	+/-	(146)
Thrombospondin-1	-	(147)

Abbreviations: VEGF, Vascular Endothelial Growth Factors; NOS, Nitrous Oxide Synthases; Ang, Angiopoietin; FLT, Fms-related receptor Tyrosine Kinase 1; Kdr, Kinase Insert Domain Receptor; PLGF, Placenta Growth Factor; PAI-1, Plasminogen Activator Inhibitor-1 ;SCF, Stem Cell Factor; SDF-1, Stromal-Derived growth Factor-1; uPA, Urokinase-type Plasminogen Activator ; TIMP-1, Tissue Inhibitor of Metalloproteinase-1; FGF, fibroblast growth factor; PDGF, Platelet-Derived Growth Factor; MCP-1, Monocyte Chemoattractant Protein-1; Tie-2, TEK tyrosine kinase endothelial-2

Table 1.3 Table of the effect of hypoxia, in relation of HIF, on molecules involved in angiogenesis. Adapted from Pugh & Ratcliffe 2003 (1), with permission under the terms and conditions provided by Springer Nature and Copyright Clearance Center (CCC).

1.4.2 Effects of intermittent hypoxia

In vivo angiogenesis is a process fundamentally regulated by the local oxygen environment surrounding the cells (148). It is widely accepted that hypoxia is one of the main stimuli for the process of angiogenesis (149). However, the chronological stability of HIF-1α in different oxygen environments is still unclear. Under normoxic conditions, HIF-1α has a very short half-life (<5 minutes), rendering it highly unstable as it is rapidly degraded in the presence of oxygen (99,150,151). Hypoxia can help prolonged its half-life, allowing its accumulation and the formation of the complexes within the cell nucleus. (see Figure 1-6B) The rate of degradation and how the hypoxia and variations in oxygen tension can affect this has been the focus of much research (152).

Oxygen levels *in vivo* are normally held in a constant state of flux and change depending on their anatomical location (84,88,153,154). Constant fluctuations lead to cyclical periods of hypoxia and re-oxygenation, a term known as intermittent or cyclical hypoxia (155). These extreme changes in oxygen level are demonstratable in patients with obstructive sleep apnoea (OSA), where transient pauses in breathing causes repetitive episodes of hypoxemia-reoxygenation during the sleep cycle, hence exposing the body to long-term pathological levels of intermittent hypoxia (156). It is interesting to note that these patients are also known to be at an increased risk of developing conditions such as hypertension, atherosclerosis, myocardial infarction, stroke, inflammation and cancer (155–160). Scientists and clinicians have alluded to the fact that cyclic hypoxic conditions can contribute to this via the stabilisation of HIF-1α which can lead to these potential pathological sequels downstream.

Conversely, HIF-1α stabilisation has been positively indicated in therapeutic ischaemic pre-conditioning for cardio and neuroprotection. Therapeutic ischemic preconditioning (IPC) aims to enhance the resistance of tissues to subsequent ischemic injury by inducing brief cycles of transient ischemia either locally or remotely (161). This phenomenon was first described by Murry and colleagues in 1986 (162). They found that exposing the heart to short (5 minutes) bursts of ischemia and

reperfusion *in vivo* via circumflex artery occlusions protects the heart against injury caused by a subsequent prolonged (30 minutes) episode of ischemia-reperfusion (162). Since then, remote IPC (RIPC), as a procedure, has been implemented for translational practice (163–165). RIPC involves subjecting limbs to brief cycles of ischaemic-reperfusion via a pressure cuff in an attempt to increase peripheral circulation of HIF-1α (165,166). Eckle et al. demonstrated that HIF-1α played a significant role in this process via the use of *in vivo* small interfering RNA, which interfered with cardiac HIF-1α expression, resulting in the loss of cardioprotection by IPC in a murine model (167). In a seminal randomised clinical trial published in 2010, the use of RIPC demonstrated an increase in myocardial salvage in patients with myocardial infarction when applied in the ambulance before percutaneous coronary intervention. The use of RIPC appears to have similar benefits in stroke (168–171). Several pre-clinical and clinical studies have reported improved cerebral ischaemic tolerance, reduction in infarct size, improved neurological function and systemic modulation of the inflammatory response, amongst many other positive outcomes (172–176). Similar benefits of ischemic protection have also been reported in other organ types (177,178), rendering the RIPC a highly promising translational intervention for the reduction of organ-related ischaemic injury (179). Figure 1-7 features the other biological pathways involved in RIPC which could be responsible for the cardioprotective nature of the procedure, the details of which would unfortunately go beyond the scope of this thesis. Given the mechanisms are comparable on a macro level, it would not be unreasonable to confer the same therapeutic benefits of IPC towards the pre-conditioning of cells using intermittent/cyclical hypoxia (180,169,166,181).

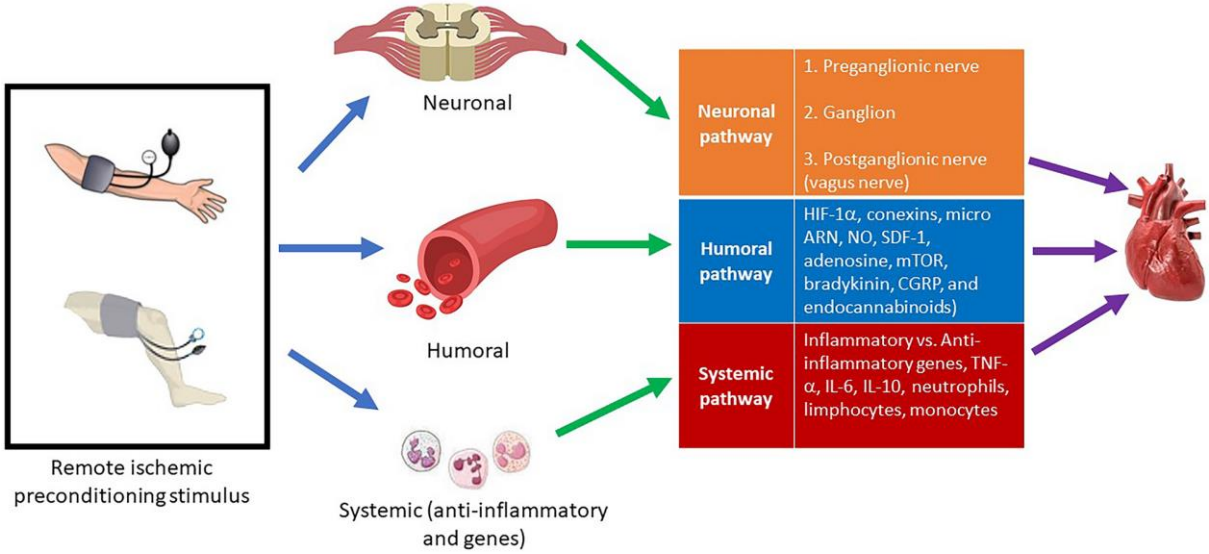

Figure 1-7 Illustration of the possible neuronal, humoral and systemic mechanism behind remote ischaemic preconditioning (RIPC) response which is responsible for *in vivo* cardioprotection. Figure was reproduced from Donato et al. (181) with permission and license under the terms and conditions provided by Springer Nature and Copyright Clearance Center (CCC).

On the cellular scale, research has shown that hypoxic effects on MSC behaviour are likely to be biphasic in nature and are also largely coordinated by HIF-1α (81). Increasing attention has been drawn to understanding cyclical/intermittent changes in hypoxia and their effect on cellular physiology, especially relating to their pro-angiogenic behaviours (182,183). Similar to OSA and IPC, much of this has been linked to the stabilisation of HIF-1α (184,185). These effects are summarised in Figure 1-8. The terms ‘cyclical’ and ‘intermittent’ hypoxia has been used interchangeably in published literature. It has been shown that chronological variation of levels of oxygen can have a significant impact on cell physiology (81,157,158,186,187). However, the understanding of the exact nature and effects of cycling hypoxia is still limited. Although there has been much research on the effects of hypoxia, most reported experimental models to use stable or chronic levels of hypoxia for their hypoxic exposures. The level of hypoxia used also varies from 0-10% (81). Intermittent hypoxia (hours to days) was shown to increase HIF-1α activity and stabilise the expression in the initial period (157). Cyclical hypoxia has been shown to influence the trans-differentiation of MSC to osteoblast, which conferred clinically to demonstrate higher bone mineral density in elderly patients (117). Prolyl-hydroxylase 2 silencing of human bone marrow MSC was shown to increase post-ischemic neovascularisation in diabetic mice with chronic limb ischaemia and offered a higher protection against apoptosis *in vitro* and with an increased rate of survival

when transplanted to ischemic tissue (188). Toffoli et al. showed that endothelial cells responded to intermittent hypoxia by increasing the expression of pro-angiogenic and pro-inflammatory genes (183). They observed the activities of three oxygen-sensitive transcription factors: HIF-1, nuclear factor erythroid 2-related factor 2 (Nrf2), and Nuclear factor-κB (NF-κB) and found that only HIF-1α had an increase in transcriptional activity under intermittent hypoxia. On the other hand, Nrf2 and NF-κB transcription factors, regulators of cellular resistance to oxidants and inflammation respectively, were not increased. They also found an increase in endothelial cell migration and tubulogenesis with alternating hypoxia–normoxia cycles. These all point to intermittent hypoxia exerting a clear pro-angiogenic effect on the cells. However, compared to chronic hypoxia, the molecular mechanisms driving cell behaviour in intermittent hypoxia are less well understood, likely due to the difficulties with modelling this in the laboratory setting where specialist equipment is required. It is only recently, through the availability of specialised hypoxia equipment (which will be elaborated further in Chapter 4 of this thesis), that we are able to observe more published data on the effects of intermittent/cyclical hypoxia on cells. However, due to the lack of consistency and variation in defining of the hypoxia culture environment, there are still inconsistencies in reporting of cellular response to intermittent and chronic hypoxia, making the subject even more challenging to understand. For example, in lower states of hypoxia (< 5%), a slight rise in apoptosis was reported in MSC; Zhu et al. and Chang et al. showed an increase in cell death in rat-derived MSC after short-term exposure of 3–24 hours of hypoxia (0–5% O_2) (189,190). Conversely, this effect is seemingly reversed with prolonged culture in hypoxia. Lavrentieva and colleagues demonstrated that a slight increase in the duration of hypoxia showed the opposite effect to short-term culture, with an increase in the proliferation rate observed after 3 to 4 days in 1% oxygen for both human umbilical cord and bone marrow-derived MSC (bmMSC) (191). However, it would be difficult to draw a comparison between the studies due to the fact that serum deprivation with used concurrently with the rat-derived MSC, likely masking and confounding the hypoxic effect on the cells, as well as different species and source of MSC used. Another controversy was shown in the reporting of NF-κB regulation in intermittent hypoxia on different cell types. As mentioned above, NF-κB was not found to be activated in intermittent hypoxia in endothelial cells by Toffoli et al (183).

However, the opposite was reported in human bmMSC by Crisostomo and colleagues, where NF-kB was activated after 24 hours of exposure to 1% O_2 (192).

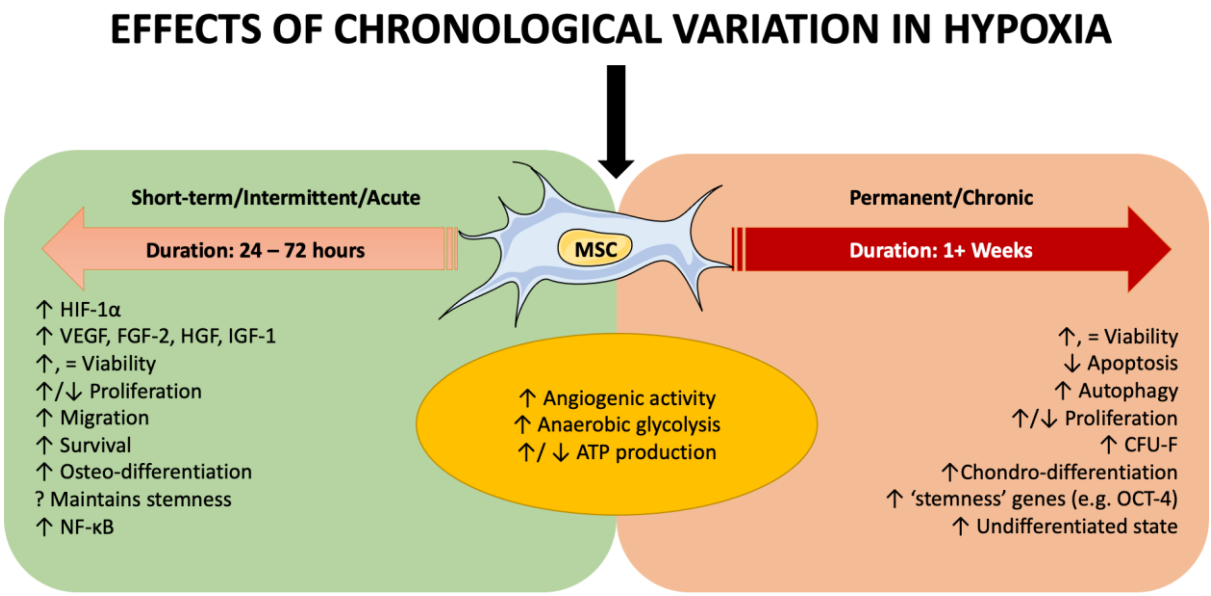

Figure 1-8 Diagrammatic representation of intermittent and chronic hypoxic effects on MSC. Due to the lack of standardisation and defined hypoxic range across published data, the cellular response to the different exposure durations can be contradictory such that both the inhibitory and potentiating activities have been reported for the same effect. The text in the middle circle highlights the common phenomena for both intermittent and chronic exposures. The figure above is adapted from Buravkova et al. 2014 (81) with permission under the terms and conditions provided by the publisher Elsevier and the Copyright Clearance Center (CCC).

Therefore, it was encouraging to see certain evidence from Martinez and colleagues, who have recently shown in their cell lines a decrease in HIF-1α mRNA in chronic hypoxia and an increase in HIF-1α mRNA following intermittent hypoxia relative to normoxia (187). They proposed a novel mechanism behind the upregulation of HIF-1α in recently identified enzymatic oxygen-sensitive pathways, known as the KDM histone demethylase family (KDM4A, KDM4B and KDM4C). Intermittent hypoxia can affect the demethylation of histones bound to the HIF-1α gene due to some availability of oxygen and subsequently increases HIF-1α mRNA expression. This would then have the downstream effect of increasing overall HIF-1 activity and expression of HIF target genes. In chronic hypoxia, however, HIF-1α is stabilised initially, increasing HIF-1 transcriptional activity and the expression of HIF-1α target activity. But these increased enzyme levels, KDM4A, KDM4B and KDM4C are largely inactive due to limited oxygen availability, which are required for KDM activity. This will then lead to an increase in Histone 3 lysine 9 trimethylation (H3K9me3), including

at the HIF-1α locus, which ultimately decreases the amount of HIF-1α mRNA transcribed. Hence, their data indicate that expression of HIF-1α is controlled differently in intermittent hypoxia compared to chronic hypoxia (187). This pathway is summarised in Figure 1-9. It highlights the key concept that increase in HIF-1α and HIF target gene expression is related to hypoxic exposure in a dose-dependent, chronological manner (187).

If we were able to better understand the exact cyclical or dynamic hypoxic levels which can achieve the best pro-angiogenic response for the cell type of interest, it would be possible to 'commandeer' this system to its therapeutic benefits with a simple adjustment of the *in vitro* culture environment to achieve this (82,193,194). Pre-conditioning regiment of cells in hypoxia was proposed by Rosova et al. to integrate into pre-transplantion protocol steps, to enable cells to resist apoptotic stimuli when transplanted into a hostile *in vivo* environment with severe hypoxia, such as ischaemic tissues from chronic wounds or other sites of injury (87). Other advantages of hypoxia on MSC are the maintenance of stemness and multipotency, which could have major therapeutic benefits when used in areas where regeneration of tissue is desired (63,195). Hence, priming of the cells via hypoxic induction could be an excellent strategy for the optimisation of therapeutic angiogenesis when pre-conditioned cells are transplanted for tissue engineering purposes (194,196).

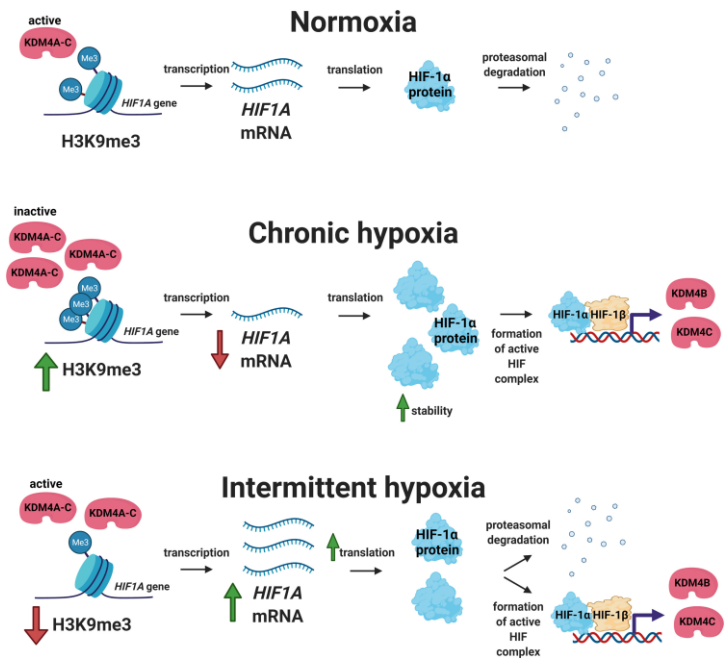

Figure 1-9 Mechanism of HIF-1a activation and degradation in intermittent versus chronic hypoxia as depicted by Martinez et al. 2022 (187). Although degradation of HIF-1a protein is decreased in chronic hypoxia, HIF1A mRNA expression also decreases due to increase in Histone 3 lysine 9 trimethylation (H3K9me3) secondary to inactive KDM histone demethylase enzymes. By contrast in intermittent hypoxia, there is an increase in HIF1A mRNA due to decreased H3K9me3. This promotes the availability of HIF-1a protein and downstream effects. Whether this increases the overall activity of HIF-1a was dependent on the stability of the protein and the rate of degradation which varies with individual conditions. Adapted and reproduced under the terms and conditions of the Creative Commons CC-BY license.

1.5 Vascularisation Strategies for Tissue Engineered Scaffolds

Low-volume, thin or hollow organs, such as TE skin, vascular grafts and heart valves, are the few TE products which have successfully ventured into mainstream clinical use. There has been very limited success seen in other more complex TE human tissue or larger solid organs, such as liver or kidney (197). Amongst the many challenges and difficulties faced in the manufacturing of TE organs for clinical translation, the failure to overcome potential nutrient limitations in more complex 3D structures seems to be the commonly reported problem (5). Adequate vascularisation is one of the greatest challenges scientists currently face in the upscaling of larger three-dimensional (3D) TE constructs containing living cells, as it is crucial for the efficient delivery of nutrients and oxygen following *in vivo* implantation (198). Without adequate vascularisation, cells within the core of a 3D scaffold would face inevitable

ischaemia and necrosis, resulting in poor survivability of the scaffold *in vivo*. The problem relates to the average growth rate of microvasculature being approximately 5 μm/h for individual vessels (199) and the diffusion limit for O_2 to cells was found to be approximately 170 μm from the closest vessel (29,200,201). Hence, if left to nature, no construct larger than 120-170 μm would be viable after a few days. Improving rapid neo-angiogenesis is pivotal to its success *in vivo*. It is no surprise that currently, greater research efforts are being geared towards improving neovascularisation and integration with the host vascular network in the development of TE constructs, as evident by the increase in yearly publication relating to this subject as shown in; there is a 6 fold increase in publications on this subject compared to 20 years ago (2493 in 2022 compared to 375 in 2002).

Several TE vascularisation strategies have been proposed by researchers. They can be broadly classified into the *in vitro* and *in vivo* approaches. These approaches use the fundamental concepts of TE in the fusion of matrix/scaffold, cells, and bioactive stimuli within a nominated bioreactor, either in a man-made equipment or a living host, to achieve its desired outcome.

4 Pillars of Tissue Engineering

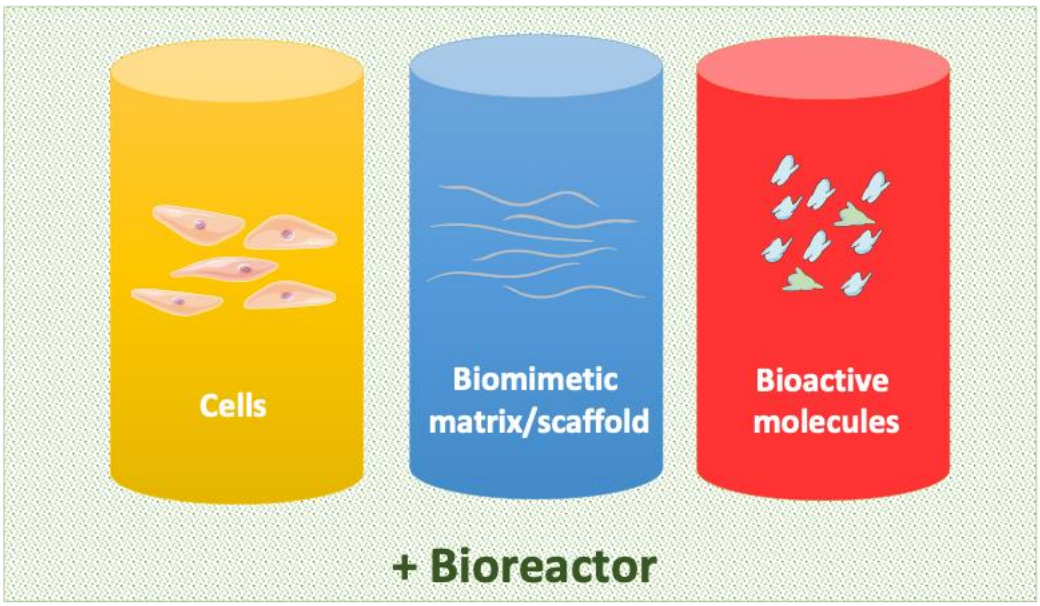

In vitro Approach

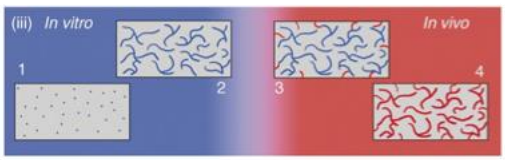

Cells-based:
- Pre-conditioned or genetically modified seeded cells (e.g. MSC, iPSC, precursor EC)
- Co-culture
- Spheroids

Biomolecular-based:
- Cytokines/Growth Factors
- Encapsulated within scaffold for time-release of GFs

Scaffold-based:
- Organ-specific scaffolds incorporate cells and bioactive molecules as mentioned above.
- Biomimetic materials with ECM (e.g. decellularized tissue/organ)
- Bioprinting to include microchannels for vascularisation

'Bottom up' approach
- 3D bioprinting with cells
- Microfluidics

In vivo Approach

Extrinsic

Implanted into region with rich blood supply (omentum, mesentery, muscle fascia, subcutaneous)

Arteriovenous loop

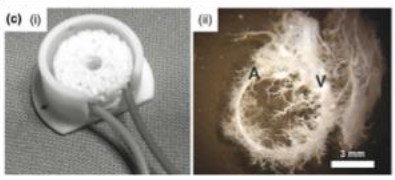

Intrinsic

Multistaged process

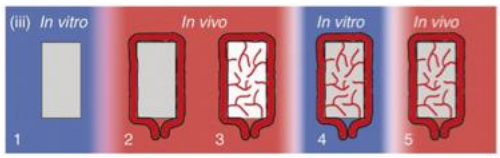

Figure 1-10 Approaches to vascularisation of TE organs. *In vitro* vascularisation. 1: A tissue construct containing endothelial cells is prepared in vitro. 2: The endothelial cells organize into a vascular network (blue). 3: The tissue construct is implanted and host vessels (red) grow into the construct. 4: When the host vessels reach the precultured vascular network, the vessels connect and the entire construct becomes perfused. *In vivo* approach: 1: Tissue construct preparation *in vitro.* 2: Implantation at the prevascularisation site, supplied by a vascular axis. 3: Formation of a microvascular network by vessel ingrowth from the vascular axis. 4: Explantation of the prevascularised construct with the vascular axis. 5: Implantation of the construct at the defect site and surgical connection of the vascular axis to the vasculature. Images within the diagrams are taken from Rouwkema et. al. 2008 (202) adapted with permission under the terms and conditions provided by Elsevier and Copyright Clearance Center.

In vitro approach of pre-vascularising tissue constructs involves using a scaffold, biomolecular or cell-based techniques (see Figure 1-10) (203). Scaffold-based techniques come from manufacturing and altering the basic raw materials that make up the scaffold in order to enhance their angiogenic qualities. Biomaterials used include a range of synthetic to biological or hybrid of the two. This includes changing the biomaterial's porosity or stiffness to encourage the ingrowth of blood vessels (204,205). Chemical-based approach can involve the use of biological products, such as growth factors and other matrix proteins, which are used to be incorporated into the scaffold. However, problems have been reported with the use of growth factors such that no single delivery of growth factor has resulted in true therapeutic angiogenesis *in vivo* such that induced stabilised vessels have been shown to regress with time in absence of true physiological stimulus. Cell-based approach involves using either endothelial cells or supporting mural/perivascular cells to assist with the angiogenic process. Cells are often co-cultured to allow for early vasculogenesis in situ prior to angiogenesis *in vivo* (209). Newer technologies using the 'bottom-up' approach to prevascularisation, integrates more innovative microfluidics and 3D bioprinting techniques, which can incorporate all of the above features and more, making this field highly attractive to modern tissue engineers (210,211).

The *in vivo* approach uses the body as a natural bioreactor for vascular ingrowth into the scaffold of interest as an extrinsic source of blood supply. (see Figure 1-10) Due to the reliance on the natural development of vascular ingrowth, this is a longer and more laborious process, which is consider too slow to satisfy the level of therapeutic support required for scaling up to meet widespread demand. As such, this is currently reserved only for thicker, larger TE graft transplants. A well-described method is to

implant the TE graft into a region of rich vascular supply (such as flaps of the omentum, mesentery or muscle fascia) during surgery and allow for extrinsic blood supply to occur via vascular ingrowth from the surrounding tissue (198). Another approach is a multi-staged, more cumbersome method of initiating intrinsic blood supply to prevascularise the scaffold. Scaffolds are subjected to heterotopic transplant first, either around an existing artery or via the use of a constructed arterial-venous loop and then removed and implanted at the site of the defect with its surrounding vasculature (212,213). The main disadvantage is that it requires three separate surgeries to complete, imposing undue morbidity on the patient.

The concept of regulating stem cell paracrine actions via different culture methods is a known strategy (60). Due to the vast scale of the vascularisation issue in TE, it is necessary to approach this problem from a multidisciplinary perspective, with the most clinically translatable method relevant to the organ-specific need. The following section will describe a pertinent clinical problem of wound healing and the proposed strategies for the evaluation of angiogenesis in this study.

1.6 Candidate tissue-engineered scaffolds for the study of angiogenesis

There is a plethora of choices for TE scaffolds available for regenerative purposes, however choosing the right TE model to study angiogenesis should ideally be from an organ with the greatest translational potential to wider clinical applications and relevance to other disease processes. The skin is the largest organ in the body, plays an important role in immune-protection and homeostasis. It is constantly challenged by external factors and is highly susceptible to trauma and disease. It is also one of the most researched and translatable forms of tissue-engineered organs currently in use in the clinical setting. Complex biological mechanisms which are triggered after skin trauma have very similar processes to those seen in myocardial infarction or spinal cord injury (214,215). Hence, and due to its accessibility, skin is thought to be one of the best models for the study of tissue repair mechanism and the development of new strategies in regenerative medicine (216).

Given the significant burden of disease from skin pathologies arising from trauma, burns, and other chronic diseases (such as diabetes and vasculopathy) causing poorly healing chronic wounds, the need to explore more innovative means to alleviate the problems in wound healing is greater than ever. In the UK, the management of wounds cost the NHS £8.3 billion in 2018, of which £5.6 billion was associated with managing non-healing chronic wounds (217). It is estimated to cost the NHS 5.5% of its annual budget (218). In the United States, it has been reported that there are over 6.5 million patients with wounds, and an associated healthcare cost of US$25 billion annually (219). Put this into a more global perspective, according to the Global Burden of Disease latest study results from Giesey et al., it showed that skin and subcutaneous disease, of which includes chronic wounds, grew by 46.8% between 1990 to 2017 and is ranked fourth by the incidence of all causes of disease (220).

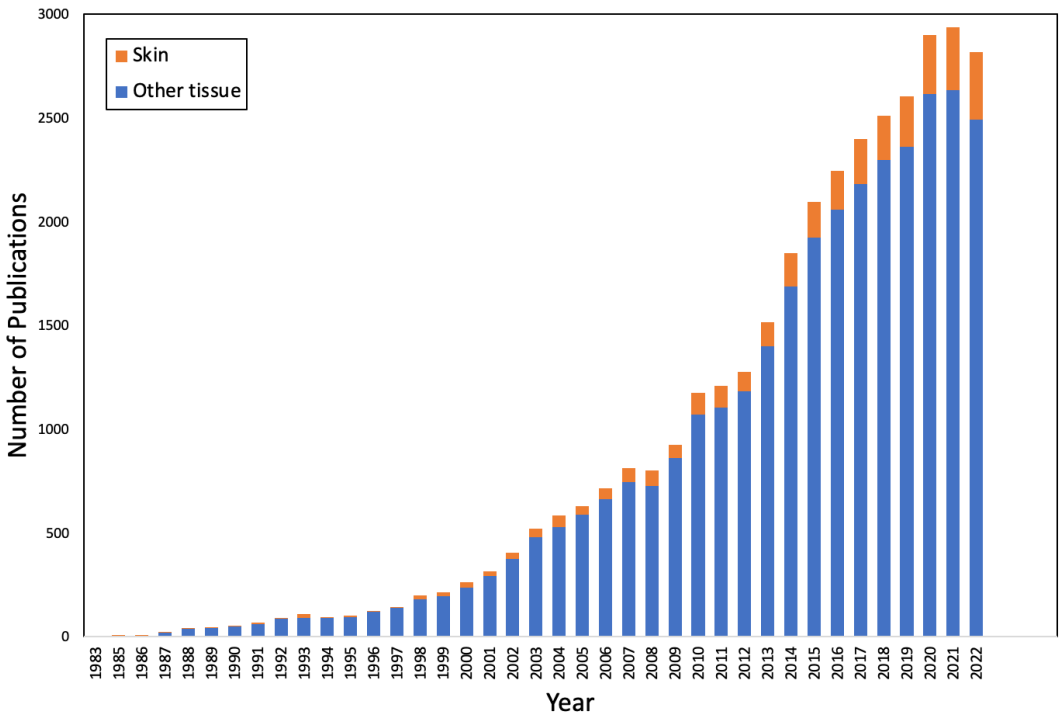

Figure 1-11 Publications associated with vascularisation in the field of tissue engineering is on the increase year on year. Papers on vascularisation in skin-related tissue engineering is also increasing. Data was obtained by Pubmed search with the keywords 'tissue AND engineering AND vascularization' which was compared to 'skin AND engineering AND vascularization', performed on the 31st December 2022.

The skin is one of the simplest forms of organ to tissue engineered due to the relative simplicity of tissue layer components in relation to other organs in the body. It is one

of the first tissue-engineered construct to be grafted onto patients and has the long track record for clinical investigations and innovation. All types of wound healing require *de novo* angiogenesis for the transportation of systematic oxygen, nutrients and other important factors into proximal wounded sites during the reparative process (221). (A detailed description of the process is covered in the Section 6.3.3 of Chapter 6 in the thesis.) A well-vascularised wound bed is crucial for the healing of skin defects. The gold standard for the treatment of significant wound defects is the use of substitute dermal and epidermal layers. This usually involves either the use of an autologous composite skin flap or a substitute dermal scaffold and an autologous epidermal tissue (222,223). The mass availability of off-the-shelf clinical-grade tissue-engineered scaffolds for dermal regeneration (SDR), also known as acellular dermal matrix (ADM), has become a game-changer in this field (223). However, the vascularisation of these ADM can take up to 3 weeks to complete, and successful completion of this step is crucial for the onward application of autologous epidermal layer in the form of a split skin graft (223). Prolong delays in epidermal coverage is usually caused by slow vascularisation of scaffold can impact on the successful use of dermal scaffold in treatment of skin pathologies, such as burns and diabetic ulcers, due to the increased risk of infection from the lack of definitive barrier. Hence, the use of ADM is limited due to infection rates and a low regenerative capacity in these patient, mainly due to lack of oxygen and nutrients driven by the poor blood supply to the wound area (224,225). Therefore, the lack of adequate neovascularisation of the surrounding wound is considered one of the main limiting factors for the clinical success of tissue-engineered scaffolds (226). The importance of this subject is reflected in publications related to skin vascularisation. Related articles have consistently increased year on year, taking up more than 10% of yearly publications since 2019. (Figure 1-11) The acceleration of vascularisation of dermal scaffolds can be improved by way of introducing angiogenic factors or gene vectors or pre-vascularisation of the scaffold prior to implantation (227).

TE matrix scaffolds can also function as a stem cell delivery vehicle. There are several pre-clinical studies showing successful use of SDR to seed cells for enhanced therapeutic effects (228–241). Using therapeutic cells to promote neovascularisation will help overcome challenges of applying TE skin clinically. MSC can act as a trophic factory for the release of angiogenic factors and can respond

appropriately to the needs of the local microenvironment, as well as function as a recruiter of host cells to the transplanted area for the purpose of regeneration (242). Bone marrow-derived MSC have also been shown to contribute to the wound healing process by migrating to the wound site and differentiating into fibroblast. (243) A recent study showed that the MSC autophagy-mediated paracrine effects played a crucial role in therapeutic wound healing by promoting endothelial cells-driven angiogenesis (244). Hence, this demonstrated the importance of auto-regulation in the paracrine secretion of VEGF in MSC, and how it would directly benefit cutaneous regeneration. A diagrammatic summary of the therapeutic effects of MSC in skin regeneration and wound healing is shown in Figure 1-12.

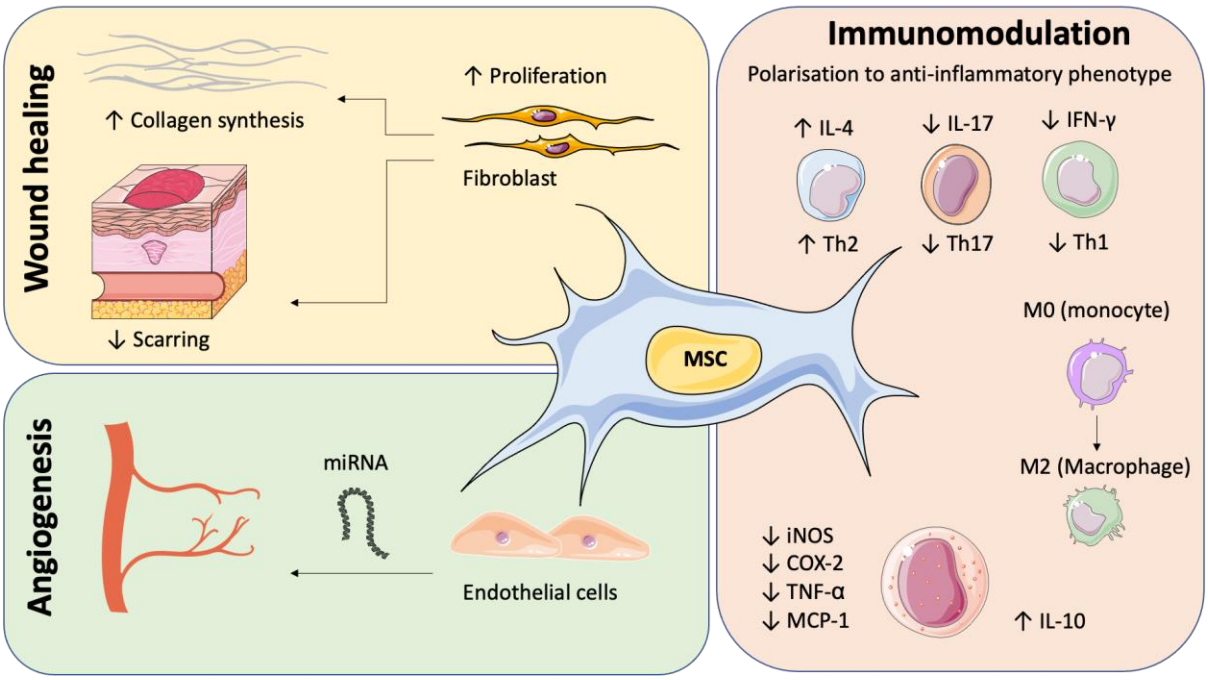

Figure 1-12 Therapeutic effects of MSC-based therapy for skin regeneration and wound healing. MSC mesenchymal stem cells, IL interleukin, INF -γ interferon γ , iNOS inducible nitric oxide synthase, COX -2 cyclooxygenase-2, TNF -α tumour necrosis factor-α, MCP-1 monocyte chemoattractant protein-1. Adapted from Wang et al. 2021 as permitted by Crown Copyright (242).

There are many different TE skin products available commercially, such as epidermal, dermal and composite constructs, which have been implemented for clinical use (222). This makes the skin an ideal candidate scaffold for the delivery of therapeutic cells for regenerative purposes. The use of clinical products will also help inform future clinically-relevant research on the potential relevance of combining cell-base therapies on such scaffolds. There are now several published data to support

the cytocompatibility of dermal matrices such as INTEGRA® and Matriderm (229,233,234,236,238,240,241,245–252).

The harsh microenvironment of damaged tissues is often hypoxic and nutrition poor, which can trigger cell death and apoptosis of seeded cells. It is widely accepted that MSC survival after *in vivo* transplantation is limited. Their main regenerative effects are mainly attributed to their trophic or immunomodulatory means (58). Ensuring MSC viability long enough to elicit their therapeutic effect *in situ* is an important issue to overcome. Therefore, the main challenges to address are poor cell engraftment and survival following transplant for cell-based therapy (253). Many studies have shown that hypoxic preconditioning could enhance the seeded MSC survivability and inhibit cell apoptosis through the autophagy process (106,121,254–256), and as such MSC have been described as exhibiting hypoxic-resistance (257).

The main aim of this study will therefore be heavily focused on clinically translatable approaches which can be adopted easily and swiftly through proof of concepts around ideas that are already in existence which can be verified on therapeutic products already in use clinically.

With these concepts in mind, I hypothesise that pre-conditioned MSC in dynamic hypoxia seeded in dermal matrix scaffold will help accelerate neo-angiogenesis from host tissue and allow for improved wound healing in an *in vivo* diabetic murine model.

2 General Materials & Methods

2.1 Human Mesenchymal Stem Cell (MSC) in 2D culture

2.1.1 Cell Source and Expansion

Ethically approved human bone marrow-derived MSC (bmMSC) from cryopreserved sampled were obtained from femoral hip tissue discarded from patients having hip surgery at the Royal National Orthopaedic Hospital. Cells were isolated using the method adapted from Igarashi et al. (258). Briefly, bone marrow aspirates were transferred to a sterile centrifuge tube containing 10ml Dulbecco's Modified Eagle's Medium (DMEM, Gibco™, #41965039) supplemented with 20% FCS and 1% Penicillin-Streptomycin (Gibco™, #15140122) and 1ml of heparin (1000IU) to prevent blood coagulation. Cells were centrifuged and resultant the lipid layer was carefully removed using a sterile Pasteur pipette. After which additional media was added to the cells and centrifuged again. The supernatant above the cell pellet was removed and cells resuspended in media. Cells were counted and seeded in T75 flasks initially. The flasks were left undisturbed for the first 72 hours to allow for the bmMSC to adhere to the tissue culture surface. After 72 hours, all floating cells were discarded, and the adherent cells were left to expand and reach confluency.

Ethically approved human umbilical cord-derived MSC (ucMSC) were obtained from neonatal umbilical cords sourced from the Anthony Nolan Trust and processed by the Process Development team under Prof Mark Lowdell's group at the Royal Free Hospital. Briefly, the collected umbilical cord collected were washed and sliced lengthways into 1cm vertical segments using a sterile scalpel. Any visible vessels were removed. These segments were placed into MACS dissociator tube with 4ml of collagenase solution (Gibco, # 17100017) and then incubated for 3 hours at 37°C. The MACS dissociator tube (Miltenyi Biotec, # 130-093-237) was then placed into the GentleMACS (Miltenyi Biotec, Germany) and spun. A monolayer was seeded into T-flask (T-175) and adherent cells were allowed to expand under these conditions.

Ethically approved human adipose derived MSC (adMSC) were isolated from surgically harvested lipoaspirate (LA) from donors. These were processed by the Process Development team under Prof Mark Lowdell's group at the Royal Free Hospital. Approximately 20mls of sample were collected from patients in Luer lock syringes. Samples were processed within 2 hours of collection. LA was incubated at 37°C in 0.15U/ml collagenase (Gibco, # 17100017) for 1 hour. The digested samples were then diluted in phosphate-buffered saline (PBS, Sigma, # D8537-500ml)/20% human albumin solution (Zenalb, Bio Products Laboratory Limited, UK) and centrifuged at 400g for 10 minutes. The fatty aqueous supernatant was discarded, and the pellet was resuspended in MSC medium (see below). A monolayer was seeded into T-flask (T-175) and adherent cells were allowed to expand until confluency.

Cells were cultured in T75 or T175cm^2 flask with seeding densities ranging from 0.5 to 5 x 10^3/cm^2 initially in order to optimise seeding density for this particular cell type. They were incubated at 37°C under an atmosphere of 5% CO_2 in either 21% O_2 (referred to as normoxia 21%), 5% O_2 (hypoxia 5%) or 1% O_2 (hypoxia 1%). The growth media use was Minimal Essential Medium alpha (MEMα, Gibco, #32561029) media containing GlutaMAX Supplement no nucleosides, supplemented with 10% Fetal Bovine Serum (FBS, Gibco, # 10270106) and 1% Anti-Anti x100 (Sigma, # A5955). The growth media was changed every 3-4 days. When cells were 90% confluent, they were sub-cultured and expanded through another passage. For each passaging, the growth medium was removed from the flasks, followed by a wash with 10mL of PBS (Sigma, # D8537-500ml). Cells were detached from the flask by using 5ml 1X TrypLE Express (Gibco, # 12604-013) solution and subsequently incubated for 3-5 minutes at 37°C. The cells were noted to be fully detached when checked under the bright field microscope for complete rounded, floating cells. The TrypLE solution was neutralised with 10mL of MEMα media. The cell suspension was transferred to a 50mL universal tube for each T75 or T175 cm² flask. The tubes were then placed in a centrifuge at 300g for 5 minutes. The supernatant after centrifuge was pipetted out without disturbing the cell pellet at the bottom of tube. The cell pellet was re-suspended in media and passaged or used for seeding in collagen hydrogels (see below Section 2.2.1).

In addition, ASC52telo immortalised hTERT adMSC isolated from a human donor was also purchased for use from ATCC (ATCC, SCRC-4000™). These cells had full certification of analysis and characterisation data through the supplier, although these were also repeated in-house to confirm the data. They were initially plated as per the manufacturer's instruction, but subsequent culture conditions were as described below.

Only bmMSC up to passage number 9 were used, although some cells were used passed passage 9 to determine when MSC lose their ability to differentiate and senesce. For ucMSC, passage up to number 14 was used due to the neonatal quality of the cells, which gives them higher proliferative capacity before cell senescence. For primary adMSC, they were used up to passage number 8. For their immortalised counterparts, they were cultured up to passage number 18 for *in vitro* optimisation experiments, although the cells which were transplanted *in vivo* were of early passages under P8 of culture.

2.1.2 Thawing and Freezing

Cryovial of MSC were removed from liquid nitrogen and disinfected with 70% ethanol (Fisher Scientific, # 10437341). In a laminar flow hood, a 1 or 2 ml sterile pipette was used to transfer the thawed cells by gently mixing in warmed media into the frozen cryovials and transferring thawed cell suspension into a 50ml sterile universal tube filled with 20ml of media, being careful to not introduce any bubbles. The tube is centrifuged at 300g for 5 minutes to pellet the cells. The supernatant is decanted to leave the pellet for resuspension with 10ml of fresh media. The cells are counted using a haemocytometer as described below. The cell suspension with the desired cell seeding density is plated into the appropriate tissue culture plate, well plates or tissue culture flask as per experiments as described.

When required, cells were frozen down in FBS (Gibco, #10270106) or 4.5% human albumin solution (Zenalb 4.5, Bio Products Laboratory Limited, #PL 08801/0006) plus 10% DMSO (CryoSure-DMSO, WAK-Chemie Medical GmbH, Germany, # WAK-DMSO-50) at a density of $1x10^6$ cells/cryovial.

2.1.3 Cell Count

Cell count was performed using a haemocytometer (Heinz Herenz Medizinalbedarf GmbH, Germany, # HERE1080339) combined with the trypan blue exclusion method. 10µl aliquot of a single cell suspension was mixed in a 1:1 ratio with trypan blue 0.4% solution (Gibco, #15250-061). The resulting cell suspension was pipetted inside the chamber between the haemocytometer glass slip and the haemocytometer. (Figure 2-1)

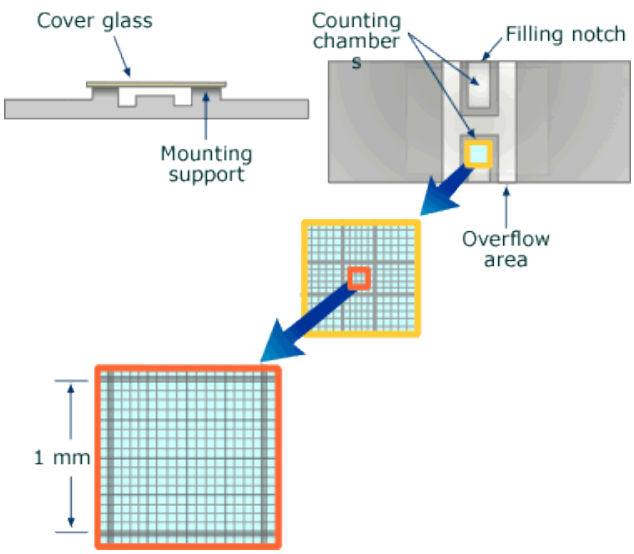

Figure 2-1 Haemocytometer used for cell counting. Image credit to: http://simulab.ltt.com.au

The cells present in the four corner primary squares of each grid (16 squares per corner) were counted under an inverted light microscope at X10 magnification. (Nikon Eclipse Ti) Counts were carried out in duplicates and averaged. Cells which did not stain blue were designated to be viable cells. As the volume in of each of the counted squares of a haemocytometer is 0.1mm^3 (or 10^{-4} ml), the number of viable cells/ml was calculated by taking the average number of cells per square and multiplying by the dilution factor and 10,000 to obtain the number of cells per ml of diluted sample. Section 0 further describes the trypan blue method for calculation of viability using the haemocytometer.

For streamlining the cell processing, Countess™ II automated cell counter (Invitrogen, Life Technologies Corporation) was also used in the later parts of the experiments to count cells, particularly where a large number of cells were required. Trypan blue was used as described above. 10µl aliquot of a single cell suspension was loaded onto the disposable Chamber Slides (#C10228, Invitrogen, Life Technologies Corporation) as per the manufacturer's instructions to obtain a readout of the cell numbers on the slides. (see Figure 2-2)

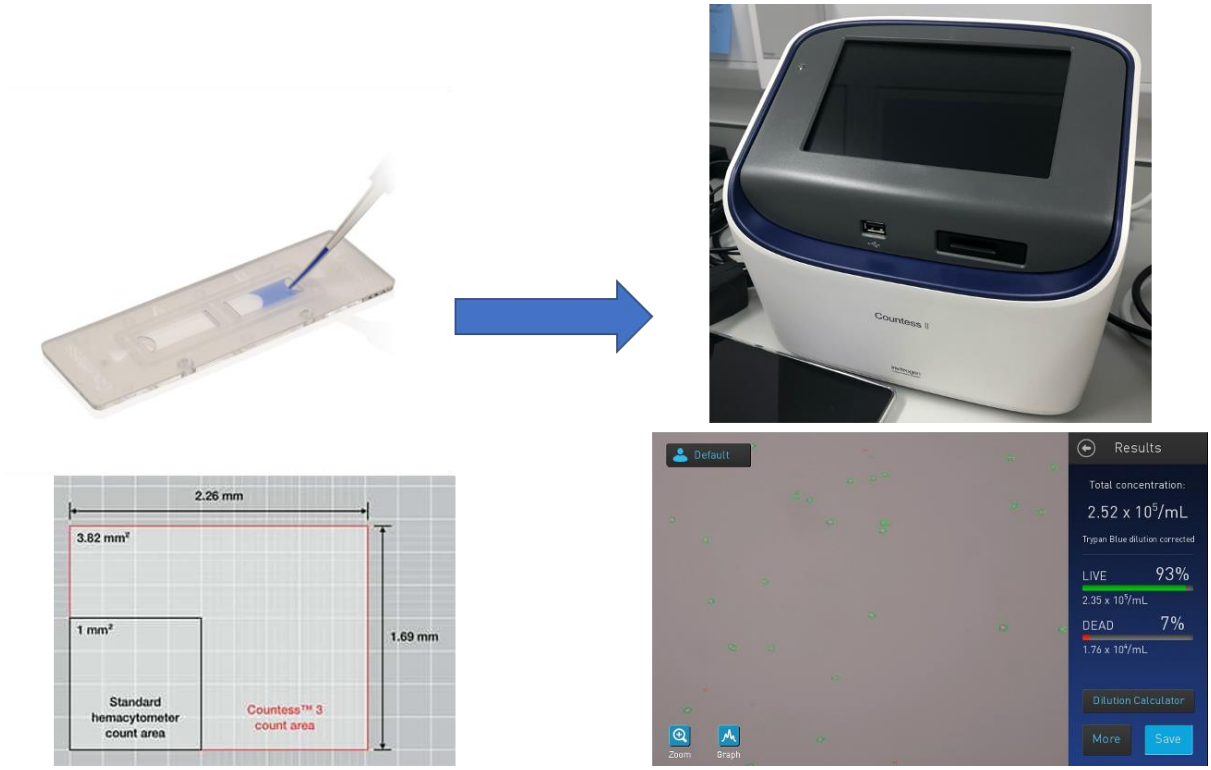

Figure 2-2 Using the Countess™ II automated cell counter system to help streamline the cell counting process with the use of the disposable Chamber Slides. The slide (top left) is loaded into the machine, which gives an accurate readout of the cell numbers in approximately 30 seconds, as shown in the lower right image. The Chamber Slides provide a larger area for the observation and counting of cells (lower left image).

2.1.4 Population doubling

Population doubling is evaluated at each passage using the following equation (259):

$$\text{Population doubling level (PDL)} = \frac{\left[\log \frac{Nn}{\log(Nn-1)}\right]}{\log 2}$$

Where:

n = cell passage,

n−1 = previous cell passage,

Nn = cell number at passage n, and

Nn−1 = number of cells plated at passage n−1.

It is important to note that passage number (n) refers only to cell transfer from one culture vessel to another but not necessarily to cell proliferation. Instead, a constant increase in PDL values confirms that cells have a prolonged life span and do not senesce. A cumulative population doubling is the sum of the population doubling values for all passages.

Population doubling time is defined as the time it takes for the population in the cell culture vessel to double. It is usually calculated using the time taken to confluency divided by the PDL value.

2.1.5 Fold increase

Fold increase is a measure of cell growth from one-time point to another. Fold increase was calculated using the following formula:

Fold increase = C(n)/C(n-1)

Where: C(n) = cell number output at each given time point
C(n-1) = cell number at a previous time point of the same experimental group

2.1.6 Cell Morphology

Morphology of cells were observed via bright field microscopy (Nikon Eclipse Ti or Invitrogen EVOS M5000) and images were captured on the Nikon software (Nikon NIS Elements BR) or EVOS (Invitrogen, Thermo Fisher Scientific) internal Imaging System for comparative analysis.

2.1.7 Flow Cytometry

To analyse cell surface markers on the MSC, flow cytometry analysis was used. Cells of interest were cultured to confluence and then trypsinised, resuspended and counted. When enough cells were obtained, they were then resuspended in 400 ul (40 ul per tube; 10 samples tubes) flow cytometry staining buffer made up of 1% BSA (Sigma-Aldrich, # 05480), 1% Sodium Azide (NaN3; Sigma-Aldrich, # S2002) diluted in PBS with 10 ul of Human Fc Receptor (FcR) blocking reagent (Miltenyi Biotec, Germany, # 130-059-901) per round-bottom Falcon polystyrene tubes (Corning, # 352052), excluding the control tubes. The cell suspension was refrigerated for 10 minutes.

Antibodies (Table 2.1) were then added into the tube and incubated in the dark for 40 minutes. This was followed by two 1% buffer wash and centrifuge (1500rpm for 5 minutes) steps. The supernatant was removed and the cells were then resuspended in 350 ul fixature solution made up of 1% formalin (Sigma-Aldrich, # HT5012-1CS) in PBS for each tube. Flow cytometry analysis was performed using MACQuant Analyzer 10 machine (Miltenyi Biotec, Germany) and analysis was done on the MAC Quantify software (Miltenyi Biotec, Germany).

Antibodies/stain (expected +/- cell surface marker for MSC)	Fluorescent marker/channel	Catalog Number	Source
CD90 Mouse Anti-Human (+)	FITC	555595	BD Pharmingen
CD73 Mouse Anti-Human (+)	PE	550257	BD Pharmingen
CD105 Mouse Anti-Human (+)	PERCP-Cy5.5	560819	BD Pharmingen
CD19 Mouse Anti-Human (-)	PE	34578 9	BD Pharmingen
CD34 Mouse Anti-Human (-)	PERCP	345803	BD Pharmingen

CD11b Rat Anti-Human (-)	FITC	ab24874	Abcam
CD45 Mouse Anti-Human (-)	PERCP	ab65952	Abcam
HLA DR Mouse Anti-Human (-)	FITC	556643	BD Pharmingen
Viability stain: TO-PRO-3	APC	T3605	Invitrogen

Table 2.1 List of antibodies/stains used for flow cytometry of ucMSC and primary bmMSC.

2.1.8 Tri-lineage Differentiation

Tri-lineage differentiation assay was performed to confirm the multipotency of the MSC for osteogenic, adipogenic, and chondrogenic potential. StemPro Differentiation Kit was used (Gibco, Adipogenesis # A1007001, Chrondrogenesis # A1007101, Osteogenesis # A1007201). bmMSC up to passage 9 were used to confirm multipotency of cells used for experiments. Manufacturer's protocol was used to differentiate the MSC for different lengths of time in 12 or 24 well plates incubated in 37°C incubator with 5% CO_2. Media was changed every 3-4 days.

2.1.8.1 Adipogenesis differentiation

MSC were cultured in a 12 well plate (Sarstedt, Germany, # 83.3921) for 14 days as per manufacturer's protocol (n=6). Seeding density of $1x10^4$ cells/cm^2 was used. After initially culturing for 24 hours in MEMα media (Gibco, # 32561029) incubated in 37°C incubator with 5% CO_2, media was replaced with chrondrogenic media supplied in the StemPro Kit (Gibco, # A1007001) with added Gentamicin (40mg/ml solution for injection, Amdipharm UK Limited, UK). At day 14, cells were first washed with PBS without calcium and magnesium (Sigma, # D8537-500ml) twice and then fixed with 4% formaldehyde solution (Merck, Germany, # 1039991000) for 30 minutes at room temperature. Plates were rinsed a further 3 times with PBS. 2ml of 60% isopropanol (MP Biomedicals, France, # 194006) was added to each well for 5 minutes and then removed. Working Oil Red O solution (Sigma-Aldrich, Germany, O0625-25G) was made up from stock solutions (300mg of Oil Red O powder in 100ml of 100% isopropanol) by diluting in 3 parts stock solution with 2 parts deionised water. 2ml of this solution was then added to each well for 10 minutes. Distilled water was used to

wash each well thoroughly. The wells were then imaged immediately under an inverted light microscope. (Nikon Eclipse Ti).

2.1.8.2 Chondrogenic differentiation

Micromass cultures of MSC were seeded on a 24 well culture plate by pipetting 5µL droplets of cell solution (1.6×10^7 cells/ml) in the centre of each well (n=12) as per manufacturer's protocol. After cultivating micromass cultures for 2 hours under high humidity conditions, warmed chondrogenesis media (Gibco, # A1007101) was added carefully to each well. After more than 14 days of culture, the micromass cell pellet was rinsed with PBS (Sigma, # D8537-500ml) once and then quickly with 1% acetic acid solution (Acros Organics, # 222140010) for 10 seconds. The cells were then stained in 0.1% Safranin O solution (Millipore Sigma, USA, # TMS-009-C) for 5 minutes and rinsed another 3 times with PBS. The cell mass was then imaged under an inverted light microscope (Nikon Eclipse Ti) at 10x for the presence of red-stained cartilage tissue.

2.1.8.3 Osteogenic differentiation

MSC were cultured in a 12 well plate (Sarstedt, Germany, # 83.3921) as per manufacturer's protocol (n=6). Seeding density of $5x10^3$ cells/cm^2 was used. After initially culturing for 24 hours in MEMα media (Gibco, # 32561029), media was exchanged for osteogenic media supplied in the StemPro Kit (Gibco, #A1007201) with added Gentamicin (40mg/ml solution for injection, Amdipharm UK Limited, UK). At day 21, cells were washed with PBS without calcium and magnesium (Sigma, # D8537-500ml) twice and then fixed with 4% formaldehyde solution (Merck, Germany, # 1039991000) for 30 minutes at room temperature. The wells were rinsed again with PBS and then with 0.05% Tween 20 (0.01 ml/10ul Tween 20 in 20ml PBS) (VWR Chemicals, USA, # 9005-64-5) as washing buffer. To detect alkaline phosphatase activity from differentiated osteoblast, BCIP-NBT (5-Bromo-4-chloro-3-indolyl phosphate-Nitro blue tetrazolium) solution (Santa Cruz Biotechnology, USA, # SC-358798) was added to the cell monolayer for 10 minutes at room temperature in the dark. Cells were washed again with PBS and the plates were observed for blue-violet

staining. To identify calcium deposits from osteogenesis, the wells were incubated with Alizarin Red S staining solution (Sigma-Aldrich, #TMS-008-C) at room temperature for 30 minutes. The excess of staining was washed three times in distilled water for 5 minutes to remove any unbound dye, and the wells were observed for orange-red staining on microscopy.

2.1.8.4 Colony Forming Unit (CFU) Capacity Assay

Clonogenicity of cells were determined using Colony Forming Unit (CFU), also known as CFU-Fibroblast (CFU-F), capacity assay adapted from Chan & Lam. (260) It is a measure of proliferation capacity commonly used for MSC. (261) Cells at the passage of interest were counted and seeded in 10ml of MEMα media (Gibco, # 32561029) at low seeding densities (e.g. 10 - 100 cells/cm^2) on 100mm tissue culture plates (Sarstedt, Germany, # 83.3902). The cells are incubated for 12 days at 37 °C in a humidified CO_2/O_2 incubator. Plates were washed with PBS (Sigma, #D8537-500ml) and stain with 0.5 % (v/v) Crystal Violet solution (Honeywell Fluka, Germany, # 32909-250ML) for 10 minutes at room temperature. The plates were then washed thoroughly with water and visible stained colonies with a diameter greater than 1 mm (>50 cells) using light microscopy were enumerated.

The number of colonies formed per a definitive number of single cells plated is called the colony-forming efficiency or potential (262). The colony-forming potential (CFP) calculated by calculating the percentage of cell-forming colonies/number of cells seeded × 100. The resultant CFP was compared between the three MSC subtypes (bmMSC, ucMSC and adMSC) across different oxygen concentrations.

2.2 Human Mesenchymal Stem Cell (MSC) in 3D culture

2.2.1 Hydrogel preparation

The collagen hydrogel preparation involved using acid soluble rat tail collagen type I solution (2.05mg/ml, First Link, Wolverhampton, UK) at an 80% final volume concentration, mixed with 10% 10x Minimum Essential Medium (MEM) (Gibco). The collagen solution was neutralised by drop-wise addition of a 5M and 1M sodium hydroxide (NaOH) solution (Fisher Scientific, # 10488790) to reach pH~7.4. Once neutralised, the colour of the collagen solution changed from yellow to light pink. (Figure 2-3)

Figure 2-3 Neutralised light pink colour of collagen hydrogel. Reproduced from author's own MSc thesis (2015).

The collagen solution was mixed into the solution of cells, in the required cell density, which was prepared in a 10% final collagen volume solution (in cell culture media). The mixed solution was pipetted into the appropriate flat bottom well-plate and placed in a humidified incubator set at 37°C for 30 minutes. For 96 well plates (Nunc, ThermoScientific, # 167008), 125µl of hydrogel was used per well; for 24 well plates (Sarstedt, # 83.3922) 500µl of hydrogel was used per well. Once gelation was complete, the corresponding media was added to culture the cells. (see Figure 2-4 for schematic diagram of steps) The resultant gel measured approximately 6 x 1mm in size in each well. For 96 well-plate, 250µl of media was added to each well; for 24 well plate, 1.5ml of media was added to each well. (Table 2.2)

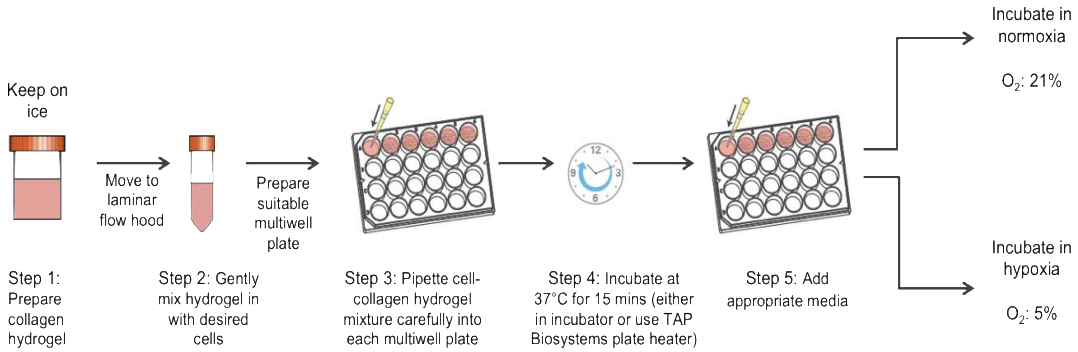

Figure 2-4 Schematic diagram of steps involved in making cellular collagen hydrogels. Reproduced from author's own MSc thesis (2015).

Well plate	Cell seeding density (cells/mL)	Cell number per gel	Vol of media added/well
96 (125 µl hydrogel)	200,000	25,000	250 µl
24 (500 µl hydrogel)	200,000	100,000	1.5 ml

Table 2.2 Different cell seeding density for the corresponding well plates are shown as are the volume of hydrogel and media used for the different plates.

2.3 Oxygen conditioning of cells using hypoxic chamber incubator

5% O_2 hypoxic conditions for cell culture were achieved by using a CO_2/O_2 incubator (Panasonic, Japan) set at 37°C, 5% CO2. Lower hypoxic culture conditions (1% O_2) were achieved in a hypoxic chamber (Stem Cells Technologies, USA, # 27310, see Figure 2-5A) by a continuous infusion of a pre-analysed gas mixture (95% N_2, 5% CO_2, 1% O_2, BOC gas), for 3-4 minutes as per manufacturer's instructions. After purging, the valves are seals and the whole chamber was placed in a general protocol incubator set at 37°C (Heratherm™, Thermo Scientific, USA). (see Figure 2-5B) Depending on the content of the hypoxic chamber, readings can go above 1% from oxygen content within the flask or plates. In such cases, it would necessitate another purge after 2 hours post-initial purging to ensure oxygen levels remain below 1% as per manufacturer's protocol.

For the purposes of this thesis, the follow definition distinguishes the different temporal hypoxic exposure of the cultured cells:

Intermittent hypoxia	< 72 hours
Persistent hypoxia	3-14 days
Chronic/permanent hypoxia	> 14 days

Table 2.3 Definition of the different chronological hypoxia.

2.3.1 Hypoxic chamber oxygen monitoring

Real-time oxygen monitoring in the chamber was measured using the Fibox 4 oxygen monitor (PreSens, Germany) with SP-PSt3-SA oxygen sensitive spot (PreSens Precision GmbH, Germany) adhered to the inside of the chamber for measurement using a fibre-optic cable sensor connected on the outside of the chamber. (Figure 2-5A) A concurrent temperature probe is also used to ensure accurate measurement of oxygen levels in the chamber. To allow for temperature equilibration with the chamber, recording of readings were only performed after 20-30 minutes of initial incubation.

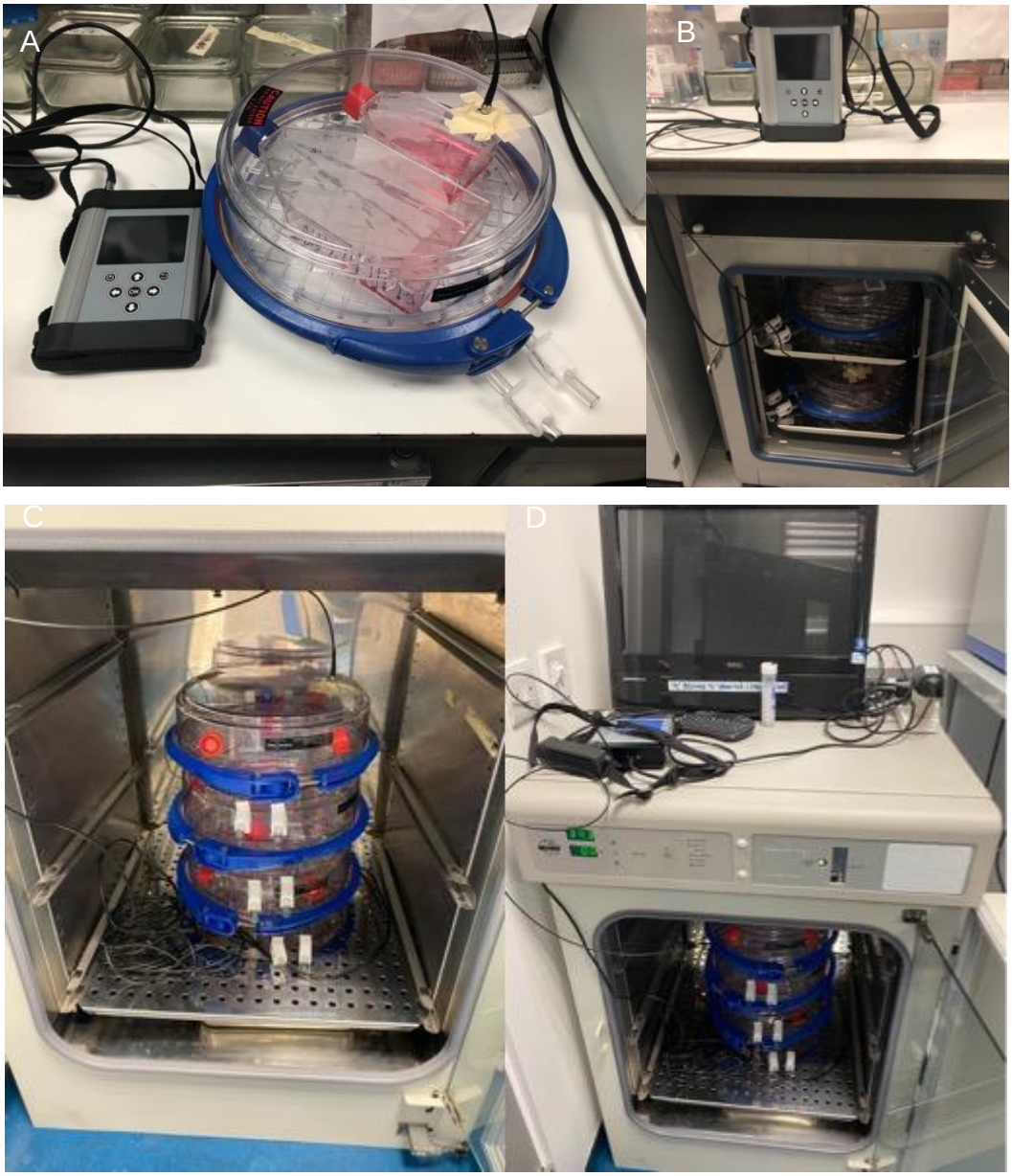

Figure 2-5 A: Hypoxic chamber set-up with Fibox 4 and fibre-optic cable attached to the chamber and the recording device on the outside; B: Smaller set-up in an incubator; C & D: Larger configuration of multiple stacked hypoxic chambers to allow for incubation of more *in vitro* samples.

2.3.2 Continuous measurement of *in vitro* vertical oxygen/hypoxic gradient using VisiSens system

The VisiSens unit is a prototype compact and portable microscopy-based imaging system (VisiSensTD, PreSens Precision GmbH, Germany) that enables non-invasive spatial and temporal monitoring of oxygen levels and their gradients within media and underneath adherent or 3D cultured cells via the use of specialist sensor foils.

The device is based on planar, biocompatible sensor foils with incorporated oxygen-sensitive luminophores. The optical signals from the sensor films are recorded without actual physical contact through a transparent vessel. This unique non-invasive nature allows for the preservation of sterility within the culture vessel. The minimum distance between the sensor film and the cells enables the direct measurement of oxygen concentration within the microenvironment of the cells with high accuracy and precision. The resultant measurements are recorded as 2D oxygen pseudocolor images or videos of a cross-section of the sample.

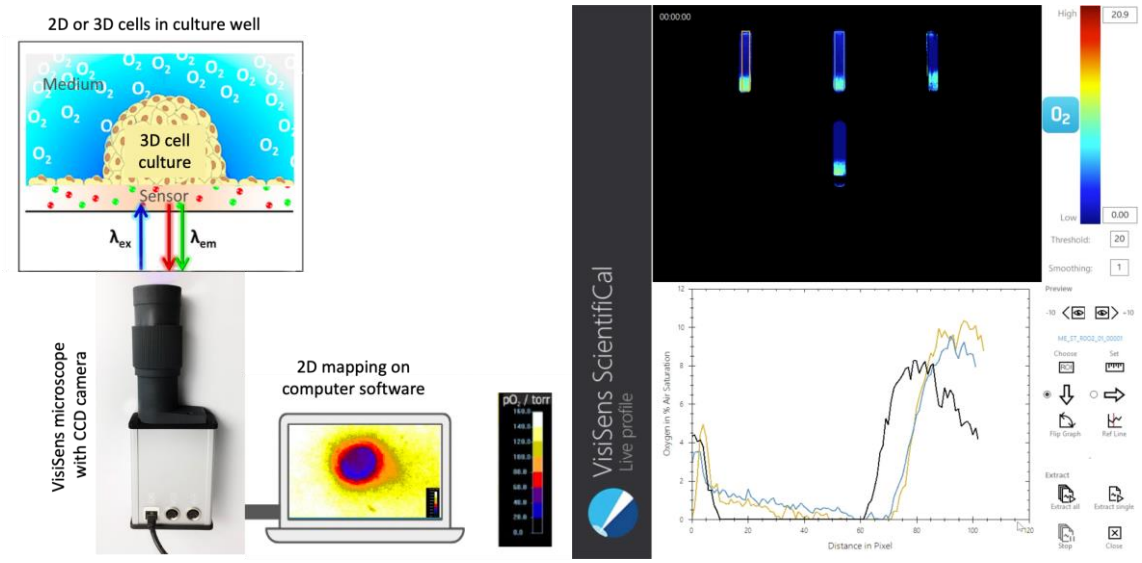

Figure 2-6 Schematic of the oxygen imaging setup which allows for the detector and the excitation unit to be incorporated in a cell culture system. The sensor foil is glued to the bottom or side of a cell culture well or plate. The foil is then placed in front of the VisiSen microscope camera unit. The oxygen-sensitive foils are excited by blue LEDs from the camera and resultant emitted fluorescence light is collected by a detector unit (consisting of a 2x microscope lens, filters and a CCD camera unit). Automated measurements are analysed by the dedicated computer software, as shown on the right-hand image.

The measurement system comes in 2 forms of oxygen sensor foil which are modular and adaptable to the culture vessel. For the thesis, the prism MIOS sensors (for 24 well plates; see Figure 2-7) and the custom cut sensor foils (for 96 well plates) were used. (see Figure 2-8)

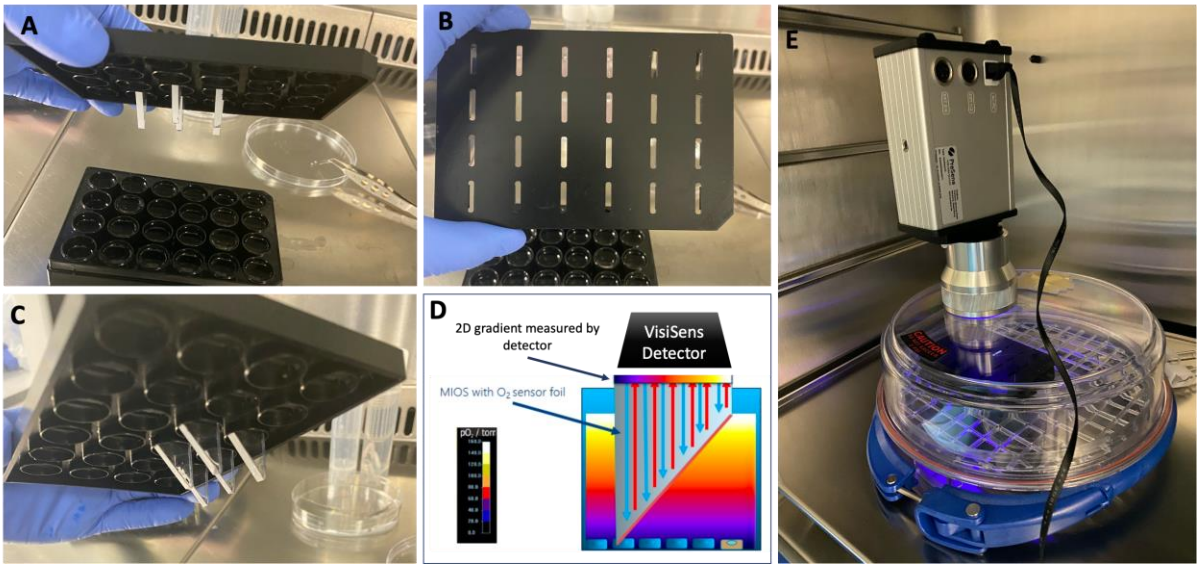

Figure 2-7 MIOS sensor foil well plate setup with VisiSens system. A, B, C:Photos show different aspects of the MIOS 3D prism-shaped sensor foil unit, which allows for the measurement of 3D gradient through media and 3D cell culture within a 24 well plate. D: Illustration of how the MIOS sensor foil is positioned through the well and is in contact with the air and media down to the bottom, where the gels/cells are attached. The Visisen unit produces blue LED light (blue arrows) which causes the sensor foil to emit luminescence detected by the VisiSen microscope camera. The resultant 3D measurements are converted into 2D gradient images, which are collected by the accompanying computer software system.

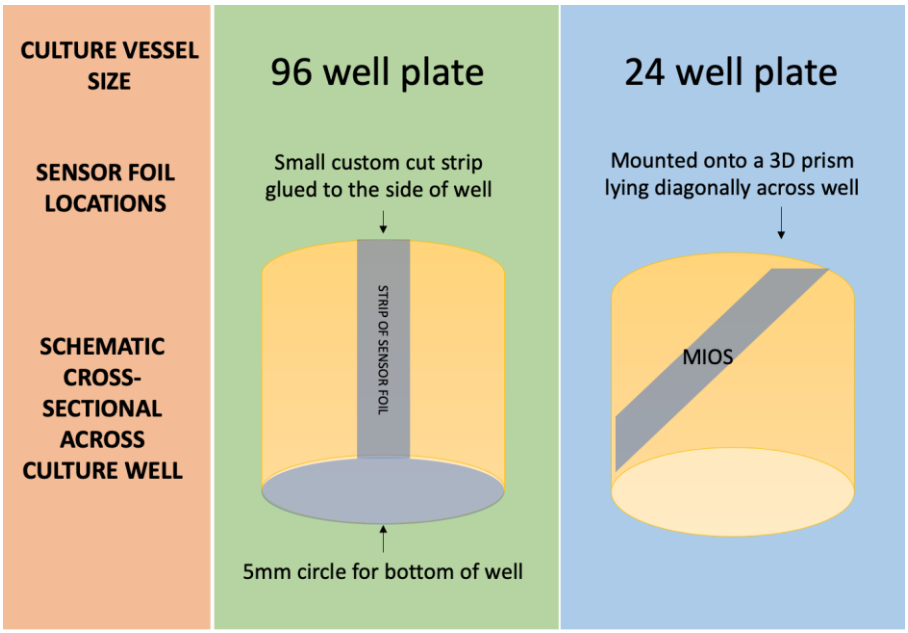

Figure 2-8 Diagram showing the setup of the two types of oxygen sensor foils used in this thesis for the measurement of oxygen gradient within cell culture vessels.

Calibration for the sensor foils was performed according to the manufacturer's guidance, using concentrated sodium sulfite solution (Honeywell Fluka, #31454-500G) and air as 0% and 21% oxygen saturations respectively.

2.3.3 Dynamic vs static oxygen pre-conditioning

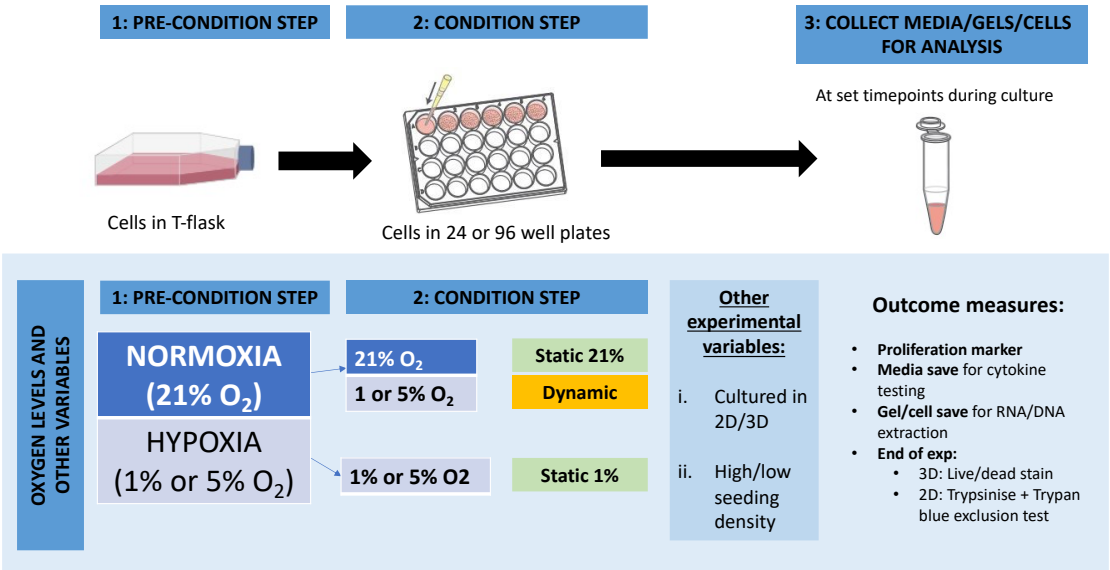

Figure 2-9. Schematic diagram of experimental flow in varying oxygen conditions with different experimental setup and their associated outcome measurements. Step 1. pre-conditioning of cells in T-flask and then 2. conditioning of cells in well-plates in different oxygen concentrations. Other experimental variables are also included at the point of seeding the cells onto well plates as shown in the yellow highlighted box. 3. At various set timepoints, analysis on cell proliferation, viability, gene and cytokine profiles will be performed.

To determine the cellular response to different oxygen levels, the experimental setup is as shown in Figure 2-9. Cells were expanded at either normoxia (21% O2) or hypoxia (5% or 1% O_2) in appropriate T-flasks. At confluency, the cells were transferred to 24 or 96 plates at either high or low seeding densities (see Table 2.2 for details). They were either seeded in 3D hydrogel as described in 2.2.1, or in 2D with the same number of cells as the 3D scaffold-free counterparts for comparative control and 2D cell culture analysis.

Outcome measures for the experimental timepoints were:

i. Viability assays for measure of cell proliferation and viability (sections 2.4.3)
ii. Media save for analysis of VEGF cytokine levels (section 2.6.1)

iii. 3D hydrogel and 2D cell save (section 2.4.2) for further RNA/DNA extraction (section 2.6.2) for PCR and DNA level measurements to determine cell numbers;

iv. End of experiment cell viability analysis using live/dead stain for 3D hydrogels (section 2.4.3.2) and trypan blue exclusion test and fold increase calculations for cells cultured in 2D (section 2.1.5 and 0).

2.4 Comparing 2D to 3D Culture

2.4.1 Seeding density in 2D/3D culture

Set experimental timepoints were 2, 4, 6, 12, 24, 48 and 72 hours for the shorten 3 day experiment and 1, 3, 5, 7, 10, 14, 21 days for the extended experiment.

Collagen hydrogels were cultured for various time-points in a humidified incubator set at 37°C (with different oxygen settings – see Figure 2-9) with media changes every 4-5 days unless media was saved for cytokine analysis. In such cases, the media was removed and replaced. Media from hydrogels which were due to be saved for further analysis were not changed for at least 24 hours prior to collection. This is to ensure an accurate representation of cytokine factor release concentrations from the cells.

In 2D culture, cells were seeded in 6 well plates at a seeding density of 1500/cm^2. In 3D culture, cells were seeded in 24 or 96 well plates at a seeding density of 200,000 cells/ml. (Table 2.2) All cell seeding densities were optimised from previous historical data in our lab.

2.4.2 Collection of 3D hydrogel and 2D cell from well-plates

For RNA and DNA extraction future experiments, as described later in this chapter, cells seeded either in 3D hydrogels or 2D directly onto the wells were collected at various timepoints. 175µl of Tri-reagent (Sigma-Aldrich, # T9424) was added to each

well in a 96 well plate or 350µl for a 24 well plate. The fluid was subsequently aspirated and transferred to a DNA/RNA free microcentrifuge tube (Eppendorf, # 022363344). The collection samples were snap frozen using liquid nitrogen before storage in the -80°C freezer to await for further analysis.

2.4.3 Viability, proliferation and growth kinetics

2.4.3.1 Trypan blue method in 2D culture

As described above in section 2.1.3, the trypan blue method determines the viability index, where cells are designated as either viable or non-viable. The index was expressed as a % of viable cells in a population: Viability index = (number of viable cells/total number of cells) × 100.

2.4.3.2 Live/Dead Assay in 3D and TE scaffold culture

Samples were washed with PBS (Sigma, # D8537-500ml) and incubated with live/dead stain (ThermoFisher Scientific, USA, # L3224) working solution composing of 2 µM calcein AM (acetoxymethyl) and 4 µM ethidium homodimer-1 (ED-1) at humidified 37 °C and 5% CO_2 incubator for 30 minutes followed by washing in the dark. Samples were observed under an inverted fluorescence microscope (Leica DMI4000b or Zeiss Axio Observer Z1 with ApoTome) analysed using FIJI image analysis software. Live cells would be stained with calcein AM, producing green fluorescence at an excited wavelength of 485 ± 10 nm, and dead cells would be stained with ED-1, emitting red fluorescence at 530 ± 12.5 nm.

2.4.3.3 Viability assay in 3D and TE scaffold culture

RealTime-Glo (Promega, # G97112) is a non-terminal ATP-independent metabolic assay measuring the viability of cells through the reduction of the metabolic (MT) cell viability pro-substrate. (Figure 2-10) The uniqueness of this assay is the ability to have a continuous read-out of measurements without lysing of the cells, unlike similar end-point assays such as Celltitre-Glo 3D (Promega, UK, # G9681). As such,

Realtime-glo can provide indirect longitudinal data for cell activity and proliferation as markers of cell health and viability. This continuous reading is possible with regular media changes containing the pro-substrate and luciferase enzyme every 72 hours, in accordance with the manufacturer's guidance.

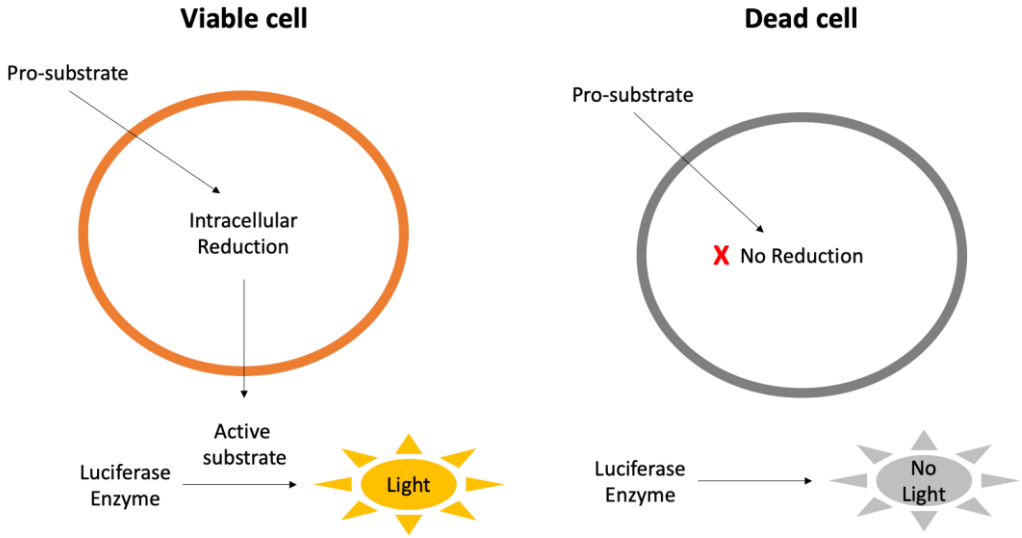

Figure 2-10 Realtime-glo cell viability assay overview, adapted from Duellman et al. (263)

Cells were seeded either directly onto the well (2D), within collagen hydrogel (3D) or INTEGRA®scaffold. Sterile white plates with clear bottoms (Corning, #3610) were used. Empty wells were positioned between each sample to ensure minimal bleeding of luminescence signals between samples. Realtime-glo solution was prepared as per manufacturer's protocol and 100ul of the substrate and pro-substrate was added to each well.

Luminescence was measured as relative light units (RLU) is measured with the TECAN infinite 200pro luminometer with 1000ms integration time with heated plate temperature set at 37.5°C to ensure no changes in metabolic activity due to temperature variations. A linearity test was performed to determine the optimum peak for the measurement of RLU for each time point. Biological triplicates of samples were used for each condition. An acellular control for every condition was used and the final calculations were normalised to the averaged control value.

To measure cell proliferation capacity from one-time point to another, the fold difference in RLU readings was calculated using the following formula:

$$\text{Fold difference} = C(n)/C(n-1)$$

Where:
C(n) = RLU reading at a given time point
C(n-1) = RLU reading at a previous time point of the same experimental group

2.5 Lentiviral transduction protocol for cells

The following details the protocol for transduction of target cells (MSC) in this study with zsGreen fluorescent protein and firefly luciferase reporter gene using lentiviral transfer vector.

Expanding lentiviral plasmid vector

Plasmid pHIV-Luc-ZsGreen was gifted from Bryan Welm's laboratory (Addgene plasmid # 39196) via the Addgene repository website. It was generated by cloning Luc2P (firefly luciferase) into the EcoRI and XbaI sites of pHIV-ZsGreen (Addgene Plasmid #18121).

The plasmid of interest was inoculated onto agar plates to allow for the growth of the bacteria-containing plasmid. To expand the plasmid for use, the bacterial stabs from the agar culture were inoculated into LB broth media, with added Ampicillin (Fisher Scientific, #10193433) at a concentration of 100ug/ml, and allowed to culture overnight in an incubator shaker (37°C at 210-230 RPM) until suitably cloudy in appearance. The LB culture was transferred into conical containers and centrifuged at 3600g for 20mins. Qiagen HiSpeed Maxi kit (Qiagen, # 12663) was used to extract plasmid from the pelleted by following the manufacturer's protocol. To determine the yield, dsDNA concentration was determined by Nanodrop UV spectrophotometry at 260 nm, with an aim of the A260 readings between 0.1 and 1.0. For long-term storage, plasmids are stored in sterile 25% glycerol stock in -80°C freezer.

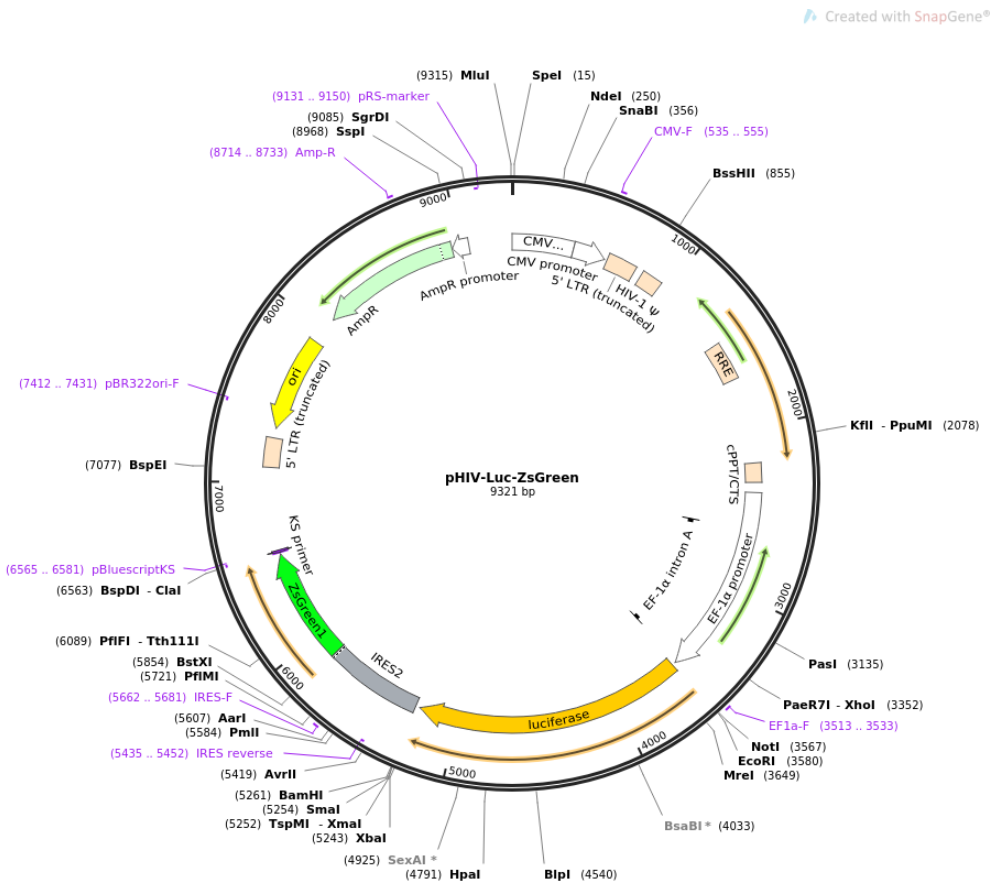

Figure 2-11 pHIV-Luc-ZsGreen plasmid sequence shown as an image. (Addgene plasmid # 39196 from Bryan Welm's laboratory)

<u>Lentivirus production using 293T packaging cells</u>

293T cells (gifted from Krishna Kolluri's lab) were cultured on T175 flask using DMEM media (Gibco™, #41965039; High glucose with L-glutamine) with 10% FBS and 1% Penicillin-Streptomycin (Gibco™, #15140122) until 80-90% confluent.

On the day of transfection, the transfection complex solution is prepared in advance. It comprises of a DNA solution and a polyethyenimine (PEI) transfection solution, which are prepared separately. The DNA solution contains lenti-vector plasmid (containing transgene of interest), Gag/Pol packaging plasmid and VSV-G envelope plasmid to make a second-generation lentiviral vector. These plasmid were gifted by Krishna Kolluri from Professor Sam Janes' lab at UCL Rayne Institute. They are diluted and sterile-filtered in 1ml of 150mM NaCl solution. Details of the plasmids for DNA solution are as follows:

a) Lenti-vector plasmid (20ug, 12KB, as above)
b) Gag/Pol packaging plasmid (13ug, pCMV-dR8.74)
c) VSV-G envelope plasmid (7ug, pMD2.G)

80ul of JetPEI® transfection solution (Polyplus Transfection, #101-10N) added to 1ml of 150mM NaCl solution and sterile filtered. The NaCl/PEI solution was added to the NaCl/DNA solution at a 1:1 volume ratio, vortexed for 10 seconds and allowed to incubate at room temperature for 20 minutes. The NaCl/DNA/PEI solution was added to 13ml of DMEM culture media used on the 293T cells. Media from the 293T cells was replaced with the NaCl/DNA/PEI/DMEM transfection complex media and allowed to incubate for 4 hours at 37°C CO_2 incubator. The transfection complex media was replaced with fresh DMEM culture media as above and allowed to incubate overnight before another media change the following morning. After 48 hours post-transfection, the media from the 293T cells can be harvested for viral supernatant. Media was collected first centrifuged for 10 minutes at 300g to remove any detached cells. The supernatant was filtered using 45um filters and transferred to a sterilise ultracentrifuge tubes and ultracentrifuged at 50,000g in 4°C for 2 hours. The supernatant was discarded and 100ul of cold Opti-mem media (Gibco™, #31985070) was added, and the tubes were allowed to incubate on ice for 1 hour. The viral pellet was resuspended using P10 pipette and aliquoted into 20ul or 40ul suspensions, which can be stored at -80°C for long-term use.

Lentiviral Vectors Titration by Flow Cytometry

The viral titre was determined using flow cytometry using 293T cells. 75,000 cells were plated into each well of a 6-well plate by adding 2ml of cell suspension from 525,000 cells diluted in 14 mL of DMEM culture media into each well. The plate was incubated overnight. The lentiviral aliquot by agitating in a 37°C warm water bath. Dilutions of the lentivirus was performed by using DMEM culture media and adding 10 µg/mL of Polybrene (Sigma-Aldrich, #TR-1003-G; 10mg/ml) as shown in Figure 2-12.

Dilution	Volume of Lentivirus Stock (µL)	Volume of DMEM complete (µL)	Volume of 10mg/mL polybrene (µL)
1:10	150	1348.5	1.5
1:25	60	1438.5	1.5
1:50	30	1468.5	1.5
1:75	20	1478.5	1.5
1:100	15	1483.5	1.5

Figure 2-12 Viral dilution table used for viral titre experiment

After overnight incubation step, media was aspirated from the cells in each well, and 1.5 mL of a viral dilution was added to each well and allowed to incubate for 48 to 72 hours. Wells containing only polybrene and cells with no virus or containing no polybrene, only cells, were included for cell counting and control. After incubation, the media was aspirated, and the wells are rinse with 1 mL of PBS. To detach the cells from the well, 0.5 ml of 1X TrypLE Express was added to each well and incubated in a CO_2 incubator for 2 minutes. 1 ml of DMEM was added to each well and mixed by gently pipetting up and down. The cell suspension was transferred to a correspondingly labelled 15 ml tube and centrifuged at 1000 rpm at room temperature for 3 minutes. The supernatant was carefully removed, and the remaining cell pellet was washed with 2 ml of PBS. The cells were centrifuged again at 1000 rpm and the PBS removed. The cells were re-suspended in 0.4 ml of fresh PBS and transferred into flow cytometry tubes. Flow cytometry analysis was performed using non-infected cells as a negative control. The percentage of fluorescent-positive cells was calculated for each well. When calculating titre, only wells with less than 40% fluorescent-positive cells was considered. This is because this method assumes one integration event per cell. When the percentage exceeds 40% there is a risk counting cells with multiple integration events leading to underestimation of the true titre value.

$$\text{Viral titre}\left(\frac{\text{TU}}{\text{ml}}\right) = \frac{\%\ \text{positive cell}\ \times\ \text{no. of cells plated}}{\text{vol. of virus added (in ul)}}$$

Where TU = transduction unit.

Transduction of MSC

MSC of interest was cultured in T175 flask as described in section 2.1.1. To prepare for transduction, an ideal multiplicity of infection (MOI) was first calculated. MOI is defined as the ratio of viral particles to target cells. (i.e. an MOI of 10 would be 10 million viruses to 1 million cells) To work out the ideal MOI for the target cells, cells are plated in a 12 well plate with 50,000 cells per well, and a range of different MOIs (i.e. different concentrations of viral particles and polybrene with media to cells plated) are introduced to each well. We used a range of 0.1 - 10 MOI. Polybrene (Sigma-Aldrich, #TR-1003-G; 10mg/ml) was diluted to a concentration of 10ug/ml and 5ug/ml for use in viral transduction. The cells were incubated overnight. The plates were checked for the percentage of GFP+ cells using both fluorescent microscopy and flow cytometry. Ideal MOI was determined by the minimum MOI required for 100% transduction (i.e. 100% GFP+ cells).

To transduce MSC, media was removed from the culture flask and replaced with MEMα culture media (Gibco, #32561029) and polybrene at a concentration of 5 µg/ml for pre-treatment for 5 minutes, followed by 12ml medium/12 µl polybrene/viral volume of ideal MOI calculated above. The transduction complex was allowed to incubate with the cells for 24 hours at 37°C. The cells were cell-sorted using fluorescence-activated cell sorting (FACS) method for GFP+ labelled cells as a marker for positive transduction. The resultant transduced cells were subsequently expanded to be used in the study for *in vitro* and *in vivo* tracking.

2.5.1 Monitoring and tracking of cells using D-luciferin and transduced MSC

Evaluation of cells using D-luciferin on transfected cells with luciferase reporter gene is valuable as a predictor of viability, metabolic activity and proliferation capacity over time.

Luciferase in metabolically active cells would break down D-luciferin to oxyluciferin, producing light in the process. This light emission (Luminescence) can be measured by a luminometer (TECAN infinite 200pro), chemiluminescent or bioluminescent imaging system (i.e. Tecan ChemiDoc or IVIS) as described in Section 2.8.3 and Chapter 4 and 6. To measure *in vitro* bioluminescent of transduced cells, twenty minutes prior to imaging, culture media was exchanged for 100ul media containing 150 µg/ml (15µl/ml) D-luciferin (# 360222, Regis Technologies Inc., USA) in the multi-well plates. Luminescence was measured as relative light units (RLU) is measured with the TECAN infinite 200pro luminometer (see section 2.4.3.3 for detailed protocol). For *in vivo* applications, see Chapter 6 for more detail.

2.6 Molecular Biology

All molecular biology protocols are outlined below. Extreme care was taken to prevent RNAse and DNAse contamination by using molecular grade reagents and consumables, particularly for PCR related techniques.

2.6.1 Cytokine Response from ELISA Assay

Media samples were saved at various time points at -20°C until ready for protein analysis of vascular endothelial growth factors (VEGF). Enzyme Linked Immunosorbent assay (ELISA) kits were purchased from R&D systems (Abingdon, #SVE00).

Media samples were thawed at room temperature. The protocol for the ELISA assays was carefully followed using the manufacturer's guidelines.

	Assay Diluent	Sample standard	Conjugate	Substrate solution	Stop solution
VEGF	50µl	200µl-2hrs	200µl-2hrs	200µl- 20mins	50µl

Table 2.4 Protein levels were quantified using ELISA. ELISA kits for VEGF (generic). The table shows the solution volumes and incubation timings used for each solution for the assays.

The resultant ELISA plates were placed on the CLARIOstar Plus plate reader (BMG LABTECH, Germany) to measure the colour absorbance set at 450nm with wavelength correction set at 570nm. The readings for the standards were used to plot a standard curve. VEGF standard curve is shown in the Appendix Figure 1. By means of interpolation using information from the standard curve, all sample readings were converted into pg/ml for analysis via the GraphPad Prism 9 software.

2.6.2 RNA and DNA Extraction from cells and tissue

RNA and DNA extraction was performed using phenol-based Tri-Reagent (Sigma-Aldrich, #T9424) phase separation method. Tri-Reagent is also commonly known as Trizol.

For 2D monolayer culture, media was removed, and the cells were washed once with ice cold PBS. PBS was aspirated and 200-400ul of Tri-Reagent (Sigma-Aldrich, #T9424) was added depending on size of well plate. The resultant Tri-Reagent mixed solution was aspirated and placed in labelled 1.5ml DNA LoBind centrifuge tubes (Eppendorf, # 0030108051). For 3D hydrogel and INTEGRA®samples, the media was removal and a one time ice cold PBS wash was performed per sample. Each sample was carefully placed into a 1.5ml PCR clean centrifuge tube followed by the addition of 400ul of Tri-Reagent solution to each sample. 3D hydrogels were processed using QIAshredder (Qiagen, # 79654) microcentrifuge spin-column homogeniser by following manufacturer's guidance. The TE scaffold samples were homogenised using mechanical homogeniser (Stuart®, Cole-Parmer, # ST1500) with single use disposable probes (Stuart®, Cole-Parmer, # ST1501) to reduce cross contamination. After thoroughly mixing, extracts were kept at −80 °C until RNA/DNA from all samples was extracted.

2.6.2.1 RNA isolation

After thawing Tri-Reagent extracts, chloroform (MP Biomedicals, # 0219400225) was added at 1:5 (v/v), and RNA was separated from DNA and proteins by multiple centrifugation and pipetting steps. The chloroform/tri-reagent mix was briefly vortexed

for 15 seconds. The samples were then centrifuged for 15 minutes at 13000 rpm at 4°C to allow for phase separation of the solution. (Figure 2-13A) The RNA (clear aqueous) layer was clearly aspirated with small RNase and DNase free low retention pipette tips with filters, between 10-100ul sizes (Starlab UK, #S1181-3810), without disturbing the interphase layer. Pipette tips were changed between samples to prevent cross contamination. If the starting sample is anticipated to be small (<106 cells or <10 mg of tissue), 5–10 µg of RNase-free molecular grade glycogen (Thermo Scientific™, #R0561) was added as a carrier to the aqueous phase to aid RNA pellet isolation later. The carefully aspirated RNA layer was placed into a new 1.5ml Eppendorf tubes with 175ul ice cold isopropanol (Fisher BioReagents™, #11388461) and vortex for 15 seconds. The tubes were centrifuged for 15 minutes at 13000 rpm at 4°C. The supernatant was aspirated with extreme caution not to touch RNA pellet at the bottom, which would appear slightly opaque. The pellet was subjected to three ethanol wash steps: 500ul ice cold 100% ethanol (Honeywell, #E7023-500ML) and centrifuged at 13000 rpm for 10 minutes at 4°C. The supernatant was aspirated and followed by another 500ml ice cold 70% ethanol wash (100% ethanol above diluted with molecular grade distilled water) and centrifuge as above, and the steps are repeated again with a final ice cold 100% ethanol wash and centrifuge. The steps were altered for hydrogels to 2 step ethanol washes to avoid loss of RNA pellet. The resultant pellet was allowed to airdry for 5-10 minutes. The pellet was resuspended in 25-50ul of distilled RNAse free water (Sigma Aldrich, #W3513-100ML). A summary of the steps are illustrated in Figure 2-13B. The samples are kept at -80°C until further evaluation.

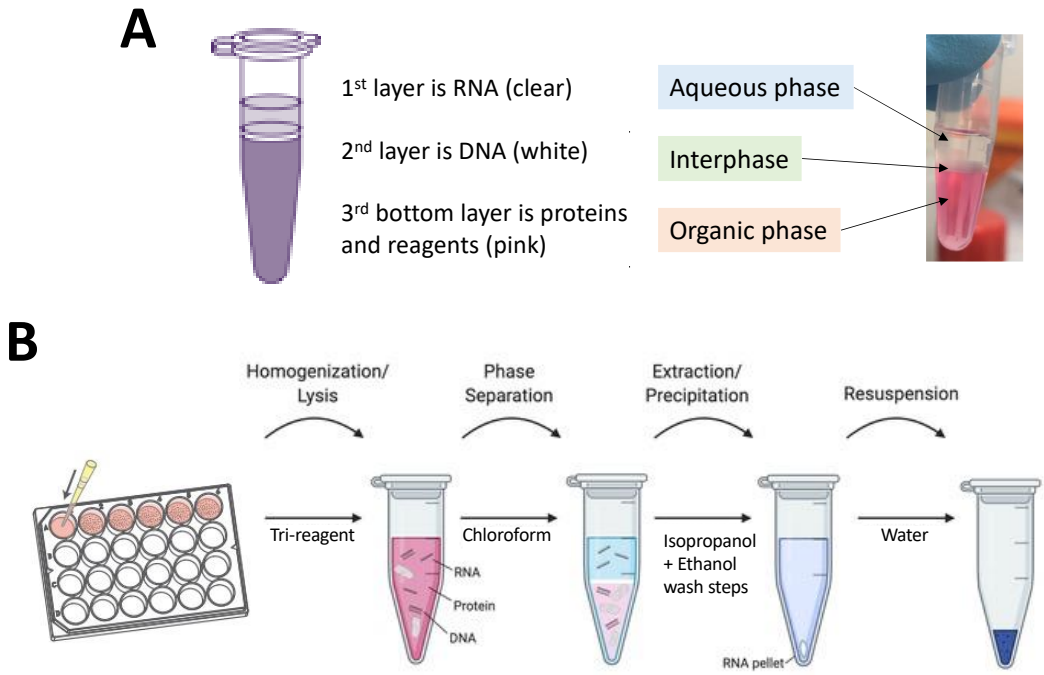

Figure 2-13 (A) Phase separation of the sample in Tri-reagent solution after the addition of chloroform. The top aqueous phase contains RNA, followed by the middle interphase layer of DNA and finally with the bottom organic phase layer made up of mainly proteins and lipids. (B) Schematic diagram showing the RNA extraction steps, which was adapted from the Addgene protocol website (264).

2.6.2.2 RNA Quantification

After RNA pellet was resuspended in distilled RNAse free water (Sigma Aldrich, #W3513-100ML), NanoDrop 1000 spectrophotometer (Thermo Fisher Scientific, USA) was used to evaluate the RNA concentration and purity. Concentration of RNA was recorded in ng/ul and the ratio OD 260/280 were noted for purity. RNA samples with an absorbance ratio OD 260/280 between 1.8–2.1 were used for further analysis. To run the qPCR experiment, the minimum concentration of RNA sample required is at least 40ng/ul per transcription reaction.

2.6.2.3 DNA isolation

Following on from the RNA extraction in section 2.6.2.1, after removal of the aqueous (chloroform) phase after phase separation, 300ul of 100% ethanol was added to the inter and organic phase later and pipetted up and down to mix. The sample was briefly centrifuged for 5 minutes at 2000 rpm and then centrifuged for 30 minutes at

maximum rpm of machine. Supernatant was removed and resuspend in 500ul of 0.1 M sodium citrate (Sigma-Aldrich, # 567446-100GM) in 10% ethanol (100% ethanol above diluted with molecular grade distilled water) adjusted to pH 8.5. The sample mixture was centrifuged for 30 minutes at 13000 rpm, followed by two short 5 minutes at 2000 rpm. The pellet was resuspend in 500 ul of 75% ethanol and centrifuged again for 5 minutes at 2000 rpm. The supernatant removed and allowed to airdry. The pellet was resuspend in 50 ul of 8 mM sodium hydroxide (Sigma-Aldrich, #72068-100ML) and centrifuged a final time for 10 minutes at 12000 rpm. The supernatant was transferred to a fresh PCR clean 200ul centrifuge tube (Starlab UK, #I1402-4300).

2.6.2.4 DNA Quantification

DNA quantification was carried out using PicoGreen dsDNA quantitation kit (Invitrogen Molecular Probes, #P-7589). The protocol for the assay was carefully followed using the manufacturer's guidelines and adapted to low DNA standard (50 ng/ml; 1:1000 of λ DNA stock) protocol (265). Reagents were prepared using manufacturer's protocol and kept away from light. 100ul of blank, DNA standard dilutions and samples were added to the wells of a white 96-well plate (Corning, #3610) in duplicates. 100ul of the PicoGreen working solution was added to each well. The sample was mixed well and incubated at room temperature for 5 minutes protected from light. The fluorescence readings were measured using CLARIOstar Plus plate reader (BMG LABTECH, Germany) at 485 nm excitation and 538 nm emission wavelength. The standard curve was created and used to calculate the DNA concentration of the samples. (see Appendix Figure 2)

2.6.3 Complementary DNA (cDNA) Transcription

Single-stranded cDNA was synthesised from 400ng of total RNA in a final volume of 10 µL. For this purpose, the High-Capacity cDNA Reverse Transcription Kit (Applied Biosystems™, #4368814) was used and the manufacturer's instructions were followed. Each reaction volume was made up of the mixture shown in Table 2.5, and placed in PCR microtubes (Starlab UK, #I1402-4300). The tubes were vortexed and

spun briefly in a mini-centrifuge and placed into the Bio-Rad T100 Thermal Cycler (Bio-Rad Laboratories, UK) using the protocol shown in Table 2.5. The resultant cDNA transcribed was stored at −20 °C.

cDNA Transcription: Master Mix per reaction	**T100 Thermal Cycler Protocol**
10 uL of sample RNA (in water containing at least 40ng/ul) + **2.0uL** 10 x RTB Buffer **0.8uL** 25 x dNTP Mix (100mM) **2.0uL** 10 x RT random primers **1.0uL** Multiscribe RTase **4.2uL** nuclease free water **Master Mix (MM)** Total reaction volume = **20ul**	Transcription reaction volume: 20 uL Step 1: 25°C (10 minutes), Step 2: 37°C (120 minutes), Step 3: 85°C (5 minutes), Step 4: 4°C (Infinite hold)

Table 2.5 cDNA transcription conditions. LEFT: Measurements of reagents for master mix (MM) and sample RNA solution to make up 20ul of reaction volume. RIGHT: Bio-Rad T100 Thermal Cycler protocol steps used.

2.6.4 Quantitative Reverse Transcription PCR (qRT-PCR)

Quantitative PCR (qPCR) was carried out using on a CFX96TM Touch System with Bio-Rad CFX Manager software (Bio-Rad Laboratories, UK). The reactions were performed in triplicates with iTaq Universal SYBR Green Supermix (Bio-Rad Laboratories, #1725121) using the manufacturer's instructions. The final reaction volume was 10uL as shown in Table 2.6, which consist of 20 ng cDNA and 0.2 µM forward and 0.2 µM reverse primers. Using 10ul low retention pipette tips, 9ul of master mix solution and 1ul of cDNA was placed into each well of the 96 well white clear bottom PCR plate (Bio-Rad Laboratories, #HSP9601) which was kept cool using IsoFreeze® PCR cooler rack (Alpha Laboratories, # LW5990P). The plate was cover with Microseal® PCR Plate Sealing Film (Bio-Rad Laboratories, #MSC1001) and spun using a PCR plate spinner at top speed for a few seconds. The amplification program on a CFX96TM Touch System is shown in Table 2.6. The temperature cycles between 95°C, to allow for DNA denaturation, followed by annealing and elongation step at 60/65°C.

After amplification, an additional thermal denaturising cycle (temperature ranged between 65 °C and 95 °C in 0.5 °C increments) was performed to obtain the melting

curves of the qPCR products and verify amplification specificity. To confirm product specificity, a melting curve analysis was performed after each amplification. The relative expression of each gene in the samples was calculated on the basis of a four-fold serially diluted standard curve derived from a pool of all the cDNA samples. This calculation of fold change was done using ΔCt and $2^{-\Delta\Delta Ct}$ methods (266,267) which normalises to a reference gene. Reference genes glyceraldehyde 3-phosphate dehydrogenase (GAPDH), an enzyme responsible for breaking down of glucose, was chosen with primers for this gene taken from literature (268). Primer sequences used are shown in Appendix Figure 3.

iTaqTM Universal SYBR® Green Supermix	**qPCR Protocol**
5uL SYBR **1uL** Forward Primer **1uL** Reverse Primer **2uL** H20 + **1uL** cDNA Master Mix (MM) Total reaction volume = **10uL**	Step 1: 95°C (30 minutes) Step 2: 95°C (5minutes)* Step 3: 60°C (30 minutes)* Step 4: 95°C (10 minutes)* Step 5: 65°C (5 minutes)* (*Repeat Steps 2 - 5 x 39 cycles) Step 6 (Final 40th Cycle): 95/0.5°C (-)

Table 2.6 qPCR conditions. LEFT: Measurements of reagents for master mix (MM) and sample cDNA solution to make up 10ul of reaction volume. RIGHT: Bio-Rad CFX96TM CFX Manager software qPCR protocol steps.

2.6.5 Primer design and efficiency calculations

RT-qPCR primer efficiency was tested for each primer pair using 10-fold serial dilutions of cDNA chosen among the samples. The mean threshold cycle (Ct) values for each serial dilution were plotted against the logarithm of the cDNA dilution factor. RT-qPCR primer efficiencies were calculated using the following equation:

$$E=((10-1slope)-1)*100$$

The efficiency of all designed primer pairs ranged from 80% to 110%, which is considered the optimal efficiency value.

2.7 Histology

Cell samples for histology are fixed in 4% paraformaldehyde (PFA) solution (Merck, Germany, # 1039991000) for 1 hour at room temperature. The plates are washed twice with PBS. The cells are then stained according to the staining protocol of each product.

Sections of *in vivo* tissue samples for histology were fixed in 4% PFA solution (Merck, Germany, Cat. No. 1039991000) or prefilled 10% formalin solution container (Richard-Allan Scientific, US; #59601) for 6-12 hours at room temperature, depending on the thickness of the sample. They were sent for histological processing using conventional techniques at the associated UCL/Yale histology laboratories for paraffin embedding and Haematoxylin & Eosin (H&E) staining. The paraffin-embedded blocks were sectioned at 4-6um thickness onto glass slides.

Prior to immunohistochemistry (IHC) staining, the slides are de-paraffinised and rehydrated with xylene and ethanol steps as follows. To deparaffinise, 3 washes with xylene at 5 minutes each was performed in a fume hood. This was followed by a decreasing concentration of ethanol to steadily rehydrate the tissue sample. Each ethanol wash step was performed twice at 10 minutes each. The first ethanol wash was at 100% followed by 95%, 70% and finally 50%. The last step comprises of 2 wash steps with deionized water at 5 minutes each.

An antigen retrieval protocol specific to the antibody stain was used with heat-induced antigen retrieval using a water bath and buffer. The sections are stained with routine or immunohistochemistry stains which will be described in further detail in the relevant chapters.

2.8 Imaging

2.8.1 Light Microscopy

Brightfield microscopy for cell culture vessels was carried out using EVOS M5000 Imaging System (Invitrogen, Thermo Fisher Scientific) Brightfield microscopy for the histological section was carried out with NanoZoomer 2.0-HT scanner (Hamamatsu Photonics K.K.). Fluorescence microscopy was carried out using Zeiss Axio Observer with ApoTome (Carl Zeiss Microscopy GmbH, Germany).

2.8.2 Scanning Electron Microscopy (SEM)

Samples were fixed in 2.5 % glutaraldehyde (Agar Scientific, #R1020) in 0.1M sodium cacodylate (no calcium) for 1 hour at room temperature. The samples were washed three times for 30 minutes with 0.1M sodum cacodylate buffer and gentle dehydration steps were performed with serial dilution in ethanol (10%, 30%, 50%, 70%, 85%, 95%, 100%). The samples were transferred to baskets put through the Balzers CPD 030 Critical Point Dryer (UK) and mounted on a stub to be coated with gold in a sputter coater (Quorum Q150T ES). Samples were analysed with JEOL JSM-6700F (Japan) SEM machine at an accelerating voltage of 5 kV.

2.8.3 Bioluminescent Imaging

Bioluminescent imaging (BLI) was performed using IVIS Lumina Series III Pre-Clinical In Vivo Imaging System (IVIS; Caliper Life Sciences Inc., USA) as previously described. (269) Living Image version 4.3.1 software (Caliper Life Sciences Inc., USA) was used for image analysis. It generated pseudocolored, scaled images overlaid upon grey scale images of the well-plates containing the seeded scaffolds, which provides 2D localisation of the source of light emission. Regions of interest (ROI) were selected using shape drawing tools, and light emission within the ROI was quantified in photons per second. ROI shapes were kept constant for each time-point measurement. This bioluminensence assay allows for tracking and monitoring of seeded transduced MSC with firefly luciferase reporter gene.

2.9 Statistical analysis

Statistical analysis was done using Microsoft Excel and Graph Pad Prism 9 software. Data were reported as mean ± standard deviation (SD), unless otherwise stated. Where appropriate, a normality test was carried out on the data sets to establish if it is normally distributed. This will help determine the most suitable statistical analysis to carry out later (i.e. parametric versus non-parametric test).

One-way analysis of variance (ANOVA) or a Kruskal-Wallis test (for non-parametric data) was used to test for differences between groups. To test for differences between multiple independent groups, a two-way ANOVA was used. Post-hoc tests (Tukey's test for parametric data or if data non-parametric, the Bonferroni test) were used to identify which group comparisons had significant differences. For categorical/nominal data between 2 outcome variables, Chi-square test was used.

Results were considered statistically significant for *p-value* < 0.05. Statistical significance was demonstrated on the graphs with asterisk. The number of asterisks would correspond to the appropriate p-value. (Table 1.1)

P value	Symbol
< 0.0001	****
0.0001 to 0.001	***
0.001 to 0.01	**
0.01 to 0.05	*
≥ 0.05	ns

Table 2.7 P-value was its corresponding symbol as denoted by number of asterisk or non-significant (ns) wording.

3 Cells in Dynamic Hypoxic Pre-Conditioning Environment

3.1 Introduction

MSC are found in most adult tissues (38). The advantages of being able to easily isolate and expand these cells in adult tissues makes these cells one of the most commonly used cell types in translational pre-clinical and clinical studies. Previous studies have shown the therapeutic potential of MSC when combined with biomaterials in wound healing (270,271). The large cohort of publications on MSC therapeutic benefits and associated safety track records adds to the appeal of using these cells for translational and tissue-engineering research.

The most prevalent and well-studied source of MSC are those from the bone marrow. This adult MSC source has been studied intensively and has the most pre-clinical and translatable evidence in published research. However, the process of harvesting this tissue is highly invasive. Hence sourcing MSC from less invasive sources, such as discarded medical waste in neonatal umbilical cord MSC which can be derived from all layers of the umbilical cord (Wharton's jelly, perivascular, membrane/sub-amnion region) and adult adipose MSC from surgical lipoaspirates, is more desirable (272,273). These alternative MSC sources have a collective advantage of potentially higher yield of harvest due to the abundance of tissue sources with little ethical concerns. The pro and cons of each cell type are listed in Table 3.1.

bmMSC	ucMSC	adMSC
Autologous and allogenic source possible	Allogenic source only	Autologous and allogenic source possible
Invasive collection from bone marrow	Easy, non-invasive collection	Invasive collection from lipoaspirate or from discarded adipose tissue from plastic surgery
Ethics will be more stringent due to morbidity from collection	Less ethical concerns with use	Ethics will be stringent due to morbidity from collection, but concerns will be less due to discarded nature of tissue collected
Limited expansion before cell senescence	Foetal in origin; they have a higher proliferation capacity than bmMSC or adMSC	Limited expansion before cell senescence
Lower cell yield which is age dependent	High cell yield	High cell yield due to larger quantities of tissue which can be harvested
Characteristic of cells vary and often decline with donor's age	Characteristics of cells are similar due to primitive nature and standard age of neonatal donors at the time of collection	Characteristics of cells may vary according to site of harvest.
Most widely studied and translatable MSC cell type	Growing body of research into its translatability	Growing body of research into its translatability due to abundance of autologous tissue source
Long history of use in clinical trials compared to other counterparts	More pre-clinical data but less clinical trials devoted to the therapeutic use of this cell type compared to bmMSCs	Similar to ucMSC, but more translatable clinical data due to the current use of autologous fat transfer techniques in surgery
Immunomodulatory capacity is widely researched	Similar and sometimes greater reported immunomodulatory capacity	Growing evidence of immunomodulation capacity
Shown to be immune evasive	Lower immunogenicity	Shown to be immune evasive

Table 3.1 Comparative list of pros and cons of using compared to bone marrow (bmMSC), umbilical cord (ucMSC) and adipose derived MSC (adMSC) for translational research from review articles (274–277).

Despite the multiple tissue sources of MSC, they all uniquely possess desirable characteristics including self-renewal, mesenchymal differentiation potential and immunomodulatory properties. MSC are also known to exhibit different cellular and therapeutic properties in relation to their original tissue source (278). Hence, a thorough pre-clinical study to evaluate of the angiogenic potential of MSC from various tissue sources is important to ensure the appropriate cell type used in the development of future therapeutic strategies.

3.1.1 The rationale of dynamic hypoxia

The literature review featured in Chapter 1 eluded to the many studies published on the hypoxic effects on cells, particularly MSC. Different cell types respond differently to their oxygen microenvironments (279). Therefore, it is important to pre-determine the effect of different levels of low oxygen on mesenchymal stem cells in view of evaluating its therapeutic potential.

Hypoxia can be defined as physiological and pathological. (see Figure 1-4) As mentioned previously in Chapter 1, physiologically cells are usually not exposed to such high levels of oxygen; cells in our tissues are normally reside between 1 - 14% O_2 (74,279). The microenvironmental niche of different MSC have been shown to reside in tissues that are physiologically low in oxygen tension. Bone marrow oxygen environments have been shown to vary between 1 - 7% and between 3-11% for adipose tissues (75–77,280). Oxygen tension in umbilical cords has been found to be lower than in the bone marrow from historic studies, with reported pO_2 between 1.3 - 2.6% in the umbilical artery and 12.3 -16.9% in the umbilical vein (281), but data is confounded with oxygen measurements at birth, which is not representative of oxygen concentration during gestation (78). Culturing cells in oxygen tension that more closely resembles the native *in vivo* microenvironment can have several positive effects. As early as 1958, studies have described some cells proliferating more rapidly in oxygen tensions that are lower than atmospheric levels (65,79). More recent studies have also shown that culturing cells under lower oxygen tensions increase self-renewal, multipotency, proliferation rate and potential as well as cell survival (63,80,81). In other words, physiological hypoxia has been shown to have an overall positive effect on cells (82,83).

	pO2 (mmHg)	**pO2 (% saturation)**	**Ref.**
Air	160	20.9	
Arterial blood	100	13.2	(78)
Venous blood	40	5.3	(78)
Cell	9.9 - 19	1.3 - 2.7	(282)
Skin	8 - 35	1.1 - 4.6	(283)
Adipose	22 - 115	3 - 15	(76,280)
Bone marrow	8 - 49	1 .1– 6.4	(75,77)
Umbilical vein	25 - 35	12.3 - 16.9	(281)
Umbilical artery	10 - 20	1.3 - 2.6	(281)

Table 3.2 Normal physiological pO2 levels in different human tissue microenvironments pertinent to the cell types studied in this thesis, expressed in mmHg and percentage of oxygen.

However, several studies have shown that the tumour environment is exposed to much lower oxygen tensions (<1%) which trigger the tumour's angiogenic response (112,284,285). This is thought to be due to the hypoxic stress response from the tumour cells driving the HIF response. This form of pathological hypoxia is defined as the oxygen level below the physiological levels in the normal tissue environment (20–100 mmHg). Such levels of hypoxia are known to be a stimulus and trigger for pro-angiogenic response from cells (73).

As mentioned in Chapter 1, the chronological stability of HIF-1α in different oxygen environments is not certain. Under normoxic conditions of atmospheric oxygen levels, HIF-1α is known to have a very short half-life of less than 5 minutes and is highly unstable as it is generally rapidly degraded in the presence of oxygen (99,150,151). Hypoxia can increase the half-life, allowing for its accumulation and the formation of the HRE complexes within the cell nucleus. (see Figure 1-6B in Chapter 1) This allows for the perseveration of the downstream HIF-1α effects on cellular activity. The rate of degradation and how the hypoxia and variations in oxygen tension on cells has been the focus of much research (152). In recent studies, intermittent hypoxia (hours to days) has been shown to increase HIF-1α activity by stabilising the expression in the initial period, as previously discussed in Chapter 1 (157).

Hence, to stimulate and recapitulate the desired pro-angiogenic hypoxic response from these cells, it would be necessary to bring the oxygen levels to lower than their physiological niche, without causing significant undesirable effects. Additionally, to test the effects of intermittent hypoxia, a unique 'dynamic hypoxia' regime will be optimised and examined with the aim of translating this hypoxic culturing process into the later pre-clinical tissue engineering section of the thesis.

For the purposes of determining the ideal pro-angiogenic hypoxic levels (physiological versus pathological), oxygen levels of 5% and 1% are chosen in the following experiments as they satisfy the three different types of MSC for the defined parameters of physiological and pathology hypoxia. (see Table 3.2 for reference values)

Hypothesis:

A regimen of dynamic hypoxia (DH) will simulate MSC to secrete more angiogenic factors via hypoxic-mediated pathways

Aim:

1. To compare different MSC cell sources and determine the most suitable type of MSC sources with the best pro-angiogenic potential in view of their translatability

2. To determine the optimal oxygen pre-conditioning regime which would produce the highest level of angiogenic paracrine response without compromising the proliferation rate of seeded cells

3.2 Materials and Methods

3.2.1 Comparing different MSC sources

MSC from the umbilical cord, bone marrow and adipose tissue were isolated as described in Chapter 2, Section 2.1. To compare the different MSC sources, cells were characterised using laboratory methods and assays detailed in Chapter 2, Section 2.1. Each primary cell source was passaged from P0 to P7 for the purposes of characterisation.

The list below summarises the different *in vitro* comparisons made to the MSC 2D cultures:

- Morphology was observed and recorded using microscopy techniques
- Cell surface markers are analysed using flow cytometry
- Multipotency of cells were determined via tri-lineage differentiation
- Proliferation rate of cells in 6 well plates

- Clonogenicity of cells were determined using Colony Forming Unit (CFU) capacity assay
- The angiogenic potential of the cells was determined by measuring VEGF cytokine from ELISA technique

In addition, ASC52telo immortalised hTERT adMSC isolated from a human donor was also purchased for use from ATCC (ATCC, SCRC-4000™). They were initially plated as per the manufacturer's instruction, but subsequent culture conditions were as described below.

3.2.2 Dynamic oxygen conditioning

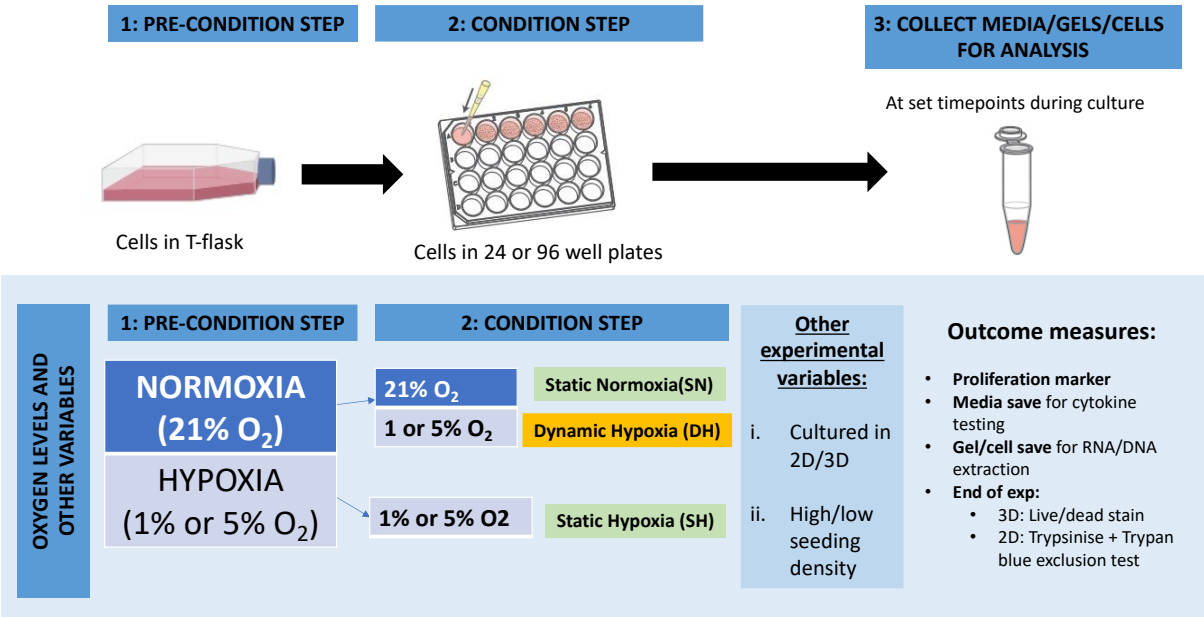

Figure 3-1. Schematic diagram of experimental flow in varying oxygen conditions with different experimental setup and their associated outcome measurements. Step 1. pre-conditioning of cells in T-flask and then 2. conditioning of cells in well-plates in different oxygen concentrations. Other experimental variables are also included at the point of seeding the cells onto well plates as shown in the yellow highlighted box. 3. At various set timepoints, analysis on cell proliferation, viability, gene and cytokine profiles will be performed.

To determine the cellular response to different oxygen levels, the experimental setup is as shown in Figure 3-1. Cells were expanded at either normoxia (21% O2) or hypoxia (1% O_2) in an appropriate T-flasks. At confluency, the cells were transferred to 24 or 96 plates, with cells seeded either in 3D hydrogel as described in 2.2.1, or in 2D with the same number of cells as the 3D scaffold-free counterparts for

comparative control and 2D cell culture analysis. From this point on, the seeded cells were conditioned in different oxygen environments as follows:

I. Static 21%; static normoxia (SN),
II. Dynamic 21-1%; dynamic hypoxia (DH)
III. Static 1%/5%; static hypoxia (SH).

The justification for the downstream oxygen conditioning environments suggested above will be discussed further in Section 3.3.1.3.2 of this chapter.

<u>Outcome measures for the experimental timepoints were:</u>

v. Measurement of cell proliferation and viability;
vi. Analysis of VEGF cytokine levels released into media;
vii. 3D hydrogel and 2D cell save for further RNA/DNA extraction for PCR and DNA level measurements to determine cell numbers;
viii. End of experiment cell viability analysis using live/dead stain for 3D hydrogels trypan blue exclusion test and fold increase calculations for cells cultured in 2D.

3.2.2.1 Continuous measurement of *in vitro* vertical oxygen gradient using VisiSens MIOS tool

To determine the exact oxygen parameters over time and through different incubator settings from incubator atmospheric air to media down to the cells, the MIOS oxygen sensor plate system (PreSens Precision GmbH, Germany) was used. The prototype VisiSens unit (VisiSensTD, PreSens Precision GmbH, Germany) was used to measure continuous readout of oxygen levels through the media and 3D hydrogel, and a detailed experimental setup is described in Chapter 2, Section 2.3.2.

Cells were seeded in hydrogel (50,000 cells per gel) and compared with a control acellular gel. The oxygen levels were measured at different time points with a continuous measurement of 45 minutes to a few hours each time. The gradient reading was divided into 3 main sections, top, middle and bottom and a separate

reading through the middle of the 3D hydrogel. The readings were averaged over 10 measurements for that time point in each separate section of the well. The averaged readings were plotted onto a graph over time. The top readings would represent the hypoxic chamber's atmospheric oxygen saturation, the middle readings would represent the section around the top of the media (at the atmospheric air/media) interface and the bottom reading would be considered peri-hydrogel layer. Readings for the middle of media was added to help capture the oxygen saturations around the middle of the media and the hydrogel interface.

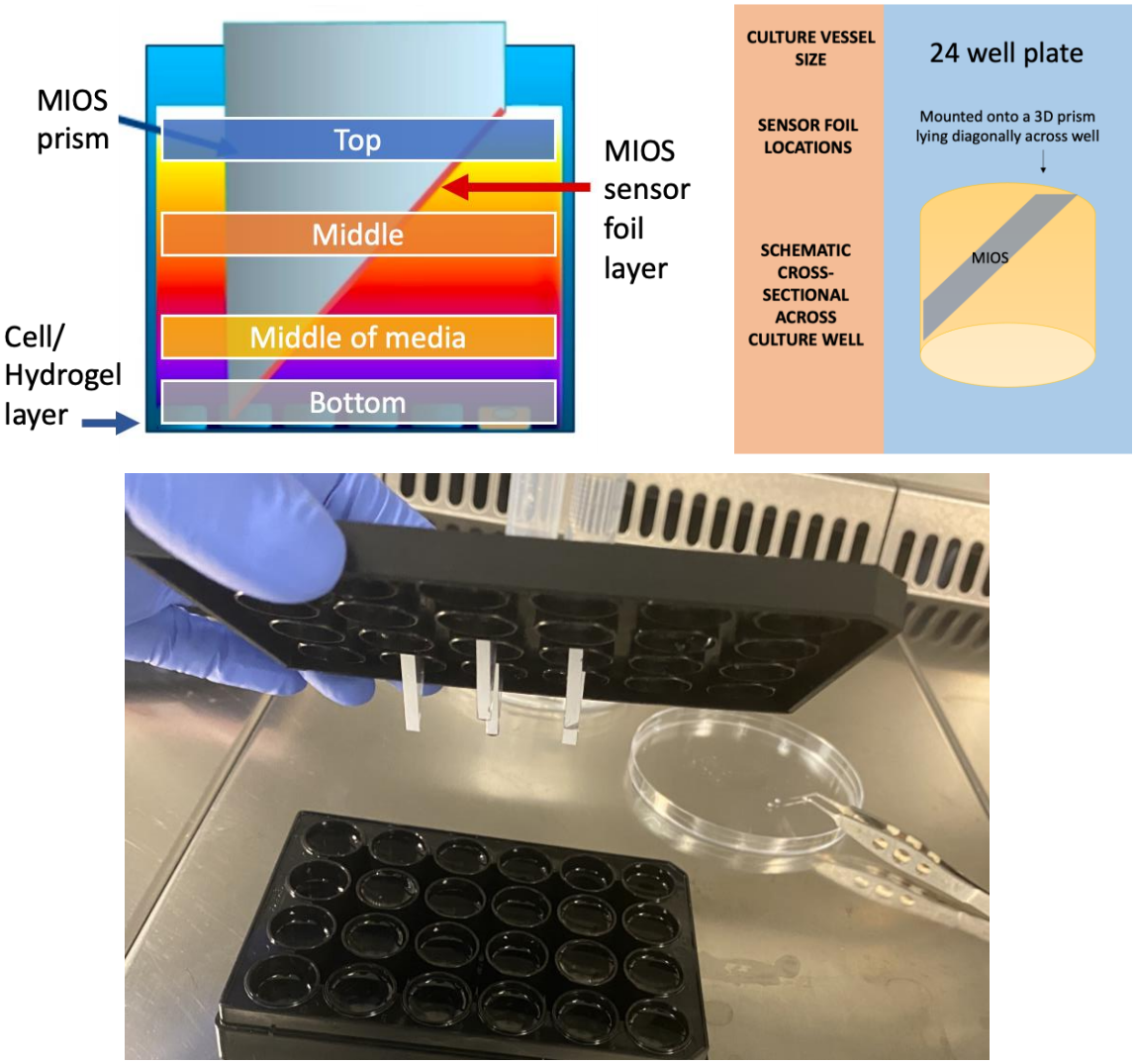

Figure 3-2 Cross-sectional diagram (top left) and schematic illustration (top right) through a culture well with MIOS sensor in situ (red coloured edge). The key sections for measurements are shown on the left image. The bottom image shows the MIOS sensor well plate system with the sensor foils (white layer) located on the side of the 3D prism inserts. (see Section 2.3.2 for detailed description of the setup).

3.2.2.2 Effects of oxygen levels on cell proliferation, viability and VEGF production

Cells were seeded at a seeding density of 14,400 cells per well in a 6 well plate for each time point and were cultured in parallel. At defined time points (Day 1,3,5,7), cells from one plate of 6 well plate were trypsinised and counted using a haemocytometer with trypan blue exclusion method. Countess™ II automated cell counter (Invitrogen, Life Technologies Corporation) with Chamber Slides (#C10228, Invitrogen, Life Technologies Corporation) was also used to validate the accuracy of the automated system against the manual haemocytometer method.

To evaluate cell metabolism and monitor activity/proliferation over time, cell counting using a haemocytometer and automated methods, DNA analysis together with cell viability assays (Realtime-glo) were performed as described in Chapter 2.

To better understand how VEGF production per cell is effected by exposure to different oxygen conditions, the VEGF concentration (pg/ml) measured from ELISA (as described in Chapter 2) was normalised to amount of cellular DNA (ng/ml) extracted for particular timepoints in culture.

3.3 Results

3.3.1 Determining Suitable Mesenchymal Stem Cell Source for Therapeutic Angiogenesis

3.3.1.1 Measurement of oxygen levels within the hypoxic chamber using Fibox sensor

Oxygen saturation real time data collected using the PreSens oxygen monitor showed that purging suitably reduced the oxygen content within the hypoxic chamber to the desired range within two minutes (Figure 3-3). Oxygen levels were maintained

below 1% in the seal chamber for more than 4 days which is about the time when media changes occur (Figure 3-4).

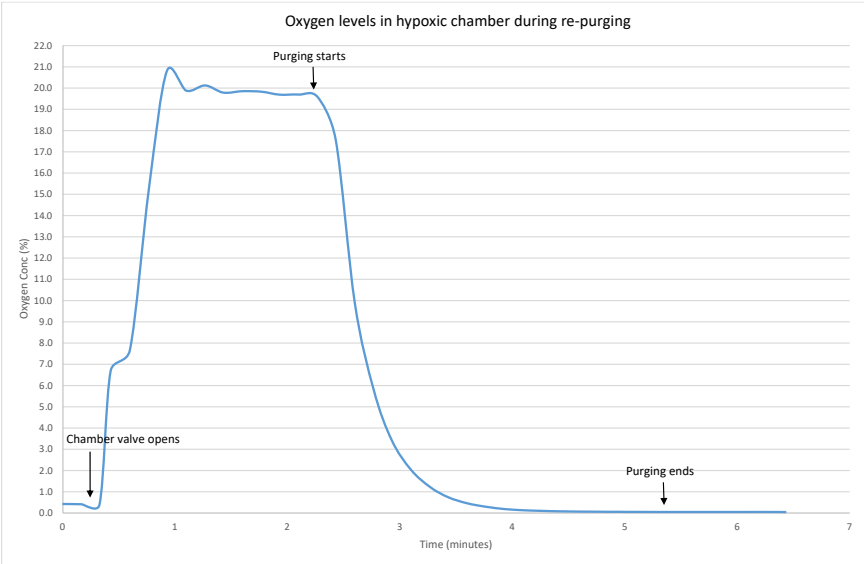

Figure 3-3 Oxygen concentration in hypoxic chamber during re-purging as measured by PreSens Fibox Oxygen Monitor. Oxygen levels deplete within two minutes of purging the chamber with 5%CO2/95%N2 mixed gas.

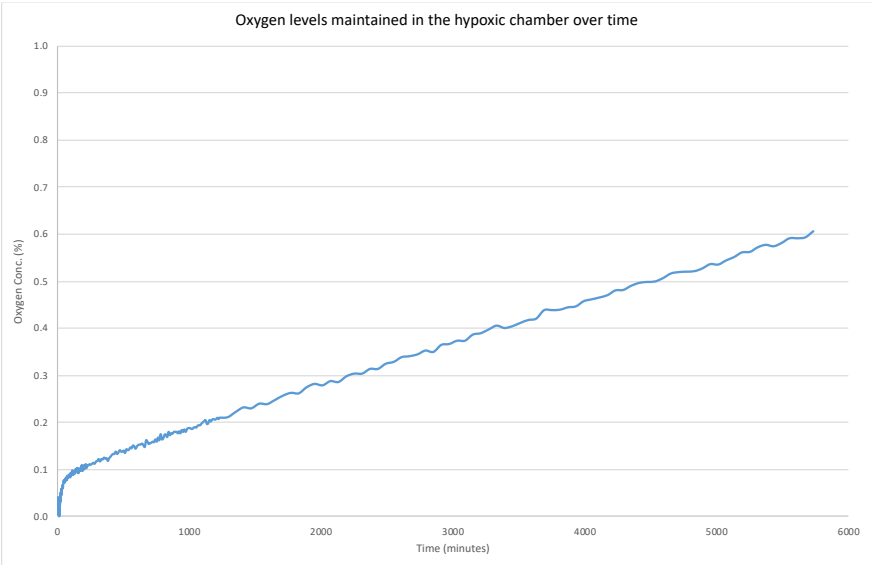

Figure 3-4 Oxygen concentrations maintained low levels of oxygen (<1%) after purging until next media change (3-4 days).

3.3.1.2 Characterisation of MSC

3.3.1.2.1 Detection of cell surface markers

Cell surface markers were determined by flow cytometry of known positive and negative cell surface markers which define MSC. The analysis of bmMSC and adMSC (primary and cell line) all showed positive expression of cell surface markers for CD90, CD73, CD105 (excess of 93% for all groups) and negative markers for CD19, CD34, CD11b, CD45 and HLA DR as shown in Figure 3-5, Figure 3-6 and Figure 3-7. For ucMSC, they were clinical grade and have been tested thoroughly by the Royal Free PD lab, which showed more than 95% of the cells expressed the antigens CD105 (98.98%), CD73 (99.75%), and CD90 (99.97%) with the same cells lacking (<2% positive) expression of CD45, CD34, CD14, CD19, and HLA-DR consistently throughout all donor sets. (Data not shown) Compensation and FMO control was performed for each marker.

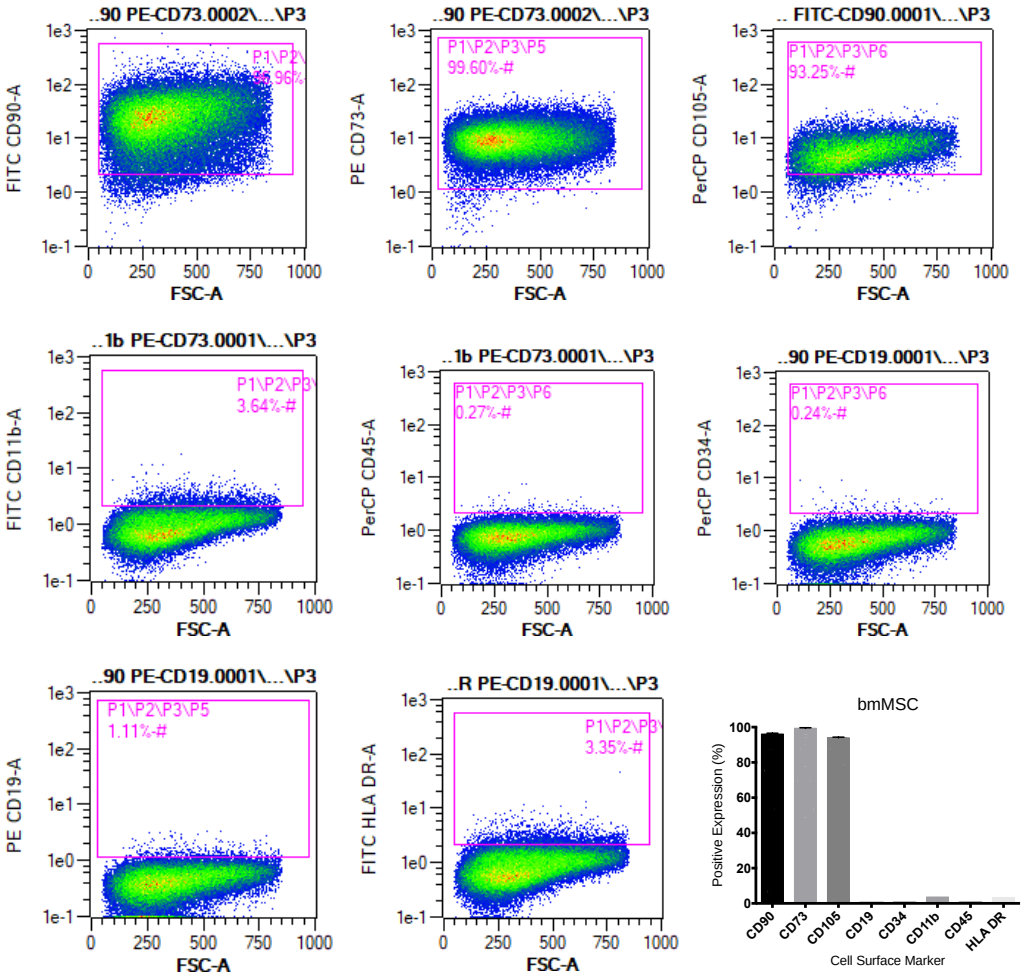

Figure 3-5 Flow cytometry dot plots for P3 bmMSC showing cells with positive markers in the purple highlighted box. Graphical profile of cell surface epitopes of P3 bmMSC. Results displayed as means ± SE of donor samples.

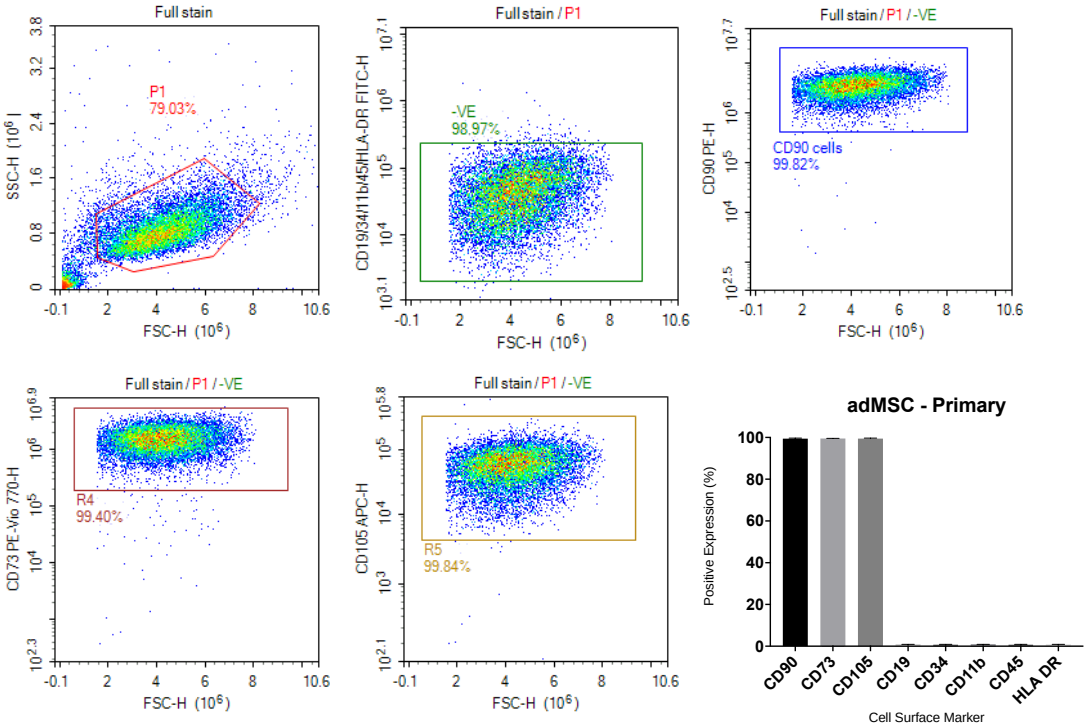

Figure 3-6 Flow cytometry dot plots for P1 primary adMSC showing cells with positive markers in the purple highlighted box. Graphical profile of cell surface epitopes of P10 cell line adMSC. Results displayed as means ± SE of donor samples (n=3).

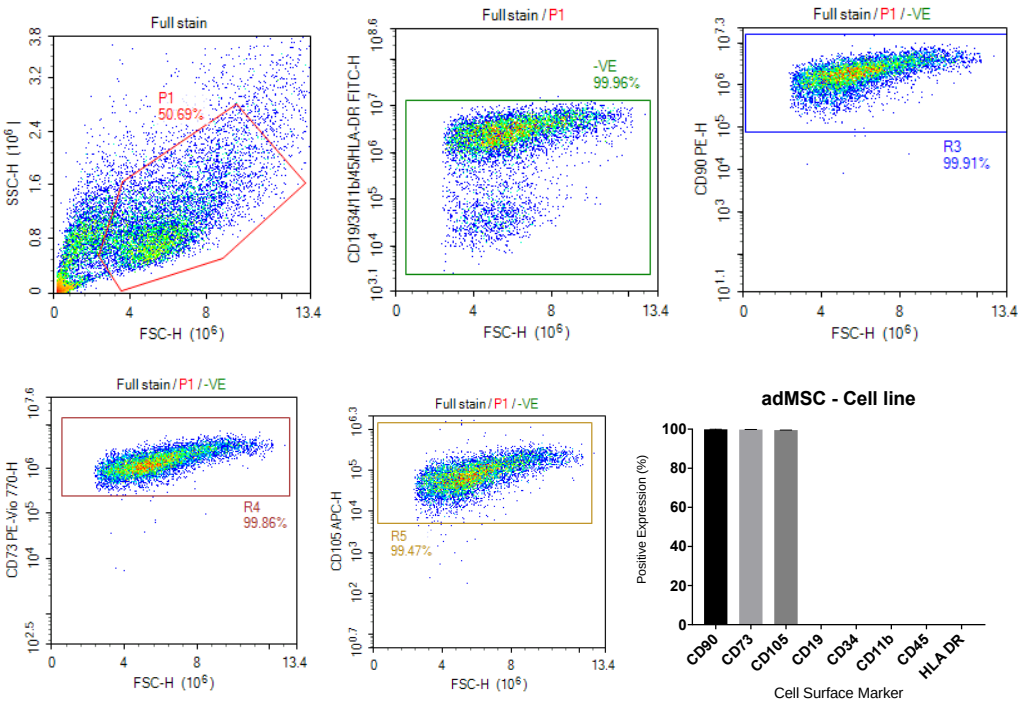

Figure 3-7 Flow cytometry dot plots for P7 immortalised cell line adMSC showing cells with positive markers in the purple highlighted box. Graphical profile of cell surface epitopes of P10 immortalised cell line adMSC. Results displayed as means ± SE of donor sample.

3.3.1.2.2 Tri-lineage differentiation of MSC

All MSC cell types: ucMSC, adMSC and bmMSC showed the ability to differentiate into adipogenic, osteogenic and chrondrogenic lineages (Figure 3-8, Figure 3-9 and Figure 3-10) when cultured in appropriate differentiation media. Phase contrast images from ucMSC were obtained from Dr Ben Weil, from Professor Mark Lowdell's group at the Royal Free Hospital, who gifted the cells for this study. Chrondrocytes from bmMSC and adMSC where positively stained with red Safranin O (see Figure 3-8A and Figure 3-9A respectively) and for ucMSC, stained blue from Alcian Blue (Figure 3-10A) after 16 days in culture. bmMSC, adMSC and ucMSC differentiated into adipose cells with lipid-filled vacuoles stained red with Oil Red O after 14 days in culture (see Figure 3-8B, Figure 3-9B and Figure 3-10B). Evidence of bmMSC differentiated osteocytes was shown from the associated alkaline phosphatase production from the osteoblast via positive blue-violet stain with BCIP-NBT solution (Figure 3-8C). Similarly, for the adMSC and ucMSC, extracellular osteoblast mineralisation was detected by the bright orange-red positive staining from Alizarin Red S within the culture. (see Figure 3-9C and Figure 3-10C) All controls (cells grown in MEMa, non-differentiating media) did not stain positive for the above. An example is shown in Figure 3-8D to demonstrate the lack of blue-violet stain with BCIP-NBT solution in the control well compared to well treated with osteogenic media.

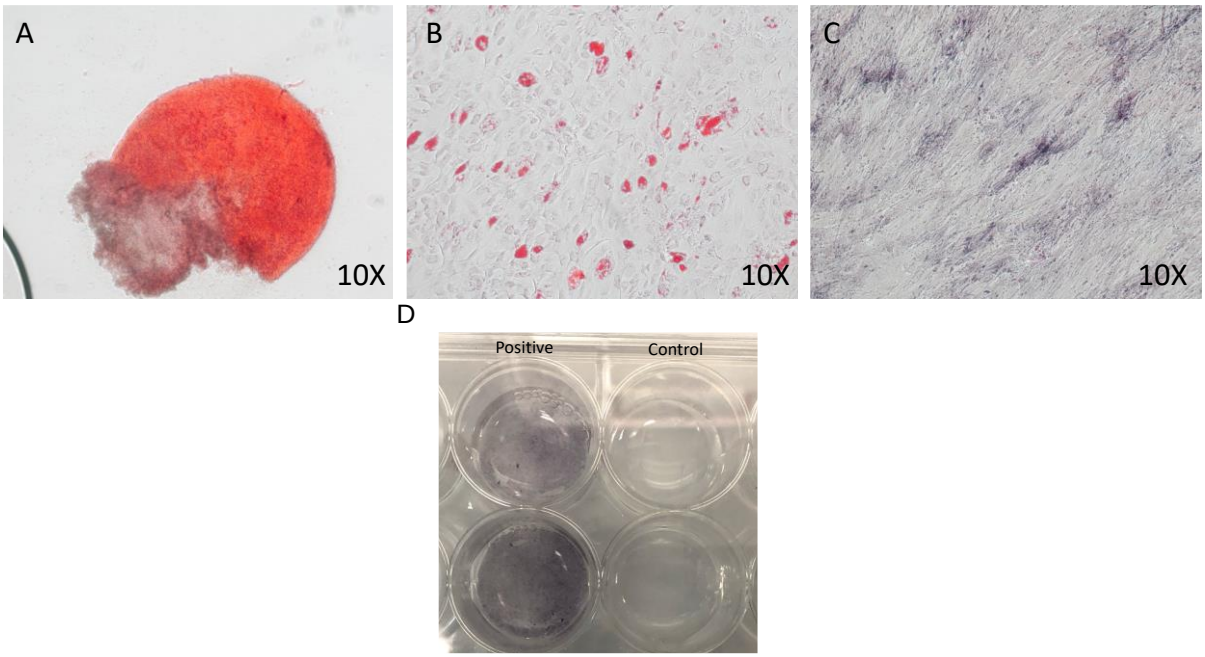

Figure 3-8 Phase contrast brightfield images showing differentiation of bmMSC to (A) chondrocyte micromass cell pellet stained with red Safranin O on a slide with coverslip, (B) adipose cells with lipid-filled vacuoles stained red with Oil Red O and (C) osteocyte matrix alkaline phosphate stained blue-violet with BCIP-NBT solution. (D) Osteocyte-associated alkaline phosphatase stained blue-violet with BCIP-NBT solution within the well-plate compared to control (bmMSC cultured in non-osteogenic media)

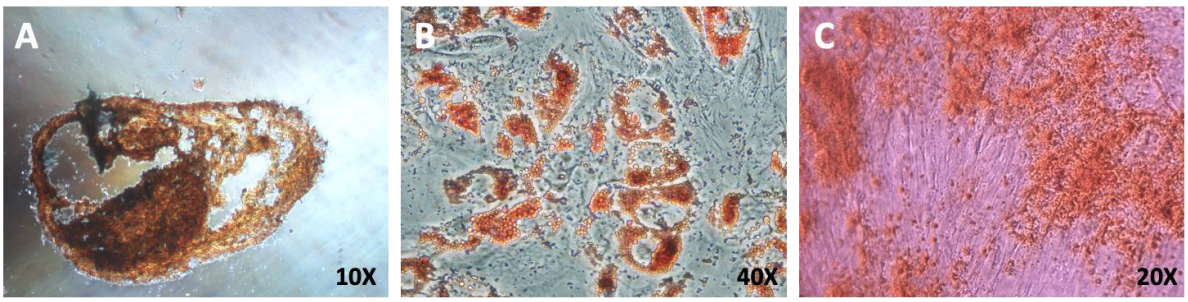

Figure 3-9 Phase contrast brightfield images of adMSC differentiating into (A) chondrocyte micromass cell pellet stained with red Safarin O on a slide (pallet lifted off the well which caused high contrast of background, affecting the visualisation of the stained micromass), (B) adipose cells with lipid-filled vacuoles stained red with Oil Red O and (C) osteocyte lineage cell matrix stained with Alizarin Red S.

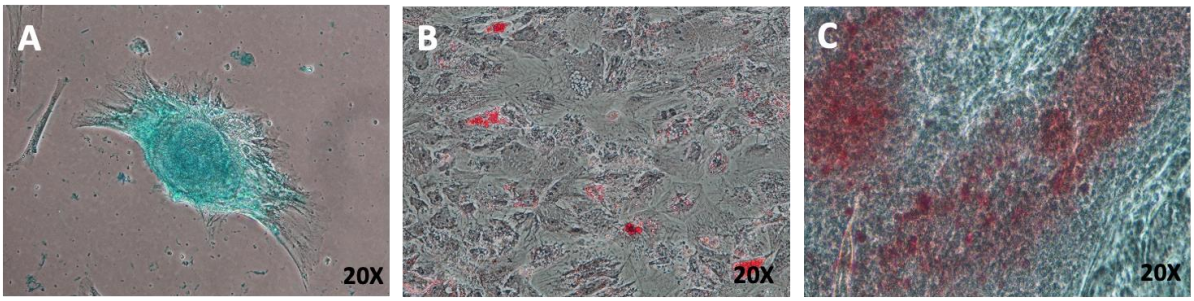

Figure 3-10 Phase contrast brightfield images of ucMSC differentiated into (A) chondrogenic micromass cell pellet stained with Alcian Blue; (B) adipocyte lipid-filled vacuoles stained with Oil Red O/HCS LipidTOX Green; (C) osteogenic lineage cell matrix stained with Alizarin Red S.

3.3.1.2.3 Cell morphology in different O2 settings

bmMSC and adMSC are morphological distinct to ucMSC as shown in Figure 3-11. bmMSC and adMSC appear fibroblastic-like, even at earlier passages, whereas ucMSC have more heterogenous cell types within the same population.

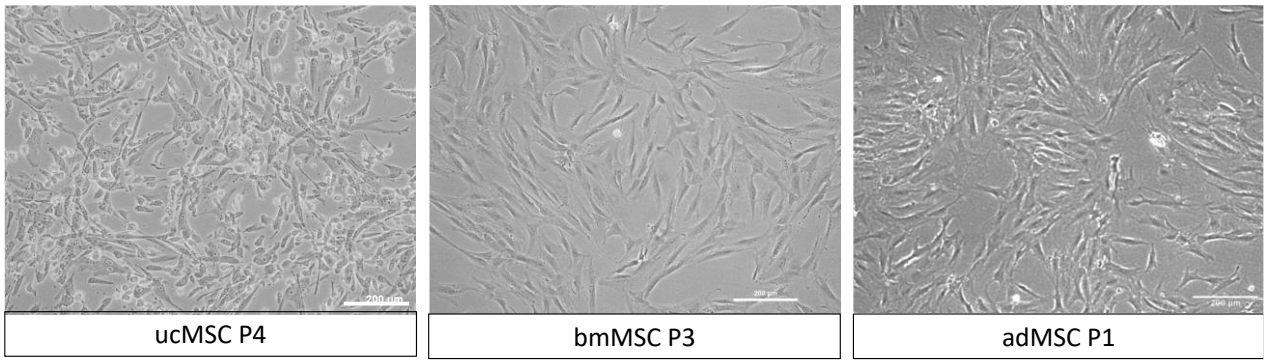

Figure 3-11 Phase contrast brightfield images showing morphological distinct appearances of ucMSC, bmMSC and adMSC at respective low passages in 21% O2 on expansion in T-flask. Scale bar = 200um.

bmMSC exposed to 1% O2 and 21% O2 during subculturing also showed morphological differences. At 80-90% confluency, hypoxically exposed bmMSC appear larger in size and appear to coalesce and overlap more than the cells in normoxia.

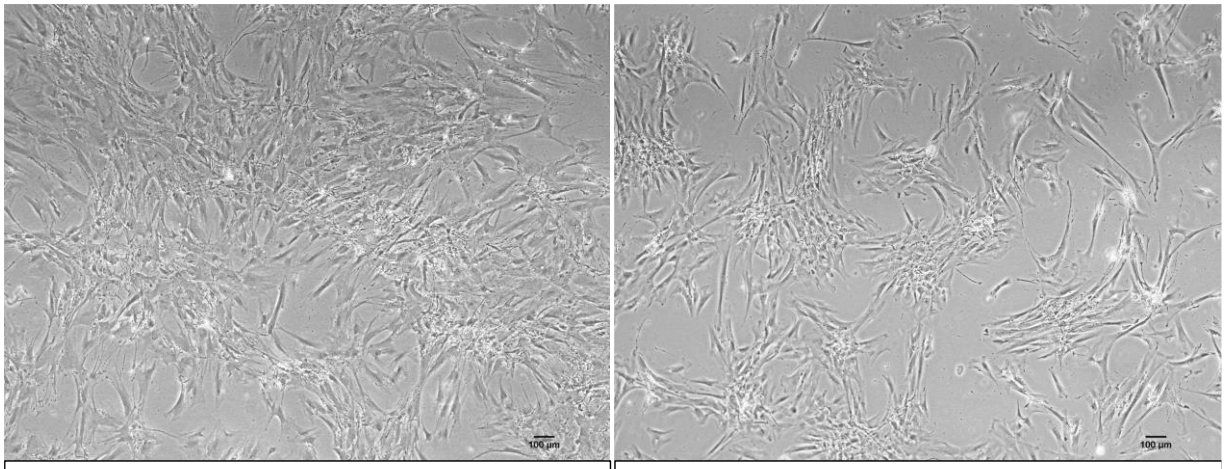

bmMSC P7 Hypoxia (1% O_2)	bmMSC P7 Normoxia (21% O_2)

Figure 3-12 Phase contrast brightfield images of bmMSC cultured in hypoxia (1% O2) compared to normoxia (21% O2) at 80-90% confluency. Scale bar = 100um.

adMSC, on the other hand, showed little morphological changes between their exposure of 1% O2 and 21% O2. At 90% confluency, their appearance was consistently fibroblastic in nature regardless of oxygen conditions.

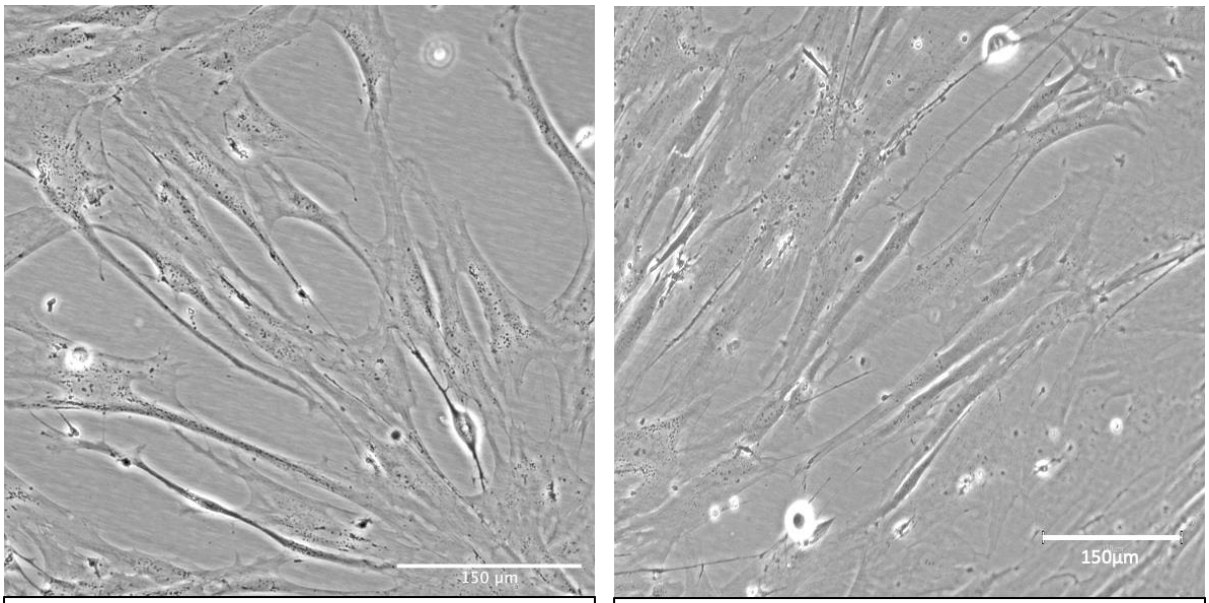

adMSC P7 in Hypoxia (1% O_2)	adMSC P7 in Normoxia (21% O_2)

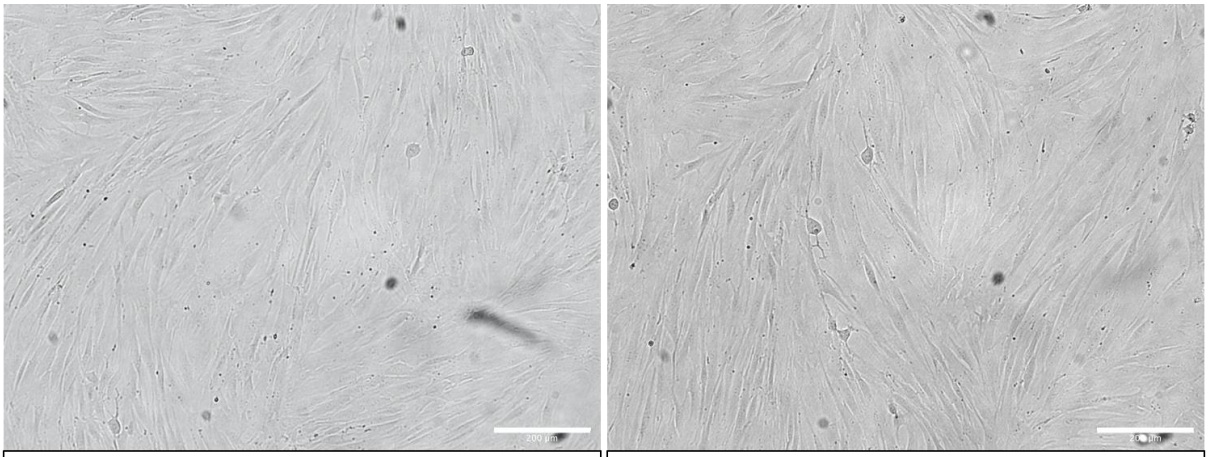

adMSC in Hypoxia (1% O_2)	adMSC in Normoxia (21% O_2)

Figure 3-13 Phase contrast brightfield images of adMSC cultured in 1% O2 and 21% O2. Top row in 10X magnification (scale bar = 150um), bottom row in 4X magnification (scale bar = 200um).

3.3.1.2.4 Proliferation profile in different O2 settings

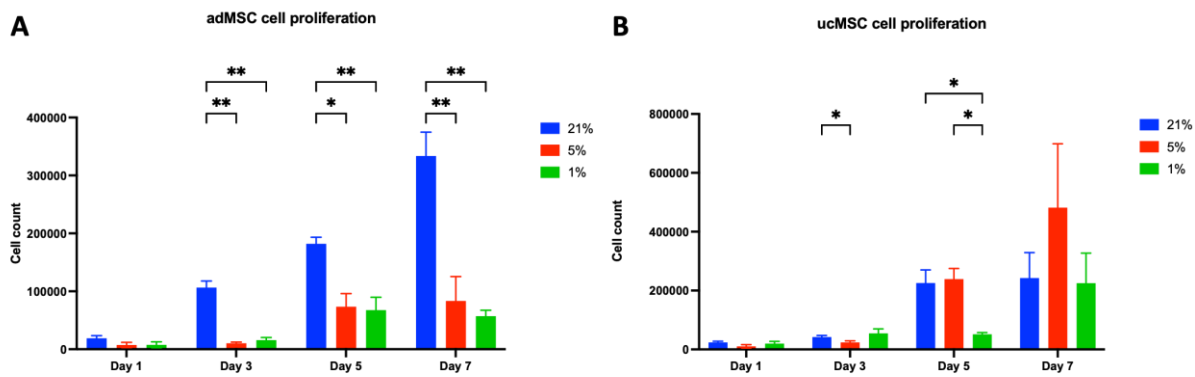

Figure 3-14 Proliferation rate of (A) adMSC and (B) ucMSC over 7 days in the different oxygen conditions. Results are displayed as mean ± standard deviation.

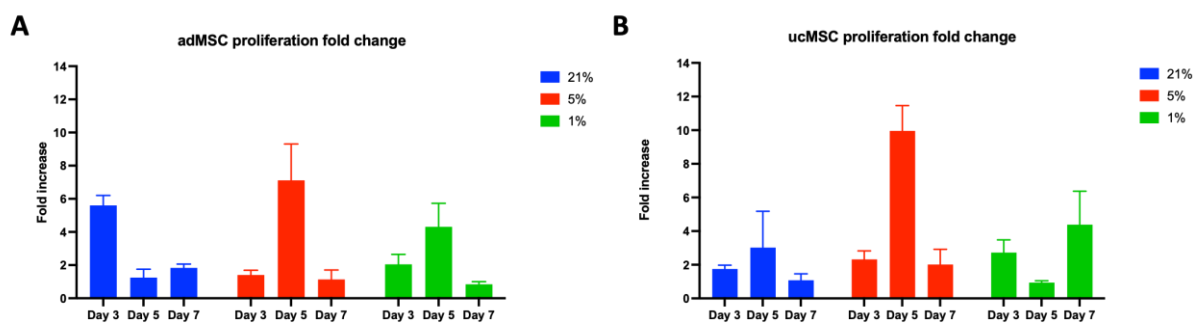

Figure 3-15 Proliferation fold increase of (A) adMSC and (B) ucMSC over 7 days in the different oxygen conditions. Each data point was compared to the value from the previous time point. Results are displayed as mean ± standard deviation.

The figures above show the proliferation rate over 7 days calculated for both ucMSC and adMSC populations in 6 well plates. There was significantly greater (four to six times more cells) absolute cell numbers on Day 7 of adMSC cultured in 21% (333,500 ± 41,307) compared to 5% (83,417 ± 42,012) and 1% (57,167 ± 10,254) culture conditions. (Figure 3-14A) A different profile was shown in the ucMSC, which showed approximately twice the cells number in the 5% oxygen condition (481,833 ± 216614) compared to 21% (242,600 ± 86242) and 1% conditions (225,167 ± 102107). (Figure 3-14B) When comparing fold-increase data, both adMSC and ucMSC showed the highest multiplication of cell numbers in 5% oxygen on Day 5 of culture. (Figure 3-15) In adMSC grown in 21% oxygen, the greatest fold increase was seen on Day 3, whereas for ucMSC in the same condition, this was seen on a slightly smaller scale on Day 5 instead. The adMSC cultured in 1% oxygen, Day 5 had the highest fold increase compared to the other days. For ucMSC in 1% oxygen, Day 7 saw the highest fold increase out of all previous days of culture.

bmMSC proliferation rate was not performed due to limited cell availability. However, population doubling time (PDT) values were plotted for bmMSC over 3 passages (P4-P6) to help give an indication of cell growth kinetics over the course of sequential cell expansion. (Figure 3-16) The results show an observable difference in the trend of the cells in different oxygen conditions, with a gradual increase in time for cells cultured in 21% compared to 5% and 1% oxygen. Cells expanded in 5% oxygen showed a more consistent PDT compared to 21% and 1% oxygen. Cells cultured in 1% oxygen demonstrated a slight increase in PDT from P4-P6.

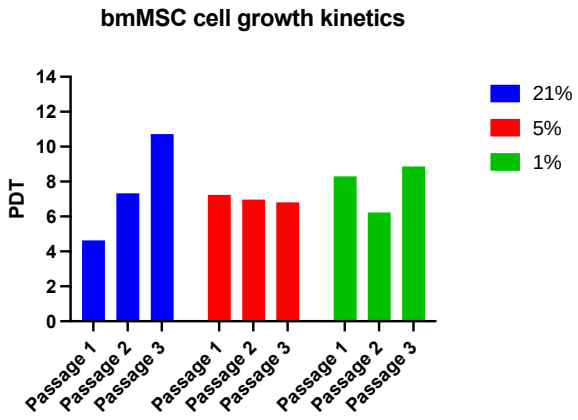

Figure 3-16 bmMSC cell growth kinetics using population doubling time (PDT) of cells growth in T-flask in different oxygen conditions over P4-6 of passage.

3.3.1.2.1 VEGF production from different cell types in different O2 settings

ELISA was performed on 72 hour conditioned media from bmMSC in 2D T-flask, which showed significantly more VEGF levels found in the media of cells cultured in 1% and 5% hypoxia (1702.4 ± 43.4 pg/ml and 1672.8 ± 189.3 pg/ml respectively) compared to cells cultured in normoxia (21% O2; 1113.0 ± 57.6 pg/ml). This was found to be statistically significant. (Figure 3-17) Comparing bmMSC and adMSC, the amount of VEGF levels was significantly higher in the adMSC compared to bmMSC in all oxygen concentrations (1%: 2205.37 ± 38.07; 5%: 2299.43 ± 10.68; 21%: 2019.88 ± 39.04). It was rather interesting and surprising to note that no VEGF was detected in ucMSC samples in any of the oxygen concentrations.

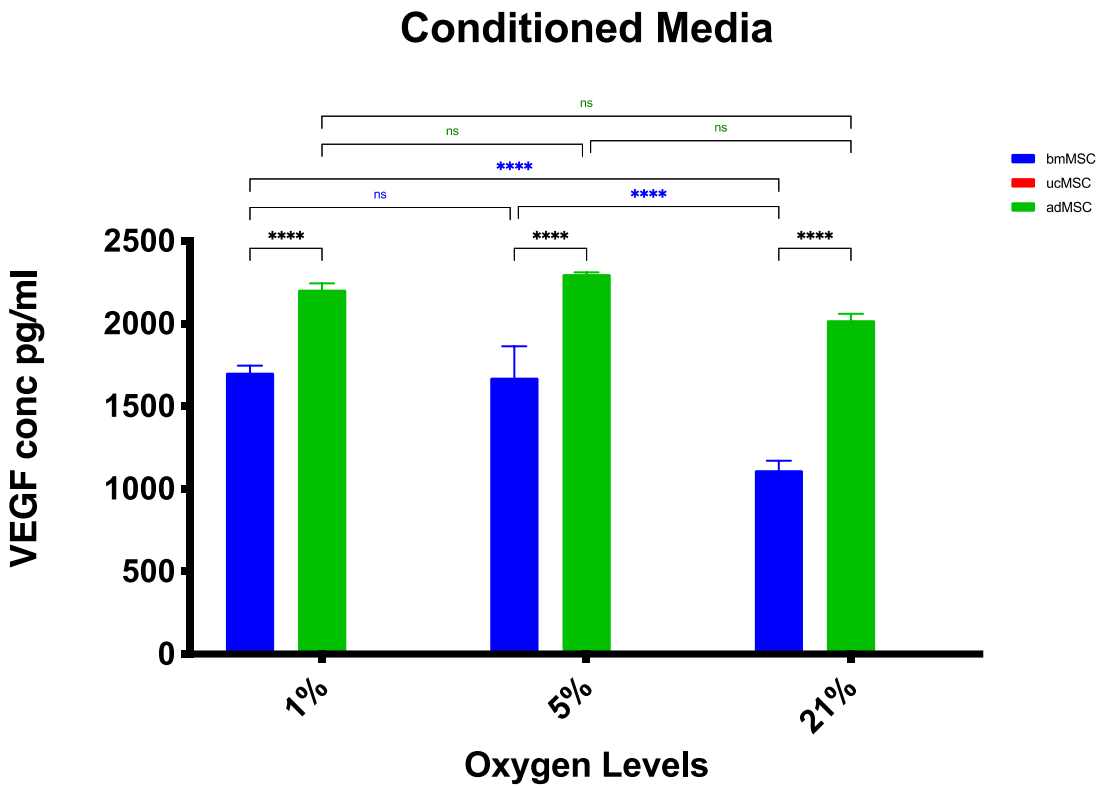

Figure 3-17 VEGF concentration from conditioned media in the different oxygen concentrations (1%, 5%, 21%) obtained from T-flask 72 hours post-media change when cells are 70-80% confluent. VEGF levels were taken from primary cells of each cell source. ucMSC showed no measurable or comparable VEGF concentration in all exposed oxygen levels. Results displayed as mean ± standard deviation.

3.3.1.2.2 Clonogenicity of cells in different O2 settings

Clonogenicity data from the MSC were obtained by colony-forming unit (CFU) assay, which is a measure of proliferation capacity commonly used for MSC. Colony-forming potential (CFP) helps standardised the data across the different cell types and allows for direct comparison by calculating the percentage of cell-forming colonies/number of cells seeded. Results are displayed as mean ± standard deviation. n-number was at least 3 or. P7 ucMSC and bmMSC showed a similar trend with CFP in different oxygen concentrations. When cells were expanded in static normoxia (SN) showed the most CFP compared to other seeding oxygen conditions (ucMSC: 2.30 ± 1.41; bmMSC: 4.17 ± 2.30). Exposure to dynamic hypoxia (DH) appeared to lower the CFP (ucMSC: 1.20 ± 0.27; bmMSC: 0.57 ± 0.38). The group with the least CFP for both bmMSC and ucMSC were the cell in static hypoxia (SH) of 1% (ucMSC: 0.60 ± 0.10; bmMSC: 0.10 ± 0.09). adMSC showed a different clonogenicity profile compared to

the other two cell sources. Cells subjected to DH had a significantly higher CFP compared to SN and SH (DH: 17.1 ± 1.72; SN: 29.6 ± 1.71; SH: 11.3 ± 3.88). This can be macroscopically appreciated in Figure 3-20.

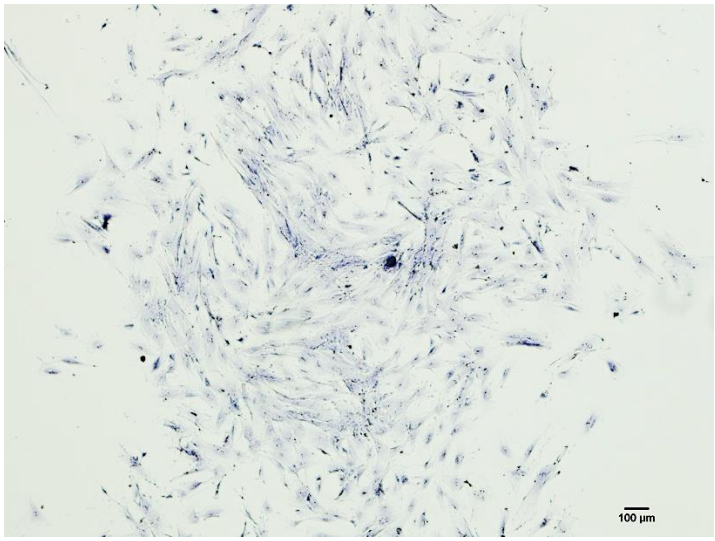

Figure 3-18 Brightfield microscopy of one colony of cells from CFU assay stained with Crystal Violet on Day 12 of CFU assay.

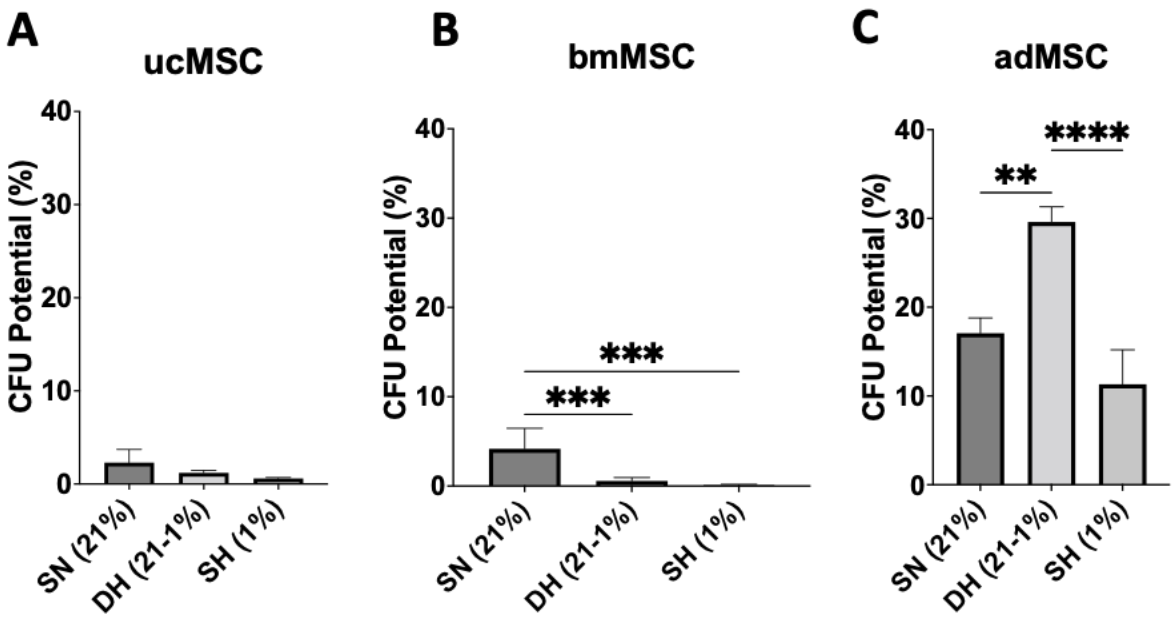

Figure 3-19 Graphs showing CFP of the different cell sources. Primary adMSC had the higher CFP across all pre-conditions. N-number >3. Results are displayed as mean ± standard deviation. SN = Static Normoxia (21%); DH = Dynamic Hypoxia (21-1%); SH = Static Hypoxia (1%).

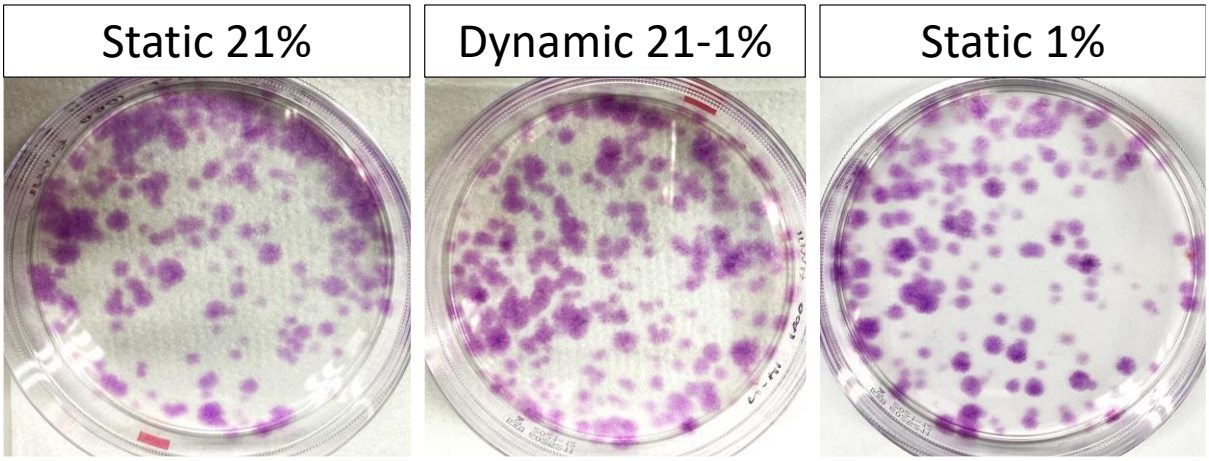

Figure 3-20 Photo of CFU assay plates with stained crystal violet colonies of adMSC. Visible differences of the CFU can be appreciated between the different oxygen pre-conditions.

3.3.1.3 Determining bioactivity of cells in different oxygen pre-condition regimens in 2D and 3D hydrogels

3.3.1.3.1 Temporal measurement of *in vitro* hypoxic gradient in culture

To help with understanding the variation in oxygen diffusion across different mediums in a well plate during the initial purging of the hypoxic chamber at set time points, the MIOS oxygen sensor well plate system was used. The top readings would represent the hypoxic chamber's atmospheric oxygen saturation (after 2 minutes of purging with the pre-mixed gas), the middle readings would represent the section around the top of the media (at the atmospheric air/media) interface and the bottom reading would be considered peri-hydrogel layer. Readings for the middle of media was added to help capture the oxygen saturations around the middle of the media and the hydrogel interface. (Figure 3-21 C)

Readings from the acellular control hydrogels were compared to the seeded cellular hydrogels (seeding density of 50,000 cells per gel). At the start of the measurements for each time point, fresh pre-conditioned (to hypoxia) media was added to the well.

The results show that there was a considerable variation in the reduction of O_2 saturation levels within the well over time.

At 24 hours of culture, the acellular control wells took approximately 25 minutes for the O_2 levels in the middle of the well to reach the same as the atmospheric O_2 readings at the top of the well, which were measured between 0-1%. The bottom and middle of media readings took a longer time to reach equilibrium with the chamber's atmospheric O_2 levels and had not reached the same level at the end of monitoring at approximately 42 minutes. (Figure 3-21 Ai) In the seeded hydrogels however, although there was a similar trend with the middle and bottom of well readings, the rate of decrease in oxygen saturation in the bottom and middle of media levels occurred more rapidly than the acellular; equilibrium of O_2 levels with the top and middle of well was reached at approximately 30 minutes post-purging of the chamber. (Figure 3-21 Bi)

At 72 hours of culture, the pattern of hypoxic variation changed in both acellular and seeded hydrogel wells. For the acellular wells, the middle of well readings started lower than the top of well readings. The bottom of well and middle of media readings, whilst they started at a higher O_2 reading of 3.8% and 5.2% respectively, reduced at a faster rate compared to the 24 hours readings and reached equilibrium with the top of well after 30 minutes of monitoring. They collectively achieved the lowest readings (which is the same as the middle of well readings) at about an hour post-purging. (Figure 3-21 Aii) For the seeded hydrogel wells, interestingly the baseline readings from the top and middle of well was recorded higher between 1.8 and 3.4% O_2 saturations. Readings from the bottom of well started at a lower O_2 level compared to the other positions in the well, which was recorded at 2.8% O_2 from the start and rapidly decreased to its lowest readings of near 0% O_2 at 42 minutes post-purging. O_2 levels for the middle of media followed the previous trend of starting at a higher O_2 measurement of 5.5%, which is above the top and middle of well initial measurement, and reached equilibrium with the top of well at about 18 minutes post-purging. (Figure 3-21 Bii) This demonstrated a more rapid reduction in oxygen levels in the seeded wells (approximately a third of the time faster than the acellular wells) compared to acellular as per the trend in the 24 hour measurements. (Figure 3-21 Bi)

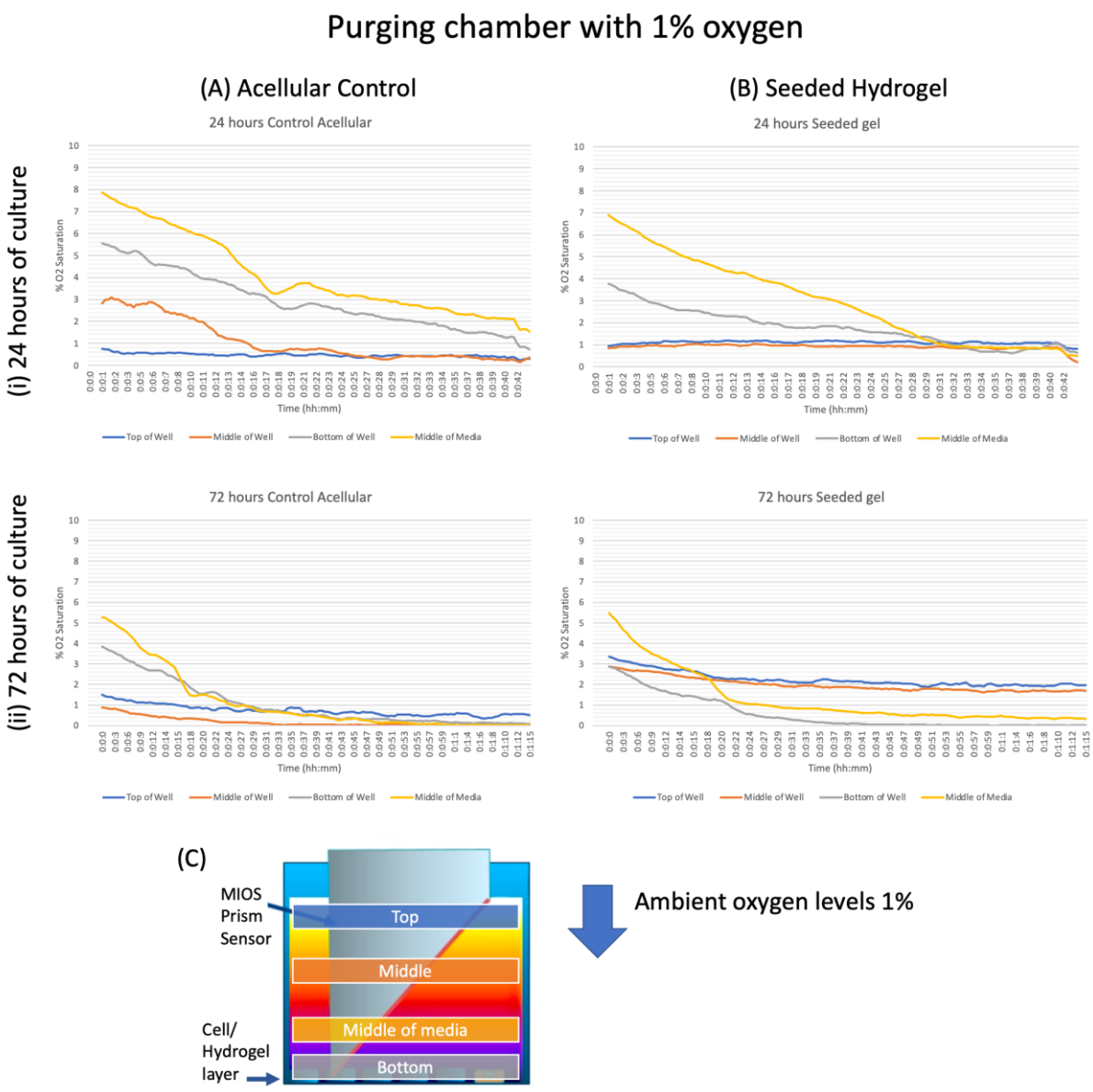

Figure 3-21 Comparison of graphs showing percentage oxygen saturations at different levels down the well as detected by the MIOS sensor.

3.3.1.3.2 Temporal VEGF levels of MSC in 2D and 3D environments in different oxygen conditions

Following on from Section 3.3.1.2.1, ELISA was performed on the adMSC in different oxygen conditions. In these experiments, the static and dynamic oxygen pre-conditioning was performed via the 2-step method as described in Section 3.2.2. These extensive and thorough experiments help to determine the best pre-condition and condition oxygen levels which would yield the highest VEGF cytokine response

from the seeded cells. Initial experiments were performed in 2D cell culture wells to interrogate various possible oxygen pre-condition environments. The cells were then seeded in 3D hydrogel to recapitulate the biomimetic environment as a form of an intermediary indication of how the cells would respond with their VEGF production in later experiments with the tissue engineered skin transplant model.

Data from the VEGF levels within conditioned media from 2D plated cells showed general upregulation of VEGF after Day 5 of culture in the oxygen conditions, particularly when pre-condition culture environment was at ‘normoxic’ 21% O2. This was found to be significant for the dynamic 21-1% O2 change when compared to static 21% on Day 7 of culture. (2431 ± 592 vs 936 ± 202; Figure 3-22A) In the 1% hypoxic pre-condition set, static 1% O2 environment had the highest and most significant VEGF levels compared to dynamic change from 1-21% on Day 7. (1904 ± 343 vs 582 ± 97; Figure 3-22B) With the 5% (physiological) hypoxia culture environment, VEGF levels were found to be lower at Day 5 and Day 7 compared to the cells cultured in 21% and 1% O2 environments, and the comparative results between variation in O2 levels did not yield any significant results. (Figure 3-22C) A comparison of the highest VEGF from three of the different O2 pre-condition data (Figure 3-22A-C) showed that the cells from dynamic 21-1% O2 culture environment have the highest reading from Day 1-7, which was shown to be significantly different by Day 7 when compared to static 1% and dynamic 5-1% O2 conditions. (2431 ± 592 vs 1904 ± 343 vs 930 ± 677 respectively; Figure 3-22D) Given these results, two O2 culture conditions of 21% and 1% were chosen to simplify the experimental process for downstream *in vitro* and *in vivo* applications. Data from dynamic 21-1%, static 1% and 21% O2 conditions were extrapolated to Graph E to help draw a comparative VEGF cellular production in these O2 environments (Figure 3-22E). Data showed that the dynamic 21-1% culture environment yield the highest VEGF levels from Day 3 – 7 and this was found to be most significant on Day 7 of culture.

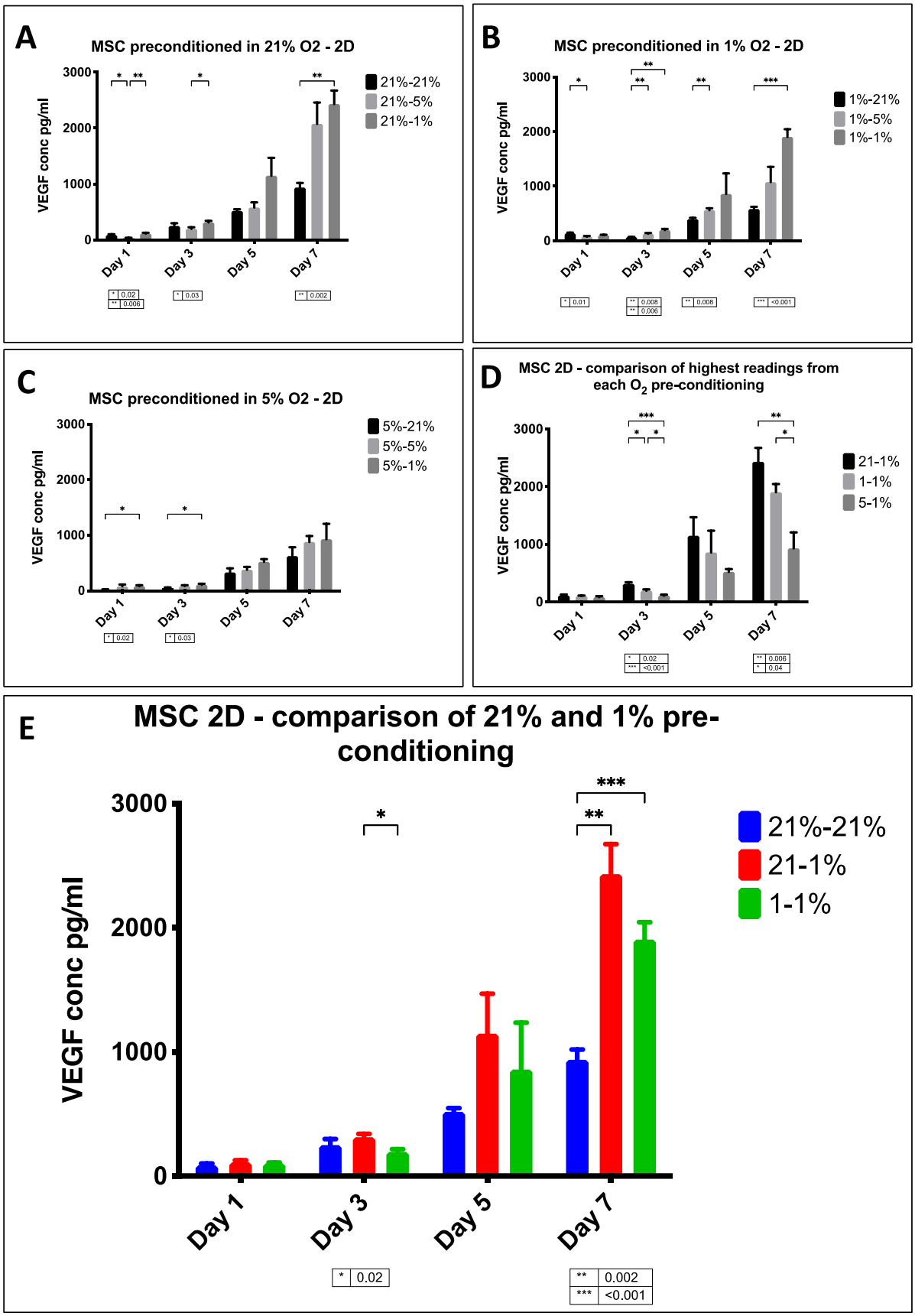

Figure 3-22 Validation of oxygen conditioning environments for optimal VEGF production from adMSC cultured in 2D cell culture. Three oxygen levels were used (1%, 5% and 21%) as shown in Graph A-C from Days 1-7. (A) Graph A shows the VEGF response from MSC preconditioned initially in 21% O2 and then

conditioned in 21%, 5% or 1% O2. (B) Graph B shows the VEGF response from MSC preconditioned initially in 1% O2 and then conditioned in 21%, 5% or 1% O2. (C) Graph C shows the VEGF response from MSC preconditioned initially in 5% O2 and then conditioned in 21%, 5% or 1% O2. (D) Graph D shows the highest VEGF readings determined from Graphs A-C from which the oxygen pre-condition and conditions yielded the highest VEGF levels. (E) Graph E combines data from the experimental oxygen conditioning chosen using 2 oxygen levels for further downstream experiments. N-number = 6 for each time point.

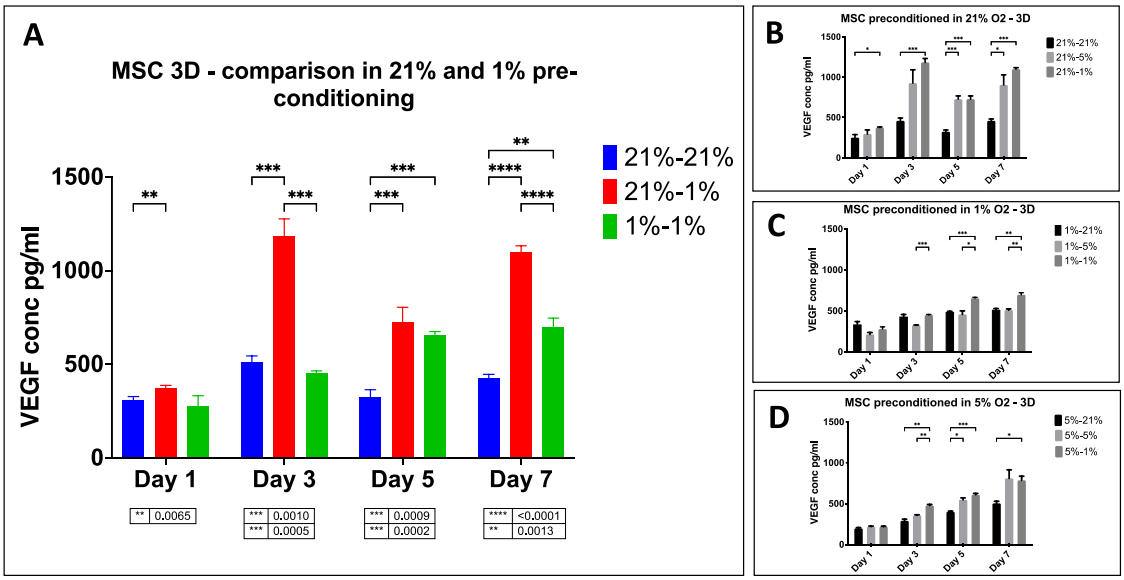

Figure 3-23 Validation of oxygen conditioning environments for optimal VEGF production from adMSC cultured in 3D (collagen hydrogel) cell culture utilising 3 different oxygen environments (1%, 5% and 21%) as per 2D culture, shown in Graph B-D from Days 1-7. (A) Utilising the same comparative experimental oxygen conditioning of 21% and 1% O2 to demonstrate the VEGF production when cells are seeded in 3D hydrogel. Graph A extracted comparative data for the same chosen O2 culture environments as Figure 3-22E. (B-D) Graph B-D showed similar results to the 2D data shown above in Figure 3-22A-C. N-number = 6 for each time point.

Equipped with the initial 2D VEGF data, the measurement of 3D VEGF production was performed to determine if similar trends would be achieved when cells are seeded into type 1 collagen hydrogel for the same pre-conditioned/conditioned O_2 environments. The highest VEGF production from each of the 3 different O_2 pre-condition environments was analogous to that of the 2D culture, with significant VEGF levels also found in the dynamic 21-1%, static 1% and dynamic 5-1% O_2 environments. (Figure 3-23B-D) Extracting the data sets for the chosen O_2 environments of 21% and 1% O2, confirmed that dynamic 21-1% O_2 environment had the highest VEGF levels when compared to the other O_2 environments, and this was found to be significant from Day 3 – 7. (Figure 3-23A)

Collectively, both 2D and 3D VEGF production data helped to justify the O_2 culture conditions of choice to use in the later sections of the thesis. This is shown in Table 3.3.

Name of conditioning regime	Acronym	Practical definition	
		Pre-conditioning O_2 during subculturing	Conditioning O_2 during seeding
Static Normoxia (21%)	SN	21%	21%
Dynamic Hypoxia (21-1%)	DH	21%	1%
Static Hypoxia (1%)	SH	1%	1%

Table 3.3 Optimised oxygen culture conditions validated for use in downstream experiments to compare therapeutic outcomes.

3.3.1.3.3 Temporal metabolic activity and proliferative capacity of cells in 2D and 3D culture in different O2 environments

Using non-terminal Realtime-Glo assay (Promega), as described in Chapter 2, to monitor temporal cellular metabolic activity, it was possible to plot the viability of cells in different seeding environments (2D/3D) at various time points. This will also provide an indirect measure of proliferative capacity over the 72-hours monitoring period.

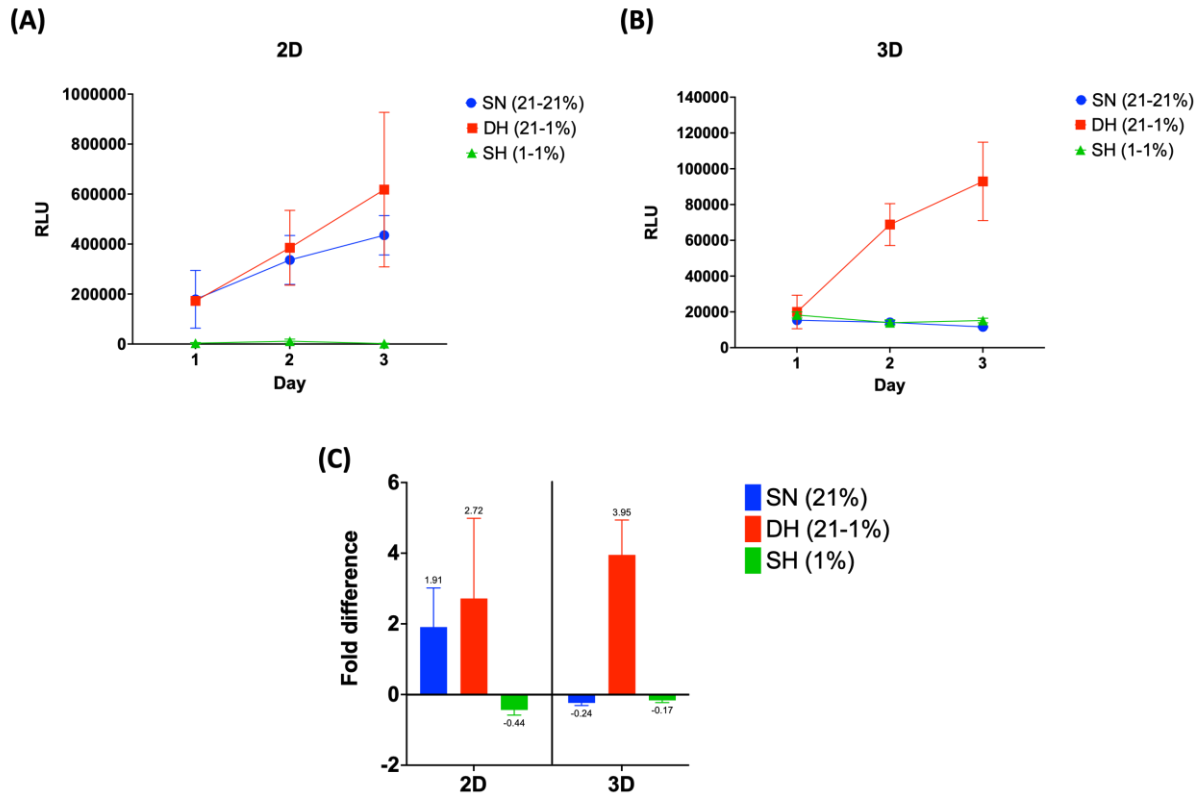

Figure 3-24 Graphs plotting viability/metabolic activity of cells over 3 days (72 hours) of continuous monitoring using Realtime-glo assay. (A) Metabolic activity/viability of cells seeded directly on well plates (2D) in different O2 conditioning environments. (B) Metabolic activity/viability of cells seeded in 3D hydrogel in different oxygen conditioning environments. (C) Comparison of fold difference in luminescence readings of Day 3 compared to Day 1 for all O2 conditions of cells seeded in 2D and 3D, with the plotted mean values on the top of each barchart.. N-number = 3 for each time point.

For 2D seeded cells, it is observed that both dynamic hypoxia (DH) and static normoxia (SN) have significantly higher RLU readings compared to static hypoxia (SH) from Day 1 to 3, as shown in Figure 3-24A (DH vs. SH: p-value = 0.02; SN vs. SH: p-value = 0.007). SH readings remained low throughout the 3 days of monitoring compared to the other O2 conditions.

When cells are seeded in 3D, as with the 2D seeded cells, DH readings were the highest on Day 2 and 3 compared to SN and SH O2 conditions, as shown in Figure 3-24B. However, unlike the 2D readings, SN has similarly lower RLU readings as SH when cells were seeded in 3D hydrogel. It is also noted that the RLU readings from 2D were ten times higher compared to the 3D counterparts. This may be partly due to the penetrative effects of the substrate in hydrogel as well as the overall effect of

the 3D microenvironment on cell metabolic activity compared to 2D. This will be examined further in the discussion section below.

The calculation of fold differences in the luminescence readings of the seeded wells on Day 1 and Day 3 allows for the indirect measure of the proliferative capacity of the cells. A higher mean fold increase was seen in the DH cells seeded in 3D hydrogel compared to 2D. For SN cells, there was a fold increase for cells seeded in 2D setting compared to 3D, which showed a fold decrease in readings. For SH, there was a fold decrease in readings for both 2D and 3D seeding environments.

Higher metabolic activity was measured in DH 21-1% O_2 conditions across all different culture environments compared to static O_2 conditions. The low RLU readings from the SH cells may be related to metabolic stress on cells from pathologically low oxygen tensions.

3.3.1.4 Temporal molecular analysis of angiogenic gene expression from MSC in 2D and 3D

RNA was extracted from adMSC seeded in 2D and 3D environments in the experimental pre-conditioning oxygen settings as described above. Molecular markers of angiogenesis, HIF1a and VEGF, were measured using qPCR technique. The ΔΔCq expression values are calculated against GAPDH housekeeping gene as described in Chapter 2.

When seeded in a 2D environment, the expression of angiogenic marker HIF1a in static normoxia (SN) 21% remained low throughout the 7 days of culture. In dynamic hypoxia (DH; 21-1%), there was an observable spike in HIF1a expression on Day 5 only. In static hypoxia (SH) 1%, 2 similar spikes in expression were noted on Day 3 and Day 7 of culture. Only cells exposed to DH showed spikes in HIF1a expression on Day 5, and a higher observable mean expression on day 7 of culture. However, none of these trends was found to be statistically significant to the other oxygen conditions. In DH, cells on day 5 of culture exhibited the highest expression VEGF expression out of all the oxygen conditionings. The mean expression (0.042 ± 0.025)

was 3 folds relative to SH (0.014 ± 0.0004) on the same culture day, but this was not found to be significant. In the SN conditioning, other than Day 1 of culture, negligible VEGF expression was found from Day 3 to 7.

Cells in 3D culture produced a different angiogenic expression profile from that of 2D culture. For HIF1a, there was a general increasing trend of expression in all oxygen conditioning groups from Day 1 to 7 of culture. The mean HIF1a expression was highest for DH compared SN and SH on the Day 1 of culture. However, this trend was not sustained from Day 3 onwards, with SH expressing a significant 1.9-fold increase relative to DH on Day 3 and superseding with the highest expression on Day 7, compared to DH and SN conditioning. The mean expression of HIF1a of cells in SN conditions appeared higher than DH on Day 3 and 7 of culture, but did not appear higher than SH conditioning throughout the 7 days. For VEGF expression of the cells, unlike that of the corresponding HIF1a expression mentioned above, both SN and DH conditioning appear to have a downward trend in levels of expression over time. For cells in SH, although the trend also appears downward in nature, there was a greater drop in the expression on Day 3 compared to Day 5 and 7, where cells had the highest mean expression relative to cells in SN and DH conditions. The highest level of expression of VEGF in the cells amongst all the oxygen conditions over 7 days of culture was on Day 1 in DH conditioning; there was a 1.9-times higher mean expression compared to SH conditioning and 2.1-times higher relative to SN conditioning. However, these comparisons were not found to be statistically significant.

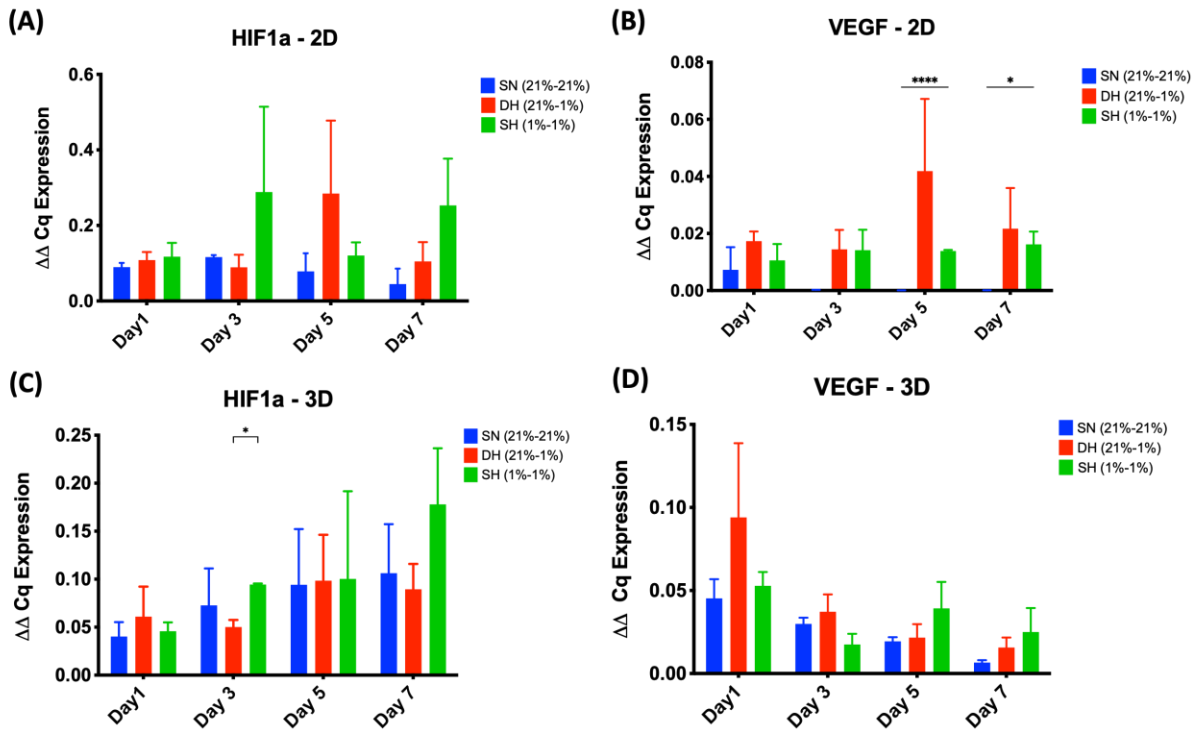

Figure 3-25 qPCR data of HIF1a and VEGF RNA expression from adMSC seeded in 2D and 3D environments in different oxygen conditions from Day 1, 3, 5 and 7. (A) HIF1a expression from 2D seeded cells, (B) VEGF expression from 2D seeded cells, (C) HIF1a expression from 3D seeded cells, (D) VEGF expression from 3D seeded cells. N-number = 3 at each time point. SN = static normoxia 21%; DH = dynamic hypoxia 21-1%; SH = static hypoxia 1%.

3.3.1.5 Temporal comparison of VEGF production potential in different oxygen conditions

To better understand the effects of different oxygen conditions on cellular potential of VEGF production, the VEGF concentration (pg/ml) measured from ELISA (as described in Chapter 2) was normalised to amount of cellular DNA (ng/ml) extracted for different timepoints in culture. For the purpose of this study, the measurement is defined as VEGF production potential.

The concentration of DNA from cells seeded in 2D environment is shown in Figure 3-26A. This value can be assumed to correlate to cell count. There is a steady increase in amount of DNA detected in all oxygen conditions over time. SN 21% conditioned cells show significantly greater DNA content than SH 1% cells at every timepoint. DH 21-1% also showed higher DNA concentration values compared to SH

1%, but it was only shown to be statistically significant on Day 1 and from Day 5 – 7. By Day 7, SN 21% cells had a marked increase in DNA concentration level, which measured the highest out of all the three oxygen conditions (6650 ± 803.37; p <0.0001). This was followed by DH cells at almost half the mean value of SN 21% (3336.67 ± 1133.59; p <0.0001) and three times the value of that from SH 1% (878.61 ± 426.12; p = 0.001). This data concurred with earlier measurements of proliferation rate of adMSC in Figure 3-14A, where highest proliferation was shown in 21% oxygen culture conditions.

When VEGF production potential was measured, the data shows the opposite trend to the DNA values shown in Figure 3-26A. VEGF per DNA of cell showed lower values in SN 21% which was decreasing over time, indicating that the cells are not producing as much VEGF proteins compared to other cells in DH or SH conditions. DH samples showed an upward trend of increasing VEGF potential value which peaks on Day 5 and then subsequently declines. SH samples, on the other hand, showed a steady high mean value from Day 1- 5, and then it starts to fall on Day 7. Thus, despite the fact that SH 1% cells do not replicate and grow as much as the DH and SN group of cells, the results indicate that per cellular DNA, SH 1% cells produce significantly more VEGF compared DH and SN samples, especially for Day 1 and 3 of culture.

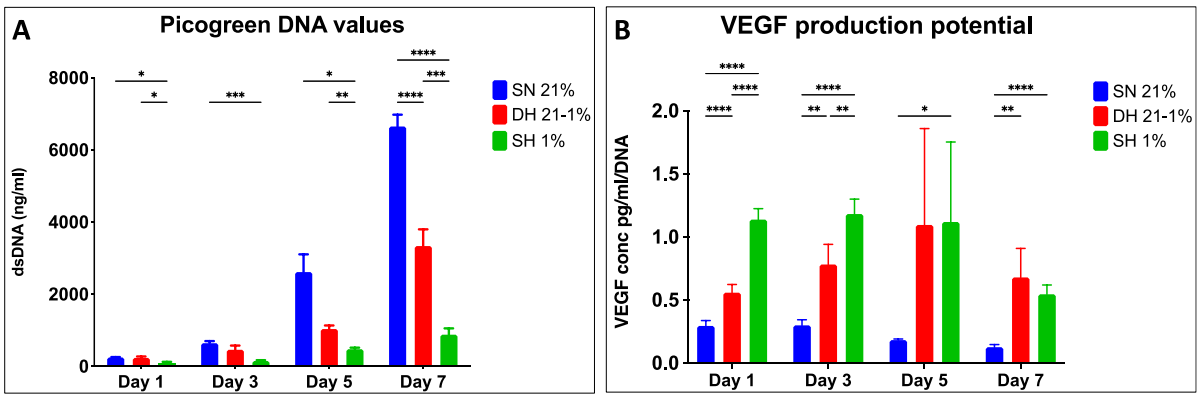

Figure 3-26 VEGF concentration are normalised to DNA content of adMSC cells in their 2D oxygen conditioning environments. (A) Extracted DNA concentration using PicoGreen kit as described in Chapter 2. (B) VEGF production potential measured as VEGF concentration per cellular DNA.

3.3.1.6 Transduction of AD-MSC with lentivirus for tracking of seeded MSC

3.3.1.6.1 Pre-experimental evaluation of transduced adMSC

Positively transduced cells do not appear morphologically different under brightfield microscopy, but they are visible under the green GPF channel of the fluorescence microscope. (Figure 3-27) This allows for the transduction process to be monitored over time using fluorescence imaging.

The cells were cell-sorted using FACS after successful transduction. To limit variation within the population post-transduction, cells were cell sorted using their zsGreen fluorescent marker benchmarked against non-transduced cells. (Figure 3-28)

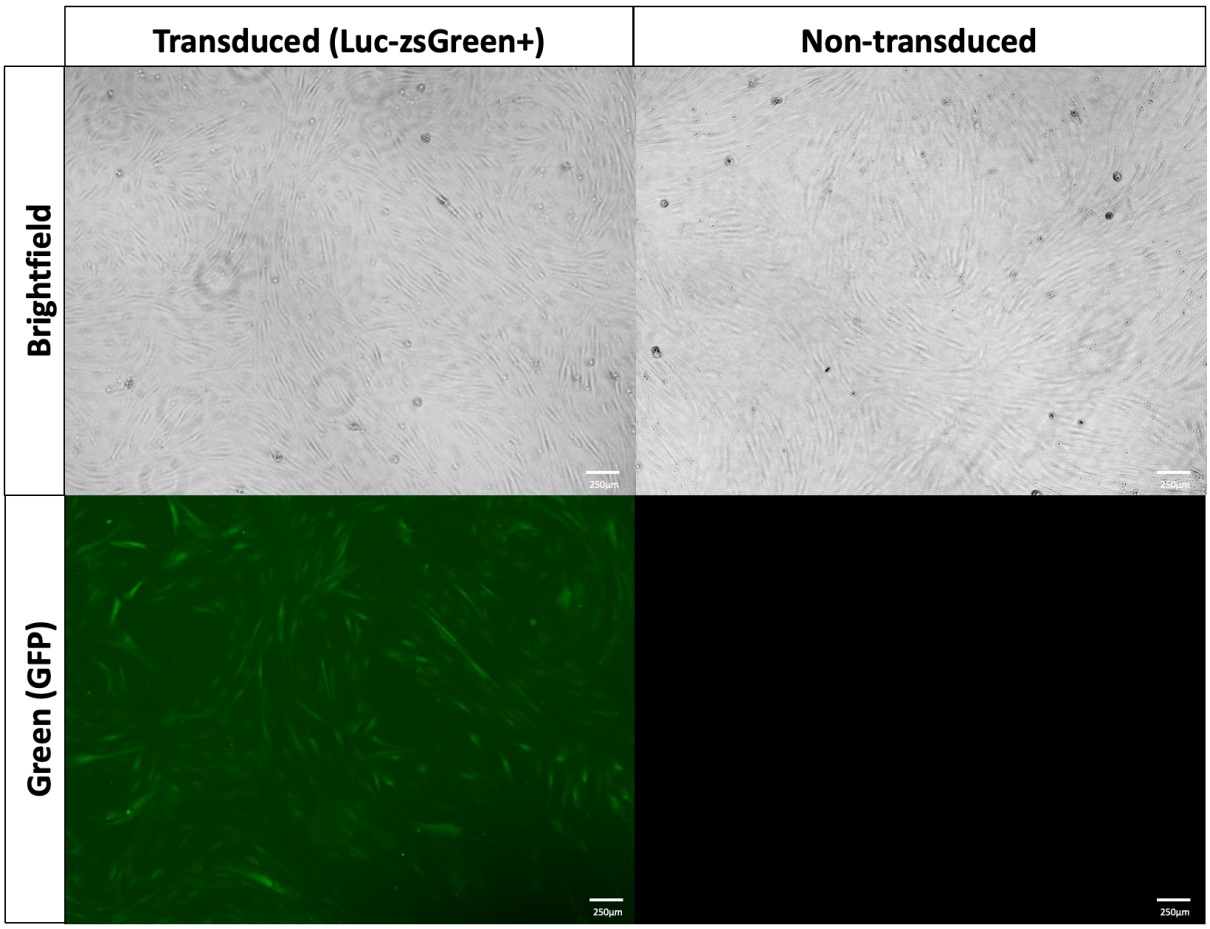

Figure 3-27 Microscopic comparison of non-transduced versus transduced adMSC in brightfield and green fluorescence (GFP+) channel. Brightfield microscopy does not demonstrate any morphological

differences between transduced versus non-transduce cells. However, only transduce cells are seen under the green GFP channel on fluorescent microscopy. Scale bar = 250µm.

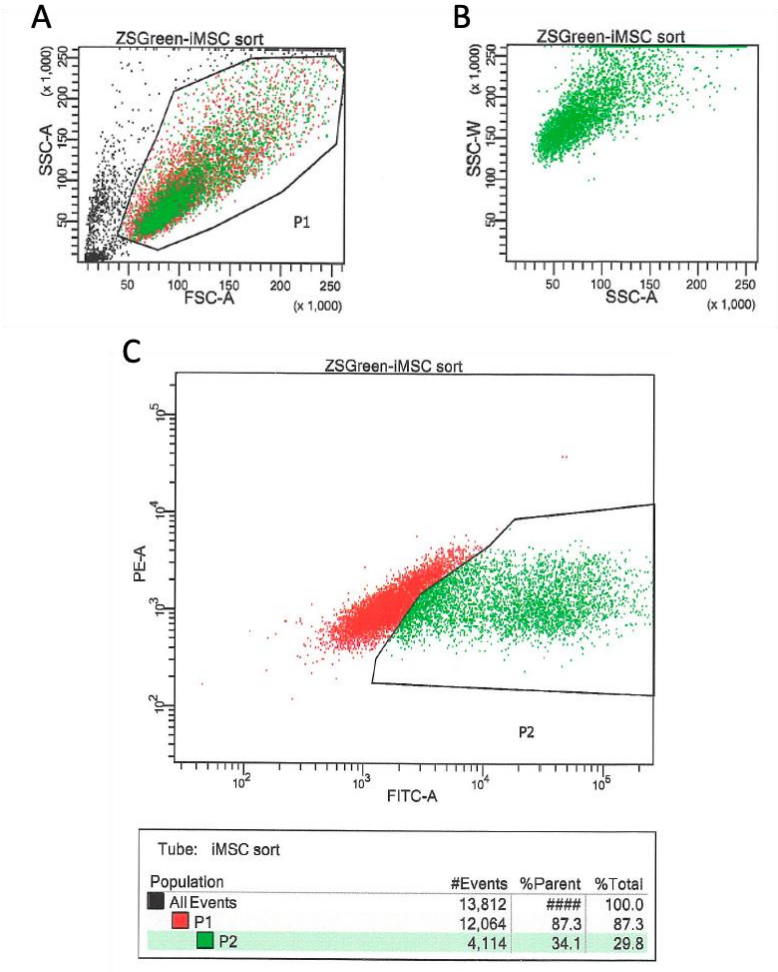

Figure 3-28 The FACS dot plots above demonstrate how positively transduced cells are sorted via the zsGreen fluorescence marker unique to these cells. Graph A and B shows the initial process of analysing for P1 and P2 events: (A) P1 events representing the entire live cell population minus the debris and dead cells, and (B) P2 events showing the gated zsGreen positive detected cells within the P1 population. (C) Plot showing the P2 against P1 events with the corresponding statistics against the total number of events.

3.3.1.6.2 Clonogenicity of transduced versus non-tranduced adMSC

There was a global reduction in the CFU count of transduced MSC (t-MSC) compared to non-transduced MSC as shown in Figure 3-29A. This was found to be

between 72-81% reduction in CFU counts across all three oxygen conditions as shown in Figure 3-29.

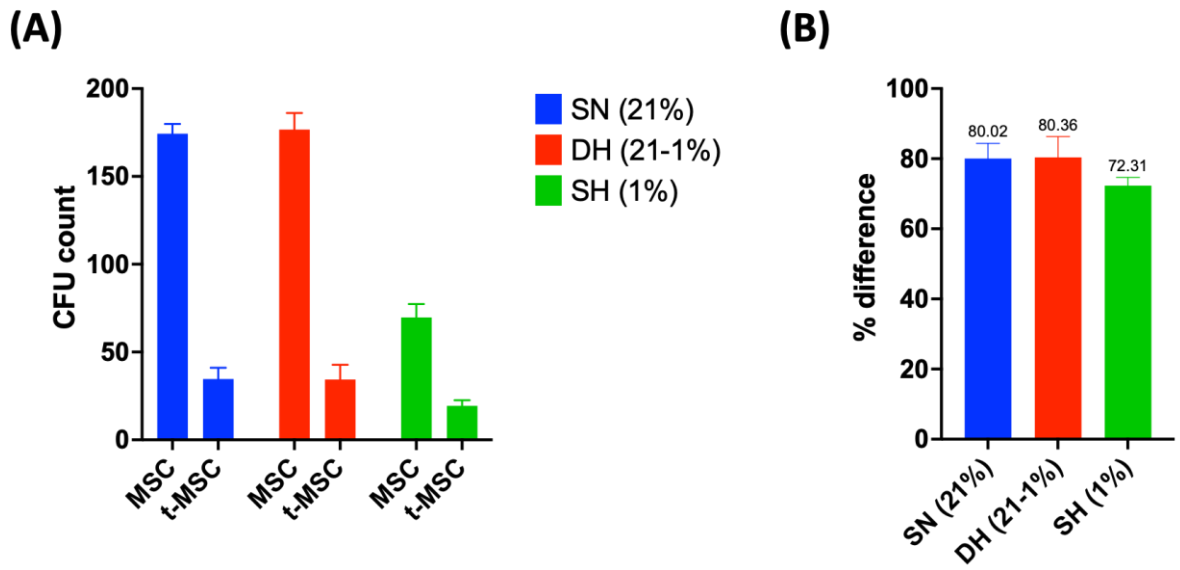

Figure 3-29 (A) Graph comparing CFU count between untransduced adMSC and transduced adMSC (shown as t-MSC on the graph). (B) Percentage difference in CFU count of MSC compared to t-MSC shown on the graph, with the plotted mean values on the top of each barchart. SN = static normoxia 21%; DH = dynamic hypoxia 21-1%; SH = static hypoxia 1%.

3.3.1.6.1 Comparing VEGF production of transduced adMSC

The mean levels of VEGF expression from transduced and untransduced adMSC seeded in INTEGRA® scaffold (see Chapter 4 for further details on this seeding methodology) were comparable from Days 1-7 of culture as shown in Figure 3-30. Untransduced adMSC showed a greater variation of expression compared to transduced cells.

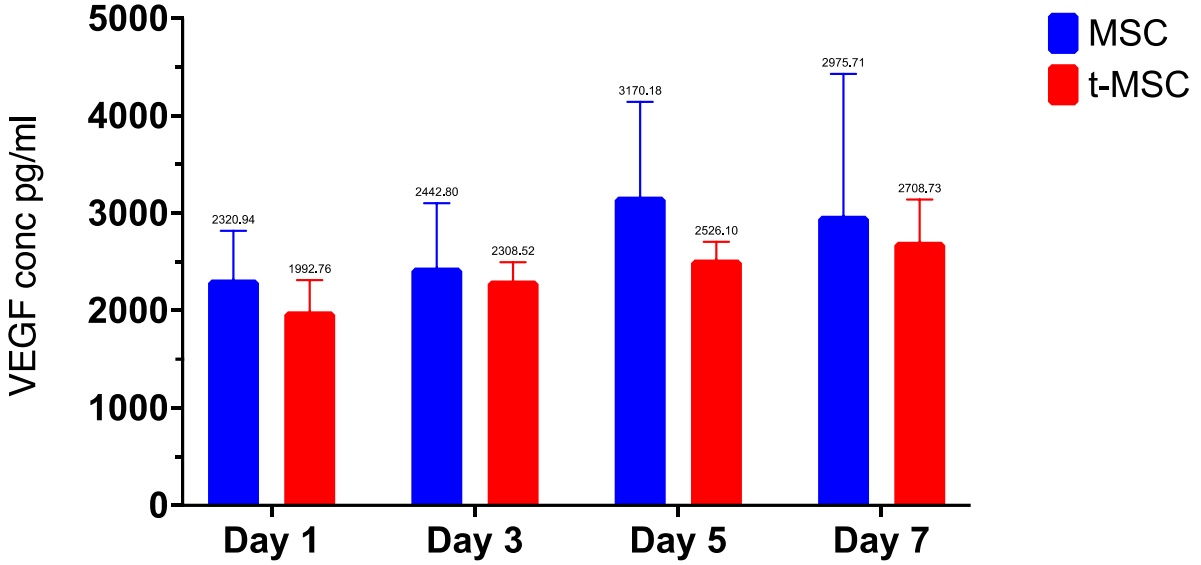

Figure 3-30 Comparing VEGF concentration between untransduced (MSC) and transduced (t-MSC) adMSC conditioned media when cultured on INTEGRA®scaffold in DH (21-1%) O2 conditions, with the plotted mean values on the top of each barchar, showed no significant difference in VEGF expression. N = 6 for each time point. *** p-value < 0.001.

3.3.1.6.2 Comparing the temporal metabolic activity and proliferative capacity of transduced adMSC

Using non-terminal Realtime-Glo assay (Promega), as described above in section 3.3.1.3.3, a comparative data set was extracted to determine the difference in cellular metabolic activity and viability of untransduced versus transduced adMSC in different seeding environments (2D/3D) at various time points. The data were plotted on the graph shown in Figure 3-31A & B. Fold difference in RLU readings from Day 3 and 1 also provided an indirect measure of the proliferative capacity of the cells. This data is shown in Figure 3-31C.

In the 2D environment, there were differences in RLU readings between the two cell types, where untransduced cells had higher RLU values compared to transduced cells. However, the proliferative capacity appeared to be greater in the transduced cells, with a higher mean fold difference of 5.41 ± 2.59 compared to untransduced cells, with 2.72 ± 2.27, but this was not found to be statistically significant ($p = 0.20$).

When the cells were seeded in 3D, the metabolic (reduction) activity from Day 1-3, as measured by the RLU readings, were analogous in trend between untransduced and transduced cells. The mean fold difference value was noted to be marginally higher in the transduced (5.27 ± 0.74) compared to the untransduced cells (3.96 ± 0.98).

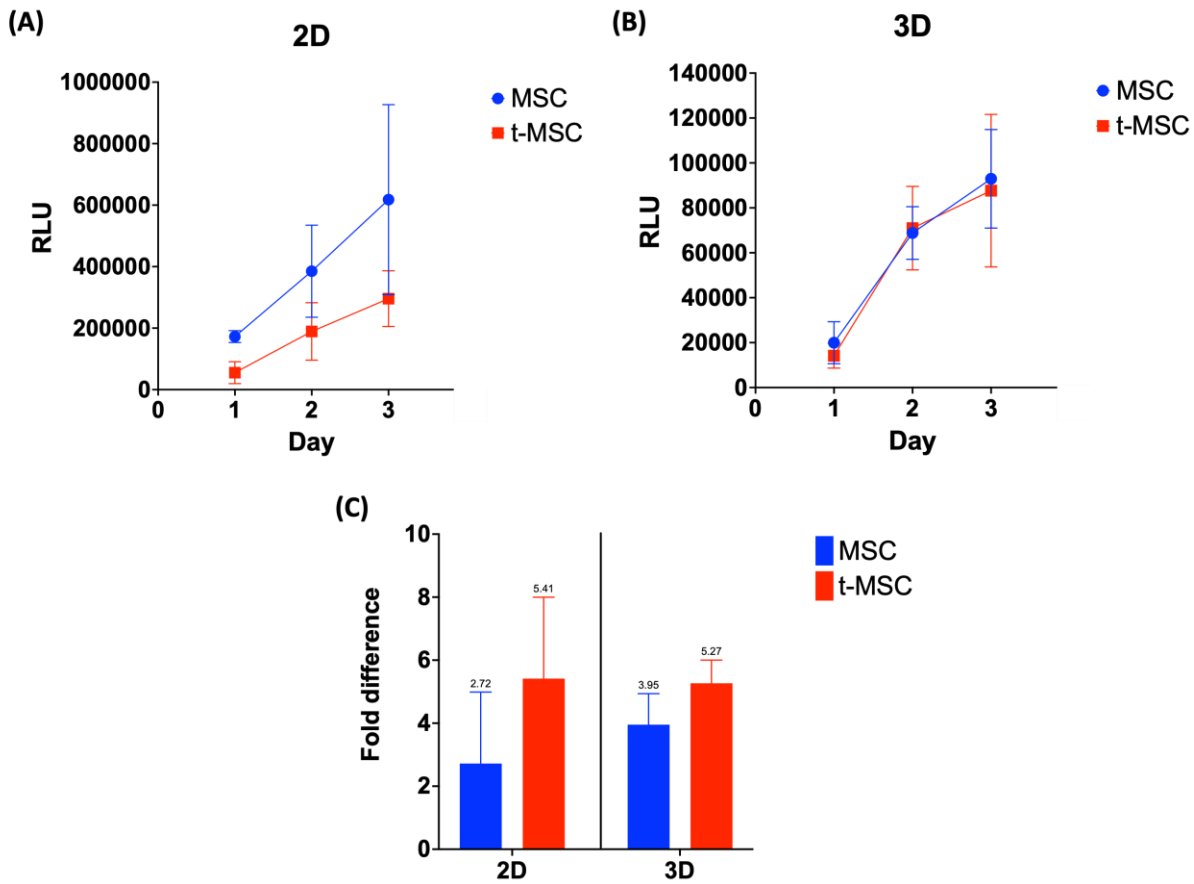

Figure 3-31 Graphs plotting viability/metabolic activity of untransduced (MSC) and transduced (t-MSC) cells over 3 days (72 hours) of continuous monitoring using Realtime-glo assay in DH (21-1%) O2 conditioning environments. (A) Metabolic activity/viability of cells seeded directly on well plates (2D). (B) Metabolic activity/viability of cells seeded in 3D hydrogel. (C) Comparison of fold difference in luminescence readings of Day 3 compared to Day 1 of cells seeded in 2D and 3D, with the plotted mean values on the top of each barchart. N-number = 3 for each time point.

3.4 Discussion

Justification for the use of adipose-derived MSC for future experiments

The three different types of MSC, from bone marrow, umbilical cord and adipose tissue, used in this study all possessed the same characteristics and trans-differentiation potential. As such, they fulfil the minimum criteria for the definition of MSC as set by the International Society for Cellular Therapy. (286) They are plastic adherent and have the ability to differentiate into osteoblasts, adipocytes and chondroblasts *in vitro*. They also express the cell surface markers for CD105, CD73 and CD90, and not CD45, CD34, CD11b, CD19 and HLA-DR molecules, as demonstrated from the flow cytometry data. Hence, they are not shown to have any phenotypic differences between the different MSC tissue types.

Morphologically, ucMSC appears to be distinctly different from bmMSC and adMSC, with a more heterogenous population noted on microscopy, especially in the earlier passages. Both bmMSc and adMSC show the typical fibroblastoid, spindle-shaped cell morphology throughout their early to late passages. (Data not shown) This difference could be a result of the neonatal nature of ucMSC compared to the adult-sourced bmMSC and adMSC, as well as the difference in techniques which were used to isolate the cells from the tissue source. In ucMSC, the removal of perivascular tissue may not be complete and may have inadvertently included other MSC-like cell types. The umbilical cord is made up of vessels, one vein and two arteries, covered by a bulk of mucoid connective tissue called the Wharton's jelly (WJ). The whole cord is lined by umbilical epithelium (287). ucMSC are primarily derived from the WJ (276). However, the umbilical cord itself, excluding the umbilical vessles, have been known to contain a reservoir of progenitor populations, which all show MSC characteristics (288). The cells would have been sourced from each component of the three stromal layers: the subamnion layer, WJ and the perivascular layer (287,289). Hence, it may be likely that the ucMSC obtain from the umbilical cord could also contain subpopulations from each stromal layer which contributes to the heterogeneity of the cells on microscopy. It is also interesting to note that some papers have described WJ-derived ucMSC as a class of unusual myofibroblast;

fibroblast-like cells with resemblance to smooth muscle cells and have features which show similarity to smooth muscle cells, such as positive stain for vimentin, desmin and a-smooth muscle actin (287,290). This ucMSC's characteristic is quite distinct from bmMSC, despite sharing the same minimum criteria for MSC definition. Studies have also shown ucMSC have the potential to change their phenotype once cultured *in vitro*. Researchers have shown that ucMSC are highly evolving when cultured moved from native tissue to *in vitro* culture, greatly changing the amount of positive cell surface markers CD73, CD90, CD105 on one single passage in a plastic tissue culture plate (291). Another showed diminishing numbers of flat, wide cells from the perivascular region with protracted cultured and persistence of fibroblast-like cells from the subamnion and WJ layer throughout the same culture (292). This is something that I have also personally observed in culture of the ucMSC in this study. One reviewer has gone as far as to say that cells isolated from the umbilical cord are not really MSC, but instead change their phenotype into MSC with *in vitro* expansion (288). This is quite controversial, but nonetheless, it is worth keeping in mind for future reference and applicability of the cell type for clinical translation. Interestingly, a paper by Hofer et al. also went into extensive detail in order to characterise the different morphological appearances of MSC, where wider 'blanket cell' types were classed as immature using a unique stromal index calculation (293). They hypothesise that the shape of cells can indicate the functional maturation of cells in culture, which can be a helpful *in vitro* parameter for future experiments.

It became apparent that the ucMSC did not produce any detectable VEGF in all different culture conditions (Figure 3-17). This was despite the pooling of several primary donor cells to reduce the significant batch-to-batch variation known to these neonatal cell types. Hence, it was decided that ucMSC should be excluded from future experiments, as the measure of angiogenic cytokine VEGF would not be a reliable indicator for this cell type's angiogenicity (294). This data was initially surprising, given the tissue origin of the cell, and how differently this has been reported in other published data (191,289,295,296). But on further investigation, it appeared that other researchers have also observed and reported similar cytokine profiles for these cells (297–299). With regards to cytokine expression of VEGF from bmMSC, as shown in Figure 3-17, there were significant differences measured between cells conditioned in 1%, 5% compared to 21%, which supported published

literature on the effects of hypoxia on cytokine expression in bmMSC (81,82,115,300,301). This also fits with the bone marrow's physiological oxygen environment as shown in Table 3.2, indicating that cells have more angiogenic cytokine profile in these oxygen environments. However, adMSC has an overall greater expression of VEGF in all oxygen tensions (1%, 5% and 21%) compared to bmMSC, which was found to be significant in nature. This supports reported data that adMSC possessed a greater potential for angiogenesis and vasculogenesis. The conditioned media from the T-flask however, did not show any significant difference between VEGF expression in 21%, 5% and 1% oxygen levels. This could be due to the pooling of media from several different T-flask, due to the larger expansion of cells from adMSC compared to bmMSC (see explanation below), or it could be due to the cell's physiological oxygen niche, where adipose tissue had a wider range of 3 – 15% pO_2 saturation compared to 1.1-6.4% in the bone marrow. On rigorous and extensive testing of various oxygen conditions in both 2D and 3D setting (see Figure 3-22 and Figure 3-23), DH conditions consistently showed much higher VEGF release compared to their 1% and 5% counterparts.

The proliferation profiles of the different cell types in different oxygen conditions also yield interesting data. Although adMSC appeared to have higher absolute cell numbers when cultured in 21% oxygen levels compared to 1% and 5% O_2 from Day 3 to 7 of culture (Figure 3-14), with the greatest fold increase noted to be from Day 1 to 3, fold increase on Day 5 was noted to be greatest on for cells in 5% O_2 instead. This trend was also shared with ucMSC for the 5% O_2 culture conditions, however, absolute cell numbers were higher in 5% oxygen conditions instead of 21% O_2. Combining this observation with the bmMSC growth kinetics with PDT shown in Figure 3-16, which was found to be more consistent in the 5% O_2 culture conditions, this was found to support published data on bmMSC (63,80,116,86,62) and ucMSC (302) on their increase in proliferation in low oxygen conditions. It was also noticed that bmMSC show signs of senescence after P9 culture, with a greatly decreased in proliferation capacity and increased time to confluence. This early senescence was also reported in the literature, where long-term hypoxia has been shown to reduce proliferation and mitochondrial activity (278,303). There were also some limitations with experimentation on bmMSC due to the lack of donor primary cells, which resulted in data that were not directly comparable, such as lack of viability and

proliferation data for bmMSC whilst seeded in well plates. Given that donor availability is one of the most important considerations to this study and for future translational purposes, this was a strong argument for using adMSC for the majority of the later parts of the thesis study. However, the proliferation profile for adMSC supported the use of 21% O_2 rather than hypoxia 1% or 5% for higher proliferation/expansion of cells. This controversial and unexpected data helped formulate and support the use of dynamic hypoxic conditioning (21-1%) from the practical aspect of cell expansion for therapeutic purposes.

In addition, the clonogenicity data demonstrated that primary adMSC has a superior colony-forming potential (CFP) compared to bmMSC and ucMSC. CFP is based on the colony-forming unit (CFU) assay. (see Chapter 2 for methodology) It was first discovered by Friedenstein et al. in the 1970s and is a time-honoured functional assay for testing the proliferative potential and self-renewal ability of progenitor-type cells such as MSC (304,305). It has been used extensively for measuring the quality of MSC in both pre-clinical and clinical trials (261,262,293,306). The number of colonies formed per a definitive number of single cells plated is called the colony-forming efficiency or potential (262). CFP values are substantially influenced by their culture conditions and hence it is a good comparative assay for the different MSC cell types in the 3 different oxygen culture conditions proposed. (Figure 3-19) The CFP appeared to be accentuated when the cells were cultured in dynamic hypoxia, which further supports the positive proliferative effects on dynamic hypoxic changes in oxygen culture conditions *in vitro*. This was also found to be higher for all oxygen culture conditions (SN, DH, SH) for the adMSC when compared to the other MSC cell types, where DH had greater CFP, followed by SN and then SH.

Given the findings above, there is a strong justification for the use of adMSC over ucMSC and bmMSC, given the ease of harvest, donor availability, higher proliferative capacity, colony forming potential and angiogenic VEGF production – all of which are highly desirable in the later experiments of this thesis. It also highlighted the practical advantage of higher proliferation at the conventional 21% oxygen (for DH 21-1% oxygen culture conditions) where the initial rapid expansion of cells can be carried out in normal 5% CO_2 incubators rather than specialist hypoxic incubators.

The effect of seeding cells into hydrogels

To understand cellular behaviour in a more biomimetic system, it was necessary to move the model from 2D to 3D (307). In this study, cells were seeded in 3D hydrogel as an intermediary optimisation step prior to their use on the tissue-engineered (TE) scaffold in the later part of the thesis. This is done to practically conserve the number of cells needed for preliminary optimisation in the TE scaffold, as cells required for seeding on TE scaffolds are in the order of 2-20 times more depending on the experiment.

Type I collagen hydrogel was used as it is the most abundant collagen subtype in the body (308). The use of 3D MSC cultures reflects a more physiologically microenvironment than 2D cultures which can have several effects. It has been shown that 3D cultures have a different metabolic activity (309), genetic expression (310) and secretome profile (66), better anti-oxidative (311,312) and anti-apoptotic functions (313) compared to 2D monolayer cultures, as well as improved therapeutic effects in some preclinical models, such as skin wound healing (312,314).

The replication of the 3D spatial effect on the cells also creates a dynamic spatial microenvironment where different layers are exposed to different levels of oxygen and nutrients, which are partly driven by cellular consumption, hence mimicking *in vivo* tissues. This is supported by the hypoxic gradient data measured by the Visisen oxygen sensor (see Figure 3-21). The significance of the hypoxic gradient on cells will be discussed further in the following chapter.

Addressing heterogeneity of primary MSC with use of immortalised hTERT adMSC

Another issue highlighted in the study is the heterogeneity of MSC in culture. This issue has hindered the progression of translational MSC research due to challenges faced with identifying and minimising the diversity of subpopulation cells with distinct biological features, resulting in high variability of outcomes in reported literature (315). Heterogenous population and anatomical variation in adMSC has been known to affect cell function and secretome profile (316–318). Although it is known that MSC heterogeneity is an inherent and unavoidable characteristic of MSC, various factors

are known to have an effect as shown in Figure 3-32. Understanding these factors can help with reducing heterogeneity and variability by standardising certain *in vitro* techniques and choice of donor and tissue sources across research laboratories. However, the control of this from a pre-clinical perspective is challenging to implement if these standardised practices have not yet been decided by larger international research groups and organisations.

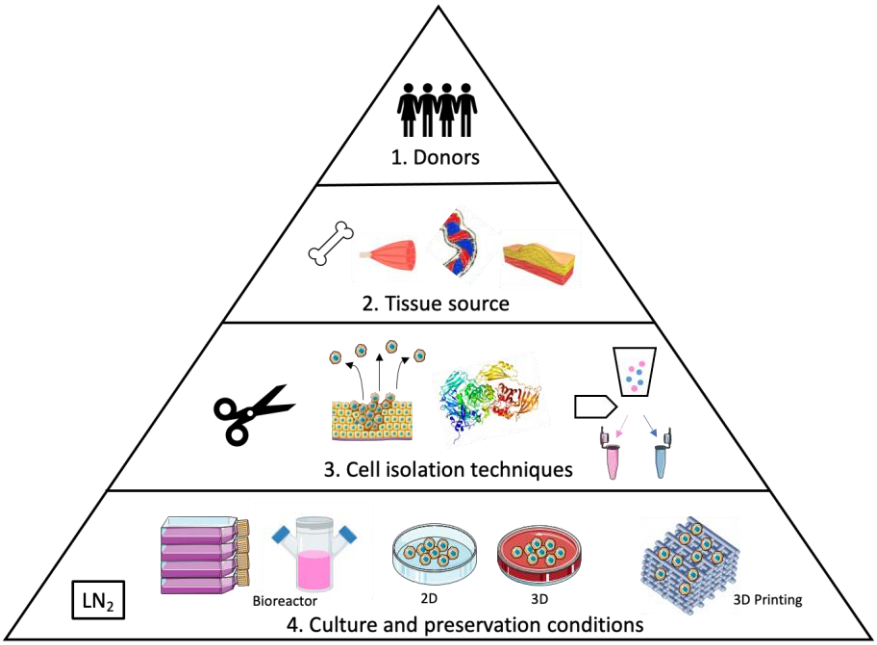

Figure 3-32 Factors which can affect the heterogeneity of MSC are shown in the figure above. MSC can exhibit heterogeneity at different levels and is not limited to the ones listed. 1) Donors of different disease backgrounds, genetics, gender, and age are known to affect the cell population. 2) Cells from different tissue sources are known to have distinct characteristics and variations in heterogeneity. 3) Cell isolation techniques may lead to distinct purity and sub-populations. 4) Cell culture environment and preservation conditions can preferentially favour certain subtypes of MSC and their differentiation potential, therefore affecting heterogeneity in culture. Adapted from Zhou et al. as permitted by Creative Commons Attribution 4.0 International License (319).

A prerequisite for successful tissue engineering outcomes is the ability to expand sufficiently large quantity of cells which can maintain their biological properties throughout extensive subculturing (320). During early optimisation experiments in this study, several issues were identified from using primary cells which were a result of cell population heterogeneity, such as donor-to-donor variability, limitation in cell expansion and varied secretome expression. For example, some of the primary donor adMSC would take 2-3 weeks to reach confluency in a T-flask, whereas others would take less than a week. It was possible to pool the donor samples, but this

resulted in a more heterogenous population of cells with time, which affected the proliferation capacity and possible earlier senescence of cells. (Data not shown) Early trials of transducing primary adMSC with lentivirus also resulted in poor viability of cells. Hence these features significantly restrict the number of experiments that can be performed with primary cells, thus limiting their research applications in fields like tissue engineering, which require a significant number of cells for optimisation during *in vitro* experiments and *in vivo* transplantation.

Recognising that the use of primary cells would have such limitations on downstream experiments and output, a solution was employed to minimise this with the use of immortalised hTERT adMSC cell line. This immortalised cell line is created by introducing the gene encoding for human telomerase reverse transcriptase (hTERT), an enzyme which helps to prevent telomere shortening, increasing the number of possible cell divisions and the resultant lifespan of the modified cells (321). From a practical perspective, they possess many advantageous features which allow their reproducible and feasible use in research: the reduction in variability/heterogeneity resulting from culture conditions, their preservation of cell traits and the lack of limited replication potential/early senescence seen in primary cells at later passage (320,322–324). This makes immortalised MSC a promising modified cell type for practical applications in tissue engineering and experimental models that can be used to establish biological mechanisms of tissue regeneration (320,322,324–326). As a result, the use of hTERT-immortalised MSC has become more widespread in recent years as a substitute for primary MSC for research. Specifically, these cells might be preferred for studying the therapeutic potential of MSC secretome expression (327) as well as genetic stability after further modifications (325).

However, there are some limitations to bear in mind. In most studies using hTERT immortalised MSC, authors assumed them to be similar to primary human MSC due to the preservation of cell traits from the original donor cells. However, a recent review article on this revealed that maintenance of these characteristics is not guaranteed by immortalisation (324). Hence, regular checkpoint testing of their desirable traits will need to be carried out periodically when expanding these cells. It is also important to remember that although heterogeneity is undesirable in pre-clinical research, donor variation is sometimes required to accurately resemble

realistic cell populations *in vivo* when considering the clinical translatability. All things considered, the advantages of using immortalised adMSC for this current study purposes far outweigh the potential disadvantages at this pre-clinical stage.

Effect of different oxygen environments and dynamic hypoxia on cell behaviour and function.

The morphology of the cells did not appear to change when altering their oxygen culture conditions for adMSC, however, there were subtle observable differences seen for bmMSC.

It is known that altering the culture conditions of MSC significantly affects the biological characteristics of MSC, where oxygen tension was found to have a profound influence on the regulatory effect of genetic stability on the cells via their effect on cell cycle checkpoint genes (335,336). This control of MSC senescence and subsequent modifications of gene expressions is critical for the translational purpose to ensure the biosafety of transplanted cells (319). Hence, if time permits, it would be helpful to assess for stemness markers in the different cell types cultured in the different oxygen conditions to determine their undifferentiated state and level of stemness throughout long-term passage, such as the use of senescence-associated β-galactosidase assay, immunophenotyping and investigating chromosomal and genetic stability (337,338).

There is also a need to understand and evaluate the variation in oxygen tension on a peri-cellular level, which has led to the in-depth oxygen measurements performed in this study using novel non-invasive oxygen sensing probes. We found a gap in research of such vital detail in the oxygen levels within the peri-cellular region which is severely lacking in published research. Very few studies have investigated the depth variation in oxygen levels within a multi-well plate for cells seeded in different scaffolds. Hence, this makes data from our study novel and unique. To determine if there are discrepancies in atmospheric oxygen within an incubator compared to the actual dissolved oxygen around the cells under a depth of liquid media and when seeded 2D or within a 3D scaffold can really help empower and guide researchers in refining their methodology; It can help define what levels of oxygen to set within the

incubator for more accurate culture conditions, as well as cell seeding densities. This was clearly demonstrated in our study, where the rate of reduction in oxygen level during culture differs from acellular and cellular hydrogels. This demonstrates that oxygen consumption of cells affects the distribution of oxygen available within the media such that the addition of cells affects oxygen distribution through the well, particularly how quickly the oxygen levels deplete around the hydrogel and media interfaces as well as the peri-cellular regions. The pattern in which this level would decrease with time according to the local atmospheric oxygen levels can help aid how we handle the exposure to hypoxic culture conditions in the hypoxic chamber. In addition, it could also explain the temporal metabolic and proliferative findings for the SH 1% sample groups, shown in section 3.3.1.3.3, where cells in both 2D and 3D environments show a distinct lack of readings and signs of proliferation over 72 hours of monitoring. This could be due to the chronic pathological levels of hypoxia which these cells have been exposed to, leading to cell death. Evidence of this can also be seen in the following chapter when cells are seeded in greater density on INTEGRA®scaffolds. The readings presented there also offer an insight into the oxygen gradient that occurs even in 21% culture, where the difference between the top and bottom of the wells differ from approximately 40% to almost 78%, depending on the seeding density, at 72 hours of culture. **(**see Chapter 4 discussion**)**

Lower proliferation and viability of adMSC in low oxygen conditions have been reported in the literature. Rybkowska et al. found that cells cultured as spheroids (3D) had slightly lower viability and a reduced proliferation rate compared to cells cultured in monolayer (2D) when cultured in 5% oxygen conditions (309). However, the lower RLU readings, and hence, metabolic activity/viability, seen in the SN 21% group in 3D compared to 2D over 72 hours is challenging to explain. One explanation could be the poorer penetrative effect of the substrate through the hydrogel, which was observed in my earlier optimisation experiments with the use of Resazurin (also known as Alamar Blue) in a reduction assay to test for the viability of cells seeded in hydrogel. Resazurin assay is based on metabolically active cells reducing resazurin (blue) into resorufin (pink) in the media. The colour change is detected using a plate/fluorescence reader. The resultant appearance of the gel after 30 minutes of incubation is shown in Figure 3-33. At this point, the picture clearly shows a discrepancy in the absorption and penetration of the Resazurin dye depending on the

position of the gel in relation to the media; Penetration was decreased when the gel sits securely within the well compared to if the gel floats on the media, due to the exposed surface area to the dye. This positional effect of the gel can affect the final output measurement. This could explain the measurement SN 21% gels in the Realtime-glo experiments above.

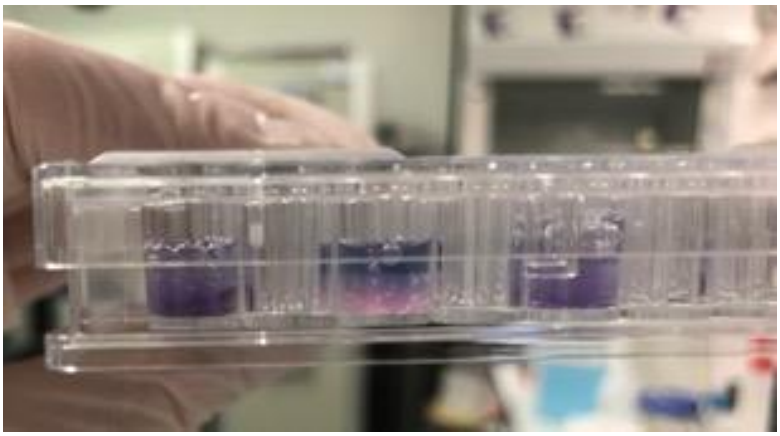

Figure 3-33 The photo shows Resazurin in the media and gel left for 30 minutes. It demonstrates the difference in absorption and penetration of the Resazurin dye depending on whether the gel is floating or sitting snuggly within the well. Penetration is decreased when the gel sits securely in the well (middle gel) compared to if the gel floats on the media (far left and far right gels) due to the exposed surface area to the dye.

However, the data shows consistently lower RLU readings throughout the 3 days of culture compared to the DH (21-1%) cells. It is likely that the transition to a more biomimetic 3D nature of the scaffold has possibly resulted in metabolic changes for cells cultured in static oxygen conditions (1% and 21%) which will be different to DH (21-1%). Certainly, calcein AM stain images of MSC seeded in hydrogel and cultured for 21 days in 21% and 5% in early preliminary experiments showed a distinctly morphological difference in shape under microscopy. (Figure 3-34) Cells from 21% oxygen culture conditions showed rounder, smaller and peri-apoptotic compared to that of cells in 5% oxygen, which appeared larger, elongated and more spindle-like cells. To explain these findings would require more extensive investigations into the metabolic pathways and oxygen consumption changes in relation to how cells interact with their surrounding ECM and their bio-physical properties. Such experiments would go beyond the scope of this thesis. However, published research have alluded to the role of ECM in modulating cellular metabolism and physiology, such as matrix stiffness and collagen density on glycolysis of cells, which can offer

valuable clues into the findings (309,339,340). Rybkowska et al. showed metabolic reconfiguration that accompanies the transition from 2D to 3D culture. They found that the change in the 3D microenvironment resulted in more active processes of mitochondrial respiration and glycolysis. They concluded that the increased metabolism might be associated with the increased demand for energy, which is required to maintain the expression of pluripotency genes and stemness state in the cells in 3D (79). Having such insight can help us plan for future experiments to understand the findings above as well as to overcome the limitations faced in this thesis.

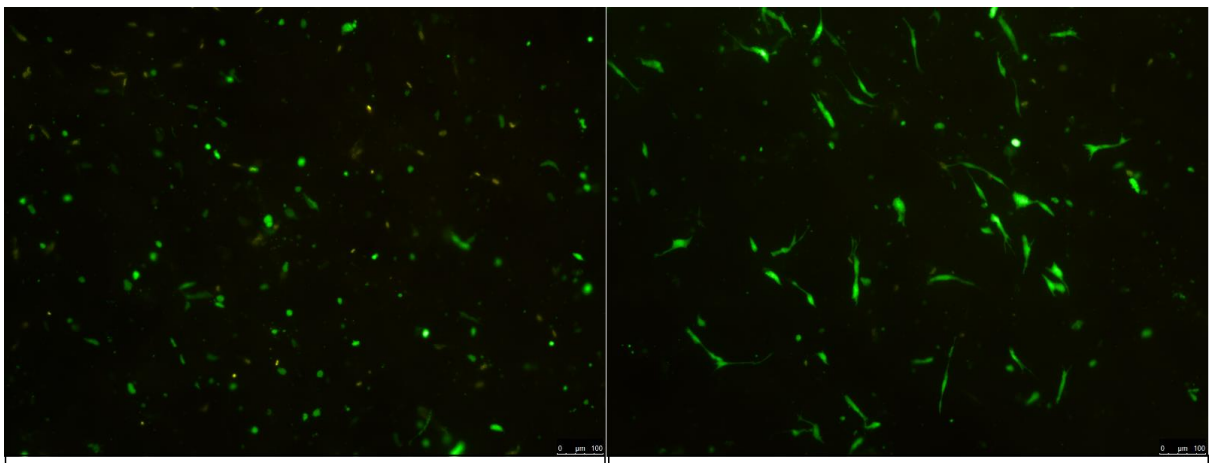

21% oxygen	5% oxygen

Figure 3-34 Morphological differences seen in calcein AM stained P2 MSC seeded in 3D hydrogel and cultured in 21% and 5% oxygen at day 21 of culture. These were microscopy images from early preliminary experiments used during the optimisation of seeding density of cells in hydrogels. Cells in 21% oxygen appeared smaller, rounder and more apoptotic-like compared to the cells in hypoxia, which appeared larger and more spindle-like. Scale bar = 100um.

Hypoxia is a crucial modulator of cell function from ion channels to chemoreceptors and surface molecules (341). Much of this modulation is regulated by HIF-1α transcription factor, as mentioned in the introduction above as well as in Chapter 1 of this thesis. Understanding the effects of different levels of hypoxia on cells predominantly comes from tumour biology and stem cell research. Several cellular mechanisms have been indicated. Reports have suggested a link between altered mitochondrial function in hypoxia and HIF activation (342–344), such that the HIF1 gene has been shown to alter mitochondrial function by suppressing mitochondrial oxygen consumption/respiration (345). This is primarily through the switch between glycolysis and oxidative phosphorylation (66,346). It has been observed that cells in

hypoxia rely mainly on anaerobic glycolysis for energy due to the lack of oxygen for oxidative phosphorylation. Glycolytic enzymes were shown to be upregulated, generating energy and NADH (345). Pyruvate substrate preferentially converts to lactate, which in turn suppresses the delivery of acetyl-CoA into the Krebs cycle. This decreases mitochondrial oxygen consumption (Figure 3-35A) (345,347). The increase in lactate also regenerates NAD+ for further glycolysis. This supports published genetic data that the regulation of glycolytic gene, such as expression pyruvate dehydrogenase kinase 1 (PDK1), is primarily mediated by the HIF1 gene, which appears to be upstream of mitochondrial function (345). In addition, Guzy and Schumacker have shown a paradoxical increase in reactive oxygen species (ROS) production under near-anoxic states which causes mitochondrial electron transport complexes to be in a reduced state (348). ROS inhibits prolyl hydroxylases (PHD), reducing its hydroxylating activity on HIF1α, which in turn helps to stabilise HIF-1α. (Figure 3-35B) All of the above metabolic changes help the cells to adapt to low-oxygen environments, which results in increased cell survival and decreased apoptosis (345). Hence modulation of this transcription factor alters the resistance of MSC to hostile environments, allowing for adaptability. Where there is overexpression of HIF-1α in MSC, there is protection against cell death and apoptosis triggered by hypoxic and oxidative stress conditions; its downregulation results in increased apoptosis and the death rate (349). More accurate measurement of metabolic activity and oxidative stress in different oxygen environments can provide a greater understanding of cellular health during culture. Given the complexity of the metabolic changes in different oxygen conditions and the potential build-up of metabolites that could influence the viability and apoptotic process of the seeded cells, it would be useful to include lactate/pH, NADH and ROS assays to evaluate and compare metabolic changes to compare to published data.

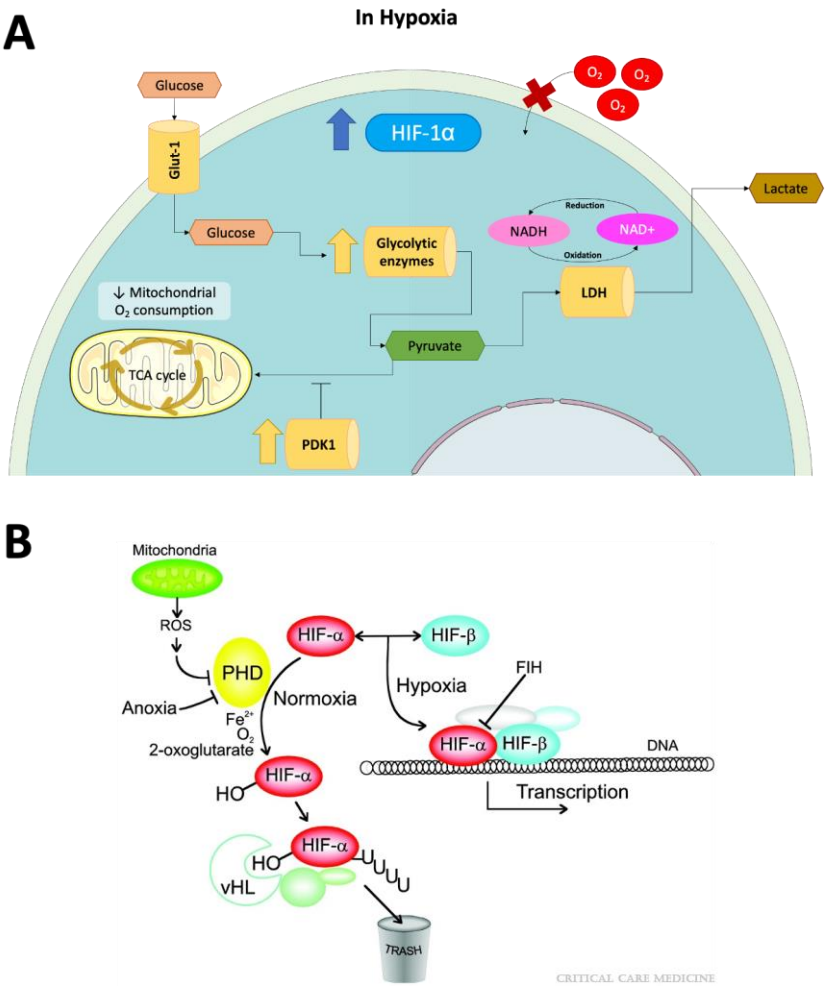

Figure 3-35 Metabolic changes seen in cellular pathways under hypoxia. (A) Increase in HIF-1 activation in hypoxic conditions result in increased glucose transporter (GLUT-1) expression which increases intracellular glucose levels. Upregulated glycolytic enzymes increase the conversion of glucose to pyruvate, which generates energy and NADH. The induction of pyruvate dehydrogenase kinase 1 (PDK1) decreases mitochondrial utilisation of pyruvate and oxygen. Lactate dehydrogenase (LDH) increases the removal of excess pyruvate as lactate and also regenerates NAD+ for increased glycolysis. Image was adapted from Papandreou et al. (345). (B) ROS generated by the mitochondrial electron transport chain can contribute to the stabilisation of HIF-α during hypoxia. PHD, Prolylhydroxylase; FIH, Factor Inhibiting HIF; VHL, von Hippel-Lindau. Figure was reproduced from Paul T. Schumacker (350) with permission under the terms and conditions provided by Wolters Kluwer Health, Inc. and CCC licence.

Intermittent or cyclical hypoxia is a well-known physiological variant that can present in human diseases, such as obstructive sleep apnoea and other respiratory disorders, which has been found to have widespread implications on the pathogenesis of various diseases such as cardiovascular disease and cancer progression (113,155,159,160,341,351). As research in this area grows, understanding the implications of varied hypoxia on cell metabolism led to an interest in how this can be adopted for use for therapeutic purposes, such as the use of

hypoxic or ischaemic pre-conditioning for cardio and neuro-protection in post-myocardial infarction and cerebral injury (168–172,174,175,177,179–181,352–354). The difference between sustained or static hypoxia and intermittent hypoxia is the limited duration and repeated exposures over time. Short-term hypoxia is known to trigger different intracellular mechanisms responsible for the development of the adaptive response, including changes in gene expression (341). The scientific basis for supporting intermittent hypoxia regimes for priming cells for therapeutic purposes is only just coming to light in recent years. Much of this is credited to original research by Martinez et al. and Rosova et al. (87,187) and their data has been covered extensively in Chapter 1.

In our study, we refer to the dramatic change in oxygen culture conditions between the cell culture and seeding process as 'dynamic hypoxia' (DH), due to the dynamic change between the expansion environment to the seeding conditions. (see Table 3.3) This regime was designed to subculture cells in 21% O_2 in T-flask followed by a dynamic switch to seed cells in hypoxia of 1% in well plates. Through the process of validating the optimum hypoxic pre-conditioning regime for the cells, it was clear that DH had advantages in cell proliferative potential, metabolic activity/viability and VEGF production compared to the other oxygen conditions, as shown above. The key to understanding this lie with the key regulator of cells in hypoxia, the HIF-1α transcription factor. Certainly, in pre-clinical studies, the hypoxic pre-conditioning mediated by short-term IH exposure has also been demonstrated to be dependent on the activation of HIF. The therapeutic effects of pre-conditioning were shown to be lost in rats with induced heterozygous deficiency for HIF-1α (355) or when HIF-1 activation was prevented (356).

Given the importance of showing HIF-1α activity in this study, qPCR was performed to investigate HIF-1α RNA expression. However, the results obtained were difficult to evaluate. There were clear discrepancies between RNA expression in cells within 2D and 3D environments. In 2D, more peaks in HIF-1α activity were observed in SH on Day 3 and 7 than DH conditions, which only peaked on Day 5. In 3D, cells showed a steady increase in HIF-1α RNA expression for all the oxygen conditions. However, there was no statistical significance in the data sets. VEGF RNA expression in 2D showed a similar peak on Day 5 of culture, but the expression pattern in 3D showed

in puzzling decrease in all groups over time. None of the above data was found to be statistically significant. Researching more around qPCR issues pertaining to hypoxic-based research, revealed a likely issue originating from the reference housekeeping gene (GAPDH) used for normalisation. GAPDH is a common housekeeping gene used for MSC qPCR research (357,358). It is also the standard reference gene used in our research group. However, on further investigation, it appears that GAPDH could be unsuitable in cells exposed to hypoxia as its expression can be affected by low oxygen conditions (357,359). In addition, HIF-1α is known to be highly sensitive to oxygen. Its rapid degradation can occur in a matter of minutes once exposed to atmospheric levels of oxygen (97,99,104). As such, it is a difficult gene to extract in standard laboratory conditions where the cells would need to be exposed to atmospheric oxygen to be processed for RNA extraction.

Methods to circumvent this issue have been proposed. The use of hypoxic workstations (see Chapter 4 discussions) to ensure the strict hypoxic processing environment should be implemented in oxygen-sensitive experiments. (see discussion section of Chapter 4) However, the cost of such equipment can be prohibitive in many laboratories. HIF-1α stabilisation agents via HIF1α hydroxylase inhibitors used to upregulate HIF-1α in culture, such deferoxamine (DFO) or dimethyloxalylglycine (DMOG), can also be used to temporarily stabilise HIF-1α for processing purposes (360).

The qPCR results have also highlighted the importance of screening and validating reference housekeeping genes in different culture conditions (361). The use of at least 2 different housekeeping reference genes from different cellular components can help minimise the issue of unaccounted genetic changes caused by low oxygen (362). These include (363):

- structure related genes [e.g. RPL13A (358)]
- metabolism related genes [e.g. HPRT(361)]
- transcription related genes [e.g. TBP (364)]

It is also worth noting that getting quality RNA from 3D hydrogels was also met with specific challenges. There are many RNA extraction kits in the market which can

significantly speed up and streamline the processing time for RNA extraction compared to the manual phase separation method described in Chapter 2. However, having tried the phenol compatible ones (Qiagen and Zymo kits shown in Figure 3-36A & B), it was not possible to get enough yield or good quality RNA, measured as absorbance ratio 260/280 between 1.8–2.1, to use for qPCR purposes. (Figure 3-36C) This revelation proved tedious and challenging to the RNA extraction process due to volume of material and processing time required for qPCR purposes.

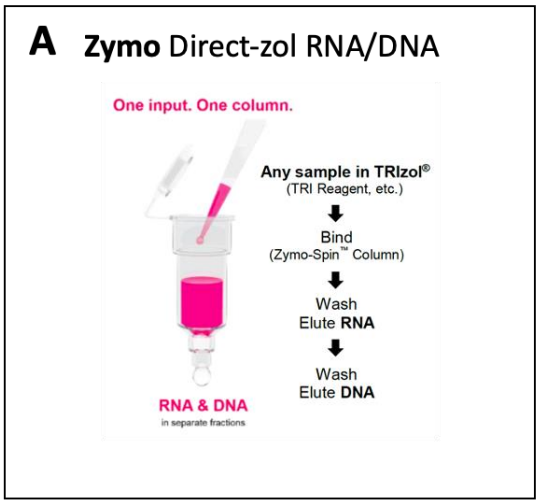

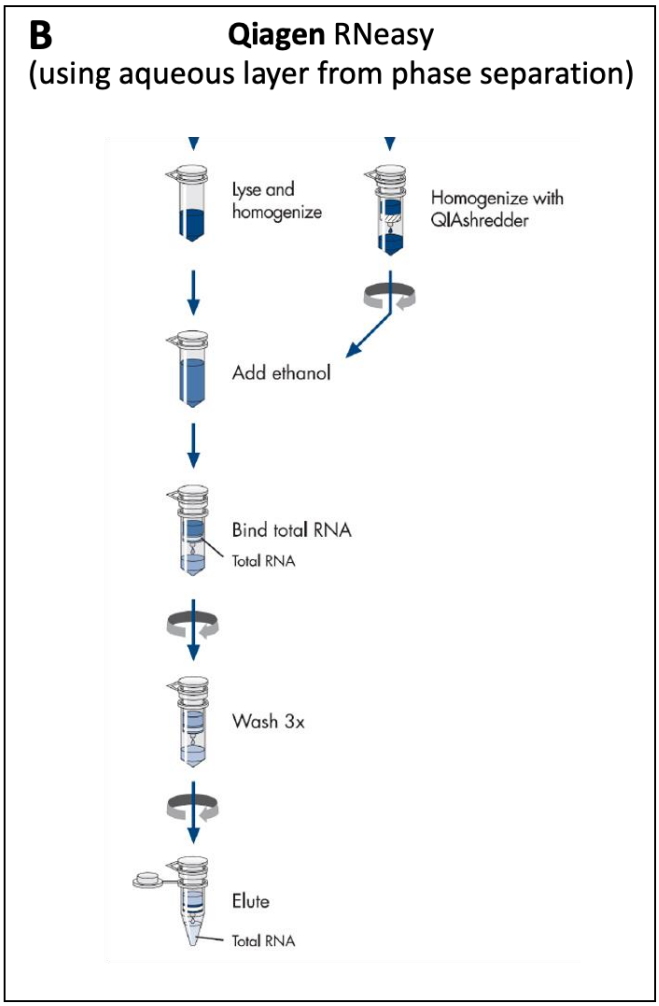

C

Requirement for qPCR:
RNA Concentration: 40ng/ul
260/280 (RNA quality): 1.8-2

Method	Sample ID	ng/ul	260/280
	7.1	9.63	1.47
	7.2	39.33	1.43
Qiagen	7.3	49.28	1.45
	7.5	11.29	1.25
	7.6	18.07	1.13
	7.7	56.15	1.29
	14.1	136.22	1.68
	14.2	26.14	1.78
Zymo	14.3	10.88	1.67

Figure 3-36 The use of commercial RNA extraction kits to help speed up RNA extraction (A) Schematic of the Zymo Direct-zol RNA/DNA kit workflow, reproduced from Zymo product website (Cat #: R2080). (B) Schematic of Qiagen RNeasy kit workflow, reproduced from Qiagen product website (Cat #: 74034). (C) Unfortunately, their use consistently showed lower yield and lower quality RNA, as shown on the table, which were unable to fulfil the requirements for downstream qPCR.

An suitable alternative to qPCR technique would be to carry out microarray analysis using several target genes of interest with set-reference genes (365). More thorough transcriptome analysis could also be carried out by RNA sequencing, but it is more

costly, with additional expertise required in bioinformatics to carry out the analysis accurately (366).

The results also queried the use of gene expression as an appropriate biomolecular marker of angiogenesis. One could argue that a more specific by-product downstream of the HIF-1α pathway, such as VEGF protein expression level, would be far more applicable and accurate in this evaluation of angiogenic potential, given their action would be more specific and easier to account for. This will be discussed further in the later chapters.

Despite growing data supporting the therapeutic benefits of hypoxic on cells, there is still much uncertainty around the detailed cellular effects of hypoxia on MSC. This is largely due to the variability of MSC tissue sources and the lack of consistency in the level of hypoxia used. In majority of the studies, the rationale behind the choice of hypoxic level is usually not justified by the authors. The inclination to use a particular hypoxic level should be guided by the cell's native oxygen microenvironment, but I have not found this to be the case. Hence, the lack of consistently can have an impact on the reproducibility of such experimental data. It is also important to note that there are limited published data on the comparative cytokine expression profiles of the different MSC sources conditioned in different oxygen levels. This may be due to the fact that the scientific community are only just becoming more aware of the significance of oxygen saturations in cell culture. Therefore, it was difficult to benchmark this study's methodology and data towards similar published research, rendering the evaluation and conclusion of the study's findings challenging from that respect.

Another important point to note is the change in the inclination to use bmMSC compared to other cell sources. This is evident by recent translational research trends where ucMSC are shown to be the next most popular tissue source, followed by adipose tissue (see Figure 3-37) (367,319,368). It is reasonable to predict that an increasing number of pre-clinical research will be focused on less invasive cell sources, such as the umbilical cord and adipose tissue. Hence, translational applications of these cells will soon catch up with bmMSC with time. However, at the moment, these changes will take a few years to become apparent. As a result, it has

been particularly challenging to tease out the different cell sources used in similar hypoxia-based studies with ‘mesenchymal stem/stromal cells’ in their description and the validity of their comparative data and references used. Most earlier publications would generically assume the cell source is from the bone marrow, but the more recent papers would have more varied cell sources. From that point of view, it is common to see references used to support their data which do not have the same tissue sources (e.g. using embryonic stem cells or bone-marrow derived cells for studies using umbilical cord MSC) to support results. This can be quite misleading, as we have shown in detail that using data from one tissue derivative does not translate easily due to differences in their cellular response to different oxygen levels. We believe we have a unique and thorough comparative dataset of these cell types which evaluates in great detail the effects of different levels of hypoxia on these three commonly used cell types.

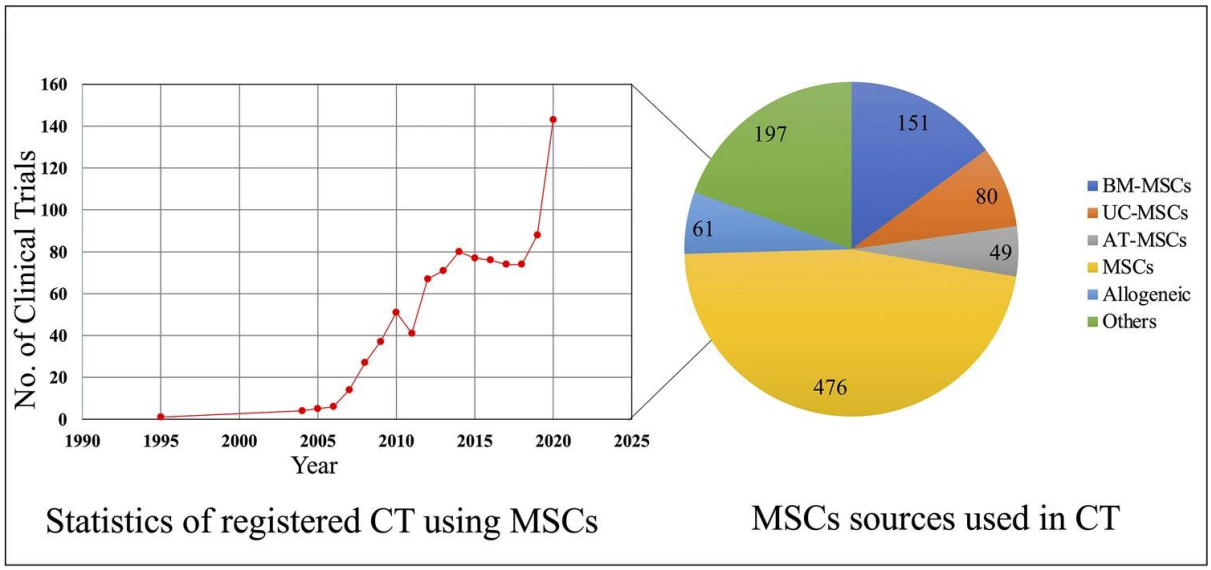

Figure 3-37 An overview of registered MSC based clinical trial (CT) growth and their cell sources. On the left shows a line plot with yearly registered MSC-based clinicals trials at ClinicalTrials.gov since the first use in 1995 up to 2020. On the right, shows a pie chart of number of CT based on main sources used: BM-MSC, UC-MSC, AT-MSC. 476 clinical trials did not disclose the sources of the MSC, ‘Others’ refers to cells derived from tissue such as placenta, dental pulp, amniotic origins. Reproduced with permission under the Creative Commons Attribution 4.0 International License from the article by Jovic et al. (368).

Despite all the above, it was interesting and crucial to note that SH 1% cells had the highest VEGF production potential, calculated as concentration of VEGF normalised to the cellular DNA, from Day 1-5 of culture. (Figure 3-26) The opposite was true for SN 21% cells. This indicates that while SH 1% cells proliferate slower and have a

lower cell population over 7 days of culture compared to SN 21% cells, each cell that was exposed to chronic hypoxia was capable of producing much more VEGF proteins than each SN 21% cells, despite the fact that was a higher cell population in SN 21% group. This proves the fact that hypoxia upregulates each cell's capabilities for production of pro-angiogenic VEGF. However, it needs to be considered that chronic hypoxia can also have a negative impact on cells as demonstrated in the cell health and viability data above. The high production of VEGF per cellular DNA could be in response to cellular stress from being in a pre-apoptotic state, such as those seen in cancer cells deep within the tumour cell undergoing necrosis (369,370). Additionally, a study by Mucci et al. showed that severe hypoxia (1%) had a negative impact on human PSC survival by inducing apoptosis through HIF-1α and P53 independent mechanisms. VEGF production potential of DH 21-1% cells sit between SH 1% and SN 21% cells. On balance, given the overall absolute VEGF levels detected in the media was the highest in DH 21-1% (see Figure 3-22 and Figure 3-23) and cells appear more resilient to the exposure to hypoxia in terms of cell proliferation, viability and CFU parameters as discussed above, there is still a strong rationale for the use of DH conditioning parameters for adMSC to encourage pro-angiogenic VEGF production.

Justification for the use of transduced MSC

Ex vivo genetic modification of MSC can help improve their therapeutic potential by altering their gene expression to match their desired therapeutic output. This technique allowed for the use of MSC for gene therapy. Using lentiviral (LV) transduction to genetically modify MSC has been gaining popularity due to its reported higher efficiency of transduction compared with other methods, such as adenovirus, adeno-associated virus (AAV), lipid transfection and electroporation (371). It has also been shown to be less prone to transcriptional silencing than other retroviral vectors (372). LV transduced MSC also showed enhanced survivability in hypoxia and ischaemia models (373).

Most modifications of genes cited in the literature are targeted for therapeutic purposes. In this study, the motivation for transducing was more practical than therapeutic in origin. During the optimisation process, it was clear that monitoring the

viability of seeded cells beyond the hydrogel model was challenging due to the opacity of the tissue-engineered material preventing visualisation of the cells on microscopy. In fact, issues with continuous monitoring of cells on a scaffold is a well-known hurdle in the progression of scaffold design and better understanding of cell-material interaction in tissue engineering (374,375). In anticipation of the *in vivo* transplant of MSC in the later part of the study, a suitable non-invasive continuous method of tracking implanted cells needed to be established. A local research collaborator recently validated a method of continuous cell monitoring by combining bioluminescence imaging and mesangioblast cells transduced with LV vector carrying reporter genes, firefly luciferase and green fluorescent protein (zsGreen), which was seeded onto TE osephageal scaffold (375). This form of 'reporter gene imaging' of cells using advancing imaging technology for cell tracking purposes is a rapidly advancing field, especially in light of the use of stem cell therapy for various therapeutic translations (376–382). By accessing the same bioluminescence imaging technology and transduction protocol as our collaborators, it was possible to non-invasively monitor MSC metabolic activity and hence the viability of cells on TE scaffold both *in vitro* and *in vivo*.

However, it was important to note that transduced cells do present with some changes compared to their untransduced counterparts in this study. Transduced MSC showed inferior CFU data, with a decrease in CFU count compared to untransduced cells. (Figure 3-29) This is likely directly due to the transduction as well as the processing of cells post-transduction. It has been noted that the use of polybrene, part of standard protocols in lentiviral transduction, can have a negative effect on MSC proliferation (383). In addition, FACS sorting has been reported to have a stressful effect on cells, where LV-transduced and FACS-sorted MSC was shown to expand at a slower rate than original parental cells (384). This highlights the possible detrimental effect of transduction on the functional outcome of transduced cells, although this is still a contentious issue in the reported literature. One study by McGinley et al. demonstrated no adverse effect on MSC morphology, viability or differentiation potential in ischaemic/hypoxic environments using second-generation lentiviral vectors (373). Conversely, although the Realtime-glo viability data in 2D showed lower readings compared to untransduced cells, the mean fold difference between Day 3 and 1 was higher than the untransduced cells, indicating

that the cells are actively proliferating despite a lower setpoint in relative RLU measurement. In addition, the RLU readings in 3D hydrogel were almost identical, highlighting changes that would affect cells when they are seeded in biomimetic conditions. (Figure 3-31C) It was also reassuring to observe that the VEGF expression of the t-MSC in DH when seeded on TE (Integra) scaffolds was comparable to the untransduced cells, albeit with slightly lower means.

It is important to note that although there have been improvements to the transduction technology using LV in the last 2 decades, there are still concerns about the genetic stability post-modification. The need to evaluate genotoxicity is an important quality control and bio-safety requirement for the clinical translatability of these cells (385). As the use of transduced cells in this study was purely to allow for practical non-invasive monitoring and *in vivo* tracking, the need to evaluate the clinical safety of these cells would go beyond the scope of this study. Hence, the decision to integrate the use of t-MSC to the later part of the *in vivo* experiments was warranted, as long as:

1. The therapeutic nature of the transduced cells was not directly due to the genetic modification itself,
2. The proposed therapeutic effect from the DH culture conditions was not affected by the transduction process, as shown in the VEGF data.

Given issues around HIF-1α stability for analysis, a potential future solution may be the insertion of a HIF reporter gene into cells, such as HypoxCR (Figure 3-38), which is a lentiviral dual fluorescent protein reporter which detects HIF active cycling cells (386). This would allow for an accurate comparative analysis of HIF activation of the cells in the different oxygen environments. It can also offer insights into the metabolic changes in the cells when changing and/or cycling cells from high to low oxygen conditions.

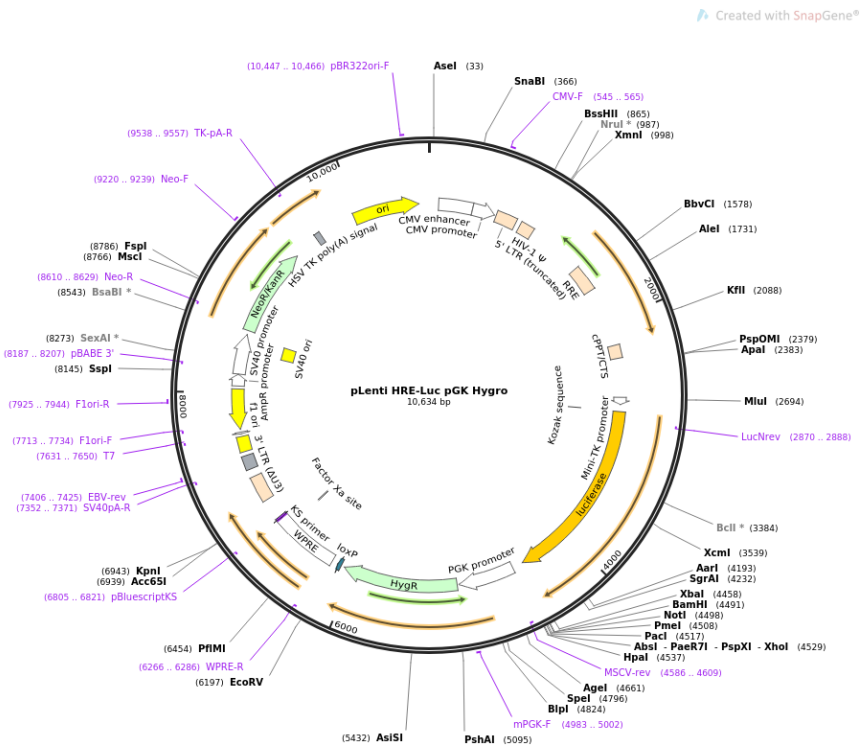

Figure 3-38 HypoxCR plasmid available from Addgene depository. (Addgene plasmid #59946 ; http://n2t.net/addgene:59946 ; RRID:Addgene_59946)

3.5 Conclusion

Adipose-derived MSC possess several benefits in comparison to other MSC population; Their harvesting is not invasive and can produce a cell yield that is more than 1000-fold higher than cord-blood derived MSC and bone-marrow derived MSC (273,275). In addition, they have demonstrated a higher proliferative capacity, longer life-span, and shorter doubling time and *in vitro* senescence when compared to bone-marrow MSC (387). Hence, they are more suitable for clinical translation purposes.

In our this study, adMSC have demonstrated higher clonogenicity, VEGF production and positive proliferative profiles. They also responded favourably to DH culture conditions from the cytokine profile results. The issues around cell heterogeneity and the need for non-invasive real-time longitudinal cell monitoring and tracking in tissue engineering were discussed. It is clear that the changes in angiogenic response are not just affected by the hypoxia preconditioning, it is also influenced by the changes in spatial effects on the cells when seeded in 3D hydrogel. The use of hTERT immortalised adMSC cell line and transduced cells were purposes as a solution to

address the above issues, and their use was debated and justified for the purposes of this study. Problems with accurately measuring HIF-1α expression from cells highlighted the issues around maintaining its stability for *in vitro* evaluation purposes as well as methodological techniques used. These are research areas that would require further improvements and additional work to help produce more reliable results. Overall, the results highlight the multitude of challenges present with the use of cell therapy in tissue engineering. Future research would need to address these challenges to help accelerate its clinical application.

4 Optimisation of Cell Seeding on INTEGRA® Dermal Matrix Scaffold

4.1 Introduction

Problems with effective cell delivery, poor cell survival and inadequate cell retention, in addition to the harsh donor site microenvironments post-transplant are all recognised barriers to the clinical success of MSC therapies. To understand the therapeutic nature of the cells for translational applications, it is also necessary to apply a more realistic 3D biomimetic environment in which the cells would reside *in vivo*. This allows for the accurate evaluation of the structural and spatial influences on the cells when they are seeded on a clinically translatable scaffold. Hence, it is necessary to optimise the transition from 3D hydrogel to a more functional tissue-engineered scaffold.

There are three main issues to address for the successful optimisation and evaluation of MSC seeded on tissue-engineered scaffold:

1. Choice of the scaffold: This would be influenced by the area of the body/organ which requires treatment/regeneration.
2. Cell seeding method: type (active/passive), timing (minutes-hours-days), use of specialised equipment (bioreactors, pumps etc.)
3. Cell seeding density: rule being the most optimal concentration of cells being delivered (i.e., the minimal quantity of cells required to give maximum cell adhesion and the proposed therapeutic effects)

This will be elaborated on in the following sections below.

4.1.1 Choice of dermal scaffold

The previous chapter looked at using 3D collagen hydrogels as a matrix to measure how cells would respond in a 3D matrix microenvironment when the oxygen tension was altered, in order to evaluate the therapeutic nature of seeded cells. To allow the application of therapeutic cells to be more translatable, increasing the complexity of the cell seeding environment was necessary. It also allows for the function assessment of the cell-scaffold complex in later studies.

Skin-based scaffolds are the most widely researched and clinically applicable tissue-engineered organ. The epidermal layer is mainly avascular and requires the underlying dermal layer for nourishment. The dermal layer plays more active role in supporting all the different skin cells and more crucially the re-epithelialisation phase during wound healing. Hence the dermal layer is key for wound healing purposes (388). Hence it is no surprise that dermal-based scaffold are the most commercially available skin scaffold used in the clinical setting (222,223). Given the critical importance of the dermis, many studies focus on dermal vascularisation as the first steps to skin bilayer reconstruction (388). Therefore, wound healing is a useful measure of functional angiogenesis (226).

For the purposes of the study, the downstream measures of cell activity ideally should use non-invasive methods where possible. This will allow for accurate optimisation of cell seeding efficiency and seeding conditions. There are many different types of commercially available tissue-engineered acellular dermal matrix (ADM). They are broadly classified into biological, synthetic or hybrid of both (222). For the purposes of this study, it was essential to use an ADM scaffold already used in the clinical setting to allow for greater translatability of the results. INTEGRA® dermal regeneration template is a commercially available scaffold which is widely used in clinical practice within Plastic Surgery (389). In addition, it has been the subject of several similar pre-clinical studies within the field of tissue engineering, which allows for greater comparative data (223,226,228–241,248,249,390,391).

4.2 Cell seeding method

The process of seeding therapeutic cells on a tissue scaffold requires a significant amount of optimisation. This is not only to ensure the survivability of cells on the scaffold but more importantly to ensure the cells are able to exert the same therapeutic effects in more complex three-dimensional environments (392).

It is equally important to appreciate that cells seeded on different scaffolds alter signalling, morphology and multiple facets of behaviour due to the changes in cell-matrix interactions and response to environmental cues (393,394). Cell seeding is considered a critical component in the construction of TE scaffolds and therefore requires some effort in its optimisation (395). Seeding techniques can also change the effect of the cells. As previously discussed, scaffold preparation, seeding density and type of seeding vessel had a significant effect on the viability of the seeded cells and their potential therapeutic (cytokine) effect (227,396,397). Seeding on scaffolds requires a delicate balance between cell survival post-seeding, cell adherence, seeding density, method of seeding (passive or active/dynamic) as well as resources available to allow for novel seeding techniques required for different scaffold types (such as the use of bioreactors) (398).

There are many different seeding techniques described in published literature and they are largely scaffold-specific (399,400). The most commonly used seeding method is static seeding (398,401). It involves passively seeding a concentrated suspension of cells directly onto the scaffold. This may not be suitable for thicker, more complex TE organs, which would require other methods of seeding, such as dynamic, magnetic, vacuum, electrostatic, and centrifugal techniques, to ensure adequate cell penetration through the structure (398,402,403).

Hypothesis:

Seeding density and changes in the oxygen pre-conditioning environment will affect angiogenic potential of the seeded adMSC on INTEGRA® ADM. This will in turn affect any functional angiogenic response.

Aim:

3. To optimise the method of seeding adMSC onto INTEGRA® ADM
4. To determine and optimise the right seeding density for adMSC for optimal cell adherence and survival
5. To determine if altering the oxygen concentration can affect seeding efficiency of cells
6. To determine if the use of transduced adMSC will allow for accurate longitudinal cell tracking for *in vivo* use.

4.3 Materials and Method

4.3.1 Preparation of INTEGRA® scaffold

INTEGRA® dermal regeneration template without silicone (Single Layer; INTEGRA® Lifesciences Corp, US; # 64101) was kindly donated by the Royal Free Hospital, Plastic Surgery Department for research purposes. In a sterile hood, identical 28.27mm^2 (6mm diameter) disc-shaped scaffolds were created from this master dermal sheet using a sterile 6mm punch biopsy device (INTEGRA® Miltex, US; #33-36). This allows for the scaffold to fit into 6mm diameter-sized wells for *in vitro* culture (non-TC treated 96 well plates or 24 trans-well plates with 6mm wide inserts). The 1.3mm thick cut-out scaffolds were stored in sterile PBS with 1% antimycotic-antibiotic solution at 4°C until further use. Dimensions and approximate area and volume are shown in Figure 4-1.

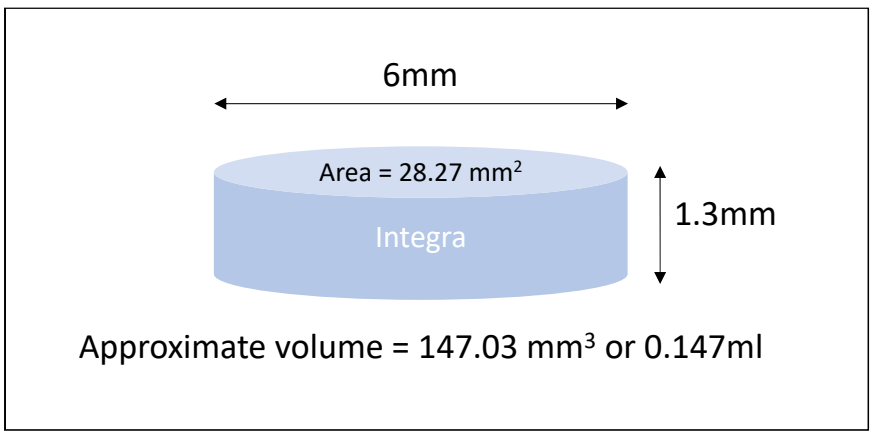

Figure 4-1 INTEGRA® dermal matrix scaffold dimensions

Initial seeding of cells on scaffolds stored only in PBS solution showed poor survival of cells. (Figure 4-11) This was likely due to the dilutional effect of the small volume of media in the cell suspensions with the storage PBS solution which has been soaked into the scaffolds. Subsequent improvement of cell adhesion and survival was achieved after scaffolds were removed from the storage PBS solution and then pre-soak with 20% FBS alpha-MEM media for up to 24 hours prior to seeding. The pre-treated scaffold in media was warmed in a 37.5ºC water bath prior to seeding.

To facilitate the absorption of cells onto the scaffold and to avoid overflow and loss of the cell suspension over the scaffold edge, the pre-treated INTEGRA® scaffold was allowed to slightly dehydrate in a sterile tissue culture hood prior to seeding. This allows for the small volume of the cell suspension to cover the entirety of the scaffold.

4.3.2 Seeding of cells on INTEGRA® scaffold

In order to evaluate the appropriate seeding density for the dermal matrix scaffold, a mix of previous seeding density experiments and published literature (392,399,404,405) was used to guide the methodological process below.

Seeding onto the INTEGRA® dermal matrix scaffold was done using a passive seeding method. After the scaffold was pretreated as described above, they were removed from the pre-soaking media and allowed to dry under a sterile hood in an open sterile dish for 10 to 15 minutes. This allows for the removal of any excess fluid/media within the matrix that may impede on the transfer and absorption of the cell suspension into the scaffold passively.

Due to the small size of the scaffold used for seeding (6mm diameter), it is necessary to concentrate the required cells in 10-15ul of media to avoid overflow over the edge of the scaffold. After some initial trial and error, the best results for the successful and accurate transfer of cells were found with the use of a 10ul or 20ul pipette tip. Figure 4-2 shows diagrammatically how this is done.

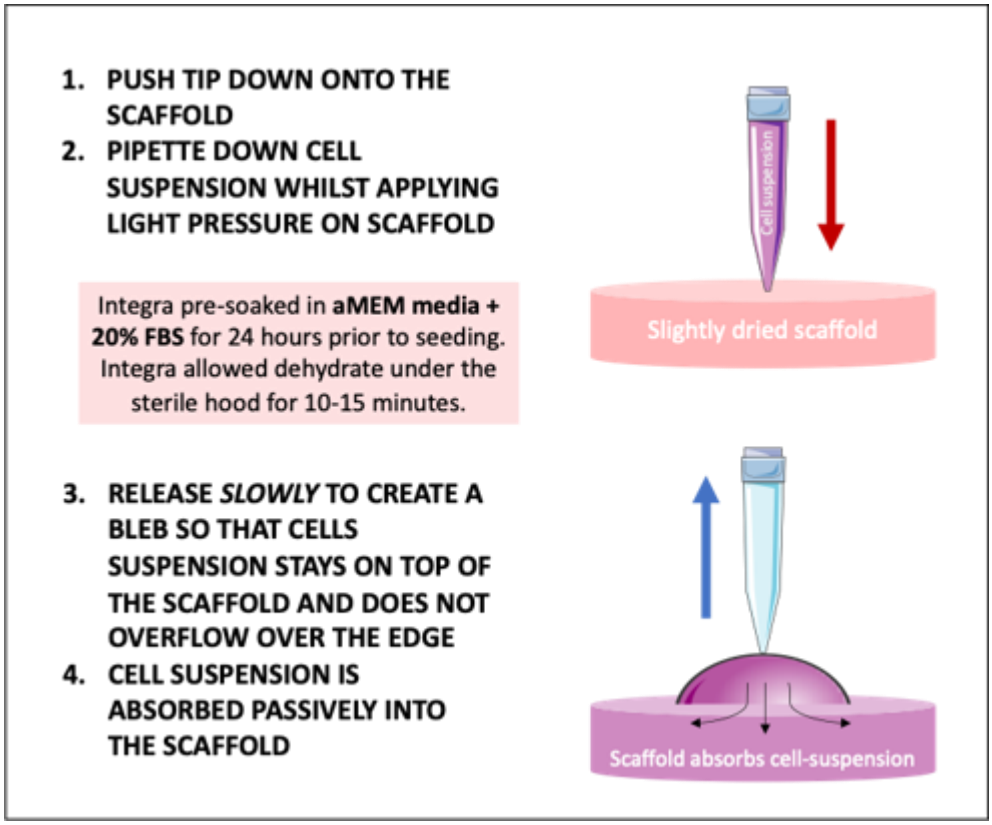

Figure 4-2 Passive cell seeding technique for 6mm INTEGRA® scaffold in non-cell adherent well plates. The required number of cells was suspended in 10-15ul of media.

The seeded scaffold was left for 6-12 hours in a 37.5ºC 5% CO_2 with 21% or 1% O_2, depending on the conditioning group (as described in Chapter 2) to allow as many cells as possible to adhere and to prevent premature washout of cells. 300ul of fresh media, pre-conditioned in either 1% or 21% O_2 for at least 2 hours prior to use, was added to each well thereafter. This ensures the consistency of the oxygen microenvironment of cells throughout the *in vitro* culture. The media was changed every 2-3 days.

To optimise and determine the most effective and pro-angiogenic cell seeding density efficiency for adMSC on the INTEGRA® matrix, a range of between 50,000 to 500,000 cells per 6mm diameter (area of 0.283 cm^2 or volume of 0.147 cm^3) scaffold was tested. This equates to between 1.77 x 10^5 cells/cm^2 to 1.77 x 10^6 cells/cm^2, or 3.4 x 10^5 cells/cm^3 to 3.4 x 10^6 cells/cm^3.

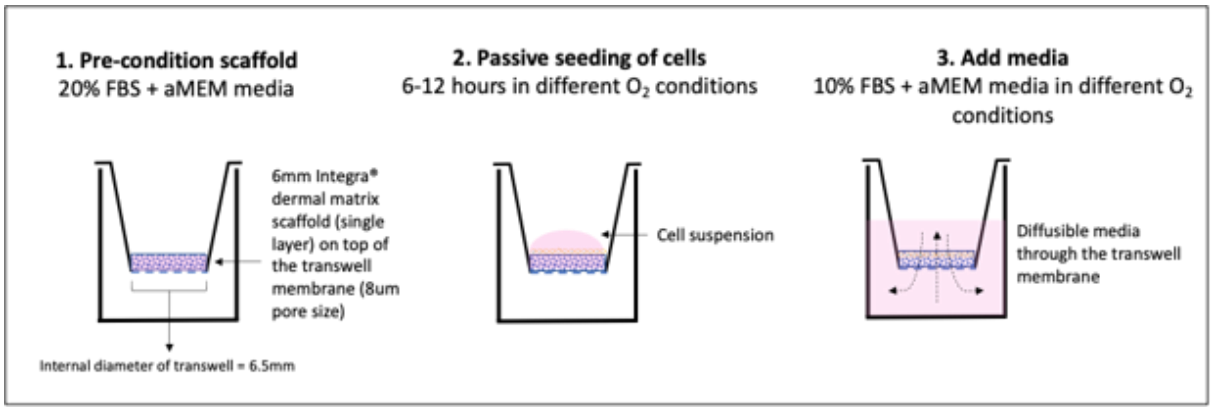

Figure 4-3 The workflow involved in the use of transwell inserts (Thincert®) for seeding of INTEGRA® dermal matrix scaffold.

To better improve the survival of seeded cells on the INTEGRA® scaffold, sterile transwell cell culture inserts in 24 well plates with PET membrane of 8um pore size (Thincert®, Greiner Bio-One International GmbH, # 662638) were used to increase the capacity of media through the scaffold by floating the scaffold centrally in a well via the inserts with a larger volume capacity for media (Figure 4-3). These inserts have a similar internal well area as the 96 well plate of 6.5mm. After initial seeding of 6-12 hours to allow for cell adhesion, a total of 1ml of fresh media was used to fill the wells (350ml into the transwell inserts and 650ml into the wells) as shown in Figure 4-4. Using the transwell setup can also help improve overall cell health and facilitate cell migration due to diffusibility of media through the pores of the transwell inserts, especially in view of the higher seeding density of cells used for the INTEGRA® dermal matrix compared to the 3D hydrogel or 2D monolayer cultures.

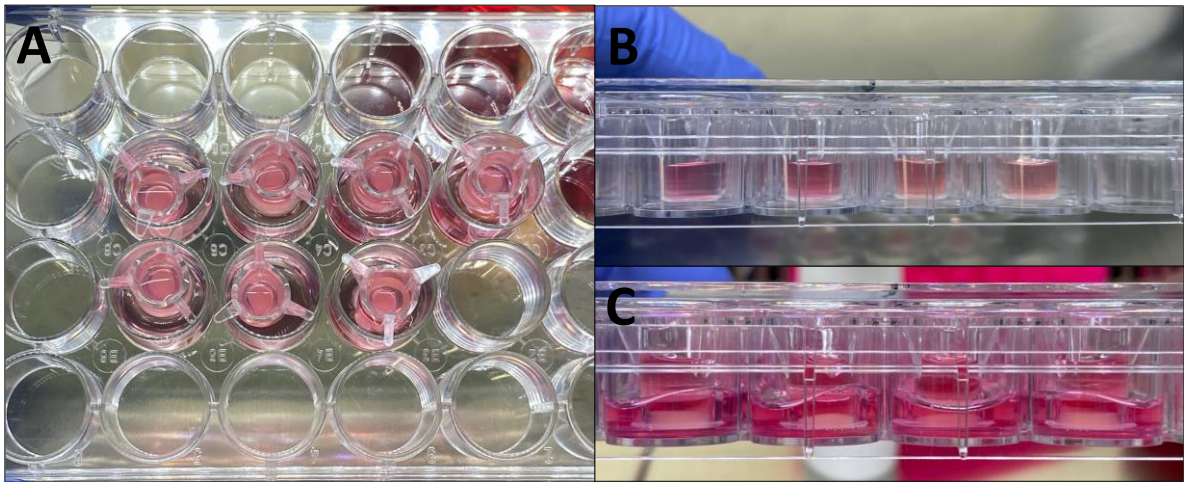

Figure 4-4 Photos of 24 well plate with transwell inserts with INTEGRA® scaffolds. (A)View of inserts from the top with media. (B) Side view of transwell insert with 350ul of media. (C) Addition of 650ul of media to the main well to make a total of 1ml media.

4.3.3 Monitoring of cells seeded on INTEGRA® scaffold

4.3.3.1 Measuring viability of seeded cells

The percentage of live/dead cells on the scaffold can be measured with the use of the Fiji image analysis software (U. S. National Institutes of Health). A 'live dead quantification' Fiji plugin and methodology were used to analyse and count the cells in the appropriate channels (406). Images in Z-stacked are analysed appropriately to ensure maximum intensity from each stack will be represented in the analysis 'Z-Project' option. The colour channels are split to allow for the analysis of the green (calcein) and red (ethidium homodimer) for live and dead cells respectively. This allows for the images to be processed accordingly by a series of 'segmentation' and 'watershed' commands. The resultant image will allow for automatic measurements with the 'analyse particle' and 'ROI manager' tool. (see Figure 4-5)

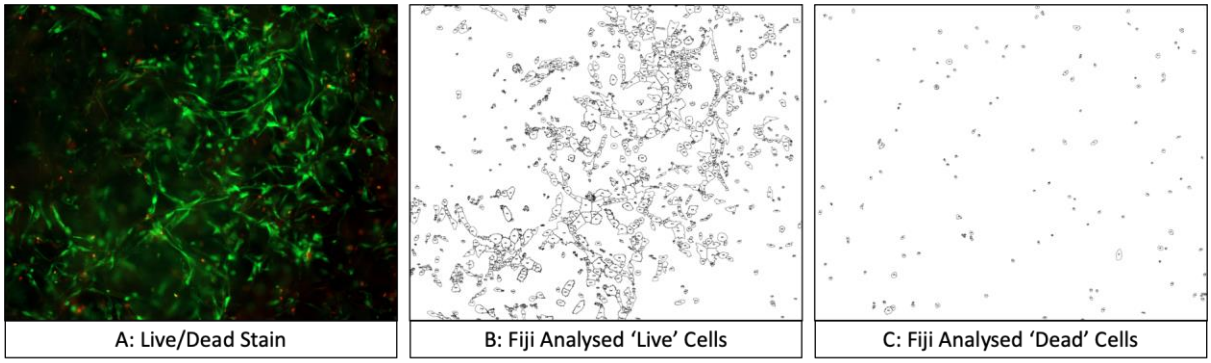

Figure 4-5 Image analysis of Live/Dead stained of cells seeded on INTEGRA® scaffold (A) using 'live dead quantification' Fiji plugin (406). B: Post-processing analysis of green (calcein-stained) cells on the green channel. C: Post-processing analysis of red (ethidium homodimer-stained) cells on the red channel.

The equation below will allow for the calculation of the percentage of live cells as a measure of viability.

$$\%\ live\ cells = \frac{No.of\ green\ (live) cells}{Total\ no.of\ green\ (live) and\ red(dead)\ cells} \times 100$$

4.3.3.2 Measuring metabolic activity

A non-terminal metabolic/viability assay, Realtime-glo (Promega, UK, # G9711), was used directly onto the samples and luminescence was measured using a plate reader as described in General Materials & Methods section.

To confirm the effects of the different oxygen culture pre-conditions on the cell-scaffold, it is crucial to evaluate the cell activity/viability once seeded as well as any pro-angiogenic effect in different oxygen conditions. To accurately access this, the seeded scaffold was evaluated up to the day of the anticipated implant *in vivo*.

To monitor cell adherence, retention and viability of cells seeded in different oxygen conditions, metabolic activity from day 1 was compared against day 0 (i.e. day 1 comparison would be indicative of metabolic activity 24 hours after seeding) or compared at endpoint versus any specific day during *in vitro* culture. This data will not only offer insight into possible metabolic differences of the seeded cells in different oxygen conditions, but it may also help infer on the most suitable day for *in*

vivo implantation of the seeded scaffold. Biological triplicates of samples were used for each condition.

4.3.4 Cell-Scaffold imaging

To monitor cell viability of cells on scaffolds at set timepoints post-seeding, the seeded scaffolds were washed in sterile PBS and diluted live/dead stain (ThermoFisher) was applied for 30 minutes at room temperature prior to imaging of cells on Zeiss Axio Observer with ApoTome (Carl Zeiss Microscopy GmbH, Germany)

Scanning electron microscopy (SEM) was performed on scaffolds before and after 72 hours of seeding to evaluate cell adhesion and morphology. As described in the 'General Materials and Methods' section, scaffolds were fixed in 2.5 % glutaraldehyde (Agar Scientific, #R1020) in 0.1M sodium cacodylate (no calcium) for 1 hour at room temperature. The samples were washed three times for 30 minutes with 0.1M sodium cacodylate buffer and gentle dehydration steps were performed with serial dilution in ethanol (10%, 30%, 50%, 70%, 85%, 95%, 100%). The samples were transferred to baskets put through the Balzers CPD 030 Critical Point Dryer (UK) and mounted on a stub to be coated with gold in a sputter coater (Quorum Q150T ES). Samples were analysed with JEOL JSM-6700F (Japan) SEM machine at an accelerating voltage of 5 kV.

4.3.5 Continuous *in vitro* vertical oxygen gradient monitoring using VisiSens unit

The prototype VisiSens unit (VisiSensTD, PreSens Precision GmbH, Germany) was used to measure continuous readout of oxygen levels through the media and seeded INTEGRA® scaffold, and a detailed experimental setup is described in Chapter 2, Section 2.3.2. Figure 4-6 show the position of the sensor foil within the well.

A comparison was made with the high (500,000 cells per scaffold) and low seeding density (100,000 cells per scaffold) scaffolds to determine if there was any difference

in oxygen levels in relation to the number of cells seeded. Measurements were performed 24 and 72 hours after initial seeding of well plates cultured in 21% oxygen (as described in Section 4.3.2). Due to the nature of the measurement, only 96 well plates were used. The captured measurements were taken from the top, middle and bottom of the well. 10 readings from each section were taken and averaged to be plotted on a graph over time.

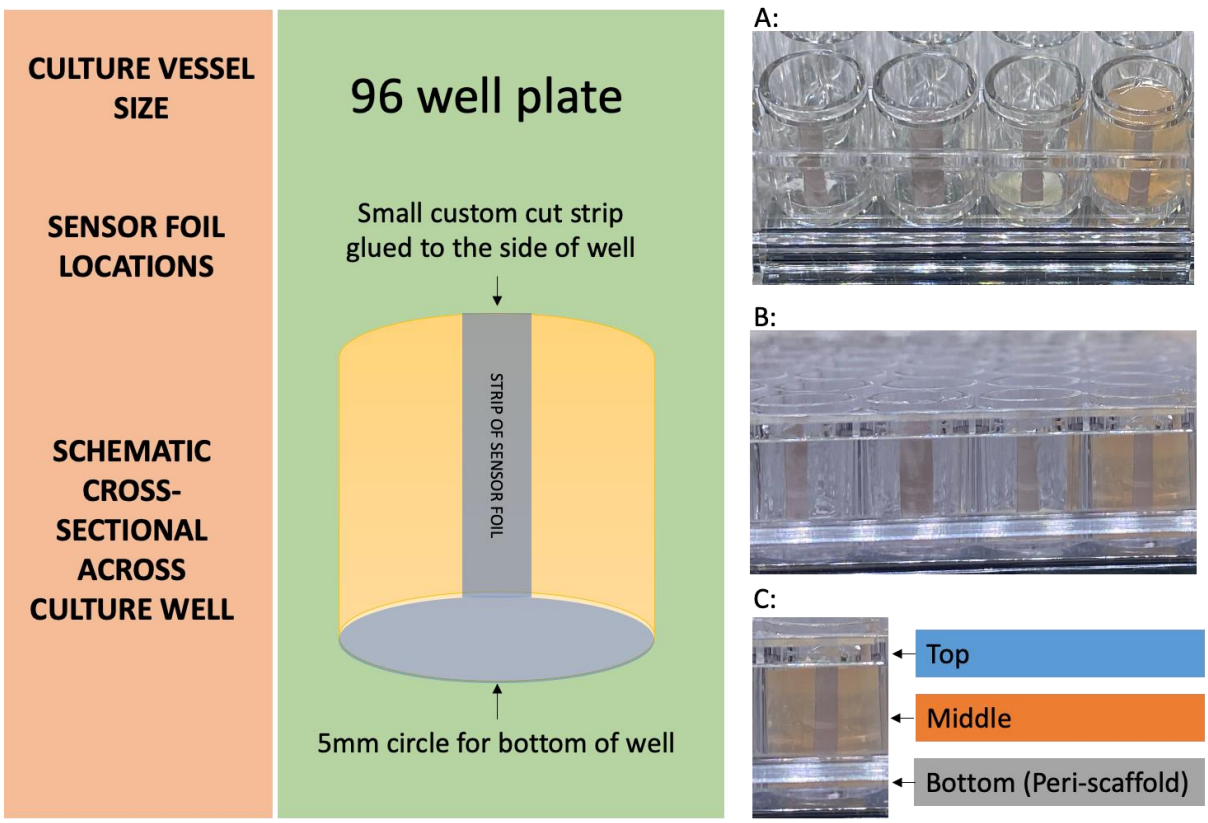

Figure 4-6 Schematic diagram of sensor foil location on a 96 well plate. A & B shows different aspects of the sensor foil location within the well. C: Region of interest for captured measurements – top, middle and bottom.

4.3.6 Measuring angiogenic effect of cells on scaffold

4.3.6.1 Cytokine response using ELISA

Media was collected at defined time points and processed as described in Chapter 2.

4.3.6.2 Angiogenesis Proteome Array

The angiogenesis proteome profile was evaluated with the use of a Human Angiogenesis Array kit (R&D systems, Cat # ARY007). This commercially available array kit features 55 target angiogenesis-related proteins. It allows for the simultaneous analysis of these soluble growth and differentiation factors, extracellular matrix components, proteases, membrane-bound receptors, and intracellular signalling molecules. The antibody array utilised a membrane-based sandwich immunoassay which endpoint produces chemiluminescence typical of immunoblotting procedures.

Conditioned media collected for the first 72 hours of cells seeded passively on INTEGRA® scaffold within non-tissue culture treated well plates. The protocol was carried out according to the manufacturer's guidelines. Briefly, 1ml of pooled media from the conditioned oxygen cell-scaffold culture just before *in vivo* implantation was collected for analysis (day 3) and centrifuged prior to use on the array membrane sheets. After processing according to the manufacturer's guidelines, each array membrane sheet was imaged using a chemiluminescence protocol a CCD imaging system ChemiDoc XR+ (BioRad, USA). The transparent acetate template overlay provided by the manufacturers was used to image the membranes for reference of coordinates. (Figure 4-7) To optimise the exposure time for the accurate detection of protein spots, ten different exposure times, ranging from 10 s to 10mins, was performed. The optimal image captured was imported into Fiji for processing and quantification of the mean pixel intensity from the protein spots. (Figure 4-8) To remove the background signal from each membrane to allow for more accurate quantification, the images were inverted to produce a white background and measurements were normalised to the averaged negative control spots (blank). Each duplicated spot representing a target protein was measured and averaged.

To measure for statistical significance between the groups, 2-way ANOVA was carried out between the averaged values of each analyte and their mean compared between the conditions. Normalised values of pre-condition results were performed by subtracting them from the control values. To better understand the significance of

the means, a measure for fold-change of a specific analyte between conditions was performed using the baseline analysis on Prism software as described here (407).

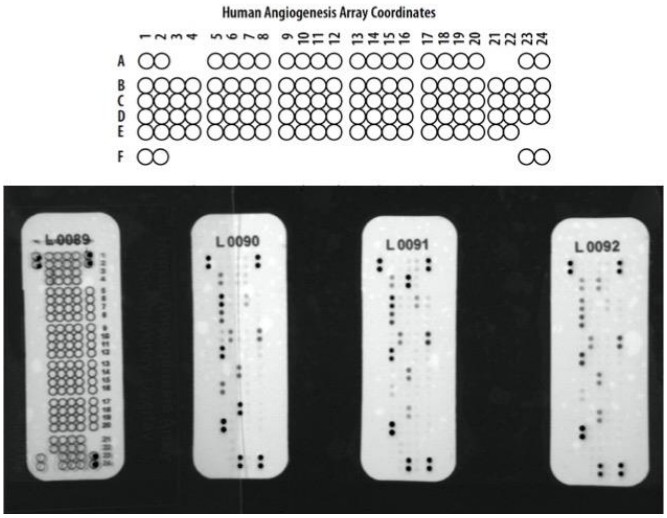

Figure 4-7 Merged image captured from chemiluminescence imager showing transparent acetate overlay (printed template shown above) which is captured to help with later processing and analysis.

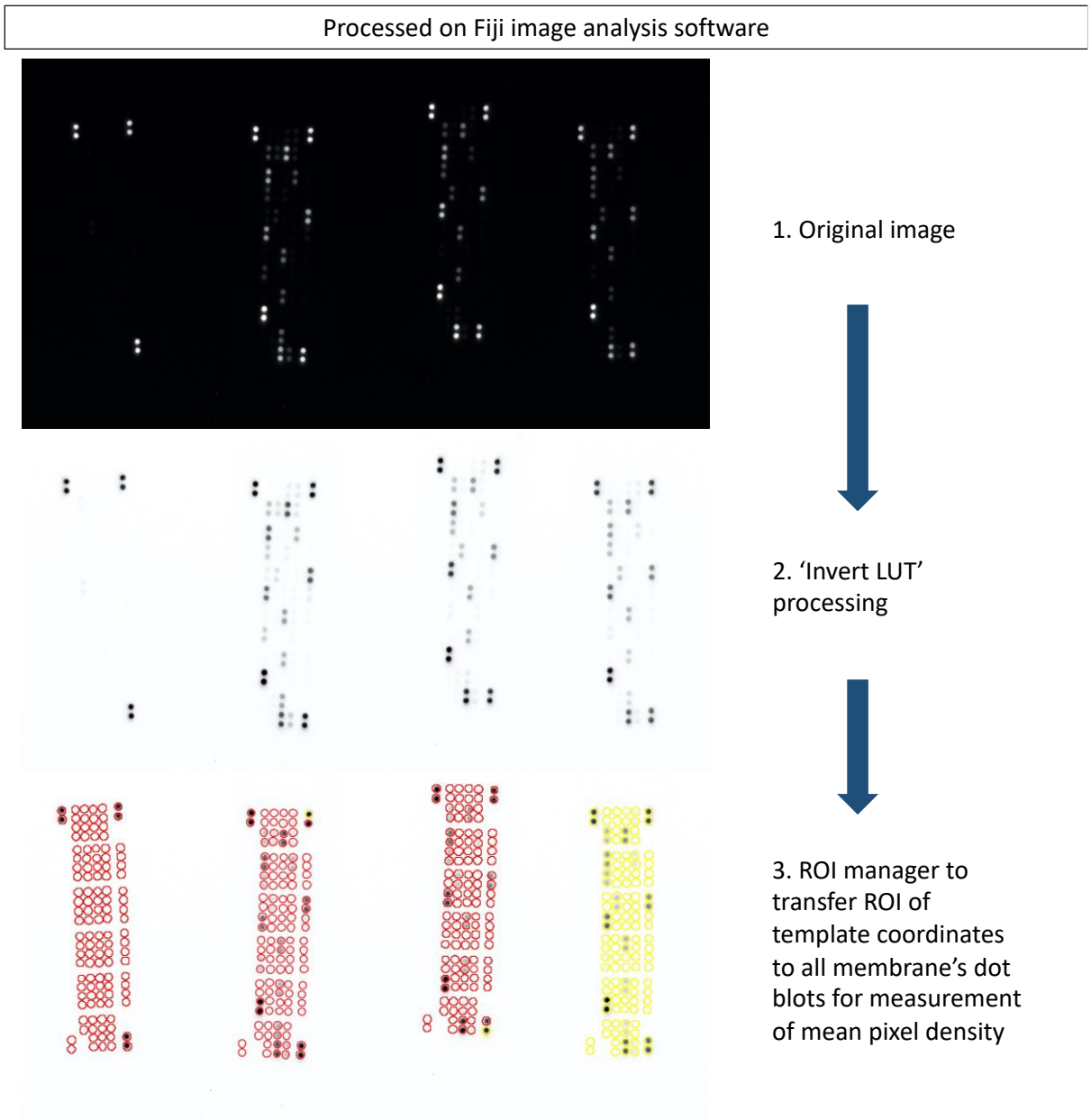

Figure 4-8 Image processing workflow of angiogenesis array membranes in Fiji software

4.3.6.3 Measuring and tracking of cells using D-luciferin and transduced MSC

Monitoring cellular activity and viability of seeded tissue-engineered scaffolds is a challenge and more innovative means to track cellular activity and viability once scaffolds are implanted *in vivo* is necessary. Only some cell tracking methods are compatible with translational research, and trackable for the duration of the desired effect. Using 'reporter gene imaging' technique as discussed in the last chapter, metabolically active cells can be monitored and tracked in real time using D-luciferin,

a substrate for the luciferase transduced MSC. A detailed methodology of this is described in Chapter 2.

4.4 Results

4.4.1 INTEGRA® scaffold characteristics and topology

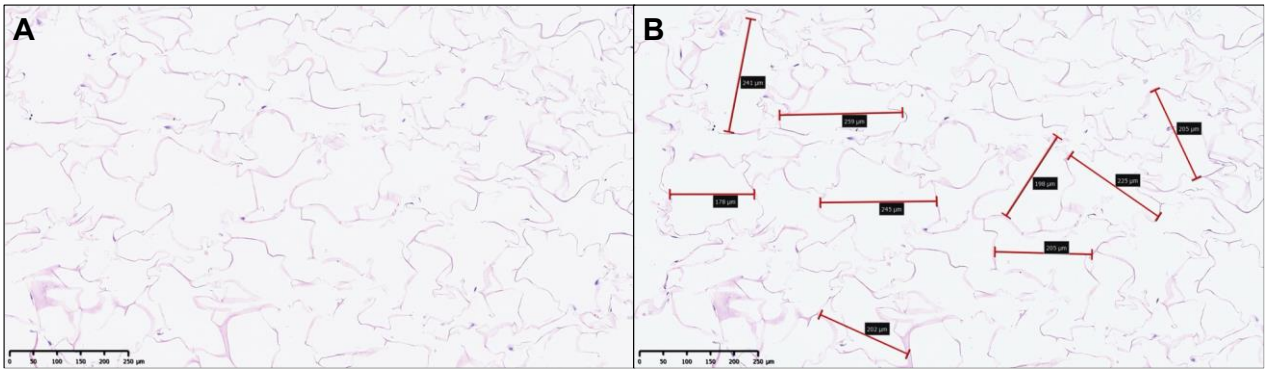

Figure 4-9 A H&E stained histological cross-section of INTEGRA® dermal regeneration template (single layer). The irregular lattice of the collagen matrix can be appreciated. The diameter of the lattice pore size is measured in 2 separate areas of the scaffold, and 9 measurements are performed in each area as shown in Figure 1B.

H&E staining of acellular INTEGRA® sections demonstrates the 2D lattice-shaped collagen matrix. (Figure 4-9) The average 2D lattice/pore diameter was calculated at 209.92 ± 31.52 µm.

SEM images of the acellular scaffold show the three-dimensional topography of the surface as well as the cross-section. (Figure 4-10) It can be appreciated how convoluted and large the pore sizes are compared to that of the size of the cell and the interconnected and fibrous nature of the layered cross-linked collagen in the cross-section.

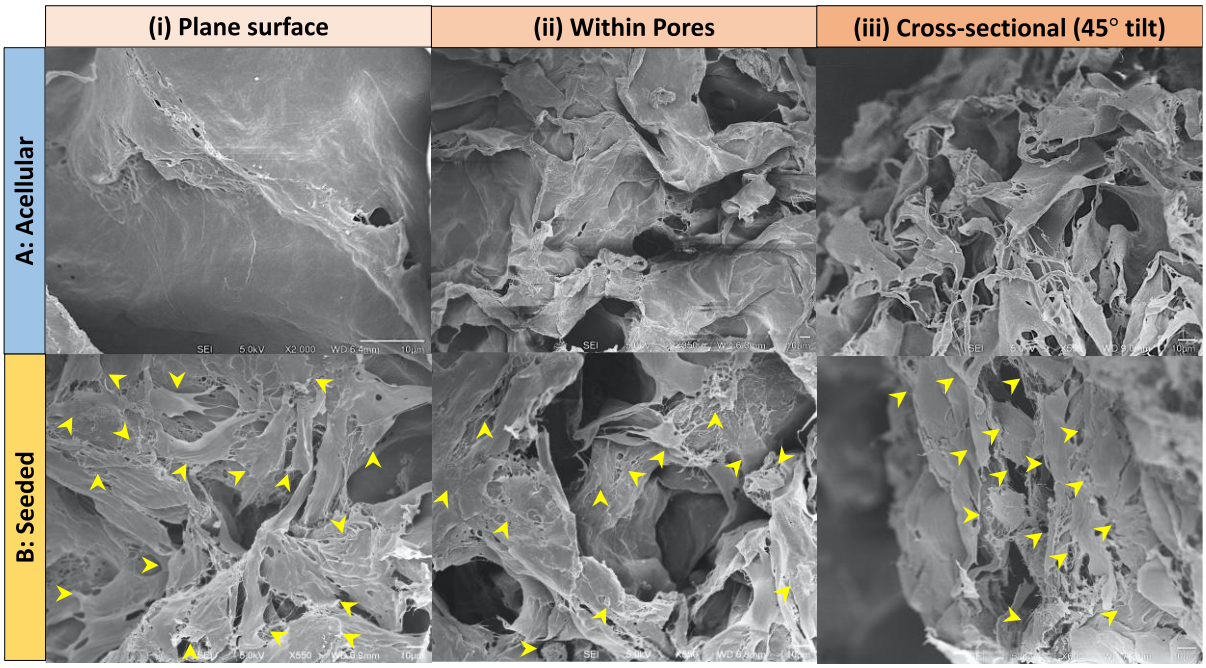

Figure 4-10 SEM of an acellular (top row A) and cellular seeded (bottom row B) scaffold showing various topographic surfaces: (i) plane, (ii) within pores and (iii) cross-section at a tilted angle of 45 degrees. (A) The acellular scaffold has varying textured surfaces, indurating to form pores visible on the surface (A)(ii). The cross-sectional image shows fibrous strands of the cross-linked collagen matrix (A)(iii). (B) The yellow arrows in the seeded matrix represent adhered MSC with a collapsed and flattened appearance. All the cells have long filopodia structures extending from the body of the cells and attaching to the surface of the scaffold. (see Figure 4-12) Cells appear on all the surfaces, including in the pores (B)(ii) and visible cross-sectionally (B)(iii). Scale bar = 10um.

4.4.2 Adhesion and morphology of cells seeded on the INTEGRA® scaffold

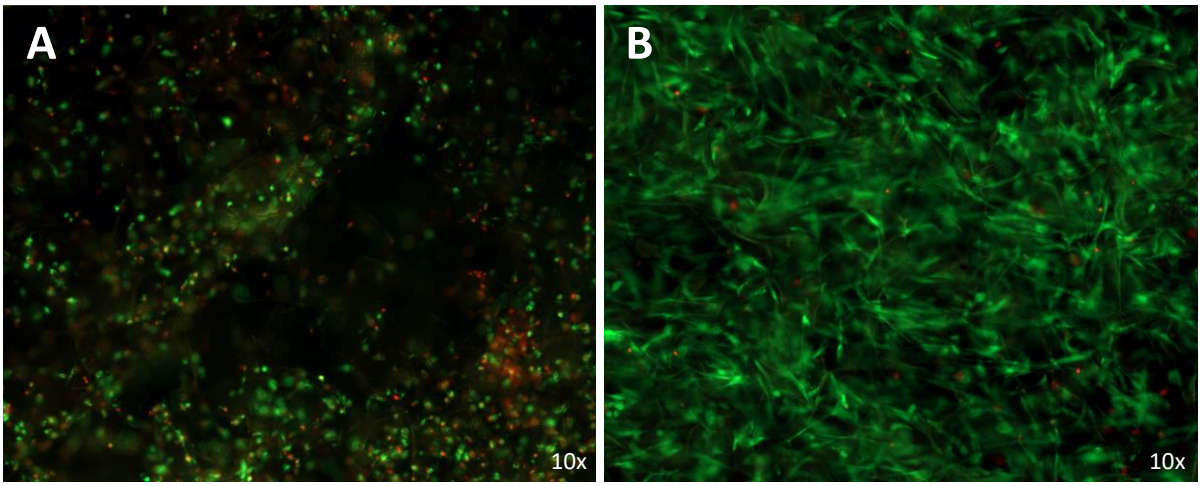

Figure 4-11 Live-Dead stain of scaffolds seeded with adMSC at day 7 of in vitro culture. (A)Cells seeded on a non-pre-treated scaffold which was previously stored in PBS. Cells are rounded and smaller with

more dead cells compared to (B) which shows cells seeded in a pre-treated scaffold in 20% FBS media. Calcein stain (green) = live cells; ethidium homodimer (red) = dead cells. 10x magnification.

Cell adhesion and survival within the scaffold were significantly affected by whether the INTEGRA® scaffolds were pre-treated in media with 20% FBS prior to seeding. It was found that scaffolds that were used directly from being stored in PBS had very poor cell attachment and survival as shown in Figure 4-11A. Once pre-soaked in aMEM media with 20% FBS for 24 hours prior to seeding, cell attachment was significantly improved. (Figure 4-11B)

Compared to the acellular scaffold, the seeded matrix showed cell coverage and adherence across the surface in Figure 4-10. The large pore sizes and interconnected nature of the lattice architecture would aid the migration of cells deeper into the scaffold post-initial seeding. This is evident by the presence of cells within the pores and the cross-sectional area of the scaffold. Morphologically, cells appear flattened, spread out with multiple long fibrillar-like filopodia attachments onto the surface, indicating healthy living cells. (Figure 4-12B) Conversely, inactive, unhealthy, or dead cells would appear small and rounded on SEM. (Figure 4-12A) This can also be further appreciated on fluorescent Live-Dead stained cells seeded in unfavourable cell culture conditions. (Figure 4-11) Due to the fibrous nature of the collagen matrix, the cells on matrix surfaces can be difficult to discern on SEM. However, these differences are more noticeable when comparing acellular scaffolds to the seeded scaffolds, due to the presence of filopodia attachments from the cell onto the scaffold surface. (see Figure 4-10B and Figure 4-12B)

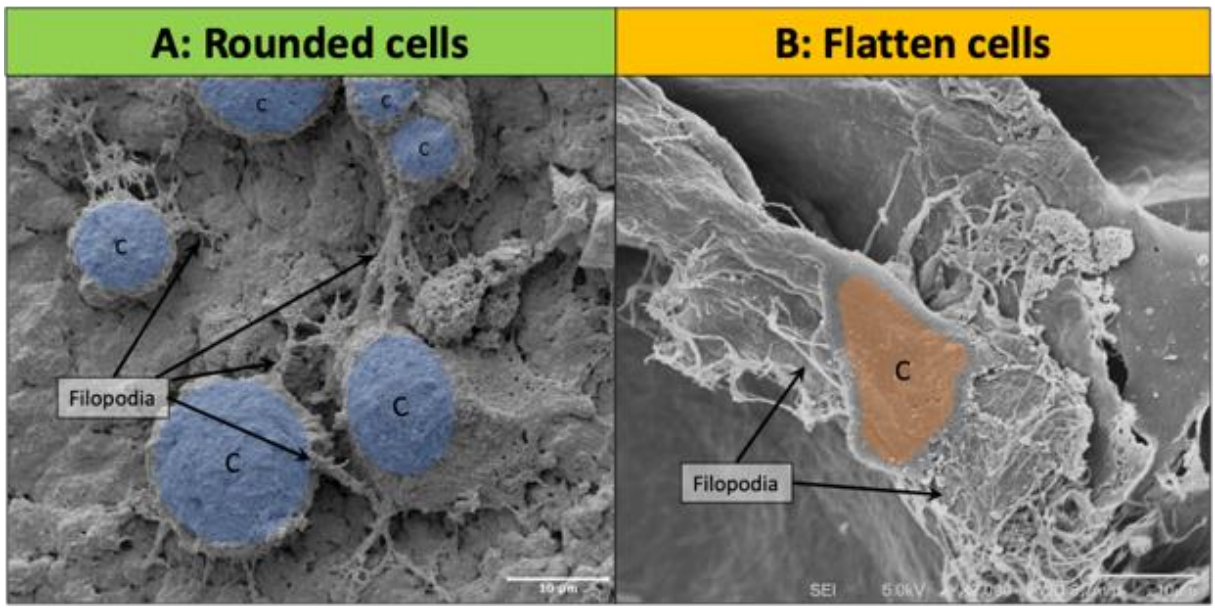

Figure 4-12 SEM of seeded cells on different scaffold surfaces. Symbol 'C' on highlighted areas of the image represents seeded mesenchymal cells (A) The rounded cells (labelled blue) on the left image are MSC seeded on decellularised trachea scaffold. (B) The right image shows a more flattened, spread-out MSC (labelled orange) with long filopodia structures anchoring the cell onto the INTEGRA® dermal matrix surface. Scale bar = 10um.

Seeded adMSC appear to align themselves into the pores of the scaffold after seeding. (Figure 4-13B) This is also appreciated from the SEM appearance of how the cells adhere tightly to the surface around the porous lattice scaffold in Figure 4-10(B)(ii) given the relatively small size of the cells to the pores. Hence, once seeding is optimised, the INTEGRA® dermal matrix is favourable for cell attachment and supporting necessary cell migration into the inner matrix of the scaffold.

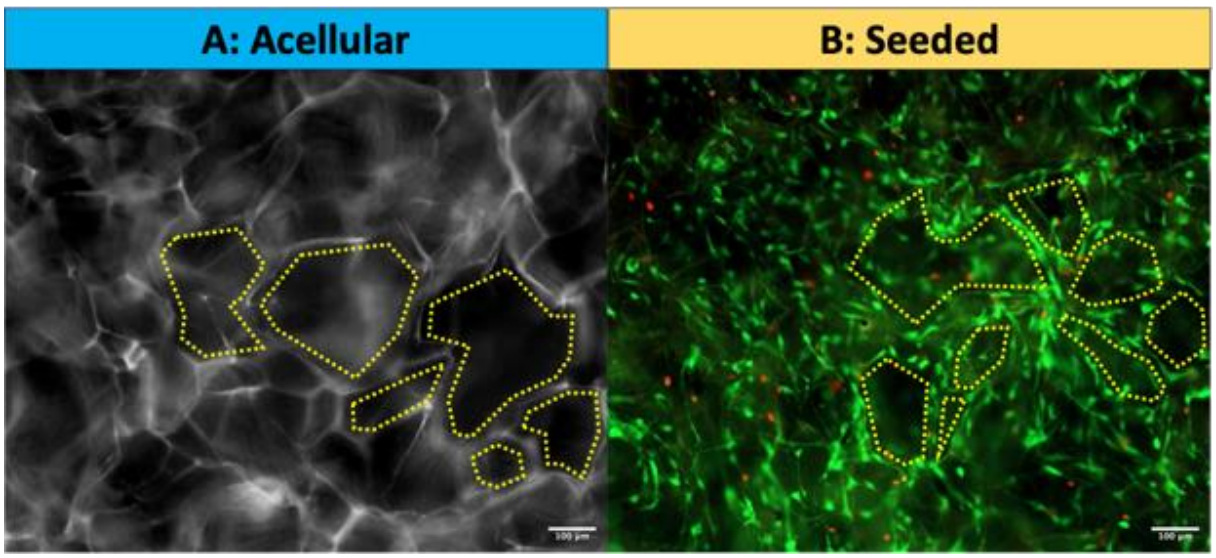

Figure 4-13 (A) Fluorescence microscopy of a control acellular INTEGRA® scaffold treated with Live-Dead stain. No cells are detected but its lattice architecture was revealed due to the autofluorescence nature of the collagen matrix, examples as highlighted by the yellow dotted outlines. (B) Fluorescence microscopy of Live-Dead stain of cells seeded INTEGRA® scaffold on day 3 of implantation. Cells appear to align to the porous outline of the scaffold, as shown by some example yellow dotted lines. Calcein stain (green) = live cells; ethidium homodimer (red) = dead cells. 10x magnification; scale bar = 100um.

4.4.3 Effect of different oxygen conditions on seeding efficiency

To determine the seeding efficiency of adMSC on the INTEGRA® scaffold, cell viability was evaluated via cell metabolic assays. Measurement of metabolic activity of cells was assessed using non-terminal, non-lytic means such as Realtime-glo and D-luciferin when transduced adMSC were used. The same pattern of cell metabolic activity was detected in both experimental modalities.

The overall percentage of non-adherent cells between the two different oxygen culture environments was calculated by the difference between the cell viability measured on Day 0 and Day 1. Day 0 reading accounts for initial non-adherent but viable floating cells in culture after the initial 6-12 hours seeding step. The luminescence, which is recorded as relative light units (RLU), detected post 24 hours after seeding reflected cell viability and an indirect measure of cell adherence onto the INTEGRA® scaffold when calculating the difference between Day 0 and Day 1 reading.

Differences in cell adherence in different oxygen pre-conditions can be observed. Figure 4-14 shows the mean percentage of non-adherent cells was higher in cells cultured in 21% (76.81± 8.84) compared to 1% (69.17 ± 10.86), but this was not found to be statistically significant.

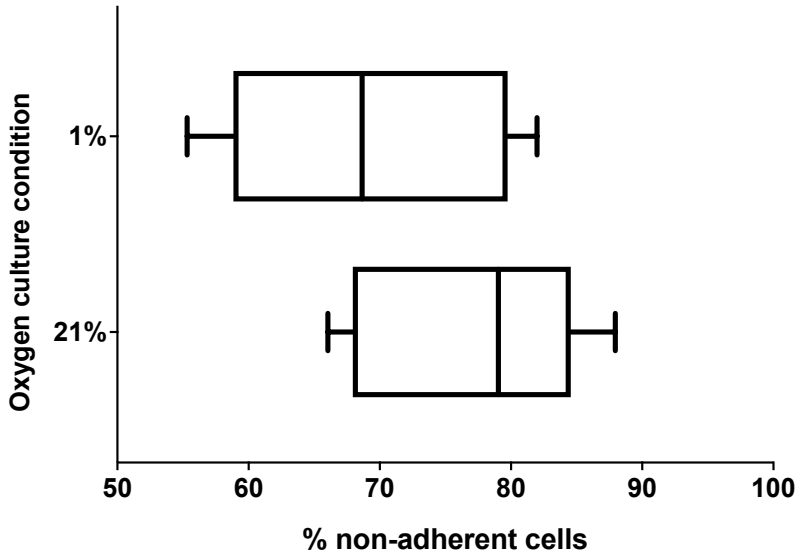

Figure 4-14 Box and whiskers plot of the percentage of non-adherent cells on the INTEGRA® scaffold. n-number = 5 per oxygen condition.

To explore this further, I performed an intricate evaluation of cell adherence and retention for various cell seeding densities (SD). Due to the complexity of the extracted data, the analysis will be explained by comparing Figure 4-15 and Figure 4-16 graphs A, B, C and D individually under the sections below:

(i) GRAPH A

To compare and assess cell seeding efficiency between different SD (50,000 – 500,000 cells per 6mm scaffold) in the two different oxygen conditions, RLU readings were compared over time. (Figure 4-15A, Figure 4-16A) A sharp drop in value from Day 0 to Day 1 suggests that not all the cells seeded would have adhered to the scaffold and survived. Conversely, any non-adherent cells would then not be viable in the seeding period, and hence the drop in RLU readings would indicate the loss of cells from this. A general decline of values (as noticed in other viability studies throughout this project) was noted followed by a subsequent plateauing of values in

all seeding densities, which may suggest that only a portion of cells adhere to the scaffold and do not proliferate past a ‘saturation’ point in the scaffold over time.

(ii) GRAPH B

Graph B shows changes in readings over time to monitor for cell proliferation or possible loss or metabolic quiescence when readings fall below 0. This was calculated by comparing RLU reading to the previous reading, which helps indicate cell proliferative activity or cell death plotted over time. Interestingly, when comparing readings from the previous day to determine the level of cell loss or cell retention/proliferation, the highest increase in RLU readings was found between Day 2 – 3 across all SD and oxygen culture levels. (Figure 4-15B, Figure 4-16B) 21% oxygen culture conditions produced the highest positive readings in 150,000 followed by 250,000 SD per scaffold (Figure 4-15B). For 1% oxygen saturations, the highest positive readings were found in 50,000 and 150,000 SD per scaffold, followed closely by 100,000 SD per scaffold (Figure 4-16B) Day 3 appears to be the most suitable time to transplant based on highest metabolically active cells.

(iii) GRAPH C

Shows percentage non-adherent cells post initial seeding, comparing readings from Day 1 compared to Day 0. For 21% oxygen conditions, 50,000 SD was found to have the lowest percentage of non-adherent cells at 36.5%, whereas the highest was 500,000 (80.1%) followed by 250,000 SD (79%). (Figure 4-15C) For 1% oxygen saturation conditions, 150,000 SD had the lowest percentage of non-adherent cells at 55.3%. The highest was found to be at 100,000 SD (82%) followed by 50,000 SD (77.5%). (Figure 4-16C)

Overall, results show that lower SD favoured 21% oxygen culture conditions in terms of initial cell adherence. The converse was seen in 1% oxygen conditions where SD between 150,000 to 500,000 was calculated to have less than 70% non-adherence. This was similar for cells cultured in 21% oxygen, where SD between 50,000 to 150,000 were calculated to have less than 70% non-adherence.

(iv) GRAPH D

To show positive cell retention on the INTEGRA® scaffold over time between seeding densities, RLU values were compared to original Day 0 readings. For cells seeded in 21% oxygen, SD of 50,000 showed higher cell retention of more than 30% over 8 days compared to the other groups. 100,000 SD also showed similar stability of readings over Day 1-3 of more than 24%. Readings from other SD fell sharply after Day 1 and remained under 7% across all groups between Day 2-8. Readings also fell from Day 3 to Day 8 for 50,000 and 100,000 SD groups. Cells seeded in 1% oxygen did not show as much percentage cell retention compared to the cells cultured in the 21% group. On Day 1, 150,000 SD had the highest cell retention percentage of 44.7% followed by 250,000 SD at 37.6%. Comparing data from Day 1 and 3, the 150,000 SD still had the highest percentage of 26.3% compared to the other groups. This was followed by 100,000 SD at 23.3% then 250,000 SD at 20.3%. However, from Day 3 to 8, data showed calculated percentages below 1% of the original readings on Day 0.

The results supported the data shown in Figure 4-15C and Figure 4-16C which showed favourable results, in terms of cell adherence and cell retention, for lower SD of 50,000 to 100,000 in cells cultured in 21% and 150,000 SD for cells cultured in 1%. When assessing for the increased cell metabolism/proliferation from Day 2-3, the concordance data from both 21% and 1% oxygen culture conditions was found in the SD of 150,000 which had the highest percentage change in reading.

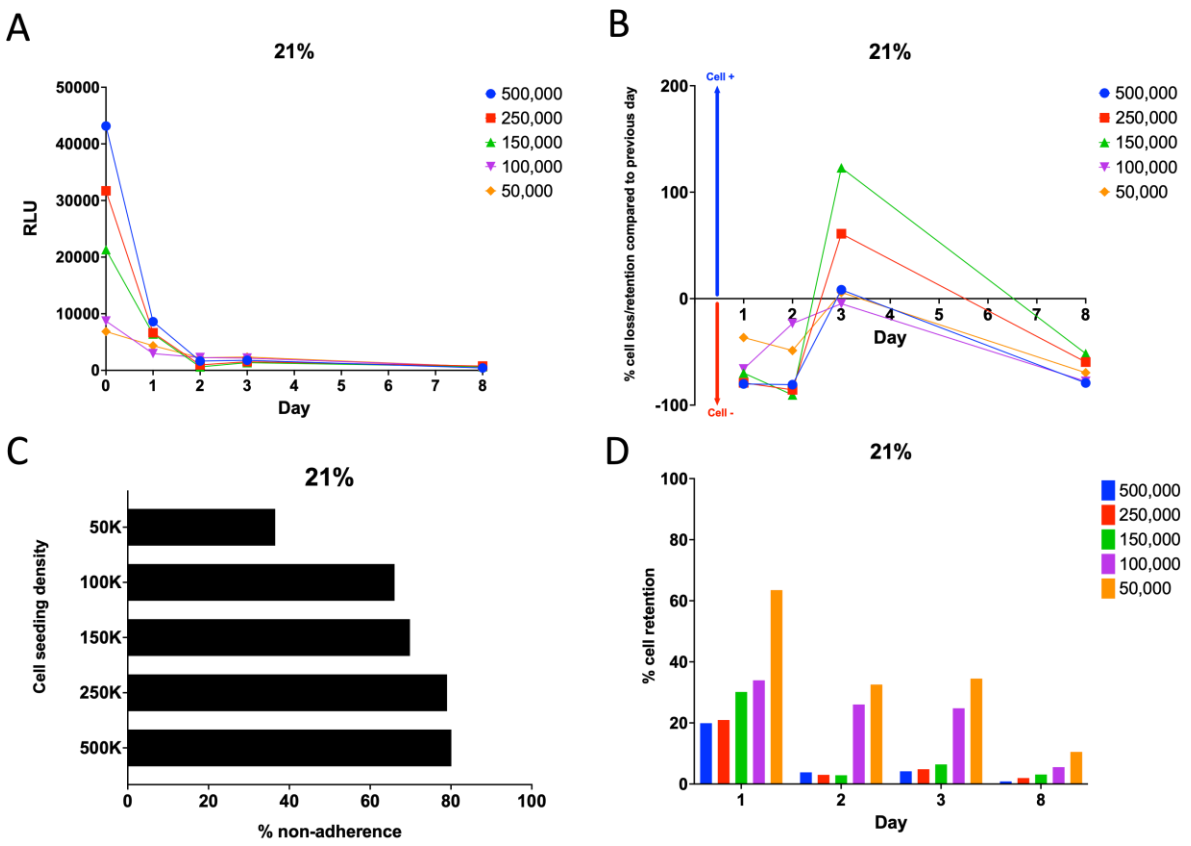

Figure 4-15 Metabolic activity from seeded cells in 21% oxygen culture environment from Day 0 - 8. (A) Luminescence readings from different seeding densities 50,000 – 500,000 cells per scaffold, measured as relative light units (RLU), are plotted against time. (B) Percentage loss or gain of RLU reading compared to the previous reading, which is indicative of cell proliferative activity or cell death, plotted over time. (C) Percentage of initial seeded cell non-adherence after 24 hours of seeding, measured by comparing Day 1 reading over Day 0. Lower the percentage of non-adherence would indicate higher cell retention. (D) Percentage cell retention over time, measured as a particular timepoint reading over Day 0 reading.

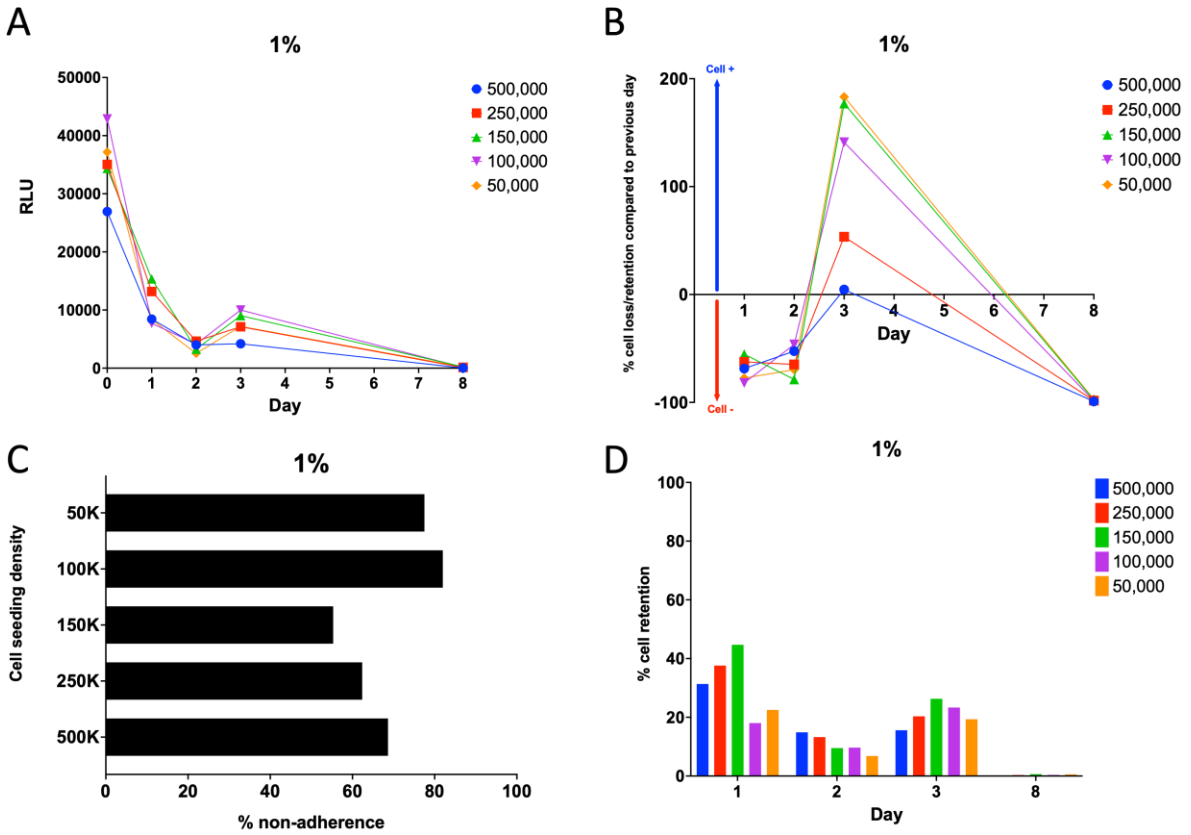

Figure 4-16 Metabolic activity from seeded cells in 1% oxygen culture environment from Day 0 - 8. (A) Luminescence readings from different seeding densities 50,000 – 500,000 cells per scaffold, measured as relative light units (RLU), are plotted against time. (B) Percentage loss or gain of RLU reading compared to the previous reading, which is indicative of cell proliferative activity or cell death, plotted over time. (C) Percentage of initial seeded cell non-adherence after 24 hours of seeding, measured by comparing Day 1 reading over Day 0. Lower the percentage of non-adherence would indicate higher cell retention. (D) Percentage cell retention over time, measured as a particular timepoint reading over Day 0 reading.

In addition, Figure 4-17 shows representative Live-Dead stained cells from Day 8 of culture in different SD for both 21% and 1% culture conditions. Cells in 21% oxygen appear to have more live cells which are highly confluent on the surface of the scaffold. Cells also appear more spindle-shaped in the lower SD with more rounded cells noted in 250,000 and 500,00 SD. Seeded cells in 1% oxygen show many more dead cells (red) with live cells (green) appearing more rounded and smaller in appearance. More dead cells were visible with increasing seeding density for both 21% and 1% groups, especially with the 1% hypoxic experimental group.

Image analysis of the Live-Dead stain data for Day 8 of culture, shown in Figure 4-18, confers with the metabolic data above where lower seeding densities between 50,000 to 150,000 in the 21% oxygen culture environment had a higher percentage of live cells compared to SD of 250,000 and 500,000. Seeded cells in 1% hypoxia showed similar trends with higher percentage of live cells in the lower SD groups compared to higher SD of 250,000 to 500,000, but the percentage of live cells were lower overall in all 1% hypoxia SD.

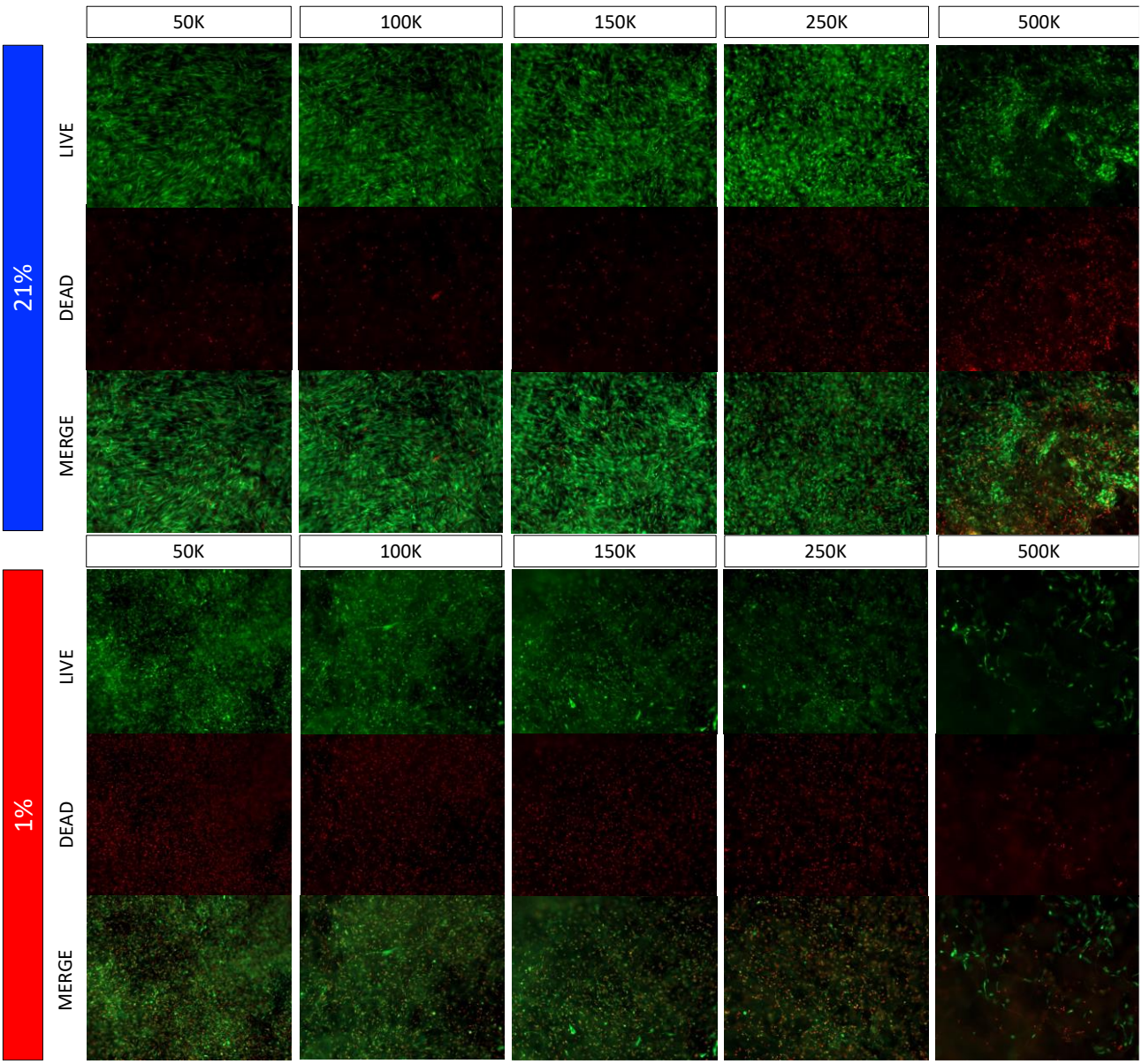

Figure 4-17 Live-Dead stain of cells on the scaffold of different seeding densities at Day 8 of culture 21% versus 1%. Merged red and green channels. Calcein stain (green) = live cells; ethidium homodimer (red) = dead cells. 10x magnification.

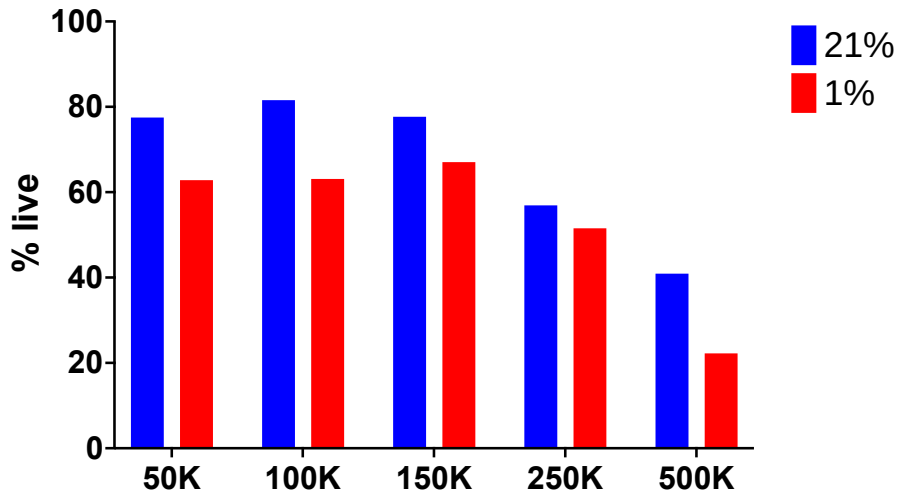

Figure 4-18 Percentage of live cells from Live-Dead stain analysis of seeded scaffold in different seeding densities on Day 8 of culture.

4.4.4 Effect of seeding density on VEGF production in dynamic compared to static oxygen conditions

To determine the choice of optimal seeding density for pro-angiogenic purposes of the seeded cells, the VEGF response in conditioned media (CM) from the different oxygen pre-conditioning environments was evaluated between high and low SD. High SD is defined as 500,000 cells per scaffold, and low SD is defined as 100,000 cells per scaffold. Only Day 1 and 3 CM was measured to show representative data on the day of the transplant.

VEGF cytokine response between the static and dynamic conditions shows some significant differences. (Figure 4-19) For the high seeding densities, static 1% hypoxia showed a higher concentration of VEGF with CM from static 21% and significantly higher results than CM from dynamic 21-1% for Day 1 and 3. In the low seeding density conditions, VEGF concentration was significantly higher in CM from the dynamic 21-1% seeded cells when compared to static 21% and static 1% for Day 1 post-seeding (***$p < 0.001$; **$p = 0.001$). However, this statistical difference was not seen on Day 3 of culture, where the dynamic 21-1% and static 1% CM showed similar VEGF concentrations (Mean ± SD: 4573.48 ± 123.44 vs 4441.31 ± 217.02)

and there was no significant difference in the results seen in the static 21% CM (4136.21 ± 35.02).

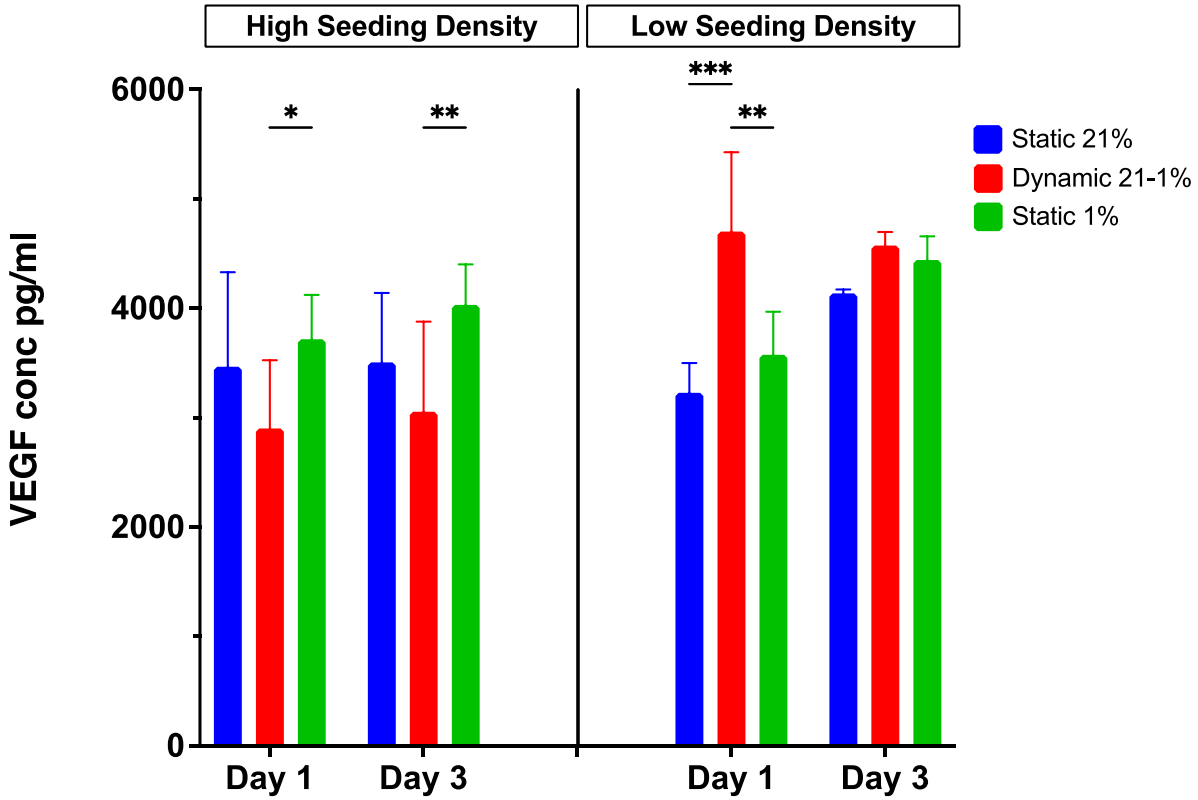

Figure 4-19 VEGF concentration from conditioned media of seeded cells in different seeding densities (SD). High SD is defined as 500,000 cells per scaffold, and low SD is defined as 100,000 cells per scaffold. n = 3 for biological replicates and n=6 for final technical replicates. *: p-value <0.033; **: p-value <0.002; ***: p-value <0.001.

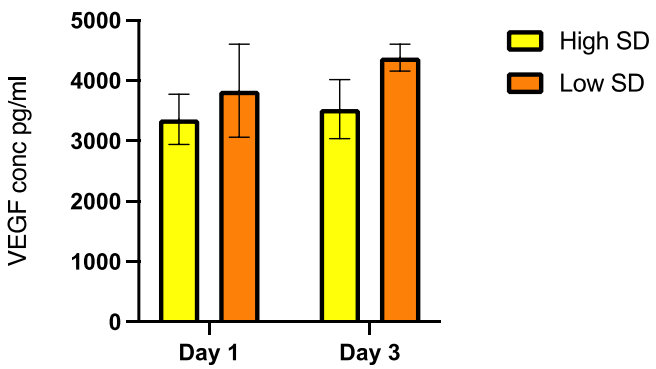

Figure 4-20 Averaged readings of all oxygen pre-conditioning groups on Day 1 and 3.

Overall averaged readings from all oxygen pre-conditioning groups on Day 1 and 3 showed higher concentration of VEGF from CM in the low SD compared to the high

SD groups (averaged Day 1: 3835.32 compared to 3361.15 and Day 3: 3530.02 compared to 4383.67).

Given the complexity of other angiogenic cytokines and growth factors (GF) which may be released together with VEGF by the seeded cells in the CM, a more extensive proteome array was performed to give a more detailed and comprehensive view of the angiogenic profile with these seeded cells. This data is presented in chapter 4.4.8.

4.4.5 Effect of seeding density on the variation of oxygen saturations within the culture well

Comparing the high and low seeding density revealed a difference in oxygen content within the media and peri-scaffold region of the 96 well culture vessel. A localised area of hypoxia between 0-1% oxygen saturation around the higher SD scaffold could be appreciated from the 'Bottom' measurements over the course of time. (Figure 4-21A) Bottom measurements are considered peri-cellular/scaffold. This similar region showed less pronounced hypoxia of between 11-15% for the low SD scaffolds. (Figure 4-21B) At 72 hours post-seeding, the pattern of hypoxia remained similar for the low SD at the initial media change, but the bottom measurement continued to decrease in percentage oxygen saturation over time, from 15% to around 10% oxygen saturation. For the high SD scaffolds, the bottom readings started higher at around 10-13% up to 23 minutes post-media change, following which the oxygen saturations started to fall to 5%. The readings in the middle of the well showed similar pattern of reduction in the fall in oxygen saturation from 15-18% up to 23 minutes, followed by a fall in readings to 12%. A much smaller drop in oxygen saturation was seen in the lower SD middle reading, from 16% to around 13% after an hour of monitoring. The other readings from the middle of well, from the high SD and low SD at 24 hours, showed more consistent readings over time.

At the end of the 1-hour monitoring post-media change, the change in oxygen gradient, from top to bottom of the well, was calculated as a percentage difference. (Figure 4-21C) For the high SD scaffolds at 24 hours of seeding, the change in

oxygen gradient was found to be 96.71 ± 0.34%, with the top of the well measuring 17.65% compared to the bottom at 0.58%. For the low SD scaffolds at the same time point, the variation in oxygen gradient was found to be much less at 40.67 ± 0.50%, with the mean oxygen level at the top measuring 19.47% and the bottom at 11.55%, but it was consistent at 72 hours of seeding, with a similar percentage change in oxygen gradient of 37.23 ± 0.46%. However, for the high SD scaffolds, there was a lower percentage difference of 77.79 ± 0.31% at the same time point. At earlier time points between 4-22 minutes, the percentage difference was 37.56 ± 1.06% before a steady increase in the difference over time. This is likely due to a time lag to equilibrate changes in oxygen consumption of the seeded cells after the media change. This phenomenon was also observed in the low seeding density curve but to a lesser extent.

A time-lapse video link of the changes in oxygen levels within the well plate can be accessed in the Supplementry section of the thesis (Supplementary Figure 1).

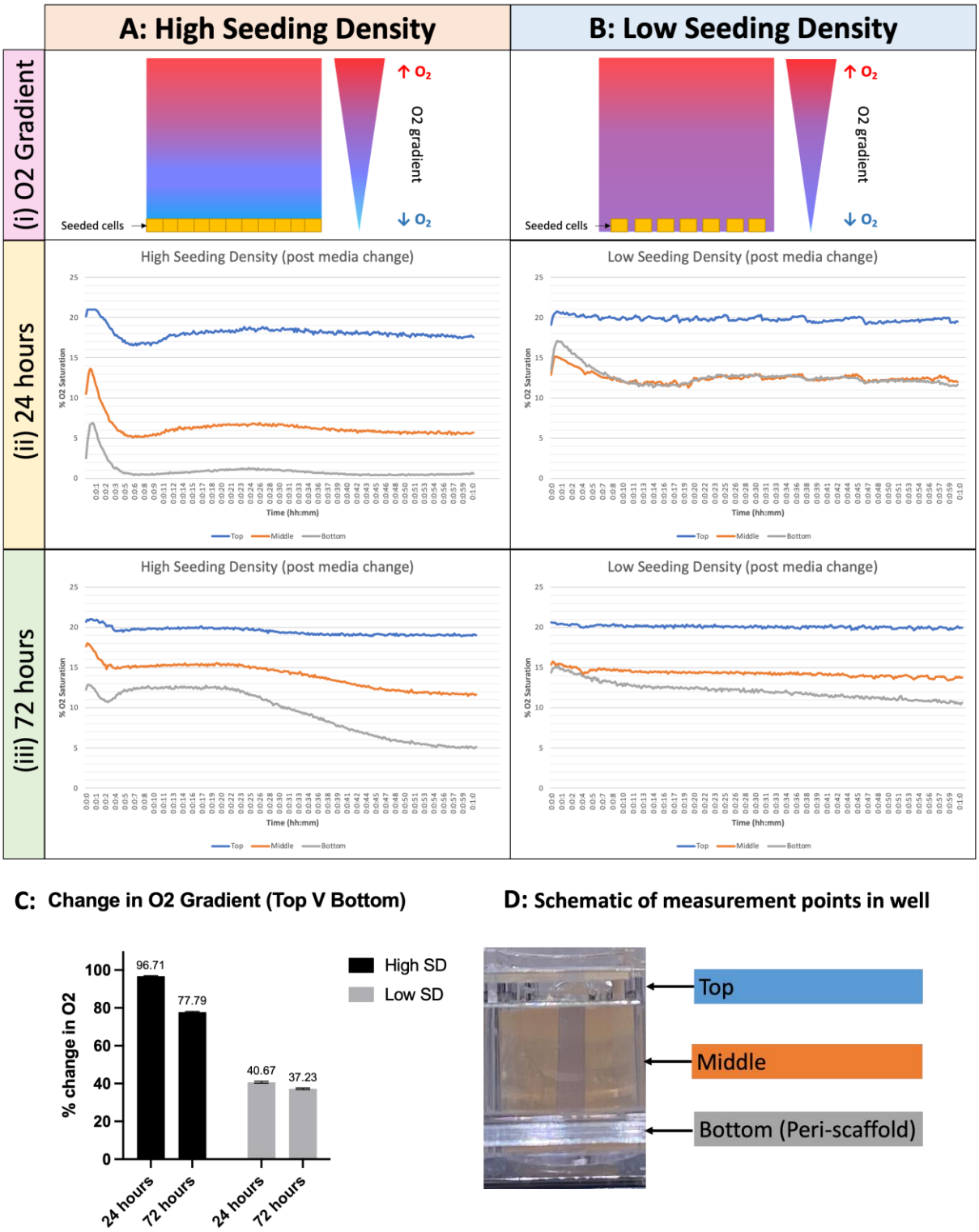

Figure 4-21 Oxygen variations within the 96 well with (A) high and (B) low seeding density (SD) scaffolds, where high SD is defined as 500,000 cells per scaffold, and low SD is defined as 100,000 cells per scaffold. (i) illustrated graphically with oxygen gradient through media. O_2 measured after media change at atmospheric oxygen (21%) incubator conditions at (ii) 24 hours and (iii) 72 hours post seeding. (C) Graph showing percentage change in oxygen saturations at the top compared to the bottom of the well (O_2 gradient), in high and low seeding densities (SD), at 1-hour post monitoring. The value shown on the top of the bar chart shows the mean percentage difference. (D) Diagram showing where the top, middle

and bottom measurements are taken within the well. The media would reach the top of the well. (see section 4.2.5)

4.4.6 Comparison of cell seeding vessels

High SD causes more cell death, likely due to the increased cellular stress from greater oxygen consumption and higher metabolic demands. This increase in cell death seen throughout the different SD is likely to be exacerbated by the small wells used in the 96 well plates despite regular media changes. Figure 4-22 shows the difference in sizes of the culture vessel.

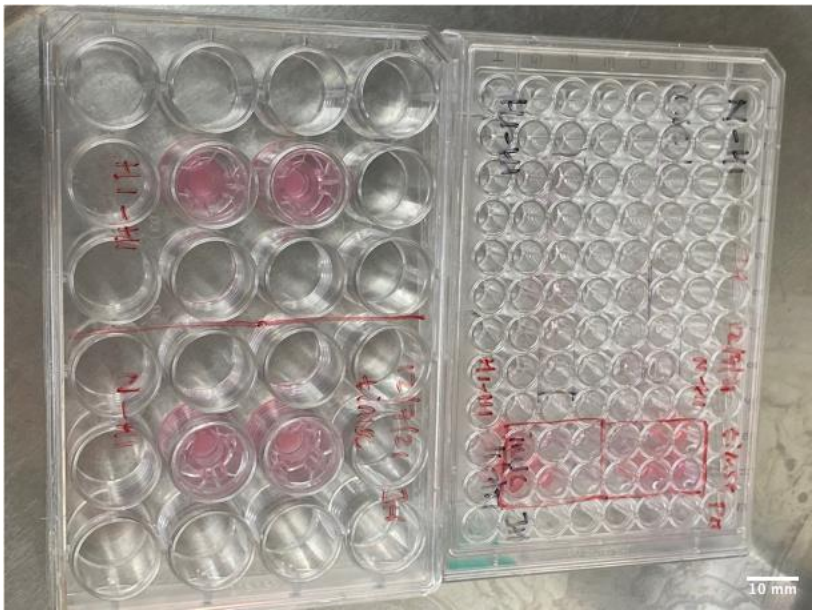

Figure 4-22 Comparison of seeding vessel sizes. 96 well plate on the right and 24 well plate with transwell insert on the left.

The effect of seeding too many cells on the scaffold and impacting on the availability of oxygen and nutritional needs of the cells would be the exertion of undue stress on the cells, which would then invariably influence the *in vitro* and *in vivo* response to hypoxia as well as the overall survivability of the seeded cells on the scaffold. It has been noted that the phenol red component in the media changes to a more yellow hue about 1-2 hours after addition of 300ul of fresh media after passive seeding of cells. This was particularly noticeable in higher seeding density wells as well as DH 21-1% cells (see Figure 4-23), an indication of more acidity from metabolic by-products of the cells such as lactate. This can help as a visual aid of increased metabolic activity in the cells, either from increased seeding density or different

oxygen pre-conditions, when compared to other wells with less metabolically demanding cells despite being cultured on the same plate and incubator. As a result, this can be a helpful indicator of cellular stress and possible poor cell survival if inadequate media is provided particularly in 96 well plates.

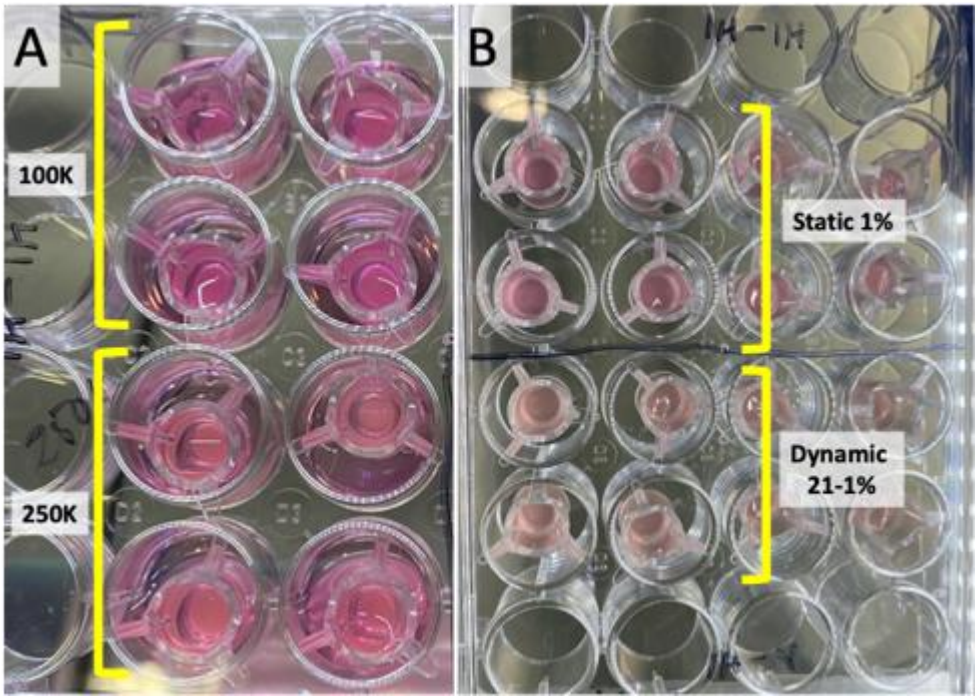

Figure 4-23 Changes in the colour of the phenol red in the media when cells are metabolising more due to increased metabolic by-products such as lactate. This is seen in higher seeding densities (SD) in (A) or different oxygen pre-conditions as shown in (B). (A) shows a transwell plate with cells cultured in static 1% environment with 2 different SD. The higher SD wells of 250,000 cells per scaffold show a more orange-yellow hue to the conditioned media compared to the lower SD wells of 100,000 cells per scaffold. (B) Transwell 24 well plate showing the wells with cells in the dynamic 21-1% group (before the addition of fresh media) producing an orange-yellow tone of media after initial seeding (post 24 hours) compared to static 1% group with more purple-pink colour of the original media.

Transwell inserts places in a 24 well plate was adopted to determine if this could improve cell viability and health of the seeded cells compared to the 96 well plate due to their larger volume capacity for media. Microscopy of Live-Dead stain of seeded scaffolds shown in Figure 4-24 display more calcein stained areas of cells in transwells cultured environment compared to 96 well plate. Hence, the analysis of the Live-Dead stain results with an improved percentage of live cells on all timepoints of measurements supported the use of transwell insert. (Figure 4-25)

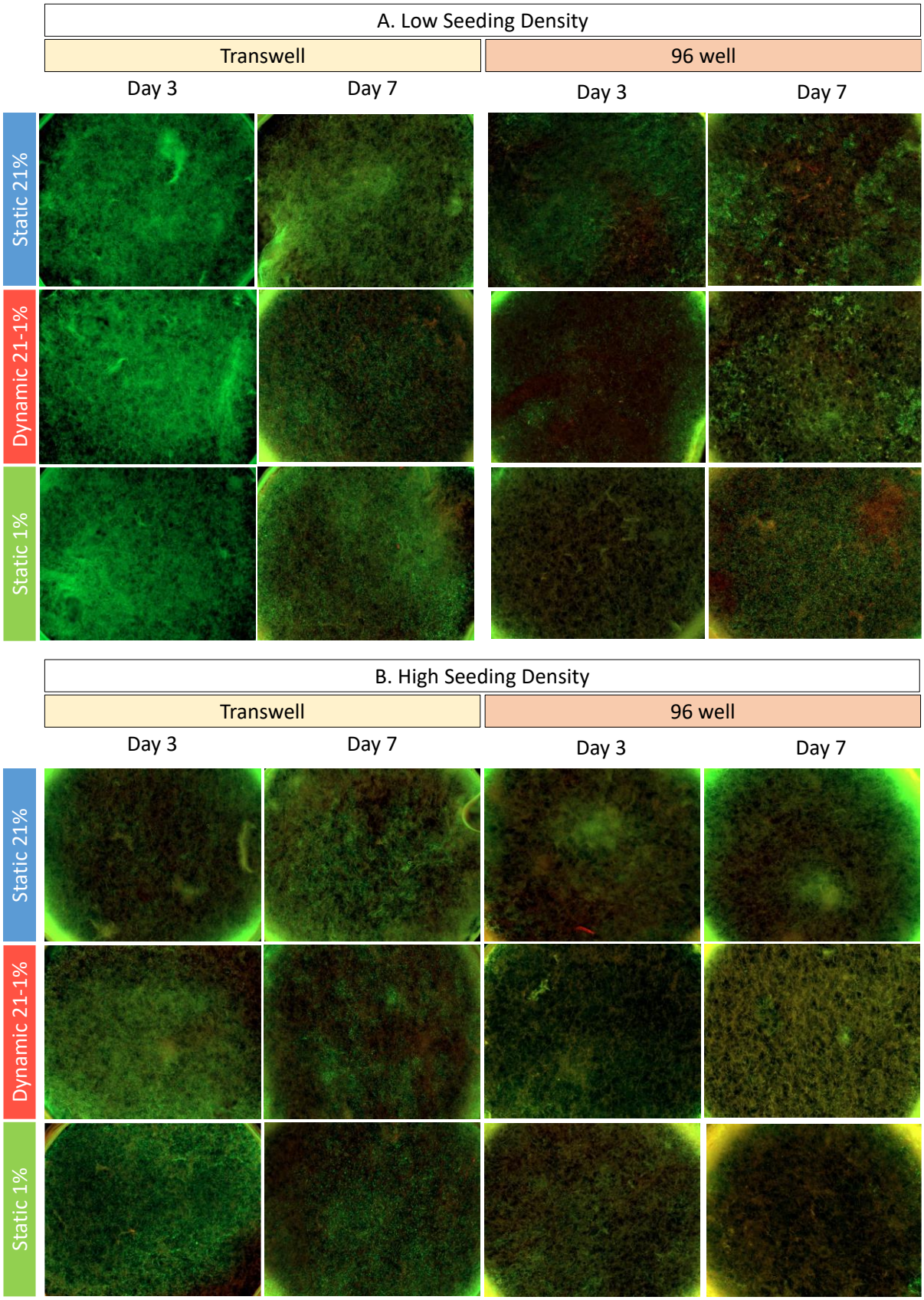

Figure 4-24 Live-Dead stain assay on seeded cells comparing transwell seeding to 96 well plate. Low magnification allows for the visualisation of the whole scaffold. (A) Low seeding density of 100,000 cells

per scaffold. (B) High seeding density of 500,000 cells per scaffold. Calcein stain (green) = live cells; ethidium homodimer (red) = dead cells. 2.5x magnification.

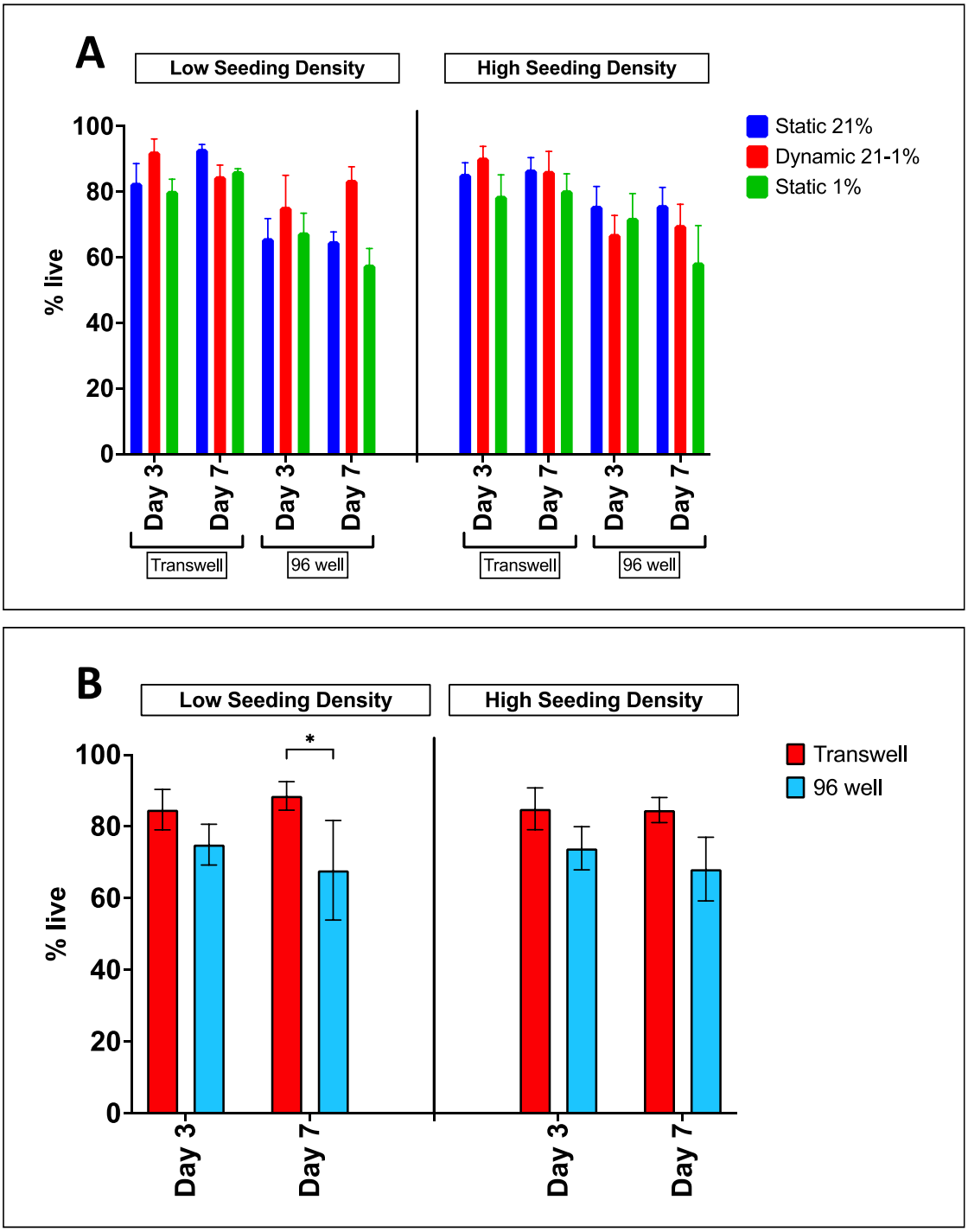

Figure 4-25 High seeding density is defined as 500,000 cells per scaffold, and low seeding density is defined as 100,000 cells per scaffold. (A) Percentage of live cells for different oxygen pre-conditions which were cultured on transwell inserts or 96 well plate on Day 3 and Day 7 analysed from Live-Dead stain assays as shown in Figure 4-25. Sample of biological replicates of n=3 for each oxygen pre-condition at different timepoints. (B) Combined average of percentage of live cells (averaged across all timepoint specific oxygen pre-condition) cultured on transwell inserts was compared to 96 well plate on Day 3 and Day 7. A graphical side to side comparison of the effect of transwell and 96 well culture

methods on low seeding density (SD) and high SD groups show a general trend of a lower percentage of live cell in the 96 well culture vessel compared to the transwell inserts.

4.4.7 Measuring of cellular bioactivity between dynamic compared to static oxygen conditions

To compare cell health between static versus dynamic oxygen pre-conditioning, cell viability and metabolic assays was performed on day 1-7 of implantation. The seeding density of 125,000 cells per scaffold used in these sets of experiments was based on the prospective assessment of optimal parameters for seeding as detailed in the discussion below.

Cell viability was measured using Live-Dead stain assay. Percentage live cells were plotted over time in Figure 4-26A. Figure 4-27 shows representative Live-Dead stain microscopy images where visual aspects of the cell health and morphology can be better appreciated. Increasingly rounded cells can be seen from Day 5-7 of the SN 21% and SH 1% images, which indicate poor health of the seeded cells. There are also more red-stained cells (ethidium homodimer = dead) seen in the SH 1% cells on Day 3 and Day 7. There seems to be some recovery on Day 5 of culture, perhaps due to the positive effect of media change.

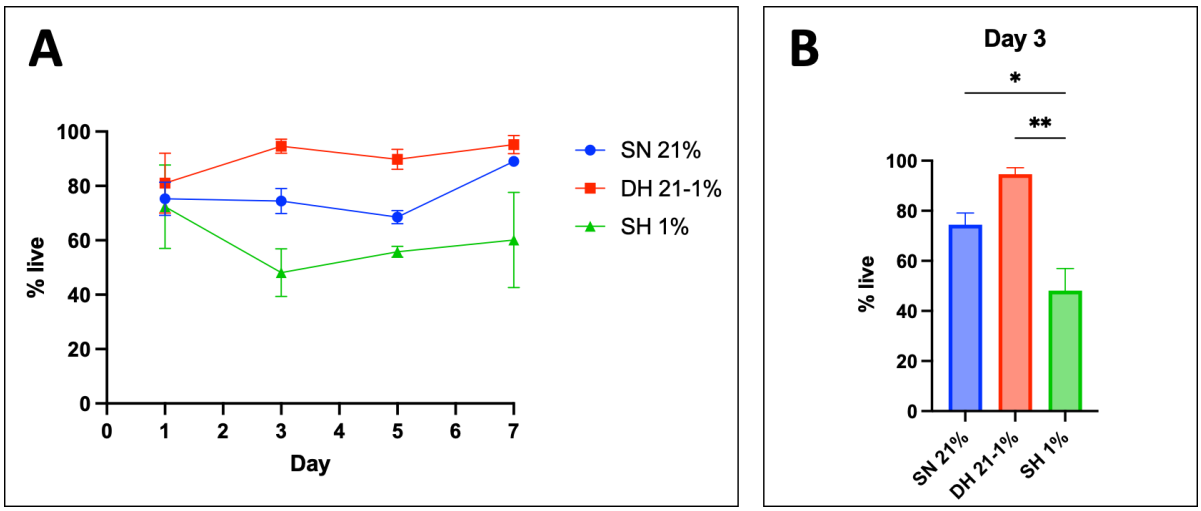

Figure 4-26 Percentage of live cells on Live-Dead stain assay for the different oxygen pre-conditions. Biological replicates of n=3 per timepoint. SN = static normoxia 21%; DH = dynamic hypoxia 21-1%; SH = static hypoxia 1%.

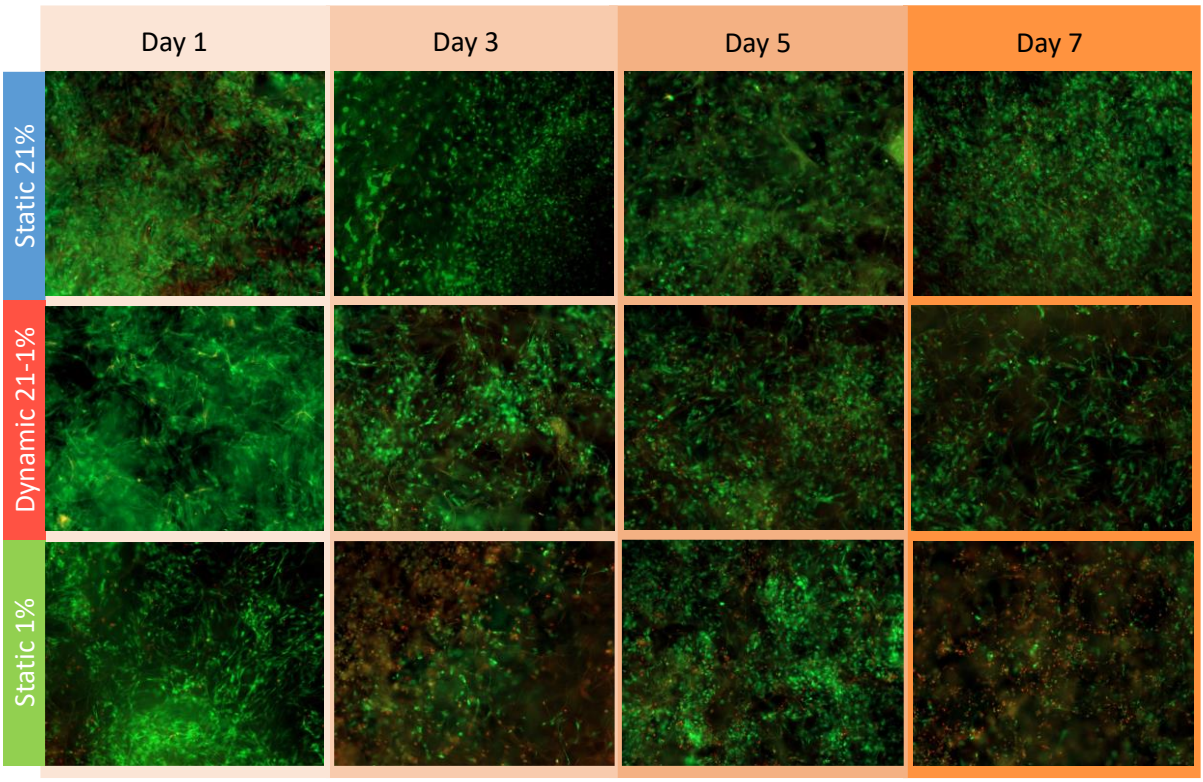

Figure 4-27 Live-dead stain of different oxygen culture conditions static versus dynamic from Day 1-7. Calcein stain (green) = live cells; ethidium homodimer (red) = dead cells. 10x magnification.

To assess the metabolic activity of the seeded cells from Day 1-3, Realtime-glo assay was used. Realtime-glo assay can be used as a continuous measure of metabolic response in the first 48 - 72 hours of culture without the need to change the media or lyse the cells seeded scaffold.

Higher metabolic activity was measured in DH 21-1% O_2 pre-conditions across all different culture environments compared to static O_2 pre-conditions. It can also indicate possible metabolic stress on cells in the dynamic oxygen group.

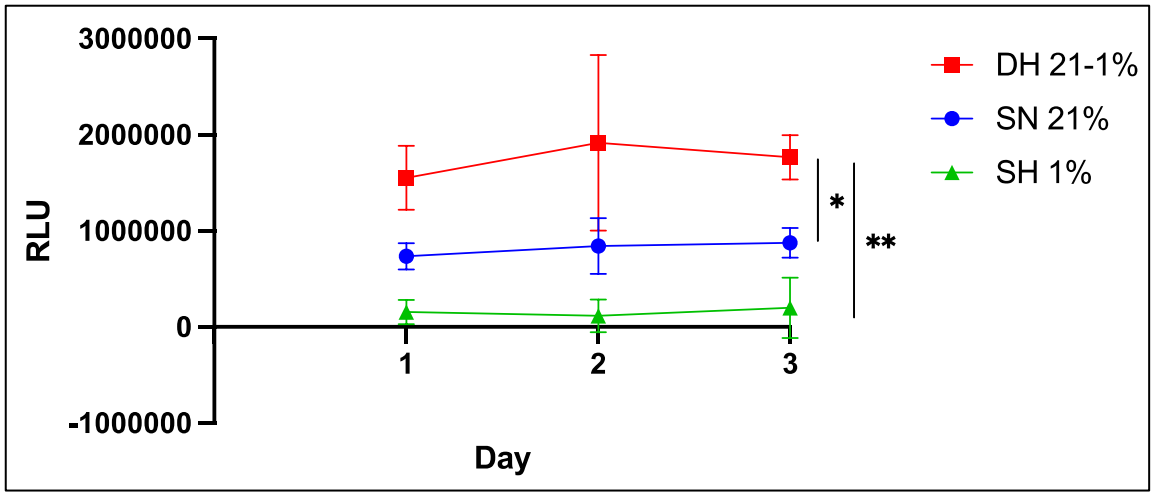

Figure 4-28 Cell viability/metabolic activity from Day 1 to 3 using Realtime-glo assay. Biological replicates of n=3 per timepoint. SN = static normoxia 21%; DH = dynamic hypoxia 21-1%; SH = static hypoxia 1%.

4.4.8 Angiogenesis proteome array profile of MSC seeded on INTEGRA®

Cytokine proteome arrays were used to measure the expression profiles of 55 angiogenic-related proteins. A summarised list of their role in angiogenesis is shown in Table 4.1. Their possible contribution to inflammation process is also shown. Inflammatory pathways are closely linked to the angiogenic and regenerative processes via potential macrophage activation.

	Angiogenic	Inflammatory
Thrombospondin-1 (TSP-1)	-	+/-
Serpin F1 (PEGF)	-	-
TIMP-1	-	+/-
TIMP-4	-	+/-
Endostatin/Collagen XVIII	-	+/-
IGFBP-3	+/-	-
VEGF	+	+
Angiogenin (ANG)	+	-
GM-CSF	+	+
MCP-1 (CCL2)	+	+
Angiopoietin-1 (Ang-1)	+	-
DPPIV (CD26)	+	+
FGF-7 (KGF)	+	+
IL-8	+	+
Leptin	+	+
MMP-8	+	+
Pentraxin 3 (PTX3)	+	+
uPA	+	+
Serpin E1 (PAI-1)	+	+
HGF	+	-
Coagulation factor III (TF)	+	+
CXCL16	+	+
GDNF	+	-
PIGF	+	-/+

Table 4.1 List of significant analytes found to be raised in the conditioned media and their corresponding known effects on angiogenesis and inflammation. '+' represents a positive association, '-' represents a negative association with the process listed in the heading, and '+/-' indicates that the analyte has been reported to have both negative and positive associations.

Results from the proteome array showed VEGF to be raised in all oxygen pre-conditions. (Figure 4-29B) In CM from cells cultured DH, we found significantly higher expression levels of the following 14 analytes compared to other conditions. (Figure 4-29 & Figure 4-30) These were Angiogenin (ANG), Angiopoietin-1 (Ang-1), Chemokine (C-X-C motif) ligand 16 (CXCL16) Dipeptidyl peptidase IV (DPPIV), Fibroblast growth factor 7 (FGF-7), granulocyte-macrophage colony-stimulating factor (GM-CSF), hepatocyte growth factor (HGF), Insulin-like growth factor binding protein-3 (IGFBP-3), Interleukin-8 (IL-8), Leptin, MMP-8, Serpin F1, Tissue Inhibitor of Metalloproteinase 4 (TIMP-4), urokinase-type plasminogen activator (uPA) and VEGF.

MMP8, uPA, Leptin and TIMP-4 expression has been shown to be significantly increased in cells pre-conditioned in the DH group compared to the SN and SH conditions, as much 3-5 fold increase. Dynamic compared to SH 21% and SN 1%, uPA had 4.67 ± 0.23 and 3.65 ± 0.18 times increased expression respectively. In a similar comparison, MMP8 expression was found to have a 4.16 ± 0.53 and 3.67 ± 0.07 fold increase respectively in the DH group compared to SN 21% and SH1% respectively. TIMP-4 was more raised when compared to SH1% than SN 21% (3.73 ± 0.80 vs 2.22 ± 0.31), whereas the converse was seen in Leptin (1.63 ± 0.30 vs 4.40 ± 0.74). When compared to the SN 21% oxygen CM, the DH group saw an approximately 2-fold increase in Angiopoietin-1 (2.08 ± SEM 1.14), FGF-7 (2.09 ± 0.24), CXCL16 (1.71 ± 0.07) and TIMP-4 (2.22 ± 0.31). HGF was found to be 2.77 fold raised in dynamic compared to static 21% (2.77 ± 0.22). Comparing SH 1% conditions, in addition to the 2-fold increase seen in Angiopoietin-1 (2.16 ± 0.84), FGF-7 (2.44 ± 0.25) and HGF (2.12 ± 0.06), CXCL16 (2.18 ± 0.04) there was an almost 4 fold increase in TIMP-4 (3.73 ± 0.80). DPPIV was also found to be 1.83 times higher (1.83 ± 0.09) in dynamic compared to static 1% group. A non-significant increase in expression was seen in IGFBP-2 (2.12 ± 0.31), HB-EGF (fold change 1.73 ± 0.90), EGF (fold change 1.62 ± 1.67), PDGF-AA (fold change 1.34 ± 0.28) and Amphiregulin (fold change 2.76 ± 0.45) was observed. These factors had low overall expression.

There was a lower expression of 4 analytes found from CM from DH compared to the SN 21% and SH 1% conditions. They are thrombospondin-1 (TSP-1), TIMP-1, Pentraxin 3 (PTX3) and MCP-1. TSP-1 and TIMP-1 are known inhibitors of angiogenesis. Serpin F1 and TIMP-4 is another known anti-angiogenic factor, which was found to be raised in DH CM compared to the other oxygen conditioning groups. The protein array also showed anti-angiogenic factors TSP1 and Serpin E1 to be detected in small amounts in the control media (aMEM). However, these quantities are far less than what was detected in the conditioned media from the different oxygen pre-conditioning groups. (Figure 4-30A&B)

Overall, CM from DH showed a greater increase in expression of 14 pro-angiogenic factors and lower expression of 2 anti-angiogenic factors and raised expression of 2 anti-angiogenic factor compared with SH 1% and SN 21% CM.

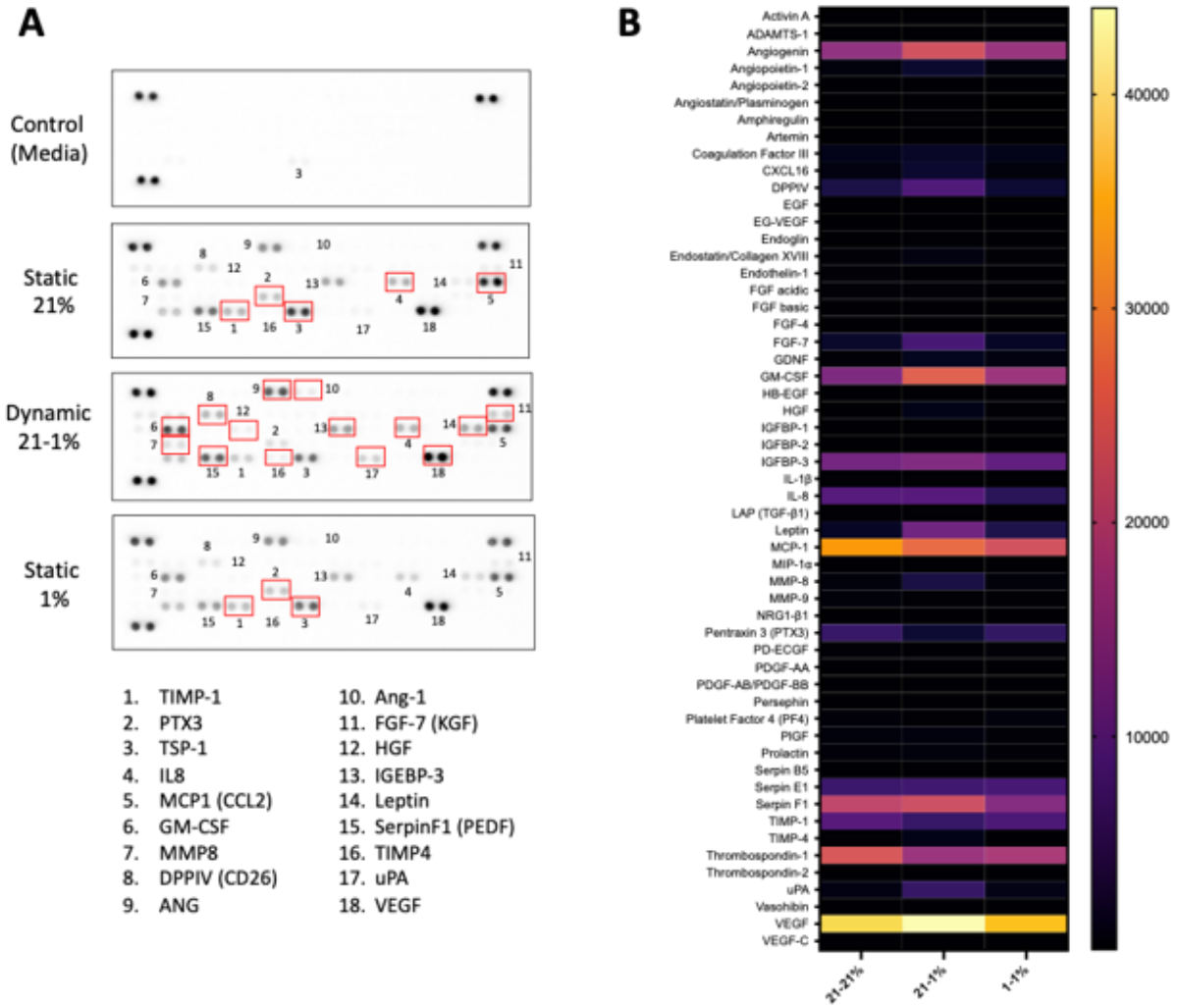

Figure 4-29 (A) Captured human angiogenesis array blots showing the corresponding conditions. (B) Normalised heat map of all 55 analytes from the angiogenesis array. Pooled CM samples taken from n=6 seeded INTEGRA® scaffold samples of different oxygen conditions. aMEM MSC culture media with 10% serum was used as control.

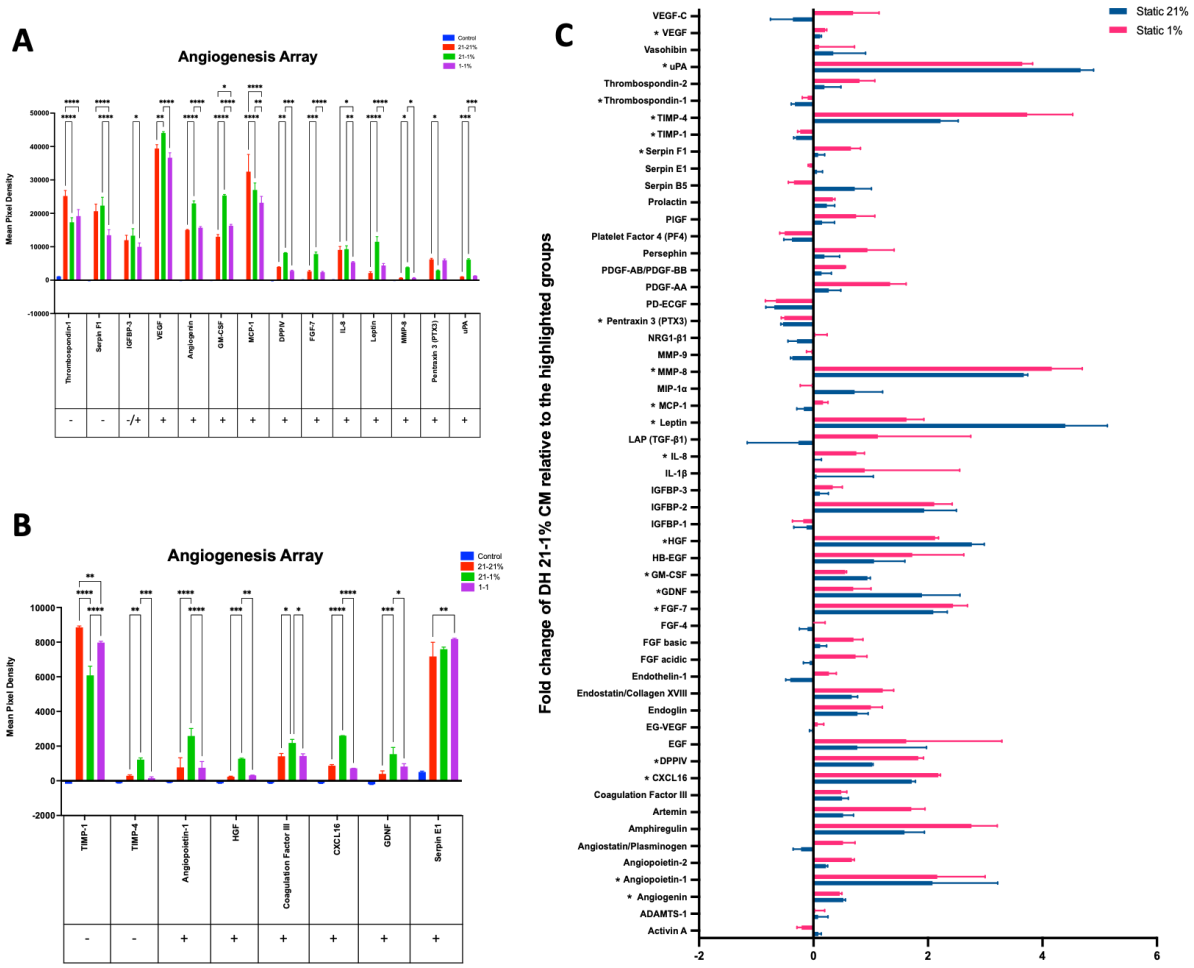

Figure 4-30 (A) & (B) Comparison of the difference in secretion of select analytes from MSC pre-conditioned in different O_2 environments. Values represent the mean of pixel intensity measurements of duplicate dots of stained membranes depicted in Figure 4-29. Symbols +/- represent whether the analyte is known to be pro or anti-angiogenic as shown in Table 4.1. (C) Fold changes in the 55 analytes in dynamic (DH) 21-1% conditioned media compared to static (SN) 21% and (SH) 1% compared to. * next to the analytes represent statistical significance between the groups.

4.4.9 Cell tracking using D-Luciferin

The use of transduced adMSC with luciferase reporter allows the non-invasive means of assessing cell viability and tracking of cells *in vivo* when D-Luciferin is added to the media. To evaluate the accuracy of measuring cell viability via the use of transduced adMSC and D-luciferin as a substrate, a preliminary comparison was made to the established use of Realtime-glo assay. (Figure 4-31) Comparing the two assays, the graphical trends look similar. The dynamic oxygen pre-conditioning group showed higher RLU values at day 1 and 3. However, day 7 data for the two assays

appear different, with the dynamic oxygen pre-conditioning group showing a sharper decline in value for the D-luciferin assay.

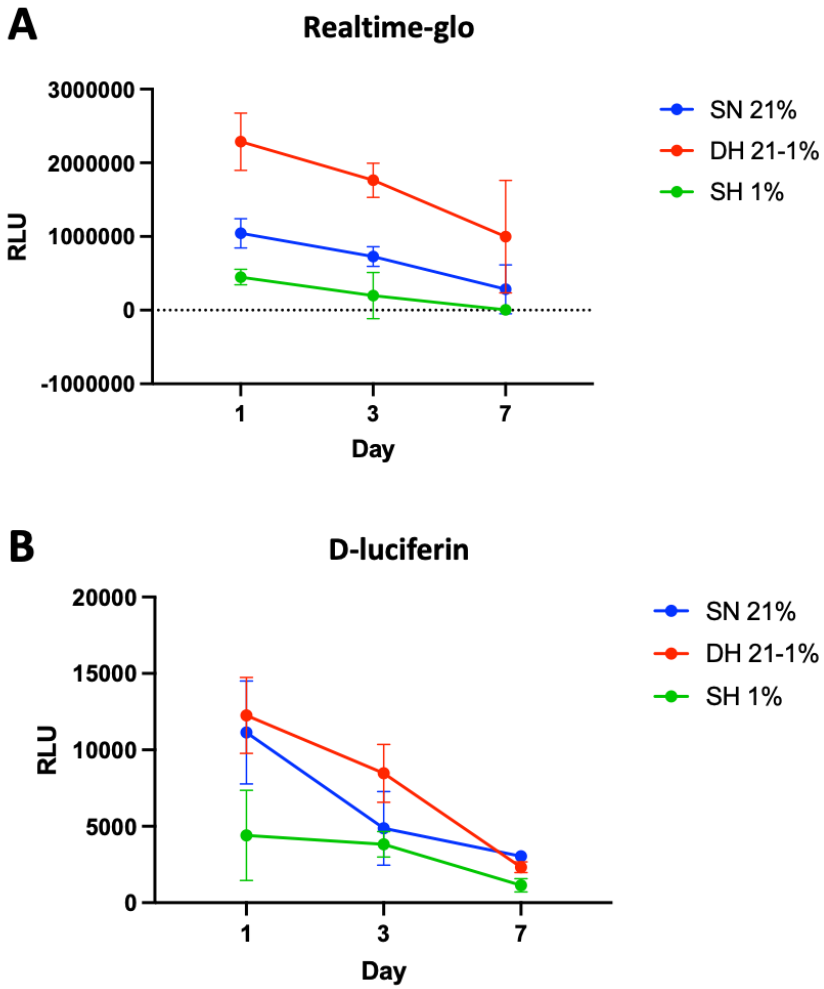

Figure 4-31 Realtime-glo assay (A) compared to D-luciferin substrate on transduced cells (B). Biological replicates of n=3 per timepoint per oxygen condition. SN = static normoxia 21%; DH = dynamic hypoxia 21-1%; SH = static hypoxia 1%.

Using D-luciferin on cells seeded on INTEGRA® showed different linearity curves compared to cells seeded on 3D hydrogel. (Figure 4-32) The difference is pronounced in the SH 1% curve in the cells seeded on INTEGRA® between 10 to 20 minutes into the assay reading, shown with a large spike in RLU value detected, before values fall back below that of the DH 21-1% and SN 21% groups. Cells seeded on the 3D hydrogel also show changes in comparable value of cells SH 1% in the first 10 minutes of reading in relation to the other oxygen pre-conditions. However, these values change after 10 minutes to overtake the other conditions. The other oxygen pre-conditions show a steady trend with decreasing measurements

after first 10 minutes in cells seeded in both INTEGRA® scaffold and 3D hydrogel settings.

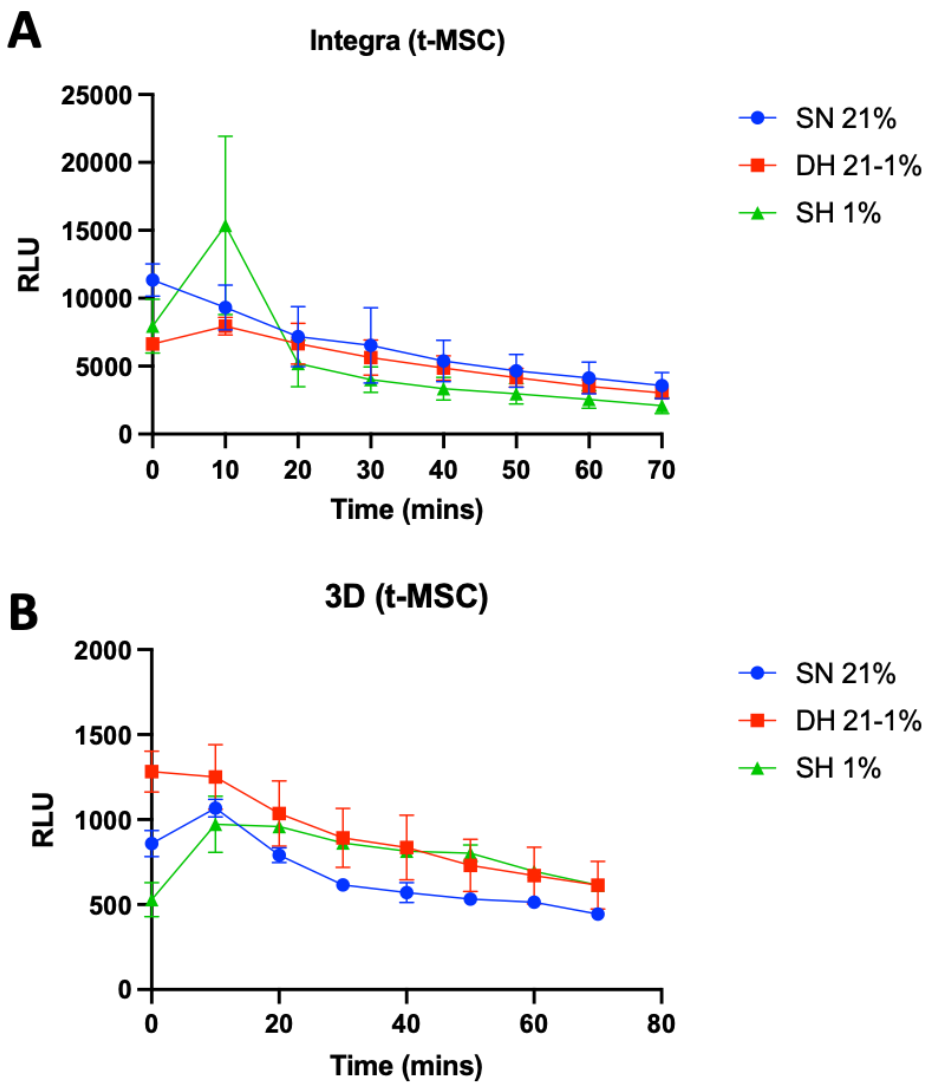

Figure 4-32 Linearity curve for D-luciferin substrate comparing transduced MSC (t-MSC) seeded on (A) INTEGRA® compared to (B) 3D hydrogel over 70 minutes from one timepoint measurement. Biological replicates of n=3 per oxygen condition. SN = static normoxia 21%; DH = dynamic hypoxia 21-1%; SH = static hypoxia 1%.

4.5 Discussion

Role of scaffold and cell morphology

Understanding the INTEGRA® scaffold architecture from a microscopic perspective is very valuable as a background in the appreciation of cell adherence to the scaffold.

The histological cross-section allowed for the visualisation of the 2D lattice shape within the scaffold. (Figure 4-9) The interconnectivity between the pores and their irregular nature can be appreciated. The 2D measurement of the pore size averaged 210µm. Early research by Klenke at al. pointed out that porosity size of 50–160 µm could support capillary ingrowth, whilst anything larger than 140 µm became necessary for the effective vascularisation of larger, denser tissues (408). A recent study by Lu et. al. found that the best pore size for hydrogel for endothelial cell migration and tissue vascularization was 200–250 µm (409), which supported previous studies which reported faster ingrowth of vessels in pore sizes greater than 250 µm (410,411). In addition, computer modelling showed that larger pore sizes with more interconnectivity and higher porosity supported accelerated angiogenesis (205). Hence, the average pore size measured in the INTEGRA® scaffold is theoretically within the ideal range for neo-vascularisation. SEM images of the seeded cells showed evidence of cell migration through the highly interconnected porous scaffold. (Figure 4-10Biii) SEM in Figure 4-10 and Figure 4-12 also show how cells were able to spread out and adhere through multiple dendritic-like attachments, called filopodia directly onto the scaffold when the micro-conditions are right. Hence, this result point to INTEGRA® as a favourable scaffold for *in vivo* neo-angiogenesis when scaffold is primed and appropriately pre-conditions. This will be further elaborated on below.

It was also possible to visualise cells on the scaffold using the Live-Dead stain assay. This was a particular advantage as INTEGRA® matrix is thin and translucent in nature so it can be imaged using an inverted fluorescent microscope. This allowed for the monitoring of cell morphology and changes in proliferation over time using this assay. The main limitation of using this assay is the inability to capture all depths of the scaffold to allow for accurate visualisation of the cells which have migrated into the deeper layers of the scaffold. Having a standardised way of imaging helped with limiting the shortcomings of this assay and to allow for cell viability calculations of cells within the scaffold over time.

<u>Cell seeding and seeding density</u>

Seeding dynamics is strongly influenced by parameters like initial cell concentration and scaffold volume (412). Seeding on the scaffold requires several stages of

optimisation and fine-tuning and can be regarded as one of the more challenging aspects of tissue engineering. However, this process cannot be overlooked, as our data above has shown. The process was highly delicate and sensitive to slight changes in the cellular microenvironment which can have significantly impact to downstream measurements, such as cell viability and cytokine expression. Hence, the experiments were tightly planned using different types of measurements to minimise on experimental variability.

One of the first challenges to overcome was ensuring cell survival on the scaffold. Unexpectedly, despite INTEGRA® being a clinically available of-the-shelf commercialised product, cells did not readily adhere and proliferate on the product without initial priming with pre-soaking in high FBS media. This could be attributed to the possible cytotoxic effects of the matrix crosslinking method used in manufacturing. INTEGRA® is a crosslinked collagen-GAG matrix. It is known that the crosslinking method, which commonly involves glutaraldehyde, can affect the cytocompatibility of cells on the scaffold (413). Capella-Monsonis et al. observed that human ADSC seeded on INTEGRA® scaffold exhibited decreased proliferation and increased metabolic activity, which could be attributed to the crosslinking method used in the manufacturing of the matrix (240). To overcome this, we primed the scaffold with 20% FBS and alpha MEM media used for cell culture. This significantly improved cell adherence and survival on the scaffold, which can be attributed to the high concentration of serum (FBS) in the media absorbed by the hydrophilic collagen-GAG based matrix in the Integra. Serum is also known to contain several ECM molecules, such as fibronectin, which can alter the surface chemistry of the scaffold. In essence, this can improve the ‘adhesive’ nature of the scaffold given cell attachment via specific integrin receptors interactions improves with the presence of serum-induced ECM molecules (412,414). Using media to pre-soak the scaffold can also displace the PBS solution within the scaffold used for storage of the INTEGRA® prior to seeding. This can theoretically create a harsh microenvironment for the cells. It was important to note that the scaffold would only be pre-soaked for a set period of time to avoid inconsistent surface chemistry between experimental sets.

The use of transwell inserts further improved cell survival and viability within the scaffold as it was evident that the media within the 96 well plates was easily

exhausted from the nutritional depletion/toxin build-up point of view. This resulted in cellular stress and poor survival as seen by the rounded, apoptotic morphology and increased dead cells detected on Live-Dead staining. There was also evidence of how quickly the media would turn yellowish in 96 well plates, which is a useful visual indicator of higher metabolic demand and greater production of acidic metabolite build-up that can cause cellular stress if allowed to accumulate in media. (Figure 4-23) Acidic metabolic waste products, such as lactate and metabolic H+, can build up within the media and this is picked up from the pH-sensitive phenol red indicator. It can also be an indicator of increased metabolic activity when shown in a side-by-side comparison in Figure 4-23, where DH 21-1% conditioned cells had a more yellowish tinge to the media compared to SH 1% approximately 12 hours post initial passive seeding. This can be a useful observation to help support the Realtime-glo cellular activity data shown in Figure 4-28 and Figure 4-31, where DH 21-1% seeded cells showed significantly higher RLU readings compared to SH 1% cells from Day 1-3.

The optimisation of cell seeding density is crucial for any tissue-engineered scaffold. Seeding density is scaffold and technique specific. This is influenced by type, size and volume of scaffold. Using the estimated volume of the INTEGRA® scaffold, seeding density was initially determined by referencing to the 3D hydrogel seeding density as described in Chapter 2, which was 2×10^5 cells/ml. Given the estimated volume of 0.147 cm^3 of a 6mm INTEGRA® scaffold, this was calculated to be approximately 30,000 cells per scaffold. However, early trial data showed very poor cell adherence and survival below 50,000 cells per scaffold. Therefore, the adoption of a higher and wider range was used for cell seeding density optimisation and a range of between 50,000 to 500,000 cells per scaffold was used, which equates to between 1.77×10^5 cells/cm^2 to 1.77×10^6 cells/cm^2, or 3.4×10^5 cells/cm^3 to 3.4×10^6 cells/cm^3 as mentioned in 4.3.2.

This is in view of 2 main driving factors considered with respect to seeding density:

1. The need for relatively short *in vitro* incubation time, due to the use of dynamic hypoxic pre-conditioning so as to prevent chronicity of the hypoxic exposure on cells.

2. The need for a greater cell number to exert the necessary paracrine effect from the seeded cells at the time of *in vivo* implant.

This is also limited by not seeding too many cells on the scaffold as it would impact oxygen and nutritional consumption and availability as shown in this study, which will be discussed further below.

It was observed that varying seeding density can affect overall cell adherence. To add to the complexity of the process, oxygen culture conditions were also found to affect cell adherence. This was shown in Figure 4-14 with cells cultured in hypoxic 1% showing slightly less non-adherence of seeded cells compared to 21% oxygen. In varying the seeding densities between 21% and 1% oxygen, it was observed that a lower seeding density of 50,000 (per scaffold) produced better initial cell adherence in 21% O_2, whereas the opposite is true for 1% oxygen. In hypoxia of 1%, seeding density of 150,000 showed better adherence than 50,000 cells per scaffold. The Live-Dead stain data confirmed that in the even higher seeding of 250,000 cells or more per scaffold, the percentage of live cells decreased across both 21% and 1% oxygen conditions. (Figure 4-18) The temporal comparison showed the greatest reduction in live cells seen in the 1% hypoxia at Day 8 of culture, possibly indicating the deleterious impact of chronic hypoxia which was mentioned earlier in this thesis. (Figure 4-16)

MSC are known to be anchorage-dependent cells. Within the collagen matrices, these cells anchor via integrins receptors to matrix ECM molecules as mentioned above (412). Integrin expression has been reported to change in response to the oxygen microenvironments. Saller et al. showed that hypoxia could alter the integrin expression of the subunits α1, α3, α5, α6, α11, αv, β1 and β3 in MSC. In particular, integrin β1-mediated cell adhesion has been shown to be crucial for MSC seeding on scaffolds (415). This may in part explain the difference in cell non-adherence reported in the different oxygen culture environments, although further experiments will be required to prove this. For future studies, this would be a useful additional experiment to evaluate such changes to better understand integrin expression by using qPCR or flow cytometry techniques. This can provide evidence for changes noted in cell adhesion on the INTEGRA® scaffold in the different oxygen conditions.

Data in Figure 4-26 shows clear differences in SH 1% versus DH in live-dead staining when calculating the percentage of live cells. Lower viability of cells was noted in the SH group. As mentioned previously, this assay has the limitation of not accounting for the deeper sections of the scaffold for stained cells. Using this stain also terminalise the experiment which increases the inter-specimen variability within each group. To overcome the difficulty of longitudinal monitoring of cell viability using terminal assay, the use of the non-lytic Realtime-glo assay was employed as a continuous measure of metabolic response in the first 48 - 72 hours of culture without the need to change the media or lyse the cells seeded scaffold. It offered a more accurate chronological metabolic activity of the seeded cells. For the first 3 days of culture, the data appears to confer with the percentage of live cells from the Live-dead stain assay shown in Figure 4-28. However, as the assay continued, there was a fall in measured activity from all oxygen pre-condition group in the RLU readings (Figure 4-31). It supports the theory that the acute and dynamic nature of the oxygen change from DH 21-1% can only be observed within the first 3 days of culture. Any further time in culture at 1%, the hypoxic exposure would be considered chronic and/or static in nature. Hence, this further supports the data that long-term, chronic levels of hypoxia has a negative impact on cell viability.

Through this optimisation experiments, I was able to show that:

- Seeding density is balanced by cell viability over time and the pro-angiogenic cytokine expression profile;
- Lower seeding density (between 100,000-150,000 per scaffold) ensures desired cell viability and cytokine expression;
- Seeding density is also restricted by the practical considerations of the timing of *in vivo* implantation and as well as the nature of the dynamic and acute nature of the hypoxic exposure to the cells. Too long in culture would negate the acuteness of the low oxygen exposure.

Jones and Cartmell found that in passive seeding of their gelatin sponge scaffolds with MG63 human osteoblast-like cells, low-volume seeding provided greater cell

seeding efficiency compared to high volume seeding (400). It is also interesting to note that varying the location of where hypoxic cells are seeded within the culture has been shown to influence the vessel infiltration density and morphology in 2D and 3D computational modelling. In the mathematical model by Moreira-Soares et al., the hypoxic cells functioned as production sites for angiogenic factors until vessels merge via anastomosis (416). Their data suggests that *in vivo* seeded cells promote anastomosis by cytokine driven response and can help overcome variations in the endothelial cell's proliferation and the tip cell chemotactic response. Other studies have also experimentally demonstrated that spatial distributing pro-angiogenic growth factors *in vivo* can influence on sprouting capabilities (417,418) and sites of functional neo-vasculatures (419).

In our results, we have also demonstrated how seeding density can also play a significant role in the VEGF expression from the cells. As shown in Figure 4-19, higher VEGF concentration were found in conditioned media from DH pre-conditions in the lower seeding density, but not in the higher seeding density counterparts. This was interesting to observe as it further highlights the importance of taking into account cell viability and metabolic activity findings into consideration for the differences in cytokine response when the cell density is increased. It is postulated that the environment in the SN 21% in the higher seeding densities group created a localised area of hypoxia in media from increased oxygen consumption. Certainly aspects of this were shown in the oxygen monitoring data in section 4.4.5, where rapid depletion in oxygen levels around the peri-cellular region of wells with higher seeding density was observed. These localised hypoxic gradients regulated by cellular seeding densities could have created a micro-environment that the DH environment sought to achieve within a SN 21% culture conditions. This theory is supported by published studies demonstrating the oxygen changes within the media environment, where the oxygen consumption around the media close to cells and the effect of oxygen diffusion limitation of the media itself creates a naturally hypoxic environment around the cell culture (420–422). Depending on the depth and volume of media, the oxygen diffusibility could be vastly altered through the aqueous solution, causing a mismatch in the levels supplied by the incubator and the pericellular level (423). This issue with oxygen diffusion discrepancy and effect on cell viability was highlighted more than a century ago by Dr. August Krogh, but it is

often still overlooked in modern day cell culture experiments (424). Keeley and Mann recently demonstrated the use of mathematical modelling to predict pericellular changes as shown in Figure 4-33 below (84). The modelling takes into account the changes in oxygen consumption of cells (V) in relation to oxygen availability, which includes the following parameters: surface area at gas/liquid interface (A); O2 diffusivity in liquid (D); fluid height (d); O2 solubility in liquid (k); pericellular PO2 (P); PO2 at gas/liquid interface (Ps) and cellular density (p) as measurable factors. (Figure 4-33) Therefore, it was highly insightful to measure oxygen availability at different sections within the media in real time with varying seeding densities with the VisiSen system. The results offers an idea of how the changes in oxygen levels relate to the cellular consumption from low to high seeding densities. It is encouraging that our current results supports previous pivotal work by McLimans et al., whose group discovered that oxygen consumption rate (OCR) of monolayer cells at the bottom of the cell culture dish can easily exceed the diffusion rate of oxygen through the culture medium (420,421). Hence, based on his study findings, McLimans adviced against culturing cells at too high density or at excessive medium depths due to significant risk of exposing cells to undue oxygen deficiency which could reach anoxic levels. There is now a wealth of evidence demonstrating that high density seeding of cells can result in altered cell proliferation profile, aberrant signalling and metabolic changes, all of which can affect cell experimental validity (425–427). With this in mind, it is likely that an increased cellular strain in higher seeding densities, combined with the increased oxidative stress from the rapid change in oxygen conditions in the DH 21-1% group. This combination would have an overall deleterious effect on the cells that might have resulted in the reduction in VEGF response when cell density is high. Combining the findings from the Live-Dead stain assay and the metabolic activity data in Figure 4-15, Figure 4-16, Figure 4-17 and Figure 4-18, it consistently showed the poor cell viability at higher seeding densities. Hence there is overwhelming supportive data to back the use of lower seeding density for future experiments in this thesis for pro-angiogenic purposes.

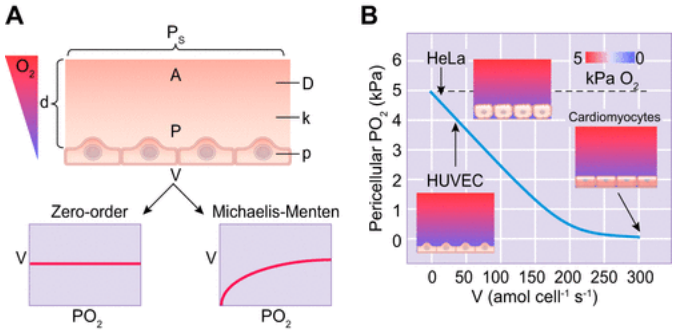

Figure 4-33 Mathematical modelling for predicting peri-cellular PO2 in cell monolayers as described by Keeley and Mann's paper (84). (A) Parameters critical in predicting pericellular PO2 in cultured cells where the gradient of high to low oxygen levels can be influenced by various factors: A =surface area at gas/liquid interface; D = O2 diffusivity in liquid; d = fluid height; k = O2 solubility in liquid; p = cell density; P = pericellular PO2; Ps = PO2 at gas/liquid interface; V= O2 consumption rate (OCR). The value of V can be simplified by considering a 'zero-order' modelling as described by Yarmush et al. (428) or 'Michaelis–Menton' kinetics as described by Powers et al. (429) As O2 consumption is affected by O2 availability, predictions will have more accuracy if V is modelled using 'Michaelis–Menton' kinetics. (B) Illustration of the relationship between pericellular PO2 and cellular OCR, with commonly used cell types annotated according to published values. Cell types with high OCR such as cardiomyocytes or hepatocytes can initiate a self-inflicted hypoxia when ambient PO2 is low. The above figures were reproduced with permission under the terms and conditions provided by the publisher The American Physiological Society and the Copyright Clearance Centre.

The oxygen measurement data also highlighted a delay for oxygen levels to decrease in the 72 hours measurements compared to 24 hours. (Figure 4-21) This time needed for equilibration of oxygen was also mentioned in a review article by Place et al. (422) which highlighted the need for a dynamically moving media to encourage constant flux of oxygen through media to reduce this equilibration time. This is useful data to help support future modifications to the culture vessel, such as the addition of stirring or rotating media, to reduce oxygen variation in media and ensure a constant oxygen saturation throughout.

Given the complexity around angiogenesis, it is likely not to be mediated by VEGF alone, although it is likely to still play a huge role in the process, as discussed above and in detail within Chapter 1. Building an angiogenic profile by measuring other angiogenic-related protein expressions allows for a more detailed analysis of how the cells are responding to different oxygen pre-conditioning environments. The proteins found in the conditioned media of the 3 different oxygen pre-conditions reflected the cellular response on the anticipated day of implant for the *in vivo* experiments (within 3 days of seeding). The collective high expression of VEGF in all conditioned groups

supports the use of adMSC as a candidate cell type for seeding. It validated the VEGF cytokine results shown in the 2D and 3D hydrogel in the last chapter, with seeded cells in the DH showing a significant difference in VEGF expression compared to the SH 1% and SN 21% groups. However, it was interesting to note that VEGF levels in the between DH 21-1% and SH 1% group on the ELISA assay (from the high and low seeding density optimisation process) failed to show the same trend. (Figure 4-19) This discrepancy can only be explained by the possible experimental variability from uncontrolled parameters, such as inevitable exposure to atmospheric oxygen for hypoxically cultured cells, which may have occurred during the optimisation process with multiple seeding densities. Due to time constriants, it was not possible to repeat the experiment to confirm this. However, it will be reflected upon in the next section with potential solutions in minimising this effect for future experiments. Overall, we did not feel that this had a significant impact on the decision made to use a lower seeding density due to the fact that other factors, such as cell viability and adherence, played a more significant role.

With regards to the reliability of the conditioned media used for the angiogenic array in view of the discrepancies above, it was felt that this data was more robust and representative. All the optimisation steps in seeding vessel and seeding density had been finalised and implementated into the experimental workflow when the conditioned media was collected for this experiment. The final seeding density also differred slightly at 125,000 cells per scaffold compared to the low seeding density of 100,000 cells per scaffold used in the optimisation steps for comparison with high seeding density of 500,000 cells. In addition, more stringent steps were also made to ensure little exposure to atmospheric oxygen during culture. Hence, there is greater confidence in the data retrieved from the angiogenic array analysis. This group of seeded cells was also subsequently used for further downstream *in vitro* and *in vivo* experiments and therefore depicted the most representative measure of protein activity in the subsequent experiments.

Encouragingly, the overall results show that the proteins raised in conditioned media from the DH pre-conditioned cells were mostly pro-angiogenic in bioactivity. Raised expression of FGF-7, also known as KGF, also points to the wound regenerative potential of the conditioned cells. KGF is known to play an important role in both

angiogenesis and wound healing (430). HGF is a known mitogen of endothelial cells and is a potent angiogenic co-activator of VEGF (431). It is an important cytokine known for promoting angiogenesis, anti-inflammation and anti-apoptosis functions. It has been reported that HGF secreted from injected MSC helps with cardio-protection in myocardial infarction (432). IL-8 also acts directly on endothelial cells and promotes angiogenesis (433). Leptin was also found to be increased in DH conditioned cells. It is a circulating hormone secreted by adipocytes and can act locally on endothelial cells via paracrine pathways and elicit an angiogenic response that maintains an appropriate balance between blood supply and fat depot size (434,435). Interestingly, leptin was also found to have a protective effect on the MSC themselves. In a study by Wang et al, leptin was increase in hypoxic pre-conditioning of bmMSC, which was in turn was shown to protected the cells from apoptosis via promoting leptin induced cell autophagy (121). MMP-8 zinc-dependent proteinase and uPA, a serine protease play important role in ECM degradation for EC angiogenesis (436,437). TIMP-4, IGFBP-3 and Serpin-F1 were the only anti-angiogenic factor found to be significantly raised in the DH group compared to the static counterparts. Published literature describes some ambiguity with regard to the anti-angiogenic effect of TIMP-4 and IGFBP-3 (438,439). A study by Fernández and Moses showed that although TIMP-4 is an inhibitor of capillary endothelial cell migration, it did not affect endothelial cell proliferation or angiogenesis *in vivo* (439). Another study by Ma et al. showed increased expression of TIMP-4 in corneal wounds which may suggest its positive role in regulating healing and angiogenesis (440). IGFBP-3 has both pro- and anti-angiogenic properties reported in published literature (438). It is the most common circulating transport protein for IGF and has a diverse range of effects on cellular mechanisms which can be manipulated according to the cellular environment (441). In the context of hypoxia, it is encouraging to note that IGFBP-3 has a largely reported pro-angiogenic role (438,442,443). IGFBP-3 has also been shown to act directly on endothelial cells and regulate sprouting angiogenesis, which is highly desirable in the initial stages of neoangiogenesis (444). Serpin-F1, also known as pigment epithelium-derived factor (PEDF), has an inhibitory effect on angiogenesis in microvascular endothelial cells (445). Given it is the only factor with the predominant anti-angiogenic activity of all the protein expressions raised, it may not have an overarching dominant effect. As with most *in vivo* cytokine activity, it is driven by a balance between pro- and anti-factors within

the body. Interesting, in a similar experiment, Fierro et al. found that bone marrow MSC seeded in dermal scaffolds when exposed to hypoxia for 48 hours showed significantly elevated levels of Angiogenin and IL-8 and decreased expression of Serpin E1, uPA (237).

MSC are known to produce not only pro-angiogenic GF, but also express factors which regulate hematopoietic cell function, such as SDF-1/CXCL12, vascular cell adhesion molecules 1, IL-7, Ang-1, and osteopontin (446). It was interesting to note that the significantly high expression of GM-CSF in the dynamic hypoxia CM. GM-CSF is a cytokine that acts on the bone marrow to mobilise and induces haematopoietic cells and their progenitor cells (447). It can be expressed by many different cell types, such as adipocytes, in response to injury or infection and can have multifaceted activity in the regulation of immunity and inflammation (448). It has also been found to influence non-haematopoietic cell types such as endothelial cells, and hence contribute to angiogenesis, neovascularisation and wound healing (449–451). The use of exogenous GM-CSF has been found to upregulate and maintain VEGF expression and increase the expression ratio of Ang-1/Ang-2 and the phosphorylation of Tie-2 (451). This was shown to increase new blood vessel formation and wound healing in *in vivo* burn wound model.

Overall, DH 21-1% CM showed greater expression of pro-angiogenic factors, which play a significant role in promoting angiogenesis *in vivo*, compared to the other conditioning groups. These proteomic results will hopefully translate to better functional EC angiogenic properties as well as *in vivo* angiogenic response in the later experiments.

Tracking of *in vitro* metabolic change

Theoretically, the use of D-luciferin on transduced cells would allow for longitudinal imaging using luminescence technology such as chemiluminescence detectors. As a prelude to the *in vivo* use, we sought to validate this technique by comparing it to Realtime-glo. Although the data was not directly comparable as the use of D-luciferin resulted in lower RLU readings, the data was proportionately similar to allow for this method to be used for the analysis of initial cell seeding efficiency and cell metabolic

activity at 21% and 1%. (see Figure 4-31) However, one challenge was that the luminescence readings from the transduced cells using D-luciferin as a substrate showed varying results over time. (see Figure 4-32) It was difficult to optimise the readings and standardise the condition settings to allow for the values to be comparable at a particular measurement time from the linearity curve. This was certainly more pronounced in the SH 1% samples, likely due to a sudden change in oxygen levels during the plate reading process. Although readings are possible from transduced cells seeded on the INTEGRA® scaffold, and maximum effort was made to limit the exposure of SH 1% cells to atmospheric oxygen, their stability of use in the monitoring of the cell's metabolic activity may not be the most suitable for different oxygen conditions used in this study. Understandably, with the lack of ideal expensive hypoxia incubator modular add-on to plate readers, this is an experimental limitation that needs to be considered especially with the interpretations of results.

4.6 Conclusion

Although there is enough data to support the pro-angiogenic effect of dynamic hypoxia of adMSC in 2D and 3D culture as shown in Chapter 3, the data in this chapter highlights the complexity and challenges faced when translating the results to cells seeded onto a more sophisticated matrix such as the INTEGRA® dermal template scaffold. Thorough optimisation in cell seeding was required as this was shown to significantly affect cytokine VEGF expression as well as cell viability and adherence/retention. Taking into account the accumulated data presented above in chapters 4.4.3 and 4.4.4, the overall results favour a lower seeding density between 100,000 and 150,000 to cater for the best overall cell adherence, cell retention over time and positive cell metabolic changes from Day 2-3 for both oxygen conditions 21% and 1%. It also considered the higher overall VEGF concentrations measured in the low SD data compared to the high SD. Hence, 125,000 per 6mm scaffold was chosen for future INTEGRA® seeding density. In addition, the data supported the timing of Day 3 to be the ideal transplantation time for downstream *in vivo* experiments.

4.7 Future methodological improvements

Most *in vitro* oxygen diffusion and saturation studies are carried out on monolayer cells. The added complexity of having TE materials used in cell culture means that there is a crucial parameter missing from the modelling oxygen diffusion, flux and rate of oxygen consumption through media for tissue engineering and regenerative medicine purposes. Oxygen monitoring data in media and within hydrogel can help determine the diffusion coefficient of oxygen in the materials. The collagen hydrogel diffusion coefficient of oxygen has already been established (452–454). However, data from more complex TE scaffolds is still lacking (455). For further work, it would be interesting to investigate the difference in the coefficient of oxygen in hydrogel and in INTEGRA® scaffold. This would complete the pericellular oxygen mathematically modelling to the above forementioned parameters. (Figure 4-33) Such data would add significantly to vital knowledge and data around oxygen culture conditioning for tissue engineering purposes that is currently lacking within the scientific community.

To further complete the data on oxygen variation of seeded cells in different media or oxygen conditions, it is possible to employ mathematical models such as one shown in Figure 4-33, to help work out the exact oxygen consumption rate of the cells in different oxygen conditions. This would help to standardise the pO_2 at the pericellular region by working out and altering the changeable parameters such as the exact atmospheric oxygen levels to be used for cell culture, the cell density to be used in relation to cell O_2 consumption, as well as height of the media used. However, with advancing technology, such measurements are now possible to monitor and analyse accurately in real time using the novel Seahorse XF Real-Time Cell Metabolic Analyser by Agilent (456). The equipment can measure rates of mitochondrial oxygen flux and extracellular acidification rate through real-time and live cell analysis and allows the interrogation of key cellular functions such as oxygen consumption rate (OCR) and extracellular acidification rate (ECAR) in a multiwell format (457). Given how important changes in oxygen levels would be to hypoxic pre-conditioning studies, this can help offer not just insight into detailed changes in cellular metabolism, but the data can also be used to reduce variability of oxygen levels and

prevent undesirable anoxia levels at the pericellular level, allowing for more reproducible data for future applications.

During this study, we trialled two different UK-manufactured hypoxic workstations from Oxford Optronix and Don Whitley Scientific. (Figure 4-34) These workstations allowed for tightly controlled hypoxic environments throughout the experimental workflow, which is crucial for hypoxia-related research. The consistent use of these workstations helps prevent oxygen variability during culture and their effect on oxygen sensitive outcome measures such as protein or gene expression, such as HIF1a. But due to the high initial upfront cost and ongoing maintenance associated with the use of this specialised equipment, the adoption of this workstation did not materialise due to funding limitations. This may highlight the possible limitations in hypoxia-related research and may explain why this field is unexplored in non-cancer related publications. If resources allow, these hypoxic workstations would certainly be advocated as a worthwhile vital investment for lab groups carrying out hypoxic based cellular therapeutics. Modular add on components, such as bioreactors, live cell imaging analysis and molecular pre-processing areas are available for these workstations. It would be highly beneficial to allow for processing of samples in such a tightly controlled oxygen environment offered by such systems for more reliable data for future experiments.

Figure 4-34 Hypoxic workstation allows for an all-in-one heated and humidified incubator with enclosed sterile work space via the use of sleeved ports. It provides a stable hypoxic environment which reduces

variability in oxygen tension during cell culture. HypoxyLab by Oxford Optronix is shown on the top and Don Whitley Scientific's H35 hypoxystation on the down.

5 Functional In Vitro Evaluation of Angiogenic Potential of Seeded Cells

5.1 Introduction

Angiogenesis is the process by which new capillaries arise from pre-existing vasculature. It involves the migration and proliferation of endothelial cells (EC) during the out-sprouting process as discussed in Chapter 1. To model the process of angiogenesis and to evaluate the effects of relevant biomolecules on the process, different functional angiogenesis assays are employed. They are classified into *in vitro*, *ex vivo* and *in vivo* methods. *In vitro* and *ex vivo* methods are used for early evaluations and to monitor specific stages in the angiogenesis process.

5.1.1 Types of Angiogenesis Assays

Most *in vitro* angiogenesis employs the use of EC in their methodology. EC play a central functional role in this process as they are key cells of interest in neovascularization and are responsive to pro-angiogenic biomolecules (458). The use of EC in angiogenesis assays allows for the direct observation of the effect of biomolecules from MSC exosomes on EC migration, proliferation as well as their organisation into pre-capillary structures (459). It forms a useful measure of pro-angiogenic activity on host vasculature.

However, EC only makes up one component of the angiogenesis neovasculature. *Ex vivo* organ culture assay attempts to mimic more realistic *in vivo* processes by utilising the tissue component surrounding nonendothelial cells (such as smooth muscle cells and pericytes) and a supporting matrix. A genuine concern for the vascularisation of tissue-engineered products is the maintenance of mature, stable and functional vessels after implantation in the host. Hence, the ability to investigate and observe how a collection of cells of interest from a vascular organ would behave in culture would be highly beneficial.

Cost-effective assays are important tools in the development of new therapeutic strategies to modulate neovascularisation. *In vitro* angiogenesis assays are generally low-cost, easily accessible and can offer specific experimental outcomes against cellular and cytokine effects of seeded cells on important aspects of angiogenesis. However, the cost does increase with complexity of the assay. Due to the need for animal-derived material in the ex vivo assays, they tend to be more costly compared to *in vitro* assays.

A summary of the different methods and their details are shown in Table 5.1. The list below generalises the main difference between *in vitro* and *ex vivo* assays:

1. *In vitro* assays recognises direct effects on endothelial cell function while *ex vivo* assays involve multiple cell types and processes. Hence, *ex vivo* assays increases the complexity and takes into account cell-to-cell interactions of EC and other supporting cells.
2. *In vitro* assays analyse isolated processes of angiogenesis consisting of proliferation, migration, differentiation, morphogenesis and/or matrix degradation of endothelial cells. E*x vivo* assays aims to study all these processes collectively and hence it closely mimics *in vivo* angiogenesis.
3. In *In vitro* assays technical skill in animal handling is not needed compared with that of *ex vivo* assays.
4. *In vitro* assays are less expensive than *ex vivo* assays.
5. *In vitro* angiogenesis assays often can be quantified more easily but careful interpretation of *in vitro* assays is required due to the use of endothelial cells in isolation.

	Angiogenic functions assessed	Description of assay	Pros	Cons
In vitro				
Wound healing/ Scratch assay	Migration/ Proliferation	2D migration into a defined gap	• Simple • Qualitative compared to other migration-based assays • Can be adapted for large-scale high-throughput assays • Multiple time points can be assessed using the same wells	• Variability between wells due to varying cell confluency • Reproducibility issue: Difficulty with standardising scratch width/edge/shape (depending on the methodology, this can be overcome – see Section 4.3) • Difficulty with quantification of gap size and rate of closure • Does not delineate chemokinesis or chemotaxis of cells
Endothelial tubular formation assay	Morphogenesis	Formation of endothelial tube-like structures on 3D matrix	• Measures differentiation and restructuring ability of endothelial cells • Semi-automated software for quantification of sprouting area is available	• The matrix effect on endothelial cellular morphogenesis is difficult to delineate
Transwell migration assay (Modified Boyden chamber assay)	Migration	Measures 2D migration of cells through a transwell/chamber	• High sensitivity to small differences in concentration gradients, • high reproducibility, • Quick and easy to set up	• Technically challenging to set-up • Maintenance of transwell gradients for the duration of the experiments • Inability to observe cell migration during the experiment
Zymogen assay	Migration/Matrix degradation	Assessment of MMP activity of endothelial cells	• Inexpensive • Easy to get basic information	• Technically challenging to set-up • Time-consuming
Ex vivo				
Organ culture assay Examples include: □ Rat/mouse aortic ring assay □ Chick aortic arch assay □ Mouse metatarsal assay	All - migration, proliferation, morphogenesis, matrix degradation	Organ is embedded into a 3D matrix and sprout formation is assessed	Closely mimics *in vivo* cellular microenvironment and offer more realistic representation of *in vivo* angiogenesis cellular behaviour as: 1) All of the key steps of the angiogenesis process are represented 2) Multiple cell types are represented 3) Endothelial cells within the organ explant have not been pre-selected by passaging and are therefore not in a proliferative state	• Technically challenging procedures with a steep learning curve • The success of assay relies heavily on technical skills of operator • Donor tissue variability in angiogenic responses • Difficulty quantification of microvessel outgrowth in 3D setting • *In vivo* angiogenesis normally occurs from micro-vessels, but larger vessels such as aorta used in assay instead • Use of non-human tissues would impact on the clinical translatability of data

Table 5.1 The most commonly used angiogenesis assays to evaluate angiogenesis modulators (459).

In order to determine if seeded adMSC in different oxygen conditioning would have a desirable effect on EC, conditioned media was collected and tested in both *in vitro* and *ex vivo* angiogenesis assays. Each separate assay section below will have a description of the methodology used.

Hypothesis:

Chemokine and paracrine material within conditioned media from seeded adMSC in dynamic hypoxia (DH) 21-1% pre-conditioning will produce pro-angiogenic features in the *in vitro* and *ex vivo* angiogenic modelling.

Aim:

7. To determine if conditioned media from DH pre-conditioned adMSC can increase endothelial cells' angiogenic functions (morphogenesis, migration, and proliferation) from *in vitro* angiogenesis assays (endothelial scratch assay and tubular formation assay).

8. To determine if conditioned media can help with early stage (sprouting) angiogenesis using *ex-vivo* organ culture assays.

5.2 In Vitro Angiogenesis Assay: Endothelial scratch assay

The wound healing or scratch assay is a good measure of cell migration and proliferation within defined and controlled conditions. The most characteristic readout of a wound healing and migration assay is the change of the cell-covered area (gap closure) over time. The type of collective cell migration probed by the this assay is known as sheet migration. This migration is exhibited by confluent epithelial and endothelial monolayers that move in two dimensions while maintaining their intercellular junctions. Sheet migration involves a complex interplay among mechanical forces, molecular interactions and biochemical cascades that are triggered by the exposure of the cellular monolayer to free space as well as the surrounding extracellular molecules present in the culture media.

Conducting a wound healing/scratch and migration assay is a relatively simple procedure which involves the following three steps: 1. create a physical gap within a confluent cell monolayer, 2. monitor the process of cell migration into the gap with live cell imaging or by taking microscopic images at different time points, 3. analyse the gap closure rate using image analysis. Despite the apparent simplicity of a wound healing assay, many factors can influence the experimental outcome and therefore the experiment must be tightly controlled in order to achieve reproducible and robust results.

It is also a simple assay which can also play host to a variety of other cell types. For example, when dermal fibroblasts are used, an extrapolation on wound healing potential of the testing agent can be explored. If endothelial cells are used, effects on vascular cell migration and proliferation can be determined through this assay.

5.2.1 Materials and Method

Traditionally, scratch/wound assays were done with a pipette tip or needle to scrape a line through a confluent cell monolayer at the bottom of a well plate, in effect 'wounding' the site in an *in vitro* setting. The main drawback of this method is the difficulty with standardising this scratch area to ensure equal boundary and thickness amongst all the wells when performing this manually. To overcome this issue, 2 silicone well culture inserts provided in the Ibidi wound healing and migration assay kit reduce such variability and ensure the same reproducible wound gap across all experimental groups (460). It is important to note, however that the loss of the traumatising effect of scraping of the cells mean loss of cell damage effect and resultant cellular signalling from necrotic or apoptotic cells. This may or may not be desirable, depending on the rationale behind the experiment. For example, in wound healing models, the traumatisation of cells may be more representative of the disease process since it may simulate a migratory response similar to that *in vivo*.

The use of the well inserts allows significant ease of the procedure throughout the assay and for any repeated experiments at a later date. The inserts allow for wells to grow cells to confluency and the removal of the insert will provide a standard 500um cell-free gap to be created. In this experiment, 2 well culture-insert pre-assembled in a 24 well plate (Ibidi GmbH, #80241) was used. The manufacturer's protocol is illustrated in the steps shown in Figure 5-1. Primary HUVEC isolated from 3 different ethically approved human umbilical cords were pooled and grown to P1. 70ul of HUVEC cell suspension was added onto the 2 well inserts at a density of 5-7 x 10^5 cells/ml. The plate was incubated at 37 °C in a CO_2 incubator for 24 hours to allow for cell adherence. The well inserts were removed carefully with a sterile forceps and wash gently with warmed PBS to remove cell debris and non-adherent cells. The wells were then filled with the respective conditioned media (CM) collected from MSC seeded in tissue-engineered scaffolds (static 1%, static 21% and dynamic 21-1%). Control media of EGM-2 and alpha MEM (aMEM) was used. 1ml of media was added to each 24 well. There were n=4 per experimental group.

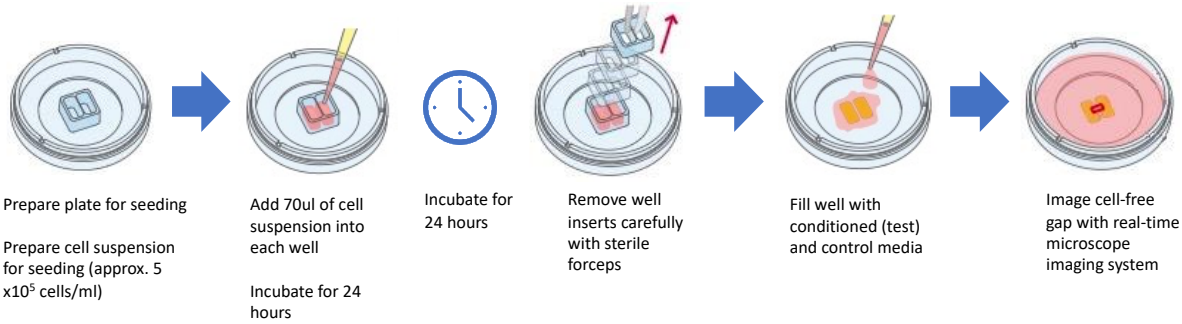

Figure 5-1 Schematic workflow of the Ibidi wound assay. Adapted from Ibidi GmbH (https://ibidi.com/img/cms/support/AN/AN21_Wound_Healing_Assay.pdf)

5.2.1.1 Image capture, analysis and quantification

Plates were serially imaged and monitored at regular intervals using EVOS FL Auto 2 Imaging System (Invitrogen, Thermo Fisher Scientific). Images taken were analysed and gap area was serially quantified using the 'MRI Wound Healing Tool' plugin on Fiji imaging software (U. S. National Institutes of Health) (461).

Figure 5-2 Serial images were taken automatically using the Invitrogen™ EVOS™ FL Auto 2 Imaging System (Thermo Fisher Scientific). An experimental specific protocol was set up within the microscope software to ensure the same fields were captured over time to allow for accurate analysis with Fiji software.

Original gap area was measured by averaging all gap area in wells at 0 hour timepoint. Gap area was plotted over the experimental timeline to represent the

amount of cell migration into the gap. To access rate of gap closure, percentage gap closure was calculated using the equation below:

$$Percentage\ gap\ closure\ (\%) = \frac{(original\ gap\ area - gap\ area\ at\ timepoint)}{original\ gap\ area} \times 100\%$$

This was plotted over time and a linear regression analysis of all the plotted points was obtained using the Prism 9 software (GraphPad Software, LLC). The gradient of the line represented the rate of gap closure (% per hour). To calculate the rate of gap closure in um^2 per hour, the gradient value of the linear regression line was multiplied by the averaged original gap area at 0 hours.

$$Rate\ of\ gap\ closure\ (um^2\ per\ hour) = gradient\ (\%\ per\ hour) \times original\ gap\ area\ (um^2)$$

All statical analysis was carried out using the Prism 9 software (GraphPad Software, LLC). All results represented mean ± standard deviation (error bars).

5.2.2 Results

The most common information derived from the wound healing assay is the rate of gap closure, which is a measure of the speed of the collective migration of the cells. In this way, the underlying mechanisms governing sheet migration can be determined (460).

There were 4 wells per experimental condition; 2 separate images of gap area from each well were analysed. (n=8 per experimental group) Serial images of all wells were taken at 0, 1, 5, 12, 17, 21 and 27 hours of culture. Gap areas at 0 hours from all wells were measured and averaged to calculate the mean of ‘original gap area’, which was 1559140.84um^2. Due to technical constraints within the experimental setup, the assay had to be terminated at 27 hours. Only HUVEC cultured in EGM-2 media migrated quickly and achieved full gap closure by 21 hours. (Figure 5-3)

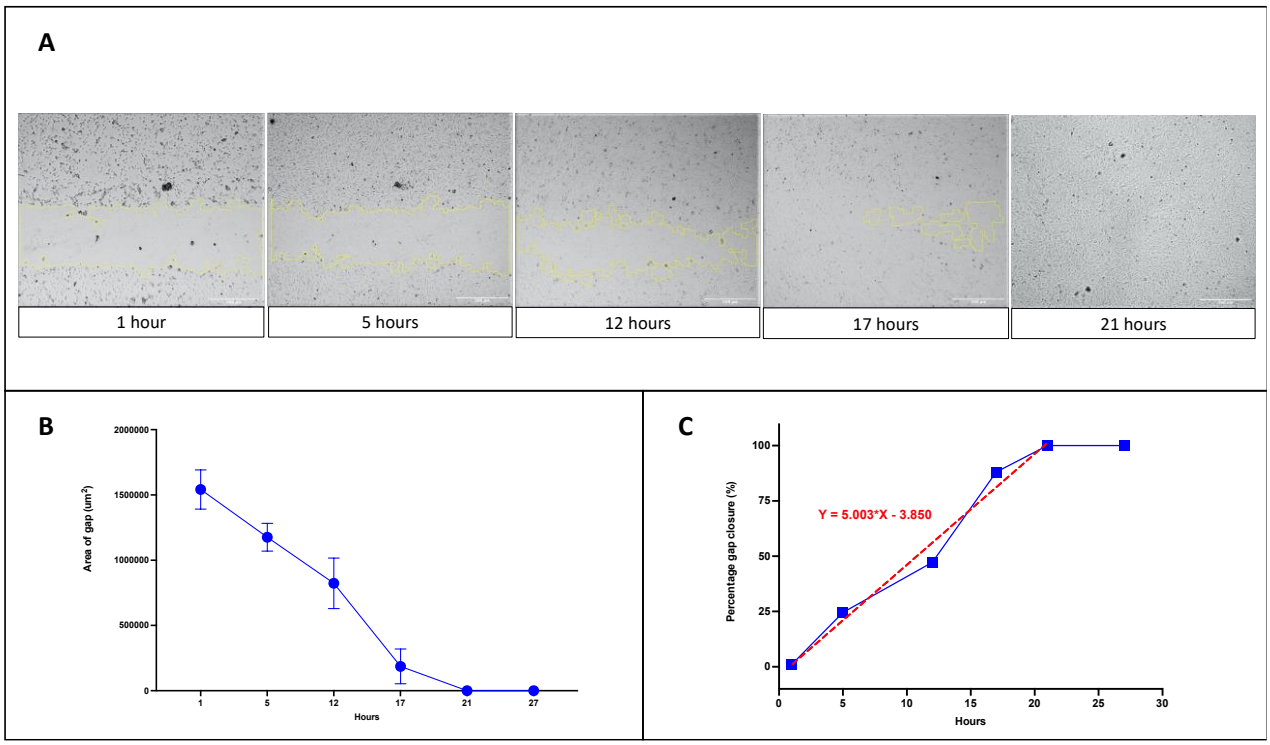

Figure 5-3 Representative time-lapsed images and corresponding measurements of the effect of EGM-2 media on the endothelial scratch assay. Assay was performed over 27 hours. A: Full gap closure was achieved by 21 hours. B: The area of gap closure (um^2) was plotted against time (hours). C: The same data set was averaged and graphed as percentage closure over time. The linear relationship between the percentage closure and time allows for the calculation of the rate of closure for this given condition. Percentage gap closure = [(Original gap area – averaged area of gap measured at particular timepoint)/ Original gap area] *100. 'Original gap area' is the average value of all gaps measured at 0 hours, which was found to be 1559140.84um^2. The slope of the linear phase revealed an average scratch closure rate of approximately 5% of the original gap area (78003.816um^2) per hour (y=5.003x-3.850).

A

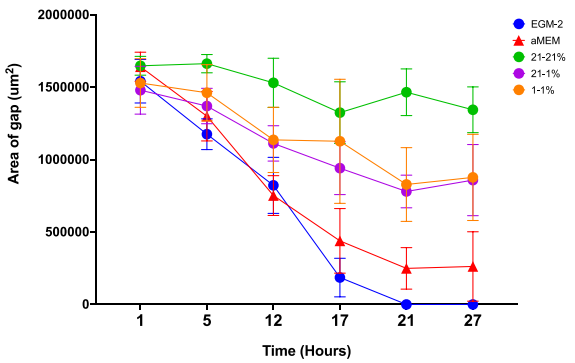

B

Media type	Rate of gap closure (um²/hr)
EGM-2	78003.816
aMEM	56783.909
Conditioned Dynamic 21-1%	28594.643
Conditioned Static 1-1%	28220.449
Conditioned Static 21-21%	12989.202

C

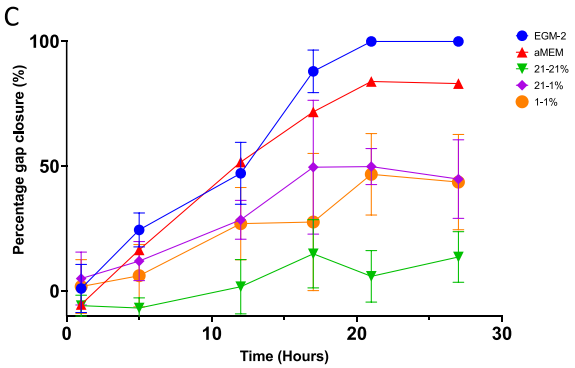

D

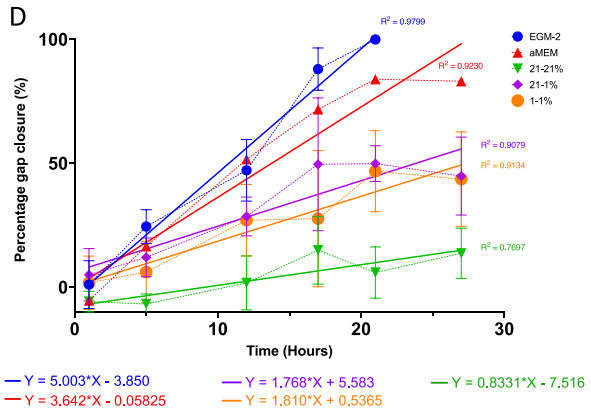

Figure 5-4 Plotted graphs comparing gap closure of HUVEC over time in the different media conditions. A: Area of gap in um² over time. B: Tabulated rate of gap closure (um²/hr) for all media types calculated from the gradient value of linear equation in graph D. C: Percentage gap closure calculated of the different media conditions over time. D: Linear regression line for plotted points for each group are shown (this was only calculated until 100% of gap closure was reached, which for the EGM-2 media group was till 21 hours of culture). The respective linear equations are shown at the bottom of the graph and their R-square values are plotted next to each graph. Differences between the gradients of each line (rate of gap closure/migration of cells) are considered very significant (P<0.0001). All error bars = standard deviation.

Within the control groups, HUVEC in EGM-2 media migrated fastest into the cell-free gap, with the gap closed by 21 hours of culture, compared to aMEM media, which did not achieve full gap closure at 27 hours. (rate of closure =78003.816 um²/hr compared to 56783.909 um²/hr). (Figure 5-4A,B) However, both control groups have significantly increased rates of closure compared to the CM groups. (Figure 5-4D) Comparing the rate of gap closure from cell migration within the CM groups, the dynamic 21-1% group (28594.643 um²/hr) had the faster rate of migration of cells, and this was followed closely by SH 1% group (28220.449 um²/hr). The SN 21% group showed the least cell migration into the gap, at the rate of 12989.202 um²/hr.

Linear regression curves were achieved for all groups with most R-square values (goodness of fit) calculated at > 0.9, except for static 21-21% conditioned media.

5.3 In Vitro Angiogenesis Assay: Endothelial cell tube formation assay

Endothelial cell tube formation assay is one of the most widely used in vitro angiogenesis assays to model the reorganisation stage of new vessel formation. *In vitro* angiogenesis assays take advantage of the tendency of vascular endothelial cells to form tubular structures when cultured on a supportive matrix (basement membrane) and have been used successfully to identify pro-angiogenic factors and inhibitors. Hence, it offers a high-throughput screening platform to test angiogenic compounds and their effects on endothelial cell tube formation.

The assay measures the ability of endothelial cells, plated at subconfluent densities with the appropriate extracellular matrix support, to form capillary-like tubular structures. It can be used to determine the ability of various compounds to promote or inhibit tube formation. Upon plating, endothelial cells attach and generate mechanical forces on the surrounding ECM to create tracks or guidance pathways that facilitate cellular migration. The resulting cords of cells will eventually form hollow lumens.

5.3.1 Materials and Method

5.3.1.1 Endothelial cells and BME preparation

The formation of capillary-like structures was assessed in a 96 well plate using material from a commercially available in vitro angiogenesis assay tube formation kit (Cultrex®, # 3470-096-K). Following manufacturer's protocol, 50ul of reduced growth factor BME without phenol (Cultrex®, # 3433-005-01) was alliquoted per well. The BME was allowed to gel at 37°C for 30 to 60 minutes after a brief centrifuging at 250 x g in 4°C to ensure the removal of any air bubbles. Primary HUVEC isolated from 3 different ethically approved human umbilical cords were pooled and grown to P1. They were used to seed onto the gelled BME at a density of 1 to 3 x 10^4 cells/100ul. The plate is at 37 °C in a CO_2 incubator, with serial images taken of the wells starting at 1 hour of incubation, and up to 24 hours post-seeding. Conditioned media (CM)

from MSC from the 3 experimental groups (static 21%, static 1%, and dynamic 21-1%; cultured up to day 3) were used to determine the effect on tubular formation. Endothelial Growth Medium-2 (EGM-2) media (Lonza) with 30ng/ml of human VEGF (Peperotech) was used as the positive control, and Endothelial Basal Medium-2 (EBM-2) (Lonza) with 5uM of sulforaphane (Cultrex®, # 3470-096-02) per well was used as the negative control. Sulforaphane [1-isothiocyanato-(4R)-methylsulfinyl)-butane], is a naturally occurring cancer chemopreventive agent, and is provided as a negative control for inhibition of *in vitro* endothelial cell tube formation. At the end of the assay, 100ul of Cell Staining Solution (Cultrex®, #: 3470-096-01) was used per well after fixing with 150ul of ice-cold methanol with several wash steps of ddH2O in between.

5.3.1.2 Image capture, analysis and quantification

The number of junctions or tubes between cells were monitored and imaged in real time using Invitrogen™ EVOS™ FL Auto 2 Imaging System (Thermo Fisher Scientific) at 4x objective. Images taken were analysed and quantified automatically using the validated 'Angiogenesis Analyzer' plugin on Fiji imaging software (U. S. National Institutes of Health) (462).

Analysis was performed on central well images at 4x magnification. Measurements were based on the following definitions: **Junctions** are nodal points with at least 3 tubules branching off from them (forming a tree). **Segments** are sections of tubules bounded by two junctions. **Branches** are features bounded by a junction and tubular sprout. Hence, the number of branches is a measure of the number of sprouts originating from a single tubule, without necessarily forming an extended network. On the other hand, the number of segments would equate to the measure of the number of tubules that form part of other segments, and hence an extended network of other connected tubules. **Meshes** are areas enclosed by tubular segments. (see Figure 5-5) To measure the overall tubular formation capacity of the CM on endothelial cells, the number of junctions, branches, segments and lengths measured would reflect on the **branching point potential**. Mesh areas, the formation of hollow capillary-like

lumens, and their corresponding measurements would reflect on the **vascular drift of the cells**.

All statical analysis was carried out using the Prism 9 software (GraphPad Software, LLC). All results represented mean ± standard deviation (error bars).

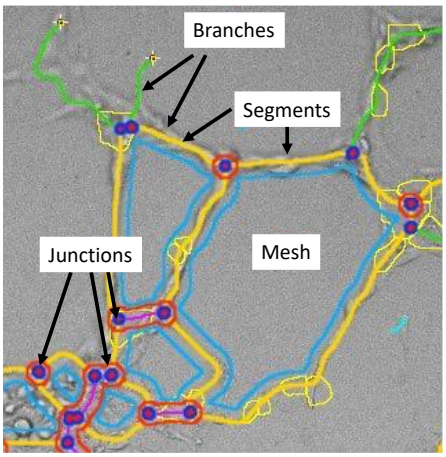

Figure 5-5 Visual illustration of labelled measurements obtained from the Angiogenesis Analyzer in Fiji software. Briefly, junctions are points associated with 3 branches (red circled spots); segments are tubules between two junctions (yellow line); branches are any tubular outsprouting from one junction (yellow or green lines); Mesh is an area enclosed by segments (blue outlined area).

5.3.2 Results

HUVEC in culture wells presented a wide range of network patterns after about 4 hours of culture, as observed by phase-contrast microscopy. They range from short and isolated segments to highly developed meshing, depending on the treatment conditions. It was noted that earlier time points would show more coalesced and clumpy endothelial cell segments. (Figure 5-6) The networks then appear to mature and peak at about 6-8 hours and appeared to lose their tubular networks and undergo apoptosis by 24 hours into the culture. (Figure 5-7)

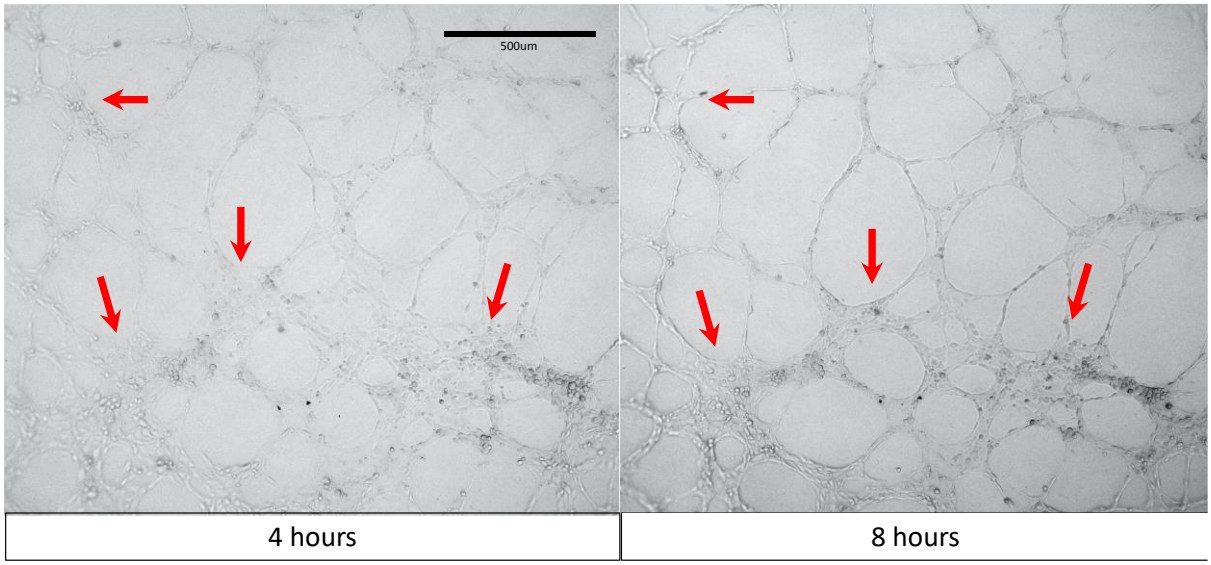

Figure 5-6 Phase contrast images of positive control well showing more coalesced and clumpy endothelial cell segments (highlighted by red arrows) in the earlier time point of 4 hours compared to the same section at 8 hours, which appear more mature from further junctional segments to create more hollowing of the network. Scale bar = 500um.

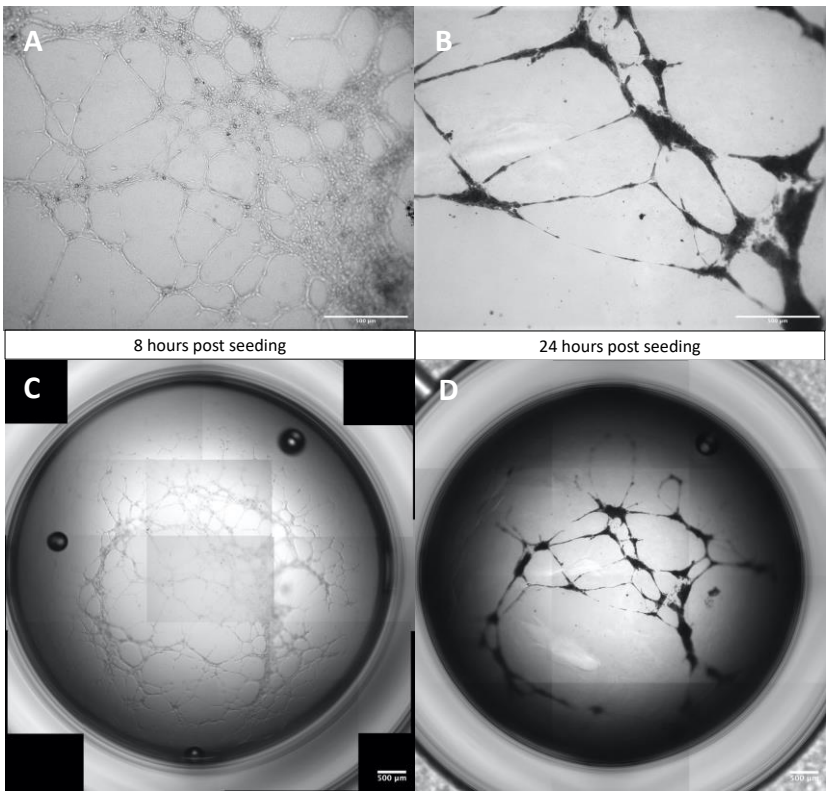

Figure 5-7 Comparative phase contrast images taken of the same area of the gel in a positive control well at 8 hours post seeding compared to 24 hours post seeding (end point of the assay). A,B: Images at 4x objective. C,D: Several images taken automatically and stitched together by EVOS™ FL Auto 2 Imaging System (Thermo Scientific) to show the entire well. Cells at 24 hours were fixed (B,D) and stained with the cell staining solution. Endothelial cells appear to have lost much of their networks by 24 hours of culture. Scale bar: 500um.

A general visual comparison of the network patterns, as shown in Figure 5-8, revealed wells with DH (21-1%) and the positive control media demonstrated the most meshed and complex network patterns. On the opposite end, the negative control wells showed clear evidence of reduced tubular and mesh networks. Both SN 21% and SH 1% conditions have meshed tubular networks, but they don't appear as prolific or complex in pattern as the DH and positive control wells.

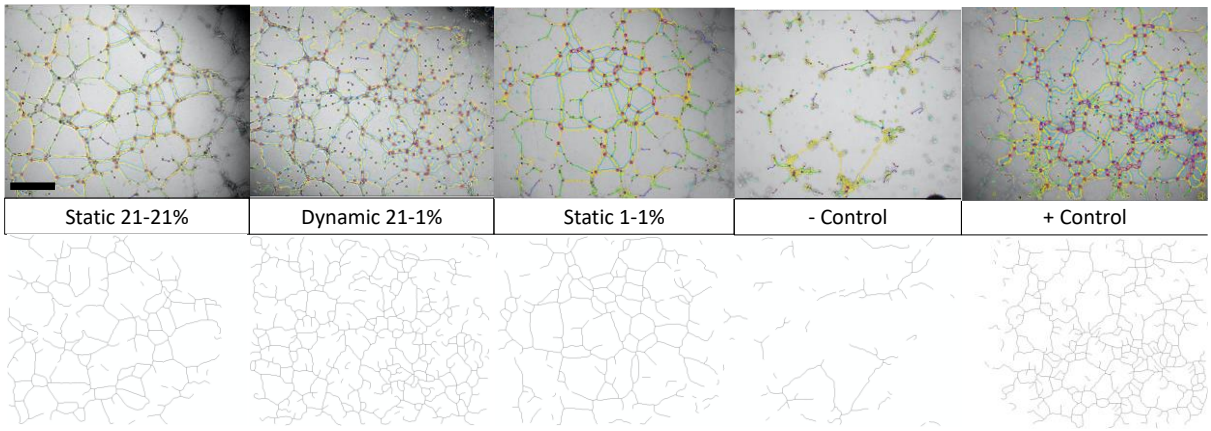

Figure 5-8 Comparative network patterns of HUVEC at 6-8 hours of culture. Top row: Phase contrast images with the superposition of vectorial objects obtained from computer analysis using the "Angiogenesis Analyzer" for Fiji are shown: green, Branches; magenta, Segments; red surrounded by blue, Junctions; cyan, Meshes; violet, Anchorage Junctions; red circle, Sphere. Bottom row: Skeletonised binary images obtained from the same software to show extent of networks formed. Scale bar: 500 µm.

Results from the measured parameters show that CM from DH (21-1%) demonstrated superior branching point potential, with higher number of measured branches, segments and junctions, with mean values, matching that of the positive control values. (DH 21-1%: NB = 85.00 ± 6.959; NS = 187.6 ± 31.59; NJ =154.1 ± 22.60; Pos. control: NB = 77.17 ± 5.782; NS = 189.8 ± 78.12; NJ = 151.5 ± 52.63) (Figure 5-9A,D,G) The average branching length, measured as branching interval, was similar throughout all experimental groups, indicating that the number of endothelial tubules between each junction and any terminal branches was similar and may not a good measure of tubular angiogenesis potential.

CM from DH (21-1%) group also exhibited enhanced vascular drift, with higher capillary-like tubular formation showing more meshed area that exhibit smaller luminal structures (from mean mesh size measurement) compared to the other adMSC CM groups. (Figure 5-9H, I) The overall total length of tubules formed was

also longer, as were the segments length and branching length in the DH (21-1%) group. (Figure 5-9F,C,E) These measurements were statically significant when compared to negative control (sulforaphane) group.

Both HUVEC in DH and SH CM demonstrated a similarly high total mesh area compared to the other groups, including the positive control. However, the mean mesh size appears to be largest with the SH 1% and positive control group and decreases in size from DH to SN and finally to the smallest mean mesh size in the negative control group. The inter-experimental groups were not found to be significant for these measurements.

Overall, the CM from the DH (21-1%) environment showed the most statically similar endothelial tubular formation response to the positive control for all measured parameters representing the branching point potential and vascular drift.

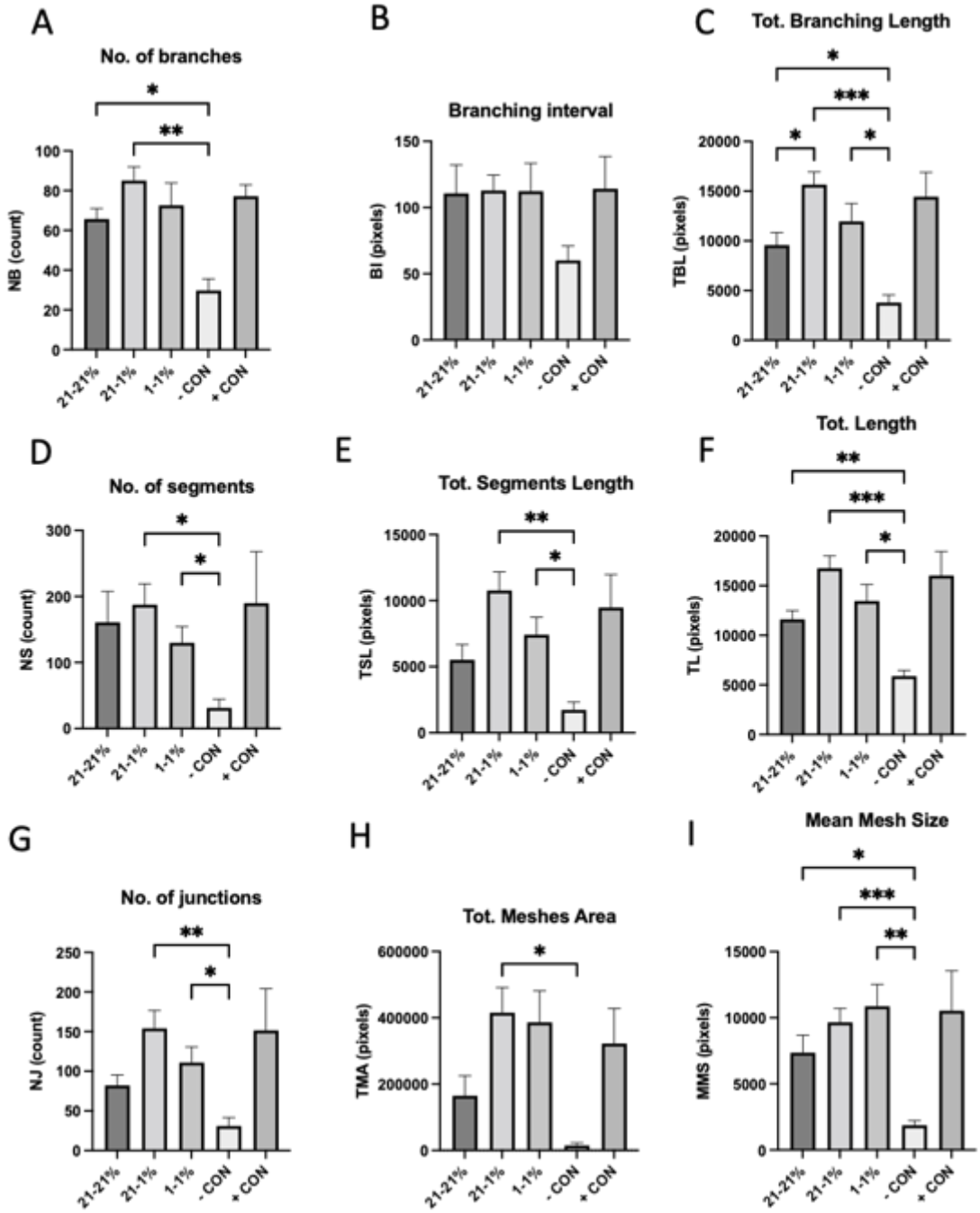

Figure 5-9 Comparative measurement of parameters obtained from image analysis. HUVEC were cultured for up to 9 hours in reduced GF BME (Cultrex). Negative control (-CON): sulforaphane was used; Positive control (+CON: EGM-2 media with the addition of 30ng/ml VEGF was used. Number of branches (NB) = number of branches in the analysed area. Number of junctions (NJ) = number of junctions in the analysed area. Number of segments (NS) = number of segments in the analysed region. Total branching length (TBL) = sum of the length of the trees composed of segments and branches in the analysed area. Branching interval (BI) = mean length between two branches in the trees in the analysed area (Tot. segments length / No. of branches). Total mesh area (TMA) = sum of mesh areas detected in the analysed area. Mean mesh area (MMA) = mean mesh size in the analysed area. Total length (TL) = sum of the length of segments and branches of tubules in the analysed area. Total segments length (TSL) = sum of length of the segments in the analysed area. Statistical analyses were performed by One-way ANOVA followed

by post-hoc Dunnet's T3 multiple comparison test. The means of each result were compared to the corresponding groups. (*p < 0.03; **p < 0.002; ***p < 0.0002; ****p < 0.0001). Error bars correspond to the number of analysed images (n = 8 acquired from 4 wells) ± SEM. Four biological replicates of wells for each experimental condition were carried out with 2 technical replicates for each well performed.

5.4 Ex vivo Angiogenesis Assay: Human arterial ring assay

Ex vivo assay uses whole organ culture, such as aortic ring assay. These assays mimic in vivo situations because they contain surrounding nonendothelial cells (such as smooth muscle cells and pericytes) and a supporting matrix.

The experiment, described in this section, is based on the rat aortic ring assay. It was originally described and developed by Nicosia et al. (463,464) which involves embedding an excised segment of the rat thoracic aorta into a three-dimensional matrix and culturing *in vitro* to investigate new blood vessel growth. This was thought to be triggered by injury from the dissection and mediated by intrinsic growth factors produced from the explant. Test substances will then be added to the culture to analyse for their pro- or anti-angiogenic effects. This assay would offer a remarkably similar microenvironment that one would expect from a transplant *in vivo* model, due to the composition of tissue and cells within the organ of note and the microenvironment triggered by trauma. As a result, it is the most widely-performed *ex vivo* model for studying angiogenesis to date (465).

One of the main drawbacks of an animal-derived organ culture assay is the use of xenographic material which may not offer a representative picture of the cells of interest for translational purposes. Several research articles have attempted to address this issue and the consensus is largely supportive of the use of xenographic representative organs for pre-clinical testing of anti-angiogenic evaluation (466,467). However, the publication for pro-angiogenic studies are still limited (468). Human and murine VEGF and their receptors is known to share about 85% of their sequence (469,470) and these could be species-specific in response (471). Hence, where available, the use of human-derived organ would be a much better tissue for *ex vivo* testing mainly for accuracy, representation and translatability of findings to clinically

relevant scenarios. In this study, we aim to overcome issues of using murine aorta by adapting the assay with human artery derived from the umbilical cord. This also offers an additional advantage over animal-based organ assays by not requiring the sacrificing of the animal donor.

5.4.1 Materials and Method

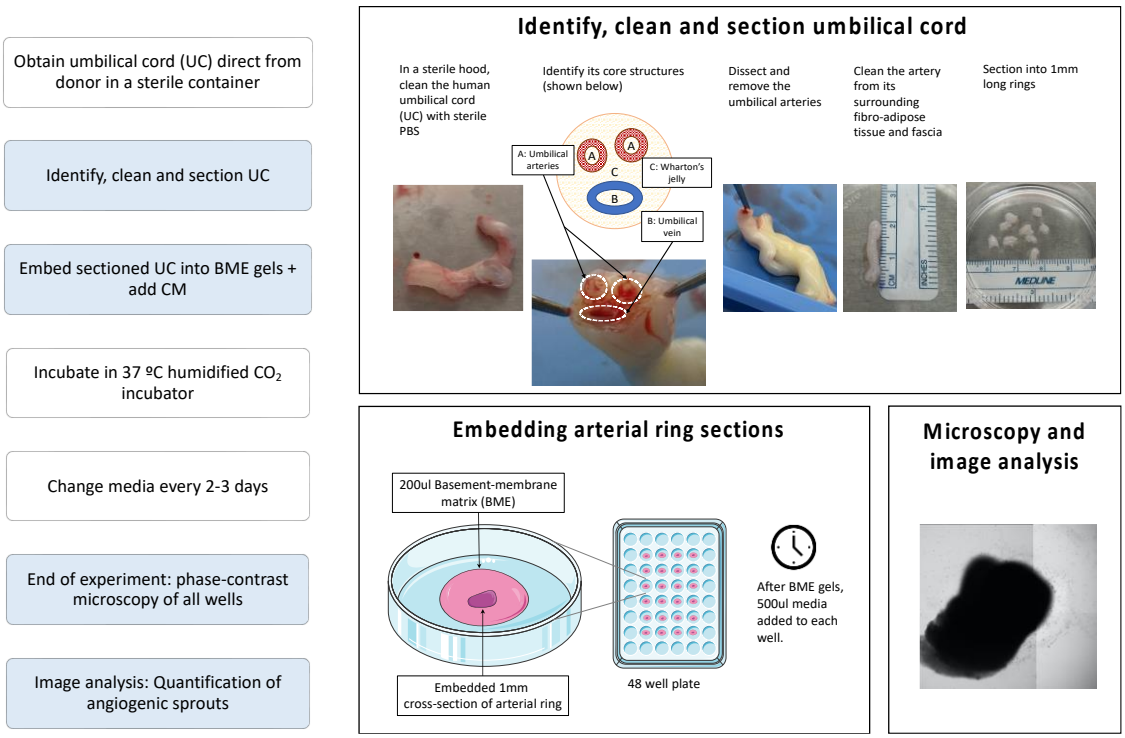

Figure 5-10 Schematic of human umbilical arterial ring assay methodology as adapted from Seano and Primo (472).

Fresh human umbilical cord was obtained from the Vascular Biology and Therapeutics Program (Yale University) via the Labor & Birth department of the Yale New Haven Hospital. The ethical use of this material was approved for research use by the Yale Human Investigations Committee.

The umbilical cord was processed using the protocol described by Seano and Primo for human arterial ring assay (472). The protocol, summarised in Figure 5-10, involved cleaning and dissecting the umbilical cord carefully to separate the umbilical artery. The surrounding fibro-adipose connective tissue and fascia were gently removed and the artery was sectioned into 1mm ring-like segments. These rings were embedded into 200ul of Geltrex™ LDEV-Free Reduced Growth Factor (Gibco,

#A1413201) basement membrane matrix (BME), prepared carefully using manufacturer's recommendations, within 48 well plates and allowed to gel at 37°C for 30 minutes. 500ul of conditioned media from the seeded cells on INTEGRA® was added to each well. EGM-2 media was added as control. For each oxygen condition, 6 separate samples were used. The well plate was incubated in 37°C humidified CO_2 incubator and the media was changed every 2-3 days with either conditioned media or EGM-2 media. All of the above procedure was carried out under sterile conditions. At the end of the assay, phase contrast microscopy using EVOS FL Auto 2 was used to image the wells and image analysis of the wells was carried out using Fiji. Observation for angiogenic dynamics, such as sprouting of capillary-like tubular structures and cellular outgrowth, were made for each of the wells. Cellular outrgowth was measured by taking the longest distance outgrowth for each embedded sample. Due to time limitations, the experiment was terminated on day 13 of culture. In the ideal scenario, the assay should be allowed to carry on for at least 15 days or more.

5.4.2 Results

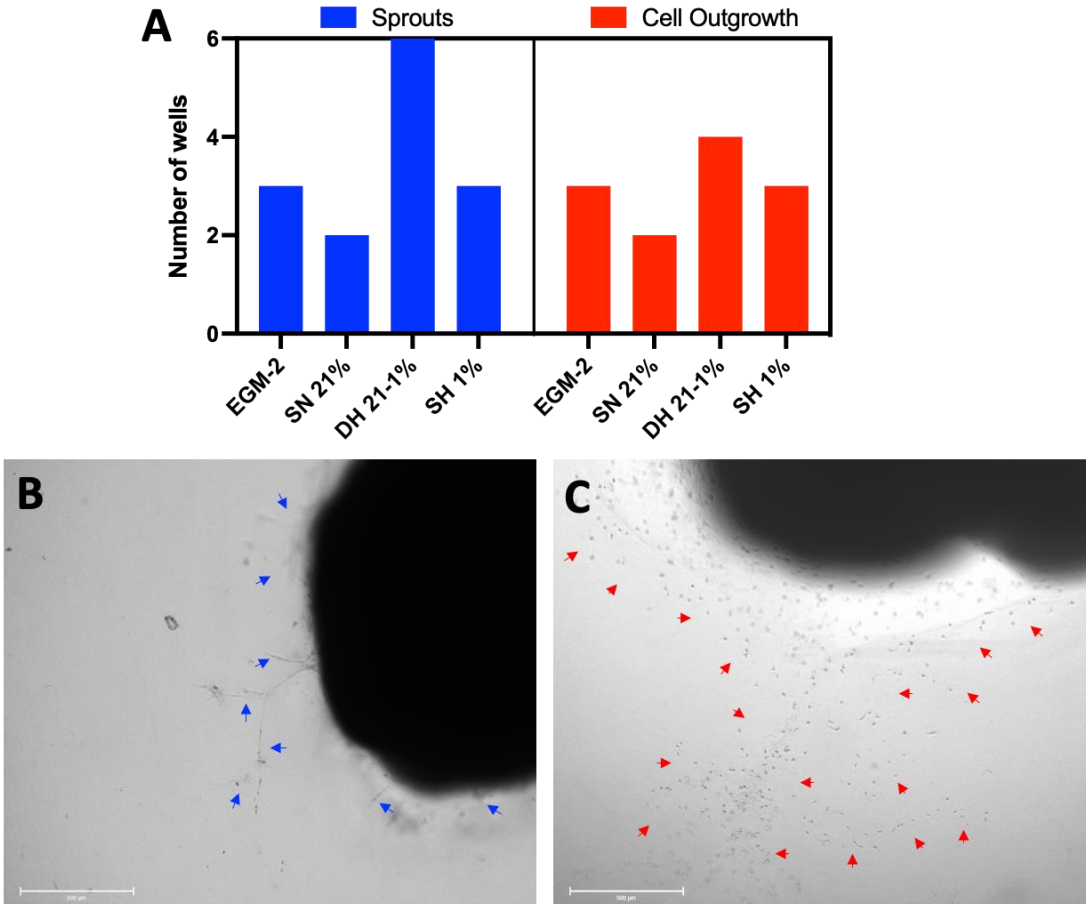

Figure 5-11 (A) Count of wells showing endothelial out-sprouting (blue graph) and cellular outgrowth (red graph); (B) Phase contrast microscopy image of capillary-like tubular sprouting from embedded arterial ring (blue arrows); (C) Phase contrast microscopy image of cellular outgrowth and migration (red arrows). Scale bar = 500um.

In observing for angiogenic changes in the wells, evidence of sprouting of capillary-like tubular structures was mostly seen in arterial ring wells cultured with DH 21-1% conditioned media (CM), in 6 out of the 6 wells (Figure 5-11B). This was compared to only 3 wells for EGM-2 media and SH 1% CM, and SN 21% CM showing only 2 wells, which was the lowest number counts overall for sprouting. (Figure 5-11A) Similar observational trends were seen with cellular outgrowth and migration (Figure 5-11C), where 4 out of 6 of the wells showed evidence of cellular migration from the embedded vessel from the DH CM. This is followed by SH 1%CM and EGM-2 media with 3 wells with cell outgrowth seen, followed lastly by SN 21% CM with 2 wells. EGM-2 media had same trends as the SH 1% CM for both sprouting and cellular outgrowth.

Measuring the cellular outgrowth distance from the embedded arterial ring (Figure 5-12), arterial rings cultured in DH 21-1% conditioned media had the furthest mean cell migration (0.352 ± 0.077mm) from the embedded ring compared to SN 21% (0.290 ± 0.087), SH 1% (0.282 ± 0.168) and EGM-2 media (0.300 ± 0.122). However, the data was not found to be statistical significance.

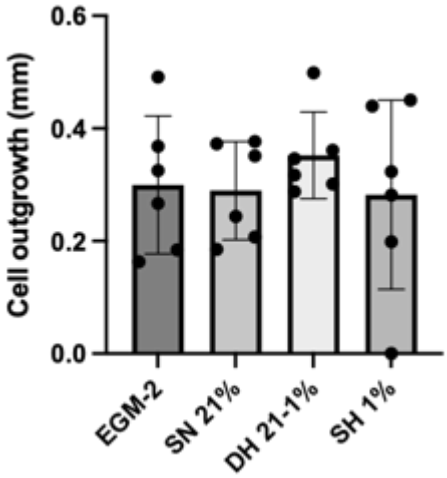

Figure 5-12 Measurement of cellular outgrowth from the embedded umbilical arterial ring. Each column represents the type of media used to culture the arterial ring. Sample n-number = 6 per condition.

5.5 Discussion

The assays performed in this chapter demonstrate, in varying degrees, the cytokine effects of conditioned media on the endothelial cells and their ability to respond in a pro-angiogenic manner. Increasing *in vitro* assays' complexity to *ex vivo* assays is useful to be able to demonstrate the effects of MSC conditioned media on not just endothelial cell behaviour, but also surround cells from composite vascular tissues. This is important as endothelial, and their supportive mural cells forms the main cellular building blocks for the angiogenesis process in the body.

Understanding the concept of vasculogenesis and angiogenesis is crucial in interpreting the results. The process of vasculogenesis involves endothelial cells remodelling into tubular structures to form primitive vascular plexus. (See Chapter 1, Figure 1.1) This process is largely driven by the presence of VEGF (21). Angiogenesis, on the other hand, describes the process of the formation of new blood vessels from pre-existing ones. The process is regulated by a tight balance

between pro- and anti-angiogenic agents (7). At the cellular level, angiogenesis involves at least two distinct cell types, endothelial cells and supporting mural cells (pericytes and vascular smooth muscle cells, as described in Chapter 1). It involves a number of cellular functions, such as migration, proliferation, differentiation and morphogenesis of these cells (8). To promote new blood vessel formation, endothelial cells from their quiescent state in pre-existing blood vessels will need to be stimulated to migrate, proliferate, and invade into surrounding tissue or matrix as described in Chapter 1, Figure 1-2.

Using *in vitro* angiogenesis assays can help identify of media containing substances which can influence specific mechanisms of angiogenesis. Each *in vitro* assay aims to represent one aspect of this angiogenic process (see Table 5.1). The monolayer endothelial scratch assay in some respects resembles the quiescent state of endothelial cells. When ‘wounded’, as such in the scratch assay, the monolayer closure of the area would involve both proliferation and migration of EC (10). VEGF stimulation is known to accelerate this process (10). Hence, this assay can be used to test whether the presence of such angiogenic factors, or indeed the amount contained in media, would influence the rate of endothelial cell proliferation and migration.

In view of the angiogenic proteomic assay previously presented in Chapter 4, it was expected that the DH 21-1% CM would achieve better results in the rate of closure compared to the other oxygen conditions. The final data did reflect this: SN 21% CM had the poorest performing result out of the CM groups. This was concordant with the other assays in this section. However, rather surprisingly, aMEM media alone achieved gap closure much faster than all the adMSC CM. Therefore, this result brings into question if CM itself would be of benefit or a hinderance to EC migration. In context of the methodological process, the pooled CM from all the wells in each set of oxygen condition were directly used in this assay with no prior processing or addition of fresh media to mix and use for the EC migration application. As a result, these CM are likely to be serum depleted during their previous culture. The serum poor could account for the relatively poor cell migration seen in the CM groups. In retrospect, a mix of 50:50 CM with fresh aMEM would have been a better comparison if fresh aMEM were used as the control. Conversely, aMEM with no

serum could be used as a control instead. However, due to time limitations, a repeat of these assay using the above suggested improvements was not possible. These suggestions can serve as a helpful recommendation for future modifications of the same experimental design. On further investigation into the use of CM on EC, it was also interesting to find that full-length VEGF-A (165) b isoform which are usually present in the CM can actually have an inhibitory effect on endothelial proliferation and migration in a dose-dependent manner (473). The existence of inhibitory forms of VEGF may play a role in the transition of an anti-angiogenic state to a pro-angiogenic phenotype (473). For future studies, it would be helpful to further investigate the different types and amount of VEGF-A isoforms present in CM from adMSC to directly correlate this with the pro-angiogenic EC migration effects.

Encouragingly, the other angiogenesis assays were able to provide greater insight into the effect of CM on other endothelial functions. Endothelial tubular formation assay aims to replicate the morphogenesis process of activating endothelial cells to organise into primitive tubular-like structures, This may eventually form into hollow tubes as part of a capillary plexus (459). This assay is thought to be more sensitive to pro-angiogenic factors, such as those described in Chapter 1 Figure 1.2, than the scratch assay. Endothelial tubular assay showed CM from MSC cultured DH 21-1% condition to be most conducive to tubule formation in the form of enhanced branch point efficiency of the embedded endothelial cells (Figure 5-9). DH 21-1% CM also appear to enhance ‘vascular drift’ of the EC, a term used to describe as how likely EC in the conditioned well would form capillary-like hollow luminal ‘mesh’ structures, which can be easily visually appreciated from the comparative skeletonised binary images shown in Figure 5-8. Overall, DH 21-1% results were similar to those of the positive control media (EGM-2 + 30ng/ml VEGF) group, demonstrating that they had a measurable pro-angiogenic tubular effect by enhancing EC morphogenesis.

In the context of new vessel formation from the tissue engineering perspective, endothelial cell migration, proliferation, morphogenesis and matrix degradation are all critical to the process (7). Cellular and molecular machinery underlying endothelial cell behaviour have been obtained mostly from observations of cell culture systems. But unlike the culture of an endothelial monolayer, the formation of a new sprout *in vivo* requires endothelial cells to invade the surrounding tissue or matrix (21). Even

three-dimensional EC morphogenesis and matrix degradation assays do not fully model vessel assembly, as the *in vivo* vessel tube formation occurs in the absence of surrounding mural cells and tissue (474). Organ culture assays aims to encompass the evaluation of all these processes. Therefore, data from this essay is thought to be a better predictor of *in vivo* angiogenesis of therapeutic agents. In the arterial ring assay, DH 21-1% CM clearly showed more cell outgrowth and sprouting compared to other conditioned media as well as EGM-2 media, which is a HUVEC-specific media. However, this preliminary data did not achieve more complete quantifiable parameters as those seen in published literature, such as angiogenic outgrowth, sprout length and branching index, due to time limitations. As there have only been 2 publications by the same author of using human umbilical artery for this organ culture assay, it may be possible that all the technical challenges have not been fully addressed (472,475). Compared to the well-documented and published rat aortic ring assay first described by Nicosia in 1982 (463), which has gone through many iterations, validations and further modifications, the use of the human arterial ring assay not been published by any other research group in the same field at the time of writing this thesis. It is likely due to the fact that human umbilical cords are not easy to obtain for research purposes, as there is an additional need for research ethical approval for material transfer agreement between healthcare services and research labs, as well as the high cost of obtaining such tissue. It was nonetheless a worthwhile experience to carry out this assay to allow for the appreciation and understanding of the difference between rat aortic ring and human arterial ring assay. Whilst carrying out this novel experiment in a limited time frame, I have identified a few possible reasons for the difficulty in obtaining quantifiable parameters on the cultured organ from a technical perspective. The incomplete removal of the outer connective tissue surrounding organ vessel has been known to affect angiogenic outgrowth. This issue has been highlighted extensively in literature for murine-derived aortic ring assays. Hence, the vessel is usually manipulated quite thoroughly, but as gently as possible during the processing step (465). However, the handling of the umbilical artery and its surrounding tissue could require a different dissection method due to the size of the artery as well as the anatomical and age difference of the tissue origin compared to that described in the original small-animal based assay. Given more time, for future experiments, it may be worth looking at improving quantifiable detection of the cells, structures and extracellular molecules and proteins

of interest. This was described in detail in a recent methodological paper by Kapoor et al. (465) where whole-mount immunofluorescence staining of EC and other cell types allowed for imaging using confocal microscopy. Subsequent imaging tools can be employed to accurately determine sprouting ability such as the use of fluorescent intensity and 3D rendering of Z-stack imaging. In addition, protein and RNA extraction can be performed as an extension on this assay to help identify changes in extra- and intra-cellular changes for different culture conditions using Western immunoblotting and qPCR techniques (465,472). However this is likely to be technically demanding due to the multitude of steps required to extract the relevant molecules and genetic material from a complex structure embedded in an already factor-enriched BME matrix. Commercial BME is usually purified from Engelbreth-Holm-Swarm (EHS) tumour, is commonly known by the original commercial brand Matrigel™, although there are many other company's which now manufacture this type of BME such as Geltrex™ used in this study. BME typically polymerises at room temperature to form a reconstituted protein matrix consisting of mainly laminin, collagen IV, entactin, and heparin sulphate proteoglycan. For the purposes of this assay, a reduced growth factor was used to prevent obscuring the pro-angiogenic factors from the conditioned media with intrinsic factors within the BME (476). Despite this, the product is still prone to batch-to-batch variation arising from the xenographic nature of its derivative (477).

Greater understanding of the angiogenic effects of the adMSC CM on endothelial and supportive mural cells requires more robust assays accompanied with the additional experiments mentioned above. This will certainly help to characterise the crucial angiogenesis process and offer more greater insights into the molecular changes which can occur with the use of CM or other angiogenic agents on the cells involved in neovascularisation. Looking further into the future, such data can support future studies on the use of CM products, such as exosomes and microvesicles, derived from adMSC for therapeutic purposes. This is an emerging and popular field which is gaining traction amongst regenerative medicine academics owning to the cell-free nature and the theoretical advantage from the ease of manufacturing off-the-shelf products. This will be discussed in further detail in the final chapter.

5.6 Conclusion

Conditioned media contains important cellular exosomes and cytokines released from the adMSC during culture. Combining the angiogenic proteomic data from the previous chapter and the functional assay results from this chapter, there is evidence of angiogenic promotion from adMSC CM in the oxygen culture condition of choice on endothelial and supporting mural cells: CM from DH 21-1% out-performed SH 1% in the scratch assay and endothelial tubular assay. Preliminary results from the whole organ arterial ring assay also showed an indication of the superior angiogenesis ability in DH 21-1% CM. CM from SN 21% condition appear to produce the poorest performing results on endothelial cells and vascular organ assay out of the three different oxygen conditioning groups. Therefore, these overall results would help support the use of DH 21-1% for *in vitro* conditioning of adMSC prior to transplantation *in vivo*.

6 In Vivo Evaluation of Angiogenic and Regenerative Potential of Seeded Cells

6.1 Introduction

Angiogenesis is largely an *in vivo* process and therefore a comprehensive evaluation of the angiogenic effect of the pre-conditioned cell products seeded on the INTEGRA® dermal matrix would require an *in vivo* host environment.

The choice of an appropriate *in vivo* assay requires important considerations. Due to the clinical relevance of angiogenesis in several different clinical pathologies, such as cancer and cardiovascular diseases, there are many established *in vivo* models of angiogenesis.

It is also important to understand if the seeded cells on clinically translatable scaffold would produce functional improvement in a given pathological process. Combining acellular dermal matrix (ADM), with MSC for the treatment of chronic skin ulcers and wound repair is a strategy that has been extensively explored. Published results so far support the strategy of “bio-activating” INTEGRA® dermal matrix by pre-seeding it with MSC (222,223,230,233,234,237,245,248,250,252,390,399,478–481). Hence, part of the onward experiments below investigates if this combination will result in improved wound healing in established murine models.

6.1.1 Types of *In Vivo* Angiogenesis Assays

There are several different types of *in vivo* angiogenesis assays described in the literature. As angiogenesis is a highly dynamic process which often requires multifactorial input from a living system, *in vivo* assays have a clear advantage over *in vitro* assays of being more representative of mimicking the biological processes of the human body. It is often a vital pre-clinical step for any potential therapeutic agent

prior to any larger animal or clinical studies. These established assay types are shown in Table 6.1.

Assay Types	Model	Types of materials used	Disadvantages
Dorsal air sac	Air pocket on the dorsum of murine models	• Tumour cells • Other test substrate	• Technically challenging
Dorsal skinfold chamber	Two symmetrical circular frames attached to the dorsum of the skin to create a skin window for experimentation. Mouse, rats, rabbits and hamster models have been described.	• Cellular implants (tumour etc) • Biomaterials • Xenografts	• Technically challenging • Uncomfortable for animals during extended assays
Zebrafish	Direct implantation of test substance onto adult or embryo of zebrafish	• Angiogenesis inhibitors	• Technically challenging
Matrigel plug implantation	Test substance/material mixed with Matrigel carrier scaffold injected subcutaneously into animals, usually murine model.	• Pro- and anti-angiogenic substrates	• Experimental challenges with the use of Matrigel as a carrier • Need to explant for analysis
Sponge matrix implantation	Test substance/material, loaded onto sponge or polymer matrices, implanted subcutaneously, usually murine model	• Study of formation of fibrovascular tissue	• Experimental challenges with the use of polymer as a scaffold • Need to explant for analysis
Corneal chamber	Test substance/material implanted directly into the corneal micropocket of mouse, rats, guinea pigs and rabbits.	• Tissue/cellular material (tumour etc) • Conditioned medium/substrate	• Technically challenging
Chorioallantoic membrane (CAM)	Direct implantation of test substance onto the growing chorioallantoic membrane of chick embryo, either in ovo or ex ovo. See section…	• Cultured human cancer material • Benign/malignant tissue/explants • Tissue engineered grafts/implant • Xenografts	• Difficult interpretation of results

Table 6.1 Different types of *in vivo* angiogenesis assays (482,483).

6.1.2 Wound healing model

The greatest question in this *in vivo* study is whether the combination of seeded cells within its scaffold will continue to produce the right factors which will lead to functional tissue regeneration. Hence, it is important to consider disease models which would benefit from both angiogenesis and regeneration of tissue. Given the scaffold of choice here is a dermal regeneration matrix, a disease model involving chronic wounds, such as diabetic wound, would be relevant to concluding any functional benefits of the seeded pre-conditioned cells.

Part of wound healing pathophysiology involves neovascularisation into the wound site. When wound fail to heal in the appropriate timeframe, chronic wounds develop. Chronic wounds have difficulty healing due to several factors depending on the background aetiology. These would include chronic infection, poor blood supply,

abnormal immune systems and abnormal pressure loading onto the wound site amongst many others ().

Hypothesis:

Seeded INTEGRA® ADM with adMSC pre-conditioned in dynamic hypoxia will increase angiogenesis and encourage wound healing *in vivo*.

Aim:

1. To determine the *in vivo* angiogenesis ability of seeded INTEGRA® scaffold in CAM model;
2. To determine the *in vivo* functional angiogenesis and regenerative ability of seeded INTEGRA® using a murine diabetic wound model;
3. Method development and modification of the CAM assay to improve data collection for future works.

6.2 Chorioallantoic Membrane (CAM) Assay

The chick embryo chorioallantoic membrane (CAM) is a developing chick embryo's extra-embryonic membrane covered by a rich vasculature. The location of the CAM is shown in Figure 6-1. It comprises a multilayer epithelium: the ectoderm at the air interface, mesoderm (or stroma) and endoderm at the interface with the allantoic sac (484). It functions mainly as an organ of gaseous exchange for the embryo's vasculature. It also actively transports sodium and chloride ions and supplies calcium from the eggshell into the developing embryo (485).

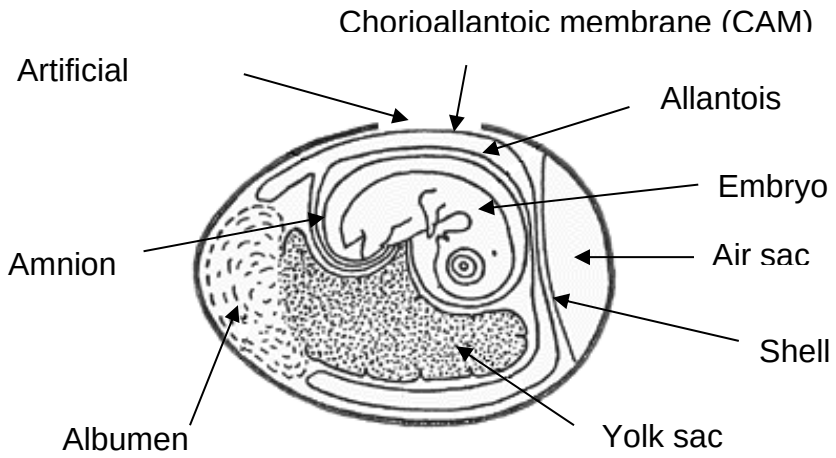

Figure 6-1 Diagram showing the anatomical structures within a developing chick at day 10 of incubation. A 2cm artificial window is cut open on the eggshell on incubation day 3 to expose the chorioallantoic membrane for experimental accessibility. Image adapted from Valdes et al. (484) and reproduced from author's own MSc thesis (2015).

Due to its unique highly vascular and easily accessible surface within a living host, this layer was ingeniously adapted as an *in vivo* testing model by Judah Folkman's team for analysing angiogenic activity of tumours in the 1970's (486–489). From the assays listed in Table 6.1, the CAM model is one of the most readily accessible *in vivo* methods. It is technically the least challenging, cheap to perform and maintain, and easiest to replicate within a short period. If embryos are used before E14 of development, it has little ethical concerns with good compliance with the 3Rs principles (replacement, reduction, and refinement) for animal-based research. (see Appendix Figure 4) The absence of a mature immune system with an underdeveloped lymphoid system in the early stages of embryogenesis (prior to E18) means that the chick embryo is naturally immunodeficient. This immunotolerance characteristic of the chick embryo to grafted tissues and cells without species-specific restrictions gives the CAM assay an added advantage in xenographic experiments (490–492). Hence it is an ideal model for evaluating angiogenesis in therapeutic products, particularly those involving human or other animal-derived cells and products. It also eliminates the possible immune-mediated inflammatory component, which could skew results in other *in vivo* models. Hence, it is one of the most widely used assays for angiogenic research, especially in the tissue-engineering field (483,493).

However, despite the above points, there are still several disadvantages to this model. It is a non-mammalian system, so results need to be interpreted with care. Reassuringly there is evidence from research which have drawn convincing similarities of the CAM to the mammalian *in vivo* models (484). As the viability of the CAM's angiogenic response is largely due to the different developmental stages of each embryo, large numbers of eggs are required to be able to obtain consistently high-powered and statistically significant results. The CAM is also subject to influences by environmental factors ranging from oxygen tension to pH, osmolality and the amount of keratinisation, which has a significant effect on the CAM response to angiogenic stimulation (494,495). Hence, the incubation conditions will need to be strictly monitored.

Regardless of certain shortcomings, the CAM technique can provide useful information relevant to studies on angiogenesis, particularly when the subjective CAM method is supplemented by histological evaluation of grafted tissues (496).

6.2.1 Materials and Method

The use of embryonated chicken eggs for research is governed by the UK Home Office under the Animals (Scientific Procedures) Act 1986 Amendment Regulations 2012 (SI 2012/3039) amended the Animals (Scientific Procedures) Act 1986 (ASPA) covering European Directive 2010/63/EU in the United Kingdom. The guidance states that if the embryo is not allowed to enter the start of the final third of the incubation period, no licence is required as it is classified as a non-protected animal. (497) The incubation period until hatching is 21 days for chicks; therefore, procedures until E14 of incubation are not regulated by ASPA. The same guidance was also stipulated in the Institutional Animal Care and Use Committee (IACUC) (498,499) and the National Institutes of Health in the USA (500), where it was established that a chick embryo under 14 days of gestation would not experience pain and can therefore be used for experimentation without any ethical restrictions or prior protocol approval (501). As this study terminates at 14 days of gestation (two-thirds of the incubation period), it did not require ethical approval for animal experimentation.

Fertilised White Leghorn chicken eggs were purchased from Henry Stewart & Co. Ltd (Norfolk, UK). The *in ovo* CAM assay procedure was adapted from previously described methods (502–504). The eggs were laid horizontally on egg trays and incubated at 37°C in a humidified atmosphere (>60% relative humidity) in a specialist egg incubator (Ova-Easy Advance Series II with humidity pump; Brinsea, UK). After 3 days, the eggs were ready for windowing the outer shell. Under the lamina flow hood, the shell of the egg at the pointed end and the windowing area was gently cleaned with small amount of 70% ethanol on gauze. 3-4 ml of albumen was removed with a 5ml syringe (BD Plastipak™) and 19-G gauge hypodermic needle (Terumo Neolus®) from the pointed end of the shell (to avoid disturbing the air cell pocket on the rounded end). This helps to create a false air sac to minimise adhesion to the shell membrane when creating the window. A rectangular window of approximately 2 x 2cm in size is cut open using a sharp curved dissecting scissors. This allows for the embryo and CAM vessels to be experimentally accessible through a cut window in the eggshell. The windows were sealed with a clear adhesive tape and re-incubated for a further 5 days until day 8, when the membrane vessels were well developed and ready for grafting of the seeded collagen hydrogel or INTEGRA® scaffold. The implants were carefully placed on the CAM between branches of the blood vessels as shown in Figure 6-2A & B.

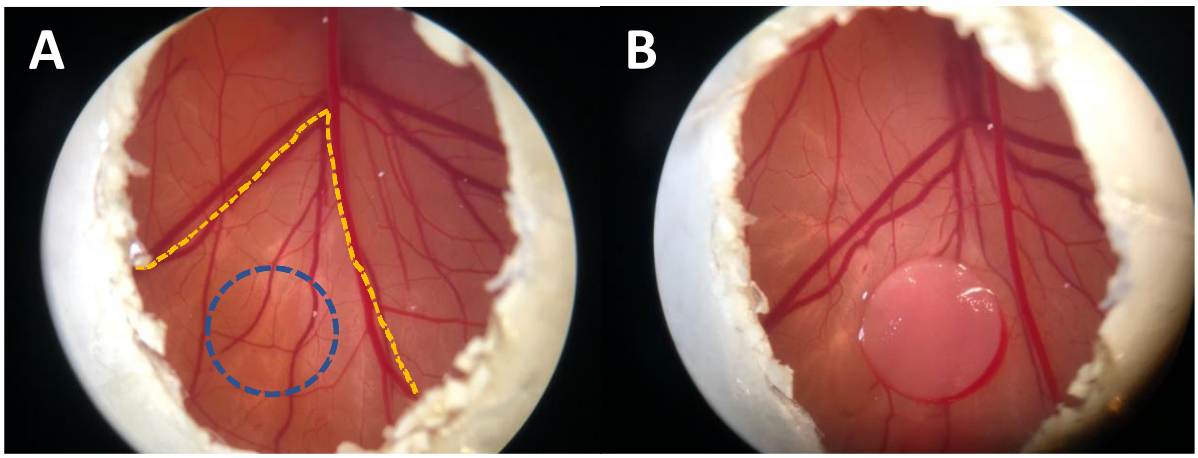

Figure 6-2 A: The ideal placement of the implant (blue circular overlay) to be grafted on CAM: between two large vessels (yellow dotted line) and directly on top of the region with maximal terminal capillaries. B: Actual INTEGRA®scaffold grafted on CAM on E8 of incubation (Day 0 of implantation).

The eggs were examined regularly and had their developmental stages noted via the Hamburger–Hamilton stages criteria, shown in Appendix Figure 5 (505). They were imaged on day 14 of incubation (7 days after implantation) before the explanation of constructs for histological analysis. Due to the expected variability commonly observed in *in vivo* assays and the possibility of infections to the eggs during the incubation period, at least four replicates were implanted per pre-conditioned seeded scaffold. This process is summarised in Figure 6-4A and B.

To assess the pre-conditioned cellular response on the CAM, collagen hydrogel was used initially as a matrix carrier for the cells. Pre-conditioned pooled primary adMSC or transduced adMSC was suspended in collagen hydrogel as described in Chapter 2. After 3 days of incubation, the gels were implanted into the CAM surface as shown in Figure 6-4B on E8 of incubation. Similarly, with the INTEGRA® seeded scaffolds, these pre-prepared scaffolds were implanted onto the CAM after 3 days of pre-conditioning.

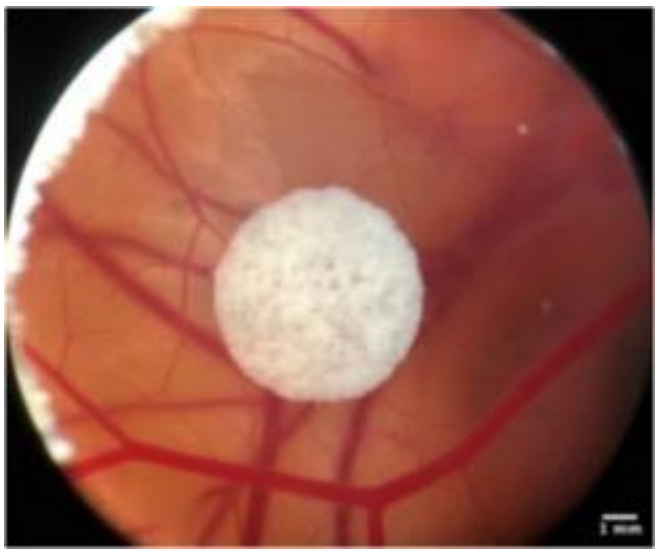

Figure 6-3 Pre-punched sterilised 6mm filter paper was placed on CAM to allow for the addition of conditioned media from cells seeded on INTEGRA®scaffolds in different oxygen pre-conditions. Scale bar = 1mm.

To assess the effect of conditioned media on the CAM, autoclaved sterilised pre-hole punched 6mm filter paper (Cat #1001325, Whatman®, UK) was placed directly on the CAM, as shown in Figure 6-3, to serve as a biological inert absorbent pad as previously described by Ma et al. and Wahl et al. (228,506). 15uL of conditioned media collected from the different pre-conditioned groups of cell-seeded scaffolds

after 72 h in culture was added to the filter paper at the time of implant. As the conditioned media was collected from the parallel implanted pre-conditioned INTEGRA® scaffolds, this allowed for the concordance assessment of media-induced angiogenesis compared to direct cellular-induced effect from the same seeded pre-conditioned scaffolds. Sterile water was used for the control filter paper group. They were imaged on day 14 of incubation (7 days after implantation) before the explanation of constructs for histological analysis as with the seeded hydrogel and INTEGRA® implants above.

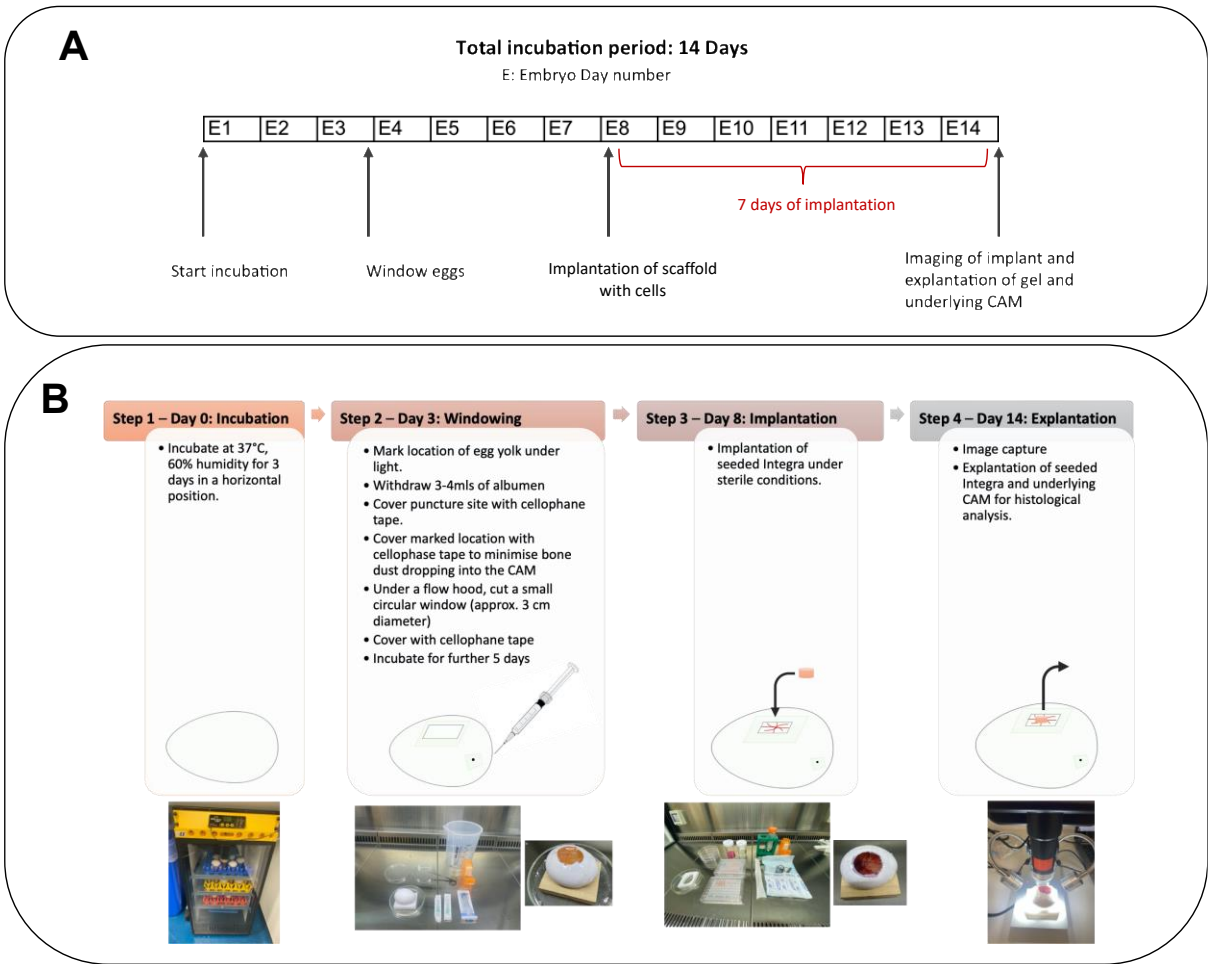

Figure 6-4 (A) Chronology of incubation period for CAM assay. Each embryo day number corresponds to the day of incubation (verification using the Hamburger–Hamilton stages of embryo development was also done to ensure consistency). Figure adapted from Borges et al. (507) (B) Four main steps involved in CAM assay as detailed as above.

After the explantation of the scaffolds, the chick embryo was euthanised via a combination of decapitation and hypothermia (-20ºC for 4 hours) methods.

6.2.1.1 Manual and software-aided vessel image analysis

The CAM assay responds to pro-angiogenic stimuli by forming new blood vessels which appear to converge toward the implant in a wheel-spoke pattern as described by Ribatti et al. and Deryugina & Quigley (504,508).

On day 14 (E14) of incubation, the peri-implant vasculature on the CAM was imaged using Leica Zoom 2000 stereomicroscope with a mounted camera adapter. To better visualise the overlying vasculature, white cream was injected underneath the CAM to obscure the underlying vessels, as described by other published CAM studies. (509,510) Captured images were cropped to 690 x 690px and processed using Fiji.

A variety of manual and automated software-aided vessel analysis methods were used to evaluate the amount of angiogenesis around the implant. Manual vessel analysis was determined by two measures: (i) vessel density, (ii) angiogenic response score.

To quantify vessel density, the green channel of the image was selected to filter the red microvasculature by contrast optimisation of the image (511). For the manual counting method, two concentric circles were digitally drawn around the implant as adapted from methods described by Dusseau et al. 1986, Harris-Hooker et al.1983, Richardson and Singh 2003, Bronckaers et al. 2013, Burggren et al. 2020 (512–516). This allows for the accurate and location-specific calculation of vessel density surrounding the implant site. The first ring surrounds the circular implant, and the second ring was drawn 1mm away from the first as shown in Figure 6-5. The intersecting vessels were counted using the Fiji counter plugin. The number of blood vessels converging towards the placed tissues in a spoke-wheel fashion were counted blindly by assessors. This was averaged and used for analysis (517). Vessels less than 10μm in diameter were included (515,517).

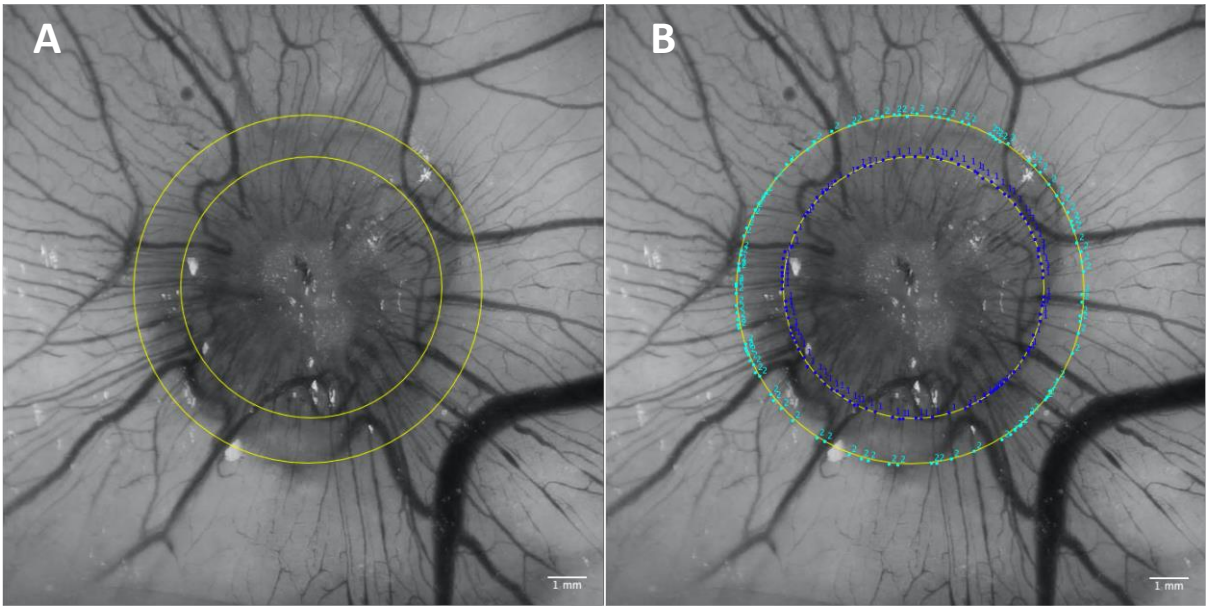

Figure 6-5 Manual counting method for vessel density of E14 implant and surrounding vasculature. This was processed on the Fiji image analysis software. A: The green channel was selected from splitting the RBG colour image and digital circular ROIs surrounding the implant were superimposed 1mm apart from each other. B: Intersecting vessels were counted using the Fiji counter plugin. Scale bar = 1mm.

To determine angiogenic response, a scoring system was adapted from Chen et al. as shown in Figure 6-6 (518). Results were assessed visually and measured semi-quantitatively using categorical data capture. The density of branching blood vessels infiltrating under the disks was scored as follows: 0, negative; 1, change in vessel architecture but not directed to the point of sample application; 2, partial spoke-wheel (one third of the circumference exhibits directional angiogenesis); 3, spoke-wheel; 4, strong and full spoke-wheel (518).

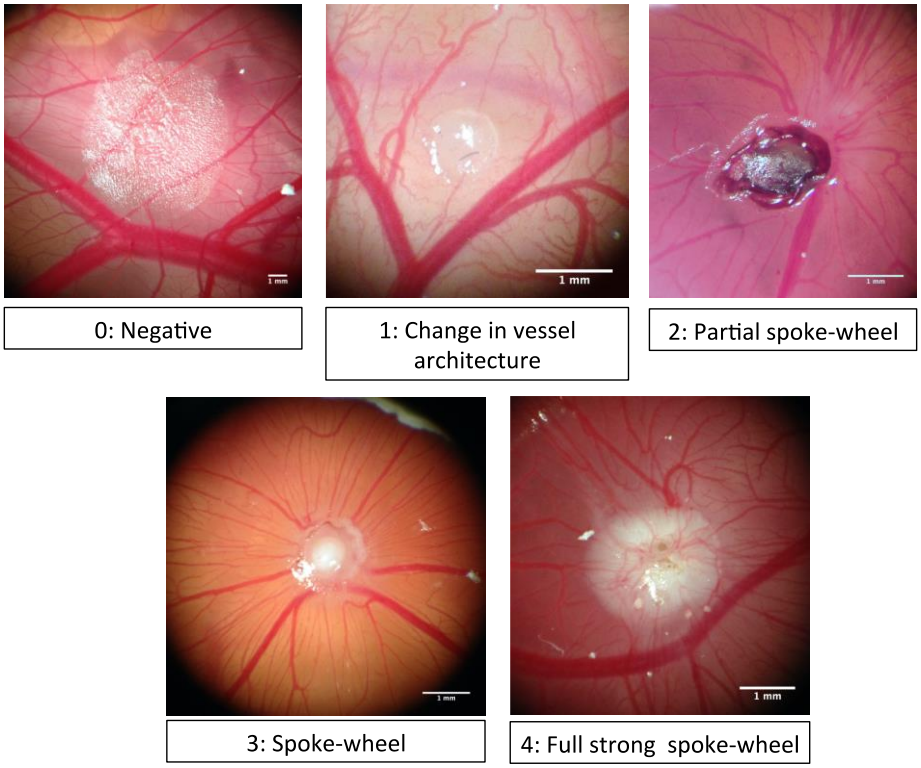

Figure 6-6 Reference images with their corresponding angiogenic score from 0-4 which were utilised for the scoring system of angiogenic response from the CAM. Images captured are of implanted cellular collagen hydrogel. Scale bar = 1mm. Reproduced from author's own MSc thesis (2015).

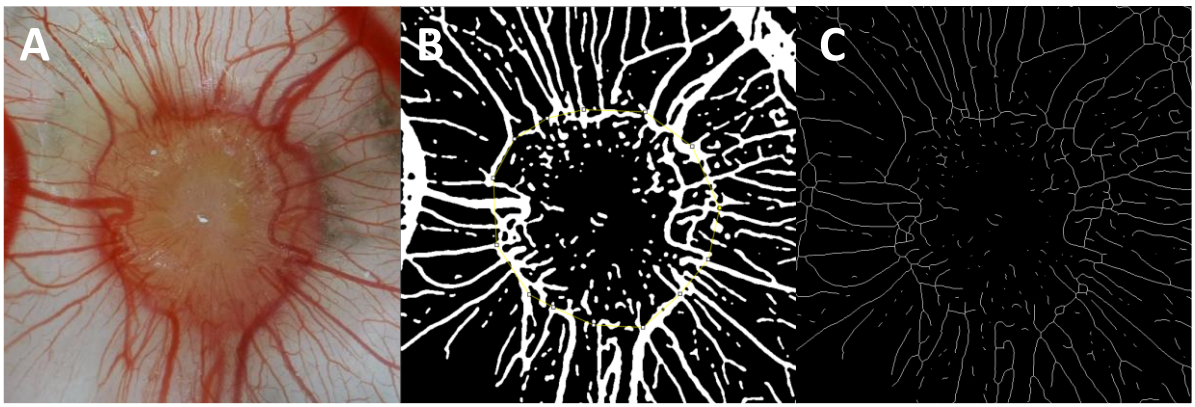

Figure 6-7 Image processing and vessel segmentation tool of CAM vasculature around implant (static 21% seeded INTEGRA®shown here on Day 14 of implant) using Fiji vessel plugin. A: original image; B: threshold and segmented image; C: binary image.

To enable automated software-aided image analysis of the vasculature for greater comparative accuracy and reduce observer bias, a vessel segmentation process was performed via a vessel analysis Fiji plugin which enabled automated vessel analysis of 'vascular density' on the defined ROI as shown in Figure 6-7 (519,520). To further increase the detail in the assessment of the vasculature, a commercial AI-based IKOSA Prisma software (KML Vision GmbH) was employed to calculate vessel area,

branching points and length parameters. Figure 6-8 shows how the software would analyse and measure vessels around the implant.

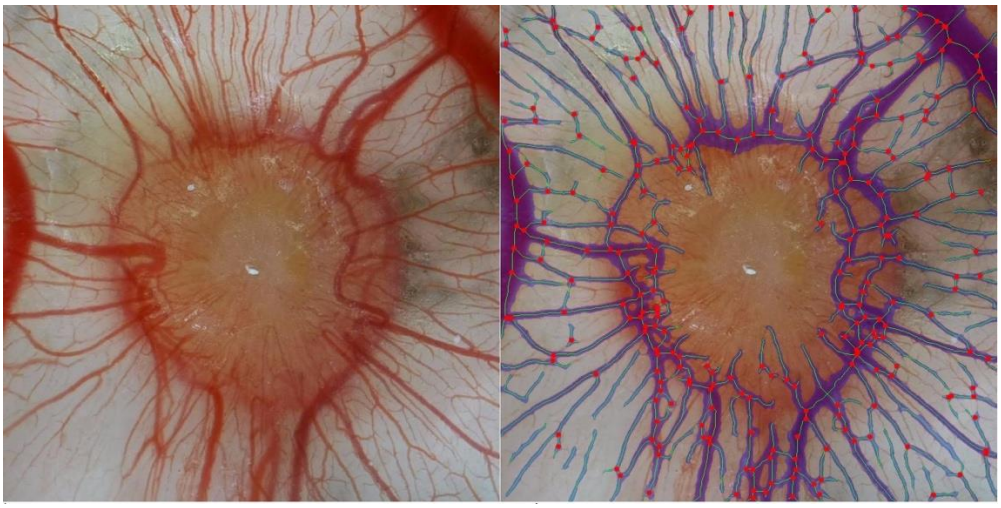

Figure 6-8 IKOSA Prisma software AI image analysis of CAM vasculature around the implant (E14 static 21% INTEGRA®scaffold) with the original image shown on left and overlayed software analysis on the right. Areas of detected vessels are shown in blue overlay, vessel paths are shown as green lines, thicker vessels are highlighted with a purple outline and vessel branching points are indicated by red dots.

6.2.1.2 Histological analysis of explanted CAM scaffold

After imaging of the implant on E14 of incubation, the CAM membrane-scaffold structures were carefully explanted using a right-angled micro-scissor. They were fixed for one hour using 4% PFA solution at room temperature followed by histological processing using varying concentrations of ethanol and xylene solutions with specimens carefully placed in a histological cassette to prepare for paraffin wax embedding. The resultant wax blocks were sectioned at 5µm thickness using a microtome machine. Each section was carefully placed on a slide and air-dried overnight. The slides were de-waxed to allow for staining of the structures using haematoxylin and eosin (H&E) staining. The resultant sections were imaged on NanoZoomer 2.0-HT scanner (Hamamatsu Photonics K.K.) Images were viewed and analysed with NDP view2 Image viewing software (Hamamatsu Photonics, Japan).

The presence of red blood cells was used as a marker of vessel infiltration into the scaffold. The depth of chick vascular infiltration was measured on the histological explanted tissue and scaffold in three different areas of the scaffold. These measurements were averaged, and vascular infiltration was calculated as a

percentage of the maximum depth of the combined explanted scaffold and CAM tissue (see Figure 6-9). At least n=3 (biological triplicates) were used per pre-conditioned group. For measuring CAM tissue layer infiltration into the filter paper implants, the same method was used as per vessel infiltration, but instead, six different areas of the implant with n=2 biological replicates were measured due to experimental limitations.

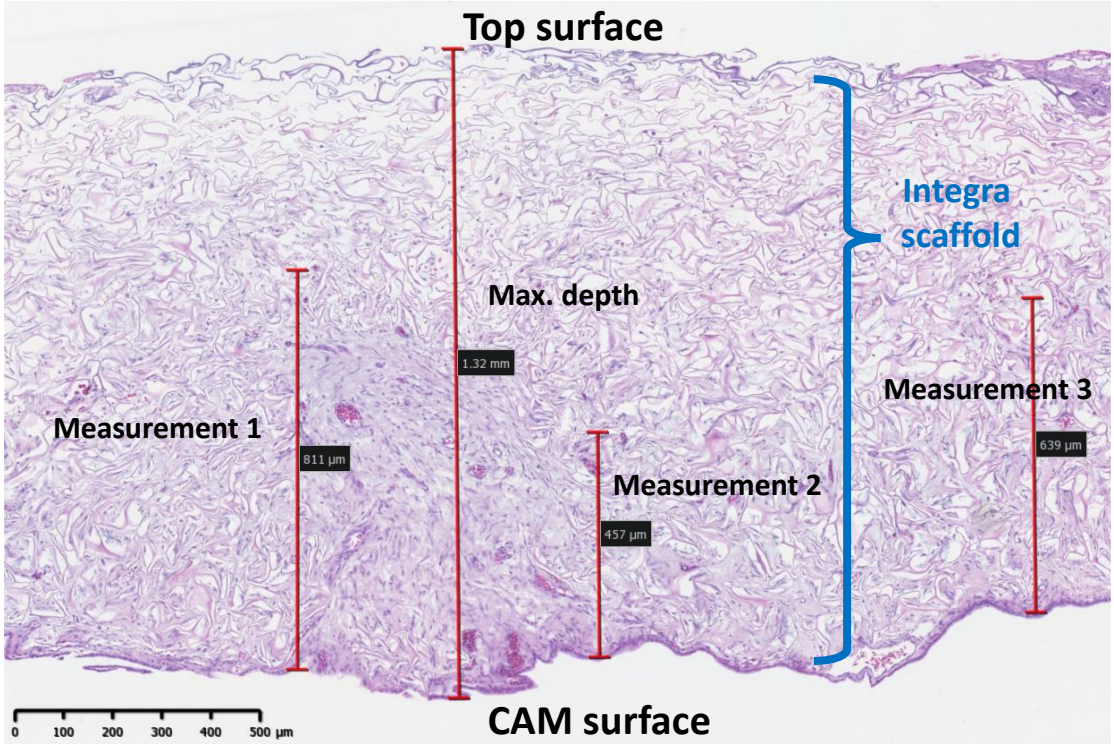

Figure 6-9 Histological section of implant on CAM with 3 reference measurement of vessel infiltration depth into the INTEGRA® scaffold from the CAM surface. Scale bar = 500um.

6.2.2 Results

6.2.2.1 Angiogenesis response to seeded hydrogel implant

From previous studies from our lab, we know that acellular collagen hydrogel does not elicit an angiogenic response on the CAM. Hence in this section, we will analyse the effect of the pre-conditioned cells seeded in a simple 3D collagen hydrogel matrix to be able to delineate mainly the cellular effect on the CAM.

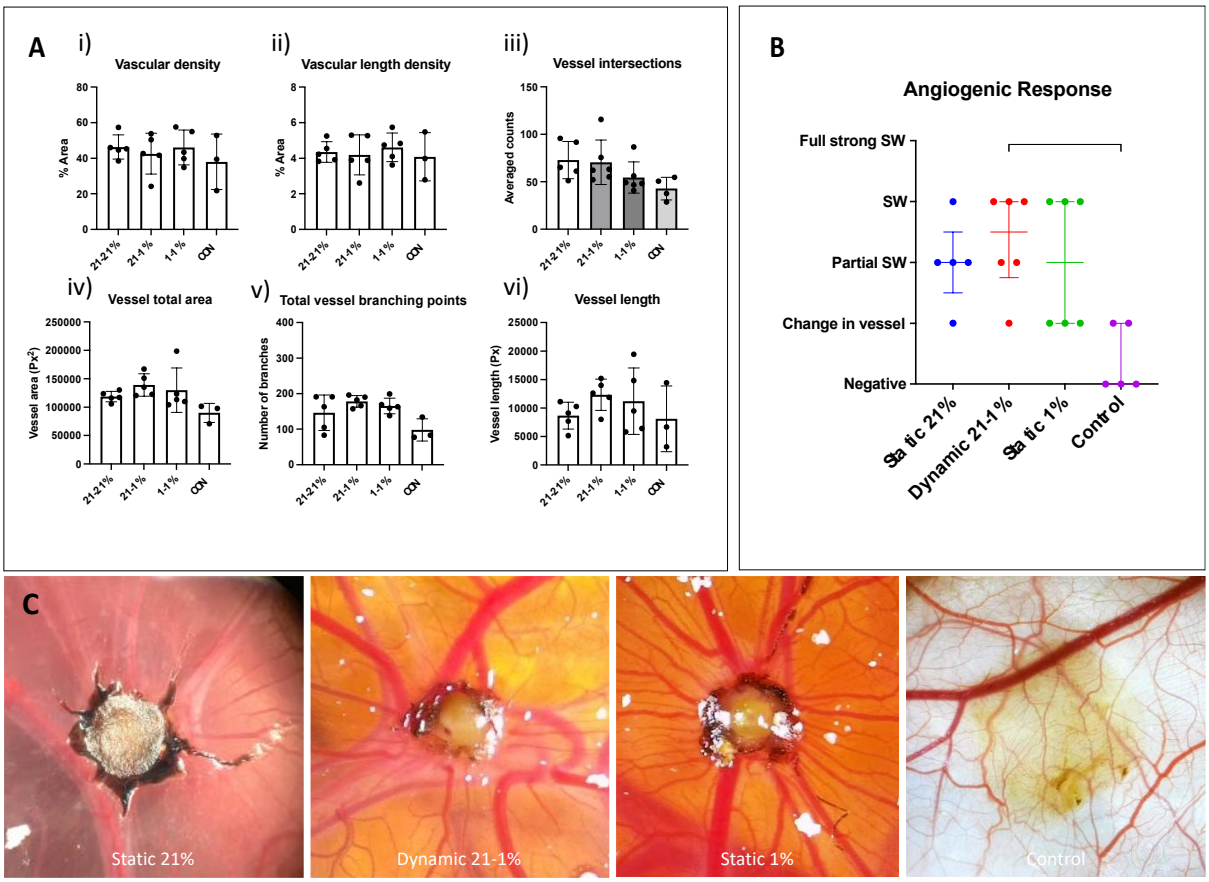

Figure 6-10 CAM vessel analysis results for primary adMSC seeded on collagen hydrogel. (A) Graphs of vessel analysis parameters. (B) Scatter graph of angiogenesis response scoring results. Results are shown as median with interquartile range due to the ordinal nature of the data set. (C) Representative images of the pre-conditioned hydrogel groups on the day of explant (E14). Acellular collagen hydrogel was used as control. Results shown as mean ± SD.

Vessel analysis from hydrogel seeded with primary adMSC using automated Fiji plugin showed no difference in vascular density or vascular length density between all the groups (Figure 6-10A i) and ii)). Analysing other vessel parameters such as total area, branching points and vessel lengths (Figure 6-10A iv), v), vi)) using IKOSA automated image analysis software showed no statistically significant difference between the groups. However, the means of the vessel total area, branching points, and vessel length in the dynamic (DH) 21-1% group show a generally higher value compared to the other groups. Averaged vessel intersection count shown in Figure 6-10A iii) also determined no statistical difference between the groups. However, the means were similarly higher in the static (SN) 21% and DH 21-1% groups compared to static (SH) 1% and control [72.80 ± 19.62 and 70.50 ± 23.50 vs 54.42 ± 16.48 and 42.75 ± 11.95 (Mean ± SD)]. The angiogenic response showed a significantly higher median score in the DH 21-1% group compared to the control (p-value = 0.02), but

no statistical difference was detected between the pre-conditioned groups. This can be further appreciated in the representative surrounding CAM vasculature of the different pre-conditioned hydrogel implants shown in Figure 6-10C.

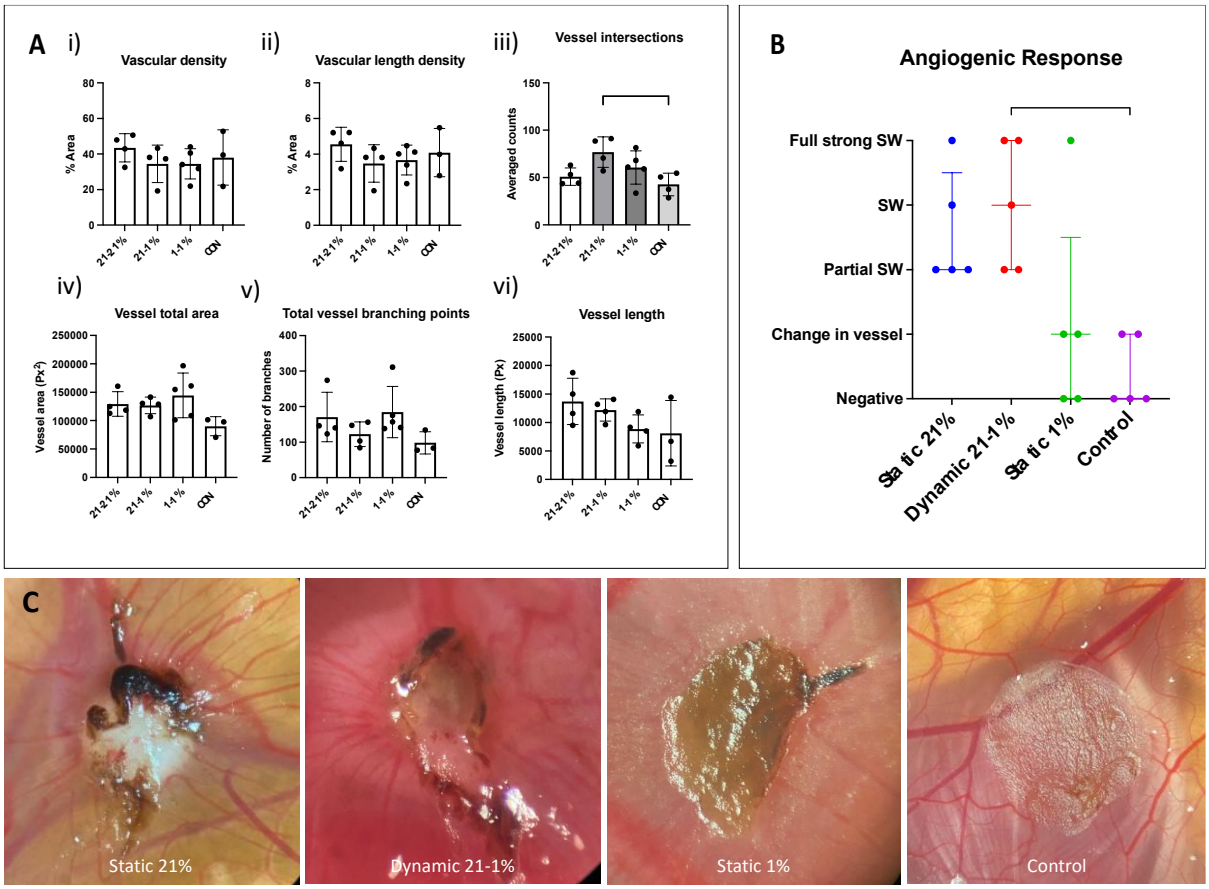

Figure 6-11 CAM vessel analysis results for transduced adMSC seeded on collagen hydrogel. (A) Graphs of vessel analysis parameters. (B) Scatter graph of angiogenesis response scoring results. Results are shown as median with interquartile range due to the ordinal nature of the data set. (C) Representative images of the pre-conditioned hydrogel groups on the day of explant (E14). Acellular collagen hydrogel was used as control. Results shown as mean ± SD.

To determine if there are differences in *in vivo* angiogenic response to primary adMSC, transduced adMSC were seeded and monitored. Vessel analysis from these seeded hydrogels showed non-significant changes between the groups for vessel total area, branching points and length. (Figure 6-11A) Compared to primary adMSC, increase in vessel length in the SN 21% group. There was a significant increase in vessel intersections around the implant noted in the DH 21-1% group compared to the control [76.75 ± 16.02 vs. 42.75 ± 11.95 (Mean ± SD); p-value = 0.05]. The angiogenic response from visual scoring showed that the SH 1% seeded transduced cells had lower scores than the seeded primary adMSC for the same hypoxic pre-

conditioning. (see Figure 6-10B compared to Figure 6-11B) Similar to the primary adMSC cells, there was no statistical significance detected between the pre-conditioned groups, but the DH 21-1% group showed a significantly higher median score compared to the control (p-value = 0.02). In addition, there were more 'Full strong Spokewheel' responses noted in the seeded transduced cells in all experimental groups compared to primary adMSC. There was also a lower median angiogenic response score for the SH 1% group in the transduced cells compared to primary adMSC. (see Figure 6-10B compared to Figure 6-11B)

6.2.2.2 Angiogenic response to seeded INTEGRA® implant

To further understand and appreciate the effects of the scaffold matrix on the cells and the overall *in vivo* angiogenic response of the cell-matrix combination on a living host, INTEGRA® seeded with transduced adMSC was implanted on CAM for further analysis. Vascular density and length occupied less percentage area of the overall ROI than the two previous hydrogel groups. However, it would be an inappropriate direct comparison as the implant type and footprint differ significantly. In addition, there is less contraction of the seeded INTEGRA® scaffold seen over the course of the implant compared to seeded hydrogel (Figure 6-11 and Figure 6-10 Ai & ii) which would suggest that different biomechanical forces are present in the two different matrices contributing to the angiogenic response of the CAM.

The analysis of the other measurable parameters, such as vessel total area, branching points and length, show higher mean values for SN 21% compared to DH 21-1% and SH 1% groups. The data from the SN 21% group are also comparable to the control, but this was not found to be statistically significant. The vessel intersection results show slightly higher mean averaged counts in DH 21-1% and SH 1% groups compared to SN 21% and control, but this was also not statistically significant. However, the angiogenic response data also showed a slightly different angiogenic profile to the other measured parameters. There was a lower median score in SH 1% compared to SN 21% and DH 21-1%. The DH 21-1% group was found to have a significantly higher median score of 'Full strong spokewheel' compared to SH 1%. The control scaffolds had a comparable angiogenic response to SN 21% seed Integra; it appears the control INTEGRA® scaffold was also capable of

stimulating a moderate degree of angiogenic response from the CAM without the addition of cells, as shown in Figure 6-12C.

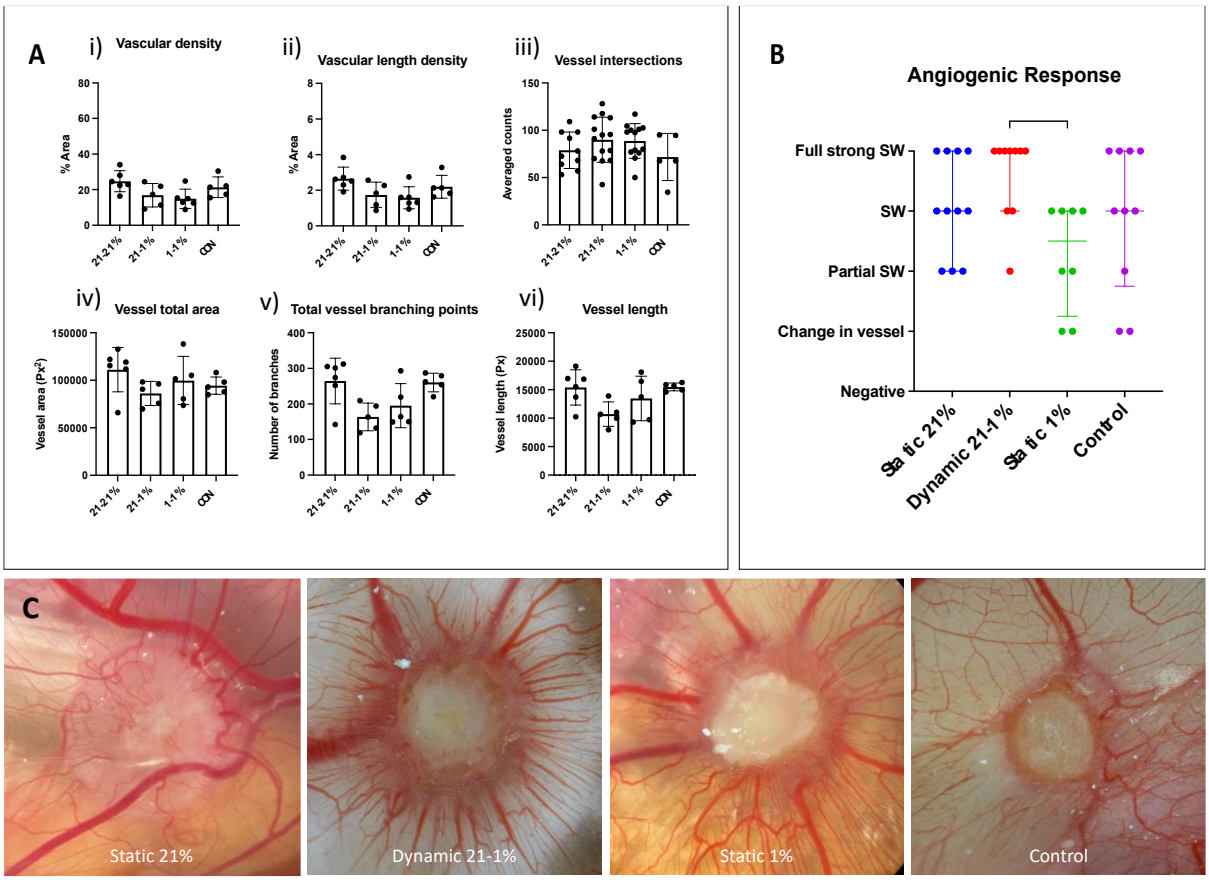

Figure 6-12 CAM vessel analysis results for transduced adMSC seeded on INTEGRA® scaffold. (A) Graphs of vessel analysis parameters. (B) Scatter graph of angiogenesis response scoring results. Results are shown as median with interquartile range due to the ordinal nature of the data set. (C) Representative images of the pre-conditioned hydrogel groups on the day of explant (E14). INTEGRA® with water (not PBS) was used as the control. Results are shown as mean ± SD.

6.2.2.3 Histological evaluation of vascular invasion

Measurement of depth of vascular infiltration into the scaffold was performed on histological H&E sections. This is calculated as a percentage of the maximum depth of the total CAM-scaffold section of each sample, to accurately account for inter-sample variation in INTEGRA® thickness.

Results (Figure 6-13A) show that the INTEGRA® scaffold with dynamic hypoxic seeded cells demonstrated a significantly higher percentage of vascular invasion compared to the control (70.05 ± 15.60% vs 41.28 ± 11.76%; P-value = 0.006). This

mean percentage of vascular invasion was also shown to be slightly higher than the SN 21% and SH 1% groups, but the difference was not found to be statistically significant (static 21%: 57.44 ± 14.54%; static 1%: 56.49 ± 22.69%).

Representative images of the H&E histological sections (Figure 6-13B i-vi) showed evidence of infiltration of vessels into the scaffold for all the pre-conditioned groups and control at varying degrees of depth and amount. Blood vessels were identified by the brightly stained red enucleated erythrocytes, otherwise known as red blood cells (RBC), within a circular vessel structure. Some RBC can be seen outside of these vessels within their surrounding tissue. This would represent extravasation of RBC, a histological finding described as erythrodiapedesis (521). It can occur where small capillaries have lost their vessel integrity and become leaky.

All INTEGRA® scaffolds, cellular or acellular control, appear to attract blood vessels deep into the scaffold layer. (Figure 6-13Bi-vi) In the acellular control scaffold, the vessel structures were smaller with fewer erythrocytes and some infiltration of nucleated host cells, likely lymphocytic in origin. (Figure 6-13Bvi & Bd) Within the cellular INTEGRA® scaffolds, more nucleated cells were seen within the scaffold layer, along with a higher density of erythrocytes for all 3 oxygen pre-conditions groups. The nucleated cells are likely to have both a mixture of seeded human adMSC and host cells in origin. Evidence of erythrodiapedesis was seen more prominently in the SN 21% pre-conditioned scaffold and these RBC appear to concentrate in the middle of the scaffold. (Figure 6-13Bi & Ba) SH 1% scaffold showed more blood vessels closer to the CAM layer. (Figure 6-13Biii & Bc) DH 21-1% scaffold appeared to have the greatest density of blood vessel infiltration into all layers of the scaffold, with less evidence of erythrodiapedesis. (Figure 6-13Bii & Bb) The vessels appeared more formed and mature and were accompanied by greater infiltration of nucleated cells similar to that seen in the SH 1% scaffold.

There also appears to be evidence of host tissue hyperplasia of the chorionic epithelium layer over the top of the scaffold in all experimental group scaffold sections, which highlights the highly biocompatible nature of the INTEGRA® scaffold on a living host. This can be further appreciated in stereoscopic macro-images

shown in Figure 6-12C, particularly of the SN 21% seeded INTEGRA® where it appears the entire CAM layer has covered over the overlying implant.

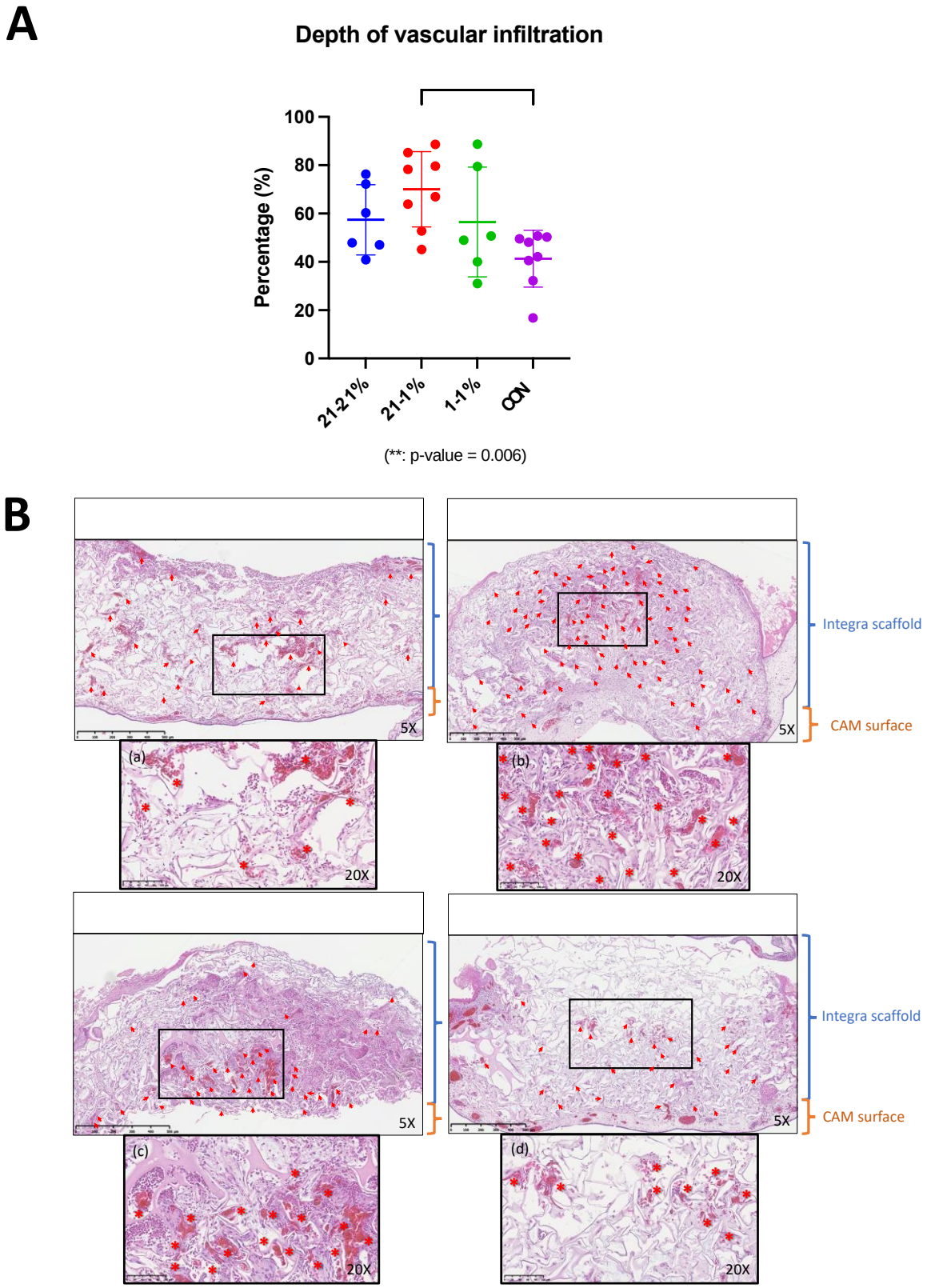

Figure 6-13 (A) Graph of the depth of vascular invasion into implant on CAM as measured on histology (H&E) sections. Results are shown as mean ± SD. N-number per group ≥ 6. (B) Representative H&E stained sections of the INTEGRA® on the CAM surface for the different experimental groups, shown in two magnifications. The CAM surface is located at the bottom of the image and is shown with the orange

bracket. The rest of the INTEGRA® implant is shown with the blue bracket. Red arrows highlight tissue regions with evidence of erythrocytes/RBC, indicative of vascular infiltration. A corresponding magnified black boxed area from the top picture is shown in the bottom picture labelled (a-d). Red asterisk symbols represent erythrocytes within blood vessel. Top picture magnification: 5X; Scale bar = 500um. Bottom picture magnification: 20X; Scale bar = 100um.

To evaluate the nature of the pro-angiogenic effects of the pre-conditioned seeded cells and their conditioned media and to be able to delineate the effects of this from scaffold-associated effect of the INTEGRA® matrix on the CAM, filter paper (FP) soaked with conditioned media (CM) collected from the different pre-conditioned groups of INTEGRA® seeded cells were used. (as shown in Figure 6-3) The filter paper is a biologically inert cellulose-based material and should not initiate any biological response or interaction with host tissue when introduced *in vivo*. However, after 7 days of implant, there was evidence of host CAM tissue layer invasion into the FP layer in all experimental groups on histological H&E sections. (Figure 6-14A) This was presented at varying degrees of integration of the FP with the CAM layer. In the SN 21% CM section, the CAM layer appears reduced in thickness, likely due to processing issues during histology, where the deeper CAM layer did not stay on the slide during sectioning (Figure 6-14Aa & i). With the SH 1% CM section, the presence of significant erythrodiapedesis in the FP layer is likely a result of the absorption of locally bleeding blood vessels at the time of explant. (Figure 6-14Ac & ii) In the SN 21%, 1% and control groups, only tissue layer infiltration was seen. (Figure 6-14Aa,c,d) The graphical representation of percentage tissue infiltration across the four groups is shown in Figure 6-14B. FP with dynamic 21-1% CM showed the highest mean percentage depth of tissue infiltration at 66.13 ± 23.79%. This was shown to be significantly higher compared to the SH 1% CM and control group (1%: 16.16 ± 9.75%, p-value <0.001; Control: 38.36 ± 9.99%, p-value = 0.01). CM SN 21% group showed a mean percentage of tissue invasion of 49.10 ± 18.85%. In the SH 1% CM, there was a significantly lower tissue ingrowth compared to all the other groups, including the control. The most striking histological finding was that vascular invasion into the FP layer was only seen in the DH 21-1% CM sections. (Figure 6-14Ab & ii) These infiltrating microvessels were also well formed with luminal-shaped cell-lined cavities filled with erythrocytes. Corresponding representative photos on day 7 of implantation support the observation of more

visible reddish vascular discolouration in the FP soaked with DH 21-1% CM (Figure 6-14Cb) than in the other experimental groups (Figure 6-14Ca-d).

A

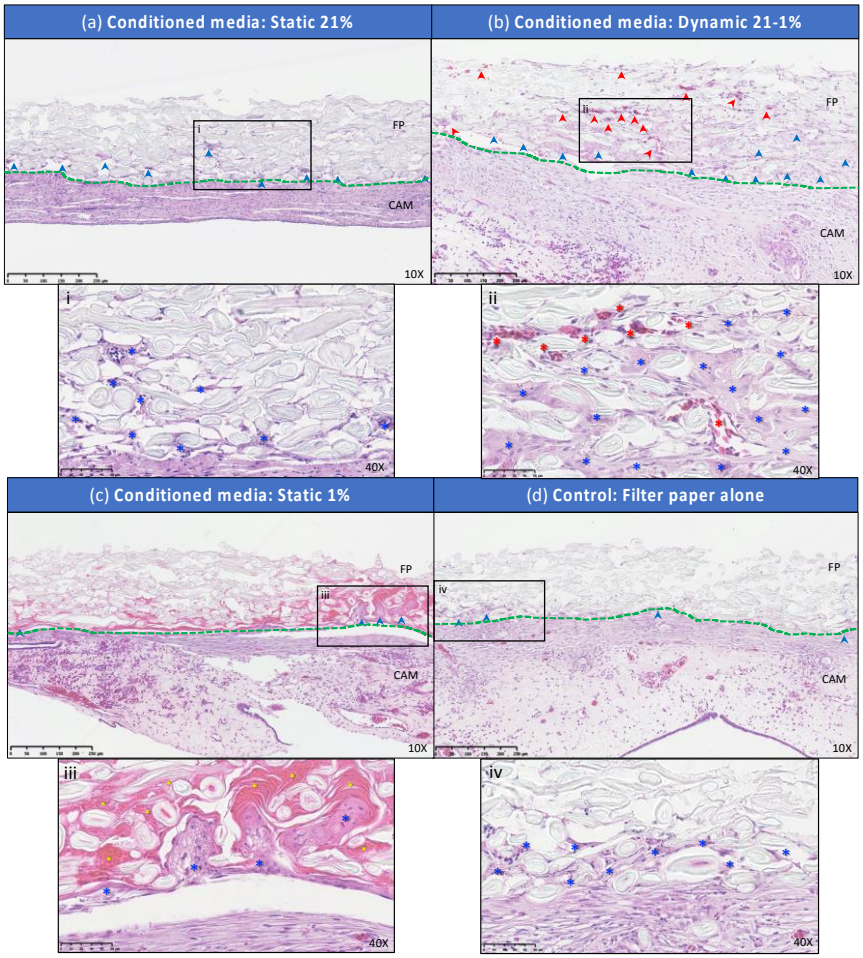
(a) Conditioned media: Static 21%
(b) Conditioned media: Dynamic 21-1%
(c) Conditioned media: Static 1%
(d) Control: Filter paper alone
FP
CAM
10X
40X
i
ii
iii
iv

B

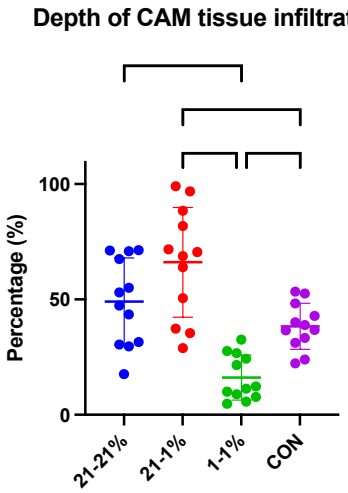
Depth of CAM tissue infiltration
Percentage (%)
100
50
0
21-21%
21-1%
1-1%
CON

C

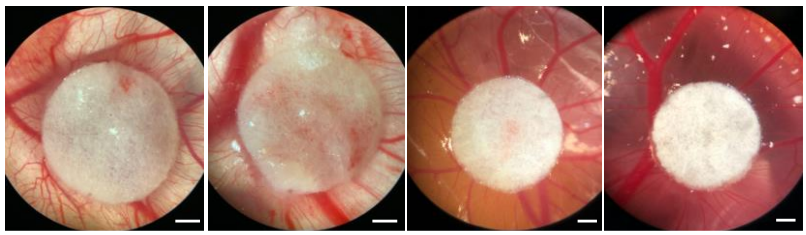

Figure 6-14 (A) Histological cross-section of H&E stained implanted filter paper on CAM in different pre-conditioned CM control groups, shown in two magnifications. Sterile water was used for control. Green dotted line: demarcates the border of the CAM (orange labelled 'CAM' text box) and filter paper (blue labelled 'FP' text box). Filter paper can be identified by the white-coloured oval/circular cross-sectional structures. Blue arrows: Evidence of invasion of the CAM tissue layer past the border into the filter paper. Red arrows: tissue regions with evidence of vascular infiltration. Only sections with dynamic 21-1% CM showed evidence of formed blood vessels within the FP layer. A corresponding magnified black boxed area from the top picture of each group is shown in the bottom picture labelled (i-vi). The blue asterisk symbol represents the area of CAM tissue infiltration; red asterisk symbol in Figure ii) represents a blood vessel; yellow asterisk symbol in Figure iii) represents regions of artificial extravasation of erythrocytes/erythrodiapedesis into filter paper, likely from contaminant during explantation. Top picture magnification: 10X; Scale bar = 250um. Bottom picture magnification: 40X; Scale bar = 50um. (B) Graph of the depth of CAM tissue infiltration into filter paper as measured on histology (H&E) sections. Results are shown as mean ± SD. Biological replicates = 2; Technical replicates = 6. (C) Representative stereoscopic images of CM-soaked filter paper on CAM at time of explant (E4 of incubation). The potential amount of vascular infiltration may be visualised by the amount of reddish colour on the white filter paper. The greatest reddish vascular discolouration was seen in the filter paper soaked with dynamic 21-1% CM. White scale bar = 1mm.

6.2.3 Discussion

<u>Understanding the angiogenic response to seeded implants on the CAM assay</u>

The angiogenic response of the CAM to the implanted scaffold was measured on several different methodologies, including manual and automated means. Angiogenic response using image analysis software would analyse and measure the vessel architecture and density using set parameters within the programme, which is standardised through the experimental set. It was clear that despite efforts to standardise the analytical process, it was still subject to variability between the samples which affected the overall results. This was highlighted particularly when it affected the image capture quality of the implant and its surrounding CAM vasculature (see Figure 6-15 and Figure 6-16). Most of the automated image analyses of the CAM vasculature showed no statistical difference between any of the pre-conditioned groups in the hydrogel or INTEGRA® scaffolds. This could be caused by the poor sensitivity of the software to small calibre microvessels, which is more important to delineate in these studies due to the acute nature of the neoangiogenesis vessels. (see Figure 6-8) With the Fiji vessel density measurements, this was also subjected to how well the vessels are segmented and

made binary through image manipulation. There was inevitability loss of some of data obtained through the process, as shown in Figure 6-7, due to a lack of sensitivity to the smaller vessels. With this in mind, a secondary manual counting of vessel intersection method was added for completeness in order to account for the smaller vessels not captured by the image analysis software. Manual vessel intersection data was able to show some differences between the pre-conditioned groups, particularly for the transduced adMSC hydrogel data, where a significantly larger amount of vessel intersections surrounding the implant were seen in the DH 21-1% group compared to the acellular control. Another widely used semi-quantitation technique of 'grading' or 'scoring' the angiogenic response around the implant was also adopted to allow for a visual assessment. Scoring strategies typically assign a number to a set of standard angiogenic responses, as shown in Figure 6-6. This method is particularly suited for quantifying angiogenic response to tumour grafts or other materials in the CAM. This is especially true for hydrogel implants, where there were no observable visual angiogenic responses seen of acellular control hydrogel on the CAM to the scaffold (see Figure 6-10C and Figure 6-11C), yet data from the image analysis software were not able to significantly differentiate or discern this from the set measurable outcomes (Figure 6-10 and Figure 6-11 i, ii, iv, v, vi). However, subjective scoring methods can render objective comparisons of data difficult, which has led researchers to develop more precise quantitative techniques, which will be discussed further in the following section on 'Future works'.

It is clear that all pre-conditioned cell-seeded hydrogels elicited an angiogenic response from the CAM, perhaps to a degree from the contractile effect of cellular proliferation within the hydrogel. It is important to determine if there are measurable differences between the primary and transduced adMSC once seeded. Due to issues with the slow growth of primary adMSC, there were difficulties faced with expanding a large enough cell population for seeding onto the INTEGRA® scaffolds. Hence, it was only possible to analyse primary adMSC on hydrogel matrix on the CAM only. Measurable differences between the primary and transduced adMSC was extrapolated for this reason. Differences in angiogenic response were seen between the two different cell types in the *in vivo* CAM assay, which was also shown and discussed previously in Chapters 3 and 4. The greatest differentiation seems to be in the SH 1% seeded cells, with a blighted response for the seeded transduce adMSC

compared to the untransduced primary adMSC. This was deemed to be an acceptable difference given that it was necessary to be able to 1) expand enough cells for *in vivo* seeding on INTEGRA® scaffold, which only adMSC cell lines were able to provide for the experimental timeline; 2) track seeded cells with the use of transduced cell lines for non-invasive monitoring after seeding and implantation into a living host. It also highlighted how important it is for researchers utilising transduced cells to thoroughly evaluate and properly account for differences in cell behaviour, especially their sensitivity to the oxygen culture environments, compared to donor primary cells. This also highlights a pertinent and commonly reported problem experienced with cell-based research for translational use, where donor primary cells require prolonged expansion *in vitro* for therapeutic use and often undergo early senescence (522). This is often the case for adult-derived cells due to the age and shorten telomeres affecting their proliferation potential.

The overall difficulties in having a conclusive finding for the set of CAM results highlights that although CAM assay generally meets the requirements to provide repeatable and reliable results at relatively low costs, it suffers from a lack of objective measures of the angiogenic response (494).

Greater insight with histological sections

Histological analysis was carried out on the seeded INTEGRA® scaffold and filter paper to understand the microscopic effect of the cells and scaffold as well as the conditioned media on vascular infiltration. Unfortunately, the seeded hydrogel scaffold was too delicate and fragile for histological processing on the day of explant. Gathering concurrent histological data alongside the vessel analysis data was critical in the evaluation of the CAM assay, given the visual vessel data varied with the type of scaffold used. Infiltration of microvessels seen on histology is also the most accurate means of evaluating host angiogenesis in the implant, where the depth of vascular invasion and vessel integrity can be better appreciated.

In many ways, histological findings on the seeded INTEGRA® scaffolds helped to conclude the initial CAM image analysis results. It is apparent that the INTEGRA® matrix itself was innately pro-angiogenic in nature from vascular changes observed

on the CAM. The histological sections helped prove and quantify this process. It delineated the degree of angiogenic potential across the different pre-conditioning groups by allowing for the microscopic examination of invading blood vessels from the presence of erythrocytes within the implant. From the data, it was shown that the INTEGRA® matrix was angiogenic in the control group even in the absence of seeded cells; just over 40% of the control INTEGRA® scaffold was shown to have vessel infiltration. With added cells pre-conditioned in either SH 1% or SN 21% oxygen, it marginally improved the average depth of vessel infiltration to about 56-57% of the scaffold. The greatest vessel infiltration was seen in the DH 21-1% pre-conditioned group with an average of 70% of the scaffold. There was also an appreciable higher density of vessels seen in the sections, although this was not quantified. There was also less extravasation of erythrocytes, otherwise known as erythrodiapedesis, seen in the DH 21-1% and SH 1% group, which could indicate better integrity of the neo-microvasculature. Extravasation of erythrocytes has been seen in leaky, excessive permeable immature vessels or in the rupture of neo-vessels in pathologies such as intraplaque haemorrhage in atherosclerosis (523). Hence, understanding vessel integrity is an important histological consideration as it not only reveals the maturation of vessels, but also predicts how functionally successful the vessels will be *in vivo,* especially in the prevention of clots in the implanted graft (524).

Due to time limitations and issues with histological processing for further endothelial cell staining of the CAM sections with CD31 positive markers, it was not possible to observe for endothelial-lined vasculature. Hence, the degree of endothelisation of the vessels observed was undetermined. Evidence of extravasation of erythrocytes is a helpful indirect indicator of poor vessel integrity in the CAM sections. Extravasation of erythrocytes can be due to immaturity or during the development of neovasculature (525), or due to pathological processes such as inflammation and oedema, causing RBC to migrate out of its host vasculature. For the sections which demonstrated less erythrodiapedesis, it could be indicative of two possible situations: 1. The additional signalling molecules from seeded cells, such as Ang-1, and/or their extracellular components affecting the maturation and integrity of the new vessels through the recruitment of EC and mural cells, or 2. Via seeded cells through their immune-modulation means to reduce inflammation and/or oedema of the surrounding tissue.

Given that the chick embryo is known to be an immunodeficient model, it is unlikely that immunomodulation resulting in a reduction in inflammation would account for these findings. Hence, it is more probable that vessel maturation from cell signalling molecules would be more accountable for this histological finding. For future experiments, it would be helpful to perform immunostaining of the sections to look for known markers of maturation and stabilisation of vessel architecture. This would involve observing for the presence of host endothelial lineage and mural cells, such as EC and pericytes and the expression of PDGF-BB and Ang1 molecule and receptor (526,527). Unfortunately, due to the low number of reagents compatible with avian species, it is very difficult to obtain antibodies, cytokines, and primers to immunostain and identify specific cell types of interest in the CAM assay sections (501).

In addition, the CAM assay could be extended to study wound repair as described by Ribbatti et al. where granulation tissue was used to recapitulate all the phases of the wound, including re-epithelisation, angiogenesis, inflammation, and fibronectin deposition, as well as resultant scar formation (528). Hence, histological identification of macrophages, fibroblasts and vessel structures could be very helpful in drawing on evidence from this aspect of the wound healing model in the CAM assay. This would help to conclude potential *in vitro* findings from the macrophage chemotaxis studies suggested in the Discussion section of Chapter 5.

How angiogenic is the conditioned media?

There were highly varied angiogenic responses within the same pre-conditioned groups, and the significance of quantifiable data would have invariably affected the overall interpretation and conclusion of the results. This was made more challenging by the fact that the INTEGRA® scaffold itself had its innate pro-angiogenic capability, marring the effect from the cells. Although this would not be surprising, given that the INTEGRA® matrix possessed the ideal pore size for vascularisation of TE scaffold, as concluded in Chapter 4.

In addition, there were encouraging angiogenic array results discussed in Chapter 4, which demonstrated significantly upregulated pro-angiogenic protein expressions

from conditioned media in the DH 21-1% seeded Integra, which made it imperative to delineate *in vivo* angiogenic response from the seeded cells, scaffold and its conditioned media. This was done using a biological inert filter paper as a wicking medium to focus on the effects of the CM alone on the CAM assay. It was shown that the ingrowth of blood vessels was only seen in the CM from the DH 21-1% pre-conditioned group. It was also interesting to note the degree of tissue infiltration into the filter paper for the different groups. Tissue infiltration into implanted material usually indicates the level of biocompatibility of the known material. As filter paper is made of cellulose porous material, the fact that there was evidence of cell and tissue infiltration within the paper scaffold is not unsurprising. In addition, cellulose paper-based cell culture systems have been described in the literature as an alternative 3D culture technique and other biomedical as well as tissue engineering applications requiring the support of cell and tissue migration (529–531). It is clear that CM from the DH 21-1% cells possess properties that not only allow for greater host cell and tissue migration into the filter paper, it also promotes blood vessel ingrowth which is not seen in the other pre-conditioned groups. It is likely that the addition of the CM would have modified the filter paper surface chemically (such as with adhesive ligands and other bioactive molecules) to allow for this favourable response (532). This would also corroborate with the proteomic data from the angiogenesis array of the conditioned cell supernatant in Chapter 4 and confirm *in vitro* to *in vivo* angiogenesis response in Chapter 5.

Increasing the complexity of the matrix from hydrogel to INTEGRA® scaffold and confounding the layers of the interplay between the cell-matrix-host effect makes the outcome parameters more challenging to decipher and conclude. A single effect from the pre-conditioned oxygen environment appears to become dilute with the increasing complexity of the cell-to-scaffold interactions. For instance, the DH (21-1%) pre-conditioned seeded transduced cells within hydrogel scaffolds appear to have an advantageous angiogenic effect when compared to the control. This appears to translate similarly to the CM response seen on the filter paper. However, the same effect was not found when the cells were subsequently seeded onto an INTEGRA® scaffold, likely due to the scaffold effect of the INTEGRA® dermal matrix being a highly biocompatible scaffold, innately pro-angiogenic in nature.

Practical considerations and limitations with the *in ovo* CAM assay

The *in ovo* CAM model was technically simple to carry out once the initial windowing method was mastered, however, there were several experimental challenges to overcome before the model was made reliable enough for data collection.

Initial experiments were carried out with silicone rings to be able to hold some volume of conditioned media over the implanted scaffold to maximise the pro-angiogenic cytokine proteins released during *in vitro* incubation. This was described by several published CAM-related studies, particularly for grafting tumour cells (533). It also prevented undesirable migration of the scaffold after implantation. However, the addition of the silicone became more of a hindrance in being able to observe and analyse the CAM at the end of the experiment. This can be appreciated in Figure 6-15A & B where the silicone ring obscured the field of view for vessel analysis. The silicone rings added unnecessary weight to the already fragile CAM surface and may negatively affect embryo/CAM development. Attempts to remove the ring for visualisation would inadvertently injure the CAM surface, preventing any possible analysis of the vessels. The use of silicone ring was discontinued for subsequent experiments for this reason.

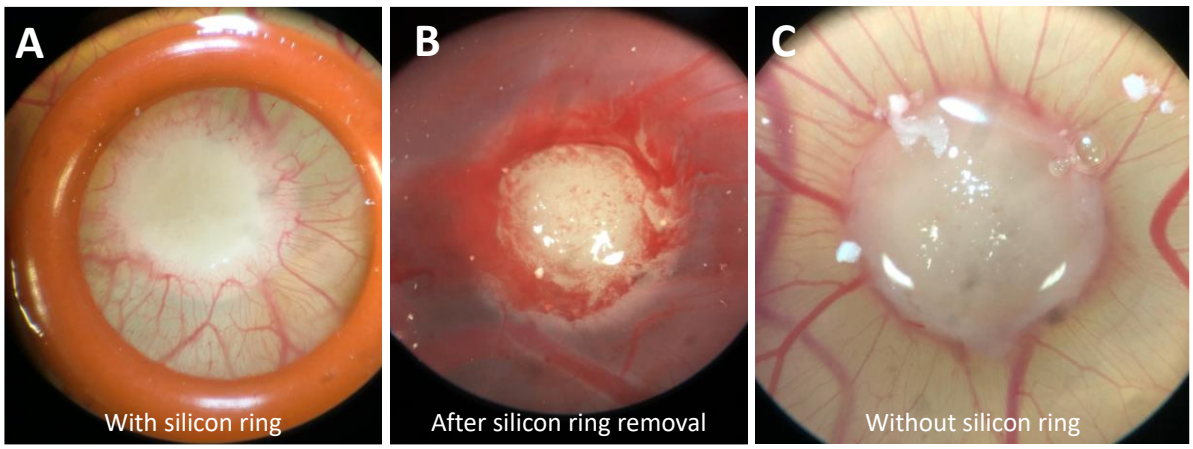

Figure 6-15 Representative comparative image of E14 CAM with 8mm silicone ring on (A) left and (B) trauma to CAM after silicone removal obscuring the surround CAM vasculature, (C) without on right with clear view of vessels. All images were grafted with INTEGRA® seeded with preconditioned static 21% adMSC.

Another common problem with the *in ovo* CAM is accessibility and visibility of the implant after 7 days. Unfortunately, the implant on the CAM can migrate during incubation and may settle on the edge of the shell. This obstructs the view of the surrounding CAM vasculature, which causes problems in the analysis of the vessels. (Figure 6-16A) Attempts to separate the CAM layer from the edge of the shell to visualise the entire CAM layer surrounding the implant usually cause trauma and bleeding, which affects the further downstream analysis of the histological sections. (Figure 6-16B)

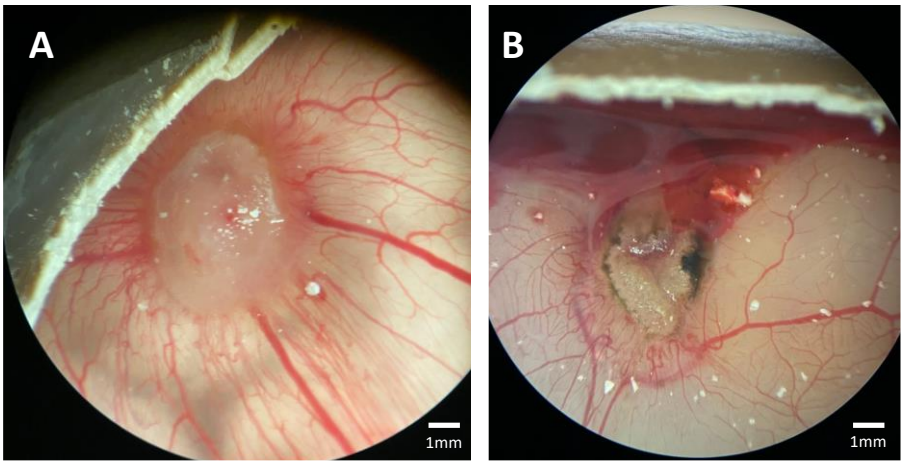

Figure 6-16 Obscured superior view of peri-implant vessels due to implant migration to the edge of shell in *in ovo* CAM assay after grafting. (A) The view of CAM layer and its vasculature surrounding the implanted scaffold (Dynamic 21-1% seeded Integra) is blocked by the shell edge. (B) Trauma on the CAM in an attempt to visualise the surrounding CAM causing bleeding of the CAM layer. Scale bar = 1mm.

There were also time limitations to explore other experimental methodologies, which reduced the potential more significant output on other measurable parameters. One such experiment would be the evaluation of the molecular evidence for the *in vivo* results visa the extraction of proteins and genetic material (RNA, DNA) which has been discussed above.

6.2.4 Method Modifications and Future Work

Since Folkman's team first used CAM as a model in the 1970s for experimenting with tumour-related angiogenesis, there have been many improvements to increase its application. Targeting one of the biggest downfalls of the CAM assay, several researchers have sought to refine the methods around vessel analysis in a region of

interest in the CAM assay. Within this thesis, we tried several of these modifications to the CAM assay, employing different techniques which have been described previously to overcome methodological difficulties encountered during the course of the experiment. The subsections in Appendix 9.1 will offer preliminary data for the *ex ovo* technique as a method modification. There will also be discussion around the pilot use of comparative imaging modalities for *in vivo* bioluminescent tracking as well as advanced microCT imaging systems to analyse the detailed 3D microvasculature.

Other useful parameters to determine for future experiments would be delineating direct cellular effect versus conditioned media response from the host as alluded to in the above results as well as data from Chapter 4 and 5 of the thesis. There is overwhelming data in the published literature that secretomes and exosomes from conditioned media containing cytokines, growth factors, and other microscopic extracellular vesicles would have a similar desired regenerative response *in vivo* (481). If time allowed for optimisation of additional experiments, it would be useful to investigate further by isolating relevant protein or RNA molecules, such as CD31, VEGF and HIF1a makers, via western blot and/or qPCR techniques to confirm or refute *in vivo* molecular changes of these pre-conditioned cells with their scaffold as well as their conditioned media to known *in vitro* data.

Important next steps to determine whether the attraction of host tissue, with chemotaxis and migration of local cells, would result in healing and regeneration *in vivo*. Hence, the following chapter will look at the murine diabetic wound healing model and determine if the pre-conditioned seeded INTEGRA® scaffolds would result in better wound healing.

6.3 Murine diabetic wound healing as a measure of functional angiogenesis

Wound healing is a form of functional angiogenesis occurring in the body through the regeneration of tissues. All types of wound healing require adequate blood supply for the reparative process (221). Hence, a well-vascularised wound bed is crucial for the healing of skin defects. Chronic non-healing wounds usually present with additional underlying pathologies which hinder healing. The most common cause for this is the lack of vascular supply to the wound. Hence it is no surprise that the aetiology of chronic wounds worldwide are from diabetic and ischaemic-related leg ulcers (563). Non-healing wound represents one of the major challenges in healthcare, costing the NHS in excess of £5.6 billion, representing an estimated 5.5% of its annual budget (217,218). As yet, no satisfactory therapy has been identified to treat such difficult wounds.

The gold standard for the treatment has been the use of off-the-shelf clinical-grade tissue-engineered scaffolds for dermal regeneration (SDR), also known as acellular dermal matrix (ADM) (223). However, the vascularisation of these ADM can take up to 3 weeks to accomplish (223). Lack of epidermal coverage or dermal graft adherence is usually caused by slow vascularisation of the scaffold. This can further impact on the successful use of dermal scaffolds. In the treatment of skin pathologies, such as burns and diabetic/vascular ulcers, this can become more apparent due to the lack of oxygen and nutrients driven by the poor blood supply which has resulted from the underlying disease (224,225). This is then exacerbated by an increased risk of infection from delayed establishment of a skin barrier. Hence, lack of adequate and rapid neovascularisation is considered one of the main limiting factors for the clinical success of ADM (226). Combination of cell therapy and tissue engineering may be the solution to this highly challenging problem. Fierro et al. mentioned the advantages of ‘bio-activating’ dermal scaffold with MSC to enhance angiogenesis and the recruitment of native cells by secreting paracrine factors to help overcome the clinical difficulties seen with ADM success due to poor vascularisation (237). Several other published studies have also supported the strategy of “bio-activating” INTEGRA® scaffold specifically by pre-seeding it with

MSC (222,223,230,233,234,237,245,248,250,252,390,399,478–481). Promising evidence of enhanced wound healing from the use of TE scaffold seeded with cells have also been extensively reported (223,224,228,233,236,238,242,564–567).

In order to determine if pre-conditioning of seeded adMSC on INTEGRA® ADM would result in successful functional angiogenesis in the form of wound regeneration, a pre-clinical wound model would need to be adopted. This wound model would ideally replicate aspects of chronic wound pathophysiological processes without the need to use human volunteers. Diabetic animal models have been used extensively in pre-clinical chronic wound research (568). The mouse model is the most accessible animal model due to the low cost and high availability of immunodeficient breeds to allow for xenotransplant of human cells without mounting any undesirable immune response. Previous studies have also used ADM such as INTEGRA® on mice with success (223,228–241,248,249,390,391). Given the above, we aim to deliver pre-conditioned adMSC seeded on INTEGRA® scaffold to a previously described splinted full-thickness diabetic mouse wound model to determine the *in vivo* therapeutic potential in this translationally relevant model (247,569,570).

6.3.1 Materials and Method

6.3.1.1 Animals

All animal studies and protocols were performed in compliance with federal guidelines and reviewed and approved by Yale University's Institutional Animal Care and Use Committee (IACUC). 24 male athymic homozygous Foxn1^{nu} nude mice (8–12 weeks; body weight 20–30 g; Jackson Laboratory, ME, USA) were used for the diabetic wound model. As there is a statistically higher male disposition for diabetic foot ulcers globally, a male-only mice population was chosen to offer a more representative profile for this disease model (571).

The mice were allowed to acclimatise for a week prior to diabetes induction in 12 hours light/dark cycle within a temperature-controlled environment. Special provisions were made for housing the animals in autoclaved cages with white

bedding and floor feeding with autoclaved diet and water as per Yale Animal Care guidelines for athymic nude mice. Post-operatively, the mice were singly housed to avoid wound disturbances from other animals during convalescence. At the end of the study, the mice were humanely euthanised via cervical dislocation under general anaesthesia in accordance with approved regulatory and protocol guidelines.

6.3.1.2 Induction of diabetes in mice

To induce diabetes, a low-dose streptozotocin (STZ) protocol was used as previously described to avoid any unwanted toxicity to other organs (569,572). Streptozotocin (Tocris Biosciences, Bristol, UK; #16-215-00) was dissolved in sterile-filtered 50 mM sodium citrate buffer (pH 4.5) immediately prior to administration and protected from light. The mice were injected daily for 7 days (50 mg/kg IP) using 30G 1ml insulin syringes (BD Medical, US; #328411). Daily body weights were recorded to guide the dosage of streptozotocin for each mouse. Blood glucose levels were monitored daily after completion of the 5 days STZ injections. Blood glucose was measured using a needle prick of the tail vein with a handheld glucometer (AimStrip® Plus, Germaine Laboratories Inc, TX, US; #37321). The mice were considered suitability hyperglycaemic after three consecutive blood glucose measurements of 300 mg/dl or higher.

6.3.1.3 Splinted dorsal wound model

Circular ring splints were made by punching out 0.5mm thick silicone sheets (Invitrogen, ThermoFisher Scientific; #P18178) with 7mm and 10mm punch biopsy (AcuPunch, Acuderm Inc; #P725, #P1025) and sterilised with the autoclave prior to use.

On the day of surgery, the diabetic mice were anaesthetised with vaporized isoflurane and laid on a heated mat set at 37.5°C throughout the surgery. With the mouse laid in prone position, the operative area was covered with Press'n Seal plastic wrap (Glad, US; #70441) with a defined surgical field exposed. (Figure 6-17A) 10% povidone-iodine solution (Humco, US; #232598001) was used to prep the skin

for surgery. (Figure 6-17B) Two silicone splints were sutured bilaterally on the upper dorsum of each animal. (Figure 6-17C) Anchoring stitches were made to secure the splint using 6-0 nylon sutures. Two full-thickness wounds, including the panniculous carnosus, were made centrally within skin exposed by the splint with a sterile 6mm punch biopsy device (INTEGRA® Miltex, US; #33-36) and excised fully using sterile dissecting scissors. (Figure 6-17D) The 6mm pre-seeded INTEGRA® dermal scaffolds were carefully placed in the wound area, with the cell-seeded side facing the wound bed and sutured in place with two to four interrupted 10-0 monofilament sutures to ensure adherence to the underlying wound. (Figure 6-17E) Scaffolds were left in place for the duration of the experiment until day 14 or until termination of the animal. We used 14 days as a marker as this is the length of time seen in vascularisation of tissue-engineered skin enabling graft survival. A semi-occlusive Opsite Flexifix dressing (Smith & Nephew, UK; # 66000040) was used to cover the wound site and was changed daily to ensure wound hygiene and prevention of infection. (Figure 6-17F) All mice were provided with 3 days of post-operative analgesia in the form of buprenorphine (0.05 mg/kg S/C; Par Pharmaceuticals, NY, US; # 42023-179-05).

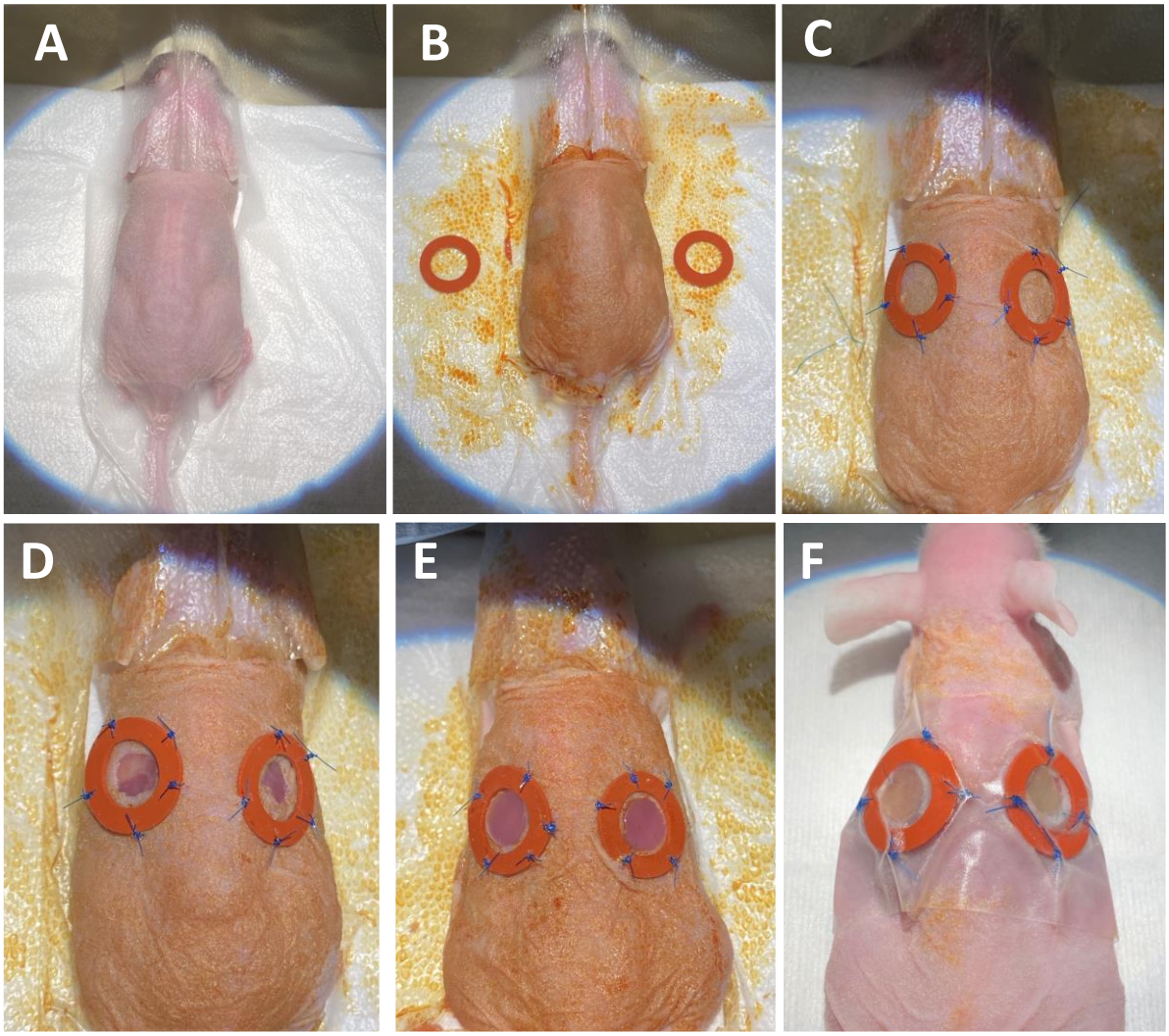

Figure 6-17 A-F Peri-operative pictures illustrating steps involved in creating two dorsal splinted wounds on a nude mouse.

Dressings were removed and wounds were examined daily from post-operative day (POD) 0-7 and every other day from day 7-14. Mice were briefly anesthetised using isoflurane and wounds were photographed at a fixed distance with a camera microscope adapter on a Leica MZ9.5 10X eyepiece stereomicroscope connected to Leica KL 1500 LCD illuminator.

6.3.1.4 Wound analysis

Stereoscopic images taken of the wound were analysed using Fiji polygonal tool to measure the area of the wound over the course of the study.

6.3.1.5 Histology and analysis

At termination of procedure, which was scheduled at post-operative day (POD) 14, full-thickness wound tissue samples were removed and placed in prefilled 10% formalin solution container (Richard-Allan Scientific, US; #59601) for 12 hours at room temperature. The solution was replaced with 70% ethanol solution and processed for histology as per General Methods chapter.

Microscopy of the histological sections were captured using the NanoZoomer 2.0-HT scanner (Hamamatsu Photonics K.K.). Resultant images were viewed and analysed with NDP.view2 Image viewing software (Hamamatsu Photonics, Japan)

Blood vessel density was measured by counting the number of vessel-shaped lumens with visible erythrocytes per field, which are stained pink due to their enucleated nature, at 40X field of view as described by Zomer et al. (249). A total of 8 regions of interest from 2 different histological sections from each wound sample were analysed and counted. The measurements were averaged and plotted as an individual value for each wound sample. Two main regions of interest, from within the scaffold and within the dermis, were analysed. (see Figure 6-23)
Dermal thickness was measured using the measurement tools within NDP.view2 Image viewing software (Hamamatsu Photonics, Japan). (Figure 6-18) A total of 8 separate measurements from 2 different histological sections from each wound were analysed. Measurement of dermal thickness includes the grafted INTEGRA® scaffold. The measurements were averaged and plotted as an individual value for each wound sample.

For controls, these included wounds with acellular INTEGRA® scaffolds as well as normal skin for histological analysis. For measurement of dermal thickness, it was possible to obtain some samples from healed areas of the skin with no scaffolds (due to early loss of scaffold prior to termination from acellular controls) for visual comparison purposes in the H&E sections (see Figure 6-27) Due to low sample numbers, these non-scaffold wounds were not included in the quantitative analysis.

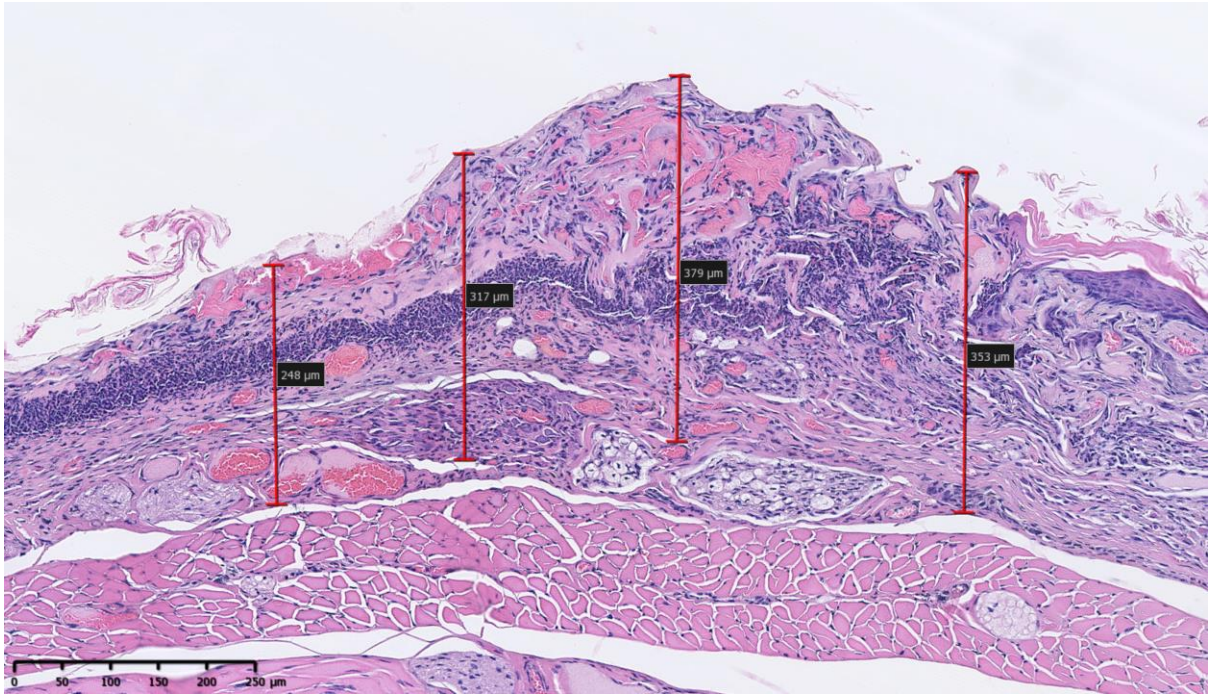

Figure 6-18 Measuring the dermal thickness of a dynamic hypoxic seeded INTEGRA® scaffold section at 10X magnification. 4 measurements per section is shown. There were 2 separate sections per sample, giving a total of 8 measurements per sample.

6.3.2 Results

6.3.2.1 Animals

All mice tolerated the STZ induction process. Most mice (22/24) measured blood glucose levels of more than 300 by day 8 of induction. The other 2 mice became suitably hyperglycaemic on day 10 and 11. (Figure 6-19A) The average blood glucose for the newly diabetic mice was 416.96 ± 81.16 mg/dl. The average weight loss observed from induction to termination was 4.48%, which is expected from post-STZ induced diabetic murine models (572). The post-operative survival curve is shown in Figure 6-19B. The overall attrition rate was 25% (6/24); One mouse died on the day of the operation, likely due to anaesthetic complications, and the rest are likely due to complications from diabetes/hyperglycaemia. A small number of mice (3/24) developed swollen abdomens filled with fluid (ascites), likely secondary to hepatotoxicity from STZ use. (see discussion below) The maintenance of consistently covered dressings on the back of the mouse was difficult and daily wound checks and dressings changes were necessary at least for the first post-operative week. As

a result, re-suturing of some of the loose sutures was required to ensure that the splints were properly secure throughout the experiment.

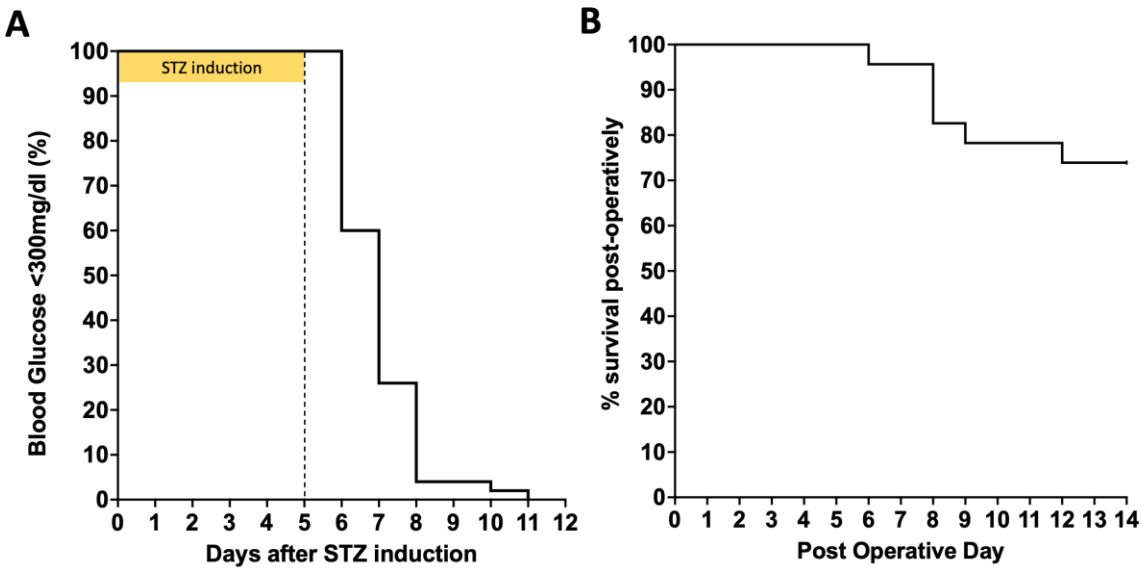

Figure 6-19 (A) Graph A shows percentage of mice with blood glucose <300mg/dl (non-diabetic) plotted over time after 1st STZ injection. The development of diabetes occurs when blood glucose is greater than or equal to 300 mg/dL. Day 0-5 represent the induction period where no glucose monitoring was performed. 100% of mice developed diabetes after day 11 of TSZ induction. (B) Percentage survival, post-death and early euthanasia, after diabetes induction is presented as Kaplan–Meier estimates plotted over time after transplant.

6.3.2.2 Wound vascularisation

Increased erythema was noted around and within the scaffold for cell-seeded scaffolds compared to acellular control scaffolds from day 5 onwards. (Figure 6-20) This is indicative of the early vascularisation process which was supported by histological evidence of increased blood vessels within and surrounding the cellular implants. (

Figure 6-23) Erythematous changes in the scaffold were noted in varying degrees on the other seeded scaffolds, but they were certainly more evident in the DH 21-1% seeded scaffolds. (Figure 6-20 and Figure 6-25) Although macroscopic findings were not quantified, there was histological evidence which will be further elaborated below.

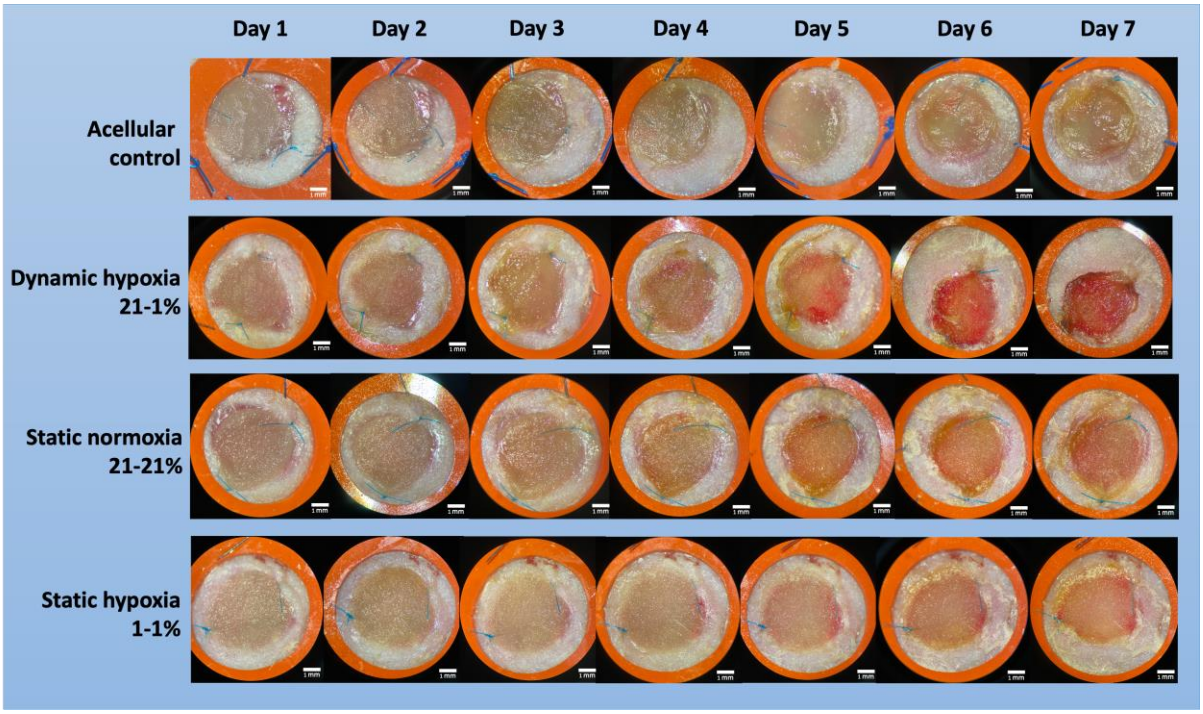

Figure 6-20 Representative macroscopic images of dorsal splinted wounds from day 1-7 of implant. Increased erythema noted around the edges of the cellular implants from day 5 onwards. Scale bar = 1mm.

Mice which were terminated early in the experiment (on day 7 and 8) had their scaffolds explanted for visual inspection of the posterior aspect of the wound as shown in Figure 6-21. These macroscopic images helped to corroborate the erythema finding on the anterior macroscopic appearance of the wound to underlying vascularisation, as shown in the smaller angiogenic vessels infiltrating into the edges of the wound and into scaffold.

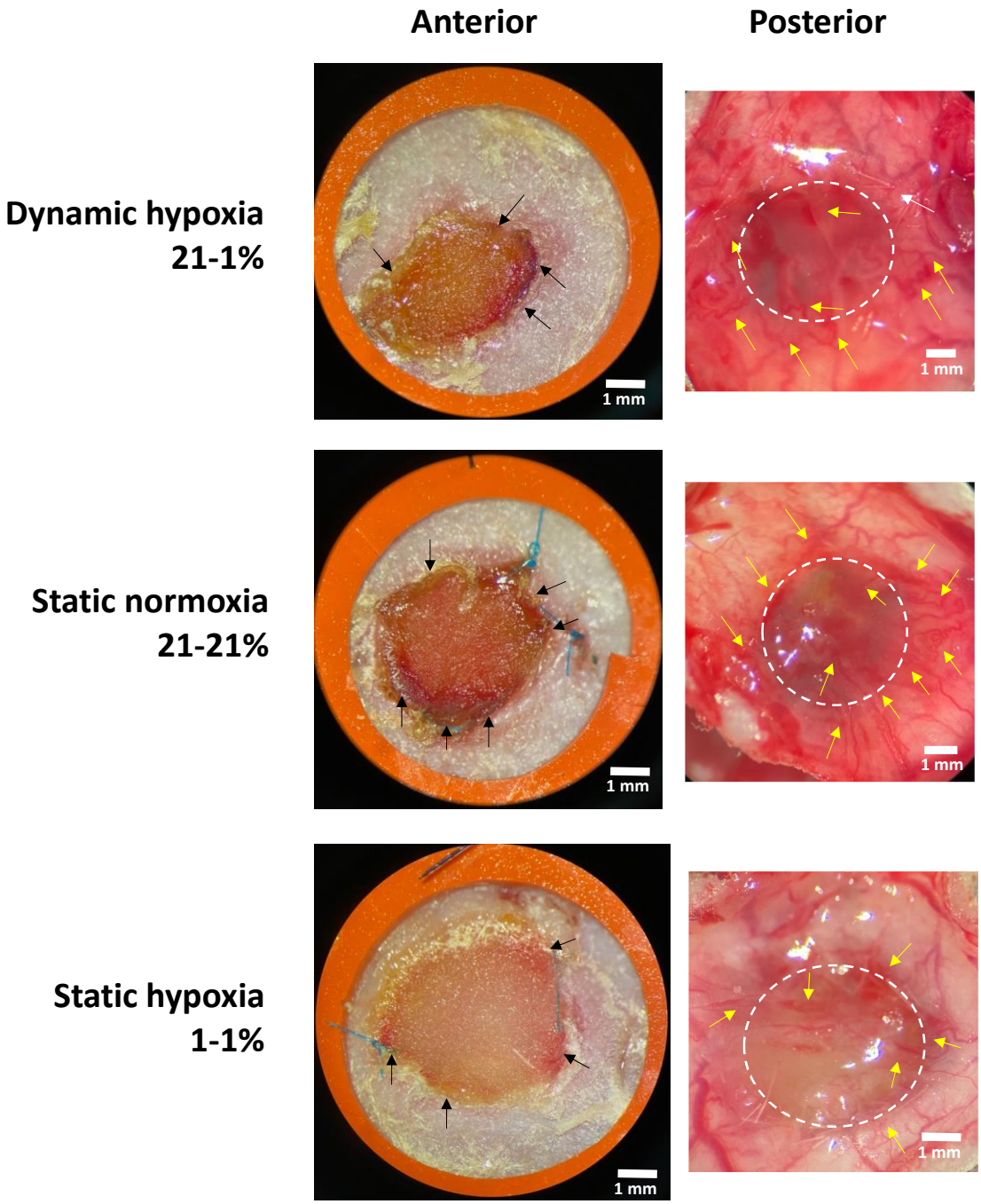

Figure 6-21 Macroscopic wound images of dorsal splinted wounds on day 7/8 of implant on terminated mouse. The three different oxygen conditions are represented. The increased erythema around the edges of the cellular implants can be seen in all scaffolds shown on the left. This is marked by black arrows, which corresponded well with visual evidence of underlying angiogenesis (yellow arrows) from the surrounding tissue into the wound and scaffold, as shown on the right images of the posterior aspect of the wound and scaffold. The scaffold parameter is encircled with a white dotted line. Scale bar = 1mm.

Histological analysis of the scaffold showed significantly increase in mean vessel density in the DH seeded wounds (26.6 ± 14.7) compared to SN 21% (14.7 ± 9.47),

SH 1% (8.84 ± 6.01) and control (3.89 ± 3.44). Cross sectional analysis of the dermal layer also showed increased mean vessel density noted in the DH seeded wounds (13.8 ± 7.45) compared to other groups. Vessel density in SN 21% (9.20 ± 5.84) were found to be similar to SH 1% (9.01 ± 5.16). Interestingly, the control dermal mean vessel density measured slightly higher at 10.3 ± 7.21 count per 0.055um^2. N-numbers varied across the different conditions, but at least n=3 of biological replicates were performed for each condition. Differences in analysed sample numbers in each condition were partly due to some samples lost during histological processing. This was particularly with the scaffold layer separating from the dermal layer during processing.

These findings can be appreciated visually via the representative cross-sectional histological sections shown in Figure 6-23. DH scaffolds showed significantly greater blood cells or erythrocytes seen within the scaffolds, some were organised within cell-lined lumens, which are likely made of endothelial cells. However, there is also concurrently increase in extravasation of these erythrocytes seen in both the scaffold and dermal area. The scaffold layer also appeared more densely packed then the other static conditions (SN and SH). The same extravasation of erythrocytes could also be seen in the control scaffolds but to a lesser extent. Within the peri-scaffold dermal layer, all conditions showed more organised cell-lined lumens containing erythrocytes.

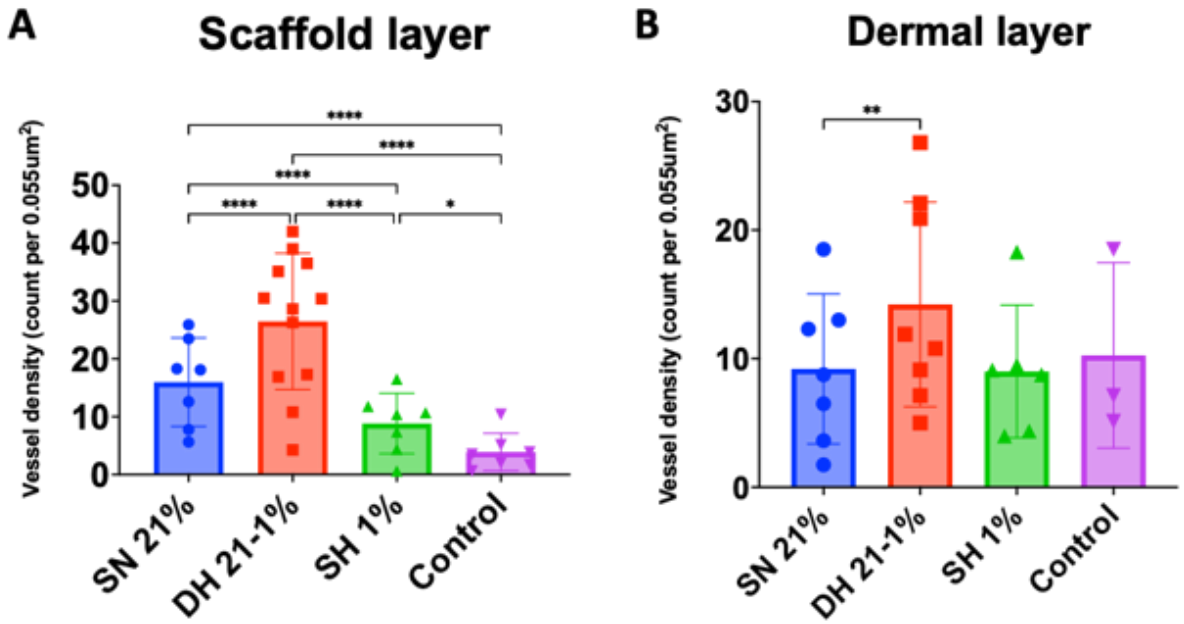

Figure 6-22 Graphical analysis of vessel density on histology sections within the scaffold (A) and dermal (B) layer of the implant on the day of harvest. N-numbers varied across the different conditions, as shown on the scatter dot plot, but at least n=3 biological replicates were performed for each condition. Differences in analysed sample numbers in each condition were partly due to sample lost during histological processing.

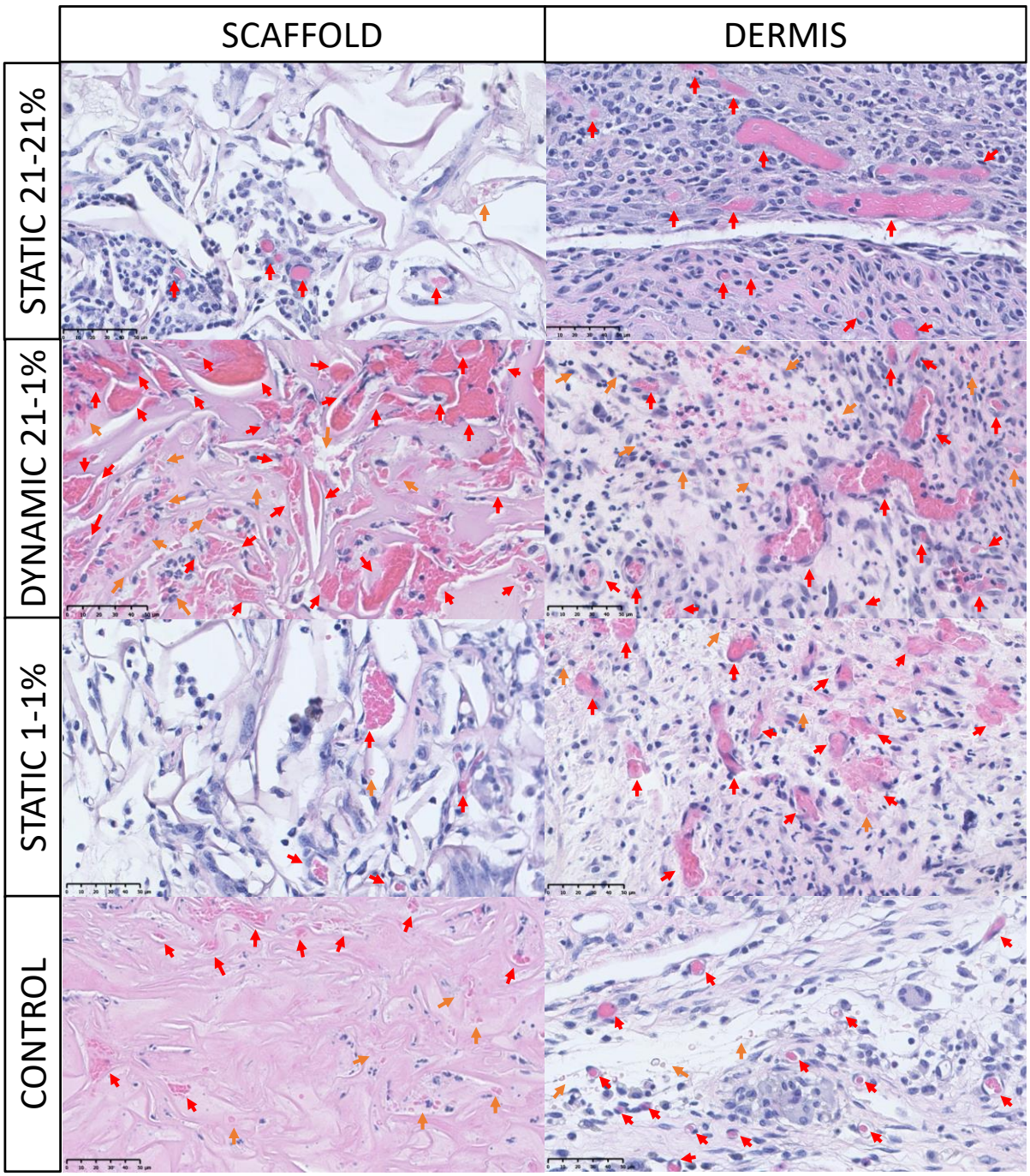

Figure 6-23 Representative histological H&E sections of the scaffold and dermis at 40X magnification for the different oxygen conditions and acellular control. Red arrows = vessels; Orange arrows = extravasation of erythrocytes into surrounding parenchyma.

6.3.2.3 Wound healing analysis

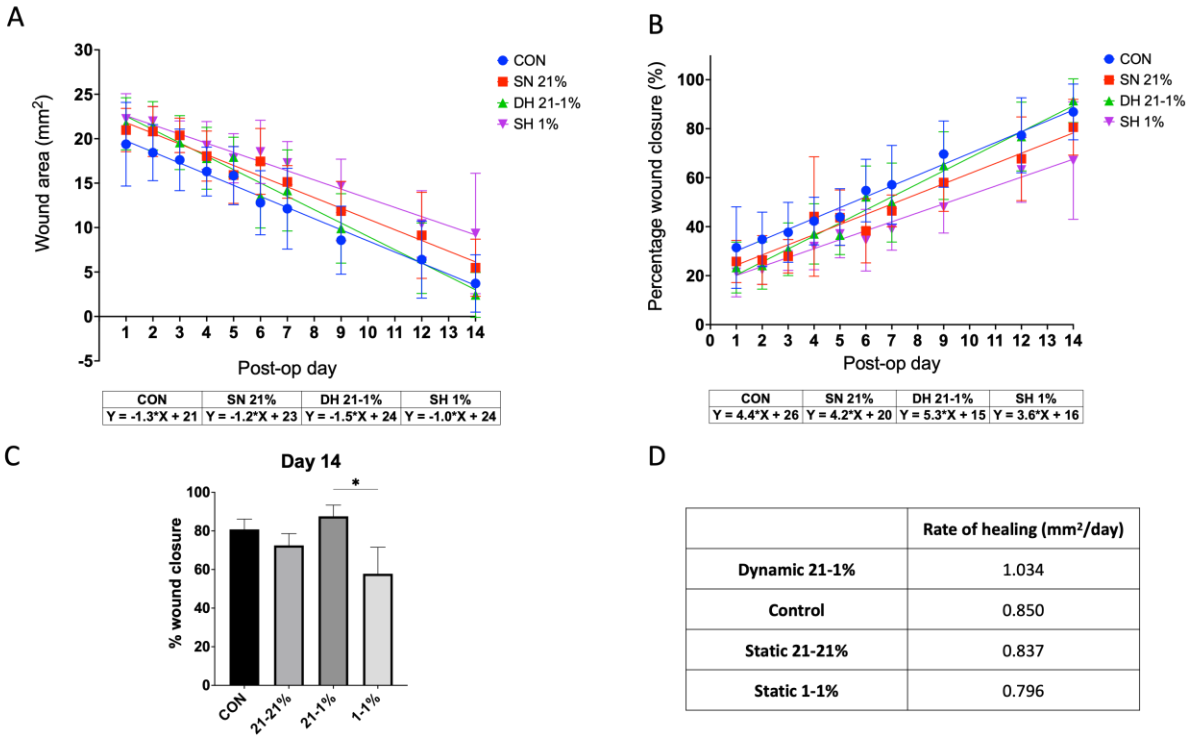

	Rate of healing (mm²/day)
Dynamic 21-1%	1.034
Control	0.850
Static 21-21%	0.837
Static 1-1%	0.796

Figure 6-24 Graphical data representation of wound healing measurements comparing seeded scaffolds with different oxygen conditioning and acellular control. (A) Graph plotted with the mean wound area of each condition over 14 post-operative days. (B) Percentage wound closure compared to original 6mm² punch biopsy wound (28.27mm²) over 14 post-operative days. (C) Comparative bar chart of percentage wound closure on POD 14. (D) Tables displaying the average rate of healing in the different oxygen conditions and acellular control listed in descending order. N-number > 5 of biological replicates per condition.

Initial wound size varies across the different groups. Hence it was necessary to normalise the values to the average wound size for each group to calculate the percentage of wound closure for each time point. Figure 6-24A shows that the control and DH INTEGRA® scaffolds achieved a smaller average wound area compared to the static hypoxic and normoxia groups. This is also demonstrated in Figure 6-24B and C with percentage wound closure over time and on Day 14 of wound analysis. The gradient of the linear regression graph of each group gives an indication of the rate of healing. Hence, it is possible to calculate the rate of healing shown in the table in Figure 6-24D. Measuring for the rate of wound closure relative to the variable initial wound size, wounds treated with DH cells when shown to healed 1.22 to 1.30 times faster compared to the other cellular and acellular counterparts.

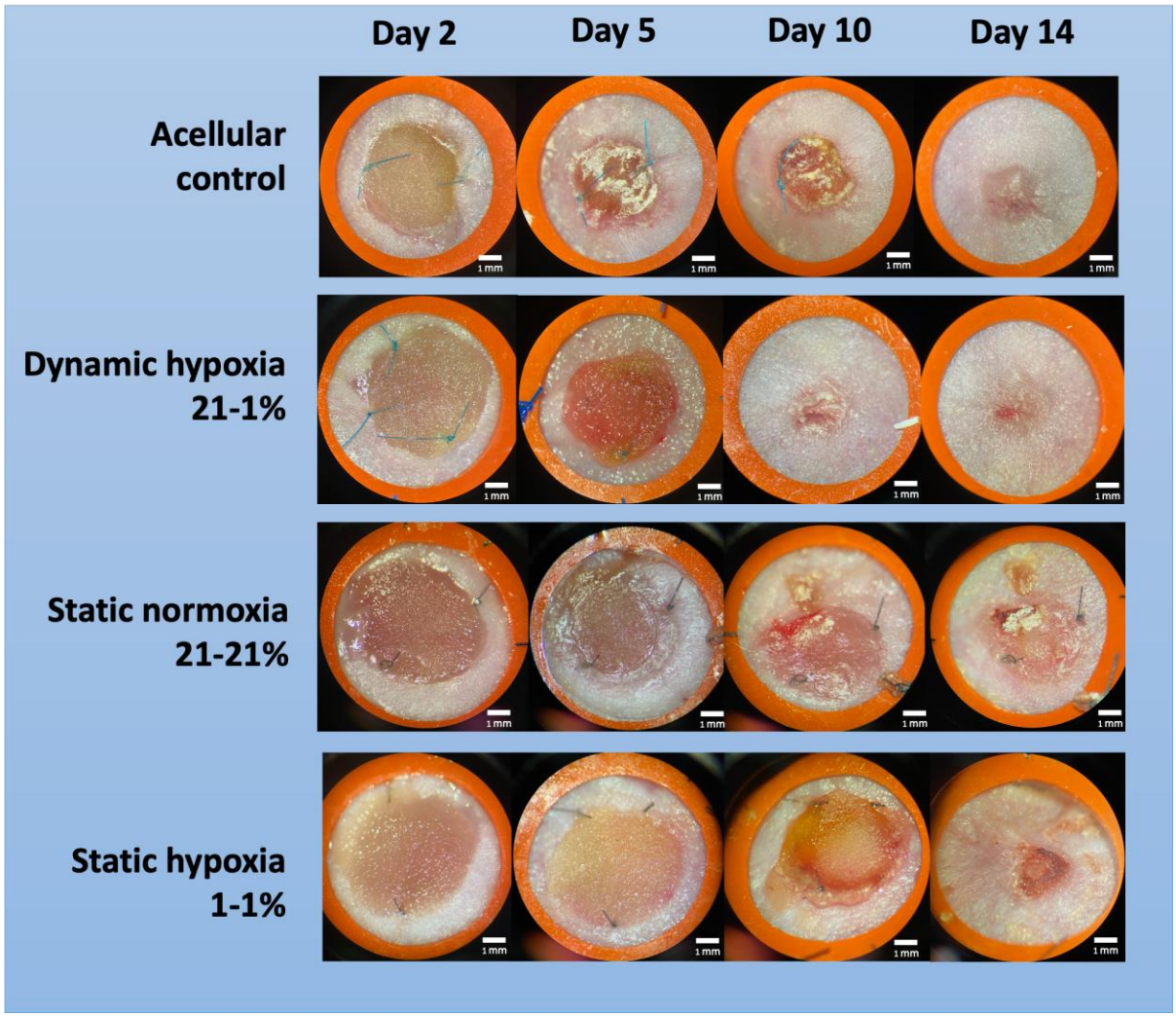

Figure 6-25 Representative photographs of the chronological healing of dorsal wound from day 2 to 14. Scale bar = 1mm.

Visual representation of wound closure over the course of healing is demonstrated in Figure 6-25. The problem with graft take and integration to the wound site can be appreciated from the static normoxia 21% on day 14. Some of the grafts do not adhere properly onto the mouse skin, sometimes leaving a layer of scab such as that seen in static hypoxia on day 14. This was found mostly in mice with wound dressing issues, where the dressings would be removed either by the host animal or fall off in between monitoring and dressing changes. The suture positions around the scaffold would stay intact. Hence, it can be appreciated that there is a degree of wound contracture occurring over time despite the use of splints circumferentially around the scaffold/wound site. There is an overall decrease in scaffold and wound size from Day 2 compared to Day 14.

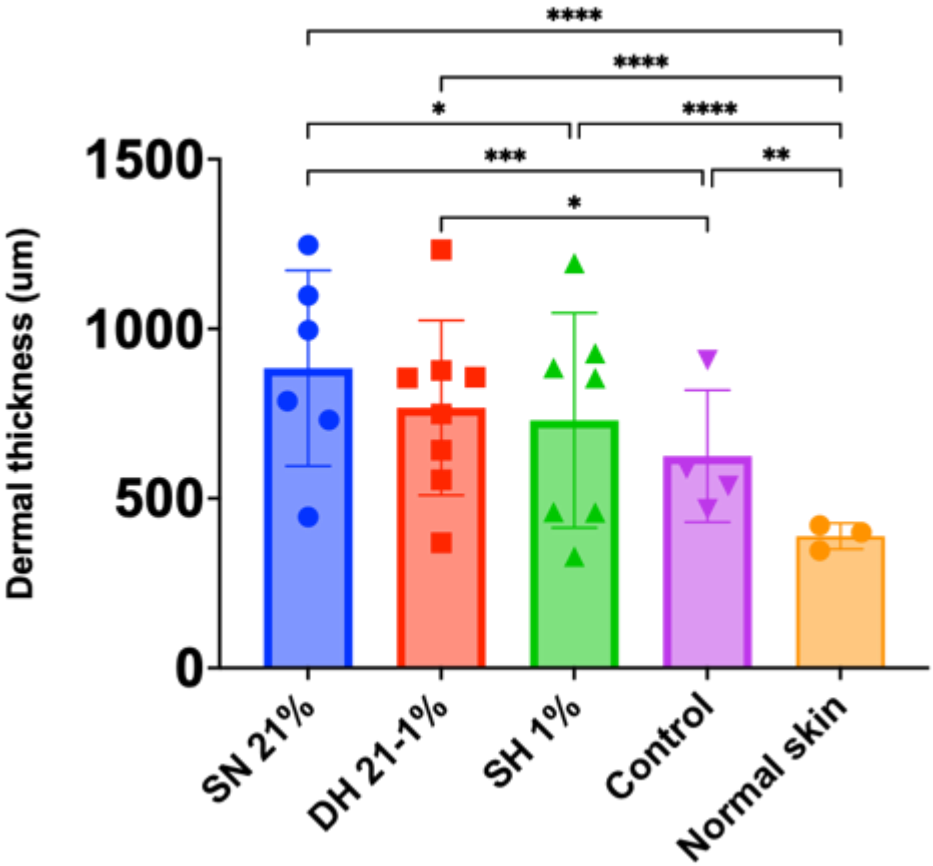

Figure 6-26 Dermal thickness of wound with implanted cellular and acellular scaffold compared to normal skin. N-numbers varied across the different conditions, but at least n=3 biological replicates were performed for each condition. Differences in anlaysed sample numbers in each condition were partly due to sample lost during histological processing.

Dermal layer thickening and granulation tissue were noted in all cell-seeded scaffolds. Cellular infiltration was also seen in all INTEGRA®scaffolds, including controls, although the degree of infiltration varied throughout the scaffold making it difficult to quantify. Compared to normal skin, all sample groups had significantly thicker dermal wound thickness. SN 21% wounds presented with the thickest mean dermal measurement (884 ± 323 um), which was found to be significantly different when compared to the SH 1%, control and normal skin dermal measurements. These happened to be the 3 groups with the thinner dermal layer compared to SN and DH groups. DH and SH mean dermal thickness were similar in measurement (767 ± 275 um and 730 ± 307 um respectively).

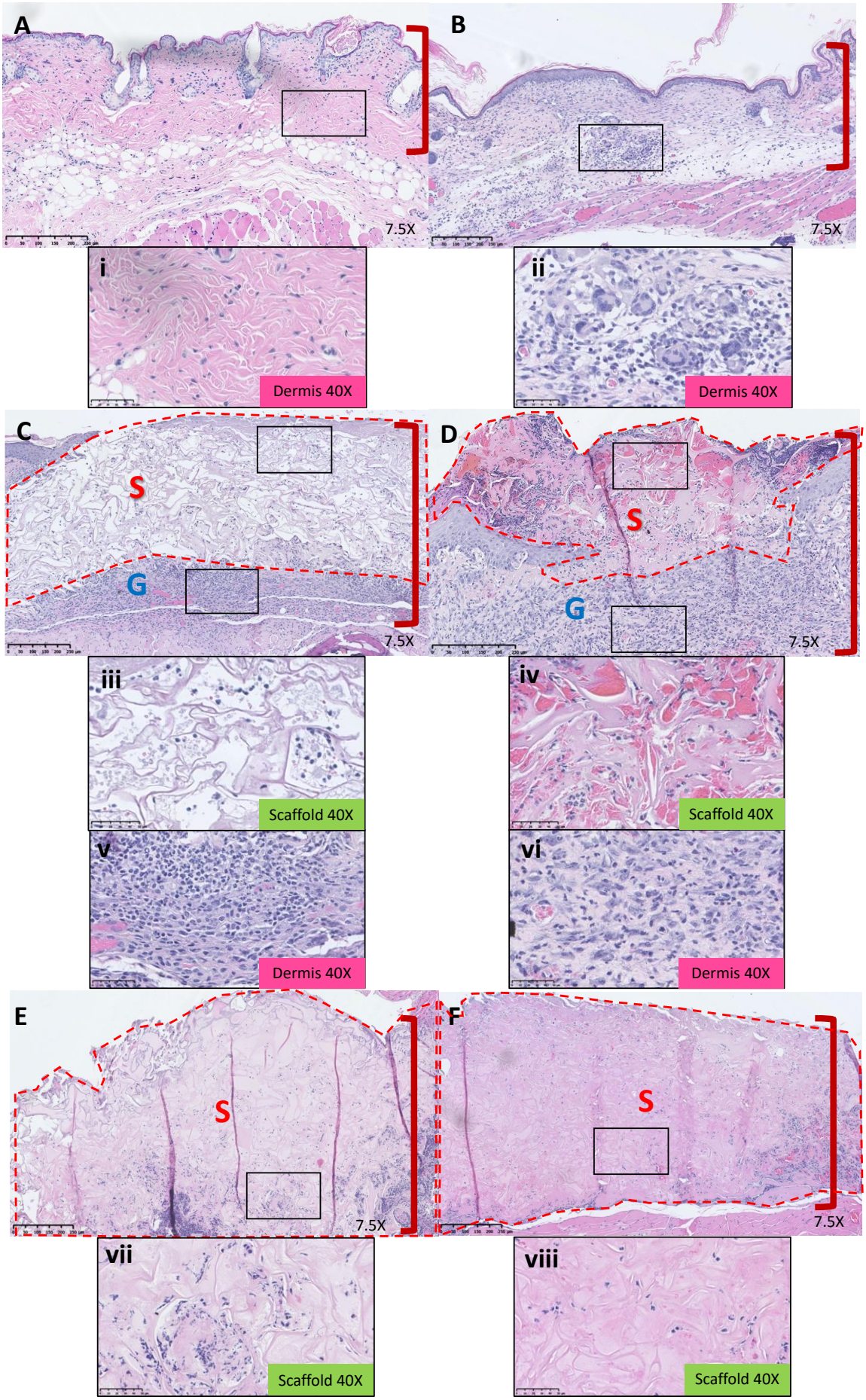
A
7.5X
B
7.5X
i
Dermis 40X
ii
Dermis 40X
C
S
G
7.5X
D
S
G
7.5X
iii
Scaffold 40X
iv
Scaffold 40X
v
Dermis 40X
vi
Dermis 40X
E
S
7.5X
F
S
7.5X
vii
Scaffold 40X
viii
Scaffold 40X

Figure 6-27 Representative H&E stained histological sections of mouse skin under brightfield microscopy at 7.5X magnification. Red brackets demarcate the dermal layer; 'S' label represents the INTEGRA® scaffold which is demarcated by red dotted line; 'G' label represents granulation tissue. (i) – (viii) represent zoomed-in areas, at 40X magnification, of the dermis and scaffold of marked-out areas in the 7.5X microscopy images above. (A) Normal skin section demonstrating a thin layer of the epidermis, marked by the densely packed cells, on the top of a thicker dermis, which is made up of connective tissues (consisting of mainly collagen and elastin fibres), followed by the hypodermis subcutaneous layer. This layer is made up of mainly adipose tissues which cover the underlying muscle. Both dermis and hypodermis are interspersed with blood vessels, as evidenced by luminal structures containing enucleated red blood cells which are stained pink; (B) Cross-section through a healed full-thickness wound with no dermal scaffold; (C) Cross-section through adMSC seeded (static 21%) Integra; (D) Cross-section through adMSC seeded (dynamic 21-1%) Integra.; (E) Cross-section through adMSC seeded (static 1%) Integra.; (F) Cross-section through control acellular INTEGRA® scaffold.

On examination of the histological sections, it was possible to make some visual comparisons between the different dermal sections. There is also an additional benefit of imagining healed wound sections which do not have an overlying scaffold to allow for comparative histological differences to wounds with scaffolds. They were obtained from acellular control wound edge in one mouse and sectioned to enable comparison of the layers in the scaffolded wounds. Wounds with scaffolds tend to have significantly altered skin anatomy. Healed wounds with no INTEGRA® layer demonstrated similar skin layers as normal skin. There was a fully epithelialised layer, but the dermis lacks the same amount of connective tissue as normal skin. There is also an increased density of cells within the dermis, representing granulation/scar tissue. There is also a loss of subcutaneous tissue. Both dermal and muscle layers show some increase in vessels compared to normal skin, but this was not quantified. In the SN 21% representative sections, cellular infiltration was seen throughout the scaffold with granulation tissue forming between the scaffold and the muscle layer. This could be indicative of scaffold integration. There was also increased vascularisation seen in this layer and evidence of epithelisation of the scaffold which was seen around the edge of the wound. In DH sample sections, the scaffold itself appeared densely packed with cells and vessels within the parenchyma. The dermal granulation layer is also thicker, with signs of remodelling by the presence of irregular connective tissue heavily populated with fibroblast-like cells. There was also evidence of epithelialisation on top of the INTEGRA® scaffold from the wound edge. The scaffold integration was certainly more evident compared to SN (Figure 6-27C), SH (Figure 6-27E) and the control (Figure 6-27F). For SH 1%

dermal-scaffold layer, although there was cellular infiltration within the scaffold, it is less pronounced compared to (C) and (D), with cells noted mainly on the wound bed where the adMSC seeded cells would reside. Within the control scaffold-dermal layer, cellular infiltration was clearly noted from the wound edges, whereas there are few cells seen on the wound bed compared to the cell-seeded counterparts seen in Figure 6-27 C, D, E. Using the control layer to compare with the SH sections, there was only a slight appreciable difference in cellular infiltration, which could indicate either loss of implanted adMSC in the SH scaffolds or less host cell infiltration into the scaffold layer.

It was interesting to observe that re-epithelisation was noted in some of the cellular scaffolds on H&E staining (Figure 6-28) but this was not all consistent across the grafts. Hence, not much significance can be placed on these histological observations other than to show that the INTEGRA® dermal scaffold is capable of supporting simple murine re-epithelisation without the need for an additional transplanted epithelial layer, unlike that required in human subjects.

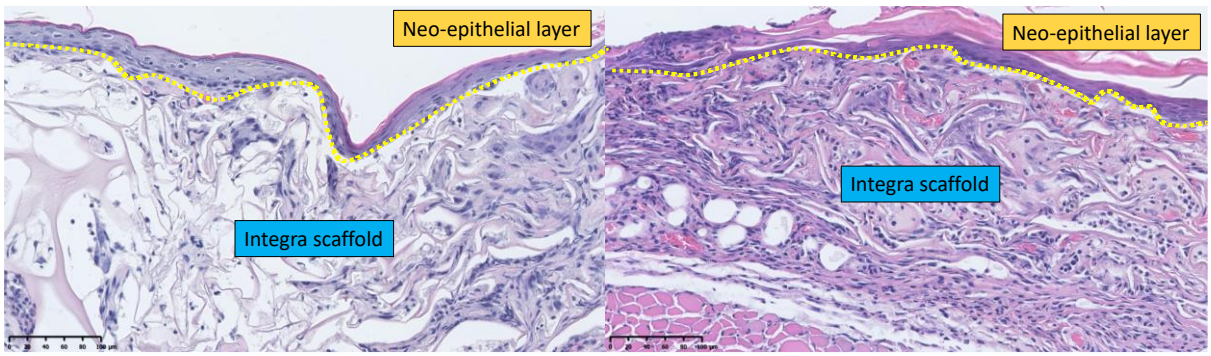

Figure 6-28 Re-epithelialisation of INTEGRA® scaffold at day 14 of implantation at 20X magnification. The yellow dashed line demarcates the neo-epithelium from the underlying dermis/INTEGRA® layer. The right image represents dynamic hypoxic seeded scaffold, the left image shows static 21% seeded scaffold.

6.3.3 Discussion

<u>Functional angiogenic and regenerative wound healing response</u>

In order to properly evaluate wound healing *in vivo*, it is necessary to understanding the key mechanism involved in the process. The phases of wound healing are shown in Figure 6-29, and consist of three main phases: inflammatory, proliferative, and

remodelling. The last phase can be further divided into early and late stages. The initial inflammatory phase usually last for a few days to a week after wounding (214,573). A platelet plug forms as part of the homeostasis process and creates a fibrin-rich matrix, which in turn acts as a scaffold for influx of inflammatory-mediated cells. They are the first line of defence against bacterial infection and mainly consist of neutrophils and monocytes, which later differentiate into macrophages (574). Macrophages play a significant role in coordinating later events in response to injury and continue their effects through into the remodelling phase (249). The next proliferative phase takes over swiftly from the inflammatory phase and usually beginnings within 48-72 hours after injury. It is characterised by the cellular proliferation and migration of different cell types such as keratinocytes, fibroblast, vascular endothelial cells, as well as supportive mural and mesenchymal stem cells (575,576). Angiogenesis plays a crucial role in this phase and is heavily coordinated by the cellular response to trauma in the form of cytokines and growth factors such as VEGF and bFGF (577,578). This allows for more influx of cells and granulation tissue develops, resulting in dermal thickening and a protective scab or eschar forming on the overlying wound. Problems at this phase in healing usually result in chronic non-healing wounds (579). The final phase involves a manifold of processes which begins 2-3 weeks after injury and can last for months to years. This phase crucially determines the final outcome wound healing and involves remodelling and maturation of the ECM and re-epithelialisation of the overlying skin. These are influential to how much scarring occurs.

Due to shorter life span and greater turnover of cells and tissue compared to humans, there is some limitation with the representation of chronological healing in mouse wounds compared to humans. Leonardi et al. suggested that data obtained between day 4 and in mouse would be more comparable to the initial stages of wound healing for humans (233). Therefore this study was focused on the inflammatory, proliferative and early remodelling phases of wound healing.

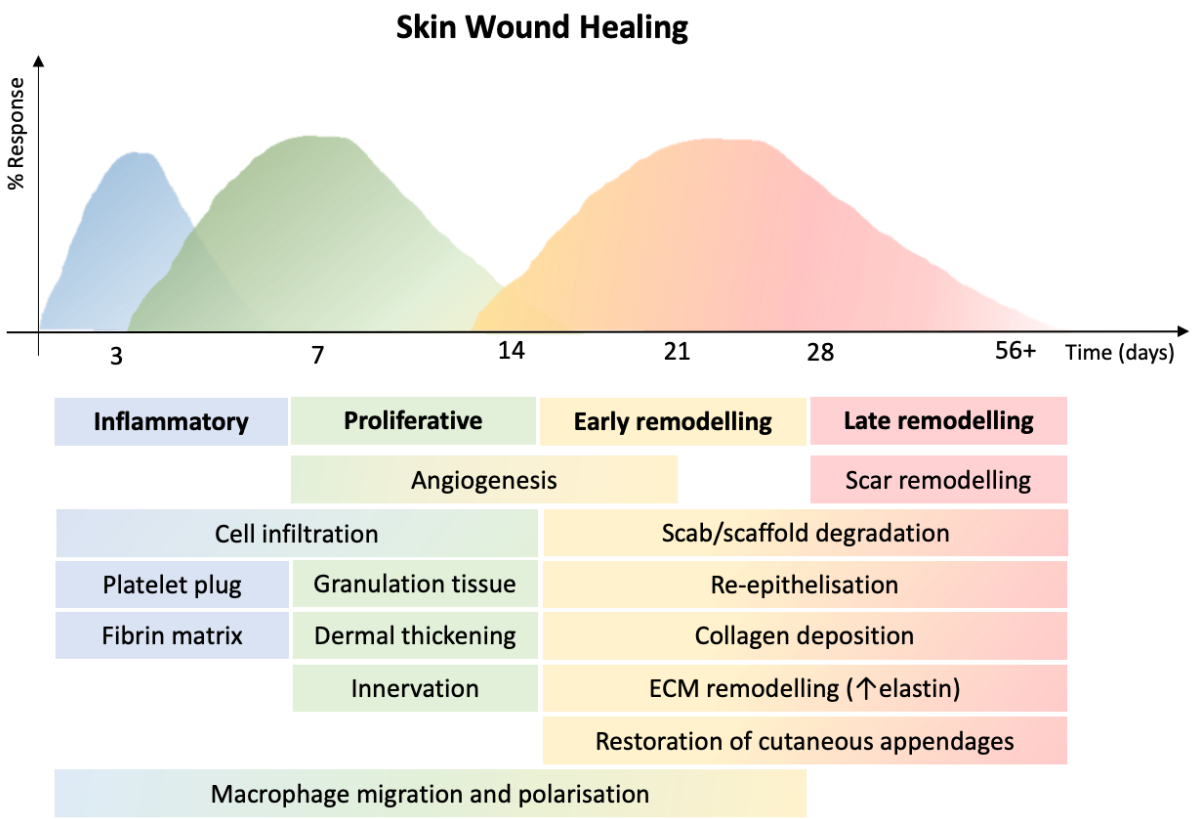

Figure 6-29 Phases of skin wound healing shown on a time scale graph. The key biological and physiological processes involve in each phase are listed under each heading, some of which would overlap with one another (214).

Multiple studies have shown that MSC, with or without scaffolds, can enhance wound healing and vascularisation (42,233,242,246,249,296,478,570,580–589). Walter et al.demonstrated that human bone marrow-derived MSC increased wound closure rate by increasing the *in vitro* migration of fibroblasts and keratinocytes (590). In a similar study to that proposed in this thesis, hypoxia pre-treated bone marrow-derived mesenchymal stem cells seeded in collagen-chitosan sponge showed accelerated wound closure via the reduction of inflammation and enhanced angiogenesis in diabetic rats with hindlimb ischemia (581). Though the results from the data were encouraging, there were a few discrepancies and issues noted between their study and this study: As Wistar rats were used they were not immunodeficient and hence are not suitable for xenographic transplant of cells due to the immune-mediated response. The wounds were not splinted, therefore contraction mediated wound closure via the panniculus carnosus layer will influence wound healing. This is important to note as in order to accurately replicate human wound healing in rodents, splinting is required so that the healing would be predominantly dependent on

epithelisation, cell proliferation and angiogenesis (388). Splinted models are also found to be more reproducible than non-splinted models (591).

From an *in vivo* angiogenesis perspective, it is evident that DH 21-1% conditioned adMSC seeded scaffold produced consistent pro-angiogenic results in both the *in vivo* CAM assay and murine models. Visually, the DH scaffolds showed greater erythema and bleeding around implant during the first week of healing. Bleeding into implants was also noted during the vascularisation process between day 6 and 10 by Später et al. (395) and can be a helpful indication of an active angiogenesis process taking place in the underlying wound. The same conditioning group also showed significantly better CAM tissue infiltration into the implant as well as improved rate of healing study's hypothesis that cells conditioned in DH environments produced factors that encouraged both neoangiogenic and tissue filtration, the two important parameters that can aid and accelerate wound healing. However, this wound healing effect was not found to be statistically significant.

SN 21% conditioned cells also showed mixed response in angiogenesis and wound healing. Whilst the vessel density data demonstrated that SN 21% scaffolds had a greater vascular infiltration than SH 1% and control samples, the wound healing rate was not found to be better than the control. Given this the typical culture condition for cells in most laboratories, the results serve as a good standard practice benchmark for comparative purposes to published data. Hence this finding was surprising given that most published literature have shown improved parameters. It is also quite challenging to explain why the SH 1% cells did not perform as well as the control acellular INTEGRA® for wound healing. The inferior, 'blighted' angiogenic response was previously noted in the CAM assay. This correlated with the lower vessel density in the INTEGRA® scaffold on the murine model observed in this conditioning group. CAM host tissue infiltration was also significantly reduced in the SH 1% seeded cells, which could perhaps explain the poor rate of healing seen in the murine wound healing parameters. It appears this is the global consequence of chronical hypoxia specific to transduced adMSC, affecting *in vivo* chemotaxis and angiogenic potential of the implanted INTEGRA® scaffold. There is some indication from the comparative hydrogel data that primary adMSC may response differently. But for reasons of cell availability, transduced adMSC cells lines had to be used for *in vivo* transplant.

Published paper on utilising hypoxia conditioning on seeded MSC show positive effect on wound healing and angiogenesis. However, most of these studies utilised 5% oxygen as hypoxia. One paper by Yusoff et al. incubated the cells in 1% oxygen but only for 24 hours (115). This regime replicates the DH 21-1% conditioning proposed in this study, and therefore not relevant to SH 1% cells. The chronic 1% hypoxia used in the study would likely have a negative impact on cell viability as alluded to in Chapter 4. The added cellular stress from the implantation to a harsh *in vivo* environment with limited supply of nutrients could have driven more cell death. This environment was replicated in hypoxic studies with an added serum deprivation component, which reported negative impact on cells (189,592,593). One paper by Change et al. reported 70% decrease in MSC survival when cultured in severe hypoxia (190). Another paper describes decrease in proliferation of murine adipose-derived MSC exposed to 1% hypoxia (594). But these data are not consistent was other papers describing the exact opposite findings (80,300,595–597). This significant discrepancy in literature was highlighted by Mazure and Pouyssegur (106). They saw autophagic cell death in extreme cellular stress conditions, such as severe hypoxic accompanied with nutritional restriction and metabolic stress, as a product of failed adaptation rather than HIF1a related mechanism. They also helpfully highlighted that different types of cells do not respond identically to hypoxia. This heterogeneity in reporting is problematic for hypoxic related research as data replication is near impossible due to extensive variability in cell types and hypoxic conditions used. It is likely that the increase in apoptotic material released by the non-viable cells could negatively impact on the angiogenic potential. However, this theory would require further molecular and histological evaluation to help shed more light on the metabolic state of these implanted cells.

All wound healing models rely on the final visual appearance of the wound as an important outcome measure. From a translational perspective, this is also the most clinically relevant parameter for physicians and patients. However, the evaluation of wound healing was particularly challenging, due to a multitude of factors. The major factor was issue around the INTEGRA® scaffold. This will be discussed further below. It is also important to note that in murine models, although the wound healing process can occur similarly to humans in terms of the overlapping relevant phases, there is known discrepancies such as shorter timescale to wound closure and key

differences in the anatomical, functional and immune processes involved which can impact on its relevance and applicability as a translatable *in vivo* wound healing model (216). Despite this, there are established modifications and adaptations which can be used. These include wound splinting and use of genetically modified mouse breed which can help to overcome some of these issues and to better re-capitulate the wound healing process in humans (216). However, great care still needs to be taken when interpreting the murine-based wound healing results on the basis of these known differences.

However, the data also questions whether enhanced neoangiogenesis is a prerequisite for regeneration of tissue, given acellular controls had better wound healing than seeded scaffolds with SN and SH cells. An et al. proposed that autophagy mediated paracrine of VEGF is crucial in MSC-related cutaneous wound healing, which may also provide a new therapeutic methodology for angiogenesis-related diseases (244). It is also possible that the inflammatory component has a greater influence on wound closure in the initial phases of wound healing. A crucial process in wound healing was not evaluated in this study. This was the identification of macrophage infiltration into the wound. Zomer et al. demonstrated that MSC can attenuate the inflammatory process by eliciting the polarisation of macrophages from the pro-inflammatory M1 to the regenerative M2 phenotype, which has been shown to enhance wound healing (249). These results support similar studies' findings that M2 macrophages positively influences tissue regeneration (598,599). Hence, further evaluation of macrophage phenotypes can be valuable in understanding these findings.

Choice of scaffold for *in vivo* model

An important limitation faced in this study with the use of the single-layer INTEGRA® matrix was the observation of poor integration to the wound site and a tendency for scabs to form with the INTEGRA® scaffold. This would obscure the view of the underlying wound and directly affect the accuracy of the wound measurements in some of the implant. Hence, it was necessary to test the integrity of the implant adherence on the wound site before the stereoscopic images were taken. However,

this posed a serious consideration to the compatibility of dermal scaffolds to the murine wound model, given the murine skin is much thinner in comparison (216).

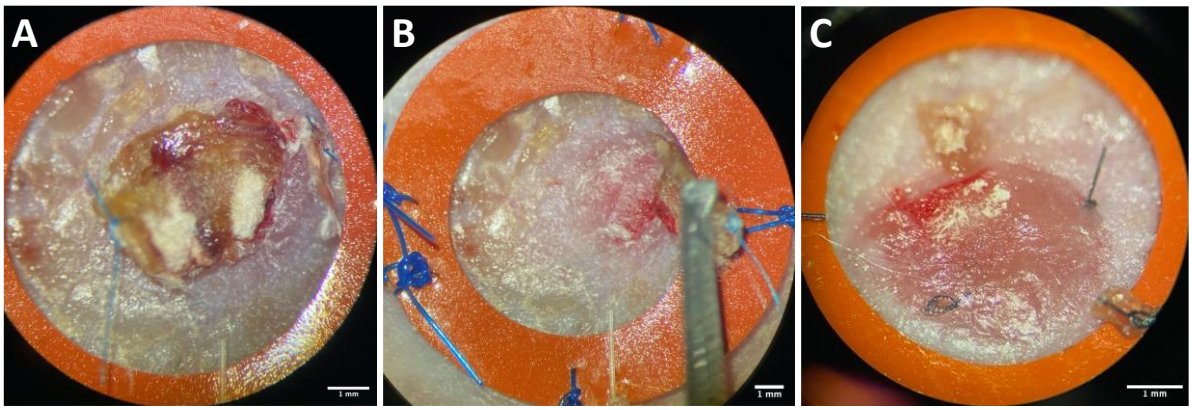

Figure 6-30 (A) Day 10 seeded (static 21%) INTEGRA® scaffold formed a scab. (B) The non-adherent INTEGRA® scab was lifted off and a smaller appearance of the underlying wound was seen. (C) By contrast, on another mouse, the day 10 seeded (static 21%) INTEGRA® scaffold showed more integration into the surrounding skin, with evidence of reepithelization, however the scar is noted to be hypertrophic in nature.

The same company also manufactures a two-layer dermal regeneration template which consists of a thin outer silicone layer, in addition to the same layer collagen-GAG matrix as used in this study. This outer layer acts theoretically as the epidermis which aims to protect the wound from infection as well as to function homeostatically to regulate temperature and moisture retention at the wound site. In the clinical setting, the silicone layer is removed at 2-3 weeks as a second stage procedure after the dermal layer is fully regenerated to allow for autologous epithelialisation. During the initial experimental planning, it was decided that the two-layer matrix was not suitable for this study due in part to the issue of having 2 staged procedures which would not be ideal for the time scale of this experiment, and also concerns around the silicone layer preventing epithelialisation of the wound which would obscure the wound healing process and downstream analysis. However, there is a consideration to whether the lack of the silicone layer would have contributed to the poor integration to the wound bed and the formation of scab seen in some of the wound sites leading to subsequent poor take of the grafts. This highlighted the need for regular wound observations and dressing changes to ensure the INTEGRA® scaffold was not exposed to risk of evaporation. Unfortunately, despite the regular dressing changes and varies modifications to dressings including full-body bandaging, some

mice were still agile enough to remove their dressings and or silicone rings within days and exposure of the scaffold to the air was not always preventable. Although this is not the first wound healing experiment performed in conjunction with the Yale University collaborators, the INTEGRA® scaffold use was a novel addition into the protocol. It was evident that some of the findings were confounded by issues with the INTEGRA® grafting properly onto the mice wounds after 7-10 days after implant. These issues prompted an in-depth discussion with the manufacturer's Research and Development department to explore if they have had similar experiences with their pre-clinical models. The discussion was proved valuable and provided useful insights for future modifications to help overcome specific experimental challenges: It transpired that the dressing over the wound was crucial, and use of a sponge layer over the occlusive dressing can help as an external pressure bandage and improve on graft integration and evaporation issues. In addition, the use of specialised 'no chew' bitter tasting vet dressings can also deter the animals from disturbing the wound area, particularly from disturbing the silicone splints.

However, problems with using these commercially available ADM for murine models is not isolated to our study. The issues with the use of INTEGRA® on nude mice was previously raised by Huang et al. (234). They found that the scaffolds were disproportionately thick and hard for use for wound healing in mice and hindered epithelial cell migration into the grafts after transplant. They overcame this by using their own processed ADM from sacrificed nude mice and seeded human cells with this matrix with success. Clinical review papers have also supported the use of decellularised skin and shown it to be more superior in performance compared to artificial cross-linked scaffolds, likely due to the 'like for like' nature of tissue replacement (223). Certainly, this form of scaffold should be considered for future cell seeded skin regeneration models. In addition, Truong et al. compared efficacy of four commercially available dermal scaffolds and process human cadaveric ADM on nude mice and found INTEGRA® to elicit the greatest inflammatory foreign body response (600). They also found similar results to this study with increased thickness of neodermis in wounds with dermal scaffolds. However, the significant of this to murine wound healing is unclear.

ADM products like INTEGRA® are purported to function as templates to assist skin regeneration. A measure of how much scarring is found in the healed wound treated with MSC seeded INTEGRA® scaffolds would be helpful to evaluate the inflammatory and immunomodulatory nature of the seeded cells and their ability to influence the scarring process.

In retrospect, it is possible that INTEGRA® is not a suitable matrix for cell seeding purposes for this angiogenesis study. From a clinical perspective, a hydrogel-like injectable ECM based scaffold which can conform into dead spaces in the body, from skin wounds to cartilage and bony defects may be a more suitable alternative scaffold (601,602). The same product could also function as ECM supportive carrier for therapeutic cell transplant and seeding purposes. It can also serve as an interface material between the scaffold, acting like a functional biological ‘glue’ between tissues and other solid organ transplants. Although there many papers published on the use of biomaterial such as fibrin, hyaluronic acid and alginate-based material, these are often too biomechanically simple and do not contain enough complex ECM to support the laborious task of regenerating tissue *in vivo*. There is increasing evidence that decellularised tissue is the most efficient biomaterial for clinical translational as it already contains all the native ECM required for cellular and tissue regeneration (603–605). Decellularised tissue can lyophilised into powder to be later reconstituted into hydrogels with numerous tissue engineering applications (601). In view of this, an attempt to develop a decellularise ECM hydrogel was made. For this pilot experiment, porcine-derived omentum was used. It was chosen because of its established clinical use as a surgical vascularised flap for *in vivo* vascularisation strategy, as well as for application to TE scaffolds (606,607). (See Chapter 1, section 1.5) The omentum was surgically harvested from pigs which were scheduled for culling at the Royal Veterinary College, Hawkshead campus, Hertfordshire. The decellularisation protocol was adapted from published papers from Porzionato et al. in Italy and Tal Dvir’s group in Israel (608–612). Lyophilisation of decellularised omentum and reconstitution to hydrogel of this decellularised tissue was done in collaboration with Molly Stevens’ group at Imperial College. Details of this can be seen in the Supplementary Figure 2. Due to time limitations, it was not possible to complete the characterisation of this omentum decellularised ECM hydrogel to allow

for use in this study. However, the preliminary data may help as a foundation for an interesting future research project.

Choice of animal wound model

Streptozotocin (STZ) is an antibiotic which has preferential cytotoxicity to pancreatic beta islet cells and can induce type 1 diabetes mellitus when administered in murine models. To reduce non-specific toxicity to other organs and tissues, the induction is normally carried out through multiple injections of low doses of STZ to cause repetitive low-grade beta islet cell damage (388). Low dose STZ protocol used in this study was adapted from two previously published protocols for mice (572,613). However, the process of STZ induced diabetes on the athymic mice can also be detrimental to their health. STZ-induced diabetic mice are known to suffer weight loss due metabolic disturbances secondary to insulin deficiency and severe hyperglycaemia (614). This was observed in this study (averaged 4.48% weight loss) and this can have varying degree of health consequence which is confounded by their immunocompromise state. On a small number of mice (3/24), significant distended abdomen from fluid accumulation (ascites) was observed at about 3 weeks post STZ induction (12-14 post-operative days). (Supplementary Figure 3) This was likely due to liver toxicity secondary to STZ induction (615). Only one of these mice died before the terminal endpoint of the study.

Athymic nude mice have been found to be advantageous as an animal model for xenographic transplants of human cells due to their immunosuppressed nature, their relatively low cost and ease of experimental repeatability (239). In addition, their hairless nature is extremely conducive to a wound healing model due to similarities of hair follicle density to humans as well as ease of experimentation without the need for repeated depilating. In this study, there were no control non-diabetic mice used to directly compare wound healing kinetics. Hence, it raises the question whether inducing diabetes on these nude mice would have any significant effect or influence on the wound healing potential of the mice. Looking at published comparison studies of different diabetic mice models and their associated wound healing potentials, it has been noted that murine wound closure rate is not significantly affected by STZ induction compared to non-diabetic controls (616,617). The most appropriate model

for studying diabetic related wound-healing was found to be in the modified type 2 diabetic (T2D) db/db mice (617). They demonstrate the most significant impairment in wound healing in all parameters, such as delay in wound closure, decreased granulation tissue formation, decreased wound bed vascularity, and significantly diminished proliferation compared to other well-accepted models. Unfortunately, db/db mice are immunocompetent and would not support xenographic (human) transplant experiments as such this study. In addition, there is a lack of commercially available immune-deficient or humanised type 2 diabetic mice breeds. The closest readily available diabetic prone mouse breed was the NOD SCID mouse, which still require STZ injections to induce diabetes, which would be more type 1 in nature (618). Another feasible way to accurately model the delayed wound healing response for this study would be to first adopt a suitable immune-deficient mouse breed and then chemically induce diabetes as above. It has been shown that high fat diet can bring about hyperinsulinemia, insulin resistance and glucose intolerance which if followed by a low dose injection of STZ to reduce functional β-cell mass can induce similar pathophysiology seen in T2D (619–622). However, a systemic review into mouse models of diabetes-associated ulcers appear to show that STZ or high fat diet regimes do not produce significant impairment in wound healing compared to established diabetic prone mouse breed such as db/db (623). Therefore, it is clear that there is still much optimisation and refinement needed to determine a suitable diabetic wound healing model/protocol which will be equally appropriate for evaluating xenographic transplantations. Unfortunately, data around this is still lacking in published literature, so any future studies would require a substantial amount of time validating and comparing against established models.

Tracking of transplanted cells *in vivo*

It is generally accepted that implanted cells do not survive for long within the scaffold. Cherubino et al. seeded human adMSC within INTEGRA® scaffold and grafted the construct onto mice and found no evidence on immunohistochemistry of human cells within the scaffold after 30 days of implant (239). Their eventual disappearance soon after engraftment show the implanted cells to be initiators of repair rather than effectors. The principle aim of seeding MSC is not therefore to ensure survival and differentiation into desired end-point cells types, but instead to utilise them as

intuitive, bioactive paracrine factories; to sense and release the necessary cytokines and growth factors according to their microenvironment. The fact that the cells have a relatively short lifespan also plays to the advantage of clinical safety concerns with possible neoplastic transformation of stem cells (42,624–626).

One of the most significant limitation and challenge experience in this study was the lack of access to a working *in vivo* bioluminescence during the *in vivo* experiments. As previously shown as a pilot proof-of-concept experiment in the *ex ovo* CAM experiments, it was possible to use the chemiluminescence detecting machine to observe for bioluminescence readings from cellular scaffolds implanted on the CAM surface. Hence, as a last resort, the same technology was unconventionally accessed for the monitoring transduced MSC transplanted on the mice. Briefly, the mouse was anaesthetised with a mix of 1 ml ketamine (Ketaset,100mg/ml) with 0.5 ml xylazine (Anased, 20mg/ml) diluted with 8.5 ml sterile saline solution. This solution was injected at a dose of 0.1 ml/10g bodyweight. D-Luciferin was injected intra-peritoneum using a 30G insulin needle and allowed to circulate for at least 30 minutes prior to detection. The anaesthetised animal was placed in the chemiluminescence machine (Syngene G:BOX Chemi XX9) with a measurement protocol set at 2 minutes cumulative integration time. (see Supplementary Figure 4)

However, due to issues with validating the methodology against the industry standard, as well as problems with standardisation of the measurement parameters for *in vivo* imaging, the images captured was not used for further quantitative analysis. Nevertheless, it was interesting to observe the presence of viable, metabolically active cells days after post-implantation through the access to this system. This imaging was performed on 9 mice at 2 or 3 timepoints. We found that cells were still viable and detectable at post-operative day 14 of transplant. (see Supplementary Figure 5) There was clear evidence of cell migration away from the seeded wound/scaffold site to other superficial anatomical areas on the mouse. Cell migration may be through the lymphatic channels as the anatomical sites of these bioluminescence cells resemble lymph nodes. It would be interesting to evaluate the migration of cells and homing sites further by tracking them in more detail using dedicated *in vivo* bioluminescence imaging, as well as performing histological

sampling of these ‘hot spots’ sites. Extended longitudinal monitoring will also allow for greater understanding on the viability of cells post-transplantation.

6.3.3.1 Study limitations

Further histological identification of the infiltrating host cells such as endothelial cells and inflammatory infiltrates, particularly macrophages, into the wounded area via appropriate immunohistological staining would also help in the comprehensive evaluation of the wound healing process. Interrogation of wound ECM would also greatly benefit the evaluation of early remodelling changes in the different seeded scaffold groups. Unfortunately, due to time and resource limitations in the study, these analyses were not performed in time for inclusion in the thesis. However, the importance of procuring this data should encourage the future completion of these experiments so that evidence of comparative changes in cellular mechanism and ECM remodelling can be accounted for.

It is important to note that several limitations experienced in this assay was mainly due to time constraints and unforeseen circumstances during COVID-19. This was also complicated by having to perform some experiments at an external overseas location (Yale University) as part of a collaborative exchange programme. To ensure relatable and comparable results with minimal variability in the *in vitro* angiogenesis assays and *in vivo* experiments, it was important that the conditioned media was collected from the seeded INTEGRA® scaffolds that would be transplanted into the *in vivo* animal models. These experiments were concentrated into a very tight time frame of less than three months with little room for error. Unfortunately, as with most cell culture experiments, it was not immune to contaminations and infected cell samples, which added greater to the workload and time needed to repeat and complete the experiments within a set timeframe.

Different lab facilities and access issues also meant that certain core equipment, such *in vivo* bioluminescence imaging machine, were not accessible. Alterative equipment had to be sourced using very creative and ingenious means in order to minimise the impact of facility problems on research output. Nevertheless, this has

meant that some of the data were not sufficiency high impact for conclusive statistically significant results due to the time constraints on the ability to perform enough experimental repeats. Hence, promising *in vitro* and *in vivo* experiments were unduly compromised in their output. In addition, due to unforeseen circumstances around shipment of samples back to UCL, the samples were irretrievable for further molecular or immunohistological analysis on the explanted scaffold as one had hoped.

6.3.4 Method Modification/Future works

Given the uncertainty around the most appropriate diabetic wound model to use as discussed above, confounded by the ambiguity around the degree of relevance of functional angiogenesis within such models, other alternative wound healing models were sought and tested for feasibility. This is discussed in further detail in Appendix section 9.2. The use of latest imaging devices to monitor vascularisation is key to longitudinal evaluation of ischaemic wounds and can help dramatically improve quantification of therapeutic angiogenesis *in vivo* and play a crucial role in producing quality reproducible data. Therefore, their inclusion in future study designs cannot be understated. Hence, Appendix section 9.3 also discussed imaging devices which were tested for feasibility.

6.4 Conclusion

As per published literature, there is clearly a role in the use of adMSC to 'bioactivate' tissue engineered scaffolds in order to enhance the regenerative potential (59). In this *in vivo* study, DH 21-1% conditioned adMSC scaffolds showed enhanced angiogenesis in the CAM and wounds models. It also demonstrated an increase rate of wound healing. However, the implantation of INTEGRA® seeded with cells pre-conditioned in either SN 21% or SH 1% did not show consistent results across the in vitro and *in vivo* experiments. SH 1% seeded cells appeared to negatively impact on wound closure compared to control acellular scaffold. Mechanism around cellular input to wound healing is still largely unclear. The data shows that the INTEGRA®

scaffold is highly biocompatible and elicits the necessary wound healing response *in vivo*, much to the manufacturer's achievements. However, the data also questions whether enhanced neoangiogenesis is a necessary prerequisite for regeneration of tissue, given acellular controls had better wound healing than seeded scaffolds with SN and SH cells. There is likely an inflammatory component which has a greater influence on wound closure. The compatibility issues of INTEGRA® as a scaffold as well as other methodological issues around the *in vivo* model and incomplete histological data is likely to have affected the inconclusive nature of the findings. To increase the relevance of the *in vivo* model for more conclusive outcomes on the effect of MSC, an alternative model with predominantly ischaemic component, as well as alternative scaffolds were discussed. The piloting of suggested improvements revealed that the bipedicle ischaemic wound model was the most feasible alternative to the splint wound model for this study. The studies in the thesis confirm the importance of access to advancing and innovative technology and how that can assist high-yield research output. The pilot use of innovative imaging technologies was carried out and the practicalities around their use was discussed to better understand the pros and cons of use. Careful selection of collaborators and detailed grant application for appropriate costing to access the latest technology in the field is highly important.

Despite the many experimental challenges which confronted in this study, the experience facilitated the identification of potential areas of improvements and opened the platform for the in-depth discussion of possible solutions to help circumvent these challenges. The adoption of the forementioned improvements to future study designs, in conjunction with access to the novel *in vivo* imaging technology, will undoubtedly help improve the quality of the research outcomes. It will also help produce more clinically relevant and translatable data to help increase understanding and progression in this field of research.

7 Final Discussion & Future Perspective

The understanding that oxygen levels can have a potent effect on the biological functions of cells formed the basis of the hypoxic pre-activation hypothesis used in this study. We demonstrated through the simple manipulation of MSC oxygen culture conditions can help to trigger a hypoxic induced response which would enhance the pro-angiogenic ability of seeded MSC within the scaffold. Even though our data consistently showed that dynamic hypoxic (DH) conditioning increases the angiogenic potential of adMSC *in vitro*, the *in vivo* effects were more variable.

<u>MSC optimisation – a challenging process:</u>

The initial optimisation steps with the interrogation of the three most commonly used MSC for pre-clinical research, bmMSC, ucMSC and adMSC, found that hypoxia did not uniformly affect the MSC in the same manner. adMSC was found to be the most suitable candidate for angiogenic and translational purposes. However, this discovery was not always consistent with published research and posed significant issues with the comparative outcomes of MSC irrespective of their tissue origin. An added appreciation of their native tissue oxygen levels helped to offer further insight into the discrepancies with their cellular response to varying oxygen levels. We also noted a change in the therapeutic efficacy of MSC in 2D and 3D environments. Changing from a simple 3D collagen gel to a more complex porous tissue-engineered dermal scaffold (INTEGRA®) altered the *in vivo* response further. Some of the results were unexpected, which can only be explained by the difficulties faced by the increasing complexity of experiments and unforeseen complications in the methodological process. The use of genetically modified cell lines also demonstrated deviations in response to hypoxia. Nevertheless, DH seems to consistently improve the pro-angiogenic nature of adMSC when compared to other control oxygen conditions.

Through this process of optimisation MSC on TE scaffolds, our understanding the cellular physiology in certain cultured environments was greatly enhanced. We appreciated the stem cell niche is highly sensitive to change and conserving and accounting for every alteration was paramount. This is because a small change in the

microenvironment, from the seeding vessel to scaffold storage conditions and media used, can all significantly affect their cellular response. Unfortunately, some of these highly sensitive parameters were only accounted for after an initial period of optimisation. This protracted optimisation process invariably impacted the time constraints which affected later experiments. Hence, this study highlighted the level of complexity involved in the refining and optimisation of translational regenerative medicine research. This is important to appreciate as reproducibility and repeatability of the experiments are critical for translational purposes. Therefore, good quality research data in cell-based tissue engineering are always hard to attain in that respect, largely due to difficulties with maintaining consistency across the myriad of factors.

Translatability of pre-clinical data:

As I consolidate my data on the cellular effect on tissue regeneration and angiogenesis, it is apparent that cells don't always produce the expected pre-clinical data, with huge variations in outcomes seen. This contributed to some of the non-significant findings. As mentioned, this could largely be due to the heterogeneity of cell populations and variation in their secretome profiles, as reported by other studies (316). But it is also becoming increasingly clear from other researchers that cellular behaviour is highly unpredictable once transplanted *in vivo*. I was particularly frustrated with the non-cohesive findings between the *in vitro* and *in vivo* experiments. This is mainly due to unforeseen factors and levels of uncertainties affecting the performance of cells once *in vivo*. This variable nature of their cellular response along with the lack of jurisdiction over the cell's microenvironment once cells are transplanted *in vivo* can be incredibly disconcerting to the conscientious researcher or clinician attempting to translate the cells to the clinical setting.

Further limitations on *in vivo* interrogation between the interplay and crosstalk biological agents, such as cells and their paracrine functions, makes for a very challenging discussion as well. We were less able to differentiate between the individual processes required for finetuning and control. Hence this 'blindness' to the *in vivo* processes can significantly affect how accurately the *in vitro* conditions can be replicated for further evaluation of the processes.

Although it is possible to conclude that MSC shows great potential in regenerative therapy, the uncertainty and potential unreliability of the product once *in vivo* would likely hinder the translatability to clinical use. Limitations such as poor survival, limited differentiation, and uncertainty around de-differentiation of cells with passaging and donor site morbidity affect translational cell use (654). Until we find a universally compatible cell type that can be used 'off-the-shelf', it is likely that the optimisation and validation process to ensure that it is GMP compliant would be a very burdened process due to the uncertainty observed in this study with cell use (655).

Study limitations and challenges:

Due to limited time and resources as well as unforeseen circumstances from changes to scaffold focus to the Covid-19 pandemic, this study has faced several significant challenges throughout its lifetime, which has undoubtedly led to compromises in the level of research output. Extenuating events included Covid and Brexit-related delivery issues, mycoplasma infection of external collaborator's cells, and global stock issues with research items due to the global pandemic. The other challenges were less mitigating and more circumstantial, such as the limited expertise available from being in a small and isolated research group with little access to critical mass know-hows, the unexpected loss lab and office space from non-Covid and Covid related reasons and delays in exchange programme due to visa issues. All of these have impacted to varying degrees the overall research experience and the execution of the research design.

Where are we now with MSC-based therapy?

After more than two decades worth of MSC research, a major question remains on whether MSC therapy can result in tangible clinical benefit. Without any suitable optimisation or manipulation, MSC are not expected to achieve significant therapeutic efficacy due to their poor survival and limited paracrine activity post-transplantation. The therapeutic efficacy largely depends upon the number of cells, how the cells are administered, any prior pre-activation of specific cellular functions and the condition

they are proposed to treat (59,367,656). Hence it is imperative that MSC survival is optimised for transplantation in order to enhance therapeutic outcomes in treated patients.

Due to the ongoing challenges to the translatability of MSC preclinical outcomes as discussed above, there is much debate around the uncertain equivalency in human clinical trials. One paper describes this ‘cognitive dissonance’ between pre-clinical and clinical trial outcomes (657). This was thought to result from apparent discrepancies in immune compatibility, dosing, and fitness of culture-adapted MSC between data from murine and human subjects (657). In that respect, there is still some distance to go before there is absolute certainty in the therapeutic benefits of MSC administration in humans.

Future perspectives – towards cell-free approaches:

To overcome the unpredictability of cell-based therapies, it may be necessary to seek alternative cell-free therapeutic solutions which offer more consistent and predictable outcomes. Recently, there is growing evidence to suggest that bioactivity originates from factors released from cells which are contained within their *in vitro* conditioned media (CM). Secretomes contained within conditioned media from MSC have been consistently shown to provide therapeutic benefits to many degenerative diseases and traumatic injuries (658).

Secretomes consist of soluble factors such as cytokines, chemokines and growth factors, and insoluble nano/microscopic extracellular vesicles (EV). The International Society for Extracellular Vesicles describes EV as particles with a lipid bilayer, that are naturally released from the cells and cannot replicate (659). EV are extruded from cells as microvesicles or exosomes, depending on the size of vesicles, exosomes being the smallest of them. They contain nucleic acids, proteins and lipids from cells and act as important mediators for intracellular crosstalk, which is seen as a key advantage over soluble secretomes (660). The most abundant of these are exosomes, which have a diameter of 40–100 nm, and can be isolated by well-described centrifugation methods (661,662). Exosomes are known to regulate

intracellular signal transduction by delivering proteins, mRNA, and microRNA (miRNA) to targeting cells and tissues (663).

The use of these secretomes and isolated EV have demonstrated comparable effects to that of ‘whole-cell’ MSC therapy. Exosomes from human MSC have been shown to contain immunoregulatory miRNAs and immunomodulatory proteins to inflammatory immune cells (M1 macrophages, dendritic cells, CD4+Th1 and Th17 cells), altering their activity and differentiation (664). There is also an increasing body of evidence to support the use of MSC secretomes in wound healing (665). The application of these secretomes have been shown to accelerate wound healing due to their growth factors, particularly VEGF and PDGF (42,589). Furthermore, it is generally understood that the cellular origin of EV significantly moderates their biological function (666–669). Hence, manipulation of the microenvironment and physiological state of cells, such as through hypoxic pre-conditioning, can influence the EV contents and their biological functions. Mao et al. evaluated the use of EV from hypoxic pre-conditioned MSC (MSC-EV) to enhance the survival of other cell types of interest such as cardiomyocytes. Hypoxia pre-conditioning was shown to enhance and strengthen the tolerance and adaptability of cardiomyocytes to an anoxic environment, inflammation, and oxidative stress (670). Zhang and colleagues also showed improved chondrocyte proliferation and migration and greater suppression of chondrocyte apoptosis with hypoxia-preconditioned MSC-EV compared to normoxia-preconditioned MSC-EV. These changes were detectable in the microRNA expressed by hypoxia-preconditioned MSC-EV (671). In fact, the first clinical application demonstrating the feasibility of secretomes from MSC was derived from hypoxic pre-conditioned MSC for the management of severe COVID-19 patients in Indonesia (669). The preliminary results reported promising changes to the clinical outcomes with a reduction in excessive pro-inflammatory cytokine storm activity as well as improved lung injury parameters.

Research into EV has gained a lot of attention in recent years due to its unique therapeutic and diagnostic potential (664,670–675). They are also able to circumvent many of the challenges of cell-based therapies, such as versatility of use, lower risks associated with the administration step, and the avoidance of cell-fate control and any potential risk of tumorigenesis (660). Being nanoparticles, exosomes can avoid

the problems associated with the transfer of mutated or damaged DNA, immunological rejection, and avoid the first-pass effect (lodging in capillaries of lungs, liver, kidneys) that is associated with systemic MSC administration (672). Genetically modified MSC can also be used to produce specific secretomes for therapeutic purposes (57). In fact, vesicle content themselves can also be genetically modified for optimal therapeutic affinity (676). Exosomes are also released mainly by healthy cells, which makes them self-selecting in terms of the quality of content and predictability of action (677–679). Hence, they can act as potent biological carriers for therapeutic agents. Almost all cells have the potential to release EV. As MSC have an excellent capacity for proliferation, they have the potential to produce a large quantity of EV (674). EV contains specific markers which have helped with the isolation and extraction from the extracellular space (680). The development of a liposomal format of therapeutic exosome content will likely result in an effective, standardised, safe and relatively inexpensive preparation which can have a long and stable self-life (681). Hence, EV products are much more amenable to the Good Manufacturing Practice (GMP) compliant large-scale production compared to cellular therapy (662). All in all, EV therapy offers a significant safety and regulatory advantage over stem cells from a translational point of view (662).

Considering these advantageous properties, the future of therapeutic angiogenesis is likely to lie in the combination of custom pre-conditioned MSC-EV products with bespoke TE scaffolds for regenerative purposes.

8 Supplementary

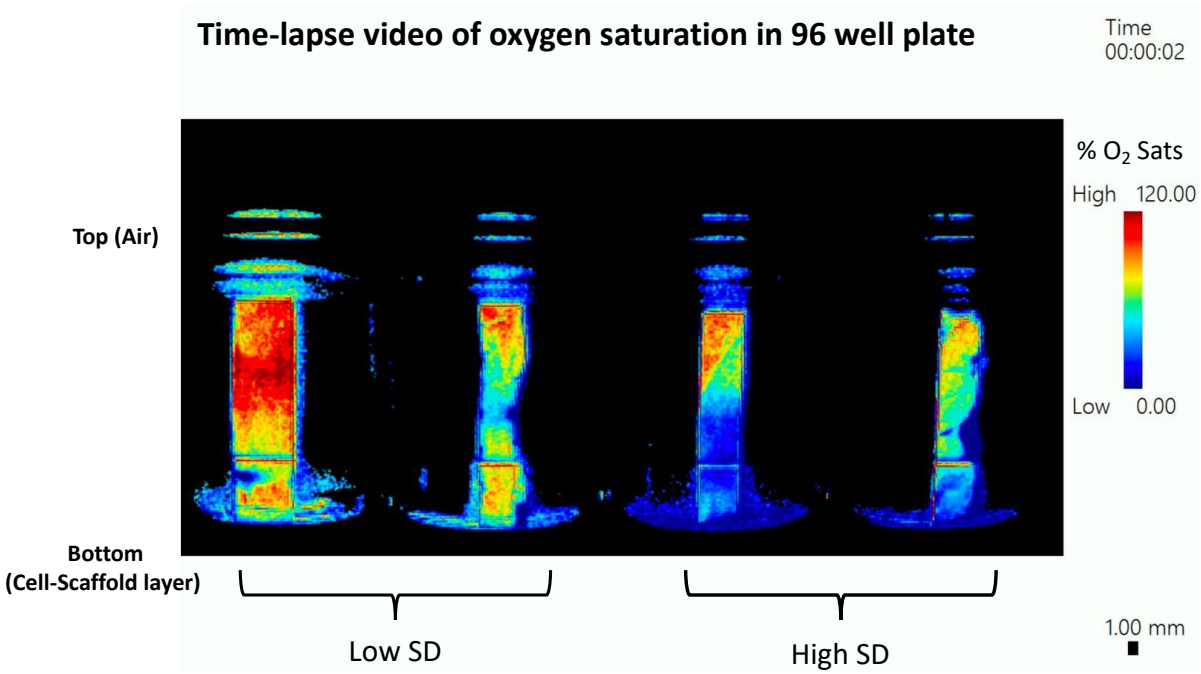

Supplementary Figure 1: Annotated screen capture of time-lapse video using VisiSen imaging to compare oxygen levels of 96 wells over time in high and low seeding density of cells seeded on INTEGRA® scaffold. Supplementary video link here: http://bit.ly/3xjZyTu

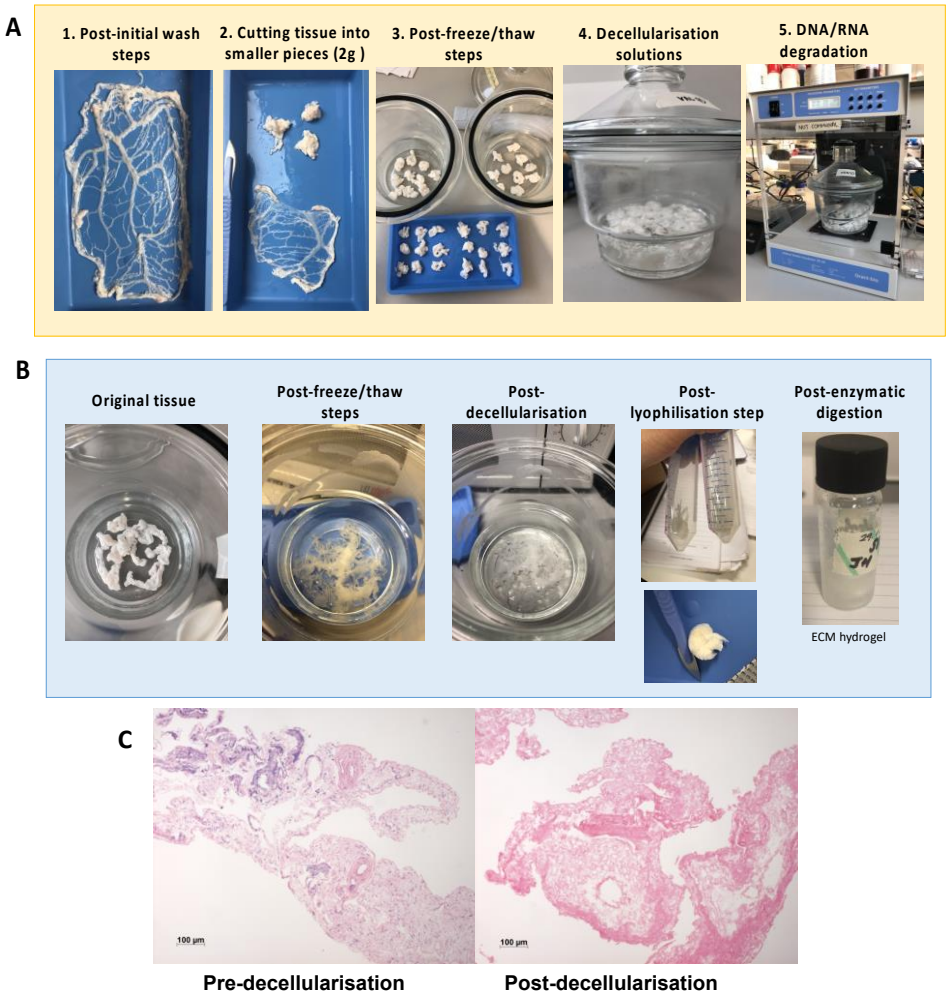

D

Steps	Duration	Temp	Day
Collection, PBS wash **+ A/A 1%**, Hypotonic solution	<24 hours	4	1
Freeze step I	Until ready	-80	1
Thaw step I in Hypotonic solution		RT	2
Freeze/Thaw II in Hypotonic solution		-80/RT	2
Freeze/Thaw III in Hypotonic solution		-80/RT	2-3
Dehydration (70%; 100%)	30mins; 30mins	RT	3
Lipid extraction (Acetone)	3x 30mins	RT	3
Lipid extraction (60/40 Hexane: Acetone)	24 hours (3x changes)	RT	3-4
Rehydration (100%; 70%)	30mins; ON	4 ON	4-5
PBS wash (pH 7.4) **+ A/A 1%**	4x 30mins	RT	5
Cell extraction I (1% SDC) in 50mM Tris COMBINE WITH 1% Triton X	ON	4 ON	5/6
PBS wash with 1.5M NaCl (Hypertonic solution) **+ A/A 1%**	24 hours (3x changes)	4 ON	6/7
Nuclear degradation (DNAse/RNAse) in HBSS ++	20-24 hours	37	7
PBS wash **+ A/A 1%**	3x 30mins	RT	8
Double distilled water wash	3x 20mins	RT	8
Sterilisation step – approx 2 hrs			
Freeze in -20 or -80	Until ready for Freeze-dry/Lyophilising	-	8
Lyophilisation + Mill to powder	48-72 hours	RT	9
Enzyme digestion with pepsin	96 hours	RT	12

Equipment

- Glass containers 500ML – 1L
- Glass bottles 500ML – 1L
- 50ml falcon tubes (CLS430829-500EA)
- Sterile forceps
- -20 freeze space (for tissue storage post-lyophilisation)
- -80 freezer space (for freeze/thaw steps and storage)
- 4 degrees fridge (for overnight decellularization steps)
- Autoclave
- Freeze dryer
- Orbital shaker/Roller
- Magnetic stirrer
- 37 degrees incubator (for DNAse/RNAse step)
- Fume hood
- Biological Safety Cabinet hood (for sterilisation steps)
- Freeze-drier
- Wiley Mini-Mill (Thomas Scientific)

Reagents

- PBS Solution
- HBSS Solution
- Antibiotic Antimycotic Solution (100×) (A5955)
- Tris-HCl
- Tris-Base
- EDTA
- Ethanol (70%, 100%)
- Acetone
- Hexane
- SDC
- Triton X100
- RNase
- DNase
- Hypotonic Buffer Solution (10 x 10−3 mM Tris, 5 x 10−3 mM EDTA, pH 8)
- Hypertonic solution (1.5 m NaCl)
- Tris-HCl (Sigma), Tris-Basic (Sigma)
- EDTA (Sigma)
- Deionised millipore water
- Vacuum filter flask 22um
- Pepsin (Sigma-Aldrich, 4000 U mg-1)
- 5M NaOH

(To prepare 500mL Hypotonic Buffer solution: 100mL 0.05M Tris stock solution + 5mL 0.5M EDTA stock solution + 395mL Millipore water)

Supplementary Figure 2: Omentum decellularisation pilot study. (A) Decellularisation steps illustrated in photos. (B) Gross tissue changes through the decellularisation protocol. (C) H&E staining of omentum

pre and post decellularisation, demonstrating complete microscopic removal of cellular nuclei (D)Table of steps used in the decellularisation protocol and list of experimental materials.

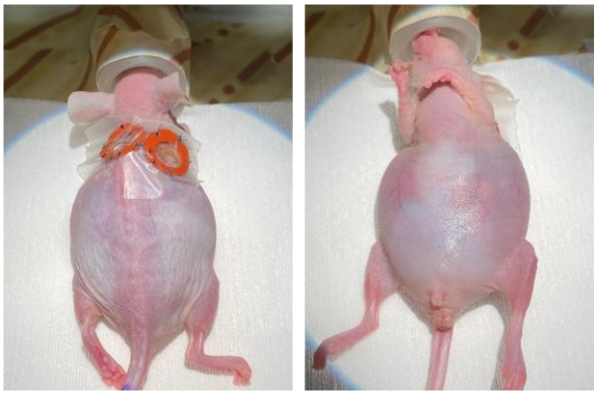

Supplementary Figure 3: Highly distended abdomen featuring profound ascites (build-up of fluid in the abdominal cavity) in one of the STZ induced diabetic athymic mice at post-operative day (POD) 12. The exact cause of this is unknown, but it is likely to relate to sensitivity to STZ toxicity. Such presentation would fulfil the humane endpoint criteria which would trigger early termination and euthanasia of the animal.

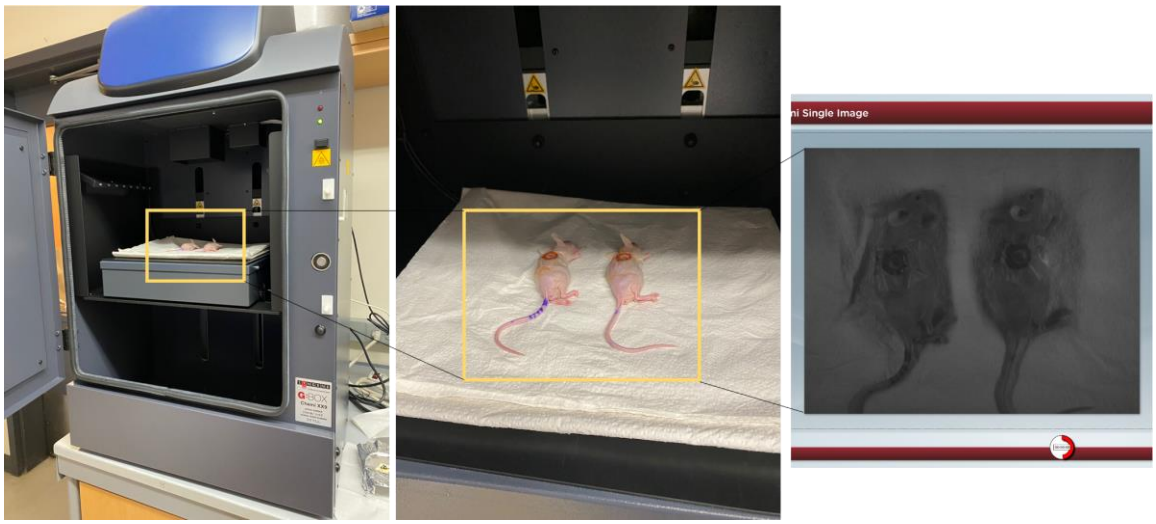

Supplementary Figure 4: Images showing the unconventional use of a chemiluminescence imaging system to observe for viable transplanted transduced adMSC.

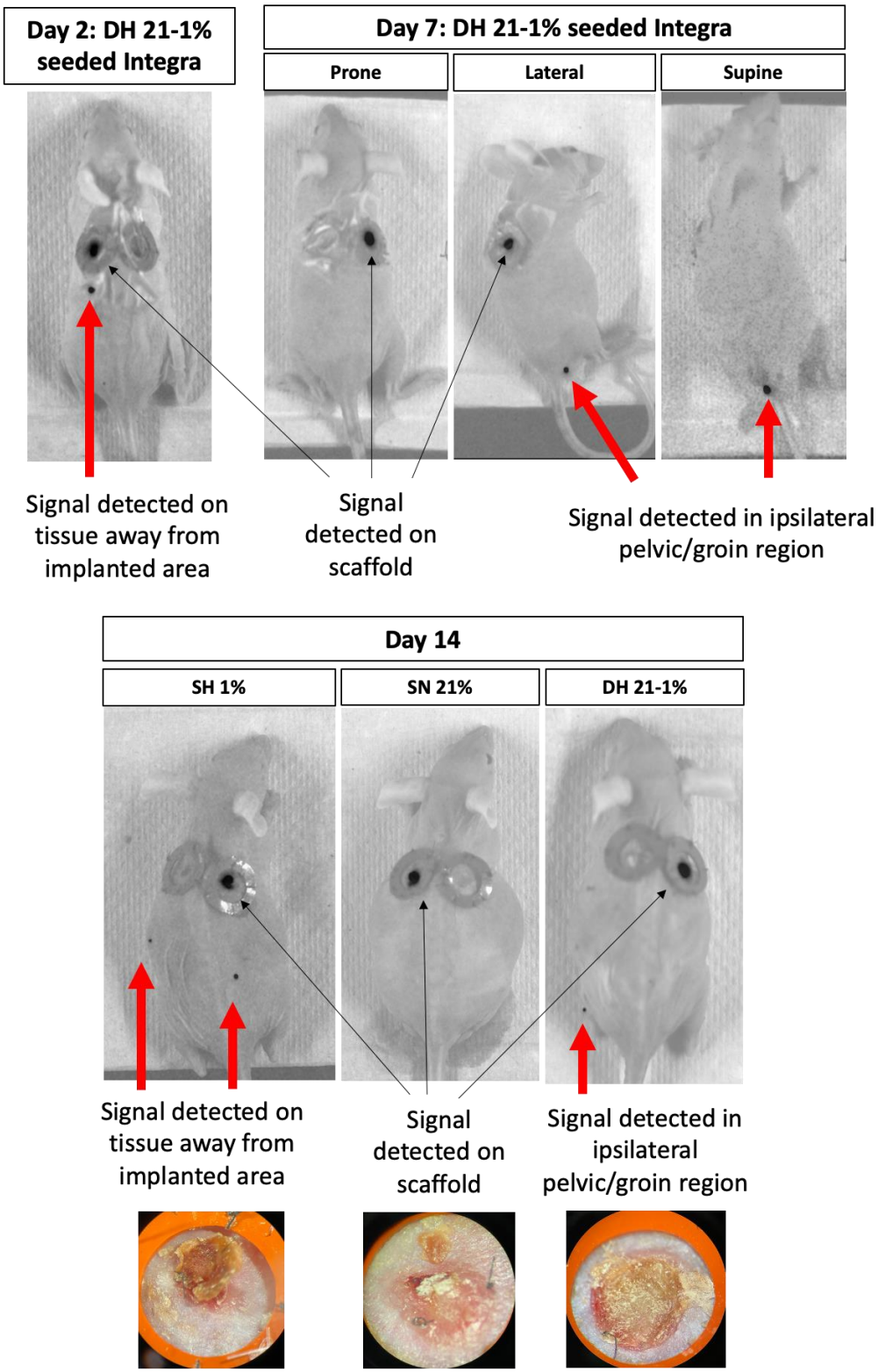

Supplementary Figure 5: Images of bioluminescence detected from transduced adMSC seeded on INTEGRA® scaffold at different timepoints. Signal outside of the transplanted scaffold/wound site were noted. In POD 7, one of the mouse detected signal in a distant groin site, indicating that the cells were able to migrate away of the transplanted scaffold to other regions of the body and remain viable. For final POD 14, side by side comparison of different oxygen conditions showing bioluminescence signals from wound site and respective are shown.

9 Appendix

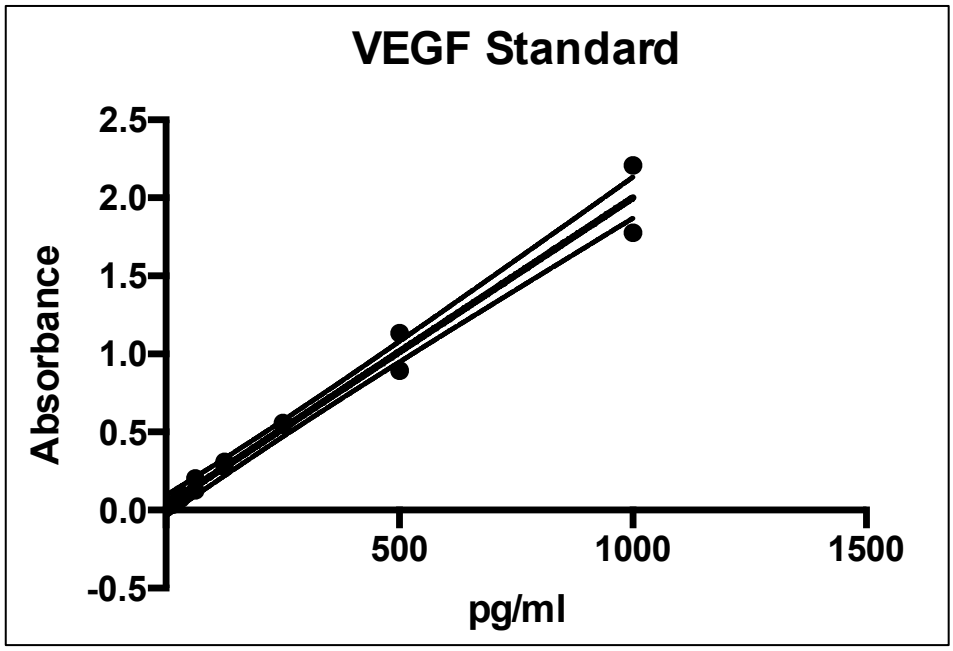

Appendix Figure 6: Standard curve for ELISA VEGF assay.

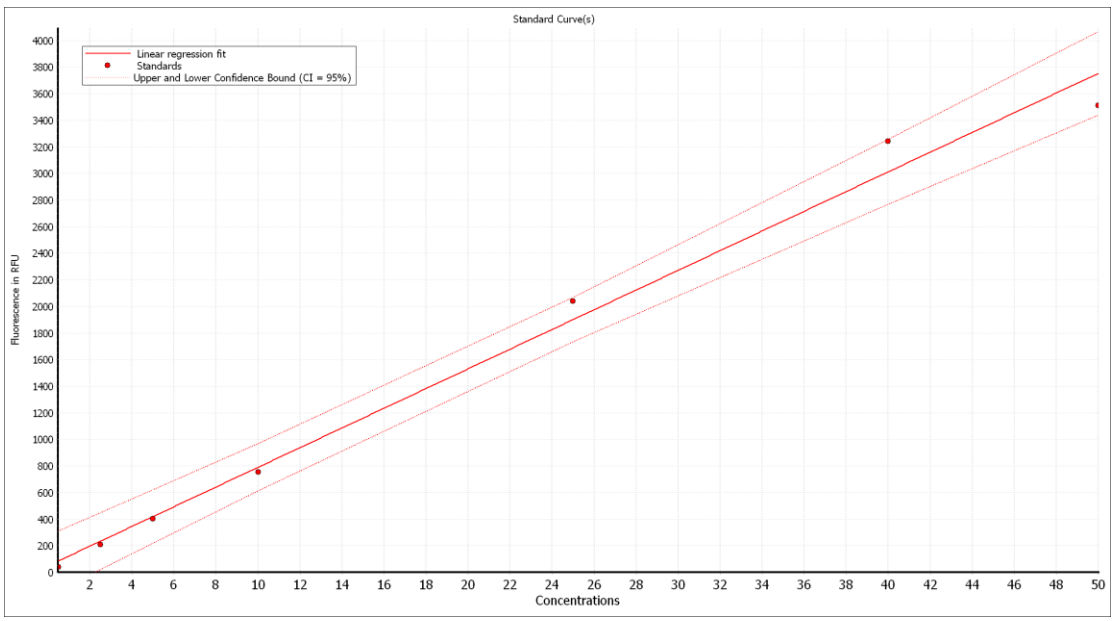

Appendix Figure 7: Standard curve for PicoGreen dsDNA quantitation. Linear regression curve equation: Y = 74.07 * X + 49.50; R^2 = 0.990.

Primer	F’	R’
GAPDH	GCTCTCTGCTCCTCCTGTTC	CGACCAAATCCGTTGACTCC
VEGF	GCCTTGCCTTGCTGCTCTAC	GAAGATGTCCACCAGGGTCTCG
HIF1a	CCAGCAGACTCAAATACAAGAACC	TGTGGGTAGGAGATGGAGATGC

Appendix Figure 8: A table of primer sets used to conduct gene expression using qPCR. Abbreviations: F, Forward (5’-3’); R, Reverse (3’-5’)

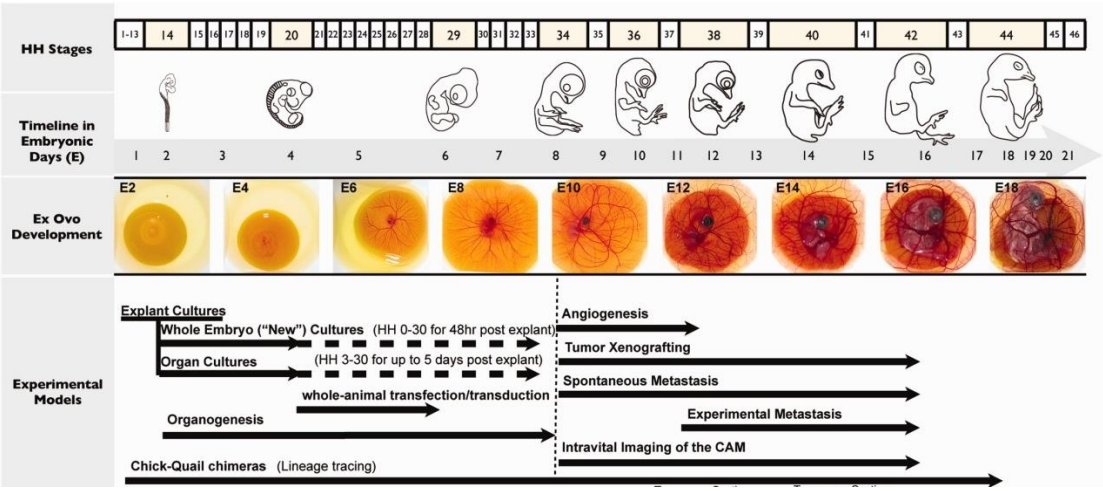

Appendix Figure 9: Chick embryo staging and the experimental timeline with Hamburger–Hamilton (HH) stages for referencing, as published by Kain et al., reproduced with licensed permission from Wiley Materials and Copyright Clearance Centre (683). Chick embryos were only carried until E14 of development in this thesis’ study.

9.1 Pilot feasibility results: *Ex ovo* CAM assay

To overcome the issue of limited access and visibility of implant in an *in ovo* CAM model, *ex ovo* techniques have been described. This system has several advantages: the accessibility of the embryo is greatly improved outside of the shell and is much more amenable to live imaging than *in ovo* techniques; it is also a more preferred technique compared to the *in vivo* system as it allows the quantification of the response over a wider area of the CAM and benefits from being able to test a large number of samples and conditions in one chick embryo (501). Therefore, biological inter-variability can be reduced, and the time required for gathering adequate results is generally shorter. However, long-term viability is often lower in the *ex ovo* system, mainly due to the embryo being at risk of drying out or reduced temperatures due to the shell-less environment.

Variations of this method have been described extensively in published literature (492,510,533–539). The *ex ovo* technique used here was adapted to the cling-film method described by Schomann et al., Kohli et al. and most recently by García-Gareta et al. due to the reported higher survivable rates of the embryos (534,536,537). The method draws parallels with the *in ovo* method up to day 3 of incubation. Fertilised White Leghorn chicken eggs were obtained from Henry Stewart & Co. Ltd (Norfolk, UK) and kept in a specialised incubator (Ova-Easy Advance Series II with humidity pump; Brinsea, UK) at 37°C in a humidified atmosphere (>60% relative humidity). After 3 days, the embryos were transferred to a shell-less culture system consisting of a glass–cling film set-up. Everything from this stage would be performed in a sterile hood with a warmed heat mat set at 38°C. Briefly, glass cups of 8 cm diameter (#1017AB06, Duralex Gigogne 22cl, France) were autoclaved and filled up to three-quarters with sterile water, and then a clean cling film layer (sterilised with 70% ethanol and left to dry) was placed inside the glasses with the bottom of the cling film floating on the top of the pre-warmed water. 1ml of 1% penicillin-streptomycin (diluted with sterile water) was added to the cling film. Eggs were wiped clean with 70% ethanol and then cracked open against the sharp edge of a triangular block, and the contents were transferred swiftly and carefully to the glass-cling film set-up. Viability was confirmed from visualisation of the embryo's

heartbeat within the egg yolk. The glasses were then covered with a 10 cm petri dish and transferred to a CO_2 incubator until E8 at 38°C in 80%–90% humidity and 2% CO_2. The viability of the embryo was checked on a daily basis. At day 8 of incubation, the relevant scaffolds with or without cells are implanted into the CAM in the same manner as the *in ovo* CAM. On day 14 of incubation, the implants were imaged and extracted followed by the termination of the study as per *in ovo* CAM assay.

Due to the increased access to the CAM surface on the *ex ovo* embryo, it was possible to monitor and measure many different outputs directly. Novel imaging modalities were piloted on the *exo ovo* CAM assay as a proof of concept of the experimental setup as described below (see Appendix Figure 10).

Using the Visisen TD modular imaging sensor (PreSens Precision Sensing GmbH, Germany) with the relevant sterile sensor foil, it is possible to detect oxygen levels and the 2D distribution of oxygen on the surface of the implant and the surrounding CAM. (Appendix Figure 10B) Visisen TD system can also be calibrated to measure pH using the appropriate sensor foil on the implant. When optimised for this purpose, pH sensor can be a valuable indirect measure of metabolic activity due to acidic metabolites released from cellular activity. However, only oxygen levels were measured as a test of feasibility.

Due to practical issues experience with transporting the chick embryos to the IVIS bioluminescence machine at a different site, the ChemiDoc system was trialled as an alternative imaging modality to allow for intravital tracking of the seeded cells. The chemiluminescence protocol was chosen with a manual exposure setting of 240s with cumulative images taken at separate timepoints within 0-240s to obtain the best images without too much saturation using the ‘Signal Accumulation Mode’ in the Bio-Rad Image Lab™ Software. Images taken from the IVIS and ChemiDoc were compared to observe for signal detection potential from the two modalities.

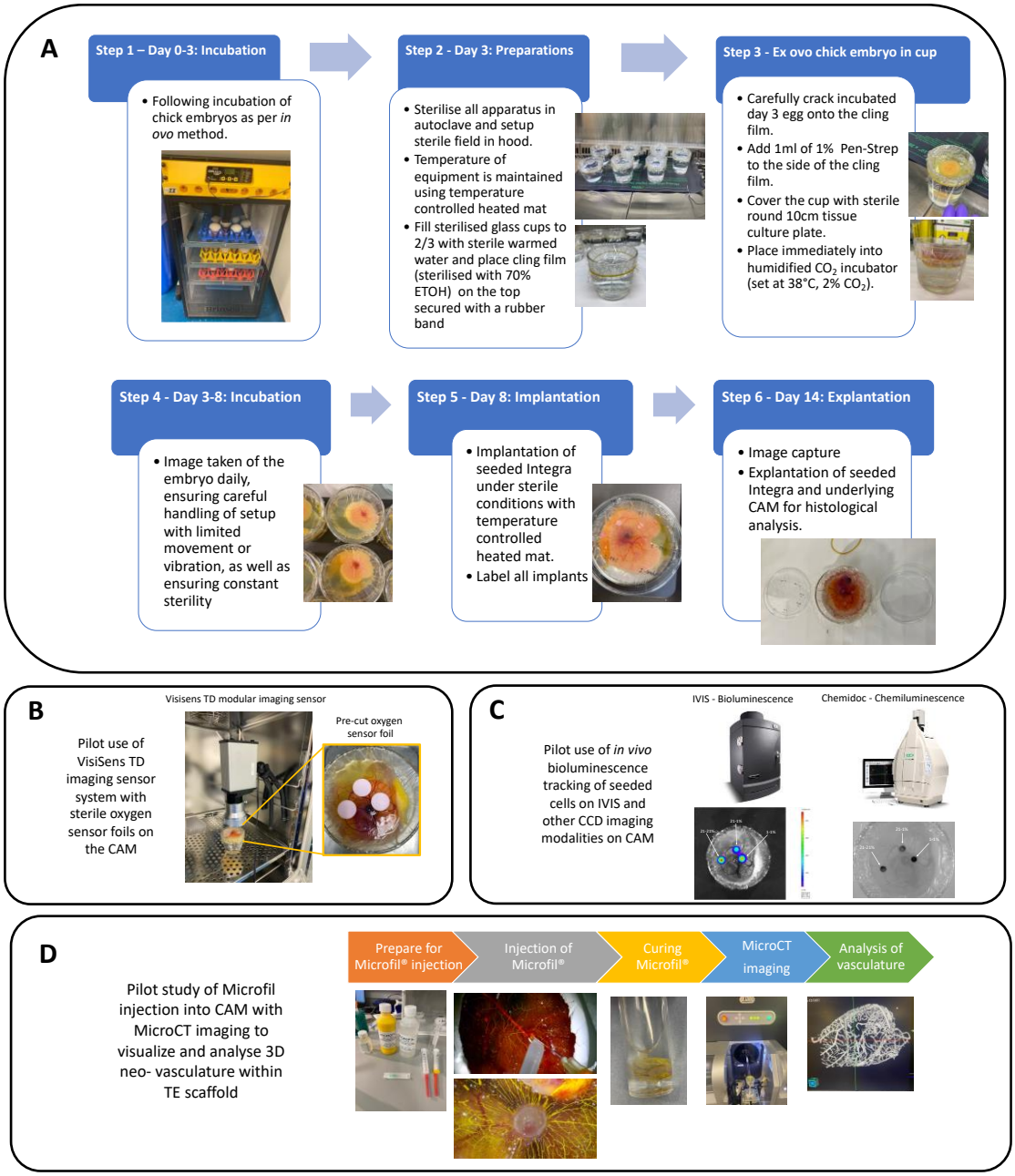

Appendix Figure 10: (A) Steps involved in *ex ovo* CAM assay (B) The use of Visisen TD oxygen sensor imaging module made possible on the *ex ovo* CAM. (C) *In vivo* bioluminescence tracking of seeded cells on *ex ovo* CAM and concurrent pilot testing of a non-conventional chemiluminescence CCD camera. (D) 3D angiography using Microfil and microCT scanning to visualise vsacularisation into TE scaffold.

9.1.1 *Ex ovo* and *in ovo* comparison

The field of view was significantly increased in the *ex ovo* CAM setup compared to *in ovo*, as shown in Appendix Figure 11A. Images from Appendix Figure 11B and C demonstrate the ease of visually tracking the scaffold and surrounding vasculature

around the implant over time. The embryonic development can also be monitored easily.

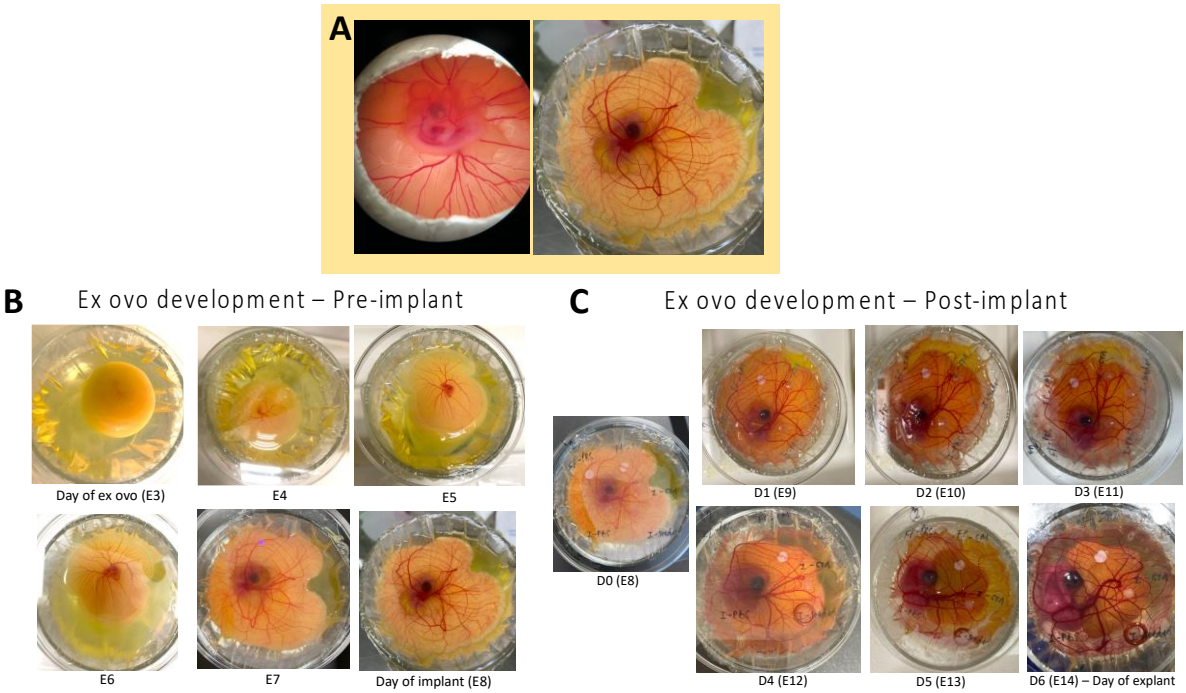

Appendix Figure 11: (A) Comparative field of view of the *in ovo* CAM (left) compared to *ex ovo* CAM (right). (B) Pre-implant *ex ovo* CAM images tracking development from E3 to E8. (C) Post-implant CAM images from the day of implant (suffixed D) from E8 to E14.

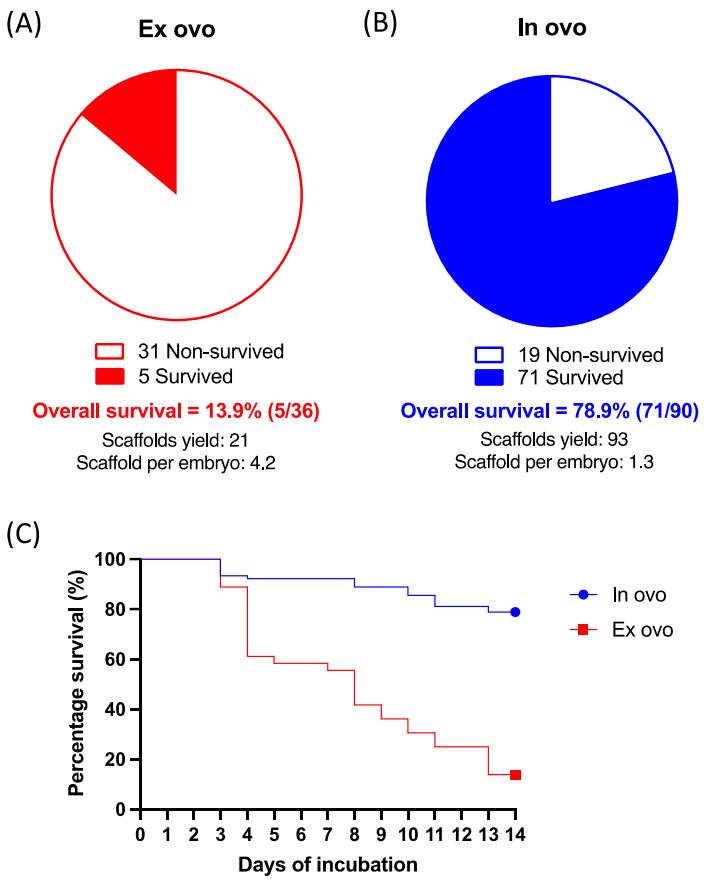

Appendix Figure 12: Comparing *ex ovo* and *in ovo* survival rates. (A) Pie chart of *ex ovo* embryo survival at E14 of gestation. Relevant statistics are detailed under the graph with overall survival shown in red. (B) Pie chart of overall *in ovo* embryo survival at E14 of gestation. Relevant statistics are detailed under the graph with overall survival shown in blue. (C) Survival curve using Kaplan-Meier survival analysis to compare *in ovo* and *ex ovo* survival rates over 14 days of incubation (equating to 14 days of gestation).

In this study, the *ex ovo* survival rates were much lower than *in ovo* group at E14 of incubation. (13.9% vs 78.9%). (Appendix Figure 12A & B) The survival curve shows how dramatic a drop in survival was noted in the first 4-5 days of incubation. This would correspond to published literature, where *ex ovo* survival rates were reported to be between 15-55% and *in ovo* between 85-95%. (510,538,539) It was noted within the *in ovo* group, which was repeated three times, that with each repeated experiment was met with higher survival rates; the initial set of *in ovo* survival rate was calculated at 62.5% (20 out of 32 embryos), followed by 82.6% (19 out of 23) and finally at 91.4% (32 out of 35) with the last batch of embryos.

Another interesting set of statistic comes from the scaffold yield per embryo. This is calculated as the number of successfully implanted scaffolds retrieved at the end of

the study (E14) divided by the number of surviving embryos. As it is possible to implant more than two scaffolds in an *in ovo* scaffold, the overall scaffold yield was found to be 1.3 scaffolds per *in ovo* embryo, which is an expected low yield due to the limited access and space within the intact eggshell. When the shell-less method was adopted, despite its poor survivability, the scaffold yield increased more than three times to 4.2 per embryo, giving a much higher yield and power to the assay. It also reduced the experimental time required to obtain results due to the high n-number possible per embryo.

9.1.2 Monitoring surface oxygen with VisiSen TD imaging sensor

On E14, three different ex ovo samples were taken for VisiSen imaging of surface oxygen saturations. (Appendix Figure 13) The ability to measure these changes in oxygen around and within the implant over time could offer potential insight into the rate of angiogenesis as well as oxygen consumption of the seeded cells if the concurrent metabolic activity of the cells could be determined using the same imaging sensor modality. The preliminary imaging demonstrated that it was possible to detect changes in oxygen levels on the surface of the implant. This technique still requires further optimisation and validation in order to obtain quantifiable results for sample comparison.

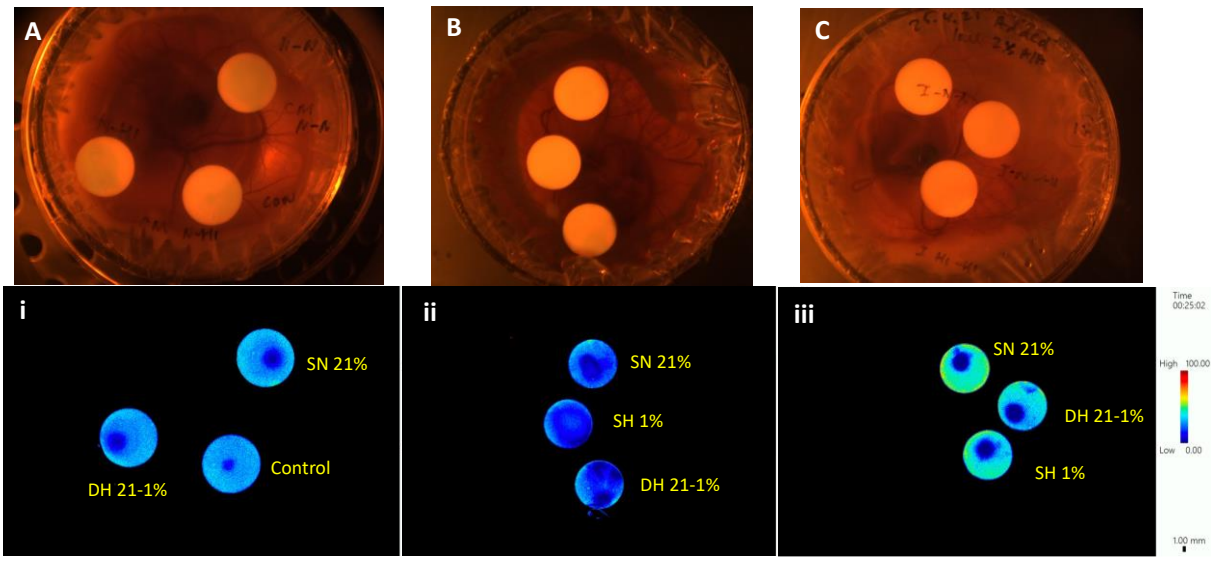

Appendix Figure 13: VisiSen imgaes of oxygen sensor foil placed on 3 different scaffolds implanted on CAM surface in 3 separate *ex ovo* assays. Above (A-C): Photos taken by CCD camera above *ex ovo* CAM with scaffolds *in situ*. Below (i-ii): VisiSen system detecting chemiluminescence changes on the oxygen sensor foil calibrated to the oxygen saturations (colour scale bar of oxygen percentages shown on the right). Images shown are taken at 25 minutes after equilibration to normoxic incubator. Scale bar shown = 1mm.

9.1.3 Live tracking of seeded transduced adMSC

Realtime tracking of transduced adMSC is possible via the use of bioluminescence imaging technology such as the IVIS spectrum in vivo imaging system (PerkinElmer). The ChemiDoc (Bio-rad) imaging system, which used for chemiluminescence imaging, was reported used on CAM assay by Naik et al. in order to utilise the CCD camera component for imaging of the vasculature. (535) As both devices use the same technology, in theory the ChemiDoc can be used to measure viability of transduced seeded cells when D-luciferin is added. The preliminary comparative data demonstrated some correlation in the images obtained from the two modalities used on the same *ex ovo* CAM. (Appendix Figure 14) However, this would need to be further validated in future experiments.

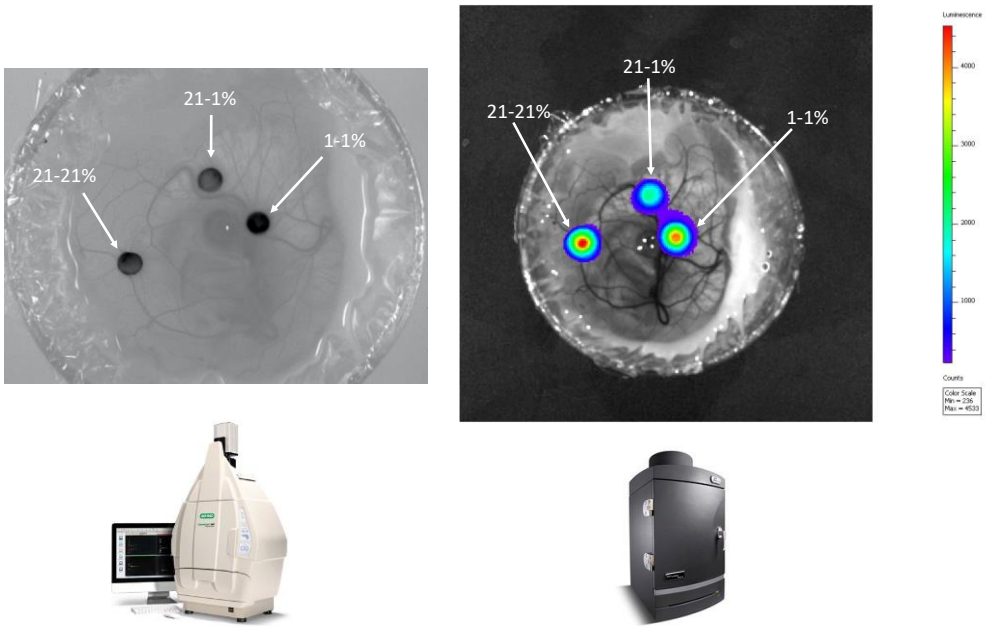

Appendix Figure 14: Images of the same *ex ovo* CAM assay with 3 scaffolds implanted with scaffold from different oxygen conditioning, (LEFT) taken on Chemidoc and (RIGHT) IVIS BLI machine to detect luciferin from seeded transduced adMSC.

9.1.4 3D imaging of the CAM vasculature

The main issue with the CAM assay for quantification of angiogenesis is the lack of a reliable three-dimensional system to measure vessel ingrowth. This is certainly an issue from the 2D image analysis of capture surface of the CAM. As mentioned previously, some implants can. migrate close to the edge of the shell/window and the view of vessels on one side is obscured.

The use of a mesh grid system was previously described to try to overcome this problem (Appendix Figure 15) (540–542). However, we found this system quite invasive and adds an unnecessary artificial layer and thickness in between the implant and CAM surface, which would likely affect overall results. Hence, we attempted a different imaging techniques described below to see if we could obtain quantifiable 3D vasculature data using current imaging technology (543–545).

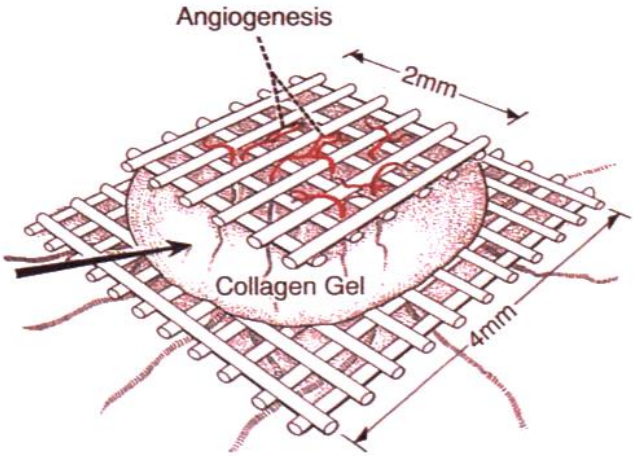

Appendix Figure 15: Earlier account of using nylon mesh grid technique for vessel quantification in pro-angiogenic assays as described by Nguyen et al. (540). Reproduced with permission from Elsevier and Copyright Clearance Center.

9.1.5 Use of whole mount fluorescence staining

Due to difficulties with obtaining chick-specific antibody for staining endothelial cells, visualisation of the endothelial lined vessel using of lectin-based histochemistry can be used as an alternative (546). This use of lectin has been well described in the literature for the for this purpose. In particular, *Lens culinaris* agglutinin (LCA), concanavalin A, and wheat germ agglutinin was found to be effective for the binding and visualisation of vessels of chicken embryos. It helps to overcome known issues with bright autofluorescence background often seen in immunohistochemistry especially in CAM samples (544,546).

The benefit of using *ex ovo* CAM assay is the ability to perform fluorescent intravital lectin perfusion/angiography into the chick embryo to allow for visualisation of vasculature into the implanted scaffold *in situ* (501,543,547,548). This would allow for the measurement of the vessel density as well as the architecture of vessels in and around the implant. It has the additional benefit being able to visualise and track the grafted transduced cells, which are zsGreen positive, on the implanted scaffold during fluorescent microscopy. Unfortunately, this method requires a specialised epi-fluorescent microscope, due to positioning of the implant on the CAM, with access to intricate perfusion apparatus, both of which were very difficult to source. The use of whole mount staining technique previously described for visualising different types of

tumour vasculatures is a suitable alternative (508,538). For this technique, we adapted the published protocols by Mangir et al. (549) and Deryugina (550) and attempted initial intravital lectin perfusion of 100µl of a 5 µg/ml Biotinylated LCA labelled tetramethylrhodamine isothiocyanate (TRITC/Rhodamine) (GlycoMatrix™, # 21761034-2) per chick embryo, using a 30G hypodermic needle attached to a 1 ml syringe. Haemostasis was achieved by using a silver nitrate stick to cauterise the bleeding vessel The embryo was allowed to incubate for a further 5-10 minutes to allow the LCA to circulate. Embryos were then sacrificed by cutting the vitelline arteries. Implant with CAM were excised with a 1cm margin around them and fixed in 4% paraformaldehyde (PFA) solution (Merck, Germany, Cat. No. 1039991000) in PBS. The explant was prepared for whole mounting via equilibrating in decreasing glycerol (Thermo Scientific, #J16374.K2) concentration (100%, 75% and 50%). At 50% glycerol, the CAM explant was mounted whole in 50% glycerol onto a glass confocal 34mm dish (VWR, #734-2905) and imaged using a confocal fluorescent microscope (Zeiss LSM 880) to record images and perform Z-stacking. Unfortunately, due to time limitations and problems with processing of the samples as well as technical issues with the confocal microscope, we were unable to image in time to obtain usable results for analysis or Z-stacking. Further improvements can be made to the processing step prior to imaging to allow for better LCA binding to vasculature via longer incubation and optimisation of fixation protocols, as well as optimisation of the embedding protocol which would need to be specifically tailored to the confocal microscope used for imaging.

9.1.6 Use of vascular casting and microCT imaging

To overcome the issues with LCA staining technique described above, we attempted to improve the accuracy of 3D vessel analysis via the use of microCT scanner. In this technique, the CAM vasculature would be injected with a radio-opaque substance, such as Omnipaque™ (Iohexol) or Microfil®, to image using radiological methods (551–555). There is only a handful of publications describing the use of microCT imaging on the chick embryo/CAM assay (551–555). We were fortunate to have a state-of-the-art imaging suite based at UCL Centre for Advanced Biomedical Imaging (CABI) and were able to access their microCT scanner there. Microfil® was deemed

a more appropriate injectable material as its resin-based property suited the terminal nature of the assay.

To assess the feasibility of this technique, a published protocol was adapted on a set of *in ovo* CAM as described by Woloszyk et al. (551–553). In brief, at E14 of CAM assay, 33G needle and 1ml containing 500ul of prepared Microfil® medium mixture (Yellow #MV-122) according to manufacturer's instructions was injected into a large primary artery of the CAM. The needle was secured with superglue during the infusion. After withdrawal of the needle, haemostasis was achieved by using a silver nitrate stick to cauterise the bleeding vessel. The chick embryo was sacrificed by sacrificed by cutting the vitelline arteries and placed in the fridge at 4°C overnight to allow for complete curing of the Microfil® material. The CAM with explant scaffold was then excised and fixed in 4% PFA (Merck, Germany, #1039991000) for at least 6 hours in room temperature. This was followed by three PBS wash steps and the explant was placed in 70% ethanol and stored in 4°C until microCT imaging. MicroCT was performed on the Perkins Elmer Quantum GX2 machine. High resolution parameters of 2.3 µm, energy level of 90 kV, intensity of 88 µA, and 57 minutes integration time was used to obtain high quality images for analysis. The workflow of this technique is summarised in Appendix Figure 16.

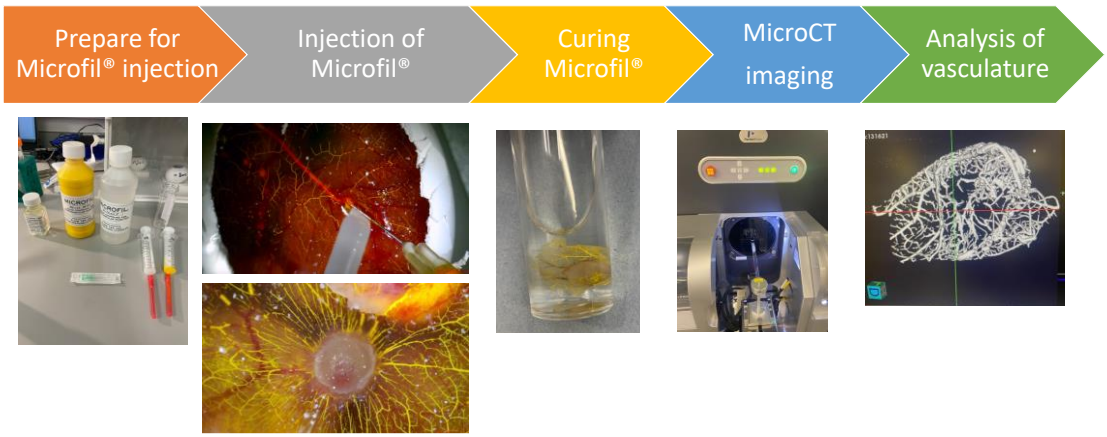

Appendix Figure 16: The workflow of microCT angiography of CAM vasculature using intravital injection of radio-opaque Microfil®.

Pilot data is showed in Appendix Figure 17, which includes 3D rendered videos of the imaged CAM explants which can be accessed using the weblink.

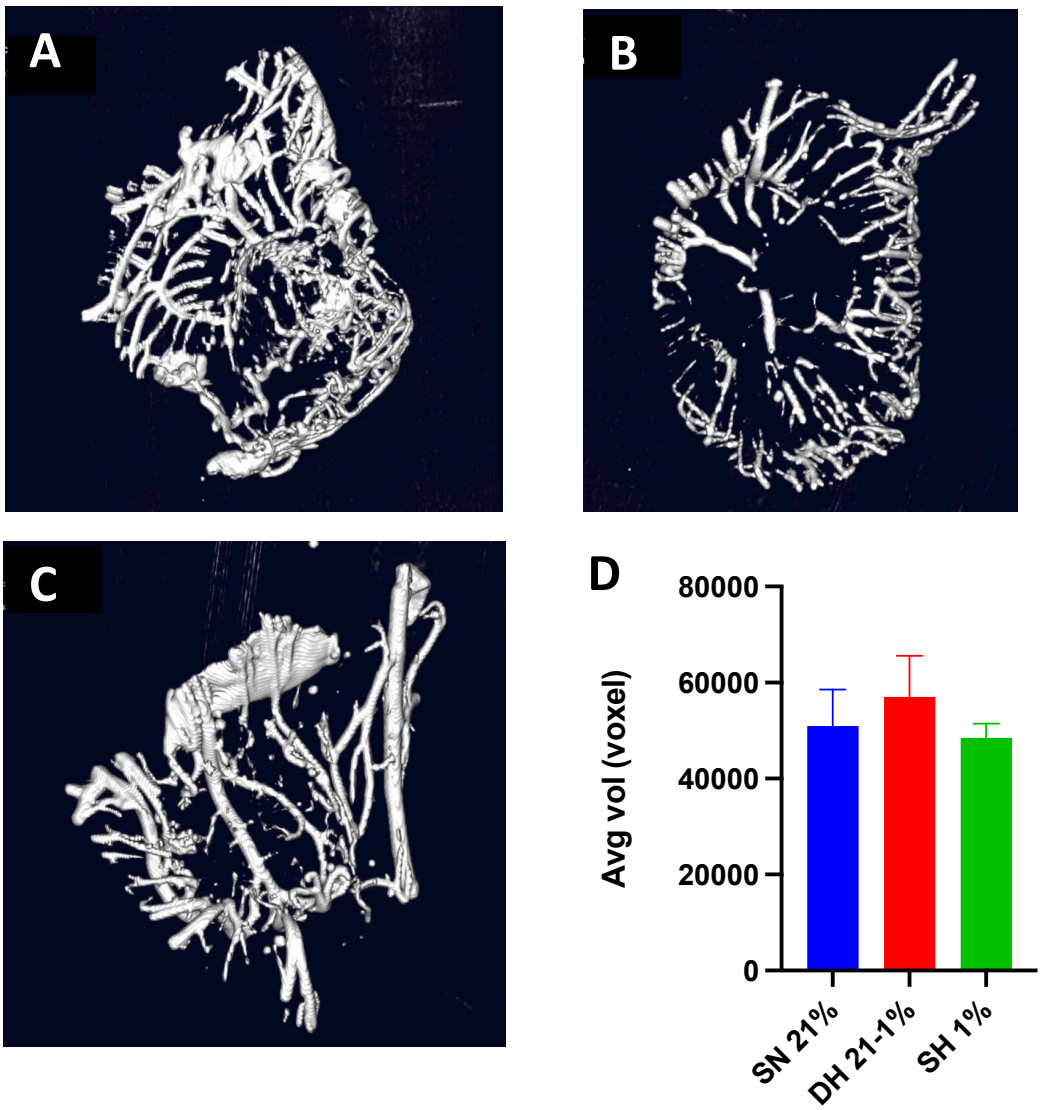

Appendix Figure 17: 3D volume rendered microCT images of CAM vasculature around implanted INTEGRA® scaffold. Vessels are visable from the radio-opaque Microfil injected into the CAM. (A) Static normoxia 21% adMSC seeded scaffold (video link here: https://bit.ly/3E5pOVc), (B) static hypoxia 1% adMSC seeded scaffold (video link here: http://bit.ly/3XpNhHB), (C) dynamic hypoxia 21-1% seeded scaffold (video link here: https://bit.ly/3E5px4C), (D) graph showing averaged volume of CAM vasculature (measured in voxels) for the 3 different scaffolds. Data was not statistically significant. n=2 per oxygen pre-conditions.

9.1.7 Use of photoacoustic imaging technology

Photoacoustic imaging (PAI) is a novel hybrid technology uses a combination of light (photo) and ultrasound (acoustic) techniques to visualise blood vessels without the need for any invasive procedure or staining. It has been used extensively in research and is described in detail in a paper by our collaborators at the Department of

Medical Physics and Bioengineering (556). It is based upon ultrasound waves being generated on stimulation and absorption of low energy laser pulses by tissue chromophores, such as haemoglobin. These waves are subsequently detected on the surface using a dedicated ultrasound probe. This can be used to reconstruct a 3D image of specific internal tissue structures such as blood vessels. Certainly, the availability of commercial units by manufacturer Fujifilm Visualsonic (Fujifilm Vevo F2 LAZR-X) would increase the application and popularity of this a promising imaging alternative compared with more complex and invasive imaging modalities. As we have previously accessed the use of PAI for a tissue engineering application in an *in vivo* murine angiogenesis models, we did explore the prospect of applying it to the CAM model (557). Unfortunately, the PAI machine at our collaborator's institute had not been validated for use with chick embryos/CAM models. Therefore, we were unable to trial this modality the CAM during this study. As there is only a handful of publications using this technology for the CAM assay (558–562), it would be a worthwhile venture to further adapt this novel imaging technology for future CAM studies.

9.1.8 Discussion on *ex ovo* CAM assay

The *ex ovo* CAM proved to be a technically challenging procedure with a known steep learning curve. The survivability of the embryo is also known to be directly proportional to technical expertise. This is largely attributed to the experience of the person carrying out the assay, as highlighted by other researchers (510,534,536–539). Only one set of this *ex ovo* Cam assay was performed due to time limitations, as its main purpose was to function as a feasibility experiment. With the *in ovo* CAM assay, there were improvements noted to the embryo's survivability with each repeated experiment. It is likely that with increased technical experience, the survivable rated of the *ex ovo* CAM assay will also improve.

The CAM is also particularly sensitive to modification in environmental factors, such as changes in oxygen tension, which is less variable in the shelled *in ovo* methods, pH, osmolarity (495). Hence, the *in ovo* and *ex ovo* CAM could give very different results which will need to be taken into account. A comparative study between the

two models would be very useful to evaluate the changes in oxygen environment and its effects on the biological *in vivo response*.

Unfortunately, due to issues around imaging of the CAM and poor survivability of the embryos, it was not possible to obtain quantifiable and comparable datasets to present on the angiogenicity of the implants. There were also issues around the possible cross-reactivity of the different pre-conditioned scaffolds on the same embryo (due to anatomical distance from each other), which could affect the overall results. Hence, there is still much more optimisation of this method required. However, the practical advantages to novel imaging techniques for longitudinal monitoring is a valuable feature of using the *ex ovo* model which should not be overlooked. The *ex ovo* CAM itself has shown itself to be a worthy alternative to the *in ovo* technique in carefully selected conditions done with the right technical expertise.

9.2 Identifying an alternative ischaemic wound model

Given the uncertainty around the most appropriate diabetic wound model to use as discussed above, confounded by the ambiguity around the degree of relevance of functional angiogenesis within such models, other alternative wound healing models were sought and tested for feasibility.

The ideal wound model for this study would need to feature angiogenesis as the main stimulus for the healing/regenerative process. It is known that the best *in vivo* animal wound healing model is in porcine skin given that both human and pig skin share many similarities from epidermal thickness to similar skin appendages, blood vessels and dermal collagen content, even down to their response to growth factors (627). A study by Suvillan et al. found porcine wound models to be 78% concordant with human studies (628). However, pig models are notoriously expensive to carry out, and the animal is tricky to handle due their large size resulting in anaesthetic issues and difficulty with *in vivo* monitoring in general due to compatibility of laboratory devices. Hence small animal *in vivo* models still have a significant role in

wound modelling. After facing the challenges of diabetic wound healing model above, I sought to try 2 other models which are shown in Appendix Figure 18.

The dorsal skinfold chamber pre-clinical model using a specialised apparatus for visualisation of neovascularisation dynamics and process has been described extensively in literature (Appendix Figure 18C) (629–639). Most models utilise mice, but hamsters have also been used successfully owning to their loose skin nature (633). The dorsal skinfold chamber apparatus was custom made via 3D printing technology with the help of a collaborator with access to medical grade 3D printing resin material (640). The model design was based off published papers and commercially available chambers from USA (631,636,641) and design iterations for our device are shown in Appendix Figure 19. The use of transillumination and intravital microscopy (brightfield or fluorescence) opens many possibilities of monitoring new blood vessel growth into scaffold in real-time, allowing for angiographic studies as well as intravital tracking of seeded cells via the readily accessible window. The chamber also doubles as a reliable splint for the skin, preventing the undesirable wound contracture. However, to run such a model successful requires access to specialised microscopy instruments which were unfortunately not available during the *in vivo* part of the study. Nevertheless, the apparatus was trialled as shown below and highlighted several practical issues which is worth bearing in mind for future studies. (Table 9.1)

The ischaemic flap model is another possible wound healing model which uses a more complex full thickness skin flap design to orchestrate an oxygen gradient via physical obstruction of the feeding vessels to the flap, forcing blood supply from only one end of the flap. (see Appendix Figure 18D) The dorsal skin flap model was originally suggested by McFarlane et al. in 1965 to study skin necrosis (642). Since then, this experimental model has been adopted as gold standard for models requiring the evaluating of viability of axial flaps (643). Hence the basis of the model is not a true wound healing assay, but it does allow for the functional assessment of neovascularisation via pro-angiogenic means. The evaluation however requires specialist imaging devices which can be costly and tedious, requiring expert input for analysis. Given the objectives of this thesis is to enhance angiogenesis into tissue engineered scaffold, this model would not be suitable for this study's purpose.

Wound healing models

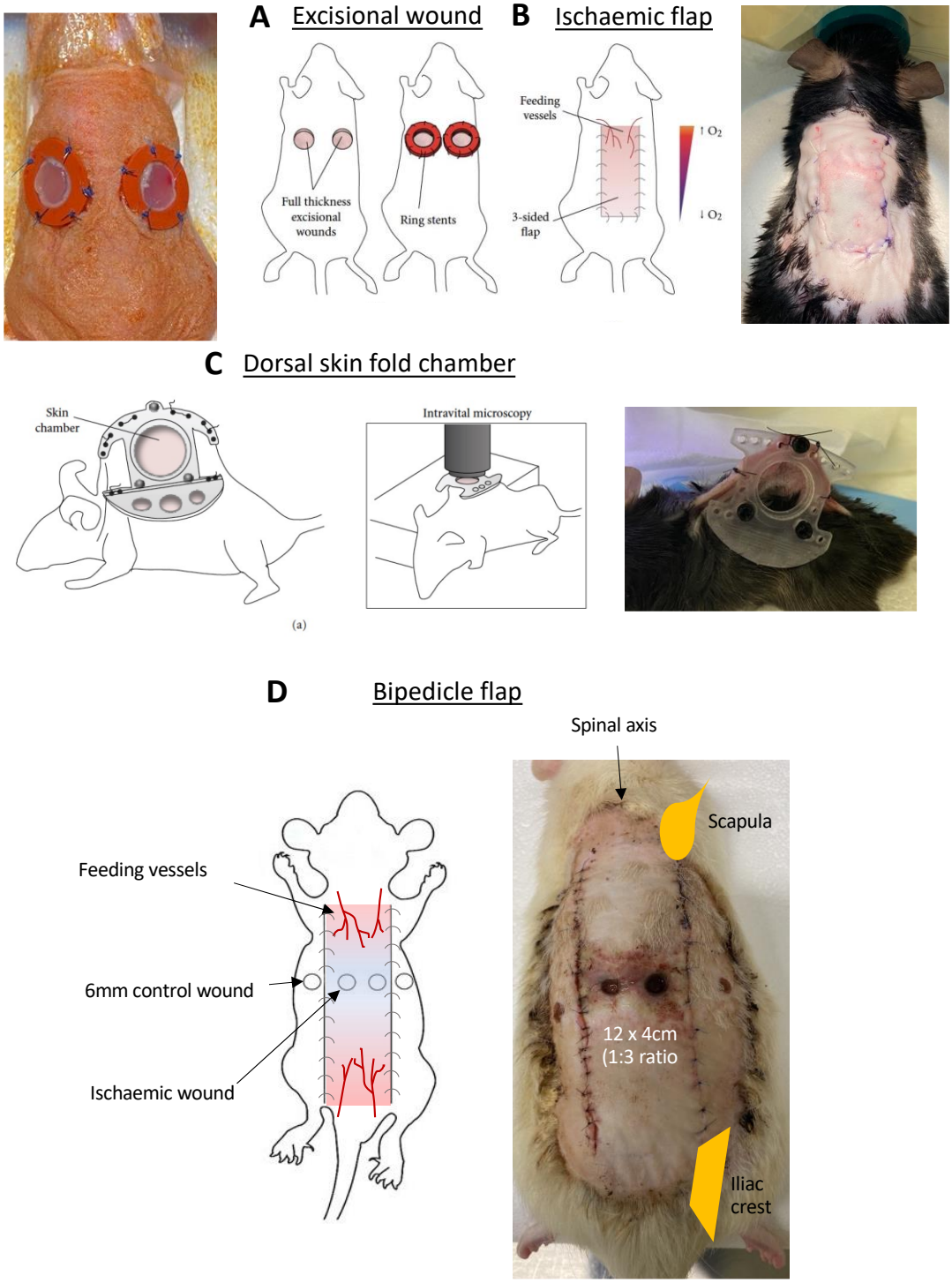

Appendix Figure 18: Surgical models of different wound healing models are shown with associated schematic images taken from Wong et al., reproduced under the Creative Commons Attribution License (CC BY 3.0). (682) Mouse photos (A) – (C) are trial experiments done in this study as an attempt to trial alternative models and to test for feasibility. (A) Excisional model, described extensively in this chapter, is a full-thickness splinted wound model aimed to mimic simple wound healing. (B) Ischaemic flap model aims to replicate blood supply issues influencing wound healing on a larger tissue surface, particularly to

the extremities of the full thickness skin flap. (C) Dorsal skin fold chamber model aims to assessment vascular physiology over time with ease of longitudinal monitoring using intravital microscopy. (D) Bipedicle flap raised on a Wistar rat with full-thickness 6mm wounds in the ischaemic region of the flap and parallel non-ischaemia wounds outside flap area as control. Schematic image on the left, adapted from Gould et al. (644), shows the area of ischaemia (blue) poorly supplied by the feeding vessels in the extremes of the pedicle. On the right rat image, the bony landmarks are highlighted yellow with surgical incisions parallel to the spinal axis on either side shown in white. Area of ischaemia can be observed around the wounds on the pedicle.

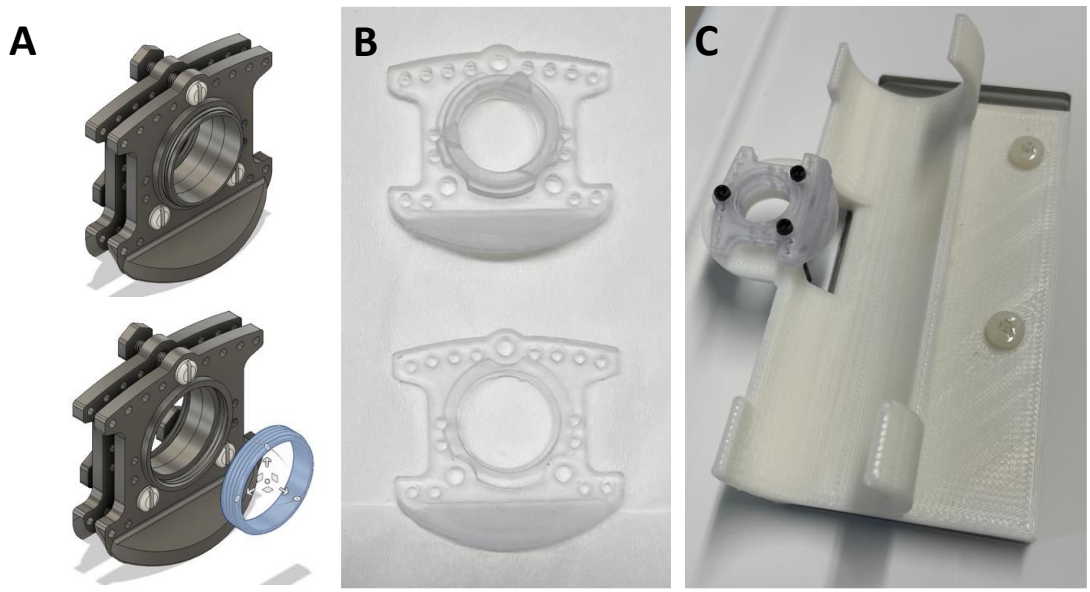

Appendix Figure 19: Dorsal skin fold chamber device design, product, and assembly. (A) Custom CAD illustrations of proposed 3D printing of chamber and compatible plastic screw with 15 mm removal glass coverslip insert. (B) MRI safe autoclavable 3D printed chambers using medical grade biocompatible resin, BioMed Clear (Formlabs Inc., USA) (C) Assembled dorsal skin fold chamber in situ with 3D printed jig for animal positioning. 3D CAD images and custom-made devices were kindly provided by Dr An Vuong of Autobiologic Inc., USA.

Modifications of the ischaemic flap to produce an ischaemic wound model was the next possible step in designing an improved wound healing model to suit our experimental needs. On further research, a bipedicle flap combined with full thickness excision wounds described by Lisa Gould's group, has been successfully adapted to rat and pig models (644,645). It has been used to model chronic ischaemic wound pathologies normally seen in diabetic and vascular ulcers (646). Adapted from Gould's 2005 and Schwarz's 1995 model (644,647), bony landmarks of the scapula and iliac crest were identified as described by McFarlane et al. (642) the spinal axis was identified on a rat, and the surgical parameters of the skin flap was

designed over this axis at a length/breadth 3:1 ratio, as described by Roy et al. (645), to ensure adequate ischaemia in the central segment of the flap. This ratio had been optimised to create an ischaemic flaps that would survived between 4 to 6 weeks (645). In theory, this ratio can be adjusted to suit the degree and period of ischaemia required, with increasing ratio causing a greater central area of ischaemia (648). The hair over the rats were removed and two parallel lines which make the pedicle flap were drawn with a surgical marker pen. The flap was raised with a scalpel and a sterile medical grade silicone sheet was placed between the flap and the underlying fascia to prevent vascularisation from the subcutaneous layer. 6mm full thickness wounds (including the panniculus carnosus) were made in the central portion of the flap and one each on either side of the flanks away from the flap as control wounds. (see Appendix Figure 18D) Ischaemia is subsequently monitored using laser doppler. This model is particularly useful for evaluating therapeutic systemic interventions for chronic ischaemic wound pathologies, although local agents are also possible. By rendering the host diabetic, a diabetic ulcer model can be created for potential therapeutic interventions (649). Hence, out of all the wound healing models described above, this is the most promising model at replicating the pathophysiology around chronic diabetic/ischaemic wounds.

Models	Pros	Cons	Ref.
Excisional splinted wound	• Conventional well-established model • Easy to implement • Low cost	• Model needs to be splinted for rodents due to panniculus carnosus (absent in humans) • The need to change wound dressings regularly • Not optimal evaluation of epithelisation	(650)
Ischaemic flap	• Accurate and reproducible model that replicates characteristics of ischaemic tissue • Allows for the study of hypoxic gradient in tissues • Effective for study of neovascularisation and perfusion into full thickness skin flap	• Not true wound healing model as no epithelialisation or skin replacement possible • Need surgical expertise in designing and implementing flap on animals • Difficult to visualise underlying vasculature	(134, 651)

	• Positive effects of treatment are measured via extent of flap necrosis/perfusion into flap	• Heavy reliance on imaging modalities (e.g. laser doppler) to analyse for vascularisation	
Dorsal skin fold chamber	• Allows for easy visualisation and microscopic imaging of vasculature accessible through the window • With intravital fluorescence microscopy, enbles real-time high-resolution imaging of various physiological parameters such as vessel growth, microvascular perfusion, vascular permeability and cell interactions. • Compatible with other measurement modalities, such as VisiSen TD oxygen sensor foil	• Requires access to specialist equipment and expertise • Technically very challenging to implement (many parts, stay sutures and screws) • Requires custom made chambers that is small and light enough to not constrict on the animal's movement or breathing functions • Due to the invasive nature of the contraption, the need for regular analgesia for the animals might affect outcome from a pharmacological perspective	(631)
Ischemic wound (bipedicle flap)	• Useful model for the study of chronic, non-healing wounds • Wound healing times are deliberately lengthened via reduction in blood flow to area of skin • Age or disease related modelling is possible	• Requires larger sized rodents (i.e. rats) to have enough space for wounding • Labour intensive • Costly	(645)

Table 9.1 List of *in vivo* models and their advantage and disadvantages in view of studying angiogenesis and wound healing.

9.3 Devices for *in vivo* tissue monitoring

One of the major limitations in the study of angiogenesis is the ability to visualise neovasculature using high fidelity scanner/imaging system. Particularly with the ischaemic wound/flap models described above, the need for a low-cost, accessible, reliable and non-invasive procedure for characterisation and quantification of angiogenesis using clinical translational methods is essential. Fortunately, the skin is an easily accessible organ, hence the use of different types of modalities is more applicable and translatable to the clinical setting with the use of advancing technology.

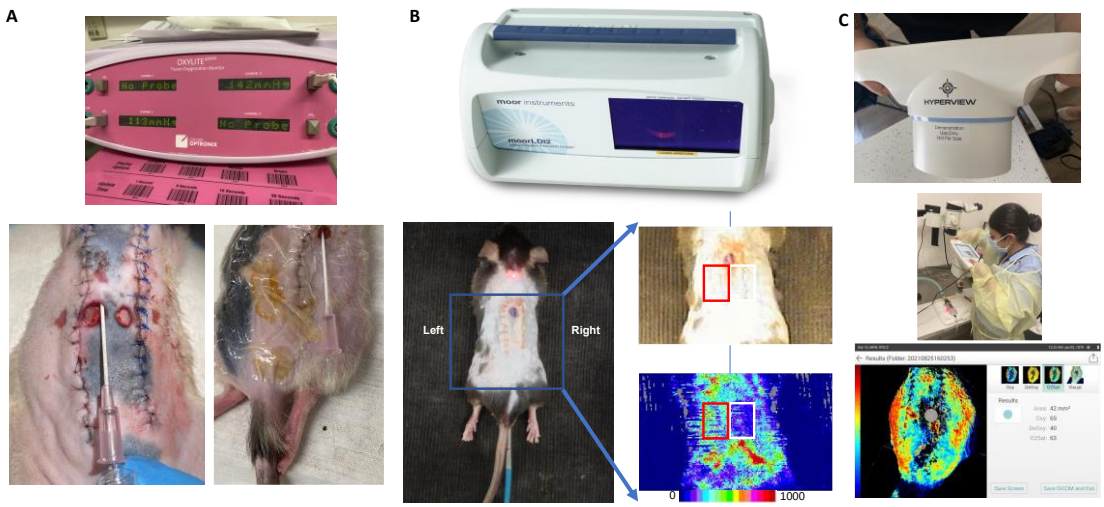

Appendix Figure 20: Trial of three different modalities for measurement of oxygen saturations in ischaemic wounds. (A) Fibreoptic instrument based Oxylite 4000E (Oxford Optronics, UK) (top) which needed to be inserted into the tissue of interest as shown in the rat model below. A plastic cannula was inserted as guide into the wound area. (B) Laser doppler system, MoorLDI2™ (Moor Instruments, USA) used to scan the surface of the skin to monitor blood perfusion through the flap. (C) Hyperspectral based point-and-shoot imaging device, HyperView™ (HyperMed Imaging, USA)

In our study, we trialled different tissue oxygen saturation modalities (see Appendix Figure 20) for the pilot ischaemic wound models. The first device, shown in Appendix Figure 20A, is a fibreoptic-based tissue oxygenation monitor OxyLite™ 4000E (Oxford Optronics, UK) which directly measures the tissue via a filament probe in contact with the tissue. This instrument is invasive in nature and was unsuitable for later parts of wound healing process due the probe necessitating trauma to the tissue site of interest during the measurement process. It also required a fair amount of optimisation with temperature probes and atmospheric oxygen normalisation prior to each use which became a practical hindrance as values fluctuate dramatically, leading to inaccuracies. The area of measurement was also very limited as it only detects oxygen where the probe is in contact with.

The second device is a laser doppler imaging device, Moor LDI2™ (Moor Instruments, USA), which measures tissue perfusion on the skin. (Appendix Figure 20B) This device offers accurate topographic measurement of surface oxygen saturations and underlying perfusion over a larger area, which is useful for flap monitoring studies (652,653). But problems with using it on pigmented animal skin limited its application on immunocompromised R/NU rats (shown in Appendix Figure

20A) It is also costly to run due to the need for technical expertise to use this specialist instrument.

The third device is the more promising a hyperspectral device HyperView™ (HyperMed Imaging, USA), which uses a non-invasive technique for measuring the oxyhaemoglobin/ deoxyhaemoglobin ratio on the surface of the skin (Appendix Figure 20C). With the ease of non-invasively measuring large area of skin, as with the Moor LDI2™ instrument above, the Hyperview's advantage is in its portability and ease of data gathering without the need for expert input. The device is still faced the same issue with pigmented skin, but the effect is less pronounced than that seen with the LDI instruments.

If the access to the more expensive photoacoustic imaging device is a possibility, then the use of Fujifilm Vevo F2 LAZR-X, shown in Appendix Figure 21, is probably the most sophisticated and superior device as it can help to visualise more 3D perfusion through the implanted scaffold using the in-build ultrasound doppler probe and blood vessel quantification.

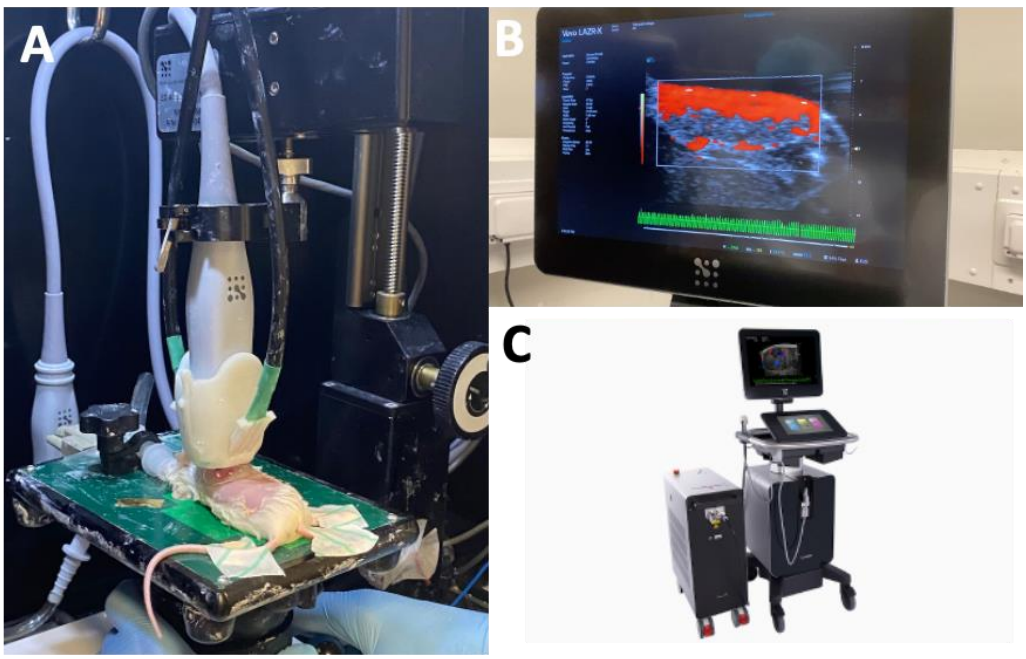

Appendix Figure 21: Photoacoustic imaging of INTEGRA® scaffold implanted on a mouse as a feasibility trial of technique. (A) Setup of the probe with animal *in situ*. (B) Realtime scanning showing ultrasound doppler flow around the implant. (C) Photo representation of the Fujifilm Vevo F2 LAZR-X machine used for this trial.

10 References

1. Pugh CW, Ratcliffe PJ. Regulation of angiogenesis by hypoxia: role of the HIF system. Nat Med. 2003 Jun;9(6):677–84.

2. Lechler RI, Sykes M, Thomson AW, Turka LA. Organ transplantation—how much of the promise has been realized? Nat Med. 2005 Jun;11(6):605–13.

3. Tresoldi C, Pellegata AF, Mantero S. Cells and stimuli in small-caliber blood vessel tissue engineering. Regen Med. 2015 May;10(4):505–27.

4. Langer R, Vacanti JP. Tissue Engineering. Science. 1993 May 14;260(5110):920–6.

5. Hassanzadeh P, Atyabi F, Dinarvand R. Tissue engineering: Still facing a long way ahead. J Controlled Release. 2018 Jun 10;279:181–97.

6. Swift MR, Weinstein BM. Arterial–Venous Specification During Development. Circ Res. 2009 Mar 13;104(5):576–88.

7. Carmeliet P. Mechanisms of angiogenesis and arteriogenesis. Nat Med. 2000 Apr;6(4):389–95.

8. Risau W. Mechanisms of angiogenesis. Nature. 1997 Apr;386(6626):671–4.

9. Chinoy MR. Lung growth and development. Front Biosci-Landmark. 2003 Jan 1;8(4):392–415.

10. Gerhardt H. VEGF and Endothelial Guidance in Angiogenic Sprouting . Madame Curie Bioscience Database . Landes Bioscience; 2013. Available from: https://www.ncbi.nlm.nih.gov/books/NBK6141/

11. Carmeliet P, Jain RK. Molecular mechanisms and clinical applications of angiogenesis. Nature. 2011 May 19;473(7347):298–307.

12. Carmeliet P. Angiogenesis in health and disease. Nat Med. 2003 Jun;9(6):653–60.

13. Yancopoulos GD, Davis S, Gale NW, Rudge JS, Wiegand SJ, Holash J. Vascular-specific growth factors and blood vessel formation. Nature. 2000 Sep 14;407(6801):242–8.

14. Saksela O, Moscatelli D, Rifkin DB. The opposing effects of basic fibroblast growth factor and transforming growth factor beta on the regulation of plasminogen activator activity in capillary endothelial cells. J Cell Biol. 1987 Aug;105(2):957–63.

15. Neufeld G, Cohen T, Gengrinovitch S, Poltorak Z. Vascular endothelial growth factor (VEGF) and its receptors. FASEB J. 1999 Jan 1;13(1):9–22.

16. Beck L, D'Amore PA. Vascular development: cellular and molecular regulation. FASEB J Off Publ Fed Am Soc Exp Biol. 1997 Apr;11(5):365–73.

17. Cockerill GW, Gamble JR, Vadas MA. Angiogenesis: Models and Modulators. Int Rev Cytol. 1995;159:113–60.

18. Abramsson A, Lindblom P, Betsholtz C. Endothelial and nonendothelial sources of PDGF-B regulate pericyte recruitment and influence vascular pattern formation in tumors. J Clin Invest. 2003 Oct 15;112(8):1142–51.

19. Hirschi KK, Rohovsky SA, Beck LH, Smith SR, D'Amore PA. Endothelial Cells Modulate the Proliferation of Mural Cell Precursors via Platelet-Derived Growth Factor-BB and Heterotypic Cell Contact. Circ Res. 1999 Feb 19;84(3):298–305.

20. Hirschi KK, Skalak TC, Peirce SM, Little CD. Vascular assembly in natural and engineered tissues. Ann N Y Acad Sci. 2002 Jun;961(1):223–42.

21. Davis GE, Senger DR. Endothelial extracellular matrix: biosynthesis, remodeling, and functions during vascular morphogenesis and neovessel stabilization. Circ Res. 2005 Nov 25;97(11):1093–107.

22. O'Reilly MS, Holmgren L, Shing Y, Chen C, Rosenthal RA, Cao Y, et al. Angiostatin: A Circulating Endothelial Cell Inhibitor That Suppresses Angiogenesis and Tumor Growth. Cold Spring Harb Symp Quant Biol. 1994 Jan 1;59:471–82.

23. Nyberg P, Xie L, Kalluri R. Endogenous Inhibitors of Angiogenesis. Cancer Res. 2005 May 16;65(10):3967–79.

24. Cao L, Mooney DJ. Spatiotemporal control over growth factor signaling for therapeutic neovascularization. Adv Drug Deliv Rev. 2007 Nov 10;59(13):1340–50.

25. Richardson TP, Peters MC, Ennett AB, Mooney DJ. Polymeric system for dual growth factor delivery. Nat Biotechnol. 2001 Nov;19(11):1029–34.

26. Chu H, Wang Y. Therapeutic angiogenesis: controlled delivery of angiogenic factors. Ther Deliv. 2012 Jun;3(6):693–714.

27. Lee K, Silva EA, Mooney DJ. Growth factor delivery-based tissue engineering: general approaches and a review of recent developments. J R Soc Interface R Soc. 2011 Feb 6;8(55):153–70.

28. Madeddu P. Therapeutic angiogenesis and vasculogenesis for tissue regeneration. Exp Physiol. 2005;90(3):315–26.

29. Jain RK, Au P, Tam J, Duda DG, Fukumura D. Engineering vascularized tissue. Nat Biotechnol. 2005 Jul 1;23(7):821–3.

30. Gaengel K, Genové G, Armulik A, Betsholtz C. Endothelial-Mural Cell Signaling in Vascular Development and Angiogenesis. Arterioscler Thromb Vasc Biol. 2009 May;29(5):630–8.

31. Raza A, Franklin MJ, Dudek AZ. Pericytes and vessel maturation during tumor angiogenesis and metastasis. Am J Hematol. 2010;85(8):593–8.

32. Potente M, Gerhardt H, Carmeliet P. Basic and Therapeutic Aspects of Angiogenesis. Cell. 2011 Sep 16;146(6):873–87.

33. Lutolf MP, Hubbell JA. Synthetic biomaterials as instructive extracellular microenvironments for morphogenesis in tissue engineering. Nat Biotechnol. 2005 Jan;23(1):47–55.

34. Mason C, McCall MJ, Culme-Seymour EJ, Suthasan S, Edwards-Parton S, Bonfiglio GA, et al. The Global Cell Therapy Industry Continues to Rise during the Second and Third Quarters of 2012. Cell Stem Cell. 2012 Dec 7;11(6):735–9.

35. Mason C, Brindley DA, Culme-Seymour EJ, Davie NL. Cell therapy industry: billion dollar global business with unlimited potential. Regen Med. 2011 May;6(3):265–72.

36. Karamysheva AF. Mechanisms of angiogenesis. Biochem Mosc. 2008 Aug 3;73(7):751.

37. Nombela-Arrieta C, Ritz J, Silberstein LE. The elusive nature and function of mesenchymal stem cells. Nat Rev Mol Cell Biol. 2011;12(2):126–31.

38. Meirelles L da S, Chagastelles PC, Nardi NB. Mesenchymal stem cells reside in virtually all post-natal organs and tissues. J Cell Sci. 2006 Jun 1;119(11):2204–13.

39. Pittenger MF, Mackay AM, Beck SC, Jaiswal RK, Douglas R, Mosca JD, et al. Multilineage Potential of Adult Human Mesenchymal Stem Cells. Science. 1999 Apr 2;284(5411):143–7.

40. Ankrum JA, Ong JF, Karp JM. Mesenchymal stem cells: immune evasive, not immune privileged. Nat Biotechnol. 2014 Mar 23;32(3):252–60.

41. Caplan AI, Dennis JE. Mesenchymal stem cells as trophic mediators. J Cell Biochem. 2006;98(5):1076–84.

42. Chen L, Tredget EE, Wu PYG, Wu Y, Wu Y. Paracrine factors of mesenchymal stem cells recruit macrophages and endothelial lineage cells and enhance wound healing. PLoS ONE . 2008 Apr 2;3(4).

43. Caplan AI, Correa D. The MSC: an injury drugstore. Cell Stem Cell. 2011;9(1):11–5.

44. da Silva Meirelles L, Caplan AI, Nardi NB. In Search of the In Vivo Identity of Mesenchymal Stem Cells. Stem Cells. 2008 Sep 1;26(9):2287–99.

45. Cunningham CJ, Redondo-Castro E, Allan SM. The therapeutic potential of the mesenchymal stem cell secretome in ischaemic stroke. J Cereb Blood Flow Metab. 2018 Aug 17;38(8):1276–92.

46. Qi S, Pan J. Cell-Based Therapy for Therapeutic Lymphangiogenesis. Stem Cells Dev. 2015 Feb;24(3):271–83.

47. Han Y, Yang J, Fang J, Zhou Y, Candi E, Wang J, et al. The secretion profile of mesenchymal stem cells and potential applications in treating human diseases. Signal Transduct Target Ther. 2022 Mar 21;7(1):1–19.

48. Home - ClinicalTrials.gov . [cited 2022 Nov 11]. Available from: https://clinicaltrials.gov/ct2/home

49. Tsuji K, Kitamura S, Wada J. Secretomes from Mesenchymal Stem Cells against Acute Kidney Injury: Possible Heterogeneity. Stem Cells Int. 2018 Dec 16;2018:e8693137.

50. Sze SK, de Kleijn DPV, Lai RC, Khia Way Tan E, Zhao H, Yeo KS, et al. Elucidating the Secretion Proteome of Human Embryonic Stem Cell-derived Mesenchymal Stem Cells*. Mol Cell Proteomics. 2007 Oct 1;6(10):1680–9.

51. Liu CH, Hwang SM. Cytokine interactions in mesenchymal stem cells from cord blood. Cytokine. 2005 Dec 21;32(6):270–9.

52. Oskowitz A, McFerrin H, Gutschow M, Carter ML, Pochampally R. Serum-deprived human multipotent mesenchymal stromal cells (MSCs) are highly angiogenic. Stem Cell Res. 2011 May 1;6(3):215–25.

53. Hoch AI, Binder BY, Genetos DC, Leach JK. Differentiation-Dependent Secretion of Proangiogenic Factors by Mesenchymal Stem Cells. PLOS ONE. 2012 Apr 20;7(4):e35579.

54. Aggarwal S, Pittenger MF. Human mesenchymal stem cells modulate allogeneic immune cell responses. Blood. 2005 Feb 15;105(4):1815–22.

55. Zhang H, Yang R, Wang Z, Lin G, Lue TF, Lin C. Adipose Tissue-Derived Stem Cells Secrete CXCL5 Cytokine with Neurotrophic Effects on Cavernous Nerve Regeneration. J Sex Med. 2011 Feb 1;8(2):437–46.

56. Arthur A, Cakouros D, Cooper L, Nguyen T, Isenmann S, Zannettino ACW, et al. Twist-1 Enhances Bone Marrow Mesenchymal Stromal Cell Support of Hematopoiesis by Modulating CXCL12 Expression. Stem Cells. 2016 Feb 1;34(2):504–9.

57. Nie WB, Zhang D, Wang LS. Growth Factor Gene-Modified Mesenchymal Stem Cells in Tissue Regeneration. Drug Des Devel Ther. 2020 Mar 26;14:1241–56.

58. Murphy MB, Moncivais K, Caplan AI. Mesenchymal stem cells: environmentally responsive therapeutics for regenerative medicine. Exp Mol Med. 2013 Nov;45(11):e54–e54.

59. Li M, Jiang Y, Hou Q, Zhao Y, Zhong L, Fu X. Potential pre-activation strategies for improving therapeutic efficacy of mesenchymal stem cells: current status and future prospects. Stem Cell Res Ther. 2022 Apr 4;13(1):146.

60. Madrigal M, Rao KS, Riordan NH. A review of therapeutic effects of mesenchymal stem cell secretions and induction of secretory modification by different culture methods. J Transl Med. 2014 Oct 11;12(1):260.

61. Bernardo ME, Fibbe WE. Mesenchymal Stromal Cells: Sensors and Switchers of Inflammation. Cell Stem Cell. 2013 Oct 3;13(4):392–402.

62. Basciano L, Nemos C, Foliguet B, de Isla N, de Carvalho M, Tran N, et al. Long term culture of mesenchymal stem cells in hypoxia promotes a genetic program maintaining their undifferentiated and multipotent status. BMC Cell Biol. 2011 Mar 30;12(1):12.

63. Grayson WL, Zhao F, Izadpanah R, Bunnell B, Ma T. Effects of hypoxia on human mesenchymal stem cell expansion and plasticity in 3D constructs. J Cell Physiol. 2006;207(2):331–9.

64. Lash GE, Fitzpatrick TE, Graham CH. Effect of Hypoxia on Cellular Adhesion to Vitronectin and Fibronectin. Biochem Biophys Res Commun. 2001 Sep 28;287(3):622–9.

65. Cooper PD, Burt AM, Wilson JN. Critical effect of oxygen tension on rate of growth of animal cells in continuous suspended culture. Nature. 1958 Nov 29;182(4648):1508–9.

66. Hsu SH, Chen CT, Wei YH. Inhibitory effects of hypoxia on metabolic switch and osteogenic differentiation of human mesenchymal stem cells. Stem Cells. 2013 Dec;31(12):2779–88.

67. Potier E, Ferreira E, Meunier A, Sedel L, Logeart-Avramoglou D, Petite H. Prolonged Hypoxia Concomitant with Serum Deprivation Induces Massive Human Mesenchymal Stem Cell Death. Tissue Eng. 2007 Jun;13(6):1325–31.

68. Minchenko A, Bauer T, Salceda S, Caro J. Hypoxic stimulation of vascular endothelial growth factor expression in vitro and in vivo. Lab Investig J Tech Methods Pathol. 1994 Sep 1;71(3):374–9.

69. Horino Y, Takahashi S, Miura T, Takahashi Y. Prolonged hypoxia accelerates the posttranscriptional process of collagen synthesis in cultured fibroblasts. Life Sci. 2002 Nov 15;71(26):3031–45.

70. Steinbrech DS, Longaker MT, Mehrara BJ, Saadeh PB, Chin GS, Gerrets RP, et al. Fibroblast response to hypoxia: the relationship between angiogenesis and matrix regulation. J Surg Res. 1999 Jun 15;84(2):127–33.

71. Kanichai M, Ferguson D, Prendergast PJ, Campbell VA. Hypoxia promotes chondrogenesis in rat mesenchymal stem cells: a role for AKT and hypoxia-inducible factor (HIF)-1alpha. J Cell Physiol. 2008 Sep;216(3):708–15.

72. Malladi P, Xu Y, Chiou M, Giaccia AJ, Longaker MT. Effect of reduced oxygen tension on chondrogenesis and osteogenesis in adipose-derived mesenchymal cells. Am J Physiol-Cell Physiol. 2006 Apr;290(4):C1139–46.

73. Knighton DR, Hunt TK, Scheuenstuhl H, Halliday BJ, Werb Z, Banda MJ. Oxygen Tension Regulates the Expression of Angiogenesis Factor by Macrophages. Science. 1983 Sep 23;221(4617):1283–5.

74. Stamati K, Mudera V, Cheema U. Evolution of oxygen utilization in multicellular organisms and implications for cell signalling in tissue engineering. J Tissue Eng. 2011 Jan 1;2(1):2041731411432365.

75. Chow DC, Wenning LA, Miller WM, Papoutsakis ET. Modeling pO(2) distributions in the bone marrow hematopoietic compartment. I. Krogh's model. Biophys J. 2001 Aug 1;81(2):675–84.

76. Bizzarri A, Koehler H, Cajlakovic M, Pasic A, Schaupp L, Klimant I, et al. Continuous oxygen monitoring in subcutaneous adipose tissue using microdialysis. Anal Chim Acta. 2006 Jul 28;573–574:48–56.

77. Harrison JS, Rameshwar P, Chang V, Bandari P. Oxygen saturation in the bone marrow of healthy volunteers. Blood. 2002 Jan 1;99(1):394.

78. Carreau A, Hafny-Rahbi BE, Matejuk A, Grillon C, Kieda C. Why is the partial oxygen pressure of human tissues a crucial parameter? Small molecules and hypoxia. J Cell Mol Med. 2011 Jun 1;15(6):1239–53.

79. Zwartouw HT, Westwood JC. Factors affecting growth and glycolysis in tissue culture. Br J Exp Pathol. 1958 Oct;39(5):529–39.

80. Grayson WL, Zhao F, Bunnell B, Ma T. Hypoxia enhances proliferation and tissue formation of human mesenchymal stem cells. Biochem Biophys Res Commun. 2007 Jul 6;358(3):948–53.

81. Buravkova LB, Andreeva ER, Gogvadze V, Zhivotovsky B. Mesenchymal stem cells and hypoxia: Where are we? Mitochondrion. 2014 Nov 1;19:105–12.

82. Das R, Jahr H, van Osch GJVM, Farrell E. The Role of Hypoxia in Bone Marrow–Derived Mesenchymal Stem Cells: Considerations for Regenerative Medicine Approaches. Tissue Eng Part B Rev. 2010 Apr;16(2):159–68.

83. Estrada JC, Albo C, Benguría A, Dopazo A, López-Romero P, Carrera-Quintanar L, et al. Culture of human mesenchymal stem cells at low oxygen tension improves growth and genetic stability by activating glycolysis. Cell Death Differ. 2012 May;19(5):743–55.

84. Keeley TP, Mann GE. Defining Physiological Normoxia for Improved Translation of Cell Physiology to Animal Models and Humans. Physiol Rev. 2019 Jan;99(1):161–234.

85. Williams JL, Weichert A, Zakrzewicz A, Da Silva-Azevedo L, Pries AR, Baum O, et al. Differential gene and protein expression in abluminal sprouting and intraluminal splitting forms of angiogenesis. Clin Sci. 2006 Apr 11;110(5):587–95.

86. Buizer AT, Bulstra SK, Veldhuizen AG, Kuijer R. The balance between proliferation and transcription of angiogenic factors of mesenchymal stem cells in hypoxia. Connect Tissue Res. 2018 Jan 2;59(1):12–20.

87. Rosová I, Dao M, Capoccia B, Link D, Nolta JA. Hypoxic Preconditioning Results in Increased Motility and Improved Therapeutic Potential of Human Mesenchymal Stem Cells. Stem Cells. 2008 Aug 1;26(8):2173–82.

88. Tsai AG, Johnson PC, Intaglietta M. Oxygen Gradients in the Microcirculation. Physiol Rev. 2003 Jul;83(3):933–63.

89. Graeber TG, Osmanian C, Jacks T, Housman DE, Koch CJ, Lowe SW, et al. Hypoxia-mediated selection of cells with diminished apoptotic potential in solid tumours. Nature. 1996 Jan 4;379(6560):88–91.

90. Levine AJ. The p53 tumor suppressor gene and gene product. Princess Takamatsu Symp. 1989 Jan 1;20:221–30.

91. Wang GL, Semenza GL. General involvement of hypoxia-inducible factor 1 in transcriptional response to hypoxia. Proc Natl Acad Sci U S A. 1993 May 1;90(9):4304–8.

92. Wang GL, Semenza GL. Purification and Characterization of Hypoxia-inducible Factor 1. J Biol Chem. 1995 Jan 20;270(3):1230–7.

93. Semenza GL, Wang GL. A nuclear factor induced by hypoxia via de novo protein synthesis binds to the human erythropoietin gene enhancer at a site required for transcriptional activation. Mol Cell Biol. 1992 Dec;12(12):5447–54.

94. Kamura T, Sato S, Iwai K, Czyzyk-Krzeska M, Conaway RC, Conaway JW. Activation of HIF1α ubiquitination by a reconstituted von Hippel-Lindau (VHL) tumor suppressor complex. Proc Natl Acad Sci. 2000 Sep 12;97(19):10430–5.

95. Maxwell PH, Wiesener MS, Chang GW, Clifford SC, Vaux EC, Cockman ME, et al. The tumour suppressor protein VHL targets hypoxia-inducible factors for oxygen-dependent proteolysis. Nature. 1999 May;399(6733):271–5.

96. Ivan M, Kondo K, Yang H, Kim W, Valiando J, Ohh M, et al. HIFα Targeted for VHL-Mediated Destruction by Proline Hydroxylation: Implications for O2 Sensing. Science. 2001 Apr 20;292(5516):464–8.

97. Salceda S, Caro J. Hypoxia-inducible Factor 1α (HIF-1α) Protein Is Rapidly Degraded by the Ubiquitin-Proteasome System under Normoxic Conditions: its stabilization by hypoxia depends on redox-induced changes*. J Biol Chem. 1997 Sep 5;272(36):22642–7.

98. Semenza GL. Hydroxylation of HIF-1: Oxygen Sensing at the Molecular Level. Physiology. 2004 Aug;19(4):176–82.

99. Jewell UR, Kvietikova I, Scheid A, Bauer C, Wenger RH, Gassmann M. Induction of HIF–1α in response to hypoxia is instantaneous. FASEB J. 2001;15(7):1312–4.

100. Wenger RH, Stiehl DP, Camenisch G. Integration of Oxygen Signaling at the Consensus HRE. Sci STKE. 2005 Oct 18;2005(306):re12–re12.

101. Manalo DJ, Rowan A, Lavoie T, Natarajan L, Kelly BD, Ye SQ, et al. Transcriptional regulation of vascular endothelial cell responses to hypoxia by HIF-1. Blood. 2005 Jan 15;105(2):659–69.

102. Semenza GL. HIF-1 and human disease: one highly involved factor. Genes Dev. 2000 Aug 15;14(16):1983–91.

103. Choudhry H, Harris AL. Advances in Hypoxia-Inducible Factor Biology. Cell Metab. 2018 Feb 6;27(2):281–98.

104. Lee JW, Bae SH, Jeong JW, Kim SH, Kim KW. Hypoxia-inducible factor (HIF-1)α: its protein stability and biological functions. Exp Mol Med. 2004 Feb;36(1):1–12.

105. Lee SH, Golinska M, Griffiths JR. HIF-1-Independent Mechanisms Regulating Metabolic Adaptation in Hypoxic Cancer Cells. Cells. 2021 Sep;10(9):2371.

106. Mazure NM, Pouysségur J. Hypoxia-induced autophagy: cell death or cell survival? Curr Opin Cell Biol. 2010 Apr 1;22(2):177–80.

107. Majmundar AJ, Wong WJ, Simon MC. Hypoxia-Inducible Factors and the Response to Hypoxic Stress. Mol Cell. 2010 Oct;40(2):294–309.

108. Kierans SJ, Taylor CT. Regulation of glycolysis by the hypoxia-inducible factor (HIF): implications for cellular physiology. J Physiol. 2021;599(1):23–37.

109. Semenza GL. Hypoxia-Inducible Factor 1: Control of Oxygen Homeostasis in Health and Disease. Pediatr Res. 2001 May;49(5):614–7.

110. Forsythe JA, Jiang BH, Iyer NV, Agani F, Leung SW, Koos RD, et al. Activation of vascular endothelial growth factor gene transcription by hypoxia-inducible factor 1. Mol Cell Biol. 1996 Sep;16(9):4604–13.

111. Ejtehadifar M, Shamsasenjan K, Movassaghpour A, Akbarzadehlaleh P, Dehdilani N, Abbasi P, et al. The Effect of Hypoxia on Mesenchymal Stem Cell Biology. Adv Pharm Bull. 2015 Jun;5(2):141–9.

112. Emami Nejad A, Najafgholian S, Rostami A, Sistani A, Shojaeifar S, Esparvarinha M, et al. The role of hypoxia in the tumor microenvironment and development of cancer stem cell: a novel approach to developing treatment. Cancer Cell Int. 2021 Jan 20;21(1):62.

113. Michiels C, Tellier C, Feron O. Cycling hypoxia: A key feature of the tumor microenvironment. Biochim Biophys Acta BBA - Rev Cancer. 2016 Aug 1;1866(1):76–86.

114. Bayer C, Vaupel P. Acute versus chronic hypoxia in tumors. Strahlenther Onkol. 2012 Jul 1;188(7):616–27.

115. Yusoff FM, Nakashima A, Kawano K ichiro, Kajikawa M, Kishimoto S, Maruhashi T, et al. Implantation of Hypoxia-Induced Mesenchymal Stem Cell Advances Therapeutic Angiogenesis. Stem Cells Int. 2022 Mar 20;2022:e6795274.

116. Park IH, Kim KH, Choi HK, Shim JS, Whang SY, June Hahn S, et al. Constitutive stabilization of hypoxia-inducible factor alpha selectively promotes the self-renewal of mesenchymal progenitors and maintains mesenchymal stromal cells in an undifferentiated state. Exp Mol Med. 2013 Sep;45(9):e44–e44.

117. Camacho-Cardenosa M, Quesada-Gómez JM, Camacho-Cardenosa A, Leal A, Dorado G, Torrecillas-Baena B, et al. Effects of normobaric cyclic hypoxia exposure on mesenchymal stem-cell differentiation–pilot study on bone parameters in elderly. World J Stem Cells. 2020 Dec 26;12(12):1667–90.

118. Fink T, Abildtrup L, Fogd K, Abdallah BM, Kassem M, Ebbesen P, et al. Induction of Adipocyte-Like Phenotype in Human Mesenchymal Stem Cells by Hypoxia. Stem Cells. 2004 Dec 1;22(7):1346–55.

119. Alvarez-Tejado M, Naranjo-Suárez S, Jiménez C, Carrera AC, Landázuri MO, Peso L del. Hypoxia Induces the Activation of the Phosphatidylinositol 3-Kinase/Akt Cell Survival Pathway in PC12 Cells: protective role in apoptosis. J Biol Chem. 2001 Jun 22;276(25):22368–74.

120. Dong Z, Wang JZ, Yu F, Venkatachalam MA. Apoptosis-Resistance of Hypoxic Cells: Multiple Factors Involved and a Role for IAP-2. Am J Pathol. 2003 Aug 1;163(2):663–71.

121. Wang L, Hu X, Zhu W, Jiang Z, Zhou Y, Chen P, et al. Increased leptin by hypoxic-preconditioning promotes autophagy of mesenchymal stem cells and protects them from apoptosis. Sci China Life Sci. 2014 Feb 1;57(2):171–80.

122. Zhang J, Xiong L, Tang W, Tang L, Wang B. Hypoxic culture enhances the expansion of rat bone marrow-derived mesenchymal stem cells via the regulatory pathways of cell division and apoptosis. Vitro Cell Dev Biol - Anim. 2018 Oct 1;54(9):666–76.

123. Vito A, El-Sayes N, Mossman K. Hypoxia-Driven Immune Escape in the Tumor Microenvironment. Cells. 2020 Apr;9(4):992.

124. Liu Y, Cox SR, Morita T, Kourembanas S. Hypoxia Regulates Vascular Endothelial Growth Factor Gene Expression in Endothelial Cells. Circ Res. 1995 Sep;77(3):638–43.

125. Goldberg MA, Schneider TJ. Similarities between the oxygen-sensing mechanisms regulating the expression of vascular endothelial growth factor and erythropoietin. J Biol Chem. 1994 Feb 11;269(6):4355–9.

126. Simon MP, Tournaire R, Pouyssegur J. The angiopoietin-2 gene of endothelial cells is up-regulated in hypoxia by a HIF binding site located in its first intron and by the central factors GATA-2 and Ets-1. J Cell Physiol. 2008;217(3):809–18.

127. Melillo G, Musso T, Sica A, Taylor LS, Cox GW, Varesio L. A hypoxia-responsive element mediates a novel pathway of activation of the inducible nitric oxide synthase promoter. J Exp Med. 1995 Dec 1;182(6):1683–93.

128. Tuder RM, Flook BE, Voelkel NF. Increased gene expression for VEGF and the VEGF receptors KDR/Flk and Flt in lungs exposed to acute or to chronic hypoxia. Modulation of gene expression by nitric oxide. J Clin Invest. 1995 Apr 1;95(4):1798–807.

129. Gerber HP, Condorelli F, Park J, Ferrara N. Differential Transcriptional Regulation of the Two Vascular Endothelial Growth Factor Receptor Genes: Flt-1, but not flk-1/kdr, is up-regulated by hypoxia*. J Biol Chem. 1997 Sep 19;272(38):23659–67.

130. Waltenberger J, Mayr U, Pentz S, Hombach V. Functional Upregulation of the Vascular Endothelial Growth Factor Receptor KDR by Hypoxia. Circulation. 1996 Oct;94(7):1647–54.

131. Takahashi Y, Takahashi S, Shiga Y, Yoshimi T, Miura T. Hypoxic Induction of Prolyl 4-Hydroxylase α(I) in Cultured Cells*. J Biol Chem. 2000 May 12;275(19):14139–46.

132. Ben-Yosef Y, Miller A, Shapiro S, Lahat N. Hypoxia of endothelial cells leads to MMP-2-dependent survival and death. Am J Physiol-Cell Physiol. 2005 Nov;289(5):C1321–31.

133. Han ZB, Ren H, Zhao H, Chi Y, Chen K, Zhou B, et al. Hypoxia-inducible factor (HIF)-1α directly enhances the transcriptional activity of stem cell factor (SCF) in response to hypoxia and epidermal growth factor (EGF). Carcinogenesis. 2008 Oct 1;29(10):1853–61.

134. Ceradini DJ, Kulkarni AR, Callaghan MJ, Tepper OM, Bastidas N, Kleinman ME, et al. Progenitor cell trafficking is regulated by hypoxic gradients through HIF-1 induction of SDF-1. Nat Med. 2004 Aug;10(8):858–64.

135. Graham CH, Fitzpatrick TE, McCrae KR. Hypoxia Stimulates Urokinase Receptor Expression Through a Heme Protein-Dependent Pathway. Blood. 1998 May 1;91(9):3300–7.

136. Liao H, Hyman MC, Lawrence DA, Pinsky DJ. Molecular regulation of the PAI-1 gene by hypoxia: contributions of Egr-1, HIF-1 α, and C/EBPα. FASEB J. 2007;21(3):935–49.

137. Hassan SJ, Babapoor S, Jee KJ, Puchner B, Deshpande M, Semenza GL, et al. Hypoxia Inducible Factor-1 Upregulates the Expression of Plasminogen Activator Inhibitor-1 in Retinal Endothelial Cells to Promote their Survival in Proliferative Diabetic Retinopathy Patients. Invest Ophthalmol Vis Sci. 2015 Jun 11;56(7):4282.

138. Schelter F, Halbgewachs B, Bäumler P, Neu C, Görlach A, Schrötzlmair F, et al. Tissue inhibitor of metalloproteinases-1-induced scattered liver metastasis is

mediated by hypoxia-inducible factor-1α. Clin Exp Metastasis. 2011 Feb 1;28(2):91–9.

139. Norman JT, Clark IM, Garcia PL. Hypoxia promotes fibrogenesis in human renal fibroblasts. Kidney Int. 2000 Dec 1;58(6):2351–66.

140. Kai AKL, Chan LK, Lo RCL, Lee JMF, Wong CCL, Wong JCM, et al. Down-regulation of TIMP2 by HIF-1α/miR-210/HIF-3α regulatory feedback circuit enhances cancer metastasis in hepatocellular carcinoma. Hepatology. 2016;64(2):473–87.

141. Kuwabara K, Ogawa S, Matsumoto M, Koga S, Clauss M, Pinsky DJ, et al. Hypoxia-mediated induction of acidic/basic fibroblast growth factor and platelet-derived growth factor in mononuclear phagocytes stimulates growth of hypoxic endothelial cells. Proc Natl Acad Sci. 1995 May 9;92(10):4606–10.

142. Gleadle JM, Ebert BL, Firth JD, Ratcliffe PJ. Regulation of angiogenic growth factor expression by hypoxia, transition metals, and chelating agents. Am J Physiol-Cell Physiol. 1995 Jun;268(6):C1362–8.

143. Bosch-Marce M, Okuyama H, Wesley JB, Sarkar K, Kimura H, Liu YV, et al. Effects of Aging and Hypoxia-Inducible Factor-1 Activity on Angiogenic Cell Mobilization and Recovery of Perfusion After Limb Ischemia. Circ Res. 2007 Dec 7;101(12):1310–8.

144. Rey S, Semenza GL. Hypoxia-inducible factor-1-dependent mechanisms of vascularization and vascular remodelling. Cardiovasc Res. 2010 May 1;86(2):236–42.

145. Negus RPM, Turner L, Burke F, Balkwill FR. Hypoxia down-regulates MCP-1 expression: implications for macrophage distribution in tumors. J Leukoc Biol. 1998;63(6):758–65.

146. Currie MJ, Gunningham SP, Turner K, Han C, Scott PA, Robinson BA, et al. Expression of the angiopoietins and their receptor Tie2 in human renal clear cell carcinomas; regulation by the von Hippel-Lindau gene and hypoxia. J Pathol. 2002;198(4):502–10.

147. Phelan MW, Forman LW, Perrine SP, Faller DV. Hypoxia increases thrombospondin-1 transcript and protein in cultured endothelial cells. J Lab Clin Med. 1998 Dec 1;132(6):519–29.

148. Rouwkema J, Khademhosseini A. Vascularization and Angiogenesis in Tissue Engineering: Beyond Creating Static Networks. Trends Biotechnol. 2016 Sep 1;34(9):733–45.

149. Stein I, Neeman M, Shweiki D, Itin A, Keshet E. Stabilization of vascular endothelial growth factor mRNA by hypoxia and hypoglycemia and coregulation with other ischemia-induced genes. Mol Cell Biol. 1995;15:5363–8.

150. Huang LE, Gu J, Schau M, Bunn HF. Regulation of hypoxia-inducible factor 1α is mediated by an O2-dependent degradation domain via the ubiquitin-proteasome pathway. Proc Natl Acad Sci. 1998 Jul 7;95(14):7987–92.

151. Wang GL, Jiang BH, Rue EA, Semenza GL. Hypoxia-inducible factor 1 is a basic-helix-loop-helix-PAS heterodimer regulated by cellular O2 tension. Proc Natl Acad Sci. 1995 Jun 6;92(12):5510–4.

152. Salceda S, Beck I, Caro J. Absolute Requirement of Aryl Hydrocarbon Receptor Nuclear Translocator Protein for Gene Activation by Hypoxia. Arch Biochem Biophys. 1996 Oct 15;334(2):389–94.

153. Martinez CA, Cistulli PA, Cook KM. A Cell Culture Model that Mimics Physiological Tissue Oxygenation Using Oxygen-permeable Membranes. Bio-Protoc. 2019 Sep 20;9(18):e3371–e3371.

154. Hammarlund EU. Harnessing hypoxia as an evolutionary driver of complex multicellularity. Interface Focus. 2020 Aug 6;10(4):20190101.

155. Somers VK, White DP, Amin R, Abraham WT, Costa F, Culebras A, et al. Sleep Apnea and Cardiovascular Disease (National Institutes of Health). J Am Coll Cardiol. 2008 Aug 19;52(8):686–717.

156. Basner RC. Continuous Positive Airway Pressure for Obstructive Sleep Apnea. N Engl J Med. 2007 Apr 26;356(17):1751–8.

157. Hunyor I, Cook KM. Models of intermittent hypoxia and obstructive sleep apnea: molecular pathways and their contribution to cancer. Am J Physiol-Regul Integr Comp Physiol. 2018 Oct;315(4):R669–87.

158. Sharma P, Dong Y, Somers VK, Peterson TE, Zhang Y, Wang S, et al. Intermittent hypoxia regulates vasoactive molecules and alters insulin-signaling in vascular endothelial cells. Sci Rep. 2018 Sep 20;8(1):14110.

159. Baguet JP, Barone-Rochette G, Tamisier R, Levy P, Pépin JL. Mechanisms of cardiac dysfunction in obstructive sleep apnea. Nat Rev Cardiol. 2012 Dec;9(12):679–88.

160. McNicholas WT. Obstructive Sleep Apnea and Inflammation. Prog Cardiovasc Dis. 2009 Mar 1;51(5):392–9.

161. Zheng J, Chen P, Zhong J, Cheng Y, Chen H, He Y, et al. HIF-1α in myocardial ischemia-reperfusion injury (Review). Mol Med Rep. 2021 May 1;23(5):1–9.

162. Murry CE, Jennings RB, Reimer KA. Preconditioning with ischemia: a delay of lethal cell injury in ischemic myocardium. Circulation. 1986 Nov;74(5):1124–36.

163. Przyklenk K, Bauer B, Ovize M, Kloner RA, Whittaker P. Regional ischemic ‘preconditioning’ protects remote virgin myocardium from subsequent sustained coronary occlusion. Circulation. 1993 Mar;87(3):893–9.

164. Günaydin B, Çakici I, Soncul H, Kalaycioglu S, Çevik C, Sancak B, et al. Does remote organ ischaemia trigger cardiac preconditioning during coronary artery surgery? Pharmacol Res. 2000 Apr 1;41(4):493–6.

165. Kharbanda R k., Mortensen U m., White P a., Kristiansen S b., Schmidt M r., Hoschtitzky J a., et al. Transient Limb Ischemia Induces Remote Ischemic Preconditioning In Vivo. Circulation. 2002 Dec 3;106(23):2881–3.

166. Heusch G, Bøtker HE, Przyklenk K, Redington A, Yellon D. Remote Ischemic Conditioning. J Am Coll Cardiol. 2015 Jan 20;65(2):177–95.

167. Eckle T, Köhler D, Lehmann R, El Kasmi KC, Eltzschig HK. Hypoxia-Inducible Factor-1 Is Central to Cardioprotection. Circulation. 2008 Jul 8;118(2):166–75.

168. Hess DC, Blauenfeldt RA, Andersen G, Hougaard KD, Hoda MN, Ding Y, et al. Remote ischaemic conditioning—a new paradigm of self-protection in the brain. Nat Rev Neurol. 2015 Dec;11(12):698–710.

169. Wang Y, Reis C, Applegate R, Stier G, Martin R, Zhang JH. Ischemic conditioning-induced endogenous brain protection: Applications pre-, per- or post-stroke. Exp Neurol. 2015 Oct 1;272:26–40.

170. Landman TRJ, Schoon Y, Warlé MC, de Leeuw FE, Thijssen DHJ. Remote Ischemic Conditioning as an Additional Treatment for Acute Ischemic Stroke. Stroke. 2019 Jul;50(7):1934–9.

171. Hao Y, Xin M, Feng L, Wang X, Wang X, Ma D, et al. Review Cerebral Ischemic Tolerance and Preconditioning: Methods, Mechanisms, Clinical Applications, and Challenges. Front Neurol . 2020;11.

172. Koch S, Katsnelson M, Dong C, Perez-Pinzon M. Remote Ischemic Limb Preconditioning After Subarachnoid Hemorrhage. Stroke. 2011 May;42(5):1387–91.

173. Meng R, Ding Y, Asmaro K, Brogan D, Meng L, Sui M, et al. Ischemic Conditioning Is Safe and Effective for Octo- and Nonagenarians in Stroke Prevention and Treatment. Neurotherapeutics. 2015 Jul 1;12(3):667–77.

174. Mi T, Yu F, Ji X, Sun Y, Qu D. The Interventional Effect of Remote Ischemic Preconditioning on Cerebral Small Vessel Disease: A Pilot Randomized Clinical Trial. Eur Neurol. 2016;76(1–2):28–34.

175. Yang J, Liu C, Du X, Liu M, Ji X, Du H, et al. Hypoxia Inducible Factor 1α Plays a Key Role in Remote Ischemic Preconditioning Against Stroke by Modulating Inflammatory Responses in Rats. J Am Heart Assoc. 2018 Feb 24;7(5):e007589.

176. Du X, Yang J, Liu C, Wang S, Zhang C, Zhao H, et al. Hypoxia-Inducible Factor 1α and 2α Have Beneficial Effects in Remote Ischemic Preconditioning Against Stroke by Modulating Inflammatory Responses in Aged Rats. Front Aging Neurosci . 2020;12.

177. Cochrane J, Williams BT, Banerjee A, Harken AH, Burke TJ, Cairns CB, et al. Laboratory Study: Ischemic Preconditioning Attenuates Functional, Metabolic, and Morphologic Injury from Ischemic Acute Renal Failure in the Rat. Ren Fail. 1999 Jan 1;21(2):135–45.

178. Kume M, Yamamoto Y, Saad S, Gomi T, Kimoto S, Shimabukuro T, et al. Ischemic preconditioning of the liver in rats: Implications of heat shock protein induction to increase tolerance of ischemia-reperfusion injury. J Lab Clin Med. 1996 Sep 1;128(3):251–8.

179. Bøtker HE, Kharbanda R, Schmidt MR, Bøttcher M, Kaltoft AK, Terkelsen CJ, et al. Remote ischaemic conditioning before hospital admission, as a complement to angioplasty, and effect on myocardial salvage in patients with acute myocardial infarction: a randomised trial. The Lancet. 2010 Feb 27;375(9716):727–34.

180. Hausenloy DJ, Yellon DM. Remote ischaemic preconditioning: underlying mechanisms and clinical application. Cardiovasc Res. 2008 Aug 1;79(3):377–86.

181. Donato M, Bin EP, D´Annunzio V, Gelpi RJ. Myocardial remote ischemic preconditioning: from cell biology to clinical application. Mol Cell Biochem. 2021 Oct 1;476(10):3857–67.

182. Dewhirst MW. Relationships between Cycling Hypoxia, HIF-1, Angiogenesis and Oxidative Stress. Radiat Res. 2009;172(6):653–65.

183. Toffoli S, Roegiers A, Feron O, Van Steenbrugge M, Ninane N, Raes M, et al. Intermittent hypoxia is an angiogenic inducer for endothelial cells: role of HIF-1. Angiogenesis. 2009 Mar 1;12(1):47–67.

184. Saxena K, Jolly MK. Acute vs. Chronic vs. Cyclic Hypoxia: Their Differential Dynamics, Molecular Mechanisms, and Effects on Tumor Progression. Biomolecules. 2019 Aug;9(8):339.

185. Pressley M, Gallaher JA, Brown JS, Tomaszewski MR, Borad P, Damaghi M, et al. Cycling hypoxia selects for constitutive HIF stabilization. Sci Rep. 2021 Mar 11;11(1):5777.

186. Bader SB, Dewhirst MW, Hammond EM. Cyclic Hypoxia: An Update on Its Characteristics, Methods to Measure It and Biological Implications in Cancer. Cancers. 2021 Jan;13(1):23.

187. Martinez CA, Jiramongkol Y, Bal N, Alwis I, Nedoboy PE, Farnham MMJ, et al. Intermittent hypoxia enhances the expression of hypoxia inducible factor HIF1A through histone demethylation. J Biol Chem. 2022 Sep 27;102536.

188. HoWangYin KY, Loinard C, Bakker W, Guérin CL, Vilar J, D’Audigier C, et al. HIF-Prolyl Hydroxylase 2 Inhibition Enhances the Efficiency of Mesenchymal Stem Cell-Based Therapies for the Treatment of Critical Limb Ischemia. Stem Cells. 2014 Jan 1;32(1):231–43.

189. Zhu W, Chen J, Cong X, Hu S, Chen X. Hypoxia and Serum Deprivation-Induced Apoptosis in Mesenchymal Stem Cells. Stem Cells. 2006 Feb 1;24(2):416–25.

190. Chang W, Song BW, Lim S, Song H, Shim CY, Cha MJ, et al. Mesenchymal Stem Cells Pretreated with Delivered Hph-1-Hsp70 Protein Are Protected from Hypoxia-Mediated Cell Death and Rescue Heart Functions from Myocardial Injury. Stem Cells. 2009 Sep 1;27(9):2283–92.

191. Lavrentieva A, Majore I, Kasper C, Hass R. Effects of hypoxic culture conditions on umbilical cord-derived human mesenchymal stem cells. Cell Commun Signal. 2010 Jul 16;8(1):18.

192. Crisostomo PR, Wang Y, Markel TA, Wang M, Lahm T, Meldrum DR. Human mesenchymal stem cells stimulated by TNF-α, LPS, or hypoxia produce growth factors by an NFκB- but not JNK-dependent mechanism. Am J Physiol-Cell Physiol. 2008 Mar;294(3):C675–82.

193. Ma T, Grayson WL, Fröhlich M, Vunjak-Novakovic G. Hypoxia and stem cell-based engineering of mesenchymal tissues. Biotechnol Prog. 2009;25(1):32–42.

194. Yang Y, Lee EH, Yang Z. Hypoxia-Conditioned Mesenchymal Stem Cells in Tissue Regeneration Application. Tissue Eng Part B Rev . 2021 Sep 26

195. Antebi B, Rodriguez LA, Walker KP, Asher AM, Kamucheka RM, Alvarado L, et al. Short-term physiological hypoxia potentiates the therapeutic function of mesenchymal stem cells. Stem Cell Res Ther. 2018 Oct 11;9(1):265.

196. Malda J, Klein TJ, Upton Z. The roles of hypoxia in the in vitro engineering of tissues. Tissue Eng. 2007 Sep 9;13(9):2153–62.

197. Mikos AG, Herring SW, Ochareon P, Elisseeff J, Lu HH, Kandel R, et al. Engineering Complex Tissues. Tissue Eng. 2006 Dec;12(12):3307–39.

198. Pellegata AF, Tedeschi AM, De Coppi P. Whole Organ Tissue Vascularization: Engineering the Tree to Develop the Fruits. Front Bioeng Biotechnol . 2018;6.

199. Utzinger U, Baggett B, Weiss JA, Hoying JB, Edgar LT. Large-scale time series microscopy of neovessel growth during angiogenesis. Angiogenesis. 2015 Jul 21;18(3):219–32.

200. Secomb TW, Hsu R, Braun RD, Ross JR, Gross JF, Dewhirst MW. Theoretical Simulation of Oxygen Transport to Tumors by Three-Dimensional Networks of Microvessels. In: Hudetz AG, Bruley DF, editors. Oxygen Transport to Tissue XX . Boston, MA: Springer US; 1998. p. 629–34. (Advances in Experimental Medicine and Biology).

201. Franko AJ, Sutherland RM. Oxygen diffusion distance and development of necrosis in multicell spheroids. Radiat Res. 1979 Sep;79(3):439–53.

202. Rouwkema J, Rivron NC, van Blitterswijk CA. Vascularization in tissue engineering. Trends Biotechnol. 2008;26(8):434–41.

203. Novosel EC, Kleinhans C, Kluger PJ. Vascularization is the key challenge in tissue engineering. Adv Drug Deliv Rev. 2011;63(4):300–11.

204. LaValley DJ, Reinhart-King CA. Matrix stiffening in the formation of blood vessels. Adv Regen Biol. 2014 Sep 25;1(1):25247.

205. Mehdizadeh H, Sumo S, Bayrak ES, Brey EM, Cinar A. Three-dimensional modeling of angiogenesis in porous biomaterial scaffolds. Biomaterials. 2013;34(12):2875–87.

206. Conway E, Collen D, Carmeliet P. Molecular mechanisms of blood vessel growth. Cardiovasc Res. 2001 Feb 16;49(3):507–21.

207. ANNEX B, SIMONS M. Growth factor-induced therapeutic angiogenesis in the heart: protein therapy. Cardiovasc Res. 2005 Feb 15;65(3):649–55.

208. Henry TD, Annex BH, McKendall GR, Azrin MA, Lopez JJ, Giordano FJ, et al. The VIVA trial: Vascular endothelial growth factor in Ischemia for Vascular Angiogenesis. Circulation. 2003 Mar 18;107(10):1359–65.

209. Rao RR, Peterson AW, Ceccarelli J, Putnam AJ, Stegemann JP. Matrix composition regulates three-dimensional network formation by endothelial cells and mesenchymal stem cells in collagen/fibrin materials. Angiogenesis. 2012 Jun;15(2):253–64.

210. Hoch E, Tovar GEM, Borchers K. Bioprinting of artificial blood vessels: current approaches towards a demanding goal. Eur J Cardiothorac Surg. 2014 Nov 1;46(5):767–78.

211. Zhang B, Radisic M. Organ-level vascularization: The Mars mission of bioengineering. J Thorac Cardiovasc Surg. 2020 May 1;159(5):2003–7.

212. Kokemueller H, Spalthoff S, Nolff M, Tavassol F, Essig H, Stuehmer C, et al. Prefabrication of vascularized bioartificial bone grafts in vivo for segmental mandibular reconstruction: experimental pilot study in sheep and first clinical application. Int J Oral Maxillofac Surg. 2010 Apr 1;39(4):379–87.

213. Laschke MW, Vollmar B, Menger MD. Inosculation: Connecting the Life-Sustaining Pipelines. Tissue Eng Part B Rev. 2009 Dec 4;15(4):455–65.

214. Gurtner GC, Werner S, Barrandon Y, Longaker MT. Wound repair and regeneration. Nature. 2008 May;453(7193):314–21.

215. Richardson RJ. Parallels between vertebrate cardiac and cutaneous wound healing and regeneration. Npj Regen Med. 2018 Nov 7;3(1):1–9.

216. Zomer HD, Trentin AG. Skin wound healing in humans and mice: Challenges in translational research. J Dermatol Sci. 2018 Apr 1;90(1):3–12.

217. Guest JF, Fuller GW, Vowden P. Cohort study evaluating the burden of wounds to the UK's National Health Service in 2017/2018: update from 2012/2013. BMJ Open. 2020 Dec 1;10(12):e045253.

218. Phillips CJ, Humphreys I, Fletcher J, Harding K, Chamberlain G, Macey S. Estimating the costs associated with the management of patients with chronic wounds using linked routine data. Int Wound J. 2016;13(6):1193–7.

219. Sen CK, Gordillo GM, Roy S, Kirsner R, Lambert L, Hunt TK, et al. Human skin wounds: A major and snowballing threat to public health and the economy. Wound Repair Regen. 2009;17(6):763–71.

220. Giesey RL, Mehrmal S, Uppal P, Delost G. The Global Burden of Skin and Subcutaneous Disease: A Longitudinal Analysis from the Global Burden of Disease Study From 1990-2017. SKIN J Cutan Med. 2021 Mar 6;5(2):125–36.

221. Iqbal T, Saaiq M, Ali Z. Epidemiology and outcome of burns: Early experience at the country's first national burns Centre. Burns. 2013 Mar 1;39(2):358–62.

222. Ho J, Walsh C, Yue D, Dardik A, Cheema U. Current Advancements and Strategies in Tissue Engineering for Wound Healing: A Comprehensive Review. Adv Wound Care. 2017 Jun 1;6(6):191.

223. Debels H, Hamdi M, Abberton K, Morrison W. Dermal Matrices and Bioengineered Skin Substitutes: A Critical Review of Current Options. Plast Reconstr Surg – Glob Open. 2015 Jan;3(1):e284.

224. Pham C, Greenwood J, Cleland H, Woodruff P, Maddern G. Bioengineered skin substitutes for the management of burns: A systematic review. Burns. 2007 Dec 1;33(8):946–57.

225. Heimbach D, Luterman A, Burke J, Cram A, Herndon D, Hunt J, et al. Artificial Dermis for Major Burns: A Multi-Center Randomized Clinical Trial. Ann Surg. 1988 Sep;208(3):313.

226. Edwards SS, Zavala G, Prieto CP, Elliott M, Martínez S, Egaña JT, et al. Functional analysis reveals angiogenic potential of human mesenchymal stem cells from Wharton's jelly in dermal regeneration. Angiogenesis. 2014 Oct 1;17(4):851–66.

227. Frueh FS, Menger MD, Lindenblatt N, Giovanoli P, Laschke MW. Current and emerging vascularization strategies in skin tissue engineering. Crit Rev Biotechnol. 2017 Jul 4;37(5):613–25.

228. Wahl EA, Fierro FA, Peavy TR, Hopfner U, Dye JF, Machens HG, et al. In Vitro Evaluation of Scaffolds for the Delivery of Mesenchymal Stem Cells to Wounds. BioMed Res Int. 2015 Oct 4;2015:e108571.

229. Später T, Frueh FS, Metzger W, Menger MD, Laschke MW. In vivo biocompatibility, vascularization, and incorporation of INTEGRA® dermal regenerative template and flowable wound matrix. J Biomed Mater Res B Appl Biomater. 2018;106(1):52–60.

230. Später T, Frueh FS, Menger MD, Laschke MW. Potentials and limitations of INTEGRA® flowable wound matrix seeded with adipose tissue-derived microvascular fragments. Eur Cell Mater. 2017 Apr 5;33:268–78.

231. Peña-Villalobos I, Casanova-Maldonado I, Lois P, Prieto C, Pizarro C, Lattus J, et al. Hyperbaric Oxygen Increases Stem Cell Proliferation, Angiogenesis and Wound-Healing Ability of WJ-MSCs in Diabetic Mice. Front Physiol . 2018;9.

232. Notodihardjo SC, Morimoto N, Munisso MC, Le TM, Mitsui T, Kakudo N, et al. A comparison of the wound healing process after the application of three dermal substitutes with or without basic fibroblast growth factor impregnation in diabetic mice. J Plast Reconstr Aesthet Surg. 2020 Aug 1;73(8):1547–55.

233. Leonardi D, Oberdoerfer D, Fernandes MC, Meurer RT, Pereira-Filho GA, Cruz P, et al. Mesenchymal stem cells combined with an artificial dermal substitute improve repair in full-thickness skin wounds. Burns. 2012 Dec 1;38(8):1143–50.

234. Huang SP, Hsu CC, Chang SC, Wang CH, Deng SC, Dai NT, et al. Adipose-Derived Stem Cells Seeded on Acellular Dermal Matrix Grafts Enhance Wound Healing in a Murine Model of a Full-Thickness Defect. Ann Plast Surg. 2012 Dec;69(6):656–62.

235. Frueh FS, Später T, Körbel C, Scheuer C, Simson AC, Lindenblatt N, et al. Prevascularization of dermal substitutes with adipose tissue-derived microvascular fragments enhances early skin grafting. Sci Rep. 2018 Jul 20;8(1):10977.

236. Formigli L, Paternostro F, Tani A, Mirabella C, Quattrini Li A, Nosi D, et al. MSCs seeded on bioengineered scaffolds improve skin wound healing in rats. Wound Repair Regen. 2015;23(1):115–23.

237. Fierro FA, O'Neal AJ, Beegle JR, Chávez MN, Peavy TR, Isseroff RR, et al. Hypoxic pre-conditioning increases the infiltration of endothelial cells into scaffolds for dermal regeneration pre-seeded with mesenchymal stem cells. Front Cell Dev Biol . 2015;3.

238. Doornaert M, Depypere B, Creytens D, Declercq H, Taminau J, Lemeire K, et al. Human decellularized dermal matrix seeded with adipose-derived stem cells enhances wound healing in a murine model: Experimental study. Ann Med Surg. 2019 Oct 1;46:4–11.

239. Cherubino M, Valdatta L, Balzaretti R, Pellegatta I, Rossi F, Protasoni M, et al. Human adipose-derived stem cells promote vascularization of collagen-based scaffolds transplanted into nude mice. Regen Med. 2016 Apr;11(3):261–71.

240. Capella-Monsonís H, De Pieri A, Peixoto R, Korntner S, Zeugolis DI. Extracellular matrix-based biomaterials as adipose-derived stem cell delivery vehicles in wound healing: a comparative study between a collagen scaffold and two xenografts. Stem Cell Res Ther. 2020 Nov 27;11(1):510.

241. Banakh I, Cheshire P, Rahman M, Carmichael I, Jagadeesan P, Cameron NR, et al. A Comparative Study of Engineered Dermal Templates for Skin Wound Repair in a Mouse Model. Int J Mol Sci. 2020 Jan;21(12):4508.

242. Wang M, Xu X, Lei X, Tan J, Xie H. Mesenchymal stem cell-based therapy for burn wound healing. Burns Trauma. 2021 Jan 1;9:tkab002.

243. Opalenik SR, Davidson JM. Fibroblast differentiation of bone marrow-derived cells during wound repair. FASEB J Off Publ Fed Am Soc Exp Biol. 2005 Sep;19(11):1561–3.

244. An Y, Liu WJ, Xue P, Ma Y, Zhang LQ, Zhu B, et al. Autophagy promotes MSC-mediated vascularization in cutaneous wound healing via regulation of VEGF secretion. Cell Death Dis. 2018 Jan 19;9(2):1–14.

245. Beccia E, Carbone A, Cecchino LR, Pedicillo MC, Annacontini L, Lembo F, et al. Adipose Stem Cells and Platelet-Rich Plasma Induce Vascular-Like Structures in a Dermal Regeneration Template. Tissue Eng Part A. 2021 May;27(9–10):631–41.

246. Yang H ya, Fierro F, Yoon DJ, Gallegos A, Osborn SL, Nguyen AV, et al. Combination product of dermal matrix, preconditioned human mesenchymal stem cells and timolol promotes wound healing in the porcine wound model. J Biomed Mater Res B Appl Biomater. 2022;110(7):1615–23.

247. Assi R, Foster TR, He H, Stamati K, Bai H, Huang Y, et al. Delivery of mesenchymal stem cells in biomimetic engineered scaffolds promotes healing of diabetic ulcers. Regen Med. 2016 Apr 1;11(3):245–60.

248. Wang Y, Feng Q, Li Z, Bai X, Wu Y, Liu Y. Evaluating the Effect of INTEGRA®Seeded with Adipose Tissue-Derived Stem Cells or Fibroblasts in Wound Healing. Curr Drug Deliv. 2020;17(7):629–35.

249. Zomer HD, Jeremias T da S, Ratner B, Trentin AG. Mesenchymal stromal cells from dermal and adipose tissues induce macrophage polarization to a pro-repair phenotype and improve skin wound healing. Cytotherapy. 2020 May 1;22(5):247–60.

250. Egaña JT, Fierro FA, Krüger S, Bornhäuser M, Huss R, Lavandero S, et al. Use of Human Mesenchymal Cells to Improve Vascularization in a Mouse Model for Scaffold-Based Dermal Regeneration. Tissue Eng Part A. 2009 May;15(5):1191–200.

251. Kalyanaraman B, Boyce ST. Wound Healing on Athymic Mice With Engineered Skin Substitutes Fabricated with Keratinocytes Harvested from an Automated Bioreactor. J Surg Res. 2009 Apr 1;152(2):296–302.

252. Meruane MA, Rojas M, Marcelain K. The Use of Adipose Tissue–Derived Stem Cells within a Dermal Substitute Improves Skin Regeneration by Increasing Neoangiogenesis and Collagen Synthesis. Plast Reconstr Surg. 2012 Jul;130(1):53–63.

253. Browne S, Healy KE. Matrix-assisted cell transplantation for tissue vascularization. Adv Drug Deliv Rev . 2018 Dec 31

254. Tsai CC, Chen YJ, Yew TL, Chen LL, Wang JY, Chiu CH, et al. Hypoxia inhibits senescence and maintains mesenchymal stem cell properties through down-regulation of E2A-p21 by HIF-TWIST. Blood. 2011 Jan 13;117(2):459–69.

255. Lee Y, Jung J, Cho KJ, Lee SK, Park JW, Oh IH, et al. Increased SCF/c-kit by hypoxia promotes autophagy of human placental chorionic plate-derived mesenchymal stem cells via regulating the phosphorylation of mTOR. J Cell Biochem. 2013;114(1):79–88.

256. Wu J, Niu J, Li X, Li Y, Wang X, Lin J, et al. Hypoxia Induces Autophagy of Bone Marrow-Derived Mesenchymal Stem Cells via Activation of ERK1/2. Cell Physiol Biochem. 2014;33(5):1467–74.

257. Burlacu A, Grigorescu G, Rosca AM, Preda MB, Simionescu M. Factors Secreted by Mesenchymal Stem Cells and Endothelial Progenitor Cells Have Complementary Effects on Angiogenesis In Vitro. Stem Cells Dev. 2013 Feb 15;22(4):643–53.

258. Igarashi A, Segoshi K, Sakai Y, Pan H, Kanawa M, Higashi Y, et al. Selection of Common Markers for Bone Marrow Stromal Cells from Various Bones Using Real-Time RT-PCR: Effects of Passage Number and Donor Age. Tissue Eng. 2007 Oct 1;13(10):2405–17.

259. Maramorosch K. Tissue Culture: Methods and Applications by Paul F. Kruse, Jr., M. K. Patterson, Jr. J N Y Entomol Soc. 1974;82:200.

260. Chan JKY, Lam P. Soluble Factors from Human Fetal Bone Marrow-Derived Mesenchymal Stem Cells: Preparation of Conditioned Medium and Its Effect on Tumor Cells. In Humana Press, New York, NY; 2016. p. 467–75.

261. Samsonraj RM, Rai B, Sathiyanathan P, Puan KJ, Rötzschke O, Hui JH, et al. Establishing Criteria for Human Mesenchymal Stem Cell Potency. STEM CELLS. 2015;33(6):1878–91.

262. Kuznetsov SA, Mankani MH, Bianco P, Robey PG. Enumeration of the colony-forming units–fibroblast from mouse and human bone marrow in normal and pathological conditions. Stem Cell Res. 2009 Jan 1;2(1):83–94.

263. Duellman SJ, Zhou W, Meisenheimer P, Vidugiris G, Cali JJ, Gautam P, et al. Bioluminescent, Nonlytic, Real-Time Cell Viability Assay and Use in Inhibitor Screening. Assay Drug Dev Technol. 2015 Oct 1;13(8):456–65.

264. Addgene: Kit Free RNA Extraction . [cited 2023 Feb 1]. Available from: https://www.addgene.org/protocols/kit-free-rna-extraction/

265. Lab MS. Quanti-iT^{TM} Pico Green dsDNA Assay (Invitrogen P7589). 2019 Mar 4 [cited 2023 Feb 1]; Available from: https://www.protocols.io/view/Quanti-iT-Pico-Green-dsDNA-Assay-Invitrogen-P7589-c5zy75

266. Livak KJ, Schmittgen TD. Analysis of Relative Gene Expression Data Using Real-Time Quantitative PCR and the 2−ΔΔCT Method. Methods. 2001 Dec 1;25(4):402–8.

267. Schmittgen TD, Livak KJ. Analyzing real-time PCR data by the comparative CT method. Nat Protoc. 2008 Jun;3(6):1101–8.

268. Al Hosni R, Bozec L, Roberts SJ, Cheema U. Reprogramming bone progenitor identity and potency through control of collagen density and oxygen tension. iScience. 2022 Apr 15;25(4):104059.

269. Crowley C, Butler CR, Camilli C, Hynds RE, Kolluri KK, Janes SM, et al. Non-Invasive Longitudinal Bioluminescence Imaging of Human Mesoangioblasts in Bioengineered Esophagi.

270. Hassan WU, Greiser U, Wang W. Role of adipose-derived stem cells in wound healing. Wound Repair Regen. 2014;22(3):313–25.

271. Lau K, Paus R, Tiede S, Day P, Bayat A. Exploring the role of stem cells in cutaneous wound healing. Exp Dermatol. 2009;18(11):921–33.

272. Semenova E, Grudniak MP, Machaj EK, Bocian K, Chroscinska-Krawczyk M, Trochonowicz M, et al. Mesenchymal Stromal Cells from Different Parts of Umbilical Cord: Approach to Comparison & Characteristics. Stem Cell Rev Rep. 2021 Oct 1;17(5):1780–95.

273. Locke M, Windsor J, Dunbar PR. Human adipose-derived stem cells: isolation, characterization and applications in surgery. ANZ J Surg. 2009;79(4):235–44.

274. Nagamura-Inoue T, He H. Umbilical cord-derived mesenchymal stem cells: Their advantages and potential clinical utility. World J Stem Cells. 2014 Apr 26;6(2):195.

275. Wagner W, Wein F, Seckinger A, Frankhauser M, Wirkner U, Krause U, et al. Comparative characteristics of mesenchymal stem cells from human bone marrow, adipose tissue, and umbilical cord blood. Exp Hematol. 2005;33(11):1402–16.

276. K. Batsali A, Kastrinaki MC, A. Papadaki H, Pontikoglou C. Mesenchymal Stem Cells Derived from Wharton's Jelly of the Umbilical Cord: Biological Properties and Emerging Clinical Applications. Curr Stem Cell Res Ther. 2013 Feb 1;8(2):144–55.

277. El Omar R, Beroud J, Stoltz JF, Menu P, Velot E, Decot V. Umbilical Cord Mesenchymal Stem Cells: The New Gold Standard for Mesenchymal Stem Cell-Based Therapies? Tissue Eng Part B Rev. 2014 Oct 21;20(5):523–44.

278. Kern S, Eichler H, Stoeve J, Klüter H, Bieback K. Comparative Analysis of Mesenchymal Stem Cells from Bone Marrow, Umbilical Cord Blood, or Adipose Tissue. Stem Cells. 2006 May 1;24(5):1294–301.

279. Mohyeldin A, Garzón-Muvdi T, Quiñones-Hinojosa A. Oxygen in Stem Cell Biology: A Critical Component of the Stem Cell Niche. Cell Stem Cell. 2010 Aug 6;7(2):150–61.

280. Goossens GH, Blaak EE. Adipose tissue oxygen tension: implications for chronic metabolic and inflammatory diseases. Curr Opin Clin Nutr Metab Care. 2012 Nov;15(6):539–46.

281. Sjöstedt S, Rooth G, Caligara F. The Oxygen Tension of the Blood in the Umbilical Cord and the Intervillous Space. Arch Dis Child. 1960 Dec 1;35(184):529–33.

282. Leach RM, Treacher DF. Oxygen transport2. Tissue hypoxia. BMJ. 1998 Nov 14;317(7169):1370–3.

283. Wang W, Winlove CP, Michel CC. Oxygen Partial Pressure in Outer Layers of Skin of Human Finger Nail Folds. J Physiol. 2003;549(3):855–63.

284. Eichhorn ME, Kleespies A, Angele MK, Jauch KW, Bruns CJ. Angiogenesis in cancer: molecular mechanisms, clinical impact. Langenbecks Arch Surg. 2007;392(3):371–9.

285. Baeriswyl V, Christofori G. The angiogenic switch in carcinogenesis. Semin Cancer Biol. 2009;19(5):329–37.

286. Dominici M, Le Blanc K, Mueller I, Slaper-Cortenbach I, Marini FC, Krause DS, et al. Minimal criteria for defining multipotent mesenchymal stromal cells. The International Society for Cellular Therapy position statement. Cytotherapy. 2006;8(4):315–7.

287. Corrao S, La Rocca G, Lo Iacono M, Corsello T, Farina F, Anzalone R. Umbilical cord revisited: from Wharton's jelly myofibroblasts to mesenchymal stem cells. Histol Histopathol. 2013;28(10):1235–44.

288. Davies JE, Walker JT, Keating A. Concise Review: Wharton's Jelly: The Rich, but Enigmatic, Source of Mesenchymal Stromal Cells. STEM CELLS Transl Med. 2017 Jul 1;6(7):1620–30.

289. Xu L, Zhou J, Liu J, Liu Y, Wang L, Jiang R, et al. Different Angiogenic Potentials of Mesenchymal Stem Cells Derived from Umbilical Artery, Umbilical Vein, and Wharton's Jelly. Stem Cells Int. 2017;2017:3175748.

290. Kobayashi K, Kubota T, Aso T. Study on myofibroblast differentiation in the stromal cells of Wharton's jelly: Expression and localization of α-smooth muscle actin. Early Hum Dev. 1998 Jul 10;51(3):223–33.

291. Margossian T, Reppel L, Makdissy N, Stoltz JF, Bensoussan D, Huselstein C. Mesenchymal stem cells derived from Wharton's jelly: comparative phenotype analysis between tissue and in vitro expansion. Biomed Mater Eng. 2012;22(4):243–54.

292. Karahuseyinoglu S, Cinar O, Kilic E, Kara F, Akay GG, Demiralp DÖ, et al. Biology of Stem Cells in Human Umbilical Cord Stroma: In Situ and In Vitro Surveys. Stem Cells. 2007 Feb;25(2):319–31.

293. Hofer EL, Labovsky V, La Russa V, Vallone VF, Honegger AE, Belloc CG, et al. Mesenchymal Stromal Cells, Colony-Forming Unit Fibroblasts, From Bone Marrow of Untreated Advanced Breast and Lung Cancer Patients Suppress Fibroblast Colony Formation From Healthy Marrow. Stem Cells Dev. 2010 Mar;19(3):359–70.

294. Kang I, Lee BC, Choi SW, Lee JY, Kim JJ, Kim BE, et al. Donor-dependent variation of human umbilical cord blood mesenchymal stem cells in response to hypoxic preconditioning and amelioration of limb ischemia. Exp Mol Med. 2018 Apr 20;50(4):35.

295. Widowati W, Wijaya L, Bachtiar I, Gunanegara RF, Sugeng SU, Irawan YA, et al. Effect of oxygen tension on proliferation and characteristics of Wharton's jelly-derived mesenchymal stem cells. Biomark Genomic Med. 2014 Mar 1;6(1):43–8.

296. Himal I, Goyal U, Ta M. Evaluating Wharton's Jelly-Derived Mesenchymal Stem Cell's Survival, Migration, and Expression of Wound Repair Markers under Conditions of Ischemia-Like Stress. Stem Cells Int. 2017 Feb 7;2017:1–13.

297. Wu M, Zhang R, Zou Q, Chen Y, Zhou M, Li X, et al. Comparison of the Biological Characteristics of Mesenchymal Stem Cells Derived from the Human Placenta and Umbilical Cord. Sci Rep. 2018 Mar 22;8(1):5014.

298. Arutyunyan IV, Kananykhina EYu, Fatkhudinov TKh, El'chaninov AV, Makarov AV, Raimova ESh, et al. Angiogenic Potential of Multipotent Stromal Cells from the Umbilical Cord: an In Vitro Study. Bull Exp Biol Med. 2016 May 1;161(1):141–9.

299. Arutyunyan I, Fatkhudinov T, Kananykhina E, Usman N, Elchaninov A, Makarov A, et al. Role of VEGF-A in angiogenesis promoted by umbilical cord-derived mesenchymal stromal/stem cells: in vitro study. Stem Cell Res Ther. 2016 Dec 22;7(1):46.

300. Hu X, Yu SP, Fraser JL, Lu Z, Ogle ME, Wang JA, et al. Transplantation of hypoxia-preconditioned mesenchymal stem cells improves infarcted heart function via enhanced survival of implanted cells and angiogenesis. J Thorac Cardiovasc Surg. 2008 Apr 1;135(4):799–808.

301. Wei L, Fraser JL, Lu ZY, Hu X, Yu SP. Transplantation of hypoxia preconditioned bone marrow mesenchymal stem cells enhances angiogenesis and neurogenesis after cerebral ischemia in rats. Neurobiol Dis. 2012 Jun 1;46(3):635–45.

302. Lu LL, Liu YJ, Yang SG, Zhao QJ, Wang X, Gong W, et al. Isolation and characterization of human umbilical cord mesenchymal stem cells with hematopoiesis-supportive function and other potentials. Haematologica. 2006 Aug;91(8):1017–26.

303. Pezzi A, Amorin B, Laureano Á, Valim V, Dahmer A, Zambonato B, et al. Effects Of Hypoxia in Long-Term In Vitro Expansion of Human Bone Marrow Derived Mesenchymal Stem Cells. J Cell Biochem. 2017;118(10):3072–9.

304. Friedenstein AJ, Chailakhjan RK, Lalykina KS. The Development of Fibroblast Colonies in Monolayer Cultures of Guinea-Pig Bone Marrow and Spleen Cells. Cell Prolif. 1970;3(4):393–403.

305. Penfornis P, Pochampally R. Colony Forming Unit Assays. In: Gnecchi M, editor. Mesenchymal Stem Cells: Methods and Protocols . New York, NY: Springer; 2016. p. 159–69. (Methods in Molecular Biology).

306. Yi T, Kim S na, Lee HJ, Kim J, Cho YK, Shin DH, et al. Manufacture of Clinical-Grade Human Clonal Mesenchymal Stem Cell Products from Single Colony Forming Unit-Derived Colonies Based on the Subfractionation Culturing Method. Tissue Eng Part C Methods. 2015 Dec;21(12):1251–62.

307. Caliari SR, Burdick JA. A practical guide to hydrogels for cell culture. Nat Methods. 2016;13(5):405–14.

308. Henriksen K, Karsdal MA. Chapter 1 - Type I collagen. In: Karsdal MA, editor. Biochemistry of Collagens, Laminins and Elastin (Second Edition) . Academic Press; 2019. p. 1–12.

309. Rybkowska P, Radoszkiewicz K, Kawalec M, Dymkowska D, Zabłocka B, Zabłocki K, et al. The Metabolic Changes between Monolayer (2D) and Three-Dimensional (3D) Culture Conditions in Human Mesenchymal Stem/Stromal Cells Derived from Adipose Tissue. Cells. 2023 Jan;12(1):178.

310. Kim Y, Lasher CD, Milford LM, Murali T m., Rajagopalan P. A Comparative Study of Genome-Wide Transcriptional Profiles of Primary Hepatocytes in Collagen Sandwich and Monolayer Cultures. Tissue Eng Part C Methods. 2010 Dec;16(6):1449–60.

311. Toh WS, Loh XJ. Advances in hydrogel delivery systems for tissue regeneration. Mater Sci Eng C. 2014 Dec 1;45:690–7.

312. Zhang S, Hou J, Yuan Q, Xin P, Cheng H, Gu Z, et al. Arginine derivatives assist dopamine-hyaluronic acid hybrid hydrogels to have enhanced antioxidant activity for wound healing. Chem Eng J. 2020 Jul 15;392:123775.

313. Gülcüler Balta GS, Monzel C, Kleber S, Beaudouin J, Balta E, Kaindl T, et al. 3D Cellular Architecture Modulates Tyrosine Kinase Activity, Thereby Switching CD95-Mediated Apoptosis to Survival. Cell Rep. 2019 Nov 19;29(8):2295-2306.e6.

314. Sivaraj D, Chen K, Chattopadhyay A, Henn D, Wu W, Noishiki C, et al. Hydrogel Scaffolds to Deliver Cell Therapies for Wound Healing. Front Bioeng Biotechnol . 2021;9.

315. Costa LA, Eiro N, Fraile M, Gonzalez LO, Saá J, Garcia-Portabella P, et al. Functional heterogeneity of mesenchymal stem cells from natural niches to

culture conditions: implications for further clinical uses. Cell Mol Life Sci. 2021 Jan 1;78(2):447–67.

316. Kalinina N, Kharlampieva D, Loguinova M, Butenko I, Pobeguts O, Efimenko A, et al. Characterization of secretomes provides evidence for adipose-derived mesenchymal stromal cells subtypes. Stem Cell Res Ther. 2015 Nov 11;6(1):221.

317. Schipper BM, Marra KG, Zhang W, Donnenberg AD, Rubin JP. Regional Anatomic and Age Effects on Cell Function of Human Adipose-Derived Stem Cells. Ann Plast Surg. 2008 May;60(5):538.

318. van Harmelen V, Röhrig K, Hauner H. Comparison of proliferation and differentiation capacity of human adipocyte precursor cells from the omental and subcutaneous adipose tissue depot of obese subjects. Metabolism. 2004 May 1;53(5):632–7.

319. Zhou T, Yuan Z, Weng J, Pei D, Du X, He C, et al. Challenges and advances in clinical applications of mesenchymal stromal cells. J Hematol OncolJ Hematol Oncol. 2021 Feb 12;14(1):24.

320. Kassem M, Abdallah BM, Yu Z, Ditzel N, Burns JS. The use of hTERT-immortalized cells in tissue engineering. Cytotechnology. 2004 Jun 1;45(1):39–46.

321. Bodnar AG, Ouellette M, Frolkis M, Holt SE, Chiu CP, Morin GB, et al. Extension of Life-Span by Introduction of Telomerase into Normal Human Cells. Science. 1998 Jan 16;279(5349):349–52.

322. Jing S, Zhou H, Zou C, Chen DPC, Ye Q, Ai Y, et al. Application of telomere biology and telomerase in mesenchymal stem cells. Nano TransMed . 2022 Sep 8

323. Shay JW, Wright WE. Use of Telomerase to Create Bioengineered Tissues. Ann N Y Acad Sci. 2005;1057(1):479–91.

324. Piñeiro-Ramil M, Sanjurjo-Rodríguez C, Castro-Viñuelas R, Rodríguez-Fernández S, Fuentes-Boquete IM, Blanco FJ, et al. Usefulness of Mesenchymal Cell Lines for Bone and Cartilage Regeneration Research. Int J Mol Sci. 2019 Jan;20(24):6286.

325. Wang H, Alarcón CN, Liu B, Watson F, Searles S, Lee CK, et al. Genetically engineered and enucleated human mesenchymal stromal cells for the targeted delivery of therapeutics to diseased tissue. Nat Biomed Eng. 2022 Jul;6(7):882–97.

326. Wang Y, Chen S, Yan Z, Pei M. A prospect of cell immortalization combined with matrix microenvironmental optimization strategy for tissue engineering and regeneration. Cell Biosci. 2019 Jan 5;9(1):7.

327. Kulebyakin K, Tyurin-Kuzmin P, Efimenko A, Voloshin N, Kartoshkin A, Karagyaur M, et al. Decreased Insulin Sensitivity in Telomerase-Immortalized

Mesenchymal Stem Cells Affects Efficacy and Outcome of Adipogenic Differentiation in vitro. Front Cell Dev Biol . 2021;9.

328. Katz DB, Huynh NPT, Savadipour A, Palte I, Guilak F. An immortalized human adipose-derived stem cell line with highly enhanced chondrogenic properties. Biochem Biophys Res Commun. 2020 Sep 10;530(1):252–8.

329. Nakahara H, Misawa H, Hayashi T, Kondo E, Yuasa T, Kubota Y, et al. Bone Repair by Transplantation of hTERT-Immortalized Human Mesenchymal Stem Cells in Mice. Transplantation. 2009 Aug 15;88(3):346.

330. rao Pattabhi S, Martinez JS, Keller TCS. Decellularized ECM effects on human mesenchymal stem cell stemness and differentiation. Differentiation. 2014 Nov 1;88(4):131–43.

331. Reijnders CMA, van Lier A, Roffel S, Kramer D, Scheper RJ, Gibbs S. Development of a Full-Thickness Human Skin Equivalent In Vitro Model Derived from TERT-Immortalized Keratinocytes and Fibroblasts. Tissue Eng Part A. 2015 Sep;21(17–18):2448–59.

332. Volkmer E, Kallukalam BC, Maertz J, Otto S, Drosse I, Polzer H, et al. Hypoxic Preconditioning of Human Mesenchymal Stem Cells Overcomes Hypoxia-Induced Inhibition of Osteogenic Differentiation. Tissue Eng Part A. 2010 Jan;16(1):153–64.

333. Wolbank S, Stadler G, Peterbauer A, Gillich A, Karbiener M, Streubel B, et al. Telomerase Immortalized Human Amnion- and Adipose-Derived Mesenchymal Stem Cells: Maintenance of Differentiation and Immunomodulatory Characteristics. Tissue Eng Part A. 2009 Jul;15(7):1843–54.

334. Novoseletskaya E, Grigorieva O, Nimiritsky P, Basalova N, Eremichev R, Milovskaya I, et al. Mesenchymal Stromal Cell-Produced Components of Extracellular Matrix Potentiate Multipotent Stem Cell Response to Differentiation Stimuli. Front Cell Dev Biol . 2020;8.

335. Haque N, Rahman MT, Abu Kasim NH, Alabsi AM. Hypoxic culture conditions as a solution for mesenchymal stem cell based regenerative therapy. ScientificWorldJournal. 2013 Aug 27;2013:632972.

336. Sharma S, Bhonde R. Mesenchymal stromal cells are genetically stable under a hostile in vivo–like scenario as revealed by in vitro micronucleus test. Cytotherapy. 2015 Oct 1;17(10):1384–95.

337. Meza-Zepeda LA, Noer A, Dahl JA, Micci F, Myklebost O, Collas P. High-resolution analysis of genetic stability of human adipose tissue stem cells cultured to senescence. J Cell Mol Med. 2008;12(2):553–63.

338. Nikitina V, Astrelina T, Nugis V, Ostashkin A, Karaseva T, Dobrovolskaya E, et al. Clonal chromosomal and genomic instability during human multipotent mesenchymal stromal cells long-term culture. PLOS ONE. 2018 Feb 12;13(2):e0192445.

339. Fernie AR, Zhang Y, Sampathkumar A. Cytoskeleton Architecture Regulates Glycolysis Coupling Cellular Metabolism to Mechanical Cues. Trends Biochem Sci. 2020 Aug 1;45(8):637–8.

340. Sthijns MMJPE, van Blitterswijk CA, LaPointe VLS. Synthetic Materials that Affect the Extracellular Matrix via Cellular Metabolism and Responses to a Metabolic State. Front Bioeng Biotechnol . 2021;9.

341. Shimoda LA, Polak J. Hypoxia. 4. Hypoxia and ion channel function. Am J Physiol - Cell Physiol. 2011 May;300(5):C951–67.

342. Brunelle JK, Bell EL, Quesada NM, Vercauteren K, Tiranti V, Zeviani M, et al. Oxygen sensing requires mitochondrial ROS but not oxidative phosphorylation. Cell Metab. 2005 Jun 1;1(6):409–14.

343. Guzy RD, Hoyos B, Robin E, Chen H, Liu L, Mansfield KD, et al. Mitochondrial complex III is required for hypoxia-induced ROS production and cellular oxygen sensing. Cell Metab. 2005 Jun 1;1(6):401–8.

344. Mansfield KD, Guzy RD, Pan Y, Young RM, Cash TP, Schumacker PT, et al. Mitochondrial dysfunction resulting from loss of cytochrome c impairs cellular oxygen sensing and hypoxic HIF-α activation. Cell Metab. 2005 Jun 1;1(6):393–9.

345. Papandreou I, Cairns RA, Fontana L, Lim AL, Denko NC. HIF-1 mediates adaptation to hypoxia by actively downregulating mitochondrial oxygen consumption. Cell Metab. 2006 Mar 1;3(3):187–97.

346. Semenza GL, Artemov D, Bedi A, Bhujwalla Z, Chiles K, Feldser D, et al. 'The Metabolism of Tumours': 70 Years Later. In: The Tumour Microenvironment: Causes and Consequences of Hypoxia and Acidity . John Wiley & Sons, Ltd; 2001. p. 251–64.

347. Iyer NV, Kotch LE, Agani F, Leung SW, Laughner E, Wenger RH, et al. Cellular and developmental control of O2 homeostasis by hypoxia-inducible factor 1α. Genes Dev. 1998 Jan 15;12(2):149–62.

348. Guzy RD, Schumacker PT. Oxygen sensing by mitochondria at complex III: the paradox of increased reactive oxygen species during hypoxia. Exp Physiol. 2006;91(5):807–19.

349. Kiani AA, Kazemi A, Halabian R, Mohammadipour M, Jahanian-Najafabadi A, Roudkenar MH. HIF-1α Confers Resistance to Induced Stress in Bone Marrow-derived Mesenchymal Stem Cells. Arch Med Res. 2013 Apr 1;44(3):185–93.

350. Schumacker PT. Hypoxia-inducible factor-1 (HIF-1). Crit Care Med. 2005 Dec;33(12):S423.

351. Tretter V, Zach ML, Böhme S, Ullrich R, Markstaller K, Klein KU. Investigating Disturbances of Oxygen Homeostasis: From Cellular Mechanisms to the Clinical Practice. Front Physiol . 2020;11.

352. Carter HH, Maxwell JD, Hellsten Y, Thompson A, Thijssen DHJ, Jones H. The impact of acute remote ischaemic preconditioning on cerebrovascular function. Eur J Appl Physiol. 2020 Mar 1;120(3):603–12.

353. Haller PM, Vargas KG, Haller MC, Piackova E, Wojta J, Gyöngyösi M, et al. Remote ischaemic conditioning for myocardial infarction or elective PCI: systematic review and meta-analyses of randomised trials. Eur Heart J Acute Cardiovasc Care. 2020 Mar 1;9(1_suppl):82–92.

354. Loukogeorgakis SP, Panagiotidou AT, Broadhead MW, Donald A, Deanfield JE, MacAllister RJ. Remote Ischemic Preconditioning Provides Early and Late Protection Against Endothelial Ischemia-Reperfusion Injury in Humans: Role of the Autonomic Nervous System. J Am Coll Cardiol. 2005 Aug 2;46(3):450–6.

355. Cai Z, Manalo DJ, Wei G, Rodriguez ER, Fox-Talbot K, Lu H, et al. Hearts From Rodents Exposed to Intermittent Hypoxia or Erythropoietin Are Protected Against Ischemia-Reperfusion Injury. Circulation. 2003 Jul 8;108(1):79–85.

356. Belaidi E, Beguin PC, Levy P, Ribuot C, Godin-Ribuot D. Prevention of HIF-1 activation and iNOS gene targeting by low-dose cadmium results in loss of myocardial hypoxic preconditioning in the rat. Am J Physiol-Heart Circ Physiol. 2008 Feb;294(2):H901–8.

357. Kozera B, Rapacz M. Reference genes in real-time PCR. J Appl Genet. 2013 Nov 1;54(4):391–406.

358. Amable PR, Teixeira MVT, Carias RBV, Granjeiro JM, Borojevic R. Identification of Appropriate Reference Genes for Human Mesenchymal Cells during Expansion and Differentiation. PLOS ONE. 2013 Sep 2;8(9):e73792.

359. Fink T, Lund P, Pilgaard L, Rasmussen JG, Duroux M, Zachar V. Instability of standard PCR reference genes in adipose-derived stem cells during propagation, differentiation and hypoxic exposure. BMC Mol Biol. 2008 Oct 31;9(1):1–9.

360. Taheem DK, Foyt DA, Loaiza S, Ferreira SA, Ilic D, Auner HW, et al. Differential Regulation of Human Bone Marrow Mesenchymal Stromal Cell Chondrogenesis by Hypoxia Inducible Factor-1α Hydroxylase Inhibitors. STEM CELLS. 2018;36(9):1380–92.

361. Rauh J, Jacobi A, Stiehler M. Identification of Stable Reference Genes for Gene Expression Analysis of Three-Dimensional Cultivated Human Bone Marrow-Derived Mesenchymal Stromal Cells for Bone Tissue Engineering. Tissue Eng Part C Methods. 2015 Feb 1;21(2):192–206.

362. Vandesompele J, De Preter K, Pattyn F, Poppe B, Van Roy N, De Paepe A, et al. Accurate normalization of real-time quantitative RT-PCR data by geometric averaging of multiple internal control genes. Genome Biol. 2002 Jun 18;3(7):research0034.1.

363. Eisenberg E, Levanon EY. Human housekeeping genes, revisited. Trends Genet. 2013 Oct 1;29(10):569–74.

364. Ragni E, Viganò M, Rebulla P, Giordano R, Lazzari L. What is beyond a qRT-PCR study on mesenchymal stem cell differentiation properties: how to choose the most reliable housekeeping genes. J Cell Mol Med. 2013;17(1):168–80.

365. Freeman WM, Robertson DJ, Vrana KE. Fundamentals of DNA Hybridization Arrays for Gene Expression Analysis. BioTechniques. 2000 Nov;29(5):1042–55.

366. Wang Z, Gerstein M, Snyder M. RNA-Seq: a revolutionary tool for transcriptomics. Nat Rev Genet. 2009 Jan;10(1):57–63.

367. Kabat M, Bobkov I, Kumar S, Grumet M. Trends in mesenchymal stem cell clinical trials 2004-2018: Is efficacy optimal in a narrow dose range? STEM CELLS Transl Med. 2020;9(1):17–27.

368. Jovic D, Yu Y, Wang D, Wang K, Li H, Xu F, et al. A Brief Overview of Global Trends in MSC-Based Cell Therapy. Stem Cell Rev Rep. 2022 Jun 1;18(5):1525–45.

369. Jing X, Yang F, Shao C, Wei K, Xie M, Shen H, et al. Role of hypoxia in cancer therapy by regulating the tumor microenvironment. Mol Cancer. 2019 Nov 11;18(1):157.

370. Al Tameemi W, Dale TP, Al-Jumaily RMK, Forsyth NR. Hypoxia-Modified Cancer Cell Metabolism. Front Cell Dev Biol . 2019;7.

371. McMahon J m., Conroy S, Lyons M, Greiser U, O'shea C, Strappe P, et al. Gene Transfer into Rat Mesenchymal Stem Cells: A Comparative Study of Viral and Nonviral Vectors. Stem Cells Dev. 2006 Feb;15(1):87–96.

372. Pfeifer A, Ikawa M, Dayn Y, Verma IM. Transgenesis by lentiviral vectors: Lack of gene silencing in mammalian embryonic stem cells and preimplantation embryos. Proc Natl Acad Sci. 2002 Feb 19;99(4):2140–5.

373. McGinley L, McMahon J, Strappe P, Barry F, Murphy M, O'Toole D, et al. Lentiviral vector mediated modification of mesenchymal stem cells & enhanced survival in an in vitro model of ischaemia. Stem Cell Res Ther. 2011 Mar 7;2(2):12.

374. Tonello S, Bianchetti A, Braga S, Almici C, Marini M, Piovani G, et al. Impedance-Based Monitoring of Mesenchymal Stromal Cell Three-Dimensional Proliferation Using Aerosol Jet Printed Sensors: A Tissue Engineering Application. Materials. 2020 Jan;13(10):2231.

375. Cao F, Lin S, Xie X, Ray P, Patel M, Zhang X, et al. In Vivo Visualization of Embryonic Stem Cell Survival, Proliferation, and Migration After Cardiac Delivery. Circulation. 2006 Feb 21;113(7):1005–14.

376. Vila OF, Garrido C, Cano I, Guerra-Rebollo M, Navarro M, Meca-Cortés O, et al. Real-Time Bioluminescence Imaging of Cell Distribution, Growth, and

Differentiation in a Three-Dimensional Scaffold Under Interstitial Perfusion for Tissue Engineering. Tissue Eng Part C Methods. 2016 Sep;22(9):864–72.

377. Dégano IR, Vilalta M, Bagó JR, Matthies AM, Hubbell JA, Dimitriou H, et al. Bioluminescence imaging of calvarial bone repair using bone marrow and adipose tissue-derived mesenchymal stem cells. Biomaterials. 2008 Feb 1;29(4):427–37.

378. Olivo C, Alblas J, Verweij V, Van Zonneveld AJ, Dhert WJA, Martens ACM. In vivo bioluminescence imaging study to monitor ectopic bone formation by luciferase gene marked mesenchymal stem cells. J Orthop Res. 2008;26(7):901–9.

379. Logeart-Avramoglou D, Oudina K, Bourguignon M, Delpierre L, Nicola MA, Bensidhoum M, et al. In Vitro and In Vivo Bioluminescent Quantification of Viable Stem Cells in Engineered Constructs. Tissue Eng Part C Methods. 2010 Jun;16(3):447–58.

380. Geuze RE, Prins HJ, Öner FC, van der Helm YJM, Schuijff LS, Martens AC, et al. Luciferase Labeling for Multipotent Stromal Cell Tracking in Spinal Fusion Versus Ectopic Bone Tissue Engineering in Mice and Rats. Tissue Eng Part A. 2010 Nov;16(11):3343–51.

381. Vilalta M, Jorgensen C, Dégano IR, Chernajovsky Y, Gould D, Noël D, et al. Dual luciferase labelling for non-invasive bioluminescence imaging of mesenchymal stromal cell chondrogenic differentiation in demineralized bone matrix scaffolds. Biomaterials. 2009 Oct 1;30(28):4986–95.

382. Lin P, Correa D, Lin Y, Caplan AI. Polybrene Inhibits Human Mesenchymal Stem Cell Proliferation during Lentiviral Transduction. PLOS ONE. 2011 Aug 26;6(8):e23891.

383. Kallifatidis G, Beckermann BM, Groth A, Schubert M, Apel A, Khamidjanov A, et al. Improved lentiviral transduction of human mesenchymal stem cells for therapeutic intervention in pancreatic cancer. Cancer Gene Ther. 2008 Apr;15(4):231–40.

384. Neri S. Genetic Stability of Mesenchymal Stromal Cells for Regenerative Medicine Applications: A Fundamental Biosafety Aspect. Int J Mol Sci. 2019 May 15;20(10):2406.

385. Le A, Stine ZE, Nguyen C, Afzal J, Sun P, Hamaker M, et al. Tumorigenicity of hypoxic respiring cancer cells revealed by a hypoxia–cell cycle dual reporter. Proc Natl Acad Sci. 2014 Aug 26;111(34):12486–91.

386. Hass R, Otte A. Mesenchymal stem cells as all-round supporters in a normal and neoplastic microenvironment. Cell Commun Signal. 2012 Sep 3;10(1):26.

387. Marques AP, Reis RL, Pirraco RP, Cerqueira M, editors. Skin Tissue Models. Illustrated edition. London: Academic Press; 2017. 472 p.

388. Heimbach DM, Warden GD, Luterman A, Jordan MH, Ozobia N, Ryan CM, et al. Multicenter Postapproval Clinical Trial of INTEGRA® Dermal Regeneration Template for Burn Treatment. J Burn Care Rehabil. 2003 Jan 1;24(1):42–8.

389. Hamrahi VF, Goverman J, Jung W, Wu JC, Fischman AJ, Tompkins RG, et al. In Vivo Molecular Imaging of Murine Embryonic Stem Cells Delivered to a Burn Wound Surface via INTEGRA® Scaffolding. J Burn Care Res. 2012 Mar 1;33(2):e49–54.

390. Frueh FS, Später T, Lindenblatt N, Calcagni M, Giovanoli P, Scheuer C, et al. Adipose Tissue-Derived Microvascular Fragments Improve Vascularization, Lymphangiogenesis, and Integration of Dermal Skin Substitutes. J Invest Dermatol. 2017 Jan 1;137(1):217–27.

391. Sharma V, Patel N, Kohli N, Ravindran N, Hook L, Mason C, et al. Viscoelastic, physical, and bio-degradable properties of dermal scaffolds and related cell behaviour. Biomed Mater. 2016 Sep;11(5):055001.

392. Chang HI, Wang Y. Cell Responses to Surface and Architecture of Tissue Engineering Scaffolds . Regenerative Medicine and Tissue Engineering - Cells and Biomaterials. IntechOpen; 2011.

393. Badylak SF. The extracellular matrix as a biologic scaffold material. Biomaterials. 2007 Sep;28(25):3587–93.

394. Später T, Körbel C, Frueh FS, Nickels RM, Menger MD, Laschke MW. Seeding density is a crucial determinant for the in vivo vascularisation capacity of adipose tissue-derived microvascular fragments. Eur Cell Mater. 2017 Aug 15;34:55–69.

395. Lovett M, Lee K, Edwards A, Kaplan DL. Vascularization Strategies for Tissue Engineering. Tissue Eng Part B Rev. 2009 Sep;15(3):353–70.

396. Ishak SA, Djuansjah JRP, Kadir MRA, Sukmana I. Angiogenesis in tissue engineering: from concept to the vascularization of scaffold construct. IOP Conf Ser Mater Sci Eng. 2014 Jun 23;58(1):12015.

397. Villalona GA, Udelsman B, Duncan DR, McGillicuddy E, Sawh-Martinez RF, Hibino N, et al. Cell-Seeding Techniques in Vascular Tissue Engineering. Tissue Eng Part B Rev. 2010 Jun;16(3):341–50.

398. Levin A, Sharma V, Hook L, García-Gareta E. The importance of factorial design in tissue engineering and biomaterials science: Optimisation of cell seeding efficiency on dermal scaffolds as a case study. J Tissue Eng. 2018 Jan 1;9:2041731418781696.

399. Jones G, Cartmell SH. Optimization of cell seeding efficiencies on a three-dimensional gelatin scaffold for bone tissue engineering. J Appl Biomater Biomech JABB. 2006 Dec;4(3):172–80.

400. Vitacolonna M, Belharazem D, Hohenberger P, Roessner ED. Effect of static seeding methods on the distribution of fibroblasts within human acellular dermis. Biomed Eng OnLine. 2013 Jun 24;12(1):55.

401. Selden C, Fuller B. Role of Bioreactor Technology in Tissue Engineering for Clinical Use and Therapeutic Target Design. Bioengineering. 2018 Apr 24;5(2):32.

402. Thevenot P, Nair A, Dey J, Yang J, Tang L. Method to Analyze Three-Dimensional Cell Distribution and Infiltration in Degradable Scaffolds. Tissue Eng Part C Methods. 2008 Dec;14(4):319–31.

403. García-Gareta E, Ravindran N, Sharma V, Samizadeh S, Dye JF. A Novel Multiparameter In Vitro Model of Three-Dimensional Cell Ingress Into Scaffolds for Dermal Reconstruction to Predict In Vivo Outcome. BioResearch Open Access. 2013 Dec;2(6):412–20.

404. Sharma V, Kohli N, Moulding D, Afolabi H, Hook L, Mason C, et al. Design of a Novel Two-Component Hybrid Dermal Scaffold for the Treatment of Pressure Sores. Macromol Biosci. 2017;17(11):1700185.

405. Live/Dead Quantification Using Fiji - Step-by-Step Guide . Allevi. 2020 [cited 2022 Mar 30]. Available from: https://www.allevi3d.com/livedead-assay-quantification-fiji/

406. How can I compute *fractional change* or *percent change* with Prism? - FAQ 281 - GraphPad . [cited 2022 Aug 3]. Available from: https://www.graphpad.com/support/faq/how-can-i-compute-ifractional-changei-or-ipercent-changei-with-prism/

407. Klenke FM, Liu Y, Yuan H, Hunziker EB, Siebenrock KA, Hofstetter W. Impact of pore size on the vascularization and osseointegration of ceramic bone substitutes in vivo. J Biomed Mater Res A. 2008;85A(3):777–86.

408. Lu D, Zeng Z, Geng Z, Guo C, Pei D, Zhang J, et al. Macroporous methacrylated hyaluronic acid hydrogel with different pore sizes for in vitro and in vivo evaluation of vascularization. Biomed Mater. 2022 Jan;17(2):025006.

409. Druecke D, Langer S, Lamme E, Pieper J, Ugarkovic M, Steinau HU, et al. Neovascularization of poly(ether ester) block-copolymer scaffolds in vivo: Long-term investigations using intravital fluorescent microscopy. J Biomed Mater Res A. 2004;68A(1):10–8.

410. Laschke MW, Harder Y, Amon M, Martin I, Farhadi J, Ring A, et al. Angiogenesis in tissue engineering: breathing life into constructed tissue substitutes. Tissue Eng. 2006;12(8):2093–104.

411. Doagă IO, Savopol T, Neagu M, Neagu A, Kovács E. The Kinetics of Cell Adhesion to Solid Scaffolds: An Experimental and Theoretical Approach. J Biol Phys. 2008 Oct;34(5):495–509.

412. Huang GP, Shanmugasundaram S, Masih P, Pandya D, Amara S, Collins G, et al. An investigation of common crosslinking agents on the stability of electrospun collagen scaffolds. J Biomed Mater Res A. 2015;103(2):762–71.

413. Nikolovski J, Mooney DJ. Smooth muscle cell adhesion to tissue engineering scaffolds. Biomaterials. 2000 Oct 1;21(20):2025–32.

414. Lee JW, Kim YH, Park KD, Jee KS, Shin JW, Hahn SB. Importance of integrin β1-mediated cell adhesion on biodegradable polymers under serum depletion in mesenchymal stem cells and chondrocytes. Biomaterials. 2004 May 1;25(10):1901–9.

415. Moreira-Soares M, Coimbra R, Rebelo L, Carvalho J, D. M. Travasso R. Angiogenic Factors produced by Hypoxic Cells are a leading driver of Anastomoses in Sprouting Angiogenesis–a computational study. Sci Rep. 2018 Jun 7;8(1):8726.

416. Ruhrberg C, Gerhardt H, Golding M, Watson R, Ioannidou S, Fujisawa H, et al. Spatially restricted patterning cues provided by heparin-binding VEGF-A control blood vessel branching morphogenesis. Genes Dev. 2002 Oct 15;16(20):2684–98.

417. Oh HH, Lu H, Kawazoe N, Chen G. Spatially Guided Angiogenesis by Three-Dimensional Collagen Scaffolds Micropatterned with Vascular Endothelial Growth Factor. J Biomater Sci Polym Ed. 2012 Dec 1;23(17):2185–95.

418. Elçin YM, Dixit V, Gitnick G. Extensive In Vivo Angiogenesis Following Controlled Release of Human Vascular Endothelial Cell Growth Factor: Implications for Tissue Engineering and Wound Healing. Artif Organs. 2001;25(7):558–65.

419. McLimans WF, Crouse EJ, Tunnah KV, Moore GE. Kinetics of gas diffusion in mammalian cell culture systems. I. Experimental. Biotechnol Bioeng. 1968;10(6):725–40.

420. McLimans WF, Blumenson LE, Tunnah KV. Kinetics of gas diffusion in mammalian cell culture systems. II. Theory. Biotechnol Bioeng. 1968;10(6):741–63.

421. Place TL, Domann FE, Case AJ. Limitations of oxygen delivery to cells in culture: An underappreciated problem in basic and translational research. Free Radic Biol Med. 2017 Dec 1;113:311–22.

422. Allen CB, Schneider BK, White CW. Limitations to oxygen diffusion and equilibration in in vitro cell exposure systems in hyperoxia and hypoxia. Am J Physiol-Lung Cell Mol Physiol. 2001 Oct;281(4):L1021–7.

423. Krogh A. The rate of diffusion of gases through animal tissues, with some remarks on the coefficient of invasion. J Physiol. 1919;52(6):391–408.

424. Radisic M, Malda J, Epping E, Geng W, Langer R, Vunjak-Novakovic G. Oxygen gradients correlate with cell density and cell viability in engineered cardiac tissue. Biotechnol Bioeng. 2006;93(2):332–43.

425. Gstraunthaler G, Seppi T, Pfaller W. Impact of Culture Conditions, Culture Media Volumes, and Glucose Content on Metabolic Properties of Renal Epithelial Cell Cultures. Cell Physiol Biochem. 1999;9(3):150–72.

426. Sheta EA, Trout H, Gildea JJ, Harding MA, Theodorescu D. Cell density mediated pericellular hypoxia leads to induction of HIF-1α via nitric oxide and Ras/MAP kinase mediated signaling pathways. Oncogene. 2001 Nov;20(52):7624–34.

427. Yarmush ML, Toner M, Dunn JCY, Rotem A, Hubel A, Tompkins RG. Hepatic Tissue Engineering: Development of Critical Technologies. Ann N Y Acad Sci. 1992;665(1):238–52.

428. Powers DE, Millman JR, Bonner-Weir S, Rappel MJ, Colton CK. Accurate control of oxygen level in cells during culture on siliconee rubber membranes with application to stem cell differentiation. Biotechnol Prog. 2010;26(3):805–18.

429. Peng C, He Q, Luo C. Lack of Keratinocyte Growth Factor Retards Angiogenesis in Cutaneous Wounds. J Int Med Res. 2011 Apr 1;39(2):416–23.

430. Xin X, Yang S, Ingle G, Zlot C, Rangell L, Kowalski J, et al. Hepatocyte Growth Factor Enhances Vascular Endothelial Growth Factor-Induced Angiogenesis in Vitro and in Vivo. Am J Pathol. 2001 Mar 1;158(3):1111–20.

431. Zhao L, Liu X, Zhang Y, Liang X, Ding Y, Xu Y, et al. Enhanced cell survival and paracrine effects of mesenchymal stem cells overexpressing hepatocyte growth factor promote cardioprotection in myocardial infarction. Exp Cell Res. 2016 May 15;344(1):30–9.

432. Li A, Dubey S, Varney ML, Dave BJ, Singh RK. IL-8 Directly Enhanced Endothelial Cell Survival, Proliferation, and Matrix Metalloproteinases Production and Regulated Angiogenesis. J Immunol. 2003 Mar 15;170(6):3369–76.

433. Cao R, Brakenhielm E, Wahlestedt C, Thyberg J, Cao Y. Leptin induces vascular permeability and synergistically stimulates angiogenesis with FGF-2 and VEGF. Proc Natl Acad Sci. 2001 May 22;98(11):6390–5.

434. Sierra-Honigmann MR, Nath AK, Murakami C, García-Cardeña G, Papapetropoulos A, Sessa WC, et al. Biological Action of Leptin as an Angiogenic Factor. Science. 1998 Sep 11;281(5383):1683–6.

435. Stratman AN, Saunders WB, Sacharidou A, Koh W, Fisher KE, Zawieja DC, et al. Endothelial cell lumen and vascular guidance tunnel formation requires MT1-MMP-dependent proteolysis in 3-dimensional collagen matrices. Blood. 2009 Jul 9;114(2):237–47.

436. Breuss JM, Uhrin P. VEGF-initiated angiogenesis and the uPA/uPAR system. Cell Adhes Migr. 2012 Nov 17;6(6):535–40.

437. Slater T, Haywood NJ, Matthews C, Cheema H, Wheatcroft SB. Insulin-like growth factor binding proteins and angiogenesis: from cancer to cardiovascular disease. Cytokine Growth Factor Rev. 2019 Apr 1;46:28–35.

438. Fernández CA, Moses MA. Modulation of angiogenesis by tissue inhibitor of metalloproteinase-4. Biochem Biophys Res Commun. 2006 Jun 23;345(1):523–9.

439. Ma DHK, Zhang F, Shi W, Yao JY, Hsiao CH, Wu HC, et al. Expression of Tissue Inhibitor of Metalloproteinase-4 in Normal Human Corneal Cells and Experimental Corneal Neovascularization. Ophthalmic Res. 2003;35(4):199–207.

440. Firth SM, Baxter RC. Cellular Actions of the Insulin-Like Growth Factor Binding Proteins. Endocr Rev. 2002 Dec 1;23(6):824–54.

441. Slomiany MG, Rosenzweig SA. IGF-1–Induced VEGF and IGFBP-3 Secretion Correlates with Increased HIF-1α Expression and Activity in Retinal Pigment Epithelial Cell Line D407. Invest Ophthalmol Vis Sci. 2004 Aug 1;45(8):2838–47.

442. Lofqvist C, Chen J, Connor KM, Smith ACH, Aderman CM, Liu N, et al. IGFBP3 suppresses retinopathy through suppression of oxygen-induced vessel loss and promotion of vascular regrowth. Proc Natl Acad Sci. 2007 Jun 19;104(25):10589–94.

443. Dallinga MG, Habani YI, Kayser RP, Van Noorden CJF, Klaassen I, Schlingemann RO. IGF-binding proteins 3 and 4 are regulators of sprouting angiogenesis. Mol Biol Rep. 2020 Apr 1;47(4):2561–72.

444. Cai J, Jiang WG, Grant MB, Boulton M. Pigment Epithelium-derived Factor Inhibits Angiogenesis via Regulated Intracellular Proteolysis of Vascular Endothelial Growth Factor Receptor 1*. J Biol Chem. 2006 Feb 10;281(6):3604–13.

445. Méndez-Ferrer S, Michurina TV, Ferraro F, Mazloom AR, MacArthur BD, Lira SA, et al. Mesenchymal and haematopoietic stem cells form a unique bone marrow niche. Nature. 2010 Aug;466(7308):829–34.

446. Arellano M, Lonial S. Clinical uses of GM-CSF, a critical appraisal and update. Biol Targets Ther. 2008 Mar 7;2(1):13–27.

447. Hamilton JA. Colony-stimulating factors in inflammation and autoimmunity. Nat Rev Immunol. 2008 Jul;8(7):533–44.

448. Takahashi T, Kalka C, Masuda H, Chen D, Silver M, Kearney M, et al. Ischemia- and cytokine-induced mobilization of bone marrow-derived endothelial progenitor cells for neovascularization. Nat Med. 1999 Apr;5(4):434–8.

449. Bussolino F, Colotta F, Bocchietto E, Guglielmetti A, Mantovani A. Recent developments in the cell biology of granulocyte-macrophage colony-stimulating factor and granulocyte colony-stimulating factor: activities on endothelial cells. Int J Clin Lab Res. 1993;23(1):8–12.

450. Zhao J, Chen L, Shu B, Tang J, Zhang L, Xie J, et al. Granulocyte/Macrophage Colony-Stimulating Factor Influences Angiogenesis by Regulating the Coordinated Expression of VEGF and the Ang/Tie System. PLOS ONE. 2014 Mar 21;9(3):e92691.

451. Figueiredo L, Pace R, D'Arros C, Réthoré G, Guicheux J, Le Visage C, et al. Assessing glucose and oxygen diffusion in hydrogels for the rational design of 3D stem cell scaffolds in regenerative medicine. J Tissue Eng Regen Med. 2018;12(5):1238–46.

452. van Stroe-Biezen SAM, Everaerts FM, Janssen LJJ, Tacken RA. Diffusion coefficients of oxygen, hydrogen peroxide and glucose in a hydrogel. Anal Chim Acta. 1993 Feb 15;273(1):553–60.

453. Cheema U, Rong Z, Kirresh O, MacRobert AJ, Vadgama P, Brown RA. Oxygen diffusion through collagen scaffolds at defined densities: implications for cell survival in tissue models. J Tissue Eng Regen Med. 2012;6(1):77–84.

454. Androjna C, Gatica JE, Belovich JM, Derwin KA. Oxygen Diffusion through Natural Extracellular Matrices: Implications for Estimating "Critical Thickness" Values in Tendon Tissue Engineering. Tissue Eng Part A. 2008 Apr;14(4):559–69.

455. Real-Time, Live-Cell Metabolic Assay, Seahorse Analysis | Agilent . [cited 2023 Feb 2]. Available from: https://www.agilent.com/en/product/cell-analysis/real-time-cell-metabolic-analysis/xf-analyzers

456. Zhang J, Zhang Q. Using Seahorse Machine to Measure OCR and ECAR in Cancer Cells. In: Haznadar M, editor. Cancer Metabolism: Methods and Protocols . New York, NY: Springer; 2019. p. 353–63. (Methods in Molecular Biology).

457. Fu J, Wang DA. In Situ Organ-Specific Vascularization in Tissue Engineering. Trends Biotechnol. 2018 Aug 1;36(8):834–49.

458. Stryker ZI, Rajabi M, Davis PJ, Mousa SA. Evaluation of Angiogenesis Assays. Biomedicines. 2019 Jun;7(2):37.

459. Jonkman JEN, Cathcart JA, Xu F, Bartolini ME, Amon JE, Stevens KM, et al. An introduction to the wound healing assay using live-cell microscopy. Cell Adhes Migr. 2014 Oct 31;8(5):440–51.

460. Wound Healing Tool . GitHub. [cited 2022 Apr 19]. Available from: https://github.com/MontpellierRessourcesImagerie/imagej_macros_and_scripts

461. Carpentier G, Berndt S, Ferratge S, Rasband W, Cuendet M, Uzan G, et al. Angiogenesis Analyzer for ImageJ — A comparative morphometric analysis of "Endothelial Tube Formation Assay" and "Fibrin Bead Assay". Sci Rep 2020 101. 2020 Jul 14;10(1):1–13.

462. Nicosia RF, Tchao R, Leighton J. Histotypic angiogenesis in vitro: Light microscopic, ultrastructural, and radioautographic studies. In Vitro. 1982 Jun 1;18(6):538–49.

463. Nicosia RF, Ottinetti A. Growth of microvessels in serum-free matrix culture of rat aorta. A quantitative assay of angiogenesis in vitro. Lab Investig J Tech Methods Pathol. 1990 Jul;63(1):115–22.

464. Kapoor A, Chen CG, Iozzo RV. A simplified aortic ring assay: A useful ex vivo method to assess biochemical and functional parameters of angiogenesis. Matrix Biol Plus. 2020 May 1;6–7:100025.

465. Simons BW, Brayton C. Chapter 3 - Challenges and Limitations of Mouse Xenograft Models of Cancer. In: Uthamanthil R, Tinkey P, editors. Patient Derived Tumor Xenograft Models . Academic Press; 2017. p. 25–36.

466. Lu T, Yang B, Wang R, Qin C. Xenotransplantation: Current Status in Preclinical Research. Front Immunol . 2020;10.

467. Nicosia R, Ottinetti A. Growth of microvessels in serum-free matrix culture of rat aorta. A quantitative assay of angiogenesis in vitro. Lab Investig J Tech Methods Pathol. 1990;(63(1)):115–22.

468. Popkov M, Jendreyko N, Gonzalez-Sapienza G, Mage RG, Rader C, Barbas CF. Human/mouse cross-reactive anti-VEGF receptor 2 recombinant antibodies selected from an immune b9 allotype rabbit antibody library. J Immunol Methods. 2004 May 1;288(1):149–64.

469. Liang WC, Wu X, Peale FV, Lee CV, Meng YG, Gutierrez J, et al. Cross-species Vascular Endothelial Growth Factor (VEGF)-blocking Antibodies Completely Inhibit the Growth of Human Tumor Xenografts and Measure the Contribution of Stromal VEGF *. J Biol Chem. 2006 Jan 13;281(2):951–61.

470. Mujagic E, Gianni-Barrera R, Trani M, Patel A, Gürke L, Heberer M, et al. Induction of Aberrant Vascular Growth, But Not of Normal Angiogenesis, by Cell-Based Expression of Different Doses of Human and Mouse VEGF Is Species-Dependent. Hum Gene Ther Methods. 2013 Feb;24(1):28–37.

471. Seano G, Primo L. Human Arterial Ring Angiogenesis Assay. In Humana Press, New York, NY; 2016. p. 191–203.

472. Lamalice L, Le Boeuf F, Huot J. Endothelial cell migration during angiogenesis. Circ Res. 2007 Mar 30;100(6):782–94.

473. Goodwin AM. In vitro assays of angiogenesis for assessment of angiogenic and anti-angiogenic agents. Microvasc Res. 2007 Sep 1;74(2):172–83.

474. Seano G, Chiaverina G, Gagliardi PA, di Blasio L, Sessa R, Bussolino F, et al. Modeling human tumor angiogenesis in a three-dimensional culture system. Blood. 2013 May 23;121(21):e129–37.

475. Vukicevic S, Kleinman HK, Luyten FP, Roberts AB, Roche NS, Reddi AH. Identification of multiple active growth factors in basement membrane matrigel suggests caution in interpretation of cellular activity related to extracellular matrix components. Exp Cell Res. 1992 Sep 1;202(1):1–8.

476. Aisenbrey EA, Murphy WL. Synthetic alternatives to Matrigel. Nat Rev Mater. 2020 Jul;5(7):539–51.

477. Conese M, Annacontini L, Carbone A, Beccia E, Cecchino LR, Parisi D, et al. The Role of Adipose-Derived Stem Cells, Dermal Regenerative Templates, and Platelet-Rich Plasma in Tissue Engineering-Based Treatments of Chronic Skin Wounds. Stem Cells Int. 2020 Jan 9;2020:e7056261.

478. Aoki S, Toda S, Ando T, Sugihara H. Bone marrow stromal cells, preadipocytes, and dermal fibroblasts promote epidermal regeneration in their distinctive fashions. Mol Biol Cell. 2004;15(10):4647–57.

479. Mansilla E, Spretz R, Larsen G, Nunez L, Drago H, Sturla F, et al. Outstanding survival and regeneration process by the use of intelligent acellular dermal matrices and mesenchymal stem cells in a burn pig model. Transpl Proc. 2010;42(10):4275–8.

480. Ho J, Yue D, Cheema U, Hsia HC, Dardik A. Innovations in Stem Cell Therapy for Diabetic Wound Healing. Adv Wound Care . 2022 Feb 17

481. Staton CA, Reed MWR, Brown NJ. A critical analysis of current in vitro and in vivo angiogenesis assays. Int J Exp Pathol. 2009;90(3):195–221.

482. Baiguera S, Macchiarini P, Ribatti D. Chorioallantoic membrane for in vivo investigation of tissue-engineered construct biocompatibility. J Biomed Mater Res B Appl Biomater. 2012 Jul;100(5):1425–34.

483. Valdes TI, Kreutzer D, Moussy F. The chick chorioallantoic membrane as a novel in vivo model for the testing of biomaterials. J Biomed Mater Res. 2002 Nov;62(2):273–82.

484. Gabrielli MG, Accili D. The chick chorioallantoic membrane: a model of molecular, structural, and functional adaptation to transepithelial ion transport and barrier function during embryonic development. J Biomed Biotechnol. 2010 Jan;2010:940741.

485. Auerbach R, Kubai L, Knighton D, Folkman J. A simple procedure for the long-term cultivation of chicken embryos. Dev Biol. 1974 Dec;41(2):391–4.

486. Ausprunk DH, Knighton DR, Folkman J. Differentiation of vascular endothelium in the chick chorioallantois: A structural and autoradiographic study. Dev Biol. 1974 Jun;38(2):237–48.

487. Ausprunk DH, Knighton DR, Folkman J. Vascularization of normal and neoplastic tissues grafted to the chick chorioallantois. Role of host and preexisting graft blood vessels. Am J Pathol. 1975 Jun;79(3):597–618.

488. Klagsbrun M, Knighton D, Folkman J. Tumor Angiogenesis Activity in Cells Grown in Tissue Culture1. Cancer Res. 1976 Jan 1;36(1):110–4.

489. Hincke MT, Da Silva M, Guyot N, Gautron J, McKee MD, Guabiraba-Brito R, et al. Dynamics of Structural Barriers and Innate Immune Components during Incubation of the Avian Egg: Critical Interplay between Autonomous Embryonic Development and Maternal Anticipation. J Innate Immun. 2019;11(2):111–24.

490. Schilling MA, Katani R, Memari S, Cavanaugh M, Buza J, Radzio-Basu J, et al. Transcriptional Innate Immune Response of the Developing Chicken Embryo to Newcastle Disease Virus Infection. Front Genet . 2018;9.

491. Dohle DS, Pasa SD, Gustmann S, Laub M, Wissler JH, Jennissen HP, et al. Chick ex ovo culture and ex ovo CAM assay: How it really works. J Vis Exp. 2010;(33):33.

492. Ribatti D. The Chick Embryo Chorioallantoic Membrane in the Study of Angiogenesis and Metastasis . Dordrecht: Springer Netherlands; 2010.

493. Auerbach R, Auerbach W, Polakowski I. Assays for angiogenesis: A review. Pharmacol Ther. 1991 Jan;51(1):1–11.

494. Auerbach R, Akhtar N, Lewis RL, Shinners BL. Angiogenesis assays: problems and pitfalls. Cancer Metastasis Rev. 2000 Jan;19(1–2):167–72.

495. Vu MT, Smith CF, Burger PC, Klintworth GK. An evaluation of methods to quantitate the chick chorioallantoic membrane assay in angiogenesis. Lab Investig J Tech Methods Pathol. 1985 Oct 1;53(4):499–508.

496. Home Office UK. Guidance on the Operation of the Animals (Scientific Procedures) Act 1986. London: Crown copyright; 2014.

497. IACUC. Protocol Requirements for the Use of Live Embryonated Eggs . Tufts University & Tufts Medical Center; 2022. Available from: http://viceprovost.tufts.edu/iacuc/

498. Boston University Research Support. Use of Live Embryonated Eggs of Egg-Laying Vertebrate Species (IACUC) | Research Support . 2020. Available from: https://www.bu.edu/researchsupport/forms-policies/iacuc-use-of-live-embryonated-eggs-of-egg-laying-vertebrate-species/

499. National Institute of Health. The public health service responds to commonly asked questions. Available from: http://grants.nih.gov/grants/olaw/references/ilar91.htm

500. Ribatti D. The chick embryo chorioallantoic membrane (CAM). A multifaceted experimental model. Mech Dev. 2016 Aug 1;141:70–7.

501. Baiguera S, Jungebluth P, Burns A, Mavilia C, Haag J, De Coppi P, et al. Tissue engineered human tracheas for in vivo implantation. Biomaterials. 2010 Dec;31(34):8931–8.

502. West DC, Thompson WD, Sells PG, Burbridge MF. Angiogenesis assays using chick chorioallantoic membrane. Methods Mol Med. 2001 Jan;46:107–29.

503. Ribatti D, Nico B, Vacca A, Presta M. The gelatin sponge–chorioallantoic membrane assay. Nat Protoc. 2006 Jun;1(1):85–91.

504. Hamburger V, Hamilton HL. A series of normal stages in the development of the chick embryo. J Morphol. 1951 Jan;88(1):49–92.

505. Ma J, Zhao Y, Sun L, Sun X, Zhao X, Sun X, et al. Exosomes Derived from Akt-Modified Human Umbilical Cord Mesenchymal Stem Cells Improve Cardiac Regeneration and Promote Angiogenesis via Activating Platelet-Derived Growth Factor D. Stem Cells Transl Med. 2017 Jan 1;6(1):51–9.

506. Borges J, Tegtmeier FT, Padron NT, Mueller MC, Lang EM, Stark GB. Chorioallantoic membrane angiogenesis model for tissue engineering: a new twist on a classic model. Tissue Eng. 2003 Jun 9;9(3):441–50.

507. Deryugina EI, Quigley JP. Chick embryo chorioallantoic membrane model systems to study and visualize human tumor cell metastasis. Histochem Cell Biol. 2008 Dec 13;130(6):1119–30.

508. Kocak FZ, Talari ACS, Yar M, Rehman IU. In-Situ Forming pH and Thermosensitive Injectable Hydrogels to Stimulate Angiogenesis: Potential Candidates for Fast Bone Regeneration Applications. Int J Mol Sci. 2020 Jan;21(5):1633.

509. Mangir N, Dikici S, Claeyssens F, Macneil S. Using ex Ovo Chick Chorioallantoic Membrane (CAM) Assay to Evaluate the Biocompatibility and Angiogenic Response to Biomaterials. ACS Biomater Sci Eng. 2019 Jul 8;5(7):3190–200.

510. Blacher S, Devy L, Hlushchuk R, Larger E, Lamandé N, Burri P, et al. Quantification Of Angiogenesis In The Chicken Chorioallantoic Membrane (CAM). Image Anal Stereol. 2005 Nov 1;24(3):169–80.

511. Bronckaers A, Hilkens P, Fanton Y, Struys T, Gervois P, Politis C, et al. Angiogenic properties of human dental pulp stem cells. PloS One. 2013 Jan 7;8(8):e71104.

512. Richardson M, Singh G. Observations on the Use of the Avian Chorioallantoic Membrane (CAM) Model in Investigations into Angiogenesis. Curr Drug Target - Cardiovasc Hematol Disord. 2003 Jun 1;3(2):155–85.

513. Harris-Hooker SA, Gajdusek CM, Wight TN, Schwartz SM. Neovascular responses induced by cultured aortic endothelial cells. J Cell Physiol. 1983 Mar;114(3):302–10.

514. Dusseau JW, Hutchins PM, Malbasa DS. Stimulation of angiogenesis by adenosine on the chick chorioallantoic membrane. Circ Res. 1986 Aug 1;59(2):163–70.

515. Burggren W, Rojas Antich M. Angiogenesis in the Avian Embryo Chorioallantoic Membrane: A Perspective on Research Trends and a Case Study on Toxicant Vascular Effects. J Cardiovasc Dev Dis. 2020 Dec;7(4):56.

516. Totonelli G, Maghsoudlou P, Garriboli M, Riegler J, Orlando G, Burns AJ, et al. A rat decellularized small bowel scaffold that preserves villus-crypt architecture for intestinal regeneration. Biomaterials. 2012 Apr;33(12):3401–10.

517. Chen H, Treweeke AT, West DC, Till KJ, Cawley JC, Zuzel M, et al. In vitro and in vivo production of vascular endothelial growth factor by chronic lymphocytic leukemia cells. Blood. 2000 Nov 1;96(9):3181–7.

518. Vessel Analysis . ImageJ Wiki. Available from: https://imagej.github.io/plugins/vessel-analysis

519. Elfarnawany M. Signal Processing Methods for Quantitative Power Doppler Microvascular Angiography. Electron Thesis Diss Repos . 2015 Aug 4

520. Caggiati A, Franceschini M, Heyn R, Rosi C. Skin erythrodiapedesis during chronic venous disorders. J Vasc Surg. 2011 Jun 1;53(6):1649–53.

521. Turinetto V, Vitale E, Giachino C. Senescence in Human Mesenchymal Stem Cells: Functional Changes and Implications in Stem Cell-Based Therapy. Int J Mol Sci. 2016 Jul;17(7):1164.

522. Jeney V, Balla G, Balla J. Red blood cell, hemoglobin and heme in the progression of atherosclerosis. Front Physiol . 2014;5.

523. Ben-Shaul S, Landau S, Merdler U, Levenberg S. Mature vessel networks in engineered tissue promote graft–host anastomosis and prevent graft thrombosis. Proc Natl Acad Sci. 2019 Feb 19;116(8):2955–60.

524. Zhang Y, Daubel N, Stritt S, Mäkinen T. Transient loss of venous integrity during developmental vascular remodeling leads to red blood cell extravasation and clearance by lymphatic vessels. Development. 2018 Feb 8;145(3):dev156745.

525. Jain RK. Molecular regulation of vessel maturation. Nat Med. 2003 Jun;9(6):685–93.

526. Goncharov NV, Nadeev AD, Jenkins RO, Avdonin PV. Markers and Biomarkers of Endothelium: When Something Is Rotten in the State. Oxid Med Cell Longev. 2017;2017:9759735.

527. Ribatti D, Vacca A, Ranieri G, Sorino S, Roncali L. The Chick Embryo Chorioallantoic Membrane as an in vivo Wound Healing Model. Pathol - Res Pract. 1996 Jan 1;192(10):1068–76.

528. Ng K, Gao B, Yong KW, Li Y, Shi M, Zhao X, et al. Paper-based cell culture platform and its emerging biomedical applications. Mater Today. 2017 Jan 1;20(1):32–44.

529. Wu X, Suvarnapathaki S, Walsh K, Camci-Unal G. Paper as a scaffold for cell cultures: Teaching an old material new tricks. MRS Commun. 2018 Mar;8(1):1–14.

530. Camci-Unal G, Laromaine A, Hong E, Derda R, Whitesides GM. Biomineralization Guided by Paper Templates. Sci Rep. 2016 Jun 9;6(1):27693.

531. Chen YH, Kuo ZK, Cheng CM. Paper – a potential platform in pharmaceutical development. Trends Biotechnol. 2015 Jan 1;33(1):4–9.

532. Dupertuis YM, Delie F, Cohen M, Pichard C. In ovo method for evaluating the effect of nutritional therapies on tumor development, growth and vascularization. Clin Nutr Exp. 2015 Oct 1;2:9–17.

533. Schomann T, Qunneis F, Widera D, Kaltschmidt C, Kaltschmidt B. Improved method for Ex Ovo -cultivation of developing chicken embryos for human stem cell xenografts. Stem Cells Int. 2013;

534. Naik M, Brahma P, Dixit M. A Cost-Effective and Efficient Chick Ex-Ovo CAM Assay Protocol to Assess Angiogenesis. Methods Protoc. 2018 Jun;1(2):19.

535. García-Gareta E, Binkowska J, Kohli N, Sharma V. Towards the Development of a Novel Ex Ovo Model of Infection to Pre-Screen Biomaterials Intended for Treating Chronic Wounds. J Funct Biomater. 2020 Jun 2;11(2):37.

536. Kohli N, Sawadkar P, Ho S, Sharma V, Snow M, Powell S, et al. Pre-screening the intrinsic angiogenic capacity of biomaterials in an optimised ex ovo chorioallantoic membrane model. J Tissue Eng. 2020 Jan 4;11:204173142090162.

537. Merlos Rodrigo MA, Casar B, Michalkova H, Jimenez Jimenez AM, Heger Z, Adam V. Extending the Applicability of In Ovo and Ex Ovo Chicken Chorioallantoic Membrane Assays to Study Cytostatic Activity in Neuroblastoma Cells. Front Oncol. 2021 Sep 1;0:3290.

538. Marshall KM, Kanczler JM, Oreffo RO. Evolving applications of the egg: chorioallantoic membrane assay and *ex vivo* organotypic culture of materials for bone tissue engineering. J Tissue Eng. 2020 Jan 20;11:204173142094273.

539. Nguyen M, Shing Y, Folkman J. Quantitation of angiogenesis and antiangiogenesis in the chick embryo chorioallantoic membrane. Microvasc Res. 1994 Jan;47(1):31–40.

540. Deryugina EI, Quigley JP. Chapter 2 Chick Embryo Chorioallantoic Membrane Models to Quantify Angiogenesis Induced by Inflammatory and Tumor Cells or Purified Effector Molecules. Methods Enzymol. 2008 Jan 1;444:21–41.

541. Kilarski WW, Samolov B, Petersson L, Kvanta A, Gerwins P. Biomechanical regulation of blood vessel growth during tissue vascularization. Nat Med. 2009 Jun;15(6):657–64.

542. Chen L, Wang S, Feng Y, Zhang J, Du Y, Zhang J, et al. Utilisation of Chick Embryo Chorioallantoic Membrane as a Model Platform for Imaging-Navigated Biomedical Research. Cells. 2021 Feb;10(2):463.

543. Ribatti D. The CAM assay in the study of the metastatic process. Exp Cell Res. 2021 Mar 15;400(2):112510.

544. McDonald DM, Choyke PL. Imaging of angiogenesis: from microscope to clinic. Nat Med. 2003 Jun;9(6):713–25.

545. Jilani SM, Murphy TJ, Thai SNM, Eichmann A, Alva JA, Iruela-Arispe ML. Selective binding of lectins to embryonic chicken vasculature. J Histochem Cytochem. 2003 May 1;51(5):597–604.

546. Chambers AF, Schmidt EE, MacDonald IC, Morris VL, Groom AC. Early Steps in Hematogenous Metastasis of B16F1 Melanoma Cells in Chick Embryos Studied by High-Resolution Intravital Videomicroscopy. JNCI J Natl Cancer Inst. 1992 May 20;84(10):797–803.

547. Zijlstra A, Lewis JD. Visualization and Quantification of De Novo Angiogenesis in Ex Ovo Chicken Embryos. In: Zudaire E, Cuttitta F, editors. The Textbook of Angiogenesis and Lymphangiogenesis: Methods and Applications . Dordrecht: Springer Netherlands; 2012. p. 217–40.

548. Mangir N, Raza A, Haycock JW, Chapple C, Macneil S. An improved in vivo methodology to visualise tumour induced changes in vasculature using the chick chorionic allantoic membrane assay. In Vivo. 2018 May 1;32(3):461–72.

549. Deryugina EI. Chorioallantoic membrane microtumor model to study the mechanisms of tumor angiogenesis, vascular permeability, and tumor cell intravasation. In: Methods in Molecular Biology . Humana Press Inc.; 2016. p. 283–98.

550. Woloszyk A, Wolint P, Becker AS, Boss A, Fath W, Tian Y, et al. Novel multimodal MRI and MicroCT imaging approach to quantify angiogenesis and 3D vascular architecture of biomaterials. Sci Rep. 2019 Dec 19;9(1):19474.

551. Woloszyk A, Mitsiadis TA. Angiogenesis within stem cell–seeded silk scaffolds cultured on the chorioallantoic membrane and visualized by 3D imaging. Curr Protoc Stem Cell Biol. 2017 May 1;2017(1):1F.19.1-1F.19.9.

552. Woloszyk A, Liccardo D, Mitsiadis TA. Three-Dimensional Imaging of the Developing Vasculature within Stem Cell-Seeded Scaffolds Cultured in ovo. Front Physiol . 2016;7.

553. Henning AL, Jiang MX, Yalcin HC, Butcher JT. Quantitative three-dimensional imaging of live avian embryonic morphogenesis via micro-computed tomography. Dev Dyn. 2011;240(8):1949–57.

554. Ames JJ, Henderson T, Liaw L, Brooks PC. Methods for Analyzing Tumor Angiogenesis in the Chick Chorioallantoic Membrane Model. In: Cao J, editor.

Breast Cancer: Methods and Protocols . New York, NY: Springer; 2016. p. 255–69. (Methods in Molecular Biology).

555. Laufer J, Johnson P, Zhang E, Treeby B, Cox B, Pedley B, et al. In vivo preclinical photoacoustic imaging of tumor vasculature development and therapy. J Biomed Opt. 2012 May 1;17(5):056016.

556. Ogunlade O, Ho JOY, Kalber TL, Hynds RE, Zhang E, Janes SM, et al. Monitoring neovascularization and integration of decellularized human scaffolds using photoacoustic imaging. Photoacoustics. 2019 Mar 1;13:76–84.

557. Chen H, Agrawal S, Dangi A, Wible C, Osman M, Abune L, et al. Optical-Resolution Photoacoustic Microscopy Using Transparent Ultrasound Transducer. Sensors. 2019 Jan;19(24):5470.

558. Eckrich J, Kugler P, Buhr CR, Ernst BP, Mendler S, Baumgart J, et al. Monitoring of tumor growth and vascularization with repetitive ultrasonography in the chicken chorioallantoic-membrane-assay. Sci Rep. 2020 Oct 29;10(1):18585.

559. Eom J, Park SJ, Lee BH. Noncontact photoacoustic tomography of in vivo chicken chorioallantoic membrane based on all-fiber heterodyne interferometry. J Biomed Opt. 2015 Oct;20(10):106007.

560. Khan S, Pathak P, Vasudevan S, Nayak D. Non-invasive photoacoustic screening of blood vasculature during anti-angiogenesis using CAM assay. OSA Contin. 2021 Nov 15;4(11):2821–36.

561. Pakdaman Zangabad R, Iskander-Rizk S, van der Meulen P, Meijlink B, Kooiman K, Wang T, et al. Photoacoustic flow velocity imaging based on complex field decorrelation. Photoacoustics. 2021 Jun 1;22:100256.

562. Sen CK. Human Wound and Its Burden: Updated 2020 Compendium of Estimates. Adv Wound Care. 2021 May;10(5):281–92.

563. Lopes L, Setia O, Aurshina A, Liu S, Hu H, Isaji T, et al. Stem cell therapy for diabetic foot ulcers: A review of preclinical and clinical research. Stem Cell Res Ther . 2018 Jul 11;9(1).

564. Hu MS, Leavitt T, Malhotra S, Duscher D, Pollhammer MS, Walmsley GG, et al. Stem Cell-Based Therapeutics to Improve Wound Healing. Plast Surg Int. 2015;2015:383581.

565. Zhang CP, Fu XB. Therapeutic potential of stem cells in skin repair and regeneration. Chin J Traumatol. 2008;11(4):209–21.

566. Wu Y, Zhao RCH, Tredget EE. Concise Review: Bone Marrow-Derived Stem/Progenitor Cells in Cutaneous Repair and Regeneration. Stem Cells. 2010 May 1;28(5):905–15.

567. Sanapalli BKR, Yele V, Singh MK, Thaggikuppe Krishnamurthy P, Karri VVSR. Preclinical models of diabetic wound healing: A critical review. Biomed Pharmacother. 2021 Oct 1;142:111946.

568. Gorecka J, Gao X, Fereydooni A, Dash BC, Luo J, Lee SR, et al. Induced pluripotent stem cell-derived smooth muscle cells increase angiogenesis and accelerate diabetic wound healing. Regen Med. 2020 Feb;15(2):1277–93.

569. Guo J, Hu H, Gorecka J, Bai H, He H, Assi R, et al. Adipose-derived mesenchymal stem cells accelerate diabetic wound healing in a similar fashion as bone marrow-derived cells. Am J Physiol - Cell Physiol. 2018 Dec 1;315(6):C885–96.

570. Zhang P, Lu J, Jing Y, Tang S, Zhu D, Bi Y. Global epidemiology of diabetic foot ulceration: a systematic review and meta-analysis. Ann Med. 2017 Feb 17;49(2):106–16.

571. Furman BL. Streptozotocin-Induced Diabetic Models in Mice and Rats. Curr Protoc. 2021;1(4):e78.

572. Eming SA, Martin P, Tomic-Canic M. Wound repair and regeneration: Mechanisms, signaling, and translation. Sci Transl Med. 2014 Dec 3;6(265):265sr6-265sr6.

573. Eming SA, Krieg T, Davidson JM. Inflammation in Wound Repair: Molecular and Cellular Mechanisms. J Invest Dermatol. 2007 Mar 1;127(3):514–25.

574. Rodrigues M, Kosaric N, Bonham CA, Gurtner GC. Wound Healing: A Cellular Perspective. Physiol Rev. 2019 Jan;99(1):665–706.

575. Wilkinson HN, Hardman MJ. Wound healing: cellular mechanisms and pathological outcomes. Open Biol. 2020 Sep 30;10(9):200223.

576. Werner S, Grose R. Regulation of Wound Healing by Growth Factors and Cytokines. Physiol Rev. 2003 Jul;83(3):835–70.

577. Barrientos S, Brem H, Stojadinovic O, Tomic-Canic M. Clinical application of growth factors and cytokines in wound healing. Wound Repair Regen. 2014;22(5):569–78.

578. Mustoe TA, O'Shaughnessy K, Kloeters O. Chronic wound pathogenesis and current treatment strategies: A unifying hypothesis. Plast Reconstr Surg . 2006 Jun;117(7 SUPPL.).

579. Yang HY, Fierro F, So M, Daniel |, Yoon J, Nguyen AV, et al. Combination product of dermal matrix, human mesenchymal stem cells, and timolol promotes diabetic wound healing in mice. 2020;

580. Tong C, Hao H, Xia L, Liu J, Ti D, Dong L, et al. Hypoxia pretreatment of bone marrow—derived mesenchymal stem cells seeded in a collagen-chitosan sponge scaffold promotes skin wound healing in diabetic rats with hindlimb ischemia. Wound Repair Regen. 2016;24(1):45–56.

581. Sylakowski K, Bradshaw A, Wells A. Mesenchymal Stem Cell/Multipotent Stromal Cell Augmentation of Wound Healing: Lessons from the Physiology of Matrix and Hypoxia Support. Am J Pathol. 2020 Jul 1;190(7):1370–81.

582. Shin L, Peterson DA. Human Mesenchymal Stem Cell Grafts Enhance Normal and Impaired Wound Healing by Recruiting Existing Endogenous Tissue Stem/Progenitor Cells. Stem Cells Transl Med. 2013 Jan 1;2(1):33–42.

583. Sasaki M, Abe R, Fujita Y, Ando S, Inokuma D, Shimizu H. Mesenchymal Stem Cells Are Recruited into Wounded Skin and Contribute to Wound Repair by Transdifferentiation into Multiple Skin Cell Type. J Immunol. 2008 Feb 15;180(4):2581–7.

584. Rodriguez-Menocal L, Salgado M, Ford D, Van Badiavas E. Stimulation of skin and wound fibroblast migration by mesenchymal stem cells derived from normal donors and chronic wound patients. Stem Cells Transl Med. 2012;1(3):221–9.

585. Maxson S, Lopez EA, Yoo D, Danilkovitch-Miagkova A, LeRoux MA. Concise Review: Role of Mesenchymal Stem Cells in Wound Repair. STEM CELLS Transl Med. 2012 Feb;1(2):142–9.

586. Lee DE, Ayoub N, Agrawal DK. Mesenchymal stem cells and cutaneous wound healing: Novel methods to increase cell delivery and therapeutic efficacy. Stem Cell Res Ther . 2016 Mar 9;7(1).

587. Fierro FA, Magner N, Beegle J, Dahlenburg H, Logan White J, Zhou P, et al. Mesenchymal stem/stromal cells genetically engineered to produce vascular endothelial growth factor for revascularization in wound healing and ischemic conditions. Transfusion (Paris). 2019 Feb 1;59(S1):893–7.

588. Chen L, Xu Y, Zhao J, Zhang Z, Yang R, Xie J, et al. Conditioned medium from hypoxic bone marrow-derived mesenchymal stem cells enhances wound healing in mice. PLoS ONE . 2014 Apr 29;9(4).

589. Walter MN, Wright KT, Fuller HR, MacNeil S, Johnson WE. Mesenchymal stem cell-conditioned medium accelerates skin wound healing: an in vitro study of fibroblast and keratinocyte scratch assays. Exp Cell Res. 2010;316(7):1271–81.

590. Park SA, Covert J, Teixeira L, Motta MJ, DeRemer SL, Abbott NL, et al. Importance of defining experimental conditions in a mouse excisional wound model. Wound Repair Regen. 2015;23(2):251–61.

591. Nie Y, Han BM, Liu XB, Yang JJ, Wang F, Cong XF, et al. Identification of MicroRNAs Involved in Hypoxia- and Serum Deprivation-Induced Apoptosis in Mesenchymal Stem Cells. Int J Biol Sci. 2011 Jun 9;7(6):762–8.

592. Zhang W, Su X, Gao Y, Sun B, Yu Y, Wang X, et al. Berberine protects mesenchymal stem cells against hypoxia-induced apoptosis in vitro. Biol Pharm Bull. 2009 Aug;32(8):1335–42.

593. Efimenko A, Starostina E, Kalinina N, Stolzing A. Angiogenic properties of aged adipose derived mesenchymal stem cells after hypoxic conditioning. J Transl Med. 2011 Jan 18;9(1):10.

594. Nekanti U, Dastidar S, Venugopal P, Totey S, Ta M. Increased Proliferation and Analysis of Differential Gene Expression in Human Wharton's Jelly-derived Mesenchymal Stromal Cells under Hypoxia. Int J Biol Sci. 2010;499–512.

595. Hubbi ME, Semenza GL. Regulation of cell proliferation by hypoxia-inducible factors. Am J Physiol - Cell Physiol. 2015 Dec 15;309(12):C775–82.

596. Peck SH, Bendigo JR, Tobias JW, Dodge GR, Malhotra NR, Mauck RL, et al. Hypoxic Preconditioning Enhances Bone Marrow–Derived Mesenchymal Stem Cell Survival in a Low Oxygen and Nutrient-Limited 3D Microenvironment. CARTILAGE. 2021 Oct 1;12(4):512–25.

597. Ploeger DT, Hosper NA, Schipper M, Koerts JA, De Rond S, Bank RA. Cell plasticity in wound healing: Paracrine factors of M1/ M2 polarized macrophages influence the phenotypical state of dermal fibroblasts. Cell Commun Signal. 2013;11(1):29.

598. Spiller KL, Anfang RR, Spiller KJ, Ng J, Nakazawa KR, Daulton JW, et al. The role of macrophage phenotype in vascularization of tissue engineering scaffolds. Biomaterials. 2014;35(15):4477–88.

599. Truong ATN, Kowal-Vern A, Latenser BA, Wiley DE, Walter RJ. Comparison of Dermal Substitutes in Wound Healing Utilizing a Nude Mouse Model. J Burns Wounds. 2005 Mar 14;4:e4.

600. Wolf MT, Daly KA, Brennan-Pierce EP, Johnson SA, Carruthers CA, D'Amore A, et al. A hydrogel derived from decellularized dermal extracellular matrix. Biomaterials. 2012 Oct;33(29):7028–38.

601. Saldin LT, Cramer MC, Velankar SS, White LJ, Badylak SF. Extracellular matrix hydrogels from decellularized tissues: Structure and function. Acta Biomater. 2017 Feb 1;49:1–15.

602. Song JJ, Ott HC. Organ engineering based on decellularized matrix scaffolds. Trends Mol Med. 2011 Aug;17(8):424–32.

603. Parmaksiz M, Dogan A, Odabas S, Elçin AE, Elçin YM. Clinical applications of decellularized extracellular matrices for tissue engineering and regenerative medicine. Biomed Mater. 2016 Mar;11(2):022003.

604. Moffat D, Ye K, Jin S. Decellularization for the retention of tissue niches. J Tissue Eng. 2022 Jan 1;13:20417314221101150.

605. Di Nicola V. Omentum a powerful biological source in regenerative surgery. Regen Ther. 2019 Dec 1;11:182–91.

606. Horch RE, Horbach T, Lang W. The nutrient omentum free flap: Revascularization with vein bypasses and greater omentum flap in severe arterial ulcers. J Vasc Surg. 2007 Apr 1;45(4):837–40.

607. Soffer-Tsur N, Shevach M, Shapira A, Peer D, Dvir T. Optimizing the biofabrication process of omentum-based scaffolds for engineering autologous tissues. Biofabrication. 2014 Aug;6(3):035023.

608. Shevach M, Soffer-Tsur N, Fleischer S, Shapira A, Dvir T. Fabrication of omentum-based matrix for engineering vascularized cardiac tissues. Biofabrication. 2014 Jan;6(2):024101.

609. Porzionato A. Decellularization of rat and human omentum to develop novel scaffolds to be recellularized with adipose derived stem cells. Decellularization Rat Hum Omentum Dev Nov Scaffolds Be Recellularized Adipose Deriv Stem Cells. 2011;149–149.

610. Porzionato A, Sfriso MM, Macchi V, Rambaldo A, Lago G, Lancerotto L, et al. Decellularized omentum as novel biologic scaffold for reconstructive surgery and regenerative medicine. Eur J Histochem. 2013 Jan 24;57(1):e4–e4.

611. Edri R, Gal I, Noor N, Harel T, Fleischer S, Adadi N, et al. Personalized Hydrogels for Engineering Diverse Fully Autologous Tissue Implants. Adv Mater. 2019;31(1):1803895.

612. Brosius F. Low-Dose Streptozotocin Induction Protocol (mouse). 2019 Oct 21 [cited 2023 Jan 27]; Available from: https://www.protocols.io/view/low-dose-streptozotocin-induction-protocol-mouse-8izhuf6

613. Furman BL. Streptozotocin-Induced Diabetic Models in Mice and Rats. Curr Protoc Pharmacol. 2015 Sep 1;70(1):5.47.1-5.47.20.

614. Laguens RP, Candela S, Hernández RE, Gagliardino JJ. Streptozotocin-Induced Liver Damage in Mice. Horm Metab Res. 1980 May;12(5):197–201.

615. Desmet CM, Lafosse A, Vériter S, Porporato PE, Sonveaux P, Dufrane D, et al. Application of Electron Paramagnetic Resonance (EPR) Oximetry to Monitor Oxygen in Wounds in Diabetic Models. PLOS ONE. 2015 Dec 14;10(12):e0144914.

616. Michaels J, Churgin SS, Blechman KM, Greives MR, Aarabi S, Galiano RD, et al. db/db mice exhibit severe wound-healing impairments compared with other murine diabetic strains in a silicone-splinted excisional wound model. Wound Repair Regen. 2007;15(5):665–70.

617. Gerling IC, Friedman H, Greiner DL, Shultz LD, Leiter EH. Multiple Low-Dose Streptozocin–induced Diabetes in NOD-scid/scid Mice in the Absence of Functional Lymphocytes. Diabetes. 1994 Mar 1;43(3):433–40.

618. Leguina-Ruzzi A, Ortiz R, Velarde V. The streptozotocin-high fat diet induced diabetic mouse model exhibits severe skin damage and alterations in local lipid mediators. Biomed J. 2018 Oct 1;41(5):328–32.

619. Skovsø S. Modeling type 2 diabetes in rats using high fat diet and streptozotocin. J Diabetes Investig. 2014;5(4):349–58.

620. Reed MJ, Meszaros K, Entes LJ, Claypool MD, Pinkett JG, Gadbois TM, et al. A new rat model of type 2 diabetes: The fat-fed, streptozotocin-treated rat. Metabolism. 2000 Nov 1;49(11):1390–4.

621. Jara CP, Nogueira G, Morari J, Prado TP do, Bezerra R de M, Bombassaro B, et al. A Diabetic Mice Model For Studying Skin Wound Healing . bioRxiv; 2022. p. 2022.05.28.493835.

622. Huynh P, Phie J, Krishna SM, Golledge J. Systematic review and meta-analysis of mouse models of diabetes-associated ulcers. BMJ Open Diabetes Res Care. 2020 May 1;8(1):e000982.

623. Gnecchi M, Danieli P, Malpasso G, Ciuffreda MC. Paracrine mechanisms of mesenchymal stem cells in tissue repair. In: Methods in Molecular Biology . Humana Press Inc.; 2016. p. 123–46.

624. Huang S, Wu Y, Gao D, Fu X. Paracrine action of mesenchymal stromal cells delivered by microspheres contributes to cutaneous wound healing and prevents scar formation in mice. Cytotherapy. 2015;17(7):922–31.

625. Kuchroo P, Dave V, Vijayan A, Viswanathan C, Ghosh D. Paracrine Factors Secreted by Umbilical Cord-Derived Mesenchymal Stem Cells Induce Angiogenesis In Vitro by a VEGF-Independent Pathway. Stem Cells Dev. 2015 Feb 15;24(4):437–50.

626. Abdullahi A, Amini-Nik S, Jeschke MG. Animal models in burn research. Cell Mol Life Sci. 2014 Sep 1;71(17):3241–55.

627. Sullivan TP, Eaglstein WH, Davis SC, Mertz P. The Pig as a Model for Human Wound Healing. Wound Repair Regen. 2001;9(2):66–76.

628. Harder Y, Schmauss D, Wettstein R, Egaña JT, Weiss F, Weinzierl A, et al. Ischemic tissue injury in the dorsal skinfold chamber of the mouse: A skin flap model to investigate acute persistent ischemia. J Vis Exp. 2014 Nov 17;(93):51900.

629. Langer S, Beescho C, Ring A, Dorfmann O, Steinau HU, Spindler N. A new in vivo model using a dorsal skinfold chamber to investigate microcirculation and angiogenesis in diabetic wounds. GMS Interdiscip Plast Reconstr Surg DGPW. 2016;5:Doc09.

630. Laschke MW, Menger MD. The dorsal skinfold chamber: A versatile tool for preclinical research in tissue engineering and regenerative medicine. Eur Cell Mater. 2016 Jul 1;32:202–15.

631. Lehr HA, Leunig M, Menger MD, Nolte D, Messmer K. Dorsal skinfold chamber technique for intravital microscopy in nude mice. Am J Pathol. 1993;143(4):1055–62.

632. Menger MD, Laschke MW, Vollmar B. Viewing the Microcirculation through the Window: Some Twenty Years Experience with the Hamster Dorsal Skinfold Chamber. Eur Surg Res. 2002;34(1–2):83–91.

633. Michael S, Sorg H, Peck CT, Reimers K, Vogt PM. The mouse dorsal skin fold chamber as a means for the analysis of tissue engineered skin. Burns. 2013 Feb 1;39(1):82–8.

634. Moy AJ, White SM, Indrawan ES, Lotfi J, Nudelman MJ, Costantini SJ, et al. Wide-field functional imaging of blood flow and hemoglobin oxygen saturation in the rodent dorsal window chamber. Microvasc Res. 2011 Nov 1;82(3):199–209.

635. Murray JC, Sckell A, Leunig M. Dorsal Skinfold Chamber Preparation in Mice: Studying Angiogenesis by Intravital Microscopy. In: Angiogenesis Protocols . Humana Press; 2003. p. 095–105.

636. Rücker M, Laschke MW, Junker D, Carvalho C, Schramm A, Mülhaupt R, et al. Angiogenic and inflammatory response to biodegradable scaffolds in dorsal skinfold chambers of mice. Biomaterials. 2006 Oct;27(29):5027–38.

637. Schreiter J, Meyer S, Schmidt C, Schulz RM, Langer S. Dorsal skinfold chamber models in mice. GMS Interdiscip Plast Reconstr Surg DGPW. 2017;6:Doc10.

638. Sorg H, Krueger C, Vollmar B. Intravital insights in skin wound healing using the mouse dorsal skin fold chamber. J Anat. 2007 Dec 1;211(6):810–8.

639. Autobiologic . Autobiologic. [cited 2023 Feb 3]. Available from: https://www.autobiologic.com

640. APJ Trading | Window Chambers . [cited 2023 Feb 3]. Available from: http://apjtrading.com/chambers.html

641. McFARLANE RM, DeYOUNG G, Henry RA, McFarlane RM. THE DESIGN OF A PEDICLE FLAP IN THE RAT TO STUDY NECROSIS AND ITS PREVENTION. Plast Reconstr Surg. 1965 Feb;35(2):177.

642. Lee JH, You HJ, Lee TY, Kang HJ. Current Status of Experimental Animal Skin Flap Models: Ischemic Preconditioning and Molecular Factors. Int J Mol Sci. 2022 Jan;23(9):5234.

643. GOULD LJ, LEONG M, SONSTEIN J, WILSON S. Optimization and validation of an ischemic wound model. Wound Repair Regen. 2005 Nov 1;13(6):576–82.

644. Roy S, Biswas S, Khanna S, Gordillo G, Bergdall V, Green J, et al. Characterization of a preclinical model of chronic ischemic wound. Physiol Genomics. 2009 May;37(3):211–24.

645. Nunan R, Harding KG, Martin P. Clinical challenges of chronic wounds: searching for an optimal animal model to recapitulate their complexity. Dis Model Mech. 2014 Nov 1;7(11):1205–13.

646. Schwarz DA, Lindblad WJ, Rees RS. Altered collagen metabolism and delayed healing in a novel model of ischemic wounds. Wound Repair Regen. 1995;3(2):204–12.

647. Guero SJ, Lacroix PA. An Experimental Model of Scalp Expansion: A Method of Optimizing Flap Size and Shape. Plast Reconstr Surg. 1991 Apr;87(4):776.

648. Yang P, Pei Q, Yu T, Chang Q, Wang D, Gao M, et al. Compromised Wound Healing in Ischemic Type 2 Diabetic Rats. PLOS ONE. 2016 Mar 30;11(3):e0152068.

649. Ansell DM, Campbell L, Thomason HA, Brass A, Hardman MJ. A statistical analysis of murine incisional and excisional acute wound models. Wound Repair Regen. 2014;22(2):281–7.

650. Tepper OM, Galiano RD, Capla JM, Kalka C, Gagne PJ, Jacobowitz GR, et al. Human Endothelial Progenitor Cells From Type II Diabetics Exhibit Impaired Proliferation, Adhesion, and Incorporation Into Vascular Structures. Circulation. 2002 Nov 26;106(22):2781–6.

651. Rah DK, Min HJ, Kim YW, Cheon YW. Effect of Platelet-Rich Plasma on Ischemia-Reperfusion Injury in a Skin Flap Mouse Model. Int J Med Sci. 2017 Jul 19;14(9):829–39.

652. Seki T, Fujioka M, Fukushima H, Matsumori H, Maegawa N, Norimoto K, et al. Regional tissue oxygen saturation measured by near-infrared spectroscopy to assess the depth of burn injuries. Int J Burns Trauma. 2014 Feb 22;4(1):40–4.

653. Portalska KJ, Groen N, Krenning G, Georgi N, Mentink A, Harmsen MC, et al. The Effect of Donor Variation and Senescence on Endothelial Differentiation of Human Mesenchymal Stromal Cells. Tissue Eng Part A. 2013 Nov;19(21–22):2318–29.

654. Simonacci F, Bertozzi N, Raposio E. Off-label use of adipose-derived stem cells. Ann Med Surg. 2017 Dec 1;24:44–51.

655. Heathman TR, Nienow AW, McCall MJ, Coopman K, Kara B, Hewitt CJ. The translation of cell-based therapies: clinical landscape and manufacturing challenges. Future Med Ltd . 2015 Jan 6

656. Galipeau J, Sensébé L. Mesenchymal Stromal Cells: Clinical Challenges and Therapeutic Opportunities. Cell Stem Cell. 2018 Jun 1;22(6):824–33.

657. Baraniak PR, McDevitt TC. Stem cell paracrine actions and tissue regeneration. Regen Med. 2010 Jan;5(1):121–43.

658. Théry C, Witwer KW, Aikawa E, Alcaraz MJ, Anderson JD, Andriantsitohaina R, et al. Minimal information for studies of extracellular vesicles 2018 (MISEV2018): a position statement of the International Society for Extracellular Vesicles and update of the MISEV2014 guidelines. J Extracell Vesicles. 2018;7(1):1535750.

659. Rani S, Ryan AE, Griffin MD, Ritter T. Mesenchymal stem cell-derived extracellular vesicles: Toward cell-free therapeutic applications. Mol Ther. 2015 May 9;23(5):812–23.

660. Théry C, Zitvogel L, Amigorena S. Exosomes: composition, biogenesis and function. Nat Rev Immunol. 2002 Aug;2(8):569–79.

661. Herrmann IK, Wood MJA, Fuhrmann G. Extracellular vesicles as a next-generation drug delivery platform. Nat Nanotechnol. 2021 Jul;16(7):748–59.

662. Qiu G, Zheng G, Ge M, Wang J, Huang R, Shu Q, et al. Functional proteins of mesenchymal stem cell-derived extracellular vesicles. Stem Cell Res Ther. 2019 Nov 28;10(1):359.

663. Harrell CR, Jovicic N, Djonov V, Arsenijevic N, Volarevic V. Mesenchymal Stem Cell-Derived Exosomes and Other Extracellular Vesicles as New Remedies in the Therapy of Inflammatory Diseases. Cells. 2019 Dec 11;8(12):1605.

664. Ahangar P, Mills SJ, Cowin AJ. Mesenchymal Stem Cell Secretome as an Emerging Cell-Free Alternative for Improving Wound Repair. Int J Mol Sci. 2020 Jan;21(19):7038.

665. Mathieu M, Martin-Jaular L, Lavieu G, Théry C. Specificities of secretion and uptake of exosomes and other extracellular vesicles for cell-to-cell communication. Nat Cell Biol. 2019 Jan;21(1):9–17.

666. van Niel G, D'Angelo G, Raposo G. Shedding light on the cell biology of extracellular vesicles. Nat Rev Mol Cell Biol. 2018 Apr;19(4):213–28.

667. Tkach M, Kowal J, Théry C. Why the need and how to approach the functional diversity of extracellular vesicles. Philos Trans R Soc B Biol Sci. 2017 Nov 20;373(1737):20160479.

668. Putra A, Widyatmoko A, Ibrahim S, Amansyah F, Amansyah F, Berlian MA, et al. Case series of the first three severe COVID-19 patients treated with the secretome of hypoxia-mesenchymal stem cells in Indonesia. F1000Research. 2021 Oct 22;10:228.

669. Mao CY, Zhang TT, Li DJ, Zhou E, Fan YQ, He Q, et al. Extracellular vesicles from hypoxia-preconditioned mesenchymal stem cells alleviates myocardial injury by targeting thioredoxin-interacting protein-mediated hypoxia-inducible factor-1α pathway. World J Stem Cells. 2022 Feb 26;14(2):183–99.

670. Zhang B, Tian X, Qu Z, Hao J, Zhang W. Hypoxia-Preconditioned Extracellular Vesicles from Mesenchymal Stem Cells Improve Cartilage Repair in Osteoarthritis. Membranes. 2022 Feb;12(2):225.

671. Mansoor H, Ong HS, Riau AK, Stanzel TP, Mehta JS, Yam GHF. Current Trends and Future Perspective of Mesenchymal Stem Cells and Exosomes in Corneal Diseases. Int J Mol Sci. 2019 Jan;20(12):2853.

672. Lai RC, Chen TS, Lim SK. Mesenchymal stem cell exosome: a novel stem cell-based therapy for cardiovascular disease. Regen Med. 2011 Jul;6(4):481–92.

673. Cai J, Wu J, Wang J, Li Y, Hu X, Luo S, et al. Extracellular vesicles derived from different sources of mesenchymal stem cells: therapeutic effects and translational potential. Cell Biosci. 2020 May 24;10(1):69.

674. Sisa C, Kholia S, Naylor J, Herrera Sanchez MB, Bruno S, Deregibus MC, et al. Mesenchymal Stromal Cell Derived Extracellular Vesicles Reduce Hypoxia-Ischaemia Induced Perinatal Brain Injury. Front Physiol . 2019;10.

675. Piffoux M, Silva AKA, Wilhelm C, Gazeau F, Tareste D. Modification of Extracellular Vesicles by Fusion with Liposomes for the Design of Personalized Biogenic Drug Delivery Systems. ACS Nano. 2018 Jul 24;12(7):6830–42.

676. Ratajczak J, Wysoczynski M, Hayek F, Janowska-Wieczorek A, Ratajczak MZ. Membrane-derived microvesicles: important and underappreciated mediators of cell-to-cell communication. Leukemia. 2006 Sep;20(9):1487–95.

677. Bruno S, Chiabotto G, Favaro E, Deregibus MC, Camussi G. Role of extracellular vesicles in stem cell biology. Am J Physiol-Cell Physiol. 2019 Aug;317(2):C303–13.

678. Tkach M, Théry C. Communication by Extracellular Vesicles: Where We Are and Where We Need to Go. Cell. 2016 Mar 10;164(6):1226–32.

679. Deng F, Miller J. A review on protein markers of exosome from different bio-resources and the antibodies used for characterization. J Histotechnol. 2019 Oct 2;42(4):226–39.

680. Poltavtseva RA, Poltavtsev AV, Lutsenko GV, Svirshchevskaya EV. Myths, reality and future of mesenchymal stem cell therapy. Cell Tissue Res. 2019 Mar 1;375(3):563–74.

681. Wong VW, Sorkin M, Glotzbach JP, Longaker MT, Gurtner GC. Surgical Approaches to Create Murine Models of Human Wound Healing. BioMed Res Int. 2010 Dec 1;2011:e969618.

682. Kain KH, Miller JWI, Jones-Paris CR, Thomason RT, Lewis JD, Bader DM, et al. The chick embryo as an expanding experimental model for cancer and cardiovascular research. Dev Dyn. 2014;243(2):216–28.